



UNIL | Université de Lausanne

Unicentre

CH-1015 Lausanne

<http://serval.unil.ch>

Year : 2022

BIOLOGICAL VS. DIAGENETIC CONTROLS IN MICROBIALITES FROM SPATIALLY RESOLVED IRON ISOTOPES IN PYRITE

Decraene Marie-Noëlle

Decraene Marie-Noëlle, 2022, BIOLOGICAL VS. DIAGENETIC CONTROLS IN
MICROBIALITES FROM SPATIALLY RESOLVED IRON ISOTOPES IN PYRITE

Originally published at : Thesis, University of Lausanne

Posted at the University of Lausanne Open Archive <http://serval.unil.ch>

Document URN : urn:nbn:ch:serval-BIB_0A591D875D0E3

Droits d'auteur

L'Université de Lausanne attire expressément l'attention des utilisateurs sur le fait que tous les documents publiés dans l'Archive SERVAL sont protégés par le droit d'auteur, conformément à la loi fédérale sur le droit d'auteur et les droits voisins (LDA). A ce titre, il est indispensable d'obtenir le consentement préalable de l'auteur et/ou de l'éditeur avant toute utilisation d'une oeuvre ou d'une partie d'une oeuvre ne relevant pas d'une utilisation à des fins personnelles au sens de la LDA (art. 19, al. 1 lettre a). A défaut, tout contrevenant s'expose aux sanctions prévues par cette loi. Nous déclinons toute responsabilité en la matière.

Copyright

The University of Lausanne expressly draws the attention of users to the fact that all documents published in the SERVAL Archive are protected by copyright in accordance with federal law on copyright and similar rights (LDA). Accordingly it is indispensable to obtain prior consent from the author and/or publisher before any use of a work or part of a work for purposes other than personal use within the meaning of LDA (art. 19, para. 1 letter a). Failure to do so will expose offenders to the sanctions laid down by this law. We accept no liability in this respect.



UNIL | Université de Lausanne

FACULTÉ DES GÉOSCIENCES ET DE L'ENVIRONNEMENT

INSTITUT DES SCIENCES DE LA TERRE

BIOLOGICAL VS. DIAGENETIC CONTROLS IN MICROBIALITES FROM SPATIALLY RESOLVED IRON ISOTOPES IN PYRITE

THÈSE DE DOCTORAT

Présentée à la

Faculté des géosciences et de l'environnement
de l'Université de Lausanne

pour l'obtention du grade de

Docteur en Géosciences et Environnement, spécialité sciences de la Terre

par

Marie-Noëlle Decraene

Master en Géosciences de l'Université de Lorraine

Jury

Prof. Johanna Marin-Carbonne, Univ. de Lausanne..... Directrice de thèse
Dr. Nicolas Olivier, Univ. de Clermont Auvergne..... Co-directeur de thèse
Prof. Jasmine Berg, Univ. de Lausanne..... Experte interne
Dr. Muammar Mansor, Univ. of Tübingen..... Expert externe
Dr. Christophe Thomazo, Univ. de Bourgogne..... Expert externe
Prof. Derek Vance, ETH Zürich..... Expert externe
Prof. Marie-Elodie Perga, Univ. de Lausanne..... Présidente du jury

LAUSANNE

2022



UNIL | Université de Lausanne

FACULTÉ DES GÉOSCIENCES ET DE L'ENVIRONNEMENT

INSTITUT DES SCIENCES DE LA TERRE

BIOLOGICAL VS. DIAGENETIC CONTROLS IN MICROBIALITES FROM SPATIALLY RESOLVED IRON ISOTOPES IN PYRITE

THÈSE DE DOCTORAT

Présentée à la

Faculté des géosciences et de l'environnement
de l'Université de Lausanne

pour l'obtention du grade de

Docteur en Géosciences et Environnement, spécialité sciences de la Terre

par

Marie-Noëlle Decraene

Master en Géosciences de l'Université de Lorraine

Jury

Prof. Johanna Marin-Carbonne, Univ. de Lausanne..... Directrice de thèse
Dr. Nicolas Olivier, Univ. de Clermont Auvergne..... Co-directeur de thèse
Prof. Jasmine Berg, Univ. de Lausanne..... Experte interne
Dr. Muammar Mansor, Univ. of Tübingen..... Expert externe
Dr. Christophe Thomazo, Univ. de Bourgogne..... Expert externe
Prof. Derek Vance, ETH Zürich..... Expert externe
Prof. Marie-Elodie Perga, Univ. de Lausanne..... Présidente du jury

LAUSANNE

2022

IMPRIMATUR

Vu le rapport présenté par le jury d'examen, composé de

Présidente de la séance publique :	Mme la Professeure Marie-Elodie Perga
Présidente du colloque :	Mme la Professeure Marie-Elodie Perga
Directrice de thèse :	Mme la Professeure Johanna Marin Carbonne
Co-directeur de thèse :	M. le Docteur Nicolas Olivier
Experte interne :	Mme la Professeure Jasmine Berg
Expert externe :	M. le Docteur Muammar Mansor
Expert externe :	M. le Docteur Christophe Thomazo
Expert externe :	M. le Professeur Derek Vance

Le Doyen de la Faculté des géosciences et de l'environnement autorise l'impression de la thèse de

Madame Marie-Noëlle DECRAENE

*Titulaire d'un
Master Earth and Planetary sciences
de l'Université de Lorraine_Centre de Recherches Pétrographiques et Géochimiques, France*

intitulée

BIOLOGICAL VS. DIAGENETIC CONTROLS IN MICROBIALITES FROM SPATIALLY RESOLVED IRON ISOTOPES IN PYRITE

Lausanne, le 29 novembre 2022

Pour le Doyen de la Faculté des géosciences et de
l'environnement



Professeure Marie-Elodie Perga

REMERCIEMENTS

Ces quatre années de thèse ont mis sur ma route tant de personnes formidables, qui m'ont aidée, soutenue, conseillée, motivée (et plus encore) pour réaliser ce travail. Tout cela n'aurait pas été possible sans vous.

Merci à mes deux encadrants de choc, Johanna et Nicolas. Merci pour votre confiance, votre accompagnement pendant ces quatre années et de m'avoir apporté vos visions très complémentaires. Merci pour tout ce que j'ai appris à vos côtés en France, en Suisse et même à l'autre bout du monde. Nico, merci pour tous tes conseils, ta patience et ta disponibilité malgré la distance. Johanna, je te suis tellement reconnaissante pour tout ce que tu m'as appris. Un immense merci aussi pour tous les moments de vie qu'on a partagé et que je garde bien gravés dans ma tête et dans mon cœur.

Merci à tous les membres de mon jury : Prof. Jasmine Berg, Dr Muammar Mansor, Dr Christophe Thomazo, Prof Derek Vance et Prof Marie-Elodie Perga d'avoir lu et évalué ma thèse.

Un merci particulier à Chris, pour ton soutien et tous nos échanges !

Dans les vastes couloirs de Geopolis se trouvent, au rez de chaussé, une bête que de rares magiciens sont capables de dompter : la SIMS (ou ims Cameca 1280 pour les intimes). Parmi eux, Anne-Sophie, Florent, Thomas, et anciennement Katja. Merci pour tout, d'avoir été là pour les bonnes sessions et les moments de galère. Une bête similaire est aussi enfermée dans les murs du CRPG de Nancy, là où mon aventure dans la géochimie a commencé. Merci à Etienne Deloule d'avoir été mon mentor pendant 2 ans et de toujours garder un œil bienveillant sur moi. Merci à la team de Nancy : Nordine Bouden, Johan Villeneuve, Laurette Piani, Yves Marrocchi, de m'avoir accueillie dans la bonne humeur au tout début de ma thèse.

De retour au Geopolis, il y a une autre machine capricieuse (dont on taira le nom... Non je rigole, c'est la NanoSIMS) qui m'a fait un peu suer. Merci à Stéphane Escrig et Laurent Rémusat de m'avoir donné plein de conseils quand elle n'en faisait qu'à sa tête. Merci Laurent pour l'apprentissage sur la NanoSIMS du Museum.

À toutes les personnes que j'ai côtoyé dans les labos (hors SIMS) et les couloirs, merci pour nos échanges. Parmi eux : Györgi, Benita, Alexandra, Pierre, Martin, Thierry, Othmar, Lucas, Anders, Allison, Daniela. Merci à notre super trio de secrétaires: Anne-Marie, Krystel et Anne.

En plus du côté scientifique, j'ai rencontré des copains merveilleux. Les copains de l'IDYST, qui parfois se trompaient de porte entre notre bureau et leur cafétéria, merci pour les pauses chocolat. Merci à Tom, Zoneibe, Franziska, Mathieu, Charlotte, Gab, Nat, Joanne, Gustavo, Sassi, Isabella. Un énorme merci Elisa pour tes conseils, et pour nos rendez-vous hebdomadaires du mercredi soir pour le yoga ! Pour clôturer avec l'IDYST, un grand merci à la plus belle des princesses d'Evian, Anthony, pour notre belle amitié. Maintenant, je voudrais remercier tous les copains de l'ISTE, pour tous les moments partagés, les apéros à Geopo, en ville ou en montagne, un merci particulier à Selena, Arnaud, Aurore (trio super Nana), Brahim

(depuis le premier jour), Uygur (the goat), Valentin, Gaëtan, Lorenzo et Fran.

Merci à toute l'équipe MT180 : Christelle, Johanna, Estelle, Johann, Noémie, Sandra, Laurent, Maud, Guillaume. Ça aussi ça a été une sacrée aventure !

Merci à Alexandra, David et Sylvie pour votre travail de relecture. Et un grand merci à Mersad pour ton aide à la mise en page.

Un immense merci à la team Stromata, pour TOUT. Que ce soit les conseils scientifiques ou personnels, toutes les anecdotes et les rires partagés. Merci pour votre amitié. Merci Juliette, pour ton énorme soutien en cette fin de thèse. Thank you David, soooooo much, for our friendship since Nancy. Merci Julien, pour le trio infernal que l'on forme avec Clem et tout ce qu'on a vécu depuis le début de la thèse. Merci Virgil, SIMS partner, tu as été d'un soutien incroyable dans le travail (mais pas que) et je suis très heureuse de t'avoir comme ami.

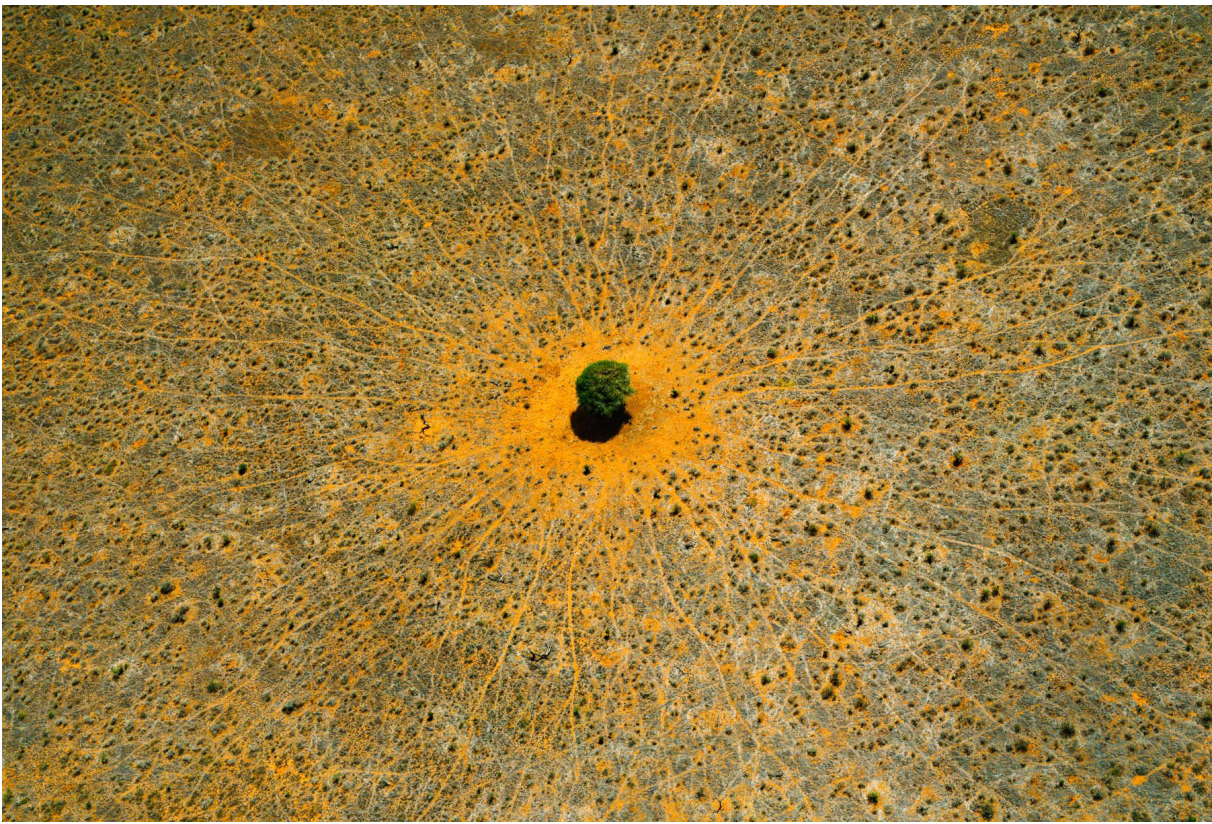
Les amis, c'est la famille que l'on peut choisir. Merci chacun d'entre vous, dispersé un peu partout (surtout en France), à commencer par Nancy, avec Alexis et Etienne, merci d'être là depuis le master. Un petit tour à Clermont pour remercier Alexiane, mon amie du lycée. Enfin on arrive dans mes belles Cévennes, pour remercier du fond du cœur mon amie adorée, ma sœur de cœur, Ju. Pour finir, de retour à Lausanne, merci à Clémence, ma co-bureau du tonerre mais surtout ma précieuse amie. Il n'y a pas de mot assez fort pour décrire à quel point ces quatre années dans notre bureau ont été formidables, folles, tellement riches en toutes sortes d'émotions. Clemino, ça résume toutes les bêtises et fous rires que l'on a partagé. Je pense d'ailleurs que nos rires sont imprégnés dans notre couloir du 4ème. Merci pour cette aventure, car elle n'aurait jamais été aussi belle sans toi.

Pendant cette thèse, la vie a remis sur mon chemin un caillou très cher à mon cœur. Merci à toi Pierre, pour ton soutien, ta patience, ton amour. Merci de me tenir la main dans notre quotidien et nos aventures. Cette thèse est aussi la tienne, alors du fond du coeur merci ♥

Enfin tout cela aurait été aussi peut-être différent sans deux personnes qui me sont très chères et qui ne sont plus là, mon Papa, qui serait je pense très fier, et ma Mamou chérie, à qui je dois tout. Tu accompagnes mes pensées au quotidien et mon coeur est à toi. Et vous vous doutez bien qu'il n'y a pas de Mamou sans Papou. Je remercie de tout mon cœur mon Papou d'amour, pour me soutenir dans tout ce que j'entreprends (même si tu n'étais pas convaincu par la géologie au début), tu m'as toujours encouragée et aidée. Merci de me distraire avec tes histoires de vie, ta force, ton caractère, merci de me ramener à l'essentiel et d'être la personne incroyable que tu es. Mon éducation c'est toi et Mamou et cette thèse c'est grâce à vous.

Marie-No

À mon Papa, Alain Decraene
À ma Mamou, Raymonde Massebeuf
À mon Papou, Georges Massebeuf.



"The tree of Life", Tsavo-East National Park, Kenya. Photo by Yann Arthus-Bertrand

RÉSUMÉ GRAND PUBLIC

Comprendre l'apparition et le développement de la vie nécessite d'étudier des roches très anciennes, vieilles de plusieurs milliards d'années. Cette quête des origines de la vie est extrêmement difficile pour deux raisons : (1) les premières traces de vie sur Terre sont microbiennes, donc extrêmement petites et (2) ces roches ont une histoire complexe, impliquant des processus qui ont modifié leurs apparences et parfois leurs compositions chimiques initiales. Heureusement, il existe encore sur Terre des roches sédimentaires laminées formées grâce à l'activité d'organismes microbiens. Ces dernières sont appelées stromatolites. Certains stromatolites sont reconnus depuis l'Archéen, soit il y a près de 3,5 Ga (pour le plus vieux spécimen découvert à ce jour), alors que d'autres sont toujours en cours de formation, par exemple dans les milieux marins peu profonds des Bahamas, de la Baie des Requins en Australie ou dans certains lacs volcaniques mexicains. Reconnaître l'origine biologique (biogénicité) de ces stromatolites anciens est un défi pour la communauté scientifique puisqu'ils ne préservent a priori pas de microorganismes fossilisés. De plus, la structure laminée qui les rend facilement reconnaissable ne peut pas être utilisée seule comme critère de biogénicité, puisque qu'elle peut également résulter de procédés abiotiques (absence d'organismes vivants). Toutefois, les stromatolites contiennent des sulfures de fer (FeS_2) micrométriques, connus sous le nom de pyrite. L'intérêt de ces pyrites réside dans leur potentiel d'enregistrer des processus de respiration microbienne à travers leurs compositions isotopiques en fer et/ou en soufre. En effet, les microorganismes ont tendance à mieux assimiler les isotopes légers (^{54}Fe ou ^{32}S) par rapport aux isotopes lourds (^{56}Fe ou ^{34}S), entraînant des différences de masse spécifiques aux différents processus microbiens. Comme le fer est un élément sensible aux réactions d'oxydation et de réduction (réactions redox), la géochimie du fer est couramment utilisée pour tracer des changements redox de l'environnement et/ou l'activité microbienne. Cette thèse se propose d'explorer la variabilité de la composition isotopique du fer des pyrites contenues dans les stromatolites à différentes périodes géologiques, afin de déterminer (1) si les pyrites peuvent être utilisées comme biosignatures, (2) l'influence et l'évolution des métabolismes microbiens utilisant le fer dans des environnements différents, (3) la capacité des compositions isotopiques en fer à renseigner des changements redox globaux comme l'oxygénation de l'atmosphère il y a 2.4 Ga et/ou des variations de l'oxygénation de l'océan pendant des crises d'extinction des espèces (exemple avec la crise du Smithien-Spathien). Pour répondre à ces questions, une comparaison d'échantillons anciens archéens (Formation de Tumbiana, 2,7 Ga) et phanérozoïques (bassin de Sonoma, 251 Ma) a été réalisée avec des microbialites modernes provenant de Cayo Coco (Cuba) et du lac Atexcac (Mexique). Dans toutes ces formations, les pyrites ont enregistré une très grande variabilité des compositions isotopiques du fer. Dans les microbialites modernes, les compositions isotopiques du fer reflètent des processus de réduction des oxydes de fer contrôlés par des microorganismes ferri-réducteurs indépendamment des conditions chimiques de l'environnement. Les compositions isotopiques

mesurées dans les sédiments du Phanérozoïque montrent un contrôle de l'environnement de dépôt (différents degrés de remobilisation des sédiments) et de la nature des dépôts (i.e. différentes signatures selon la présence ou l'absence des dépôts microbiens). Dans les échantillons archéens, la large gamme isotopique mesurée est interprétée comme résultant de procédés d'oxydation et de réduction complexes, contrôlés par l'activité des microorganismes. Cette thèse démontre l'importance de processus locaux dans la formation des pyrites préservées dans les stromatolites, comme l'influence de gradient redox à l'échelle du sédiment ou du biofilm et des différents métabolismes microbiens qui composent le biofilm. Ainsi, les pyrites associées à ces dépôts microbiens ne semblent pas permettre de reconstruire les signatures de l'environnement global. En revanche, ces pyrites peuvent être utilisées comme des biosignatures, à conditions de mener des études détaillées combinant l'isotopie du Fe, du S et minéralogie.

ABSTRACT

Recognition of fossils in the Archean sedimentary rocks is essential to constraining when and how life evolved, and the nature of the microbial metabolisms present on early Earth. Unfortunately, preservation of microorganisms is very limited in the Archean rock record. Direct observations of Archean microfossils are not convincing, yet, indirect traces of metabolic activity are described as early as ~3.5 Ga in form of stromatolites. Stromatolites are laminated organo-sedimentary benthic structures formed by the activity of microbial communities. They represent the oldest archives of life on Earth. However, laminated structures have also been reproduced by abiotic experiments, undermining the biological origin of the ancient stromatolite specimens. This thesis work focuses on refining geochemical and isotope proxies that can be used to assess the stromatolite biogenicity. I investigated pyrite, a mineral that is ubiquitous in the stromatolite record. It is well demonstrated that in modern sediments specific microorganisms produce Fe^{2+} and H_2S that ultimately lead to the formation of micrometric pyrite. Over the course of microbial activity and mineral precipitation, both sulfur and iron exhibit large isotope fractionations. Iron is transformed to pyrite through various aqueous and mineral species in the environment through redox-sensitive processes. Therefore Fe isotopes are used in reconstructing paleoredox conditions, diagenetic processes and/or metabolic signatures. Consequently, this thesis (1) tests if iron isotope compositions of micrometric pyrite can be used as a biosignature and (2) assesses sensitivity of Fe isotopes in pyrite with respect to global redox changes. I used a spatially resolved secondary ion mass spectrometry technique (SIMS) to develop a new analytical protocol to investigate the Fe isotope variability in pyrite smaller than $10\ \mu\text{m}$. In this thesis, samples of different age (modern, Mesozoic and Archean) have been selected to reconstruct the iron isotope variations through time and to differentiate the global versus local environmental influences on the pyrite isotope compositions. Modern samples are two microbialites collected from two different environments. Spatially resolved S isotope analyses is employed via nanoscale secondary ion mass spectrometry (NanoSIMS) to document the large isotope ranges and its relationship to the pyrite morphology and the activity of sulfate-reducing bacteria. As one of the main findings of the thesis, Fe isotope compositions (from -3.5 to +3.5‰) measured on a micrometer scale are consistent with a microbially-mediated Fe-oxide reduction by Fe-reducing organisms. The studied here Mesozoic samples were deposited during the Smithian-Spathian boundary (SSB, ~251 Ma), an interval post-dating the end-Permian mass extinction event. According to multiple lines of evidence, the oceans experienced abrupt swings in redox state and temperature, all of which leading to a major biotic diversity crisis. During this period of major ecological stresses, microbial communities flourished leading to deposition of a rich stromatolite record. I measured eight samples deposited along a ramp system which revealed a wide Fe isotope range (i.e. ~7‰). The $\delta^{56}\text{Fe}$ values show a clear influence of the depositional environment and the nature of deposit, i.e. the presence of microbialite. The Fe

isotope compositions collected on the Archean Tumbiana stromatolites, displayed the widest range of $\delta^{56}\text{Fe}$ values measured in the entire Archean sedimentary pyrite record (i.e. -2.2 to +4.4‰). This exceptionally large isotope range is interpreted as the result of an intense local iron cycling within the microbial mat, including repeated cycles of partial oxidation and microbially-mediated reduction processes, related to biogeochemical carbon and sulfur cycles. All together, Fe isotope compositions of micrometric pyrite grains are likely to record synsedimentary and early diagenetic processes that occur within the sediment or in the biofilm. Importantly, the seawater column has a limited influence on the final $\delta^{56}\text{Fe}$ values of pyrite. The $\delta^{56}\text{Fe}$ values measured in pyrite highlight the intimate interaction between the local pools of Fe, O, C and S. The speciation and isotope compositions of these elements are affected by the microbially mediated cycling as well as the redox gradients created abiotically. Therefore, to better understand the conditions of microbialite formation through geological time, it is critical to couple the Fe- and S-isotope measurements with detailed sedimentological and petrological studies.

RÉSUMÉ

Reconnaitre la nature et l'évolution des premières traces de vie est une tâche complexe due à la rareté et la petite taille des fossiles et à l'histoire géologique des roches qui les contiennent. Toutefois, les métabolismes microbiens peuvent laisser des traces indirectes sous forme de roche ou de minéraux. Les stromatolites sont des structures organo-sédimentaires laminées formées par l'activité de communautés microbiennes, et sont considérés comme les plus anciennes traces de vie sur Terre. Ces structures laminées peuvent aussi être produites par des expériences abiotiques, remettant en question l'origine biologique des plus anciens spécimens. Ce travail de thèse se concentre sur le développement de nouveaux traceurs pouvant permettre d'évaluer la biogénicité des stromatolites. J'ai en particulier porté mon attention sur la pyrite, un sulfure de fer ubiquiste dans les stromatolites (modernes à archéens). En effet, certains microorganismes peuvent réduire des oxydes de fer et des sulfates pour produire du Fe^{2+} et de l' H_2S et ainsi former des pyrites micrométriques. Ces processus microbiens produisent d'importants fractionnements des isotopes du Fe et du S. Puisque majoritairement contrôlé par des processus redox, l'étude du cycle géochimique du fer permet de mieux comprendre les processus redox dans les environnements anciens mais aussi l'évolution des métabolismes microbiens. Cette thèse a plusieurs objectifs : (1) tester si la composition isotopique du fer des pyrites micrométriques peut être utilisée comme biosignature et (2) évaluer l'influence des changements redox de l'environnement sur la formation des pyrites. Les analyses des isotopes du fer des pyrites ont été réalisées à très haute résolution spatiale (Secondary Ion Mass Spectrometry, SIMS) pour lesquelles un nouveau protocole analytique a été développé. Ce protocole permet dorénavant de mesurer la variabilité isotopique du Fe dans des pyrites ayant des tailles inférieures à $10\ \mu\text{m}$. Dans cette thèse, des échantillons de différentes périodes géologiques (moderne, Mésozoïque et Archéen) ont été sélectionnés pour reconstruire les variations isotopiques du fer sur une longue période, et pour différencier les influences environnementales globales et locales sur la composition des pyrites. Les échantillons modernes sont deux microbialites collectées dans deux environnements différents (un lac et un lagon). Les analyses des isotopes du S (NanoSIMS) ont mis en évidence de larges gammes isotopiques, différentes selon la morphologie de la pyrite. L'origine de ces gammes a été attribuée à l'activité des bactéries sulfato-réductrices. Les compositions isotopiques du Fe des pyrites de ces échantillons (de -3.5 à $+3.5\%$) reflètent une réduction microbienne des oxydes de Fe par des organismes ferri-réducteurs. Les échantillons mésozoïques étudiés ont été déposés à l'intervalle Smithian-Spathian (SSB, $\sim 251\ \text{Ma}$), une période postérieure à la crise d'extinction de masse de la fin du Permien. La SSB est décrite par de nombreux auteurs comme une période régie par des variations abruptes de la température et de l'état d'oxygénation des océans qui ont entraîné une baisse drastique de la biodiversité. Pendant cette période de stress écologique majeur, des dépôts microbiens - y compris des stromatolites habituellement rares dans l'enregistrement géologique du Phanérozoïque - se sont développés. J'ai mesuré huit échantillons déposés le

long d'un système de rampe qui ont mis en évidence une large gamme isotopique de Fe ($\sim 7\%$). Ces échantillons montrent une influence nette de l'environnement de dépôt et de la nature du dépôt, i.e. la présence de microbialites. Les compositions isotopiques du Fe des pyrites mesurées dans les stromatolites archéens de la formation de Tumbiana, ont affiché la plus large gamme de compositions isotopiques du fer du registre sédimentaire Archéen (i.e. $-2,2\%$ à $+4,4\%$). L'origine de cette gamme est attribuée à des cycles d'oxydo-réduction du fer au sein d'un tapis microbien, ces cycles étant influencés par des microorganismes métabolisant le soufre et le carbone. Dans l'ensemble, ces trois cibles, caractérisées par des conditions environnementales redox différentes, montrent que les pyrites micrométriques sont susceptibles d'enregistrer des processus synsédimentaires et de diagénèse précoce dans le sédiment et/ou le biofilm plutôt que l'état redox de la colonne d'eau. De plus, les signatures isotopiques du Fe associées à l'activité microbienne, dans les stromatolites et les dépôts microbiens non minéralisés, sont complexes et reflètent les interactions (microbiennes ou non) entre les cycles du Fe, du S, du C et de l'O. Par conséquent, le couplage entre isotopie du Fe, du S et des observations sédimentaires et minéralogiques (contexte de dépôt et la formation des microbialites) est crucial pour distinguer les processus locaux et globaux qui modulent les signaux isotopiques du Fe des pyrites à travers le temps.

Contents

Résumé grand public	11
Abstract	13
Résumé	15
Chapter 1. Introduction	29
1. Microbialites	30
1.1. Definition and classification	30
1.2. Microbialite formation	31
1.2.1. Metabolic activity and chemical gradients	31
1.2.2. Processes involved in the formation of microbialites	32
1.3. Stromatolite diversity through time	34
1.3.1. Stromatolite fabric	35
1.3.2. Microfossil identification	37
1.3.3. Preservation of carbonaceous material	37
1.3.4. Carbon isotope compositions	38
2. Micrometric pyrite: an ubiquitous mineral in microbialites	39
2.1. Sedimentary pyrite formation	39
2.2. Pyrite as proxy for paleoredox reconstructions	41
2.2.1. Trace elements	41
2.2.2. Pyrite morphology and size	42
2.2.3. Sulfur isotopes	43
3. Geological Fe cycling	45
3.1. Fe isotopes and nomenclature	45
3.2. Fe sources and sinks	47
3.2.1. Atmospheric dust	47
3.2.2. Benthic sediments	47
3.2.3. Hydrothermal plume	48
3.3. Microbial Fe cycling	49
3.3.1. Fe oxidation	49
3.3.2. Dissimilatory Fe reduction	50
3.3.3. Anaerobic oxidation of methane coupled to Fe (III) reduction	51
3.4. Looking into the past: Fe cycling in the Precambrian	51
3.4.1. Evolution of sulfidic and oxic Fe sinks	51
3.4.2. Pyrite Fe isotope compositions through geological time	52
4. Scope of this thesis	54
5. Literature cited	58

Chapter 2. Studied samples, geological contexts, and methods	81
1. Studied samples	82
1.1. Stromatolites from the Tumbiana Formation (2.7 Ga, Western Australia)	83
1.2. Stromatolites from the Malmani Subgroup (2.5 Ga, South Africa)	85
1.3. MISS from the Thaynes Group (251 Ma, United-States)	88
1.4. Modern microbialite from Cayo Coco (Cuba) and Atexcac lake (Mexico)	90
2. Methods	92
2.1. Sample preparation	92
2.2. Scanning electron microscopy (SEM)	93
2.3. Electron probe micro-analyses (EPMA)	94
2.4. Raman	95
2.5. Major and trace elements	96
2.6. Secondary ion mass spectrometry (SIMS) CAMECA ims 1280 HR	96
2.6.1. General principles	96
2.6.2. Instrumental description	97
2.7. Pyrite S isotope analyses	101
2.8. Analytical protocol for measuring Fe isotope compositions in micrometric pyrite	102
2.8.1. Objectives	102
2.8.2. Article published in RCM	102
3. Literature cited	118
Chapter 3. Pyrite iron and sulfur isotope signatures in modern microbialites ..	125
1. Early precipitated micropyrrite in microbialites: A time capsule of microbial sulfur cycling	128
2. Fe isotope biosignatures revealed in modern pyrite framboids	147
2.1. Interest of investigating framboids	147
2.2. Sample description	148
2.3. Results	150
2.3.1. Sample description	150
2.3.2. $\delta^{56}\text{Fe}$ values of framboids	151
2.4. Discussion	153
2.4.1. Origin of $\delta^{56}\text{Fe}$ variability under oxic conditions	153
2.4.2. Microbial Fe oxide reduction dominate the Fe isotope record in Cuba	154
2.4.3. Iron cycling model and implication for the sulfur cycling	156
3. Conclusions and perspectives	158
3.1. Main conclusions	158
3.2. Relationship between framboid and micropyrrite formation	159
3.3. Litterature cited	161

Chapter 4. Pyrite Fe cycling during biotic recovery: example with the Smithian-Spathian Boundary event	169
Pyrite iron isotope compositions track local sedimentation conditions through the Smithian-Spathian transition (Early Triassic, Utah, USA)	170
1. Introduction	172
2. Materials and methods	173
2.1. Geological context, studied section and samples	173
2.2. Methods	175
2.2.1. Petrographic observations	175
2.2.2. Hg concentrations and TOC contents	176
2.2.3. Bulk rock $\delta^{34}\text{S}$	176
2.2.4. Fe isotope analyses by SIMS	177
3. Results	178
3.1. Facies description	178
3.2. Carbon, sulfur and mercury contents	178
3.3. Bulk pyrite and CAS $\delta^{34}\text{S}$	180
3.4. Pyrite and organic matter description	180
3.5. In situ iron isotope compositions	181
4. Discussion	183
4.1. Pyrite precipitation locus and environmental redox conditions	183
4.2. Iron isotope kinetic and equilibrium isotope effects	184
4.3. Pyrite $\delta^{56}\text{Fe}$ values controlled by sedimentary depositional settings and microbial communities	184
4.3.1. Inner ramp model: $\delta^{56}\text{Fe}$ values controlled by the nature of deposit	184
4.3.2. Mid and outer ramp model: $\delta^{56}\text{Fe}_{\text{py}}$ controlled by H_2S production in a closed system	186
4.4. Pyrite formation during an interval of biotic diversity loss: a depositional environment control rather the deleterious anoxic conditions	188
5. Conclusions	188
6. Acknowledgements	189
7. Literature cited	190
Chapter 5. Microbially influenced Fe cycling in Archean stromatolites	209
Chapter 6. Malmani stromatolites: Post-depositional history and preservation of primary geochemical signatures	233
1. The Campbellrand-Malmani platform	234
1.1. Geological context and sections	234
1.2. The redox conditions of the Neoproterozoic ocean	234

2. Results	234
2.1. Petrographic observations	234
2.1.1. Facies description	234
2.1.2. Episodes of silicification	238
2.2. Geochemical analyses	238
2.2.1. Major and minor elements	238
2.2.2. Trace elements plus Rare Earth Element (REE)	240
2.2.3. Carbonaceous matter	242
2.2.4. Minor elements in pyrite (EPMA)	243
2.2.5. SIMS analyses (Fe and S isotopes)	243
3. In situ Fe and S isotope signatures previously reported	246
4. Discussion	246
4.1. Post depositional history	246
4.2. Preservation of primary grains and chemical-environmental signals?	249
5. Preliminary Conclusions	251
6. Literature cited	252
Chapter 7. General Discussion and Perspectives	257
1. Importance of post depositional processes	258
2. Beyond the post-depositional history:	
identification of primary elements and mineral phases	260
3. Environmental control on pyrite formation	261
3.1. Influence of depositional settings	261
3.2. Influence of microbial activities	262
4. Closing words: pyrite and global redox changes	264
5. Perspectives	264
5.1. Development of analytical protocol for nanoscale measurements of Fe isotopes	264
5.2. Searching for a primary signal in sedimentary rocks recording a metamorphic gradient	265
5.3. Influence of methanotrophy on pyrite formation in modern and ancient sediments	267
6. Literature cited	269

LIST OF FIGURES

Figure 1. 1: Classification of microbialites as a function of the macrofabric of microbialites, i.e. their internal structure.	30
Figure 1. 2: Structure of a microbial mat.	31
Figure 1. 3: Variation of stromatolite abundance, reported as taxa number, through Earth history.	34
Figure 1. 4: Comparison of stromatolites through time.	35
Figure 1. 5: pe-pH diagram of iron.	39
Figure 1. 6: BSE image of modern framboid grains.	42
Figure 1. 7: Secular variations of $\Delta^{33}\text{S}$ values of pyrite and sulfate and triple sulfur isotope plot.	43
Figure 1. 8: Model of the Archean sulfur cycle.	44
Figure 1. 9: Relationship between the temperature ($10^6/T^2$) and the fractionation factor ($10^3 \ln \alpha_{\text{Fe(III)aq-Fe(II)aq}}$).	46
Figure 1. 10: Fe isotope compositions measured in different natural materials.	47
Figure 1. 11: Schematic representation of iron source in the ocean.	48
Figure 1. 12: Secular variations of bulk iron isotopes of pyrite. GOE: Great Oxidation Event. Compilation from Ostrander et al. (2022).	53
Figure 2. 1: Overview of the sample collection.	82
Figure 2. 2: Geological context of the Tumbiana Fm.	83
Figure 2. 3: Geological context of the Malmani platform.	86
Figure 2. 4: Geological context of the LWC samples.	88
Figure 2. 5: Map of Cuba island with the location of Cayo Coco lagoon.	90
Figure 2. 6: Map of Mexico with the extent of the trans-mexican volcanic belt and the location of Atexcac lake.	91
Figure 2. 7: Interferometer image showing the topography of an epoxy mount along x and y profiles.	92
Figure 2. 8: Views of a sample under the microscope and the camera of the SIMS.	93
Figure 2. 9: Chemical map of framboid pyrite by SEM.	94
Figure 2. 10: Raman spectrum of pyrite in LWC88 compared to reference spectrum of pyrite from the Ruff database.	95
Figure 2. 11: Schematic of primary ion beam sputtering on a sample surface and production of secondary ions.	96
Figure 2. 12: Schematic of a CAMECA ims 1280HR ion microprobe	97

Figure 2. 13: Detailed scheme of the Cesium source	98
Figure 2. 14: Detailed scheme of the Hyperion-II source	99
Figure 2. 15: $^{57}\text{Fe}^+$ and $^{56}\text{FeH}^+$ intensity signals.	100
Figure 3. 1: BSE image of framboid pyrite.	147
Figure 3. 2: Location of the microbialite sample M2 6.8-7.1.	149
Figure 3. 3: Location of the microbialite sample ATX-2012-08.	149
Figure 3. 4: BSE images of framboid pyrite grains measured for their $\delta^{56}\text{Fe}$ values by SIMS.	150
Figure 3. 5: Fe isotope compositions measured in M2 6.8-7.1 (yellow dots) and ATX-2012-08 (green dots) represented as histograms and whisker plots.	151
Figure 3. 6: Relationship between $\delta^{56}\text{Fe}$ values and a) the $^{56}\text{Fe}^+$ ion yield, i.e. the ratio of $^{56}\text{Fe}^+$ ion intensity (in counts per second) over the primary beam intensity, and b) the framboid grain size in M2 6.8-7.1 (yellow dots) and ATX-2012-08 (green dots).	152
Figure 3. 7: Model of Fe and S cycling in microbial mat at Cayo Coco.	156
Figure 4. 1: a) Log of the LWC section with focus on Units B and C (modified after Grosjean et al., 2018). b) Early Triassic paleogeographic map showing the location of the Sonoma Foreland Basin (SFB) (modified after Brayard et al., 2013). c) Position along a ramp system and thin section pictures of studied samples (scale bar for thin sections: 2.5mm). The different star colors refer to the corresponding facies association (FA1-FA5). MHTSL: Mean High Tide Sea Level; FWWB: Fair Weather Wave Base; SWB: Storm Wave Base.	174
Figure 4. 2: Evolution of Fe isotope compositions measured by SIMS on 8 LWC samples with corresponding total organic carbon concentrations (in %), pyrite $\delta^{34}\text{S}$ values on 29 samples (LWC31 to LWC70) and carbonate associated sulfate (CAS) $\delta^{34}\text{S}$ values on 4 samples of the section. The simplified log reports lithologies and positions of samples measured by SIMS.	179
Figure 4. 3: $\delta^{56}\text{Fe}_{\text{py}}$ as a function of pyrite morphologies: euhedral, framboid, aggregate and secondary overgrowth. No clear difference is observed between each morphology.	180
Figure 4. 4: Fe isotope compositions of pyrite from the Lower Weber Canyon section as a function of depositional environments along a ramp system.	182
Figure 4. 5: Iron cycling model in the sediment from inner ramp samples.	185
Figure 4. 6: Iron cycling model in the sediment from mid and outer ramp samples.	187
Figure 6. 1: a) Geological map of the studied area with location of the sedimentary section and the outcrop of stromatolite megadomes along the road. Modified from Tyler and Tyler (1996). b) A large-scale view of the outcrop along the road made of large stromatolite megadomes several meters across. c) A close-up of a domal stromatolite. d) to g) Photographs of the different outcrops which composed the log, with rippled-dolomite (non-bioconstructed facies FA1) and stromatolites (bioconstructed facies FA2) at the top and stromatolites with various degrees of silicification throughout the section.	235

Figure 6. 2: a) Field view of the two facies associations, the non-bioconstructed (ripples) facies FA1 and the bioconstructed (stromatolite) facies FA2, identified at the top of the log. This part of the outcrop displays dolomitization with no signs of silicification. b) Field view of FA2 made of both dolomite and partially silicified stromatolites. c) Climbing ripples forming FA1 and g) microscopic view of FA1, characterized by dark and light laminae. d) Stromatolite at the top of the section (FA2) and h) microscopic view of the laminae constituting FA2. Same for e) and i) in FA2 from a stromatolite interbedded with silicified stromatolites. f) Partially silicified domal stromatolites and j) microscopic view of the dolomite-chert contact.	236
Figure 6. 3: Pictures illustrating remarkable (primary and secondary) features observed in samples:	237
Figure 6. 4: a) Ternary diagram with analyses of stromatolite samples from the studied log (Upper Monte Christo Fm). The detrital fraction is defined as the sum Al_2O_3 , Fe_2O_3 , MnO , Na_2O and K_2O (in wt.%; TiO_2 and P_2O_5 contents are below the detection limit). b) Harker diagrams with samples from the log, including samples from FA1 (green square) and stromatolite samples from FA2 (green dots) divided into partially silicified stromatolites (green dot with blue line) and fully silicified stromatolites (green dot with red line).	239
Figure 6. 5: Relationship between Sr/Ca ratio and a) the Mn content and b) the ratio Fe/Fe+Mg in samples from the section.	240
Figure 6. 6: REE+Y spectra normalized to PAAS of samples classified as a function of the lithology and the position in the log.	241
Figure 6. 7: Raman spectra of carbonaceous matter from sample 1.30 (partially silicified stromatolite from the log) fitted to the theoretical G and D-bands.	242
Figure 6. 8: Macroscopic view of samples measured for their pyrite Fe and S isotope compositions by SIMS.	244
Figure 6. 9: a) Fe isotope compositions of pyrite from AmalC4 (orange dots), MA37 (purple dots) and MA39 (yellow dots) reported using outlier box plot representation. Line crossing the box is the median and the edges of the box represent the quartiles (lower line is the 1st quartile Q1, i.e. the 25th percentile, and upper line is the 3rd quartile Q3, i.e. the 75th percentile). Lower and upper whiskers represent 1.5*IQR (interquartile range, i.e. the range between Q1 and Q3). The minimum and maximum are marked by small lines at the end of whiskers and represent respectively the lowest and highest values of the distribution. b) Multiple sulfur isotopes measured in the same samples that were used for Fe isotope analyses. Grey dots report in situ $\delta^{34}S$ and $\Delta^{33}S$ measurements in samples from the Campbellrand-Malmani platform (Farquhar et al., 2013; Fischer et al., 2014; Kamber and Whitehouse, 2007; Ono et al., 2009). $\Delta^{33}S$ is defined as $\delta^{33}S-1000*[(1+ \delta^{34}S/1000)^{33}-1]$	245
Figure 6. 10: Scheme of the different stages of post-depositional processes experienced by the stromatolite samples of the Malmani Subgroup in the eastern part of the platform. Not to scale, modified from Lawnizack (2022).	247
Figure 6. 11: Relationship between Y/Ho and element concentrated in terrigenous minerals (Al, Ga, Th and Zr). Detection limits: Y= 0.02 ppm, Ho= 0.001 ppm, Ga= 0.02 ppm, Th=0.015 ppm, Zr= 1.50 ppm . .	250

Figure 7. 1: Synthesis of secondary and primary mineral phases observed in all studied samples as a function of the maximum temperature peak they have experience, and comparison of their Fe isotope ranges. 259

Figure 7. 2: Geological map of the Transvaal sequence (South Africa) with the location of the studied site (yellow star) at the eastern part of the Malmani Subgroup and the site from where the well-preserved stromatolite was sampled (orange star; Griqualand West area; samples provided by W. Altermann; modified after Sumner and Beukes, 2006). Microscopic view of the stromatolite sample 91/55, characterized by dark carbonaceous laminae. The Raman spectra obtained on this carbonaceous material allowed to estimate a maximum peak temperature experienced by the sample of ~290°C (Kouketsu et al., 2014). Comparison with Raman spectra obtained in sample 1.30 (from the log described in Chapter 6), which have experienced a higher peak temperature of ~395°C. 266

LIST OF TABLES

Table 1. 1: Main functional groups in a microbial mat ecosystem and corresponding metabolic activity. Modified from Visscher and Stolz (2005)	32
Table 1. 2: Distribution of Archean stromatolites, their location and morphological description. Modified from Hofmann (2000).	36
Table 2. 1: Summary of main characteristics of the Tumbiana Fm and studied samples.	85
Table 2. 2: Summary of main characteristics of the Malmani Subgroup and studied samples.	87
Table 2. 3: Summary of main characteristics of the Lower Weber Canyon stratigraphic section and studied samples	89
Table 2. 4: Summary of main characteristics of sample M2 6.8-7.1 and ATX-2012-08 from Cayo Coco (Cuba) and Atexcac lake (Mexico) respectively.	91

CHAPTER 1.

INTRODUCTION

Exploring the conditions that led to the appearance and development of life is one of the central questions in science, that results in the development of interdisciplinary fields between chemistry, biology and geology. The earliest forms of life present on Earth were micrometric and refer to microorganisms (from the domains of Bacteria and Archaea). Since their first emergence at about 3.8 Ga, microorganisms have been able, through their metabolic activity, to produce a wide variety of by-product minerals which can be preserved in sedimentary rocks over the geological timescale (e.g. carbonate, sulfides, oxides; *Hansel et al., 2004; Visscher and Stolz, 2005; Aloisi et al., 2006; Picard et al., 2018*). Eventually, the activity of microorganisms, organized in a community in a microbial mat or biofilm, precipitates mineral structures called microbialites. Microbialites are observed in modern marine and lacustrine environments and have been preserved throughout the geological record since the Archean (~3.5 Ga; *Lowe, 1980; Vankranendonk et al., 2008; Wacey, 2010*). The specificity of microbially-induced minerals is their ability to preserve information (structural and chemical) about their biological origin, also known as biosignatures. Due to the scarcity of Archean rocks (4 Ga-2.5 Ga) on Earth's surface and the difficulty to identify fossils of microorganisms, the nature of the first microorganisms present on Earth can be studied by analyzing the minerals they produced. However, Archean rocks are highly affected by post-depositional processes, including metamorphism and metasomatism that may have partially or entirely modified (e.g. degrade, erase, replace among other possibilities) the primary signal.

This thesis intends to better understand processes involved in microbialite formation through the analyses of pyrite, an iron sulfide mineral composed of S and Fe whose formation may originate from microorganisms. I tested the hypothesis if pyrite Fe isotope compositions can be used as biosignatures or not. The aim of this thesis is to define isotope robust criteria of biogenicity of ancient microbialites by determining the origin of pyrite enclosed in various sedimentary rocks (e.g. modern, Early Triassic, Meso- and Neoproterozoic). Moreover, this thesis

explored different geological periods characterized by contrasting environmental redox conditions in order to test the ability of pyrite Fe isotope in pyrite to record global redox variation. This opening chapter is divided in four parts. The first introduces microbialites, how they form and why the geochemical community is interested in them. The second focuses on the formation and the use of sedimentary pyrites as a proxy of paleoredox conditions. The third part is dedicated to the Precambrian iron cycling and existing interpretations of Fe isotope signal throughout the geological record. Finally, this chapter ends by presenting the research questions and objectives of this thesis.

1. Microbialites

1.1. Definition and classification

Microbialites are defined as “organosedimentary deposits that have accreted as a result of benthic microbial community trapping and binding detrital sediment and/or forming the locus of mineral precipitation» (*Burne and Moore, 1987*). As such, microbialites are classified on the basis of their macroscopic fabric (**Fig. 1.1**). Four categories are defined (*Riding, 2011a*): the most famous are stromatolites, having a laminated organization (*Kalkowsky, 1908; Semikhatov et al., 1979*), thrombolites for clotted microbial carbonate (*Aitken, 1967*), dendrolite, displaying a dendritic fabric (*Riding, 1991*) and leiolites that are unstructured microbialites (*Braga et al., 1995*). There is, however, another category of microbialites, known as Microbially Induced Sedimentary Structures (MISS; *Noffke et al., 2001*), which does not grow vertically but rather along planar laminated structures (*Gerdes et al., 2001; Noffke and Awramik, 2013*). In the vast majority of cases, MISS develop in siliciclastic peritidal environments and result from the interaction of microorganisms with physical sedimentary processes (e.g. erosion, deposition, transport; *Noffke et al., 2003*). Through the definition of microbialites, *Burne and Moore (1987)* proposed that a stromatolite is a subset of microbialite and combined the genetic, i.e. of biological origin, and descriptive, i.e. laminated sedimentary structures, definitions. However, there are still disagreements on the way stromatolites are defined and how Archean specimens formed (*Monty,*

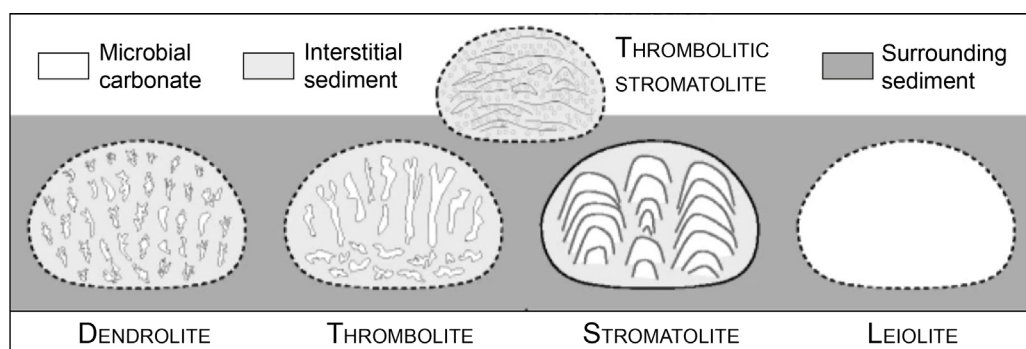


Figure 1. 1: Classification of microbialites as a function of the macrofabric of microbialites, i.e. their internal structure. Modified from *Riding (2011)*.

1977; Awramik, 1992; Grotzinger and Knoll, 1999; Riding, 2011b). In the microbialite definition, the biological origin of stromatolites is verified for modern specimens but not for ancients as old as 3.5 Ga (Walter *et al.*, 1980; van Kranendonk *et al.*, 2003). As originally defined, stromatolites are «organogenic, laminated, calcareous rock structures, the origin of which is clearly related to microscopic life, which in itself must not be fossilised» (Kalkowsky, 1908). Such a definition implies the biogenic origin of those laminated structures. Subsequently, this genetic definition has been revised into «organosedimentary structure produced by sediment trapping, binding, and/or precipitation as a result of the growth and metabolic activity of micro-organisms» (Awramik *et al.*, 1976). However, another definition describes stromatolite as «an attached, laminated, lithified sedimentary growth structure, accretionary away from a point or limited surface of initiation», allowing the use of stromatolite as a pure descriptive term (Semikhatov *et al.*, 1979). These two conflicting views (i.e. descriptive versus genetic definitions) open discussions about the reliability of Archean stromatolite structures as indicative of microbial activity back to the early Earth (Awramik and Grey, 2005). This points out the importance of having discriminant criteria between abiotic and biological processes in stromatolite formation in order to better understand how and when life evolved on Earth (Cloud and Morrison, 1979; Buick *et al.*, 1981; Walter, 1983; Hofmann *et al.*, 1999; Brasier *et al.*, 2005; Javaux, 2019; Lepot, 2020).

1.2. Microbialite formation

1.2.1. Metabolic activity and chemical gradients

Living stromatolites, and microbialites in the general term of Burne and Moore (1987) form through the activity of microbial communities gathered in a microbial mat or a biofilm (Stolz, 2000). Microbial mats can be considered as complex biofilms (Gerdes, 2007) and thus, are formed by microorganisms (and their extracellular products) that occur in an unstructured manner in a lamina (Marshall, 1992; Neu, 1994). Biofilms mainly differentiate from microbial mats by their size (pluri- μm) and their ability to develop within the sediment (Gerdes, 2010).

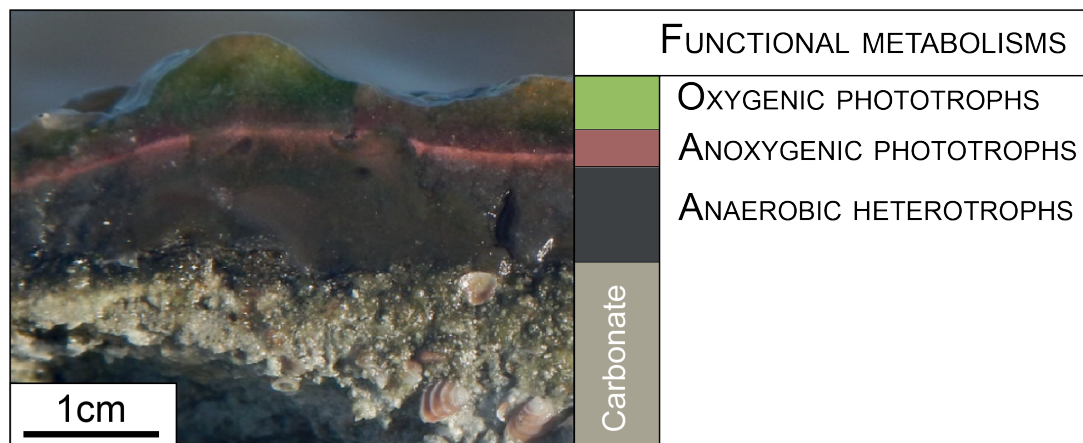


Figure 1.2: Structure of a microbial mat. Photograph of a mineralizing microbial mat with different colored layers and the associated active microbial metabolisms. Modified from Bouton *et al.* (2016).

A microbial mat is a pluri mm to cm layered structure growing at a water-substrate interface. Each layer displays a specific color and is dominated by a specific metabolic system. Together, they form an ecosystem with primary producers, consumers and decomposers (Stolz, 2000). These include oxygenic phototrophs (cyanobacteria; in most of the cases they represent the green top layer), aerobic heterotrophs, sulfide oxidizers, anoxygenic phototrophs (e.g. purple and green sulfur bacteria; pink layer) and anaerobic heterotrophs (e.g. sulfate reducers and methanogens; black layer **Fig. 1.2** and **Table 1.1**; *des Marais et al., 1992*; *Ward et al., 1992*; *Stolz, 2000*; *Visscher and Stolz, 2005*). The activity of those microorganisms tends to create steep chemical gradients (Cohen and Rosenberg, 1989) within the mat. For example, the maximum photosynthetic rate in the mat's photic zone corresponds to a maximum O₂ production, or the maximum H₂S concentration within the microbial mat matches with the activity of anaerobic heterotrophs (e.g. *Jorgensen et al., 1983*; *Ley et al., 2006*). However, this vertical stratification is more complex. For example, important rates of sulfate reduction have been observed in the oxic layer while this metabolism is normally found under the oxic/anoxic transition in mats (*Canfield and des Marais, 1993*; *Krekeler et al., 1997*; *Minz et al., 1999*; *Baumgartner et al., 2006*).

Table 1.1: Main functional groups in a microbial mat ecosystem and corresponding metabolic activity. Modified from Visscher and Stolz (2005)

Functional group	Metabolic reaction
Oxygenic phototrophs:	$\text{CO}_2 + \text{H}_2\text{O} \rightarrow \text{CH}_2\text{O} + \text{O}_2$
Aerobic heterotrophs:	$\text{CH}_2\text{O} + \text{O}_2 \rightarrow \text{CO}_2 + \text{H}_2\text{O}$
Sulfide oxidizers:	$\text{H}_2\text{S} + 2\text{O}_2 \rightarrow \text{SO}_4^{2-} + 2\text{H}^+$
Anoxygenic phototrophs:	
Fe-oxidation	$4\text{Fe}^{2+} + \text{CO}_2 + 4\text{H}^+ \rightarrow \text{CH}_2\text{O} + 4\text{Fe}^{3+} + \text{H}_2\text{O}$
S-oxidation	$\text{HS}^- + \text{HCO}_3^- \rightarrow \text{CH}_2\text{O} + \text{SO}_4^{2-}$
Anaerobic heterotrophs:	
Microbial sulfate reduction	$2\text{CH}_2\text{O} + \text{SO}_4^{2-} \rightarrow 2\text{HCO}_3^- + \text{H}_2\text{S}$
Methanogenesis	$4\text{H}_2 + \text{CO}_2 \rightarrow \text{CH}_4 + 2\text{H}_2\text{O}$

1.2.2. Processes involved in the formation of microbialites

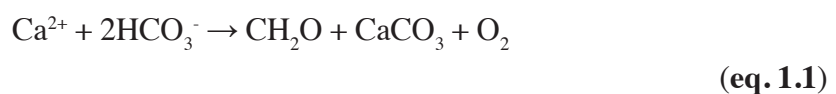
The activity of biofilms and/or microbial mats leading to the formation of microbialites is attributed to the relative expression of two main processes: (1) trapping and binding of detrital sediments, (2) mineralization, mainly carbonate precipitation (biologically-induced and/or abiotically induced; *Awramik et al., 1976*; *Burne and Moore, 1987*; *Dupraz et al., 2009*).

1.2.2.1. Trapping and binding

Trapping and/or binding of sedimentary particles depends on the microbialite surface and environmental properties. Stickiness and relief of the microbial mat allow to trap particles and are enhanced, for example, by the presence of filamentous cyanobacteria, microalgae, or diatoms (*Burne and Moore, 1987; Noffke and Awramik, 2013; Reid et al., 2003*). Moreover, the abundance and/or size of the suspended particles, as well as the local current strength and/or frequency are important environmental properties that strongly impact the trapping and/or binding process (*Riding, 1991*). Although trapping and/or binding of grains are important processes for the construction of cohesive structures, these processes alone do not lead to the formation of a microbialite.

1.2.2.2. Mineralization

In this part, I focus on carbonate formation, which is dominant in the formation of a microbialite, although microbial activity can lead to the authigenic precipitation of other mineral phases such as kerolite (Mg-silicate; *Zeyen et al., 2015*). Calcification represents the precipitation of calcium (\pm Mg) carbonates (calcite or aragonite, CaCO_3 , dolomite MgCaCO_3) which can be microbially and/or abiotically-mediated (*Grotzinger and Knoll, 1999; Dupraz and Visscher, 2005; Riding, 2011a*). Inorganic carbonate precipitation occurs frequently during evaporation of supersaturated water with respect to the mineral in confined environments and/or in environments characterized by rapid loss of CO_2 which also promote carbonate precipitation due to different CO_2 partial pressure (*Given and Wilkinson, 1985; Morse et al., 2007*). These abiotic reactions occur in various environments including areas of high energy (waterfall, shoreline), caves, springs, or streams and, for example, are dominant in the formation of travertine and microbial tufa (*Riding, 2008*). Evaporation and CO_2 degassing are two main abiotic processes that can induce carbonate precipitation in microbialites. It is well recognized that the metabolic activity of some microorganisms influences the alkalinity of the system (i.e. concentration of carbonate ions), promoting either precipitation or dissolution of carbonates (*Krumbein, 1979; Golubic, 1983; Dupraz et al., 2009; Visscher et al., 2000; Couradeau et al., 2013*). Cyanobacteria were the first microorganisms to be recognized for their role in calcification (*Roddy, 1915*). However, phototrophic microorganisms such as cyanobacteria can modify their metabolic activity as a function of diurnal cycles and thus change their regime of carbonate formation between day and night. Photosynthetic CO_2 fixation coupled to carbonate equilibrium reactions results in an increase of alkalinity and therefore promotes the precipitation of carbonate (**eq. 1.1**; *Visscher et al., 1998*):



Organic carbon produced by photosynthetic CO_2 fixation during the day is reoxidized by aerobic respiration and fermentation during the night, both of which favor the dissolution

of carbonate. This diurnal behavior is not observed for anaerobic heterotrophs such as sulfate reducers, which are known to increase alkalinity and thus support the precipitation of carbonate (Wright and Wacey, 2005; Braissant *et al.*, 2007; Gallagher *et al.*, 2012; Bontognali *et al.*, 2014). Biologically-mediated calcification is also highly modulated by environmental parameters, such as temperature, evaporation (salinity), supply of alkaline water (increasing pH) or water column turbidity, which can directly modify the alkalinity of a microbial mat and the activity of microbial metabolisms (Reid *et al.*, 2000; Visscher *et al.*, 2000; Dupraz *et al.*, 2004, 2009; Bowlin *et al.*, 2012; Jahnert and Collins, 2013).

1.3. Stromatolite diversity through time

The study of early traces of life in Archean stromatolites requires the acquisition of robust criteria of biogenicity. Although Archean sedimentary rocks are rare and have been subject to various degrees of secondary alteration, including metamorphism and metasomatism, some stratigraphic formations are interpreted to preserve primary sedimentary structures (e.g. stromatolites of the Strelley Pool (3.4 Ga), of the Tumbiana Formation (Fm, 2.7 Ga); Hofmann, 2000; Wright and Altermann, 2000; Allwood *et al.*, 2006; Gandin and Wright, 2007).

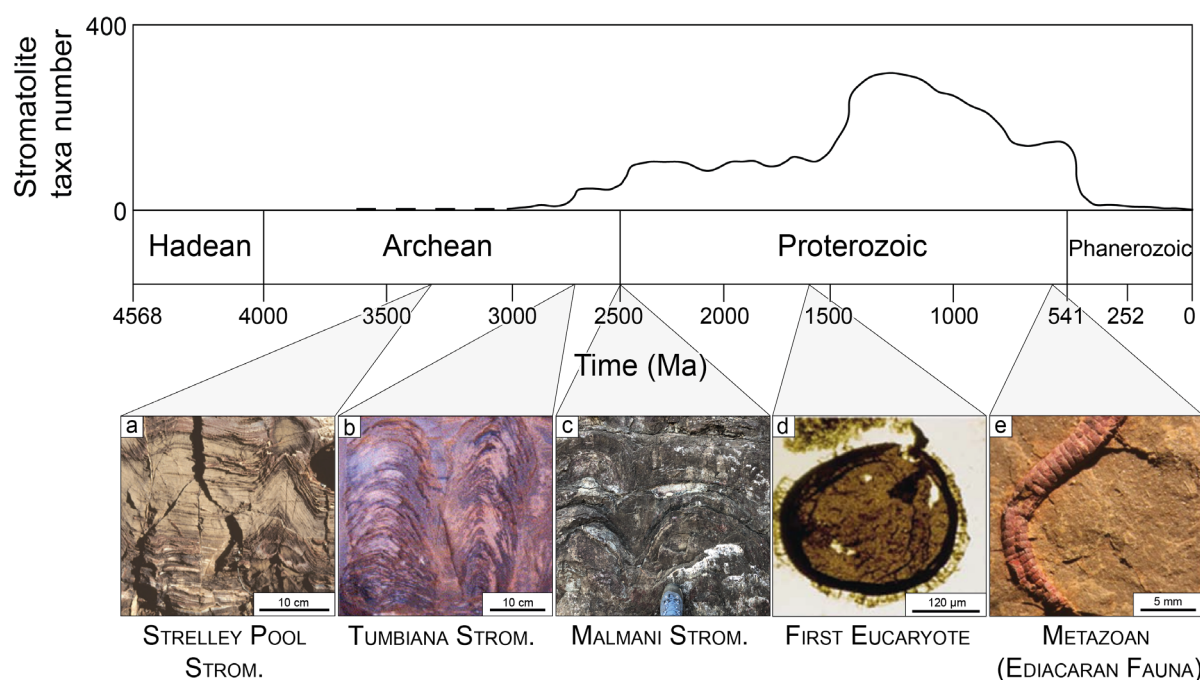


Figure 1. 3: Variation of stromatolite abundance, reported as taxa number, through Earth history. Modified from Riding (2006). It should be noted that stromatolites are not individual fossil organisms, but the most used stromatolite classification follow the conventional Linnean system. The term stromatolite “taxa” is not to be interpreted *sensu stricto* (Semikhatov and Raaben, 2000). a) Conical stromatolite from the 3.4 Ga Strelley Pool Formation (Warrawoona Group, Western Australia; Awramik, 2006); b) Columnar stromatolite from the 2.7 Ga Tumbiana Formation (Fortescue Group, Western Australia; Sakurai *et al.*, 2005); c) Large domal stromatolite from the 2.5 Ga Malmani Subgroup (South-Africa); d) Spheroidal microfossil interpreted as eucaryotic organism (1.6 Ga Ruyang Group, China; Knoll *et al.*, 2006); e) Metazoan worm fossil from the Ediacaran fauna (~570-540 Ma; Darroch *et al.*, 2018).

1.3.1. Stromatolite fabric

Based on modern analogs, stromatolites are easily recognizable through their laminated microfabric. (**Fig. 1.2**). The recognition of domical, columnar or tabular-layered morphologies allows to identify stromatolites through geological time (**Figs. 1.3** and **1.4**; *Andres and Reid, 2006*; *Altermann, 2008*; *Allwood et al., 2009*; *Bosak et al., 2009*).

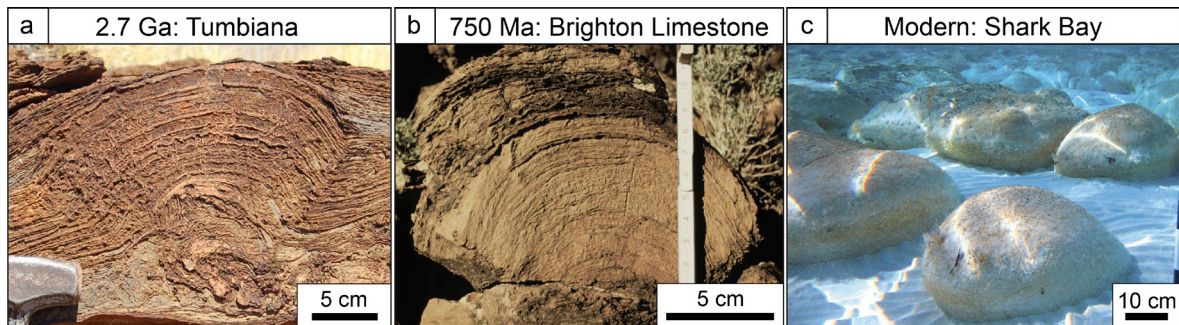


Figure 1. 4: Comparison of stromatolites through time. a) Domal stromatolite from the 2.72 Ga Tumbiana Formation (Pilbara Craton, Western Australia; *Lepot et al., 2008*); b) Cryogenian domal stromatolite from the Brighton Limestone (South Australia) and c) Modern stromatolite from Shark Bay (western Australia; *Noffke and Awramik, 2013*).

The increase in stromatolite diversity started during the Archean (4 Ga - 2.5 Ga) and reached a maximum during the Meso-Proterozoic (~1.3 Ga) (**Fig. 1.3**; *Awramik, 1991*; *Grotzinger, 1990*; *Riding, 2006*). The Meso- to Neo-Proterozoic (1.3 Ga - 600 Ma) period show a global decline in stromatolite diversity and abundance which is commonly attributed to the appearance of grazing metazoan organisms (*Walter and Heys, 1985*). However, based on the temporal gap between the decline of stromatolites and the first occurrence of metazoan fossils, *Grotzinger (1990)* proposed an alternative explanation relying on a global decrease of the ocean carbonate saturation state at that time. The biologic origin of ancient stromatolites is questioned by post-depositional deformation that mimics laminated structures of stromatolites (*Buick et al., 1981*; *Lowe, 1994*; *Wacey, 2010*; *Allwood et al., 2018*). This fuels the controversy on the interpretation of 3.7 Ga putative conical and domical stromatolites from Greenland (*Nutman et al., 2016, 2019*). Those structures were reassessed to be non-biological, resulting instead from the alteration and deformation of layered sedimentary rocks (*Allwood et al., 2018*; *Zawaski et al., 2020*). Moreover, “stromatolite-like” morphologies have been successfully reproduced during abiotic experiments (*Grotzinger and Knoll, 1999*; *McLoughlin et al., 2008*), for example by spray deposition in a turbulent flow regime that formed columnar and branched structures (*McLoughlin et al., 2008*).

The oldest occurrence of laminated sedimentary structures identified as stromatolites is observed in the 3.5 Ga Dresser Fm (Pilbara Craton, Western Australia; *Walter et al., 1980*; *Vankranendonk et al., 2008*). However, the oldest consensual biogenic stromatolites were identified in the 3.4 Ga Strelley Pool Fm (Warrawoona Group, Pilbara Craton, Western Australia; **Figs. 1.3** and **1.4**), where a large diversity of stromatolites (e.g. large domes, conical, wavy, egg-carton laminites) grew on a shallow carbonate platform (*Allwood et al., 2006*; *Wacey, 2010*;

Table 1. 2: Distribution of Archean stromatolites, their location and morphological description. Modified from Hofmann (2000).

Era	Age (Ga)	Group	Formation	Stromatolite	Ref.
Isua Supracrustal Belt, west Greenland					
Eoarchean	3.7			Biogenic stromato. ?	Nutmann et al. (2016)
Pilbara Craton, west Australia					
	3.48	Warrawoona	Dresser	Stratiform, columnar, domal, conical	Van Kranendonk et al. (2008)
	3.47	Warrawoona	Towers	Stratiform, domal pseudocolumnar,	Hofmann et al. (1999)
Paleoarchean	3.46	Warrawoona	Panorama	Stratiform, conical	Hofmann et al. (2000)
	3.43	Warrawoona	Strelley Pool	Stratiform, conical	Allwood et al. (2006)
Kaapvaal craton, Barberton Greenstone belt, South Africa					
	3.29	Onverwacht	Kromberg	Stratiform, conical pseudocolumnar,	Byerly et al. (1996)
Superior Province (Canada)					
	2.94	Red lake	Ball assemblage	Stratiform, domal pseudocolumnar,	McIntyre and Fralick (2017)
	2.80-2.78	Steepprock	Mosher Carbonate	Stratiform, domal, pseudocolumnar, conical, columnar	Fralick and Riding (2015)
Kaapvaal craton, Pongola Supergroup (South Africa)					
Mesoarchean	2.90	Nsuze	White Mfolozi	Stratiform, domal, pseudocolumnar, conical, columnar, branching	Hicks et al. (2011)
Zimbabwe craton, Masvingo Greenstone Belt (Zimbabwe)					
	2.84		Mushandike	Stratiform, pseudocolumnar, domal	Kamber et al. (2004)
Pilbara Craton, Western Australia					
	2.72	Fortescue	Tumbiana	Stratiform, domal, pseudocolumnar, conical, columnar, branching	Buick (1992)
	2.54	Hamersley	Carawine Dolomite	Stratiform, domal, pseudocolumnar, conical, columnar	Simonson et al. (1993)
Kaapvaal craton (South Africa)					
Neoarchean	2.74	Platberg	Rietgat	Pseudocolumnar, domal, branching	Buck (1980)
	2.55-2.52	Chuniespoort	All Fms. in Malmani and Campbellrand	Stratiform, domal, pseudocolumnar, conical, columnar,	Sumner and Beukes (2006)
		Ghaap	Subgr.	branching	
Zimbabwe craton, Belingwe Greenstone Belt (Zimbabwe)					
	2.60	Ngesi	Cheshire	Stratiform, domal, pseudocolumnar, conical, branching	Abell et al. (1985)

Sugitani et al., 2015). Other domical, conical and pseudo-columnar structures interpreted as stromatolites were also identified in Paleoarchean formations (3.6-3.2 Ga) (**Fig. 1.3; Table 1.2**). The Meso (3.2-2.8 Ga) and the Neoproterozoic (2.8-2.5 Ga) preserve extended carbonate platforms on which stromatolites have flourished (**Table 1.2**), such as Red Lake and Steep Rock (Canada; *Wilks and Nisbet, 1988; Fralick and Riding, 2015; McIntyre and Fralick, 2017*), the Carawine Dolomite (Western Australia; *Simonson et al., 1993; Jahn and Simonson, 1995*) and the Malmani-Campbellrand platform (South Africa; *Altermann and Nelson, 1998; Sumner and Grotzinger, 2004*). One of the most famous Neoproterozoic formations is the 2.7 Ga Tumbiana Fm (Pilbara Craton, Western Australia), which preserves an exceptional range of stromatolite morphology (*Buick, 1992; Philippot et al., 2009; Coffey et al., 2013*). Those stromatolites were also extensively studied for the characterization of early traces of microbial activity (e.g. *Hayes, 1994; Thomazo et al., 2009, 2011; Coffey et al., 2013; Stüeken et al., 2017; Marin-Carbonne et al., 2018*). Based on the observation that modern stromatolites host a wide variety of microorganisms, stromatolites constitute the oldest trace of life (i.e. microbial) on Earth.

1.3.2. Microfossil identification

Even though a large range of microfossils has been evidenced in Proterozoic sedimentary rocks and closed any debate about biogenicity of stromatolites, less than 1% of Archean stromatolites contain putative microfossils (*Grotzinger and Knoll, 1999*). Simple morphologies, like filament or spherical microstructures have been considered as Archean microfossils (*Schopf and Packer, 1987; Schopf et al., 2007; Javaux et al., 2010; Wacey et al., 2011*). However, it has been demonstrated that mineral growth (amorphous silica) or aggregation or displacement of carbonaceous matter during late recrystallization can reproduce Archean microstructures identified as microfossils (*García Ruiz et al., 2002; Jones and Renaut, 2007; Wacey et al., 2018; Nims et al., 2021*). A list of criteria for re-evaluating the antiquity and biogenicity of putative fossils is proposed in *Brasier et al. (2005)*, including (1) the geological context, i.e. samples from Archean age showing primary depositional features, replicable, microfossils included in the orientation of stromatolite growth and in a context consistent with life development; (2) biological morphology, i.e. in thin sections, microfossils should exhibit a variability in morphology, plausible shape of microorganisms (for example cell wall) or by-products and should be morphologically differentiable from abiotic fossil-like microstructures; (3) biological processing, i.e. composed of carbonaceous matter or microbially-produced minerals.

1.3.3. Preservation of carbonaceous material

The recognition of preserved organic matter in stromatolites and/or microfossils and its chemical characterization is used to discuss biogenicity of those structures (*Buick, 1984; Papineau et al., 2017; Alleon and Summons, 2019*). The structural organization, or maturity, of the aromatic skeleton of carbonaceous matter can be documented by Raman spectroscopy. This method allows the estimation of the maximal temperature peak undergone by the hosted

rock (*Beyssac et al., 2002; Kouketsu et al., 2014*) but does not document the thermal evolution of organic matter during diagenesis. The carbon speciation of carbonaceous material can be determined by scanning transmission X-ray microscopy (STXM) coupled with X-ray absorption near edge structure (XANES) spectroscopy (e.g. *Alleon et al., 2016; le Guillou et al., 2018*).

Biomarker extraction has also been conducted in bitumen contained in Neoproterozoic rocks (Hamesley basin, Pilbara Craton, western Australia), including stromatolites (*Brocks et al., 1999, 2003; Eigenbrode et al., 2008*). Those biomarkers mainly consist of lipid molecules (e.g. hopanoid, sterane) that are indicative of specific groups of Archaea and Bacteria such as cyanobacteria, anoxygenic phototrophs, methanotrophs (*Brocks et al., 1999; Rashby et al., 2007; Ventura et al., 2007; Eigenbrode et al., 2008; Welander and Summons, 2012*). Hopanoid hydrocarbons extracted from 2.7 Ga sedimentary rocks are indicative of aerobic methanotrophy and cyanobacterial activity and therefore may attest for the existence of oxygenic photosynthesis before the global atmosphere oxygenation occurring at ~2.4 Ga (*Brocks et al., 1999; Eigenbrode et al., 2008*). However, the syngeneity of these biomarkers has been challenged by evidence of surface contamination during core drilling (*Rasmussen et al., 2008; Brocks, 2011; French et al., 2015*). The existence of oxygenic photosynthesis and eukaryotes as old as 2.7 Ga, and therefore the evidence of a biological origin of the oldest stromatolites cannot be exclusively supported by biomarkers.

1.3.4. Carbon isotope compositions

Carbon has two stable isotopes, ^{12}C and ^{13}C . Microorganisms that use carbon for their metabolic activity (for example oxygenic photosynthesis) preferentially incorporate light ^{12}C isotopes compared to heavy ^{13}C isotopes. This process fractionates these two stable isotopes, reported as the ratio of $^{13}\text{C}/^{12}\text{C}$, and produces negative isotope composition (relative to the international standard V-PDB) of the produced organic matter (*Farquhar et al., 1989*). Carbon isotope compositions are widely used as a proxy for carbon source in organic matter and thus used to identify past metabolic activity (*Schidlowski, 2001; Thomazo et al., 2009; Williford et al., 2016*). However, isotope reset can occur during late metamorphic/metasomatism event, blurring the original signature carried by organic material (*van Zuilen et al., 2003; Schwab et al., 2005; Saitoh et al., 2020*). Moreover, the recognition of carbonaceous material and negative C isotope compositions is not necessarily attributed to past microbial activity as they can be reproduced by abiotic processes. For example, organic carbon (under crystalline graphite) can be formed through abiotic dissolution and reduction of carbonate in shallow subduction zones (*Galvez et al., 2013*). Experimental organic material synthesis by a Fischer-Tropsch type reaction, i.e. fluid-rock interaction under hydrothermal conditions, allowed the production of carbon isotope signatures similar to biologically-produced organic matter (*McCullom and Seewald, 2006; Taran et al., 2007*).

In conclusion, various degrees of confidence can be assigned to the different criteria used to assess the biogenicity of Archean stromatolites. Because abiotic processes are able to reproduce

stromatolite lamination, microfossil morphology and carbon isotope signatures, more proxies are needed to constrain their biological origin and to better identify the nature of the active microbial metabolisms during their formation.

2. Micrometric pyrite: an ubiquitous mineral in microbialites

2.1. Sedimentary pyrite formation

Pyrite was the first mineral to have its crystalline structure determined by X-ray diffraction (Bragg, 1914). The pure composition of pyrite is FeS_2 with a cubic (NaCl-type) structure (Kullerud and Yoder, 1959). Arrangement of atoms consists of S_2^{2-} at the center of the edges and center of the cube and Fe^{II} at the corners and center of each face of the cube. However, pyrite can incorporate minor and trace elements such as Co, Ni, Mo, Cu, Zn and As (Oertel et al., 1999). Pyrite is thermodynamically stable in anoxic low temperature environments under a large range of pH conditions (Fig. 1.5; Schoonen, 2004).

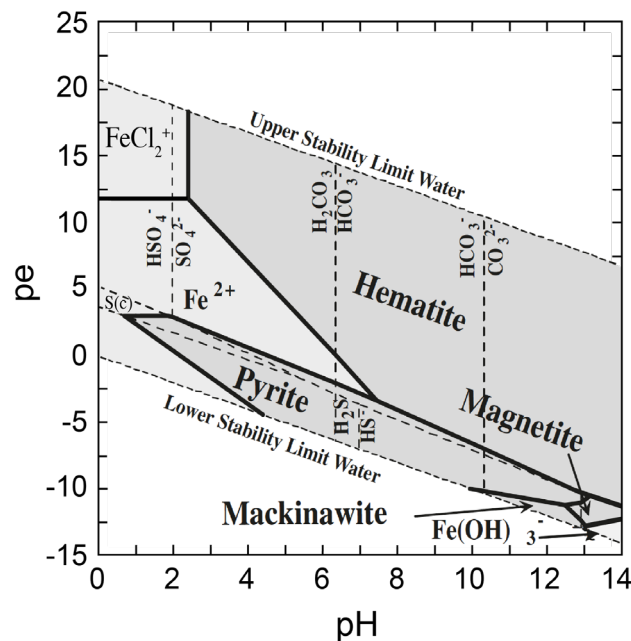


Figure 1. 5: *pe-pH* diagram of iron. This diagram shows the stability of iron sulfides and oxides in seawater (25°C, 1bar). Dashed lines report the speciation of sulfur and carbon species (Schoonen, 2004).

Pyrite formation can be divided into two processes. The first step is pyrite nucleation, a spontaneous reaction that requires supersaturated conditions with respect to pyrite (Schoonen and Barnes, 1991). Subsequently, pyrite grows until the crystal reaches its final size. Pyrites unlikely precipitate from the simple reaction between Fe^{II} and S_2^{2-} (Kamyshny et al., 2004) because pyrite formation requires a solution supersaturated with respect to amorphous FeS (Schoonen and

Barnes, 1991). Several studies synthesized abiotic pyrite in low temperature (< 100°C) aqueous solutions and pointed out the role of metastable intermediate dissolution for pyrite formation (*Luther, 1991; Rickard and Luther, 1997*). These metastable intermediates, referred to precursors, are mono- or polysulfides such as mackinawite (FeS) or greigite (Fe₃S₄). Mackinawite is the first product synthesized during abiotic low temperature experiments (*Schoonen and Barnes, 1991*) but is also precipitated in sulfate-reducing bacterial cultures (*Ivarson and Hallberg, 1976; Picard et al., 2018*). The conversion of FeS into pyrite requires (1) an electron acceptor to oxidize S₂^{-II} from FeS into a S^{-I} species and (2) the addition of sulfur or the loss of iron to reach a Fe/S molar ratio of 1:2 (see *Schoonen, 2004* for a review). Such a conversion mechanism can be reached using H₂S as electron acceptor, named the “hydrogen pathway” (**eq. 1.2**):



or via the incorporation of zero-valent sulfur species as electron acceptors (**eq. 1.3**; *Berner, 1970, 1984*):



However, the solid transformation between amorphous FeS and elemental sulfur is unlikely to form pyrite, and S₀ rather reacts to form polysulfide. The latter precipitates through the reaction of FeS and elemental sulfur (**eq. 1.4**) or through the reaction of HS⁻ and elemental sulfur (**eq. 1.5**; *Luther, 1991; Schoonen and Barnes, 1991; Wilkin and Barnes, 1996; Rickard and Luther, 1997*).



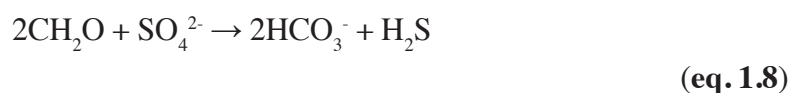
Greigite (**eq. 1.4**) can then react with elemental sulfur to precipitate pyrite as in the following equation (**eq. 1.6**):



On the other hand, polysulfides formed through **eq. 1.5** can produce pyrite by reacting with FeS as follows (**eq. 1.7**):



In modern oxic environments, pyrite forms along the course of early diagenesis once oxygen has been consumed by aerobic organic matter degradation. In anoxic sediments, organic carbon oxidation is dominantly mediated by sulfate reducers (*Jørgensen, 1982; Egger et al., 2018*), microorganisms use sulfate to sustain their metabolism and produce aqueous sulfide following the general stoichiometry of **eq. 1.8**.



Microbially-formed sulfide can subsequently interact with ferrous iron (Fe^{2+}), from abiotic (hydrothermal, weathering of ferrous Fe bearing substrate) and/or microbial reactions (dissimilatory Fe reduction or anaerobic oxidation of methane coupled to Fe-oxide reduction, cf **section 2.2**). Because Fe is in its insoluble ferric form (Fe^{3+} , forming iron (oxy)hydroxide and iron oxides) in surface environments, H_2S can directly react with ferric iron to produce Fe^{2+} (i.e. reduction-dissolution of Fe-oxide by H_2S , named hereafter sulfidation; *McAnena, 2011*).

The formation of pyrite is commonly admitted to occur under anoxia. However, the conversion of mackinawite into greigite and/or pyrite (**eqs. 1.3 to 1.5**) requires zero-valent sulfur, which is used as an oxidant. In the “hydrogen pathway”, the role of the oxidant is supported by protons (*Rickard and Luther, 1997*). However, in pure cultures of sulfate-reducing bacteria, the formation of pyrite is more efficient in the presence of other oxidants than H^+ . For example in his experiments, *Rickard (1969)* has shown that the conversion of mackinate into pyrite only occurred when goethite was involved. More recently, *Duverger et al. (2020)* and *Berg et al. (2020)* demonstrated the importance of dissolved Fe(III)-phosphate nanoparticles to precipitate pyrites in laboratory cultures of sulfate-reducing bacteria. Therefore, the precipitation of pyrite seems to not only be restricted to pure anoxic zones but can also reflect conditions of redox fluctuations.

2.2. Pyrite as proxy for paleoredox reconstructions

As a redox-sensitive mineral, sedimentary pyrite is widely used as a proxy for paleoenvironmental and paleoecological reconstructions. The trace element content, sulfur isotope signatures, pyrite texture and iron isotope signatures (this last point is detailed in **section 3.4**) are used to infer redox condition of the water column and past microbial activity (*Wilkin et al., 1996; Shen et al., 2011; Large et al., 2014*).

2.2.1. Trace elements

The incorporation of (redox-sensitive) trace elements, such as As, Ni, Co, Mo, Se, Cu, Mn, Ni, Cr, Pb, Zn and Cd, into pyrite is mediated by atomic substitution into the crystal structure or by forming for example micro- to nano-inclusions of sphalerite (*Michel et al., 1994; Gregory et al., 2015*). Such incorporation has been experimentally shown to occur during early stages of pyrite precursor formation (*Huerta-Diaz and Morse, 1992; Morse and Arakaki, 1993*). Therefore, pyrite formed within euxinic (anoxic and sulfidic) seawater or in sediment porewaters well-connected with the overlying water column are used to reconstruct paleoenvironmental (redox and microbial activity) conditions (*Dill and Kemper, 1990; Large et al., 2014*). However, because pyrite can form in sediments disconnected from the water column, the associated trace element composition may represent local conditions (*Gregory et al., 2019a*). Moreover, late fluid circulation can affect pyrite grains via partial (overgrowth formation) and/or complete recrystallization, leading to the alteration of their trace element contents (*Large et al., 2007*).

Hydrothermal alteration in pyrite can be track using Co/Ni ratios, which are usually above 2 in pyrite formed from hydrothermal fluids (*Bajwah et al., 1987*). To remove the post-depositional overprint, numerous studies promote in situ trace element analyses by laser ablation-inductively coupled plasma-mass spectrometry (LA-ICP-MS; *Large et al., 2014; Gregory et al., 2019b; Stepanov et al., 2020*). Such in-situ techniques allow to measure distinctly (i) pyrite cores, preserving the early diagenetic conditions, and (ii) secondary rims which are affected by late diagenesis (*Marin-Carbonne et al., 2014; Gregory et al., 2019b*), hydrothermal or metamorphic processes (*Large et al., 2007; Gregory et al., 2016*).

2.2.2. Pyrite morphology and size

Pyrite morphologies, but also size and the degree of pyritization, are excessively used to assess paleoredox conditions (*Wilkin et al., 1996; Roychoudhury et al., 2003; Rickard, 2019*). Framboidal pyrite, i.e. a morphology described as spherical cluster containing numerous micrometric pyrite crystals (**Fig. 1.6**), have attracted a special interest since their first description by *Rust (1935)*.

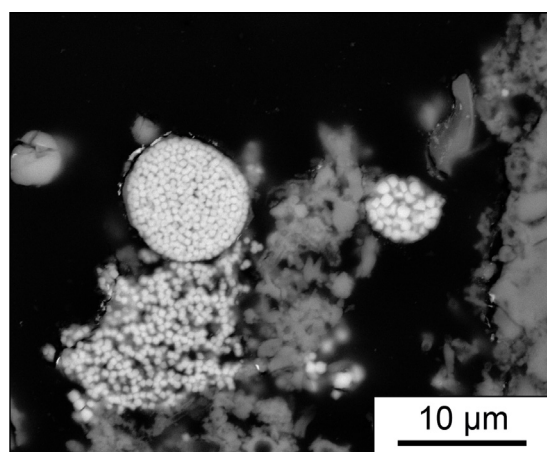


Figure 1. 6: BSE image of modern framboid grains. These pyrite grains are from microbialite samples developed in the Atexcac lake (Mexico; cf. *Chapter 3*).

Indeed, framboidal pyrite can precipitate in the water column under euxinic conditions (e.g. Black Sea) or in sediments under an oxygenated water column (*Wilkin et al., 1996*). Syngenetic framboids formed in euxinic waters are generally smaller and less variable in size ($5.0 \pm 1.7 \mu\text{m}$) than diagenetic pyrite formed in anoxic porewater sediments underlying an oxic water column ($7.7 \pm 4.1 \mu\text{m}$; *Wilkin and Barnes, 1997*). Based on these differences, many studies used framboid size distribution to define the locus of framboidal pyrite precipitation and past water column oxygenation state (*Zhou and Jiang, 2009; Wang et al., 2012; Blood et al., 2015; Huang et al., 2019*). In microbialites from the Archean to present days, pyrite size ranges between hundreds of nm to tens of μm (in average 10-20 μm) and are highly abundant in organic-rich laminae (*Folk, 2005; Cavalazzi et al., 2007; Gomes et al., 2018; Marin-Carbonne et al., 2018*). However, the occurrence of framboids in Archean sedimentary rocks is rare, the oldest being reported in the 2.9 Ga carbonaceous shale of the Witwatersrand Supergroup (South Africa; *Guy et al. 2010*).

2.2.3. Sulfur isotopes

Sedimentary pyrite sulfur isotope signatures give insights into microbial processes and atmosphere oxygenation through Earth history. Sulfur has four stable isotopes 32, 33, 34 and 36 with respective abundance of 95.02%, 0.75%, 4.21% and 0.02% (see *Sharp, 2017* for a recent review). Sulfur isotope compositions are expressed in delta notation, reporting permil variations of the $^{3x}\text{S}/^{32}\text{S}$ ratios (where x is either 3, 4 or 6), normalized to Vienna Cañon-Diablo Troilite (V-CDT) as the following (eq. 1.9):

$$\delta^{3x}\text{S} = \left[\frac{\left(\frac{^{3x}\text{S}}{^{32}\text{S}} \right)_{\text{sample}}}{\left(\frac{^{3x}\text{S}}{^{32}\text{S}} \right)_{\text{VCDT}}} - 1 \right] * 1000$$

(eq. 1.9)

Because microorganisms metabolizing sulfur in modern sediments produce specific sulfur isotope fractionations (e.g. *Harrison and Thode, 1958; Kaplan and Rittenberg, 1964; Rees, 1973; Chambers et al., 1975; Fry et al., 1986, 1988; Zerkle et al., 2009; Sim et al., 2011a, 2011b; Balci et al., 2012; Leavitt et al., 2013; Pellerin et al., 2019*, detailed in **sidebar 1, Chapter 3**), many studies are dedicated to trace metabolism-specific isotope signatures in ancient environments (*Canfield et al., 2000; Shen et al., 2001; Ono et al., 2003; Shen and Buick, 2004; Archer and Vance, 2006; Ueno et al., 2008; Roerdink et al., 2012; Zhelezinskaia et al., 2014; Marin-Carbonne et al., 2018*). In addition, ancient sedimentary rocks (i.e. Archean and early Paleoproterozoic) are also used to reconstruct the evolution of the atmosphere and oceanic oxygenation (e.g. *Farquhar and Wing, 2003; Kaufman et al., 2007; Johnston, 2011*). This is based on the observation that sedimentary rocks older than ~2.4 Ga preserve mass-independent fractionation (MIF) of sulfur isotopes (i.e. $\Delta^{33}\text{S} \neq 0$, where x refers to 3 or 6; *Farquhar et al., 2000, Fig. 1.7a*).

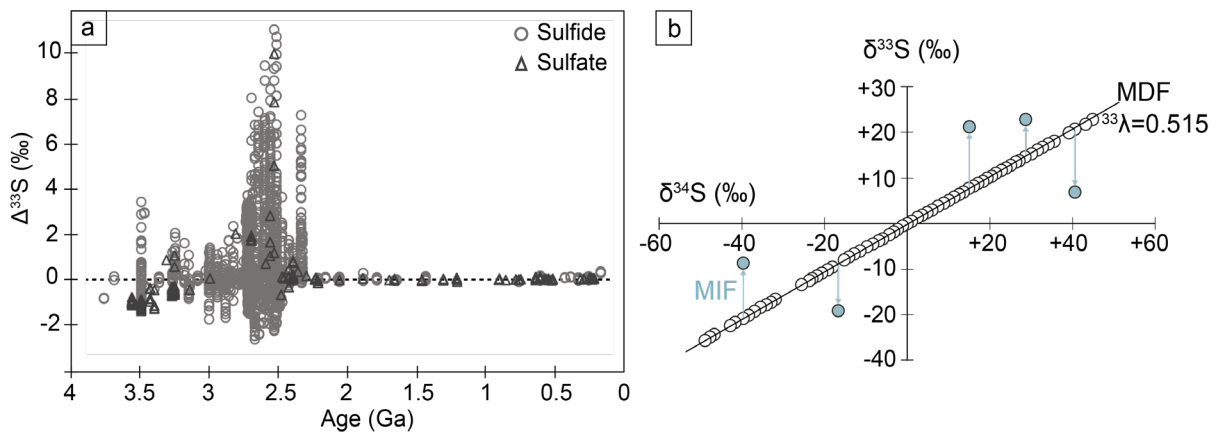


Figure 1.7: Secular variations of $\Delta^{33}\text{S}$ values of pyrite and sulfate and triple sulfur isotope plot. a) Mass-independent fractionation of sulfur isotopes (S-MIF) in both sulfide (grey dots) and sulfate (dark grey triangles) through time. S-MIF signatures are recorded in samples before 2.4 Ga and disappear after 2.4 Ga ($\Delta^{33}\text{S}=0$ reports mass dependent fractionation processes), indicative of the evolution of the atmosphere from anoxic to oxic conditions. Modified from *Zerkle et al. (2021)*. b) Illustration of samples aligned with the mass-dependent fractionation (MDF) line between $\delta^{34}\text{S}$ and $\delta^{33}\text{S}$ (slope $^{33}\lambda=0.515$). All samples deviating from this line were affected by mass-independent fractionation. Modified from *Johnston et al. (2011)*.

Mass-independent fractionation is a deviation from the theoretical equilibrium or kinetic mass law, i.e. defined as the mass difference between isotopes (**Fig. 1.7b**; *Thiemens, 1999*). Sulfur MIF is noted as Δ^{3xS} (x is either 3 or 6), described as (**eq. 1.10**):

$$\Delta^{3xS} = \delta^{3xS} - 1000 * \left[\left(1 + \frac{\delta^{34S}}{1000} \right)^{3x\lambda} - 1 \right]$$

(**eq. 1.10**)

where $^{3x}\lambda$ is the terrestrial mass fractionation array, set at 0.515 for $^{33}\lambda$ and 1.90 for $^{36}\lambda$.

Since its discovery by *Farquhar et al. (2000)*, the preservation of S-MIF in > 2.4 Ga sedimentary rocks has been used as a robust proxy for the absence of oxygen in the atmosphere (*Pavlov and Kasting, 2002*; *Halevy et al., 2010*; *Halevy, 2013*; *Ono, 2017*). Subsequently, several laboratory experiments exploring photochemical dissociation of gaseous SO_2 with UV under various anoxic conditions reveal that UV photolysis produces S-MIF signals (*Farquhar et al., 2001*; *Whitehill and Ono, 2012*; *Ono et al., 2013*). Since their production, conditions of S-MIF preservation require atmospheric oxygen below 10^{-5} present atmospheric level (PAL) in order to be incorporated in S-bearing minerals (e.g. evaporite, barite, carbonate, sulfide; *Pavlov and Kasting, 2002*). Therefore, S-MIF observation in sedimentary rocks older than 2.4 Ga is considered as strong evidence for anoxic atmospheric conditions. Experimental photochemical dissociation of SO_2 generates S-MIF in both reduced, under the form S_8 , and oxidized, as sulfuric acid aerosols H_2SO_4 species, both carrying different S-MIF signatures (**Fig. 1.8**; *Farquhar et al., 2001*; *Masterson et al., 2011*; *Franz et al., 2013*; *Endo et al., 2016*). Although the magnitude of S-MIF (Δ^{33S} and Δ^{36S}) varies with physico-chemical parameters (e.g. pressure, wavelength,

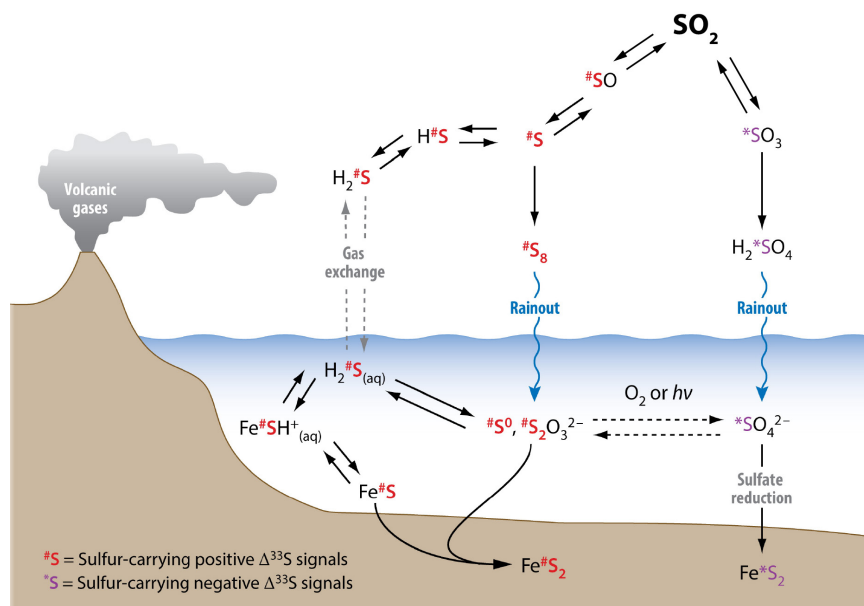


Figure 1.8: Model of the Archean sulfur cycle. The photodissociation of volcanic SO_2 produces reduced S species carrying positive S-MIF and oxidized S species carrying negative S-MIF, both transferred in the ocean where they can react with iron to produce pyrite. Modified from *Ono, (2017)*.

atmosphere composition), the canonical model emerging from experimental studies describes that atmospheric SO₂ photochemistry generates S₈ characterized by Δ³³S > 0 and Δ³⁶S < 0, directly incorporated into sulfide, and H₂SO₄, then SO₄²⁻, characterized by Δ³³S < 0 and Δ³⁶S > 0, either incorporated into minerals or microbially reduced to precipitate sulfide (**Fig. 1.8**).

3. Geological Fe cycling

3.1. Fe isotopes and nomenclature

Iron is the most abundant redox-sensitive metal in the Solar System and the fourth most abundant element in the Earth's crust. It has four stable isotopes, ⁵⁴Fe, ⁵⁶Fe, ⁵⁷Fe and ⁵⁸Fe with the respective abundances of 5.85, 91.75, 2.21 and 0.29% (*Berglund and Wieser, 2011*). Mass-dependent Fe isotope variations are usually reported as δ⁵⁶Fe, reported as permil variations of the ⁵⁶Fe/⁵⁴Fe ratio relative to the IRMM-014 international reference material as follows (**eq. 1.11**):

$$\delta^{56}Fe = \left[\frac{\left(\frac{^{56}Fe}{^{54}Fe} \right)_{sample}}{\left(\frac{^{56}Fe}{^{54}Fe} \right)_{IRMM-014}} - 1 \right] * 1000$$

(**eq. 1.11**)

An isotope exchange reaction between phases A and B can induce an isotope composition difference, better known as an isotope fractionation, defined as (**eq. 1.12**):

$$\alpha_{B-A} = \frac{R_B}{R_A}$$

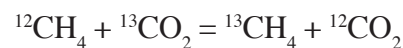
(**eq. 1.12**)

with R_A and R_B the isotope ratios of the heavy to the light isotope (for example ⁵⁶Fe/⁵⁴Fe) in phases A and B. Or can be expressed using the Δ notation as (**eq. 1.13**):

$$\Delta_{B-A} = (\delta_B - \delta_A) \approx 1000(\alpha_{B-A} - 1) \approx 1000 \ln \alpha_{B-A}$$

(**eq. 1.13**)

Isotope exchanges are categorized as equilibrium or kinetic reactions. Briefly, an equilibrium fractionation describes an isotope exchange reaction that reaches thermodynamic equilibrium (*Urey, 1947*; reviewed in *Sharp, 2017*). This means that light and heavy isotopes of an element can be completely exchanged between two substances A and B. For example, the equilibrium reaction between methane and carbon dioxide gives (**eq. 1.14**):



(**eq. 1.14**)

Equilibrium fractionation between two phases is proportional to $1/T^2$, meaning the extent of fractionation decreases with temperature increase (*Beard and Johnson, 2004* for a review). Therefore, largest fractionations are expected in low-temperature environments (**Figs. 1.9** and **1.10**). Kinetic fractionations are associated with incomplete or unidirectional reactions such as evaporation, diffusion or microbial reactions. Here, the fractionation is more dependent on the mass and the velocity of the isotope in a molecule. Therefore, isotopically lighter molecules are preferentially removed in evaporative or diffusive systems. In the case of microbial reaction, the preferential incorporation of light isotopes in the reaction product is favored by the lower dissociation energy of molecules which contain light isotopes (*Bigeleisen and Mayer, 1947* reviewed in *Sharp, 2017*)

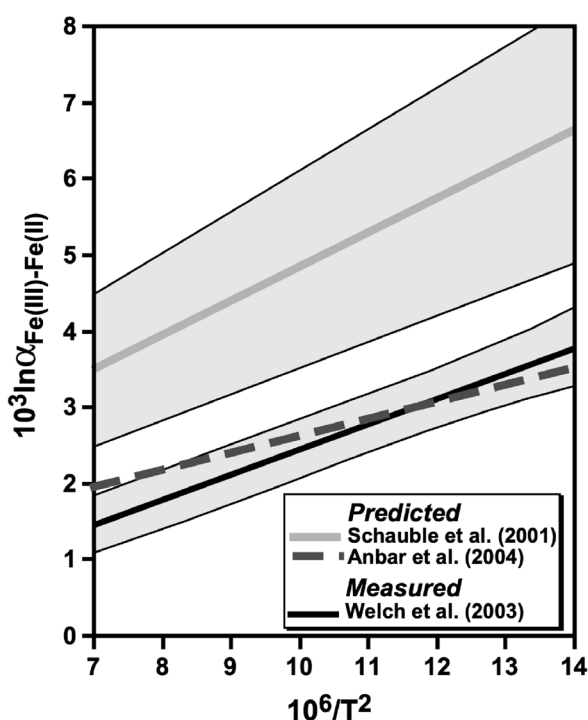


Figure 1.9: Relationship between the temperature ($10^6/T^2$) and the fractionation factor ($10^3 \ln \alpha_{\text{Fe(III)-Fe(II)}}$). The light gray and dashed gray lines correspond to the fractionation factor calculated by Schauble et al. (2001) and Anbar (2004). The black line is the fractionation factor experimentally determined (Welch et al., 2003). Modified from Beard and Johnson (2004).

Fe isotope variations in natural samples are limited, with the largest range of $\sim 6\%$ measured in Archean and Proterozoic sedimentary rocks (e.g. *Johnson et al., 2003; Dauphas et al., 2004, 2007; Rouxel et al., 2005; Yamaguchi et al., 2005; Archer and Vance, 2006; Planavsky et al., 2012; Marin-Carbonne et al., 2020, Fig. 1.10*). However, large Fe isotope fractionation are not only limited to low temperature processes, as illustrated by a 1.5% kinetic fractionation evidenced during Mg–Fe diffusion in olivine (*Teng et al., 2011; Sio et al., 2018*).

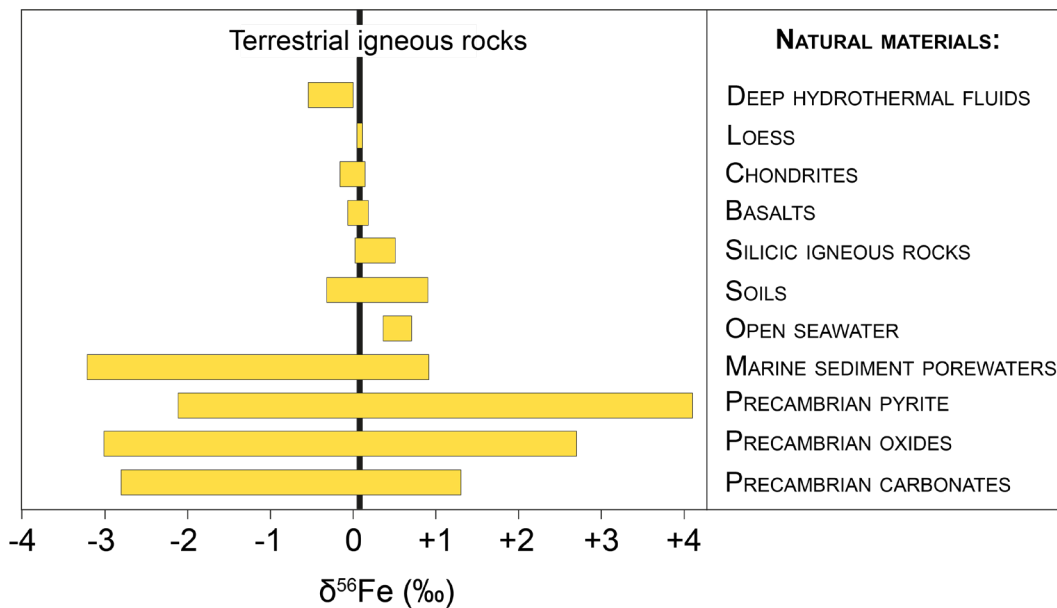


Figure 1.10: Fe isotope compositions measured in different natural materials. Modified from Johnson *et al.* (2020).

3.2. Fe sources and sinks

Despite being present in very low concentrations in the modern ocean (i.e. nM range), Fe plays an essential role as nutrient contributing to the marine primary productivity (Moore *et al.*, 2001; Morel *et al.*, 2006). Such low concentrations are explained by its rather short time of residence in the modern oceans (2 to 600 years), which results in the conversion of Fe^{2+} into insoluble Fe^{3+} in oxygenated waters (Johnson *et al.*, 1997; Moore *et al.*, 2004). This results in a heterogeneous distribution of Fe isotope compositions in the global ocean, which depends on the location and contribution of Fe sources. Bioavailable iron, in the form of Fe^{2+} , is supplied to the oceans through three major sources including (Fig. 1.11): the atmospheric dust (section 3.2.1), the benthic sediments (section 3.2.2) and the hydrothermal plume (section 3.2.3).

3.2.1. Atmospheric dust

Aeolian dust is the dominant source of Fe into the surface ocean, while dust-derived Fe fluxes are seasonally and spatially variable (Fig. 1.11). For example, the highest dust fluxes are measured in the North Atlantic in response to high input from the Sahara region (Conway and John, 2014; Jickells *et al.*, 2005; Mahowald *et al.*, 2005; Raiswell *et al.*, 2016). Although there are large uncertainties relative to the amount and solubility of Fe from atmospheric dust, a flux of $\sim 1\text{E}+11$ mol per year was estimated to be released into the ocean (Fung *et al.*, 2000) with typical continental $\delta^{56}\text{Fe}$ values of $\sim +0.5 - +0.8\text{‰}$ (Beard *et al.*, 2003; Waeles *et al.*, 2007).

3.2.2. Benthic sediments

Benthic dissolved Fe fluxes are released from continental margin sediments (Fig. 1.11). This can happen in Oxygen Minimum Zones (OMZ, such as the Peru margin, e.g. Noffke *et al.*,

2012) where the high productivity promotes organic carbon burial and consequently leads to anoxia in the upper sediments. In these sediments, Fe(III)-oxides are either reduced by biological mediation or abiotically by reaction with other reduced species. These reactions produce characteristic ^{56}Fe -depleted (up to -3%) Fe isotope compositions (Crosby *et al.*, 2005, 2007; Severmann *et al.*, 2010). However, dissolved Fe fluxes from continental shelf sediment is not limited to OMZ as they are also observed under oxygenated conditions (Jeandel *et al.*, 2011). Dissolved Fe^{2+} released into the oxygenated ocean can be preserved from oxidation through organic ligand formation (van den Berg, 1995; Witter and Luther, 1998; Boye *et al.*, 2001).

3.2.3. Hydrothermal plume

Hydrothermal fluids poorly contribute to the global balance of dissolved Fe because of rapid precipitation of Fe(III) oxide/hydroxides or Fe-metal-sulfides close to the vent (Fig. 1.11; Statham *et al.*, 2005; Tagliabue *et al.*, 2010). However, as discussed above, the stabilization of Fe^{2+} by formation of organic complexes raises hydrothermal vents as a significant source of Fe (Gledhill and van den Berg, 1994; Bennett *et al.*, 2009). The direct input of dissolved Fe^{2+} by hydrothermal vents is combined with the leaching of Fe-bearing mineral of the seafloor during fluid circulation. The Fe isotope composition of hydrothermal fluids is slightly lower than igneous rocks (0 to -0.5% ; Sharma *et al.*, 2001; Bennett *et al.*, 2009; Rouxel *et al.*, 2016), although some direct measurements of dissolved Fe^{2+} within hydrothermal plumes evidenced $\delta^{56}\text{Fe}$ values as low as -1.35% (Conway and John, 2014).

With the exception of reduced iron incorporated during carbonate precipitation (Fe-rich carbonate to siderite) and/or associated with organic matter, dissolved iron is sequestered in sediments as iron sulfide (sulfidic Fe sink) or reacts with oxygen to form insoluble Fe^{3+} (oxyhydr) oxides (oxidizing Fe sink).

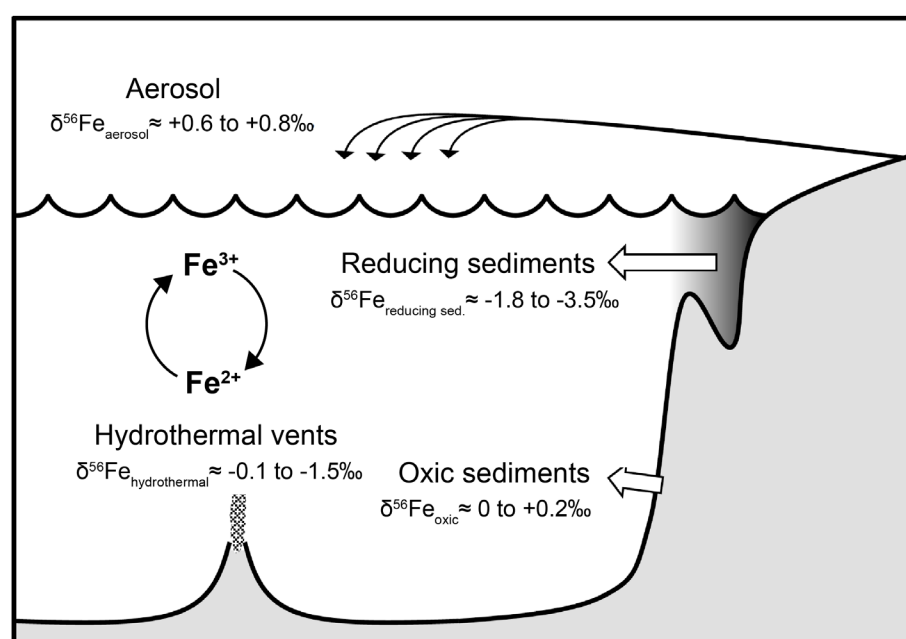


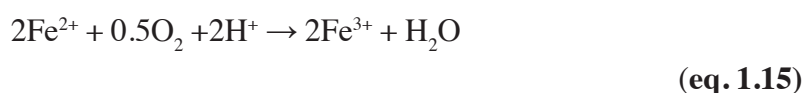
Figure 1. 11: Schematic representation of iron source in the ocean. Modified from Dauphas *et al.* (2017).

3.3. Microbial Fe cycling

The microbial reaction involved in the Fe cycle and their associated Fe isotope compositions are summarized below.

3.3.1. Fe oxidation

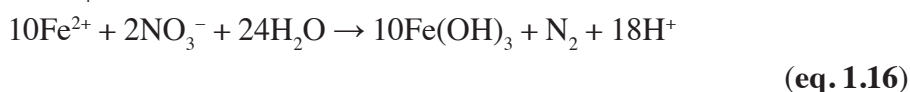
Under aerobic conditions and circumneutral pH, dissolved Fe²⁺ is thermodynamically unstable and abiotically reacts with O₂ to form Fe³⁺ phases and subsequently ferric (oxyhydro) oxides (Cornell and Schwertmann, 2003). However, abiotic Fe(II) oxidation can be disadvantaged and compete with microbial Fe(II)-oxidation (performed for example by *Gallionella*, *Sideroxydans*, *Ferriphaseus*, *Leptothrix*, *Ferritrophicum*, *Acidothiobacillus ferrooxidans* and *Leptospirillum ferrooxidans*) under low oxygen concentrations (5-20 μM) or acidic conditions (Chan et al., 2016; Mori et al., 2017). Those bacteria use O₂ as electron acceptor to form ferric iron (Emerson et al., 2010) as the following (eq. 1.15):



Experiments of bacterial Fe(II) oxidation under acidic and oxic conditions allowed to determine a Fe isotope fractionation of +2.2‰ between ferrihydrite and dissolved Fe²⁺ (Balci et al., 2006).

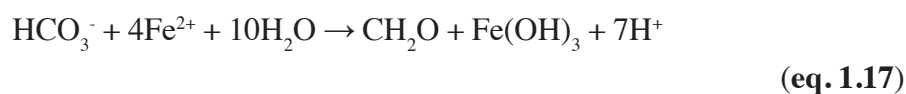
Under anoxic conditions, dissolved Fe(II) fuels a variety of Fe-oxidizing metabolic pathways including:

(1) Nitrate-reducing bacteria, a metabolic pathway using nitrate as electron acceptor to produce N₂ or ammonium NH₄⁺ (see eq. 1.16; Straub et al., 1996):



Bacteria coupling nitrate reduction to Fe(II) or sulfide oxidation, are represented by *Acidovorax spp.*, *Thiobacillus denitrificans*, *Geothrix* and *Marinobacter* and typically operate below the photic zone but can tolerate low oxygen concentrations (Edwards et al., 2003; Kappler et al., 2005a; Haaijer et al., 2007). An equilibrium Fe isotope fractionation of +3‰ between ferrihydrite precipitates and aqueous Fe(II) was determined during microbial Fe(II) oxidation coupled to nitrate reduction (Kappler et al., 2010).

(2) Anoxygenic Fe(II)-oxidizing phototrophs use light energy to transform bicarbonate into organic matter (see eq. 1.17; Widdel et al., 1993):

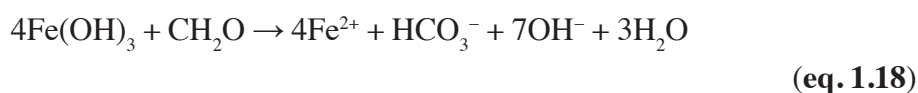


Photoferrotrophs include purple sulfur bacteria (*Thiodictyon sp.*), purple non-sulfur bacteria (*Rhodobacter ferrooxidans strain SW2*, *Rhodospseudomonas palustris strain TIE-1*, *Rhodovulum iodolum*, *Rhodovulum robiginosum*) and green sulfur bacteria (*Chlorobium ferrooxidans*,

Chlorobium phaeoferrooxidans, *Chlorobium* sp.; Ehrenreich and Widdel, 1994; Heising et al., 1999; Straub et al., 1999; Jiao et al., 2005; Croal et al., 2007; Llorós et al., 2015; Laufer et al., 2017). Those bacteria operate in restricted areas in sediments/microbial mats which combine deep enough light penetration and anoxic conditions. However, they have been shown to be also active under low oxygen concentrations and at very low light intensities (Kappler et al., 2005b). Fe isotope fractionation produced during Fe(II) oxidation by anoxygenic phototrophs resulted in the formation of ferrihydrite isotopically heavier, by +1.5‰, than dissolved Fe²⁺ (Croal et al., 2004). All together, those isotope fractionations are much larger than the fractionation factor obtained during abiotic oxidation of aqueous Fe(II) into Fe(III)-oxides ($\Delta\text{Fe}_{\text{Fe(III)-ox-Fe(II)}} = +0.9\text{‰}$; Bullen et al., 2001) but on the same order of magnitude or even lower than the equilibrium fractionation factors between aqueous Fe(III) and aqueous Fe(II) determined during abiotic oxidation experiments at room temperature ($\Delta\text{Fe}_{\text{Fe(III)aq-Fe(II)aq}} = +2.9\text{‰}$; Welch et al., 2003) and $\Delta\text{Fe}_{\text{Fe(III)aq-Fe(II)aq}} = +2.7\text{‰}$; Johnson et al., 2002). Under silica-rich conditions, a larger equilibrium fractionation, i.e. +3.99‰ between Fe(III)-Si coprecipitate and aqueous Fe(II), was determined during abiotic Fe oxidation experiments (Wu et al., 2012) with a smaller fractionation at lower Fe:Si ratio (Wu et al., 2012, in the continuity of Wu et al., 2011).

3.3.2. Dissimilatory Fe reduction

Under anaerobic conditions, a wide variety of bacteria such as *Geobacter* spp., *Shewanella* spp., *Albidoferax ferrireducens*, *Geothrix fermentans* and hyperthermophilic archaea (Lovley and Phillips, 1988; Myers and Nealson, 1990; Lovley et al., 1996; Coates et al., 1999; Tor and Lovley, 2001), known as Fe reducers, use Fe(III)-minerals as electron acceptors to produce Fe(II) coupled to the oxidation of organic matter (eq. 1.18; Lovley, 1987). This process is known as dissimilatory iron reduction, or DIR.

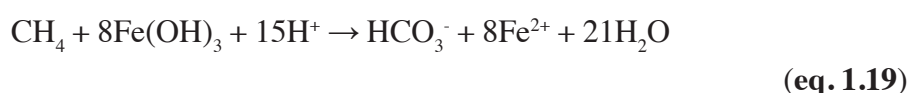


The Fe(III)-phases used by Fe reducers range from poorly ordered hydrated Fe(III) minerals, e.g. ferrihydrite, to well-crystalline phases such as hematite, goetite or lepidocrosite. Microbial Fe(III) reduction leads to the formation of by-product minerals including magnetite, siderite, green rust and sulfide (Cutting et al., 2009). Experiments documented a fractionation factor of -2.95‰ between Fe²⁺ and Fe(III)-oxides during DIR. The extent of the fractionation is independent of the stain (e.g. *Geobacter sulfurreducens*, *Shewanella putrefaciens*) or the Fe(III) substrate used (Crosby et al., 2007). This fractionation factor is consistent within error with the one determined during microbial reduction involving Fe(III)-silica precipitates (Percak-Dennett et al., 2011). Fractionation between Fe(II) and Fe(III)-oxides during DIR experiments is much larger than the fractionation of -0.8‰ between aqueous Fe(II) and Fe(III)-oxides obtained for abiotic reductive dissolution (sulfidation) of Fe(III)-oxides (McAnena, 2011) but equivalent to the Fe(II)-hematite equilibrium Fe fractionation factor of -2.8‰ during abiotic reduction (Friedrich et al., 2019).

A more recent study demonstrated the ability of some strains of Actinobacteria to perform Fe(III)-oxides (goethite and ferrihydrite) reduction under oxic and neutral pH conditions (Zhang *et al.*, 2019). The reduction of goethite in phosphate-buffered conditions leads to the formation, in addition to aqueous Fe(II), of vivianite as by-product. The isotope fractionation of Fe isotopes associated with aerobic Fe(III) reduction still needs to be constrained.

3.3.3. Anaerobic oxidation of methane coupled to Fe(III) reduction

Anaerobic methane oxidation (AOM) occurs in anoxic environments and uses various oxidized species as electron acceptor such as Fe(III)-oxides (eq. 1.19), sulfate, Mn(IV)-oxides or nitrate (Sivan *et al.*, 2011).



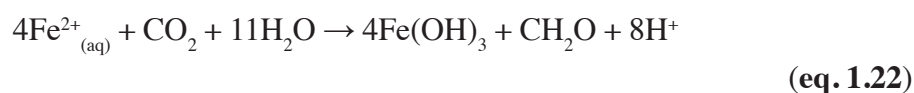
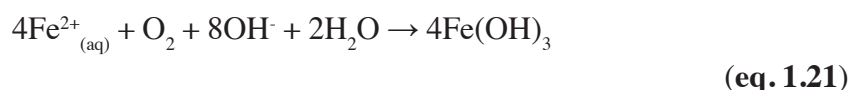
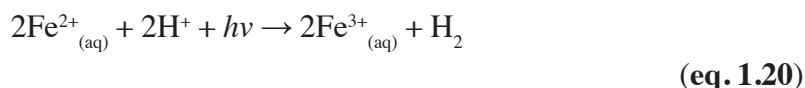
Oxidation of methane coupled to Fe(III)-oxide reduction is conducted by archaea (*Candidatus Methanoperedens nitroreducens*, *Candidatus Methanoperedens ferrireducens*; Ettwig *et al.*, 2016; Cai *et al.*, 2018) but also exist in archaea and bacteria syntrophic communities (e.g. *Methanobacterium* and *Desulfovibrio*; He *et al.*, 2019). This metabolic pathway has been described in sediments at depth where methanogens are active, in microbial mats growing in marine methane seeps or in freshwater lakes (e.g. Costello *et al.*, 2002; Greinert *et al.*, 2002; Sivan *et al.*, 2007; Ding and Valentine, 2008) and have been active in Archean stromatolites (Hayes, 1994; Thomazo *et al.*, 2009; Flannery *et al.*, 2016; Slotznick and Fischer, 2016). Fractionation factor between Fe(III) and Fe(II) species during AOM remains undocumented.

3.4. Looking into the past: Fe cycling in the Precambrian

3.4.1. Evolution of sulfidic and oxic Fe sinks

The size of the sulfidic and oxic Fe sinks evolved through time, and significantly changed at the Archean-Paleoproterozoic transition at ~2.4 Ga. This period is named the Great Oxidation Event (GOE) and describes an interval of irreversible rise of oxygen concentrations in the atmosphere and oceans ($\geq 10^{-5}$ Present Atmospheric Level; Holland *et al.*, 1986; Pavlov and Kasting, 2002; Sverjensky and Lee, 2010; Gumsley *et al.*, 2017). In the Archean, the concentration of atmospheric greenhouse gases have been much higher than today, maintaining a surface temperature allowing liquid water to be present, whereas the solar radiation was lower than today (faint young Sun paradox; Sagan and Chyba, 1997). In addition to information provided by pyrite S-MIF, the preservation of reduced minerals such as uraninite (UO₂), detrital (rounded shape) pyrite, siderite and the massive deposition of Banded Iron Formations (BIF), layered sedimentary rocks mainly made of silica, Fe-oxides and mixed-valence Fe minerals, attest for a stable anoxic atmosphere and ocean (Grandstaff, 1980; Holland *et al.*, 1986; Rasmussen and Buick, 1999; Klein, 2005). The deposition of BIF before 2.4 Ga is also indicative for the

predominance of ferruginous conditions in the Archean ocean, with estimations of dissolved iron concentrations up to 100 μM , (versus ~ 1 nM in the modern ocean; *Canfield et al., 2005*). The precipitation of Fe(II)-Fe(III) minerals in BIF also demonstrates Fe²⁺ oxidation processes via three different pathways, including atmospheric abiotic photo oxidation (**eq. 1.20**; *Braterman et al., 1983*), biologically-mediated and/or mediated by O₂ released by oxygenic photosynthetic bacteria (**eq. 1.21**; *Cloud, 1973*) and, finally, oxidation mediated by anoxygenic photosynthetic organisms where Fe²⁺ is used as an electron donor (**eq. 1.22**; *Widdel et al., 1993*; *Kappler et al., 2005b*).



The decreasing abundance of BIF and reduced minerals is concurrent with the disappearance of S-MIF and the deposition of red beds (*Eriksson and Cheney, 1992*; *Knoll and Holland, 1995*), all happening at about 2.4 Ga and leading to the increase of the Fe oxidic sink. In contrast, although the size of the sulfidic sink may have been restricted during the Archean because of lower sulfate concentrations (>2.5 μM) than modern oceans (28 mM; *Habicht et al., 2002*; *Crowe et al., 2014*), pyrite represents the main Fe sulfidic sink through Earth history, in euxinic water columns and/or sediment porewaters. Therefore, because pyrite has been a stable Fe sink since the Archean, the conditions of its precipitation can be studied on a large temporal scale.

3.4.2. Pyrite Fe isotope compositions through geological time

Through the geological record, the most negative bulk $\delta^{56}\text{Fe}$ values and the largest variations are recorded in Archean and Paleoproterozoic pyrite ($\delta^{56}\text{Fe}$ from -3.51 to +1.19‰), while Neoproterozoic to modern pyrite display narrower $\delta^{56}\text{Fe}$ ranges (-1.65 to +0.16‰) close to the average value of igneous rocks (**Fig. 1.12**; *Dauphas and Rouxel, 2006*).

While processes such as Fe²⁺ adsorption on Fe-oxides or dissociation of Fe²⁺-Fe³⁺ complexes can create significant Fe isotope fractionation, the largest isotope variations result from either abiotic and biotic redox reactions that convert Fe³⁺ bearing minerals into ferrous iron Fe²⁺, or minerals, i.e. Fe sulfide (*Matthews et al., 2001*; *Welch et al., 2003*; *Johnson and Beard, 2005*; *Teutsch et al., 2005*; *Polyakov et al., 2007*; *Guilbaud et al., 2011*). Therefore, three hypotheses are discussed in the literature to explain the negative $\delta^{56}\text{Fe}$ values that dominate the pyrite Fe isotope record (**Figs. 1.10** and **1.12**). These hypothesis are detailed below. These include: (h1) global changes of the oxygenation of the ocean (*Rouxel et al., 2005*; *Kunzmann et al., 2017*), (h2) microbial iron redox reactions due to extensive DIR (*Johnson and Beard, 2005*; *Severmann et al., 2008*) and (h3) the isotope regime of pyrite precipitation (kinetic or equilibrium), highly dependent on the sulfur availability (*Guilbaud et al., 2011*; *Mansor and Fantle, 2019*).

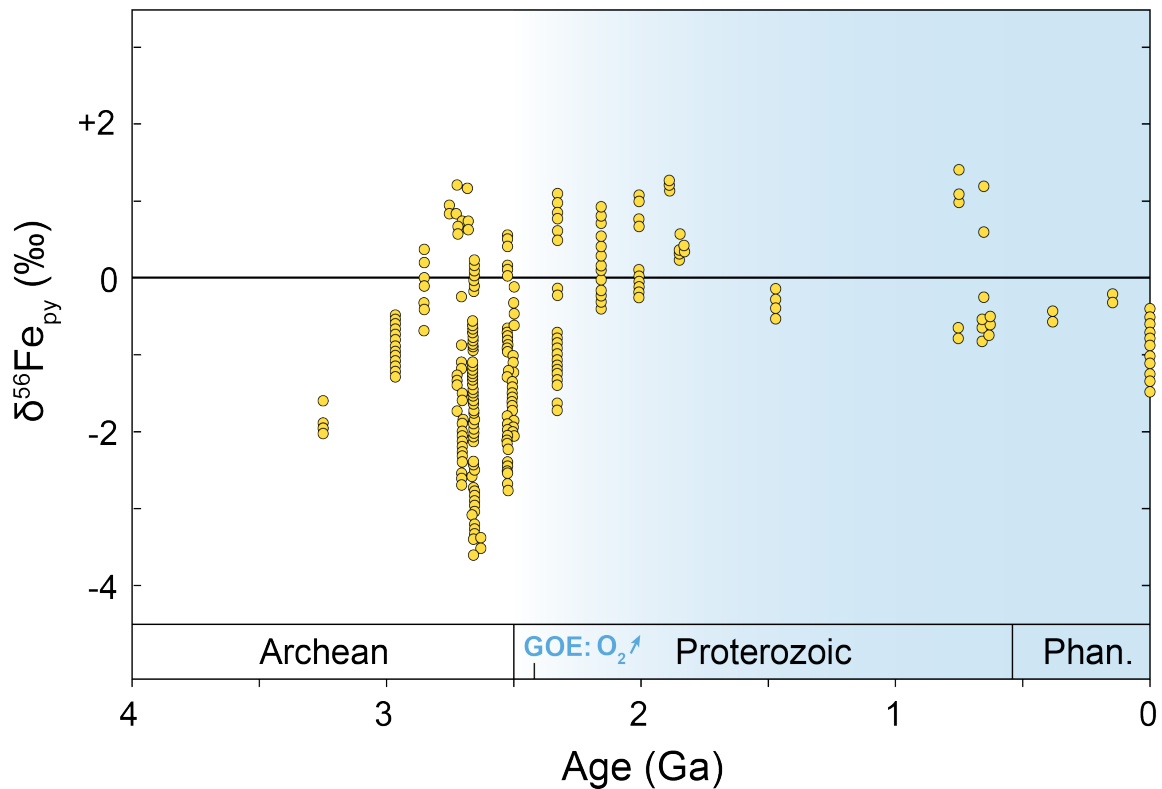


Figure 1. 12: Secular variations of bulk iron isotopes of pyrite. GOE: Great Oxidation Event. Compilation from Ostrander et al. (2022).

(h1) The partial oxidation of the ferruginous Archean ocean is an efficient way to generate ^{56}Fe -depleted values in sedimentary pyrite. This process leads to the deposition of Fe-oxide characterized by heavy $\delta^{56}\text{Fe}$ values. The precipitation of Fe-oxides is paired with the creation of a residual dissolved Fe^{2+} reservoir characterized by light $\delta^{56}\text{Fe}$ values (Rouxel et al., 2005). This hypothesis suggests that the increase of Fe isotope compositions of pyrite through the GOE reflects the growth of the oxidized Fe reservoir. Consequently, sedimentary pyrite can be used as a proxy of oceanic redox variations through time.

(h2) Dissimilatory Fe reduction is the biotic redox pathway conducted in benthic environments to produce ^{56}Fe -depleted pyrite. This metabolic pathway produces a negative dissolved Fe^{2+} pool, as low as -3‰ , compared to the Fe(III) substrate. Many studies proposed that negative $\delta^{56}\text{Fe}$ values measured in Archean shales and carbonates reflect active microbial Fe reduction (e.g. Yamaguchi et al., 2005; Heimann et al., 2010).

(h3) The partial drawdown of the dissolved Fe reservoir during pyrite precipitation (Guilbaud et al., 2011) results in a negative fractionation factor ($\sim 2.2\text{‰}$) between pyrite and dissolved Fe^{2+} . This hypothesis suggests that the Fe isotope compositions of pyrite is controlled by the availability of reactive Fe and S species for the precipitation of pyrite. Pyrite expresses negative Fe isotope compositions when the concentration of sulfate is low (Rolison et al., 2018). In that case, the shift of Fe isotope compositions from negative to positive values around 2.4 Ga reflect an increase of the concentration of sulfate in the ocean. The expansion of the sulfidic Fe sink has been demonstrated, at least partly, to control the Fe isotope variability through the Archean-

Proterozoic transition (*Heard and Dauphas, 2020*). This led to an alternative interpretation of Fe isotope ranges of pyrite through the geological record that does not involve redox reactions of Fe (*Mansor and Fantle, 2019*).

The temporal evolution of $\delta^{56}\text{Fe}$ values through time in **Figure 1.12** is representative of the Fe signal extracted from pyrite bulk analyses. By contrast, this work proposes to evidence the Fe isotope variability of pyrite through spatially resolved analyses.

4. Scope of this thesis

As already mentioned above, microbialites can be identified in the geological record from the Archean to modern time. Moreover, micrometric pyrite, which can derive from biological reactions, is a ubiquitous mineral in sedimentary rocks (*Schieber, 2002; Liu et al., 2020*). Therefore, this work focuses on the ability of pyrite to record and preserve microbial metabolic activity and redox conditions in microbialites of different ages, including modern, Early Triassic and Archean samples. First, an analytical protocol was developed to accurately measure iron isotopes in pyrites with sizes of often less than $10\ \mu\text{m}$. Then the samples were targeted according to emblematic time periods dominated by different environmental redox conditions. This includes modern microbialites forming in oxic environments, which have not yet been influenced by post-depositional processes, and thus aided in understanding the full range of $\delta^{56}\text{Fe}$ formed in microbialites. This “primary” isotope signal (i.e. mostly influenced by microbial activity) extracted from pyrite grains was subsequently compared to Early Triassic MISS/sediments and Archean microbialites, likely formed in anoxic environments and Early Triassic microbialites (and other sedimentary rocks), which deposited during a period of time that documents extensive anoxia as a result of a large environmental stress.

Two main questions drove this work:

Do Fe isotope compositions of micrometric pyrite grains preserved in microbialites reflect the activity of Fe-reducing bacteria?

As a redox sensitive element, what is the effect of global environmental changes on the Fe isotope compositions in pyrite preserved in microbialites?

To answer these questions, I focus on secondary ion mass spectrometry (SIMS) to measure spatially resolved Fe isotope compositions. Prior to this work, pyrite grains of size less than $20\ \mu\text{m}$ have never been analyzed and, consequently, required the development of a new analytical procedure, which was published in 2021 in *Rapid Communication in Mass Spectrometry* (*Decraene et al., 2021a*). This newly developed analytical procedure describes parameters used to obtain a primary beam of $3\ \mu\text{m}$ -size without sacrificing analytical precision. Analytical effects

induced by mass interferences, topography and crystal orientation are shown to be insignificant for Fe isotope compositions. **Chapter 2** also describes the geological context of all studied samples, as well as geochemical analytical methods used during the course of my PhD.

Chapter 3 explores the pyrite isotope signatures of framboidal pyrite from two modern mineralized microbialites (Cayo Coco, Cuba and Atexcac lake, Mexico). This chapter aims to define the isotope imprint of pyrite formed under microbial influence before experiencing late diagenesis and metamorphism which can impact S and Fe isotope compositions (*Williford et al., 2011; Marin-Carbonne et al., 2020*). Chapter 3 is divided into two parts: (1) the first part focuses on the S cycling that occurred in two pyrite morphologies (framboid and micrometric euhedral) identified in both microbialite samples, and (2) the second part is dedicated to the Fe cycling recorded in pyrite framboids. In the former, S isotope compositions highlight that micrometric euhedral pyrite captures undisputable signature of microbial sulfur reduction, while framboids recorded more complex signatures related to either (1) oxidation-reduction cycling in the upper layers of the microbial mat or (2) diffusive flux of isotopically heavy H₂S. This work led to a recent publication in *Geochemical Perspectives Letters* (*Marin-Carbonne et al., 2022*). The active microbial S cycling evidenced in the formation of micropyrrite, and the demonstration that sulfate reducing bacteria can take the advantage over Fe-reducers under anoxic conditions led to the question:

What is the influence of sulfate-reducers on Fe cycling?

Do framboidal pyrite grains record the isotope signature of microbial Fe-oxide reduction or does this reduction only reflect the influence of microbial H₂S fluxes?

In the latter, in situ Fe isotope compositions revealed the influence of Fe-reducing bacteria to precipitate framboid pyrite, likely beyond the zone of influence of sulfate reducers. This chapter highlights that pyrite grains precipitated in modern microbialites forming in an oxygenated water column can record incontestable microbial Fe and S isotope signatures and that those microbialites operate as independent ecological niches from environmental oxygenation state.

Chapter 4 focuses on the isotope record of pyrite deposited along a ramp system across the Smithian-Spathian boundary (SSB, Early Triassic). This period is widely studied for unstable and harsh environmental conditions, including for example spread oceanic anoxia in the aftermath of the end Permian mass extinction event (*Sun et al., 2012; Grasby et al., 2013*). At that time, various environmental stress factors caused the loss of 90% of marine species (*Bond and Grasby, 2017*) and various microbial deposits were described during the Early Triassic as “anachronistic facies”. This study includes samples distributed in different depositional environments, ranging from inner to outer ramp settings. Moreover, samples from the inner ramp can contain MISS.

This chapter focusses on two central questions:

Do pyrite isotope signatures record an oceanic redox state variation linked to the SSB?

What is the influence of the depositional environment and the nature of sediments on pyrite formation?

In relation to the latter, this study also addresses the influence of MISS on pyrite Fe isotope signatures. Through a multi-isotope proxy approach (in situ $\delta^{56}\text{Fe}$ and bulk $\delta^{34}\text{S}$) and petrographic observations, our results highlight (1) that the overlying water column was likely oxygenated and therefore pyrite likely precipitated in the upper sedimentary column, (2) the influence of the connectivity between sediment porewaters and water column (open versus closed system) controls the isotope signatures of Fe and S reservoirs and (3) heavy $\delta^{56}\text{Fe}$ compositions associated with MISS, and attributed to active Fe-redox cycling in the microbial mat. This study has been recently submitted at *Palaeogeography, Palaeoclimatology, Palaeoecology*.

Chapter 5 describes microbially-influenced Fe cycling in an Archean stromatolite (2.7 Ga, Tumbiana Formation). Indeed, past studies demonstrated active microbial cycling of N, S, C, and As (Thomazo et al., 2009, 2011; Sforza et al., 2014; Stüeken et al., 2017; Marin-Carbonne et al., 2018; Lepot et al., 2019). Together with mineralogical observations of aragonite crystals, well-preserved organic matter and diversified morphologies of stromatolites, few doubts remain about the biogenicity of those structures (Buick, 1992; Lepot et al., 2019). However, while no Fe redox cycling was first evidenced by bulk rock analyses (Czaja et al., 2010), in situ analyses on pyrite (20 to $\sim 100\ \mu\text{m}$ in size) evidenced active Fe cycling (Yoshiya et al., 2012). Microbial Fe cycling was therefore suggested but not demonstrated. This study aims to determine the existence of microbial Fe reduction in pyrite by exploring the isotope variability of micrometric pyrite grains as small as $5\ \mu\text{m}$. Those targets enclose the largest range of $\delta^{56}\text{Fe}$ values measured in Archean sedimentary pyrite, attributed to the interaction of an active microbial Fe cycle (Fe oxidation and reduction) in close association with sulfate reducers and methanotrophs. This chapter demonstrates once again the control of local redox processes on Fe isotope signatures of micrometric pyrite. This work resulted in a publication in *Geochimica et Cosmochimica Acta* (Decraene et al., 2021b).

Chapter 6 aims to assess the effect of the global rise of oxygen in the early stages of the GOE on Fe isotope signatures of pyrite from 2.5 Ga stromatolites. Another goal of this work is to evaluate the effect of intense post-deposit influence on isotope compositions of pyrite. This work, still in progress, focuses on stromatolite samples from the Campbellrand-Malmani carbonate platform, characterized by centimetric to metric stromatolite domes associated with

well-preserved sedimentary structures. This platform deposited at around 2.5 Ga, just before the GOE, where photosynthetic O₂ production have previously been documented (*Kendall et al., 2010*). Another particularity of the platform is the existence of a metamorphic gradient, from the west to the east, with metamorphic temperature increasing from 250 to > 400°C (*Button, 1973*). Moreover, the platform experienced an almost complete dolomitization and partial silicification. The main results (petrographic observations, major and trace elements, in situ Fe and S isotope compositions, minor elements in pyrite) are presented and briefly discussed in terms of primary signal preservation.

Finally, the meanings of pyrite isotope compositions in microbialites through geological time are discussed in a conclusive chapter (**Chapter 7**). This discussion is organized in three parts:

- (1) The importance to identify post-depositional processes and their impact on the mineralogy and isotope signatures
- (2) The element and mineral phases still preserved despite extensive secondary alteration and mineralogical replacement
- (3) The interpretations of isotope signals extracted from these «primary» grains

Then this chapter closes with the presentation of three future projects that I hope to pursue.

5. Literature cited

- Abell, P.I., McClory, J., Martin, A., Nisbet, E.g. 1985. Archaean stromatolites from the Ngesi Group, Belingwe greenstone belt, Zimbabwe; preservation and stable isotopes — preliminary results. *Precambrian Research* 27, 357–383. [https://doi.org/10.1016/0301-9268\(85\)90094-4](https://doi.org/10.1016/0301-9268(85)90094-4)
- Aitken, J.D., 1967. Classification and Environmental Significance of Cryptalgal Limestones and Dolomites, with Illustrations from the Cambrian and Ordovician of Southwestern Alberta. *Journal of Sedimentary Research* Vol. 37. <https://doi.org/10.1306/74D7185C-2B21-11D7-8648000102C1865D>
- Alleon, J., Bernard, S., le Guillou, C., Marin-Carbonne, J., Pont, S., Beysac, O., McKeegan, K.D., Robert, F., 2016. Molecular preservation of 1.88 Ga Gunflint organic microfossils as a function of temperature and mineralogy. *Nature Communications* 7, 11977. <https://doi.org/10.1038/ncomms11977>
- Alleon, J., Summons, R.E., 2019. Organic geochemical approaches to understanding early life. *Free Radical Biology and Medicine* 140, 103–112. <https://doi.org/10.1016/j.freeradbiomed.2019.03.005>
- Allwood, A.C., Walter, M.R., Kamber, B.S., Marshall, C.P., Burch, I.W., 2006. Stromatolite reef from the Early Archaean era of Australia. *Nature* 441, 714–718. <https://doi.org/10.1038/nature04764>
- Allwood, A.C., Grotzinger, J.P., Knoll, A.H., Burch, I.W., Anderson, M.S., Coleman, M.L., Kanik, I., 2009. Controls on development and diversity of Early Archean stromatolites. *Proceedings of the National Academy of Sciences* 106, 9548–9555. <https://doi.org/10.1073/pnas.0903323106>
- Allwood, A.C., Rosing, M.T., Flannery, D.T., Hurowitz, J.A., Heirwegh, C.M., 2018. Reassessing evidence of life in 3,700-million-year-old rocks of Greenland. *Nature* 563, 241–244. <https://doi.org/10.1038/s41586-018-0610-4>
- Aloisi, G., Gloter, A., Krüger, M., Wallmann, K., Guyot, F., Zuddas, P., 2006. Nucleation of calcium carbonate on bacterial nanoglobules. *Geology* 34, 1017. <https://doi.org/10.1130/G22986A.1>
- Altermann, W., Nelson, D.R., 1998. Sedimentation rates, basin analysis and regional correlations of three Neoproterozoic and Palaeoproterozoic sub-basins of the Kaapvaal craton as inferred from precise U–Pb zircon ages from volcanoclastic sediments. *Sedimentary Geology* 120, 225–256. [https://doi.org/10.1016/S0037-0738\(98\)00034-7](https://doi.org/10.1016/S0037-0738(98)00034-7)
- Altermann, W., 2008. Accretion, Trapping and Binding of Sediment in Archean Stromatolites—Morphological Expression of the Antiquity of Life. *Space Science Reviews* 135, 55–79. <https://doi.org/10.1007/s11214-007-9292-1>
- Anbar, A.D., 2004. Iron stable isotopes: beyond biosignatures. *Earth and Planetary Science Letters* 217, 223–236. [https://doi.org/10.1016/S0012-821X\(03\)00572-7](https://doi.org/10.1016/S0012-821X(03)00572-7)
- Andres, M.S., Reid, P.R., 2006. Growth morphologies of modern marine stromatolites: A case study from Highborne Cay, Bahamas. *Sedimentary Geology* 185, 319–328. <https://doi.org/10.1016/j.sedgeo.2005.12.020>
- Archer, C., Vance, D., 2006. Coupled Fe and S isotope evidence for Archean microbial Fe(III) and sulfate reduction. *Geology* 34, 153. <https://doi.org/10.1130/G22067.1>
- Awramik, S.M., Margulis, L., Barghoorn, E.S., 1976. Evolutionary Processes in the Formation of Stromatolites, in: *Developments in Sedimentology*. Developments in Sedimentology, pp. 149–162. [https://doi.org/10.1016/S0070-4571\(08\)71135-X](https://doi.org/10.1016/S0070-4571(08)71135-X)
- Awramik, S.M., 1991. Archaean and Proterozoic Stromatolites, in: *Calcareous Algae and Stromatolites*. Springer Berlin Heidelberg, Berlin, Heidelberg, pp. 289–304. https://doi.org/10.1007/978-3-642-52335-9_15
- Awramik, S.M., 1992. The History and Significance of Stromatolites, in: *Early Organic Evolution*. Springer Berlin Heidelberg, Berlin, Heidelberg, pp. 435–449. https://doi.org/10.1007/978-3-642-76884-2_34

- Awramik, S.M., Grey, K., 2005. Stromatolites: biogenicity, biosignatures, and bioconfusion, in: Hoover, R.B., Levin, G. v., Rozanov, A.Y., Gladstone, G.R. (Eds.), . p. 59060P. <https://doi.org/10.1117/12.625556>
- Awramik, S.M., 2006. Respect for stromatolites. *Nature* 441, 700–701. <https://doi.org/10.1038/441700a>
- Bajwah, Z.U., Seccombe, P.K., Offler, R., 1987. Trace element distribution, Co:Ni ratios and genesis of the big cadia iron-copper deposit, new south wales, australia. *Mineralium Deposita* 22. <https://doi.org/10.1007/BF00204522>
- Balci, N., Bullen, T.D., Witte-Lien, K., Shanks, W.C., Motelica, M., Mandernack, K.W., 2006. Iron isotope fractionation during microbially stimulated Fe(II) oxidation and Fe(III) precipitation. *Geochimica et Cosmochimica Acta* 70, 622–639. <https://doi.org/10.1016/j.gca.2005.09.025>
- Balci, N., Mayer, B., Shanks, W.C., Mandernack, K.W., 2012. Oxygen and sulfur isotope systematics of sulfate produced during abiotic and bacterial oxidation of sphalerite and elemental sulfur. *Geochimica et Cosmochimica Acta* 77, 335–351. <https://doi.org/10.1016/j.gca.2011.10.022>
- Baumgartner, L.K., Reid, R.P., Dupraz, C., Decho, A.W., Buckley, D.H., Spear, J.R., Przekop, K.M., Visscher, P.T., 2006. Sulfate reducing bacteria in microbial mats: Changing paradigms, new discoveries. *Sedimentary Geology* 185, 131–145. <https://doi.org/10.1016/j.sedgeo.2005.12.008>
- Beard, B.L., Johnson, C.M., Skulan, J.L., Neelson, K.H., Cox, L., Sun, H., 2003. Application of Fe isotopes to tracing the geochemical and biological cycling of Fe. *Chemical Geology* 195, 87–117. [https://doi.org/10.1016/S0009-2541\(02\)00390-X](https://doi.org/10.1016/S0009-2541(02)00390-X)
- Beard, B.L., Johnson, C.M., 2004. Fe Isotope Variations in the Modern and Ancient Earth and Other Planetary Bodies. *Reviews in Mineralogy and Geochemistry* 55, 319–357. <https://doi.org/10.2138/gsrmg.55.1.319>
- Bennett, S.A., Rouxel, O., Schmidt, K., Garbe-Schönberg, D., Statham, P.J., German, C.R., 2009. Iron isotope fractionation in a buoyant hydrothermal plume, 5°S Mid-Atlantic Ridge. *Geochimica et Cosmochimica Acta* 73, 5619–5634. <https://doi.org/10.1016/j.gca.2009.06.027>
- Berg, J.S., Duverger, A., Cordier, L., Laberty-Robert, C., Guyot, F., Miot, J., 2020. Rapid pyritization in the presence of a sulfur/sulfate-reducing bacterial consortium. *Scientific Reports* 10, 8264. <https://doi.org/10.1038/s41598-020-64990-6>
- Berglund, M., Wieser, M.E., 2011. Isotope compositions of the elements 2009 (IUPAC Technical Report). *Pure and Applied Chemistry* 83, 397–410. <https://doi.org/10.1351/PAC-REP-10-06-02>
- Berner, R.A., 1970. Sedimentary pyrite formation. *American Journal of Science* 268, 1–23. <https://doi.org/10.2475/ajs.268.1.1>
- Berner, R.A., 1984. Sedimentary pyrite formation: An update. *Geochimica et Cosmochimica Acta* 48, 605–615. [https://doi.org/10.1016/0016-7037\(84\)90089-9](https://doi.org/10.1016/0016-7037(84)90089-9)
- Beyssac, O., Goffé, B., Chopin, C., Rouzaud, J.N., 2002. Raman spectra of carbonaceous material in metasediments: a new geothermometer. *Journal of Metamorphic Geology* 20, 859–871. <https://doi.org/10.1046/j.1525-1314.2002.00408.x>
- Bigeleisen, J., Mayer, M.G., 1947. Calculation of Equilibrium Constants for Isotope Exchange Reactions. *The Journal of Chemical Physics* 15, 261–267. <https://doi.org/10.1063/1.1746492>
- Blood, D.R., Lash, G.G., Larsen, D., Egenhoff, S.O., Fishman, N.S., 2015. Dynamic redox conditions in the Marcellus Shale as recorded by pyrite framboid size distributions. *The Geological Society of America Special Papers* 515, 153–168.
- Bond, D.P.G., Grasby, S.E., 2017. On the causes of mass extinctions. *Palaeogeography, Palaeoclimatology, Palaeoecology* 478, 3–29. <https://doi.org/10.1016/j.palaeo.2016.11.005>
- Bontognali, T.R.R., McKenzie, J.A., Warthmann, R.J., Vasconcelos, C., 2014. Microbially influenced formation of Mg-calcite and Ca-dolomite in the presence of exopolymeric substances produced by sulphate-reducing bacteria. *Terra Nova* 26, 72–77. <https://doi.org/10.1111/ter.12072>
- Bosak, T., Liang, B., Sim, M.S., Petroff, A.P., 2009. Morphological record of oxygenic photosynthesis in conical stromatolites.

Proceedings of the National Academy of Sciences 106, 10939–10943. <https://doi.org/10.1073/pnas.0900885106>

Bouton, A., Vennin, E., Pace, A., Bourillot, R., Dupraz, C., Thomazo, C., Brayard, A., Désaubliaux, G., Visscher, P.T., 2016. External controls on the distribution, fabrics and mineralization of modern microbial mats in a coastal hypersaline lagoon, Cayo Coco (Cuba). *Sedimentology* 63, 972–1016. <https://doi.org/10.1111/sed.12246>

Bowlin, E.M., Klaus, J.S., Foster, J.S., Andres, M.S., Custals, L., Reid, R.P., 2012. Environmental controls on microbial community cycling in modern marine stromatolites. *Sedimentary Geology* 263–264, 45–55. <https://doi.org/10.1016/j.sedgeo.2011.08.002>

Boye, M., van den Berg, C.M.G., de Jong, J.T.M., Leach, H., Croot, P., de Baar, H.J.W., 2001. Organic complexation of iron in the Southern Ocean. *Deep Sea Research Part I: Oceanographic Research Papers* 48, 1477–1497. [https://doi.org/10.1016/S0967-0637\(00\)00099-6](https://doi.org/10.1016/S0967-0637(00)00099-6)

Braga, J.C., Martin, J.M., Riding, R., 1995. Controls on Microbial Dome Fabric Development along a Carbonate-Siliciclastic Shelf-Basin Transect, Miocene, SE Spain. *PALAIOS* 10, 347. <https://doi.org/10.2307/3515160>

Bragg, W.L., 1914. The analysis of crystals by the X-ray spectrometer. *Proceedings of the Royal Society of London. Series A, Containing Papers of a Mathematical and Physical Character* 89, 468–489. <https://doi.org/10.1098/rspa.1914.0015>

Braissant, O., Decho, A.W., Dupraz, C., Glunk, C., Przekop, K.M., Visscher, P.T., 2007. Exopolymeric substances of sulfate-reducing bacteria: Interactions with calcium at alkaline pH and implication for formation of carbonate minerals. *Geobiology* 5, 401–411. <https://doi.org/10.1111/j.1472-4669.2007.00117.x>

Brasier, M., Green, O., Lindsay, J., McLoughlin, N., Steele, A., Stoakes, C., 2005. Critical testing of Earth's oldest putative fossil assemblage from the ~3.5Ga Apex chert, Chinaman Creek, Western Australia. *Precambrian Research* 140, 55–102. <https://doi.org/10.1016/j.precamres.2005.06.008>

Braterman, P.S., Cairns-Smith, A.G., Sloper, R.W., 1983. Photo-oxidation of hydrated Fe²⁺—significance for banded iron formations. *Nature* 303, 163–164. <https://doi.org/10.1038/303163a0>

Brocks, J.J., Logan, G.A., Buick, R., Summons, R.E., 1999. Archean Molecular Fossils and the Early Rise of Eukaryotes. *Science* (1979) 285, 1033–1036. <https://doi.org/10.1126/science.285.5430.1033>

Brocks, J.J., Buick, R., Summons, R.E., Logan, G.A., 2003. A reconstruction of Archean biological diversity based on molecular fossils from the 2.78 to 2.45 billion-year-old Mount Bruce Supergroup, Hamersley Basin, Western Australia. *Geochimica et Cosmochimica Acta* 67, 4321–4335. [https://doi.org/10.1016/S0016-7037\(03\)00209-6](https://doi.org/10.1016/S0016-7037(03)00209-6)

Brocks, J.J., 2011. Millimeter-scale concentration gradients of hydrocarbons in Archean shales: Live-oil escape or fingerprint of contamination? *Geochimica et Cosmochimica Acta* 75, 3196–3213. <https://doi.org/10.1016/j.gca.2011.03.014>

Buck, S.G., 1980. Stromatolite and ooid deposits within the fluvial and lacustrine sediments of the Precambrian Ventersdorp Supergroup of South Africa. *Precambrian Research* 12, 311–330. [https://doi.org/10.1016/0301-9268\(80\)90033-9](https://doi.org/10.1016/0301-9268(80)90033-9)

Buick, R., Dunlop, J.S.R., Groves, D.I., 1981. Stromatolite recognition in ancient rocks: an appraisal of irregularly laminated structures in an Early Archean chert-barite unit from North Pole, Western Australia. *Alcheringa: An Australasian Journal of Palaeontology* 5, 161–181. <https://doi.org/10.1080/03115518108566999>

Buick, R., 1984. Carbonaceous filaments from North Pole, Western Australia: Are they fossil bacteria in Archean stromatolites? *Precambrian Research* 24, 157–172. [https://doi.org/10.1016/0301-9268\(84\)90056-1](https://doi.org/10.1016/0301-9268(84)90056-1)

Buick, R., 1992. The Antiquity of Oxygenic Photosynthesis: Evidence from Stromatolites in Sulphate-Deficient Archean Lakes. *Science* (1979) 255, 74–77. <https://doi.org/10.1126/science.11536492>

Bullen, T.D., White, A.F., Childs, C.W., Vivit, D. v., Schulz, M.S., 2001. Demonstration of significant abiotic iron isotope fractionation in nature. *Geology* 29, 699. [https://doi.org/10.1130/0091-7613\(2001\)029<0699:DOSAII>2.0.CO;2](https://doi.org/10.1130/0091-7613(2001)029<0699:DOSAII>2.0.CO;2)

Burne, R. v., Moore, L.S., 1987. Microbialites: Organosedimentary Deposits of Benthic Microbial Communities. *PALAIOS* 2, 241.

<https://doi.org/10.2307/3514674>

- Button, A., 1973. The stratigraphic history of the Malmani dolomite in the eastern and north-eastern Transvaal.
- Byerly, G.R., Kröner, A., Lowe, D.R., Todt, W., Walsh, M.M., 1996. Prolonged magmatism and time constraints for sediment deposition in the early Archean Barberton greenstone belt: evidence from the Upper Onverwacht and Fig Tree groups. *Precambrian Research* 78, 125–138. [https://doi.org/10.1016/0301-9268\(95\)00073-9](https://doi.org/10.1016/0301-9268(95)00073-9)
- Cai, C., Leu, A.O., Xie, G.-J., Guo, J., Feng, Y., Zhao, J.-X., Tyson, G.W., Yuan, Z., Hu, S., 2018. A methanotrophic archaeon couples anaerobic oxidation of methane to Fe(III) reduction. *The ISME Journal* 12, 1929–1939. <https://doi.org/10.1038/s41396-018-0109-x>
- Canfield, D.E., des Marais, D.J., 1993. Biogeochemical cycles of carbon, sulfur, and free oxygen in a microbial mat. *Geochimica et Cosmochimica Acta* 57, 3971–3984. [https://doi.org/10.1016/0016-7037\(93\)90347-Y](https://doi.org/10.1016/0016-7037(93)90347-Y)
- Canfield, D.E., Habicht, K.S., Thamdrup, B., 2000. The Archean Sulfur Cycle and the Early History of Atmospheric Oxygen. *Science* (1979) 288, 658–661. <https://doi.org/10.1126/science.288.5466.658>
- Canfield, D.E., Erik Kristensen, Bo Thamdrup, 2005. The Iron and Manganese Cycles. pp. 269–312. [https://doi.org/10.1016/S0065-2881\(05\)48008-6](https://doi.org/10.1016/S0065-2881(05)48008-6)
- Cavalazzi, B., Barbieri, R., Ori, G.G., 2007. Chemosynthetic microbialites in the Devonian carbonate mounds of Hamar Laghdad (Anti-Atlas, Morocco). *Sedimentary Geology* 200, 73–88. <https://doi.org/10.1016/j.sedgeo.2007.03.002>
- Chambers, L.A., Trudinger, P.A., Smith, J.W., Burns, M.S., 1975. Fractionation of sulfur isotopes by continuous cultures of *Desulfovibrio desulfuricans*. *Canadian Journal of Microbiology* 21, 1602–1607. <https://doi.org/10.1139/m75-234>
- Chan, C.S., Emerson, D., Luther, G.W., 2016. The role of microaerophilic Fe-oxidizing micro-organisms in producing banded iron formations. *Geobiology* 14, 509–528. <https://doi.org/10.1111/gbi.12192>
- Cloud, P., 1973. Paleocological Significance of the Banded Iron-Formation. *Economic Geology* 68, 1135–1143. <https://doi.org/10.2113/gsecongeo.68.7.1135>
- Cloud, P., Morrison, K., 1979. On microbial contaminants, micropseudofossils, and the oldest records of life. *Precambrian Research* 9, 81–91. [https://doi.org/10.1016/0301-9268\(79\)90052-4](https://doi.org/10.1016/0301-9268(79)90052-4)
- Coates, J.D., Ellis, D.J., Gaw, C. v., Lovley, D.R., 1999. *Geothrix fermentans* gen. nov., sp. nov., a novel Fe(III)-reducing bacterium from a hydrocarbon-contaminated aquifer. *International Journal of Systematic and Evolutionary Microbiology* 49, 1615–1622. <https://doi.org/10.1099/00207713-49-4-1615>
- Coffey, J.M., Flannery, D.T., Walter, M.R., George, S.C., 2013. Sedimentology, stratigraphy and geochemistry of a stromatolite biofacies in the 2.72 Ga Tumbiana Formation, Fortescue Group, Western Australia. *Precambrian Research* 236, 282–296. <https://doi.org/10.1016/J.PRECAMRES.2013.07.021>
- Cohen, Y., Rosenberg, E., 1989. *Microbial mats: physiological ecology of benthic microbial communities*. ASM, Washington.
- Conway, T.M., John, S.G., 2014. Quantification of dissolved iron sources to the North Atlantic Ocean. *Nature* 511, 212–215. <https://doi.org/10.1038/nature13482>
- Cornell, R.M., Schwertmann, U., 2003. The iron oxides: structure, properties, reactions, occurrences, and uses. *Corrosion Reviews* 15, 533–559. <https://doi.org/10.1515/CORRREV.1997.15.3-4.533>
- Costello, A.M., Auman, A.J., Macalady, J.L., Scow, K.M., Lidstrom, M.E., 2002. Estimation of methanotroph abundance in a freshwater lake sediment. *Environmental Microbiology* 4, 443–450. <https://doi.org/10.1046/j.1462-2920.2002.00318.x>
- Couradeau, E., Benzerara, K., Gérard, E., Estève, I., Moreira, D., Tavera, R., López-García, P., 2013. Cyanobacterial calcification in modern microbialites at the submicrometer scale. *Biogeosciences* 10, 5255–5266. <https://doi.org/10.5194/bg-10-5255-2013>
- Croal, L.R., Johnson, C.M., Beard, B.L., Newman, D.K., 2004. Iron isotope fractionation by Fe(II)-oxidizing photoautotrophic bacteria.

Geochimica et Cosmochimica Acta 68, 1227–1242. <https://doi.org/10.1016/j.gca.2003.09.011>

Croal, L.R., Jiao, Y., Newman, D.K., 2007. The fox Operon from Rhodospirillum rubrum Promotes Phototrophic Fe(II) Oxidation in Rhodospirillum rubrum. *Journal of Bacteriology* 189, 1774–1782. <https://doi.org/10.1128/JB.01395-06>

Crosby, H.A., Johnson, C.M., Roden, E.E., Beard, B.L., 2005. Coupled Fe(II)–Fe(III) Electron and Atom Exchange as a Mechanism for Fe Isotope Fractionation during Dissimilatory Iron Oxide Reduction. *Environmental Science & Technology* 39, 6698–6704. <https://doi.org/10.1021/es0505346>

Crosby, H.A., Roden, E.E., Johnson, C.M., Beard, B.L., 2007. The mechanisms of iron isotope fractionation produced during dissimilatory Fe(III) reduction by *Shewanella putrefaciens* and *Geobacter sulfurreducens*. *Geobiology* 5, 169–189. <https://doi.org/10.1111/j.1472-4669.2007.00103.x>

Crowe, S.A., Paris, G., Katsev, S., Jones, C., Kim, S.-T., Zerkle, A.L., Nomosatryo, S., Fowle, D.A., Adkins, J.F., Sessions, A.L., Farquhar, J., Canfield, D.E., 2014. Sulfate was a trace constituent of Archean seawater. *Science* (1979) 346, 735–739. <https://doi.org/10.1126/science.1258966>

Cutting, R.S., Coker, V.S., Fellowes, J.W., Lloyd, J.R., Vaughan, D.J., 2009. Mineralogical and morphological constraints on the reduction of Fe(III) minerals by *Geobacter sulfurreducens*. *Geochimica et Cosmochimica Acta* 73, 4004–4022. <https://doi.org/10.1016/j.gca.2009.04.009>

Czaja, A.D., Johnson, C.M., Beard, B.L., Eigenbrode, J.L., Freeman, K.H., Yamaguchi, K.E., 2010. Iron and carbon isotope evidence for ecosystem and environmental diversity in the ~2.7 to 2.5 Ga Hamersley Province, Western Australia. *Earth and Planetary Science Letters* 292, 170–180. <https://doi.org/10.1016/j.epsl.2010.01.032>

Darroch, S.A.F., Smith, E.F., Laflamme, M., Erwin, D.H., 2018. Ediacaran Extinction and Cambrian Explosion. *Trends in Ecology & Evolution* 33, 653–663. <https://doi.org/10.1016/j.tree.2018.06.003>

Dauphas, N., van Zuilen, M., Wadhwa, M., Davis, A.M., Marty, B., Janney, P.E., 2004. Clues from Fe Isotope Variations on the Origin of Early Archean BIFs from Greenland. *Science* (1979) 306, 2077–2080. <https://doi.org/10.1126/science.1104639>

Dauphas, N., Rouxel, O., 2006. Mass spectrometry and natural variations of iron isotopes. *Mass Spectrometry Reviews* 25, 515–550. <https://doi.org/10.1002/mas.20078>

Dauphas, N., Cates, N.L., Mojzsis, S.J., Busigny, V., 2007. Identification of chemical sedimentary protoliths using iron isotopes in the > 3750 Ma Nuvvuagittuq supracrustal belt, Canada. *Earth and Planetary Science Letters* 254, 358–376. <https://doi.org/10.1016/J.EPSL.2006.11.042>

Dauphas, N., John, S.G., Rouxel, O., 2017. Iron Isotope Systematics. *Reviews in Mineralogy and Geochemistry* 82, 415–510. <https://doi.org/10.2138/rmg.2017.82.11>

Decraene, M.N., Marin-Carbonne, J., Bouvier, A.S., Villeneuve, J., Bouden, N., Luais, B., Deloule, E., 2021a. High-spatial-resolution measurements of iron isotopes in pyrites by secondary ion mass spectrometry using the new Hyperion-II radio-frequency plasma source. *Rapid Communications in Mass Spectrometry* 35. <https://doi.org/10.1002/rcm.8986>

Decraene, M.N., Marin-Carbonne, J., Thomazo, C., Olivier, N., Philippot, P., Strauss, H., Deloule, E., 2021b. Intense biogeochemical iron cycling revealed in Neoproterozoic micropyrrites from stromatolites. *Geochimica et Cosmochimica Acta* 312, 299–320. <https://doi.org/10.1016/j.gca.2021.07.020>

des Marais, D.J., D'Amelio, E., Farmer, J.D., Jørgensen, B.B., Palmisano, A.C., Pierson, B.K., 1992. Case study of a modern microbial mat-building community: the submerged cyanobacterial mats of Guerrero Negro, Baja California Sur, Mexico. *The Proterozoic biosphere: a multidisciplinary study* 325–333.

Dill, H., Kemper, E., 1990. Crystallographic and chemical variations during pyritization in the upper Barremian and lower Aptian dark claystones from the Lower Saxonian Basin (NW Germany). *Sedimentology* 37, 427–443. <https://doi.org/10.1111/j.1365-3091.1990.tb00145.x>

- Ding, H., Valentine, D.L., 2008. Methanotrophic bacteria occupy benthic microbial mats in shallow marine hydrocarbon seeps, Coal Oil Point, California. *Journal of Geophysical Research: Biogeosciences* 113, n/a-n/a. <https://doi.org/10.1029/2007JG000537>
- Dupraz, C., Visscher, P.T., Baumgartner, L.K., Reid, R.P., 2004. Microbe-mineral interactions: early carbonate precipitation in a hypersaline lake (Eleuthera Island, Bahamas). *Sedimentology* 51, 745–765. <https://doi.org/10.1111/j.1365-3091.2004.00649.x>
- Dupraz, C., Visscher, P.T., 2005. Microbial lithification in marine stromatolites and hypersaline mats. *Trends in Microbiology* 13, 429–438. <https://doi.org/10.1016/j.tim.2005.07.008>
- Dupraz, C., Reid, R.P., Braissant, O., Decho, A.W., Norman, R.S., Visscher, P.T., 2009. Processes of carbonate precipitation in modern microbial mats. *Earth-Science Reviews*. <https://doi.org/10.1016/j.earscirev.2008.10.005>
- Duverger, A., Berg, J.S., Busigny, V., Guyot, F., Bernard, S., Miot, J., 2020. Mechanisms of Pyrite Formation Promoted by Sulfate-Reducing Bacteria in Pure Culture. *Frontiers in Earth Science* 8. <https://doi.org/10.3389/feart.2020.588310>
- Edwards, K.J., Rogers, D.R., Wirsén, C.O., McCollom, T.M., 2003. Isolation and Characterization of Novel Psychrophilic, Neutrophilic, Fe-Oxidizing, Chemolithoautotrophic α - and γ - Proteobacteria from the Deep Sea. *Applied and Environmental Microbiology* 69, 2906–2913. <https://doi.org/10.1128/AEM.69.5.2906-2913.2003>
- Egger, M., Riedinger, N., Mogollón, J.M., Jørgensen, B.B., 2018. Global diffusive fluxes of methane in marine sediments. *Nature Geoscience* 11, 421–425. <https://doi.org/10.1038/s41561-018-0122-8>
- Ehrenreich, A., Widdel, F., 1994. Anaerobic oxidation of ferrous iron by purple bacteria, a new type of phototrophic metabolism. *Applied and Environmental Microbiology* 60, 4517–4526. <https://doi.org/10.1128/aem.60.12.4517-4526.1994>
- Eigenbrode, J.L., Freeman, K.H., Summons, R.E., 2008. Methylhopane biomarker hydrocarbons in Hamersley Province sediments provide evidence for Neoproterozoic aerobicity. *Earth and Planetary Science Letters* 273, 323–331. <https://doi.org/10.1016/j.epsl.2008.06.037>
- Emerson, D., Fleming, E.J., McBeth, J.M., 2010. Iron-Oxidizing Bacteria: An Environmental and Genomic Perspective. *Annual Review of Microbiology* 64, 561–583. <https://doi.org/10.1146/annurev.micro.112408.134208>
- Endo, Y., Ueno, Y., Aoyama, S., Danielache, S.O., 2016. Sulfur isotope fractionation by broadband UV radiation to optically thin SO₂ under reducing atmosphere. *Earth and Planetary Science Letters* 453, 9–22. <https://doi.org/10.1016/j.epsl.2016.07.057>
- Eriksson, P.G., Cheney, E.S., 1992. Evidence for the transition to an oxygen-rich atmosphere during the evolution of red beds in the lower proterozoic sequences of southern Africa. *Precambrian Research* 54, 257–269. [https://doi.org/10.1016/0301-9268\(92\)90073-W](https://doi.org/10.1016/0301-9268(92)90073-W)
- Ettwig, K.F., Zhu, B., Speth, D., Keltjens, J.T., Jetten, M.S.M., Kartal, B., 2016. Archaea catalyze iron-dependent anaerobic oxidation of methane. *Proceedings of the National Academy of Sciences* 113, 12792–12796. <https://doi.org/10.1073/pnas.1609534113>
- Farquhar, G.D., Ehleringer, J.R., Hubick, K.T., 1989. Carbon isotope discrimination and photosynthesis. *Annu Rev Plant Physiol Plant Mol Biol* 40, 503–537.
- Farquhar, J., Bao, H., Thiemens, M., 2000. Atmospheric Influence of Earth's Earliest Sulfur Cycle. *Science* (1979) 289, 756–758. <https://doi.org/10.1126/science.289.5480.756>
- Farquhar, J., Savarino, J., Airieau, S., Thiemens, M.H., 2001. Observation of wavelength-sensitive mass-independent sulfur isotope effects during SO₂ photolysis: Implications for the early atmosphere. *Journal of Geophysical Research: Planets* 106, 32829–32839. <https://doi.org/10.1029/2000JE001437>
- Farquhar, J., Wing, B.A., 2003. Multiple sulfur isotopes and the evolution of the atmosphere. *Earth and Planetary Science Letters* 213, 1–13. [https://doi.org/10.1016/S0012-821X\(03\)00296-6](https://doi.org/10.1016/S0012-821X(03)00296-6)
- Flannery, D.T., Allwood, A.C., van Kranendonk, M.J., 2016. Lacustrine facies dependence of highly ¹³C-depleted organic matter during the global age of methanotrophy. *Precambrian Research* 285, 216–241. <https://doi.org/10.1016/j.precamres.2016.09.021>
- Folk, R.L., 2005. Nannobacteria and the formation of framboidal pyrite: Textural evidence. *Journal of Earth System Science* 114,

369–374. <https://doi.org/10.1007/BF02702955>

Fralick, P., Riding, R., 2015. Steep Rock Lake: Sedimentology and geochemistry of an Archean carbonate platform. *Earth-Science Reviews* 151, 132–175. <https://doi.org/10.1016/j.earscirev.2015.10.006>

Franz, H.B., Danielache, S.O., Farquhar, J., Wing, B.A., 2013. Mass-independent fractionation of sulfur isotopes during broadband SO₂ photolysis: Comparison between ¹⁶O and ¹⁸O-rich SO₂. *Chemical Geology* 362, 56–65. <https://doi.org/10.1016/j.chemgeo.2013.07.021>

French, K.L., Hallmann, C., Hope, J.M., Schoon, P.L., Zumberge, J.A., Hoshino, Y., Peters, C.A., George, S.C., Love, G.D., Brocks, J.J., Buick, R., Summons, R.E., 2015. Reappraisal of hydrocarbon biomarkers in Archean rocks. *Proceedings of the National Academy of Sciences* 112, 5915–5920. <https://doi.org/10.1073/pnas.1419563112>

Friedrich, A.J., Nebel, O., Beard, B.L., Johnson, C.M., 2019. Iron isotope exchange and fractionation between hematite (α-Fe₂O₃) and aqueous Fe(II): A combined three-isotope and reversal-approach to equilibrium study. *Geochimica et Cosmochimica Acta* 245, 207–221. <https://doi.org/10.1016/j.gca.2018.10.033>

Fry, B., Cox, J., Gest, H., Hayes, J.M., 1986. Discrimination between ³⁴S and ³²S during bacterial metabolism of inorganic sulfur compounds. *Journal of Bacteriology* 165, 328–330. <https://doi.org/10.1128/jb.165.1.328-330.1986>

Fry, B., Gest, H., Hayes, J.M., 1988. ³⁴S/³²S fractionation in sulfur cycles catalyzed by anaerobic bacteria. *Applied and Environmental Microbiology* 54, 250–256. <https://doi.org/10.1128/aem.54.1.250-256.1988>

Fung, I.Y., Meyn, S.K., Tegen, I., Doney, S.C., John, J.G., Bishop, J.K.B., 2000. Iron supply and demand in the upper ocean. *Global Biogeochemical Cycles* 14, 281–295. <https://doi.org/10.1029/1999GB900059>

Gallagher, K.L., Kading, T.J., Braissant, O., Dupraz, C., Visscher, P.T., 2012. Inside the alkalinity engine: the role of electron donors in the organomineralization potential of sulfate-reducing bacteria. *Geobiology* 10, 518–530. <https://doi.org/10.1111/j.1472-4669.2012.00342.x>

Galvez, M.E., Beyssac, O., Martinez, I., Benzerara, K., Chaduteau, C., Malvoisin, B., Malavieille, J., 2013. Graphite formation by carbonate reduction during subduction. *Nature Geoscience* 6, 473–477. <https://doi.org/10.1038/ngeo1827>

Gandin, A., Wright, D.T., 2007. Evidence of vanished evaporites in Neoproterozoic carbonates of South Africa. *Geological Society, London, Special Publications* 285, 285–308. <https://doi.org/10.1144/SP285.17>

García Ruiz, J.M., Carnerup, A., Christy, A.G., Welham, N.J., Hyde, S.T., 2002. Morphology: An Ambiguous Indicator of Biogenicity. *Astrobiology* 2, 353–369. <https://doi.org/10.1089/153110702762027925>

Gerdes, G., Klenke, T., Noffke, N., 2001. Microbial signatures in peritidal siliciclastic sediments: a catalogue. *Sedimentology* 47, 279–308. <https://doi.org/10.1046/j.1365-3091.2000.00284.x>

Gerdes, G., 2007. Structures left by modern microbial mats in their host sediments. *Atlas of microbial mat features preserved within the siliciclastic rock record* 5–38.

Gerdes, G., 2010. What are microbial mats?. In *Microbial Mats* (pp. 3-25). Springer, Dordrecht. https://doi.org/10.1007/978-90-481-3799-2_1

Given, R.K., Wilkinson, H.B., 1985. Kinetic Control of Morphology, Composition, and Mineralogy of Abiotic Sedimentary Carbonates. *Journal of Sedimentary Research* Vol. 55. <https://doi.org/10.1306/212F862A-2B24-11D7-8648000102C1865D>

Gledhill, M., van den Berg, C.M.G., 1994. Determination of complexation of iron(III) with natural organic complexing ligands in seawater using cathodic stripping voltammetry. *Marine Chemistry* 47, 41–54. [https://doi.org/10.1016/0304-4203\(94\)90012-4](https://doi.org/10.1016/0304-4203(94)90012-4)

Golubic, S., 1983. *Stromatolites, Fossil and Recent: A Case History*, in: *Biomining and Biological Metal Accumulation*. Springer Netherlands, Dordrecht, pp. 313–326. https://doi.org/10.1007/978-94-009-7944-4_30

Gomes, M.L., Fike, D.A., Bergmann, K.D., Jones, C., Knoll, A.H., 2018. Environmental insights from high-resolution (SIMS) sulfur isotope analyses of sulfides in Proterozoic microbialites with diverse mat textures. *Geobiology* 16, 17–34. <https://doi.org/10.1111/gbi.12265>

- Grandstaff, D., 1980. Origin of uraniferous conglomerates at Elliot Lake, Canada and Witwatersrand, South Africa: Implications for oxygen in the Precambrian atmosphere. *Precambrian Research* 13, 1–26. [https://doi.org/10.1016/0301-9268\(80\)90056-X](https://doi.org/10.1016/0301-9268(80)90056-X)
- Grasby, S.E., Beauchamp, B., Embry, A., Sanei, H., 2013. Recurrent Early Triassic ocean anoxia. *Geology* 41, 175–178. <https://doi.org/10.1130/G33599.1>
- Gregory, D.D., Large, R.R., Halpin, J.A., Baturina, E.L., Lyons, T.W., Wu, S., Danyushevsky, L., Sack, P.J., Chappaz, A., Maslennikov, V. v., Bull, S.W., 2015. Trace Element Content of Sedimentary Pyrite in Black Shales. *Economic Geology* 110, 1389–1410. <https://doi.org/10.2113/econgeo.110.6.1389>
- Gregory, D.D., Large, R.R., Bath, A.B., Steadman, J.A., Wu, S., Danyushevsky, L., Bull, S.W., Holden, P., Ireland, T.R., 2016. Trace Element Content of Pyrite from the Kapaï Slate, St. Ives Gold District, Western Australia. *Economic Geology* 111, 1297–1320. <https://doi.org/10.2113/econgeo.111.6.1297>
- Gregory, D., Mukherjee, I., Olson, S.L., Large, R.R., Danyushevsky, L. v., Stepanov, A.S., Avila, J.N., Cliff, J., Ireland, T.R., Raiswell, R., Olin, P.H., Maslennikov, V. v., Lyons, T.W., 2019a. The formation mechanisms of sedimentary pyrite nodules determined by trace element and sulfur isotope microanalysis. *Geochimica et Cosmochimica Acta* 259, 53–68. <https://doi.org/10.1016/j.gca.2019.05.035>
- Gregory, D.D., Cracknell, M.J., Large, R.R., McGoldrick, P., Kuhn, S., Maslennikov, V. v., Baker, M.J., Fox, N., Belousov, I., Figueroa, M.C., Steadman, J.A., Fabris, A.J., Lyons, T.W., 2019b. Distinguishing Ore Deposit Type and Barren Sedimentary Pyrite Using Laser Ablation-Inductively Coupled Plasma-Mass Spectrometry Trace Element Data and Statistical Analysis of Large Data Sets. *Economic Geology* 114, 771–786. <https://doi.org/10.5382/econgeo.4654>
- Greinert, J., Bohrmann, G., Elvert, M., 2002. Stromatolitic fabric of authigenic carbonate crusts: result of anaerobic methane oxidation at cold seeps in 4,850 m water depth. *International Journal of Earth Sciences* 91, 698–711. <https://doi.org/10.1007/s00531-001-0244-9>
- Grotzinger, J.P., 1990. Geochemical model for Proterozoic stromatolite decline. *American Journal of Science* 290, 80–103.
- Grotzinger, J.P., Knoll, A.H., 1999. Stromatolites in precambrian carbonates: Evolutionary Mileposts or Environmental Dipsticks? *Annual Review of Earth and Planetary Sciences* 27, 313–358. <https://doi.org/10.1146/annurev.earth.27.1.313>
- Guilbaud, R., Butler, I.B., Ellam, R.M., 2011. Abiotic Pyrite Formation Produces a Large Fe Isotope Fractionation. *Science* (1979) 332, 1548–1551. <https://doi.org/10.1126/science.1202924>
- Gumsley, A.P., Chamberlain, K.R., Bleeker, W., Söderlund, U., de Kock, M.O., Larsson, E.R., Bekker, A., 2017. Timing and tempo of the Great Oxidation Event. *Proceedings of the National Academy of Sciences* 114, 1811–1816. <https://doi.org/10.1073/pnas.1608824114>
- Guy, B.M., Beukes, N.J., Gutzmer, J., 2010. Paleoenvironmental controls on the texture and chemical composition of pyrite from non-conglomeratic sedimentary rocks of the Mesoarchean Witwatersrand Supergroup, South Africa. *South African Journal of Geology* 113, 195–228. <https://doi.org/10.2113/gssajg.113.2.195>
- Haijjer, S.C.M., Lamers, L.P.M., Smolders, A.J.P., Jetten, M.S.M., Op den Camp, H.J.M., 2007. Iron Sulfide and Pyrite as Potential Electron Donors for Microbial Nitrate Reduction in Freshwater Wetlands. *Geomicrobiology Journal* 24, 391–401. <https://doi.org/10.1080/01490450701436489>
- Habicht, K.S., Gade, M., Thamdrup, B., Berg, P., Canfield, D.E., 2002. Calibration of Sulfate Levels in the Archean Ocean. *Science* (1979) 298, 2372–2374. <https://doi.org/10.1126/science.1078265>
- Halevy, I., Johnston, D.T., Schrag, D.P., 2010. Explaining the Structure of the Archean Mass-Independent Sulfur Isotope Record. *Science* (1979) 329, 204–207. <https://doi.org/10.1126/science.1190298>
- Halevy, I., 2013. Production, preservation, and biological processing of mass-independent sulfur isotope fractionation in the Archean surface environment. *Proc Natl Acad Sci U S A* 110, 17644–17649. <https://doi.org/10.1073/pnas.1213148110>
- Hansel, C.M., Benner, S.G., Nico, P., Fendorf, S., 2004. Structural constraints of ferric (hydr)oxides on dissimilatory iron reduction and

the fate of Fe(II). *Geochimica et Cosmochimica Acta* 68, 3217–3229. <https://doi.org/10.1016/J.GCA.2003.10.041>

Harrison, A.G., Thode, H.G., 1958. Mechanism of the bacterial reduction of sulphate from isotope fractionation studies. *Transactions of the Faraday Society* 54, 84. <https://doi.org/10.1039/tf9585400084>

Hayes, J.M., 1994. Global methanotrophy at the Archaean-Proterozoic transition. *Early Life on Earth* 220–236.

He, Z., Wang, J., Hu, J., Yu, H., Jetten, M.S.M., Liu, H., Cai, C., Liu, Y., Ren, H., Zhang, X., Hua, M., Xu, X., Zheng, P., Hu, B., 2019. Regulation of coastal methane sinks by a structured gradient of microbial methane oxidizers. *Environmental Pollution* 244, 228–237. <https://doi.org/10.1016/j.envpol.2018.10.057>

Heard, A.W., Dauphas, N., 2020. Constraints on the coevolution of oxic and sulfidic ocean iron sinks from archaean-paleoproterozoic iron isotope records. *Geology* 48, 358–362. <https://doi.org/10.1130/G46951.1>

Heimann, A., Johnson, C.M., Beard, B.L., Valley, J.W., Roden, E.E., Spicuzza, M.J., Beukes, N.J., 2010. Fe, C, and O isotope compositions of banded iron formation carbonates demonstrate a major role for dissimilatory iron reduction in ~2.5Ga marine environments. *Earth and Planetary Science Letters* 294, 8–18. <https://doi.org/10.1016/j.epsl.2010.02.015>

Heising, S., Richter, L., Ludwig, W., Schink, B., 1999. *Chlorobium ferrooxidans* sp. nov., a phototrophic green sulfur bacterium that oxidizes ferrous iron in coculture with a “*Geospirillum*” sp. strain. *Archives of Microbiology* 172, 116–124. <https://doi.org/10.1007/s002030050748>

Hicks, N., Dunlevey, J.N., Liu, K.W., 2011. A new stromatolite occurrence in the Nsuze Group, Pongola Supergroup of northern kwazulu-natal, South Africa. *South African Journal of Geology* 114, 195–200. <https://doi.org/10.2113/gssajg.114.2.195>

Hofmann, H.J., Grey, K., Hickman, A.H., Thorpe, R.I., 1999. Origin of 3.45 Ga coniform stromatolites in Warrawoona Group, Western Australia. *Geological Society of America Bulletin* 111, 1256–1262. [https://doi.org/10.1130/0016-7606\(1999\)111<1256:OOGCSI>2.3.CO;2](https://doi.org/10.1130/0016-7606(1999)111<1256:OOGCSI>2.3.CO;2)

Hofmann, H.J., 2000. Archaean Stromatolites as Microbial Archives, in: *Microbial Sediments*. Springer Berlin Heidelberg, Berlin, Heidelberg, pp. 315–327. https://doi.org/10.1007/978-3-662-04036-2_34

Holland, H.D., Lazar, B., McCaffrey, M., 1986. Evolution of the atmosphere and oceans. *Nature* 320, 27–33. <https://doi.org/10.1038/320027a0>

Huang, Y., Chen, Z.-Q., Algeo, T.J., Zhao, L., Baud, A., Bhat, G.M., Zhang, L., Guo, Z., 2019. Two-stage marine anoxia and biotic response during the Permian–Triassic transition in Kashmir, northern India: pyrite framboid evidence. *Global and Planetary Change* 172, 124–139. <https://doi.org/10.1016/j.gloplacha.2018.10.002>

Huerta-Diaz, M.A., Morse, J.W., 1992. Pyritization of trace metals in anoxic marine sediments. *Geochimica et Cosmochimica Acta* 56, 2681–2702. [https://doi.org/10.1016/0016-7037\(92\)90353-K](https://doi.org/10.1016/0016-7037(92)90353-K)

Ivarson, K.C., Hallberg, R.O., 1976. Formation of mackinawite by the microbial reduction of jarosite and its application to tidal sediments. *Geoderma* 16, 1–7. [https://doi.org/10.1016/0016-7061\(76\)90089-6](https://doi.org/10.1016/0016-7061(76)90089-6)

Jahn, B., Simonson, B.M., 1995. Carbonate PbPb ages of the Wittenoom Formation and Carawine Dolomite, Hamersley Basin, Western Australia (with implications for their correlation with the Transvaal Dolomite of South Africa). *Precambrian Research* 72, 247–261. [https://doi.org/10.1016/0301-9268\(94\)00092-6](https://doi.org/10.1016/0301-9268(94)00092-6)

Jahnert, R.J., Collins, L.B., 2013. Controls on microbial activity and tidal flat evolution in Shark Bay, Western Australia. *Sedimentology* 60, 1071–1099. <https://doi.org/10.1111/sed.12023>

Javaux, E.J., Marshall, C.P., Bekker, A., 2010. Organic-walled microfossils in 3.2-billion-year-old shallow-marine siliciclastic deposits. *Nature* 463, 934–938. <https://doi.org/10.1038/nature08793>

Javaux, E.J., 2019. Challenges in evidencing the earliest traces of life. *Nature* 572, 451–460. <https://doi.org/10.1038/s41586-019-1436-4>

Jeandel, C., Peucker-Ehrenbrink, B., Jones, M.T., Pearce, C.R., Oelkers, E.H., Godderis, Y., Lacan, F., Aumont, O., Arsouze, T.,

2011. Ocean margins: The missing term in oceanic element budgets? *Eos, Transactions American Geophysical Union* 92, 217–218. <https://doi.org/10.1029/2011EO260001>
- Jiao, Y., Kappler, A., Croal, L.R., Newman, D.K., 2005. Isolation and Characterization of a Genetically Tractable Photoautotrophic Fe(II)-Oxidizing Bacterium, *Rhodospseudomonas palustris* Strain TIE-1. *Applied and Environmental Microbiology* 71, 4487–4496. <https://doi.org/10.1128/AEM.71.8.4487-4496.2005>
- Jickells, T.D., An, Z.S., Andersen, K.K., Baker, A.R., Bergametti, G., Brooks, N., Cao, J.J., Boyd, P.W., Duce, R.A., Hunter, K.A., Kawahata, H., Kubilay, N., laRoche, J., Liss, P.S., Mahowald, N., Prospero, J.M., Ridgwell, A.J., Tegen, I., Torres, R., 2005. Global Iron Connections Between Desert Dust, Ocean Biogeochemistry, and Climate. *Science* (1979) 308, 67–71. <https://doi.org/10.1126/science.1105959>
- Johnson, K.S., Gordon, R.M., Coale, K.H., 1997. What controls dissolved iron concentrations in the world ocean? *Marine Chemistry* 57, 137–161. [https://doi.org/10.1016/S0304-4203\(97\)00043-1](https://doi.org/10.1016/S0304-4203(97)00043-1)
- Johnson, C.M., Skulan, J.L., Beard, B.L., Sun, H., Neelson, K.H., Braterman, P.S., 2002. Isotope fractionation between Fe(III) and Fe(II) in aqueous solutions. *Earth and Planetary Science Letters* 195, 141–153. [https://doi.org/10.1016/S0012-821X\(01\)00581-7](https://doi.org/10.1016/S0012-821X(01)00581-7)
- Johnson, C.M., Beard, B.L., Beukes, N.J., Klein, C., O’Leary, J.M., 2003. Ancient geochemical cycling in the Earth as inferred from Fe isotope studies of banded iron formations from the Transvaal Craton. *Contributions to Mineralogy and Petrology* 144, 523–547. <https://doi.org/10.1007/s00410-002-0418-x>
- Johnson, C.M., Beard, B.L., 2005. Biogeochemical Cycling of Iron Isotopes. *Science* (1979) 309, 1025–1027. <https://doi.org/10.1126/science.1112552>
- Johnson, C., Beard, B., Weyer, S., 2020. *Iron Geochemistry: An Isotope Perspective*. Springer International Publishing, Cham. <https://doi.org/10.1007/978-3-030-33828-2>
- Johnston, D.T., 2011. Multiple sulfur isotopes and the evolution of Earth’s surface sulfur cycle. *Earth-Science Reviews* 106, 161–183. <https://doi.org/10.1016/j.earscirev.2011.02.003>
- Jones, B., Renaut, R.W., 2007. Microstructural changes accompanying the opal-A to opal-CT transition: new evidence from the siliceous sinters of Geysir, Haukadalur, Iceland. *Sedimentology* 54, 921–948. <https://doi.org/10.1111/j.1365-3091.2007.00866.x>
- Jørgensen, B.B., 1982. Mineralization of organic matter in the sea bed—the role of sulphate reduction. *Nature* 296, 643–645. <https://doi.org/10.1038/296643a0>
- Jørgensen, B.B., Revsbech, N.P., Cohen, Y., 1983. Photosynthesis and structure of benthic microbial mats: Microelectrode and SEM studies of four cyanobacterial communities. *Limnology and Oceanography* 28, 1075–1093. <https://doi.org/10.4319/lo.1983.28.6.1075>
- Kalkowsky, E., 1908. Oolith und Stromatolith im norddeutschen Buntsandstein. *Zeitschrift der deutschen geologischen Gesellschaft* 68–125.
- Kamber, B.S., Bolhar, R., Webb, G.E., 2004. Geochemistry of late Archaean stromatolites from Zimbabwe: evidence for microbial life in restricted epicontinental seas. *Precambrian Research* 132, 379–399. <https://doi.org/10.1016/j.precamres.2004.03.006>
- Kamyshny, A., Goifman, A., Gun, J., Rizkov, D., Lev, O., 2004. Equilibrium Distribution of Polysulfide Ions in Aqueous Solutions at 25 °C: A New Approach for the Study of Polysulfides’ Equilibria. *Environmental Science & Technology* 38, 6633–6644. <https://doi.org/10.1021/es049514e>
- Kaplan, I.R., Rittenberg, S.C., 1964. Microbiological Fractionation of Sulphur Isotopes. *Journal of General Microbiology* 34, 195–212. <https://doi.org/10.1099/00221287-34-2-195>
- Kappler, A., Schink, B., Newman, D.K., 2005a. Fe(III) mineral formation and cell encrustation by the nitrate-dependent Fe(II)-oxidizer strain BoFeN1. *Geobiology* 3, 235–245. <https://doi.org/10.1111/j.1472-4669.2006.00056.x>
- Kappler, A., Pasquero, C., Konhauser, K., Newman, D., 2005b. Deposition of banded iron formations by anoxygenic phototrophic

Fe(II)-oxidizing bacteria. *Geology* 33, 865. <https://doi.org/10.1130/G21658.1>

Kappler, A., Johnson, C.M., Crosby, H.A., Beard, B.L., Newman, D.K., 2010. Evidence for equilibrium iron isotope fractionation by nitrate-reducing iron(II)-oxidizing bacteria. *Geochimica et Cosmochimica Acta* 74, 2826–2842. <https://doi.org/10.1016/j.gca.2010.02.017>

Kaufman, A.J., Johnston, D.T., Farquhar, J., Masterson, A.L., Lyons, T.W., Bates, S., Anbar, A.D., Arnold, G.L., Garvin, J., Buick, R., 2007. Late Archean Biospheric Oxygenation and Atmospheric Evolution. *Science* (1979) 317, 1900–1903. <https://doi.org/10.1126/science.1138700>

Kendall, B., Reinhard, C.T., Lyons, T.W., Kaufman, A.J., Poulton, S.W., Anbar, A.D., 2010. Pervasive oxygenation along late Archaean ocean margins. *Nature Geoscience* 3, 647–652. <https://doi.org/10.1038/ngeo942>

Klein, C., 2005. Some Precambrian banded iron-formations (BIFs) from around the world: Their age, geologic setting, mineralogy, metamorphism, geochemistry, and origins. *American Mineralogist* 90, 1473–1499. <https://doi.org/10.2138/am.2005.1871>

Knoll, A.H., Holland, H.D., 1995. Oxygen and Proterozoic evolution: an update. *Effects of Past Global Change on Life* 21–33.

Knoll, A.H., Javaux, E.J., Hewitt, D., Cohen, P., 2006. Eukaryotic organisms in Proterozoic oceans. *Philosophical Transactions of the Royal Society B: Biological Sciences* 361, 1023–1038. <https://doi.org/10.1098/rstb.2006.1843>

Kouketsu, Y., Nishiyama, T., Ikeda, T., Enami, M., 2014. Evaluation of residual pressure in an inclusion-host system using negative frequency shift of quartz Raman spectra. *American Mineralogist* 99, 433–442. <https://doi.org/10.2138/am.2014.4427>

Krekeler, D., Sigalevich, P., Teske, A., Cypionka, H., Cohen, Y., 1997. A sulfate-reducing bacterium from the oxic layer of a microbial mat from Solar Lake (Sinai), *Desulfovibrio oxycliniae* sp. nov. *Archives of Microbiology* 167, 369–375. <https://doi.org/10.1007/s002030050457>

Krumbein, W.E., 1979. Photolithotropic and chemoorganotrophic activity of bacteria and algae as related to beachrock formation and degradation (gulf of Aqaba, Sinai). *Geomicrobiology Journal* 1, 139–203. <https://doi.org/10.1080/01490457909377729>

Kullerud, G., Yoder, H.S., 1959. Pyrite stability relations in the Fe-S system. *Economic Geology* 54, 533–572. <https://doi.org/10.2113/gsecongeo.54.4.533>

Kunzmann, M., Gibson, T.M., Halverson, G.P., Hodgskiss, M.S.W., Bui, T.H., Carozza, D.A., Sperling, E.A., Poirier, A., Cox, G.M., Wing, B.A., 2017. Iron isotope biogeochemistry of Neoproterozoic marine shales. *Geochimica et Cosmochimica Acta* 209, 85–105. <https://doi.org/10.1016/j.gca.2017.04.003>

Large, R.R., Maslennikov, V. v., Robert, F., Danyushevsky, L. v., Chang, Z., 2007. Multistage Sedimentary and Metamorphic Origin of Pyrite and Gold in the Giant Sukhoi Log Deposit, Lena Gold Province, Russia. *Economic Geology* 102, 1233–1267. <https://doi.org/10.2113/gsecongeo.102.7.1233>

Large, R.R., Halpin, J.A., Danyushevsky, L. v., Maslennikov, V. v., Bull, S.W., Long, J.A., Gregory, D.D., Lounejeva, E., Lyons, T.W., Sack, P.J., McGoldrick, P.J., Calver, C.R., 2014. Trace element content of sedimentary pyrite as a new proxy for deep-time ocean–atmosphere evolution. *Earth and Planetary Science Letters* 389, 209–220. <https://doi.org/10.1016/j.epsl.2013.12.020>

Laufer, K., Niemeyer, A., Nikeleit, V., Halama, M., Byrne, J.M., Kappler, A., 2017. Physiological characterization of a halotolerant anoxygenic phototrophic Fe(II)-oxidizing green-sulfur bacterium isolated from a marine sediment. *FEMS Microbiology Ecology* 93. <https://doi.org/10.1093/femsec/fix054>

le Guillou, C., Bernard, S., de la Pena, F., le Brech, Y., 2018. XANES-Based Quantification of Carbon Functional Group Concentrations. *Analytical Chemistry* 90, 8379–8386. <https://doi.org/10.1021/acs.analchem.8b00689>

Leavitt, W.D., Halevy, I., Bradley, A.S., Johnston, D.T., 2013. Influence of sulfate reduction rates on the Phanerozoic sulfur isotope record. *Proceedings of the National Academy of Sciences* 110, 11244–11249. <https://doi.org/10.1073/pnas.1218874110>

Lepot, K., Benzerara, K., Brown, G.E., Philippot, P., 2008. Microbially influenced formation of 2,724-million-year-old stromatolites. *Nature Geoscience* 1, 118–121. <https://doi.org/10.1038/ngeo107>

- Lepot, K., Williford, K.H., Philippot, P., Thomazo, C., Ushikubo, T., Kitajima, K., Mostefaoui, S., Valley, J.W., 2019. Extreme ^{13}C -depletions and organic sulfur content argue for S-fueled anaerobic methane oxidation in 2.72 Ga old stromatolites. *Geochimica et Cosmochimica Acta* 244, 522–547. <https://doi.org/10.1016/j.gca.2018.10.014>
- Lepot, K., 2020. Signatures of early microbial life from the Archean (4 to 2.5 Ga) eon. *Earth-Science Reviews* 209, 103296. <https://doi.org/10.1016/J.EARSCIREV.2020.103296>
- Ley, R.E., Harris, J.K., Wilcox, J., Spear, J.R., Miller, S.R., Bebout, B.M., Maresca, J.A., Bryant, D.A., Sogin, M.L., Pace, N.R., 2006. Unexpected Diversity and Complexity of the Guerrero Negro Hypersaline Microbial Mat. *Applied and Environmental Microbiology* 72, 3685–3695. <https://doi.org/10.1128/AEM.72.5.3685-3695.2006>
- Liu, J., Pellerin, A., Antler, G., Kasten, S., Findlay, A.J., Dohrmann, I., Røy, H., Turchyn, A. v., Jørgensen, B.B., 2020. Early diagenesis of iron and sulfur in Bornholm Basin sediments: The role of near-surface pyrite formation. *Geochimica et Cosmochimica Acta* 284, 43–60. <https://doi.org/10.1016/j.gca.2020.06.003>
- Llirós, M., García-Armisen, T., Darchambeau, F., Morana, C., Triadó-Margarit, X., Inceoğlu, Ö., Borrego, C.M., Bouillon, S., Servais, P., Borges, A. v., Descy, J., Canfield, D.E., Crowe, S.A., 2015. Pelagic photoferrotrophy and iron cycling in a modern ferruginous basin. *Scientific Reports* 5, 13803. <https://doi.org/10.1038/srep13803>
- Lovley, D.R., 1987. Organic matter mineralization with the reduction of ferric iron: A review. *Geomicrobiology Journal* 5, 375–399. <https://doi.org/10.1080/01490458709385975>
- Lovley, D.R., Phillips, E.J.P., 1988. Novel Mode of Microbial Energy Metabolism: Organic Carbon Oxidation Coupled to Dissimilatory Reduction of Iron or Manganese. *Applied and Environmental Microbiology* 54, 1472–1480. <https://doi.org/10.1128/aem.54.6.1472-1480.1988>
- Lovley, D.R., Coates, J.D., Blunt-Harris, E.L., Phillips, E.J.P., Woodward, J.C., 1996. Humic substances as electron acceptors for microbial respiration. *Nature* 382, 445–448. <https://doi.org/10.1038/382445a0>
- Lowe, D.R., 1980. Stromatolites 3,400-Myr old from the Archean of Western Australia. *Nature* 284, 441–443. <https://doi.org/10.1038/284441a0>
- Lowe, D.R., 1994. Abiological origin of described stromatolites older than 3.2 Ga. *Geology* 22, 387. [https://doi.org/10.1130/0091-7613\(1994\)022<0387:AODSO>2.3.CO;2](https://doi.org/10.1130/0091-7613(1994)022<0387:AODSO>2.3.CO;2)
- Luther, G.W., 1991. Pyrite synthesis via polysulfide compounds. *Geochimica et Cosmochimica Acta* 55, 2839–2849. [https://doi.org/10.1016/0016-7037\(91\)90449-F](https://doi.org/10.1016/0016-7037(91)90449-F)
- Mahowald, N.M., Baker, A.R., Bergametti, G., Brooks, N., Duce, R.A., Jickells, T.D., Kubilay, N., Prospero, J.M., Tegen, I., 2005. Atmospheric global dust cycle and iron inputs to the ocean. *Global Biogeochemical Cycles* 19, n/a-n/a. <https://doi.org/10.1029/2004GB002402>
- Mansor, M., Fantle, M.S., 2019. A novel framework for interpreting pyrite-based Fe isotope records of the past. *Geochimica et Cosmochimica Acta* 253, 39–62. <https://doi.org/10.1016/j.gca.2019.03.017>
- Marin-Carbonne, J., Rollion-Bard, C., Bekker, A., Rouxel, O., Agangi, A., Cavalazzi, B., Wohlgemuth-Ueberwasser, C.C., Hofmann, A., McKeegan, K.D., 2014. Coupled Fe and S isotope variations in pyrite nodules from Archean shale. *Earth and Planetary Science Letters* 392, 67–79. <https://doi.org/10.1016/j.epsl.2014.02.009>
- Marin-Carbonne, J., Remusat, L., Sforza, M.C., Thomazo, C., Cartigny, P., Philippot, P., 2018. Sulfur isotope's signal of nanopyrates enclosed in 2.7 Ga stromatolitic organic remains reveal microbial sulfate reduction. *Geobiology* 16, 121–138. <https://doi.org/10.1111/gbi.12275>
- Marin-Carbonne, J., Busigny, V., Miot, J., Rollion-Bard, C., Muller, E., Drabon, N., Jacob, D., Pont, S., Robyr, M., Bontognali, T.R.R., François, C., Reynaud, S., van Zuilen, M., Philippot, P., 2020. In Situ Fe and S isotope analyses in pyrite from the 3.2 Ga Mendon Formation (Barberton Greenstone Belt, South Africa): Evidence for early microbial iron reduction. *Geobiology* 18, 306–325. <https://doi.org/10.1111/gbi.12385>

- Marin-Carbonne, J., Decraene, M.-N., Havas, R., Remusat, L., Pasquier, V., Alléon, J., Zeyen, N., Bouton, A., Bernard, S., Escrig, S., Olivier, N., Vennin, E., Meibom, A., Benzerara, K., Thomazo, C., 2022. Early precipitated micropyrith in microbialites: A time capsule of microbial sulfur cycling. *Geochemical Perspectives Letters* 21, 7–12. <https://doi.org/10.7185/geochemlet.2209>
- Marshall, K.C., 1992. Biofilms: an overview of bacterial adhesion, activity, and control at surfaces. *Am. Soc. Microbiol. News*, 58, 202–207.
- Masterson, A.L., Farquhar, J., Wing, B.A., 2011. Sulfur mass-independent fractionation patterns in the broadband UV photolysis of sulfur dioxide: Pressure and third body effects. *Earth and Planetary Science Letters* 306, 253–260. <https://doi.org/10.1016/j.epsl.2011.04.004>
- Matthews, A., Zhu, X.-K., O’Nions, K., 2001. Kinetic iron stable isotope fractionation between iron (-II) and (-III) complexes in solution. *Earth and Planetary Science Letters* 192, 81–92. [https://doi.org/10.1016/S0012-821X\(01\)00432-0](https://doi.org/10.1016/S0012-821X(01)00432-0)
- McAnena, A., 2011. The reactivity and isotope fractionation of Fe-bearing minerals during sulfidation: an experimental approach . (Doctoral dissertation, Newcastle University).
- McCollom, T., Seewald, J., 2006. Carbon isotope composition of organic compounds produced by abiotic synthesis under hydrothermal conditions. *Earth and Planetary Science Letters* 243, 74–84. <https://doi.org/10.1016/j.epsl.2006.01.027>
- McIntyre, T., Fralick, P., 2017. Sedimentology and geochemistry of the 2930 Ma Red Lake–Wallace Lake carbonate platform, Western Superior Province, Canada. *the Depositional Record* 3, 258–287.
- McLoughlin, N., Wilson, L.A., Brasier, M.D., 2008. Growth of synthetic stromatolites and wrinkle structures in the absence of microbes – implications for the early fossil record. *Geobiology* 6, 95–105. <https://doi.org/10.1111/j.1472-4669.2007.00141.x>
- Michel, D., Giuliani, G., Olivo, G.R., Marini, O.J., 1994. As growth banding and the presence of Au in pyrites from the Santa Rita gold vein deposit hosted in Proterozoic metasediments, Goiás State, Brazil. *Economic Geology* 89, 193–200. <https://doi.org/10.2113/gsecongeo.89.1.193>
- Minz, D., Fishbain, S., Green, S.J., Muyzer, G., Cohen, Y., Rittmann, B.E., Stahl, D.A., 1999. Unexpected Population Distribution in a Microbial Mat Community: Sulfate-Reducing Bacteria Localized to the Highly Oxidic Chemocline in Contrast to a Eukaryotic Preference for Anoxia. *Applied and Environmental Microbiology* 65, 4659–4665. <https://doi.org/10.1128/AEM.65.10.4659-4665.1999>
- Monty, Cl., 1977. Evolving Concepts on the Nature and the Ecological Significance of Stromatolites, in: *Fossil Algae*. Springer Berlin Heidelberg, Berlin, Heidelberg, pp. 15–35. https://doi.org/10.1007/978-3-642-66516-5_2
- Moore, J.K., Doney, S.C., Glover, D.M., Fung, I.Y., 2001. Iron cycling and nutrient-limitation patterns in surface waters of the World Ocean. *Deep Sea Research Part II: Topical Studies in Oceanography* 49, 463–507. [https://doi.org/10.1016/S0967-0645\(01\)00109-6](https://doi.org/10.1016/S0967-0645(01)00109-6)
- Moore, J.K., Doney, S.C., Lindsay, K., 2004. Upper ocean ecosystem dynamics and iron cycling in a global three-dimensional model. *Global Biogeochemical Cycles* 18, n/a-n/a. <https://doi.org/10.1029/2004GB002220>
- Morel, F., Milligan, A., Saito, M., 2006. Marine Bioinorganic chemistry: The role of trace metals in the oceanic cycles of major nutrients. *The Oceans and Marine Geochemistry* 6.
- Mori, J.F., Scott, J.J., Hager, K.W., Moyer, C.L., Küsel, K., Emerson, D., 2017. Physiological and ecological implications of an iron- or hydrogen-oxidizing member of the Zetaproteobacteria, *Ghiorsea bivora*, gen. nov., sp. nov. *The ISME Journal* 11, 2624–2636. <https://doi.org/10.1038/ismej.2017.132>
- Morse, J.W., Arakaki, T., 1993. Adsorption and coprecipitation of divalent metals with mackinawite (FeS). *Geochimica et Cosmochimica Acta* 57, 3635–3640. [https://doi.org/10.1016/0016-7037\(93\)90145-M](https://doi.org/10.1016/0016-7037(93)90145-M)
- Morse, J.W., Arvidson, R.S., Lüttge, A., 2007. Calcium Carbonate Formation and Dissolution. *Chemical Reviews* 107, 342–381. <https://doi.org/10.1021/cr050358j>
- Myers, C.R., Nealson, K.H., 1990. Respiration-linked proton translocation coupled to anaerobic reduction of manganese(IV) and

- iron(III) in *Shewanella putrefaciens* MR-1. *Journal of Bacteriology* 172, 6232–6238. <https://doi.org/10.1128/jb.172.11.6232-6238.1990>
- Neu, T.R., 1994. Biofilms and microbial mats. *Biostabilization of sediments* 9–15.
- Nims, C., Lafond, J., Alleon, J., Templeton, A.S., Cosmidis, J., 2021. Organic biomorphs may be better preserved than microorganisms in early Earth sediments. *Geology* 49, 629–634. <https://doi.org/10.1130/G48152.1>
- Noffke, N., Gerdes, G., Klenke, T., Krumbein, W.E., 2001. Microbially Induced Sedimentary Structures: A New Category within the Classification of Primary Sedimentary Structures. *Journal of Sedimentary Research* 71, 649–656. <https://doi.org/10.1306/2DC4095D-0E47-11D7-8643000102C1865D>
- Noffke, N., Gerdes, G., Klenke, T., 2003. Benthic cyanobacteria and their influence on the sedimentary dynamics of peritidal depositional systems (siliciclastic, evaporitic salty, and evaporitic carbonatic). *Earth-Science Reviews* 62, 163–176. [https://doi.org/10.1016/S0012-8252\(02\)00158-7](https://doi.org/10.1016/S0012-8252(02)00158-7)
- Noffke, A., Hensen, C., Sommer, S., Scholz, F., Bohlen, L., Mosch, T., Graco, M., Wallmann, K., 2012. Benthic iron and phosphorus fluxes across the Peruvian oxygen minimum zone. *Limnology and Oceanography* 57, 851–867. <https://doi.org/10.4319/lo.2012.57.3.0851>
- Noffke, N., Awramik, S.M., 2013. Stromatolites and MISS—Differences between relatives. *GSA Today* 23, 4–9. <https://doi.org/10.1130/GSATG187A.1>
- Nutman, A.P., Bennett, V.C., Friend, C.R.L., van Kranendonk, M.J., Chivas, A.R., 2016. Rapid emergence of life shown by discovery of 3,700-million-year-old microbial structures. *Nature* 537, 535–538. <https://doi.org/10.1038/nature19355>
- Nutman, A.P., Bennett, V.C., Friend, C.R.L., van Kranendonk, M.J., Rothacker, L., Chivas, A.R., 2019. Cross-examining Earth's oldest stromatolites: Seeing through the effects of heterogeneous deformation, metamorphism and metasomatism affecting Isua (Greenland) ~3700 Ma sedimentary rocks. *Precambrian Research* 331, 105347. <https://doi.org/10.1016/j.precamres.2019.105347>
- Oertel, J., Ellmer, K., Bohne, W., Röhrich, J., Tributsch, H., 1999. Growth of n-type polycrystalline pyrite (FeS₂) films by metalorganic chemical vapour deposition and their electrical characterization. *Journal of Crystal Growth* 198–199, 1205–1210. [https://doi.org/10.1016/S0022-0248\(98\)01074-4](https://doi.org/10.1016/S0022-0248(98)01074-4)
- Ono, S., Eigenbrode, J.L., Pavlov, A.A., Kharecha, P., Rumble, D., Kasting, J.F., Freeman, K.H., 2003. New insights into Archean sulfur cycle from mass-independent sulfur isotope records from the Hamersley Basin, Australia. *Earth and Planetary Science Letters* 213, 15–30. [https://doi.org/10.1016/S0012-821X\(03\)00295-4](https://doi.org/10.1016/S0012-821X(03)00295-4)
- Ono, S., Whitehill, A.R., Lyons, J.R., 2013. Contribution of isotopologue self-shielding to sulfur mass-independent fractionation during sulfur dioxide photolysis. *Journal of Geophysical Research: Atmospheres* 118, 2444–2454. <https://doi.org/10.1002/jgrd.50183>
- Ono, S., 2017. Photochemistry of Sulfur Dioxide and the Origin of Mass-Independent Isotope Fractionation in Earth's Atmosphere. *Annual Review of Earth and Planetary Sciences* 45, 301–329. <https://doi.org/10.1146/annurev-earth-060115-012324>
- Ostrander, C. M., Severmann, S., Gordon, G. W., Kendall, B., Lyons, T. W., Zheng, W., Moutusi, R., Anbar, A. D., 2022. Significance of ⁵⁶Fe depletions in late-Archean shales and pyrite. *Geochimica et Cosmochimica Acta*, 316, 87-104. <https://doi.org/10.1016/j.gca.2021.10.013>
- Papineau, D., She, Z., Dodd, M.S., 2017. Chemically-oscillating reactions during the diagenetic oxidation of organic matter and in the formation of granules in late Palaeoproterozoic chert from Lake Superior. *Chemical Geology* 470, 33–54. <https://doi.org/10.1016/j.chemgeo.2017.08.021>
- Pavlov, A.A., Kasting, J.F., 2002. Mass-Independent Fractionation of Sulfur Isotopes in Archean Sediments: Strong Evidence for an Anoxic Archean Atmosphere. *Astrobiology* 2, 27–41. <https://doi.org/10.1089/153110702753621321>
- Pellerin, A., Antler, G., Holm, S.A., Findlay, A.J., Crockford, P.W., Turchyn, A. v., Jørgensen, B.B., Finster, K., 2019. Large sulfur isotope fractionation by bacterial sulfide oxidation. *Science Advances* 5. <https://doi.org/10.1126/sciadv.aaw1480>
- Percak-Dennett, E.M., Beard, B.L., Xu, H., Konishi, H., Jonhson, C.M., Roden, E.E., 2011. Iron isotope fractionation during microbial

- dissimilatory iron oxide reduction in simulated Archean seawater. *Geobiology* 9, 205–220. <https://doi.org/10.1111/j.1472-4669.2011.00277.x>
- Philippot, P., van Kranendonk, M., van Zuilen, M., Lepot, K., Rividi, N., Teitler, Y., Thomazo, C., Blanc-Valleron, M.-M., Rouchy, J.-M., Grosch, E., de Wit, M., 2009. Early traces of life investigations in drilling Archean hydrothermal and sedimentary rocks of the Pilbara Craton, Western Australia and Barberton Greenstone Belt, South Africa. *Comptes Rendus Palevol* 8, 649–663. <https://doi.org/10.1016/j.crpv.2009.06.006>
- Picard, A., Gartman, A., Clarke, D.R., Girguis, P.R., 2018. Sulfate-reducing bacteria influence the nucleation and growth of mackinawite and greigite. *Geochimica et Cosmochimica Acta* 220, 367–384. <https://doi.org/10.1016/J.GCA.2017.10.006>
- Planavsky, N., Rouxel, O.J., Bekker, A., Hofmann, A., Little, C.T.S., Lyons, T.W., 2012. Iron isotope composition of some Archean and Proterozoic iron formations. *Geochimica et Cosmochimica Acta* 80, 158–169. <https://doi.org/10.1016/j.gca.2011.12.001>
- Polyakov, V.B., Clayton, R.N., Horita, J., Mineev, S.D., 2007. Equilibrium iron isotope fractionation factors of minerals: Reevaluation from the data of nuclear inelastic resonant X-ray scattering and Mössbauer spectroscopy. *Geochimica et Cosmochimica Acta* 71, 3833–3846. <https://doi.org/10.1016/j.gca.2007.05.019>
- Raiswell, R., Hawkings, J.R., Benning, L.G., Baker, A.R., Death, R., Albani, S., Mahowald, N., Krom, M.D., Poulton, S.W., Wadham, J., Tranter, M., 2016. Potentially bioavailable iron delivery by iceberg-hosted sediments and atmospheric dust to the polar oceans. *Biogeosciences* 13, 3887–3900. <https://doi.org/10.5194/bg-13-3887-2016>
- Rashby, S.E., Sessions, A.L., Summons, R.E., Newman, D.K., 2007. Biosynthesis of 2-methylbacteriohopanepolyols by an anoxygenic phototroph. *Proceedings of the National Academy of Sciences* 104, 15099–15104. <https://doi.org/10.1073/pnas.0704912104>
- Rasmussen, B., Buick, R., 1999. Redox state of the Archean atmosphere: Evidence from detrital heavy minerals in ca. 3250–2750 Ma sandstones from the Pilbara Craton, Australia. *Geology* 27, 115. [https://doi.org/10.1130/0091-7613\(1999\)027<0115:RSOTAA>2.3.CO;2](https://doi.org/10.1130/0091-7613(1999)027<0115:RSOTAA>2.3.CO;2)
- Rasmussen, B., Fletcher, I.R., Brocks, J.J., Kilburn, M.R., 2008. Reassessing the first appearance of eukaryotes and cyanobacteria. *Nature* 455, 1101–1104. <https://doi.org/10.1038/nature07381>
- Rees, C.E., 1973. A steady-state model for sulphur isotope fractionation in bacterial reduction processes. *Geochimica et Cosmochimica Acta* 37, 1141–1162. [https://doi.org/10.1016/0016-7037\(73\)90052-5](https://doi.org/10.1016/0016-7037(73)90052-5)
- Reid, R.P., Visscher, P.T., Decho, A.W., Stolz, J.F., Bebout, B.M., Dupraz, C., Macintyre, I.G., Paerl, H.W., Pinckney, J.L., Prufert-Bebout, L., Steppe, T.F., DesMarais, D.J., 2000. The role of microbes in accretion, lamination and early lithification of modern marine stromatolites. *Nature* 406, 989–992. <https://doi.org/10.1038/35023158>
- Reid, P.R., James, N.P., Macintyre, I.G., Dupraz, C.P., Burne, R. v., 2003. Shark Bay stromatolites: Microfabrics and reinterpretation of origins. *Facies* 49, 299. <https://doi.org/10.1007/s10347-003-0036-8>
- Rickard, D., 1969. The microbiological formation of iron sulphides. *Stockholm Contributions to Geology*, 20, 49–66.
- Rickard, D., Luther, G.W., 1997. Kinetics of pyrite formation by the H₂S oxidation of iron (II) monosulfide in aqueous solutions between 25 and 125°C: The mechanism. *Geochimica et Cosmochimica Acta* 61, 135–147. [https://doi.org/10.1016/S0016-7037\(96\)00322-5](https://doi.org/10.1016/S0016-7037(96)00322-5)
- Rickard, D., 2019. Sedimentary pyrite framboid size-frequency distributions: A meta-analysis. *Palaeogeography, Palaeoclimatology, Palaeoecology* 522, 62–75. <https://doi.org/10.1016/j.palaeo.2019.03.010>
- Riding, R., 1991. Classification of Microbial Carbonates, in: *Calcareous Algae and Stromatolites*. Springer Berlin Heidelberg, Berlin, Heidelberg, pp. 21–51. https://doi.org/10.1007/978-3-642-52335-9_2
- Riding, R., 2006. Microbial carbonate abundance compared with fluctuations in metazoan diversity over geological time. *Sedimentary Geology* 185, 229–238. <https://doi.org/10.1016/j.sedgeo.2005.12.015>
- Riding, R., 2008. Abiogenic, microbial and hybrid authigenic carbonate crusts: components of Precambrian stromatolites. *Geologia Croatica* 61, 73–103.
- Riding, R., 2011a. Microbialites, stromatolites, and thrombolites. *Encyclopedia of geobiology*.

- Riding, R., 2011b. The nature of stromatolites: 3,500 million years of history and a century of research. *Lecture Notes in Earth Sciences* 131, 29–74. https://doi.org/10.1007/978-3-642-10415-2_3
- Roddy, H.J., 1915. Concretions in streams formed by the agency of blue green algae and related plants. *Proc Am Philos Soc* 246–258.
- Roerdink, D.L., Mason, P.R.D., Farquhar, J., Reimer, T., 2012. Multiple sulfur isotopes in Paleoproterozoic barites identify an important role for microbial sulfate reduction in the early marine environment. *Earth and Planetary Science Letters* 331–332, 177–186. <https://doi.org/10.1016/j.epsl.2012.03.020>
- Rolison, J.M., Stirling, C.H., Middag, R., Gault-Ringold, M., George, E., Rijkenberg, M.J.A., 2018. Iron isotope fractionation during pyrite formation in a sulfidic Precambrian ocean analogue. *Earth and Planetary Science Letters* 488, 1–13. <https://doi.org/10.1016/j.epsl.2018.02.006>
- Rouxel, O.J., Bekker, A., Edwards, K.J., 2005. Iron Isotope Constraints on the Archean and Paleoproterozoic Ocean Redox State. *Science* (1979) 307, 1088–1091. <https://doi.org/10.1126/science.1105692>
- Rouxel, O., Toner, B.M., Manganini, S.J., German, C.R., 2016. Geochemistry and iron isotope systematics of hydrothermal plume fallout at East Pacific Rise 9°50'N. *Chemical Geology* 441, 212–234. <https://doi.org/10.1016/j.chemgeo.2016.08.027>
- Roychoudhury, A.N., Kostka, J.E., van Cappellen, P., 2003. Pyritization: a palaeoenvironmental and redox proxy reevaluated. *Estuarine, Coastal and Shelf Science* 57, 1183–1193. [https://doi.org/10.1016/S0272-7714\(03\)00058-1](https://doi.org/10.1016/S0272-7714(03)00058-1)
- Rust, G.W., 1935. Colloidal primary copper ores at Cornwall Mines, southeastern Missouri. *The Journal of Geology* 43, 398–426.
- Sagan, C., Chyba, C., 1997. The Early Faint Sun Paradox: Organic Shielding of Ultraviolet-Labile Greenhouse Gases. *Science* (1979) 276, 1217–1221. <https://doi.org/10.1126/science.276.5316.1217>
- Saitoh, M., Nabhan, S., Thomazo, C., Olivier, N., Moyon, J.-F., Ueno, Y., Marin-Carbonne, J., 2020. Multiple Sulfur Isotope Records of the 3.22 Ga Moodies Group, Barberton Greenstone Belt. *Geosciences (Basel)* 10, 145. <https://doi.org/10.3390/geosciences10040145>
- Sakurai, R., Ito, M., Ueno, Y., Kitajima, K., Maruyama, S., 2005. Facies architecture and sequence-stratigraphic features of the Tumbiana Formation in the Pilbara Craton, northwestern Australia: Implications for depositional environments of oxygenic stromatolites during the Late Archean. *Precambrian Research* 138, 255–273. <https://doi.org/10.1016/j.precamres.2005.05.008>
- Schauble, E.A., Rossman, G.R., Taylor, H.P., 2001. Theoretical estimates of equilibrium Fe-isotope fractionations from vibrational spectroscopy. *Geochimica et Cosmochimica Acta* 65, 2487–2497. [https://doi.org/10.1016/S0016-7037\(01\)00600-7](https://doi.org/10.1016/S0016-7037(01)00600-7)
- Schidlowski, M., 2001. Carbon isotopes as biogeochemical recorders of life over 3.8 Ga of Earth history: evolution of a concept. *Precambrian Research* 106, 117–134. [https://doi.org/10.1016/S0301-9268\(00\)00128-5](https://doi.org/10.1016/S0301-9268(00)00128-5)
- Schieber, J., 2002. Sedimentary pyrite: A window into the microbial past. *Geology* 30, 531. [https://doi.org/10.1130/0091-7613\(2002\)030<0531:SPAWIT>2.0.CO;2](https://doi.org/10.1130/0091-7613(2002)030<0531:SPAWIT>2.0.CO;2)
- Schoonen, M.A.A., Barnes, H.L., 1991. Reactions forming pyrite and marcasite from solution: I. Nucleation of FeS₂ below 100°C. *Geochimica et Cosmochimica Acta* 55, 1495–1504. [https://doi.org/10.1016/0016-7037\(91\)90122-L](https://doi.org/10.1016/0016-7037(91)90122-L)
- Schoonen, M.A., 2004. Mechanisms of sedimentary pyrite formation. *Geological Society of America Special Paper* 379, 117–134.
- Schopf, J.W., Packer, B.M., 1987. Early Archean (3.3-Billion to 3.5-Billion-Year-Old) Microfossils from Warrawoona Group, Australia. *Science* (1979) 237, 70–73. <https://doi.org/10.1126/science.11539686>
- Schopf, J.W., Kudryavtsev, A.B., Czaja, A.D., Tripathi, A.B., 2007. Evidence of Archean life: Stromatolites and microfossils. *Precambrian Research* 158, 141–155. <https://doi.org/10.1016/j.precamres.2007.04.009>
- Schwab, V., Spangenberg, Jorge.E., Grimalt, J.O., 2005. Chemical and carbon isotope evolution of hydrocarbons during prograde metamorphism from 100°C to 550°C: Case study in the Liassic black shale formation of Central Swiss Alps. *Geochimica et Cosmochimica Acta* 69, 1825–1840. <https://doi.org/10.1016/j.gca.2004.09.011>

- Semikhatov, M.A., Gebelein, C.D., Cloud, P., Awramik, S.M., Benmore, W.C., 1979. Stromatolite morphogenesis—progress and problems. *Canadian Journal of Earth Sciences* 16, 992–1015. <https://doi.org/10.1139/e79-088>
- Semikhatov, M.A., Raaben, M.E., 2000. Proterozoic Stromatolite Taxonomy and Biostratigraphy, in: *Microbial Sediments*. Springer Berlin Heidelberg, Berlin, Heidelberg, pp. 295–306. https://doi.org/10.1007/978-3-662-04036-2_32
- Severmann, S., Lyons, T.W., Anbar, A., McManus, J., Gordon, G., 2008. Modern iron isotope perspective on the benthic iron shuttle and the redox evolution of ancient oceans. *Geology* 36, 487–490. <https://doi.org/10.1130/G24670A.1>
- Severmann, S., McManus, J., Berelson, W.M., Hammond, D.E., 2010. The continental shelf benthic iron flux and its isotope composition. *Geochimica et Cosmochimica Acta* 74, 3984–4004. <https://doi.org/10.1016/j.gca.2010.04.022>
- Sforna, M.C., Philippot, P., Somogyi, A., van Zuilen, M.A., Medjoubi, K., Schoepp-Cothenet, B., Nitschke, W., Visscher, P.T., 2014. Evidence for arsenic metabolism and cycling by microorganisms 2.7 billion years ago. *Nature Geoscience* 7, 811–815. <https://doi.org/10.1038/ngeo2276>
- Sharma, M., Polizzotto, M., Anbar, A.D., 2001. Iron isotopes in hot springs along the Juan de Fuca Ridge. *Earth and Planetary Science Letters* 194, 39–51. [https://doi.org/10.1016/S0012-821X\(01\)00538-6](https://doi.org/10.1016/S0012-821X(01)00538-6)
- Sharp, Z., 2017. *Principles of stable isotope geochemistry*.
- Shen, Y., Buick, R., Canfield, D.E., 2001. Isotope evidence for microbial sulphate reduction in the early Archaean era. *Nature* 410, 77–81. <https://doi.org/10.1038/35065071>
- Shen, Y., Buick, R., 2004. The antiquity of microbial sulfate reduction. *Earth-Science Reviews* 64, 243–272. [https://doi.org/10.1016/S0012-8252\(03\)00054-0](https://doi.org/10.1016/S0012-8252(03)00054-0)
- Shen, Y., Farquhar, J., Zhang, H., Masterson, A., Zhang, T., Wing, B.A., 2011. Multiple S-isotope evidence for episodic shoaling of anoxic water during Late Permian mass extinction. *Nature Communications* 2, 210. <https://doi.org/10.1038/ncomms1217>
- Sim, M.S., Bosak, T., Ono, S., 2011a. Large Sulfur Isotope Fractionation Does Not Require Disproportionation. *Science (1979)* 333, 74–77. <https://doi.org/10.1126/science.1205103>
- Sim, M.S., Ono, S., Donovan, K., Templar, S.P., Bosak, T., 2011b. Effect of electron donors on the fractionation of sulfur isotopes by a marine *Desulfovibrio* sp. *Geochimica et Cosmochimica Acta* 75, 4244–4259. <https://doi.org/10.1016/j.gca.2011.05.021>
- Simonson, B.M., Schubel, K.A., Hassler, S.W., 1993. Carbonate sedimentology of the early Precambrian Hamersley Group of Western Australia. *Precambrian Research* 60, 287–335. [https://doi.org/10.1016/0301-9268\(93\)90052-4](https://doi.org/10.1016/0301-9268(93)90052-4)
- Sio, C.K., Roskosz, M., Dauphas, N., Bennett, N.R., Mock, T., Shahar, A., 2018. The isotope effect for Mg-Fe interdiffusion in olivine and its dependence on crystal orientation, composition and temperature. *Geochimica et Cosmochimica Acta* 239, 463–480. <https://doi.org/10.1016/j.gca.2018.06.024>
- Sivan, O., Schrag, D.P., Murray, R.W., 2007. Rates of methanogenesis and methanotrophy in deep-sea sediments. *Geobiology* 5, 141–151. <https://doi.org/10.1111/j.1472-4669.2007.00098.x>
- Sivan, O., Adler, M., Pearson, A., Gelman, F., Bar-Or, I., John, S.G., Eckert, W., 2011. Geochemical evidence for iron-mediated anaerobic oxidation of methane. *Limnology and Oceanography* 56, 1536–1544. <https://doi.org/10.4319/lo.2011.56.4.1536>
- Slotznick, S.P., Fischer, W.W., 2016. Examining Archean methanotrophy. *Earth and Planetary Science Letters* 441, 52–59. <https://doi.org/10.1016/j.epsl.2016.02.013>
- Statham, P., German, C., Connelly, D., 2005. Iron (II) distribution and oxidation kinetics in hydrothermal plumes at the Kairei and Edmond vent sites, Indian Ocean. *Earth and Planetary Science Letters* 236, 588–596. <https://doi.org/10.1016/j.epsl.2005.03.008>
- Stepanov, A.S., Danyushevsky, L. v., Large, R.R., Mukherjee, I., Zhukova, I.A., 2020. Deconvolution of the composition of fine-grained pyrite in sedimentary matrix by regression of time-resolved LA-ICP-MS data. *American Mineralogist* 105, 820–832. <https://doi.org/10.2138/>

- Stolz, J.F., 2000. Structure of Microbial Mats and Biofilms, in: *Microbial Sediments*. Springer Berlin Heidelberg, Berlin, Heidelberg, pp. 1–8. https://doi.org/10.1007/978-3-662-04036-2_1
- Straub, K.L., Benz, M., Schink, B., Widdel, F., 1996. Anaerobic, nitrate-dependent microbial oxidation of ferrous iron. *Applied and Environmental Microbiology* 62, 1458–1460. <https://doi.org/10.1128/aem.62.4.1458-1460.1996>
- Straub, K.L., Rainey, F.A., Widdel, F., 1999. *Rhodovulum iodosum* sp. nov. and *Rhodovulum robiginosum* sp. nov., two new marine phototrophic ferrous-iron-oxidizing purple bacteria. *International Journal of Systematic and Evolutionary Microbiology* 49, 729–735. <https://doi.org/10.1099/00207713-49-2-729>
- Stüeken, E.E., Buick, I R, Anderson, I R E, Baross, J.A., Planavsky, N.J., Lyons, I T W, 2017. Environmental niches and metabolic diversity in Neoproterozoic lakes. *Geobiology* 15. <https://doi.org/10.1111/gbi.12251>
- Sugitani, K., Mimura, K., Takeuchi, M., Yamaguchi, T., Suzuki, K., Senda, R., Asahara, Y., Wallis, S., van Kranendonk, M.J., 2015. A Paleoproterozoic coastal hydrothermal field inhabited by diverse microbial communities: the Strelley Pool Formation, Pilbara Craton, Western Australia. *Geobiology* 13, 522–545. <https://doi.org/10.1111/gbi.12150>
- Sumner, D.Y., Grotzinger, J.P., 2004. Implications for Neoproterozoic ocean chemistry from primary carbonate mineralogy of the Campbellrand-Malmani Platform, South Africa. *Sedimentology* 51, 1273–1299. <https://doi.org/10.1111/j.1365-3091.2004.00670.x>
- Sumner, D.Y., Beukes, N.J., 2006. Sequence Stratigraphic Development of the Neoproterozoic Transvaal carbonate platform, Kaapvaal Craton, South Africa. *South African Journal of Geology* 109, 11–22. <https://doi.org/10.2113/gssajg.109.1-2.11>
- Sun, D., Tong, J., Xiong, Y., Tian, L., Yin, H., 2012. Conodont biostratigraphy and evolution across Permian-Triassic boundary at Yangou Section, Leping, Jiangxi Province, South China. *Journal of Earth Science* 23, 311–325. <https://doi.org/10.1007/s12583-012-0255-4>
- Sverjensky, D.A., Lee, N., 2010. The Great Oxidation Event and Mineral Diversification. *Elements* 6, 31–36. <https://doi.org/10.2113/gselements.6.1.31>
- Tagliabue, A., Bopp, L., Dutay, J.-C., Bowie, A.R., Chever, F., Jean-Baptiste, P., Bucciarelli, E., Lannuzel, D., Remenyi, T., Sarthou, G., Aumont, O., Gehlen, M., Jeandel, C., 2010. Hydrothermal contribution to the oceanic dissolved iron inventory. *Nature Geoscience* 3, 252–256. <https://doi.org/10.1038/ngeo818>
- Taran, Y.A., Kliger, G.A., Sevastianov, V.S., 2007. Carbon isotope effects in the open-system Fischer–Tropsch synthesis. *Geochimica et Cosmochimica Acta* 71, 4474–4487. <https://doi.org/10.1016/j.gca.2007.06.057>
- Teng, F.-Z., Dauphas, N., Helz, R.T., Gao, S., Huang, S., 2011. Diffusion-driven magnesium and iron isotope fractionation in Hawaiian olivine. *Earth and Planetary Science Letters* 308, 317–324. <https://doi.org/10.1016/j.epsl.2011.06.003>
- Teutsch, N., von Gunten, U., Porcelli, D., Cirpka, O.A., Halliday, A.N., 2005. Adsorption as a cause for iron isotope fractionation in reduced groundwater. *Geochimica et Cosmochimica Acta* 69, 4175–4185. <https://doi.org/10.1016/j.gca.2005.04.007>
- Thiemens, M.H., 1999. Mass-Independent Isotope Effects in Planetary Atmospheres and the Early Solar System. *Science* (1979) 283, 341–345. <https://doi.org/10.1126/science.283.5400.341>
- Thomazo, C., Ader, M., Farquhar, J., Philippot, P., 2009. Methanotrophs regulated atmospheric sulfur isotope anomalies during the Mesoproterozoic (Tumbiana Formation, Western Australia). *Earth and Planetary Science Letters* 279, 65–75. <https://doi.org/10.1016/j.epsl.2008.12.036>
- Thomazo, C., Ader, M., Philippot, P., 2011. Extreme ¹⁵N-enrichments in 2.72-Gyr-old sediments: evidence for a turning point in the nitrogen cycle. *Geobiology* 9, 107–120. <https://doi.org/10.1111/j.1472-4669.2011.00271.x>
- Tor, J.M., Lovley, D.R., 2001. Anaerobic degradation of aromatic compounds coupled to Fe(III) reduction by *Ferroglobus placidus*. *Environmental Microbiology* 3, 281–287. <https://doi.org/10.1046/j.1462-2920.2001.00192.x>

- Ueno, Y., Ono, S., Rumble, D., Maruyama, S., 2008. Quadruple sulfur isotope analysis of ca. 3.5 Ga Dresser Formation: New evidence for microbial sulfate reduction in the early Archean. *Geochimica et Cosmochimica Acta* 72, 5675–5691. <https://doi.org/10.1016/j.gca.2008.08.026>
- Urey, H.C., 1947. The thermodynamic properties of isotope substances. *Journal of the Chemical Society (Resumed)* 562. <https://doi.org/10.1039/jr9470000562>
- van den Berg, C.M.G., 1995. Evidence for organic complexation of iron in seawater. *Marine Chemistry* 50, 139–157. [https://doi.org/10.1016/0304-4203\(95\)00032-M](https://doi.org/10.1016/0304-4203(95)00032-M)
- van Kranendonk, M.J., Webb, G.E., Kamber, B.S., 2003. Geological and trace element evidence for a marine sedimentary environment of deposition and biogenicity of 3.45 Ga stromatolitic carbonates in the Pilbara Craton, and support for a reducing Archaean ocean. *Geobiology* 1, 91–108. <https://doi.org/10.1046/j.1472-4669.2003.00014.x>
- van Zuilen, M.A., Lepland, A., Teranes, J., Finarelli, J., Wahlen, M., Arrhenius, G., 2003. Graphite and carbonates in the 3.8 Ga old Isua Supracrustal Belt, southern West Greenland. *Precambrian Research* 126, 331–348. [https://doi.org/10.1016/S0301-9268\(03\)00103-7](https://doi.org/10.1016/S0301-9268(03)00103-7)
- Vankranendonk, M., Philippot, P., Lepot, K., Bodorkos, S., Pirajno, F., 2008. Geological setting of Earth's oldest fossils in the ca. 3.5 Ga Dresser Formation, Pilbara Craton, Western Australia. *Precambrian Research* 167, 93–124. <https://doi.org/10.1016/j.precamres.2008.07.003>
- Ventura, G.T., Kenig, F., Reddy, C.M., Schieber, J., Frysinger, G.S., Nelson, R.K., Dinel, E., Gaines, R.B., Schaeffer, P., 2007. Molecular evidence of Late Archean archaea and the presence of a subsurface hydrothermal biosphere. *Proceedings of the National Academy of Sciences* 104, 14260–14265. <https://doi.org/10.1073/pnas.0610903104>
- Visscher, P. T., Reid, R. P., Bebout, B. M., Hoefft, S. E., Macintyre, I. G., & Thompson, J. A., 1998. Formation of lithified micritic laminae in modern marine stromatolites (Bahamas); the role of sulfur cycling. *American Mineralogist*, 83(11-12_Part_2), 1482-1493. <https://doi.org/10.2138/am-1998-11-1236>
- Visscher, P.T., Pamela Reid, R., Bebout, B.M., 2000. Microscale observations of sulfate reduction: Correlation of microbial activity with lithified micritic laminae in modern marine stromatolites. *Geology* 28, 919. [https://doi.org/10.1130/0091-7613\(2000\)28<919:MOOSRC>2.0.CO;2](https://doi.org/10.1130/0091-7613(2000)28<919:MOOSRC>2.0.CO;2)
- Visscher, P.T., Stolz, J.F., 2005. Microbial mats as bioreactors: populations, processes, and products. *Geobiology: Objectives, Concepts, Perspectives* 87–100. <https://doi.org/10.1016/B978-0-444-52019-7.50009-7>
- Wacey, D., 2010. Stromatolites in the ~3400 Ma Strelley Pool Formation, Western Australia: Examining Biogenicity from the Macro- to the Nano-Scale. *Astrobiology* 10, 381–395. <https://doi.org/10.1089/ast.2009.0423>
- Wacey, D., Kilburn, M.R., Saunders, M., Cliff, J., Brasier, M.D., 2011. Microfossils of sulphur-metabolizing cells in 3.4-billion-year-old rocks of Western Australia. *Nature Geoscience* 4, 698–702. <https://doi.org/10.1038/ngeo1238>
- Wacey, D., Saunders, M., Kong, C., 2018. Remarkably preserved tephra from the 3430 Ma Strelley Pool Formation, Western Australia: Implications for the interpretation of Precambrian microfossils. *Earth and Planetary Science Letters* 487, 33–43. <https://doi.org/10.1016/j.epsl.2018.01.021>
- Waeles, M., Baker, A.R., Jickells, T., Hoogewerff, J., 2007. Global dust teleconnections: aerosol iron solubility and stable isotope composition. *Environmental Chemistry* 4, 233. <https://doi.org/10.1071/EN07013>
- Walter, M.R., Buick, R., Dunlop, J.S.R., 1980. Stromatolites 3,400–3,500 Myr old from the North Pole area, Western Australia. *Nature* 284, 443–445. <https://doi.org/10.1038/284443a0>
- Walter, M.R., 1983. Archean stromatolites: evidence of the Earth's earliest benthos. *Earth's Earliest Biosphere* 187–213.
- Walter, M.R., Heys, G.R., 1985. Links between the rise of the metazoa and the decline of stromatolites. *Precambrian Research* 29, 149–174. [https://doi.org/10.1016/0301-9268\(85\)90066-X](https://doi.org/10.1016/0301-9268(85)90066-X)
- Wang, L., Shi, X., Jiang, G., 2012. Pyrite morphology and redox fluctuations recorded in the Ediacaran Doushantuo Formation.

Palaeogeography, Palaeoclimatology, Palaeoecology 333–334, 218–227. <https://doi.org/10.1016/j.palaeo.2012.03.033>

Ward, D.M., Bauld, J., Castenholz, R.W., Pierson, B.K., 1992. Modern phototrophic microbial mats: anoxygenic, intermittently oxygenic/anoxygenic, thermal, eukaryotic, and terrestrial. *The Proterozoic Biosphere: a Multidisciplinary Study* 309–324.

Welander, P. v., Summons, R.E., 2012. Discovery, taxonomic distribution, and phenotypic characterization of a gene required for 3-methylhopanoid production. *Proceedings of the National Academy of Sciences* 109, 12905–12910. <https://doi.org/10.1073/pnas.1208255109>

Welch, S.A., Beard, B.L., Johnson, C.M., Braterman, P.S., 2003. Kinetic and equilibrium Fe isotope fractionation between aqueous Fe(II) and Fe(III). *Geochimica et Cosmochimica Acta* 67, 4231–4250. [https://doi.org/10.1016/S0016-7037\(03\)00266-7](https://doi.org/10.1016/S0016-7037(03)00266-7)

Whitehill, A.R., Ono, S., 2012. Excitation band dependence of sulfur isotope mass-independent fractionation during photochemistry of sulfur dioxide using broadband light sources. *Geochimica et Cosmochimica Acta* 94, 238–253. <https://doi.org/10.1016/j.gca.2012.06.014>

Widdel, F., Schnell, S., Heising, S., Ehrenreich, A., Assmus, B., Schink, B., 1993. Ferrous iron oxidation by anoxygenic phototrophic bacteria. *Nature* 362, 834–836. <https://doi.org/10.1038/362834a0>

Wilkin, R.T., Barnes, H.L., 1996. Pyrite formation by reactions of iron monosulfides with dissolved inorganic and organic sulfur species. *Geochimica et Cosmochimica Acta* 60, 4167–4179. [https://doi.org/10.1016/S0016-7037\(97\)81466-4](https://doi.org/10.1016/S0016-7037(97)81466-4)

Wilkin, R.T., Barnes, H.L., Brantley, S.L., 1996. The size distribution of framboidal pyrite in modern sediments: An indicator of redox conditions. *Geochimica et Cosmochimica Acta* 60, 3897–3912. [https://doi.org/10.1016/0016-7037\(96\)00209-8](https://doi.org/10.1016/0016-7037(96)00209-8)

Wilkin, R.T., Barnes, H.L., 1997. Pyrite formation in an anoxic estuarine basin. *American Journal of Science* 297, 620–650. <https://doi.org/10.2475/ajs.297.6.620>

Wilks, M.E., Nisbet, E.g. 1988. Stratigraphy of the Steep Rock Group, northwest Ontario: a major Archaean unconformity and Archaean stromatolites. *Canadian Journal of Earth Sciences* 25, 370–391. <https://doi.org/10.1139/e88-040>

Williford, K.H., van Kranendonk, M.J., Ushikubo, T., Kozdon, R., Valley, J.W., 2011. Constraining atmospheric oxygen and seawater sulfate concentrations during Paleoproterozoic glaciation: In situ sulfur three-isotope microanalysis of pyrite from the Turee Creek Group, Western Australia. *Geochimica et Cosmochimica Acta* 75, 5686–5705. <https://doi.org/10.1016/j.gca.2011.07.010>

Williford, K.H., Ushikubo, T., Lepot, K., Kitajima, K., Hallmann, C., Spicuzza, M.J., Kozdon, R., Eigenbrode, J.L., Summons, R.E., Valley, J.W., 2016. Carbon and sulfur isotope signatures of ancient life and environment at the microbial scale: Neoproterozoic shales and carbonates. *Geobiology* 14, 105–128. <https://doi.org/10.1111/gbi.12163>

Witter, A.E., Luther, G.W., 1998. Variation in Fe-organic complexation with depth in the Northwestern Atlantic Ocean as determined using a kinetic approach. *Marine Chemistry* 62, 241–258. [https://doi.org/10.1016/S0304-4203\(98\)00044-9](https://doi.org/10.1016/S0304-4203(98)00044-9)

Wright, D.T., Altermann, W., 2000. Microfacies development in Late Archaean stromatolites and oolites of the Ghaap Group of South Africa. *Geological Society, London, Special Publications* 178, 51–70. <https://doi.org/10.1144/GSL.SP.2000.178.01.05>

Wright, D.T., Wacey, D., 2005. Precipitation of dolomite using sulphate-reducing bacteria from the Coorong Region, South Australia: significance and implications. *Sedimentology* 52, 987–1008. <https://doi.org/10.1111/j.1365-3091.2005.00732.x>

Wu, L., Beard, B.L., Roden, E.E., Johnson, C.M., 2011. Stable Iron Isotope Fractionation Between Aqueous Fe(II) and Hydrated Ferric Oxide. *Environmental Science & Technology* 45, 1847–1852. <https://doi.org/10.1021/es103171x>

Wu, L., Percak-Dennett, E.M., Beard, B.L., Roden, E.E., Johnson, C.M., 2012. Stable iron isotope fractionation between aqueous Fe(II) and model Archean ocean Fe–Si coprecipitates and implications for iron isotope variations in the ancient rock record. *Geochimica et Cosmochimica Acta* 84, 14–28. <https://doi.org/10.1016/j.gca.2012.01.007>

Yamaguchi, K.E., Johnson, C.M., Beard, B.L., Ohmoto, H., 2005. Biogeochemical cycling of iron in the Archean–Paleoproterozoic Earth: Constraints from iron isotope variations in sedimentary rocks from the Kaapvaal and Pilbara Cratons. *Chemical Geology* 218, 135–169. <https://doi.org/10.1016/j.chemgeo.2005.01.020>

Yoshiya, K., Nishizawa, M., Sawaki, Y., Ueno, Y., Komiya, T., Yamada, K., Yoshida, N., Hirata, T., Wada, H., Maruyama, S., 2012. In situ iron isotope analyses of pyrite and organic carbon isotope ratios in the Fortescue Group: Metabolic variations of a Late Archean ecosystem. *Precambrian Research* 212–213, 169–193. <https://doi.org/10.1016/j.precamres.2012.05.003>

Zawaski, M.J., Kelly, N.M., Orlandini, O.F., Nichols, C.I.O., Allwood, A.C., Mojzsis, S.J., 2020. Reappraisal of purported ca. 3.7 Ga stromatolites from the Isua Supracrustal Belt (West Greenland) from detailed chemical and structural analysis. *Earth and Planetary Science Letters* 545, 116409. <https://doi.org/10.1016/j.epsl.2020.116409>

Zerkle, A.L., Farquhar, J., Johnston, D.T., Cox, R.P., Canfield, D.E., 2009. Fractionation of multiple sulfur isotopes during phototrophic oxidation of sulfide and elemental sulfur by a green sulfur bacterium. *Geochimica et Cosmochimica Acta* 73, 291–306. <https://doi.org/10.1016/j.gca.2008.10.027>

Zerkle, A.L., Claire, M.W., di Rocco, T., Grassineau, N.V., Nisbet, E.g. Sun, R., Yin, R., 2021. Sulfur and mercury MIF suggest volcanic contributions to Earth's atmosphere at 2.7 Ga. *Geochemical Perspectives Letters* 48–52. <https://doi.org/10.7185/geochemlet.2124>

Zeyen, N., Benzerara, K., Li, J., Groleau, A., Balan, E., Robert, J.-L., Estève, I., Tavera, R., Moreira, D., López-García, P., 2015. Formation of low-T hydrated silicates in modern microbialites from Mexico and implications for microbial fossilization. *Frontiers in Earth Science* 3. <https://doi.org/10.3389/feart.2015.00064>

Zhang, L., Zeng, Q., Liu, X., Chen, P., Guo, X., Ma, L. Z., Dong, H., Huang, Y., 2019. Iron reduction by diverse actinobacteria under oxic and pH-neutral conditions and the formation of secondary minerals. *Chemical Geology*, 525, 390-399. <https://doi.org/10.1016/j.chemgeo.2019.07.038>

Zhelezinskaia, I., Kaufman, A.J., Farquhar, J., Cliff, J., 2014. Large sulfur isotope fractionations associated with Neoproterozoic microbial sulfate reduction. *Science* (1979) 346, 742–744. <https://doi.org/10.1126/science.1256211>

Zhou, C., Jiang, S.-Y., 2009. Palaeoceanographic redox environments for the lower Cambrian Hetang Formation in South China: Evidence from pyrite framboids, redox sensitive trace elements, and sponge biota occurrence. *Palaeogeography, Palaeoclimatology, Palaeoecology* 271, 279–286. <https://doi.org/10.1016/j.palaeo.2008.10.024>

CHAPTER 2.

STUDIED SAMPLES, GEOLOGICAL CONTEXTS, AND METHODS

In this work, samples were characterized using petrographic observations and high spatial resolution geochemical measurements. Detailed descriptions of samples will be presented in chapters below, although an overview of the studied samples is given here. This chapter is divided in two parts:

(1) A brief description of studied samples, including the geological context, lithology, mineralogy, and pyrite description. Here I detail the field observations made in September 2019 in the Barberton area, South Africa.

(2) Description of analytical techniques used, i.e. scanning electron microscopy (SEM), Raman spectroscopy, electron probe micro-analyses (EPMA) and secondary ion mass spectrometry (SIMS). In the different chapters of this thesis, other analytical methods were described, such as Fe speciation, bulk rock S isotope and major and trace element measurements. These techniques were used in collaboration with other laboratories (Biogeosciences, Dijon, France; SARM, CRPG Nancy, France; Institut für Geologie und Paläontologie, Münster, Germany). In addition to present traditional methods for petrographic observations and characterization, the state-of-the-art Fe isotope measurements by SIMS are presented in detail here. These measurements are specifically customized for studying micropyrates and hence deserve a separate chapter. This analytical protocol was published in *Rapid Communications in Mass Spectrometry* (Decraene et al., 2021).

1. Studied samples

We focused on four major periods characterized either by strongly different redox conditions, i.e. Archean and Modern, or by an abrupt shift of global redox conditions, i.e. pre-GOE and after the Permian-Triassic crisis. Studied samples are microbialites, mostly stromatolites, or sediments with non-mineralizing Microbial Induced Sedimentary Structures (hereafter MISS) enclosing micrometric pyrite (**Fig. 2.1**). Because pyrite is the object of interest, samples were selected for their high pyrite contents, determined either by observation of thin sections or through high bulk sulfur content. Some key features for each sample are summarized below (**Tables 2.1 to 2.4**) and additional details are available in the following chapters. Pyrite grains have a wide diversity of morphologies, sizes, grain organizations and post-depositional alteration features (**Fig. 2.1**). From the oldest to the youngest, I studied samples from the five localities listed in **sections 1.1 to 1.4**.

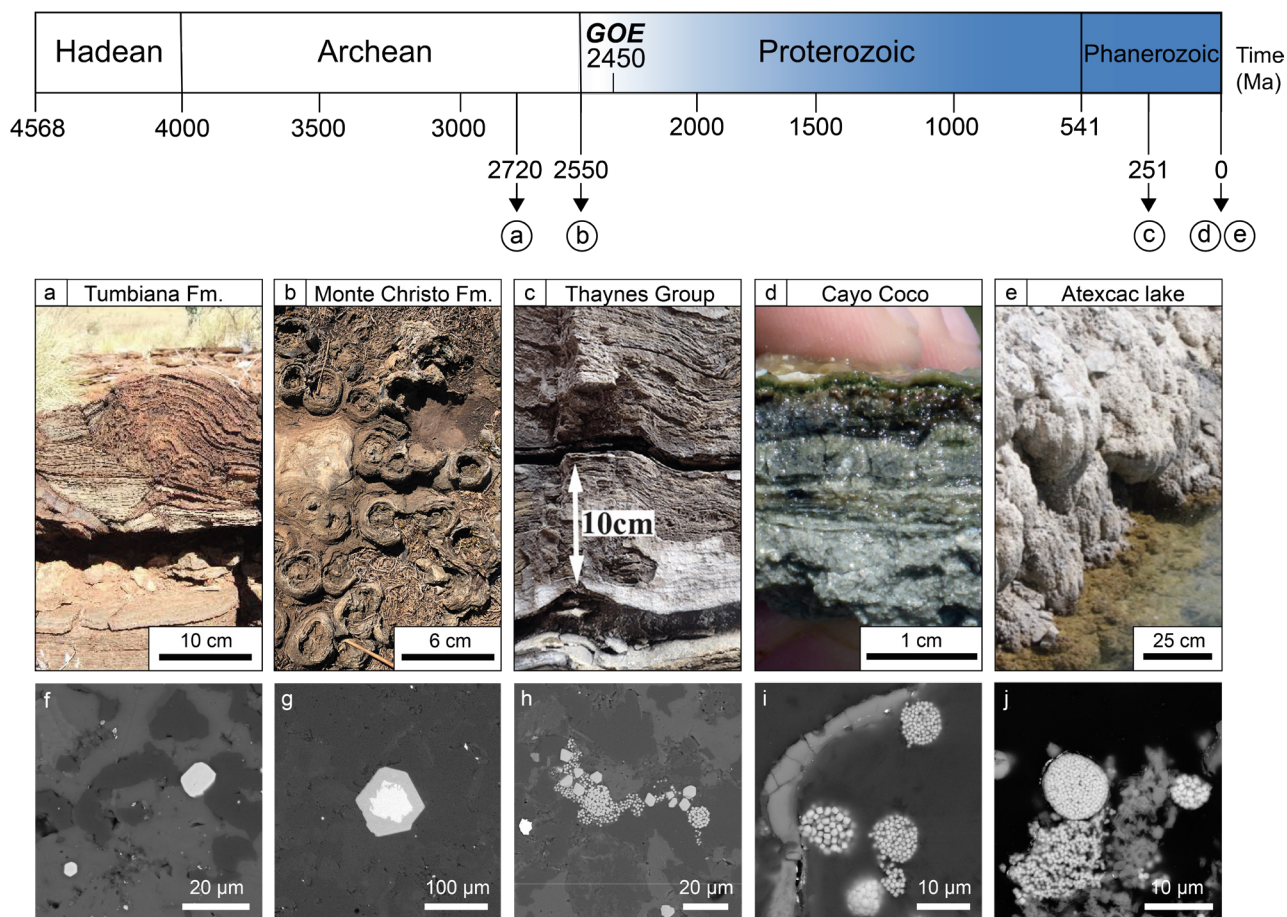


Figure 2. 1: Overview of the sample collection. Representative images of studied rocks in hand sample (in color; upper panels) along with the representative images of pyrite grains as seen in BSE images (greyscale; lower panels) from: a) Domal stromatolites from the 2.72 Ga Tumbiana Fm, Australia (Lepot et al., 2008) containing euhedral pyrite grains (f); b) Chertified concretionary domes from the 2.55 Ga Upper Monte Christo Fm (Malmani-Campbellrand carbonate platform), South Africa including euhedral pyrite with Fe(III)-oxide rim (g); c) Undulated microbial laminae in siltstones from the 251 Ma Lower Weber Canyon sedimentary section, United-States (Grosjean et al., 2018) with framboid and euhedral pyrite grains (h); d) Mineralizing microbial mat from Cayo Coco lagoon, Cuba (Bouton et al., 2020) including framboid pyrite grains (i); e) Microbialites from Atexcac lake (Mexico) developing on the crater wall (Zeyen et al., 2015), enclosing framboidal pyrite grains (j).

All samples represent a wide range of depositional environments and physico-chemical conditions (e.g. pH, temperature, water column depth and oxygenation state, iron, sulfur and organic matter concentrations and sources). Briefly, the sample collection includes:

- Stromatolites from the 2.7 Ga Tumbiana Formation that likely developed under fully anoxic conditions (Farquhar *et al.*, 2000; Thomazo *et al.*, 2009), and stromatolites from the 2.5 Ga Malmani Subgroup deposited slightly before the Great Oxidation Event (~2.4 Ga), depicting the time interval when atmosphere and oceanic evolved towards oxic conditions (Farquhar *et al.*, 2000; Pavlov and Kasting, 2002; Bekker *et al.*, 2004).

- MISS from the 251 Ma Thaynes Group in Utah (USA) deposited in the aftermath of the end Permian mass extinction event (Olivier *et al.*, 2014; Grosjean *et al.*, 2018), a period of spreading oceanic anoxia (Algeo *et al.*, 2011; Song *et al.*, 2019).

- Modern microbialites from Cuba and Mexico formed under oxygenated conditions in lagoonal (Bouton *et al.*, 2016; Pace *et al.*, 2018) and lacustrine (Zeyen *et al.*, 2015, 2017) settings, respectively.

1.1. Stromatolites from the Tumbiana Formation (2.7 Ga, Western Australia)

The Tumbiana Formation (Fm) is a succession of volcanic and sedimentary rocks deposited in the middle of the Fortescue Group of the Archean Pilbara Craton in Western Australia (Fig. 2.2a). The Tumbiana Fm was dated at 2724 ± 5 Ma by U-Pb zircons geochronology of ash layers (Blake *et al.*, 2004). This formation is covered by the basaltic flows of the Maddina Fm and rests on the aerial basalt flows of the Kylenea Fm (Thorne and Trendall, 2001). Those volcano-sedimentary deposits experienced a green-schist facies metamorphism (prehnite-pumpellyite)

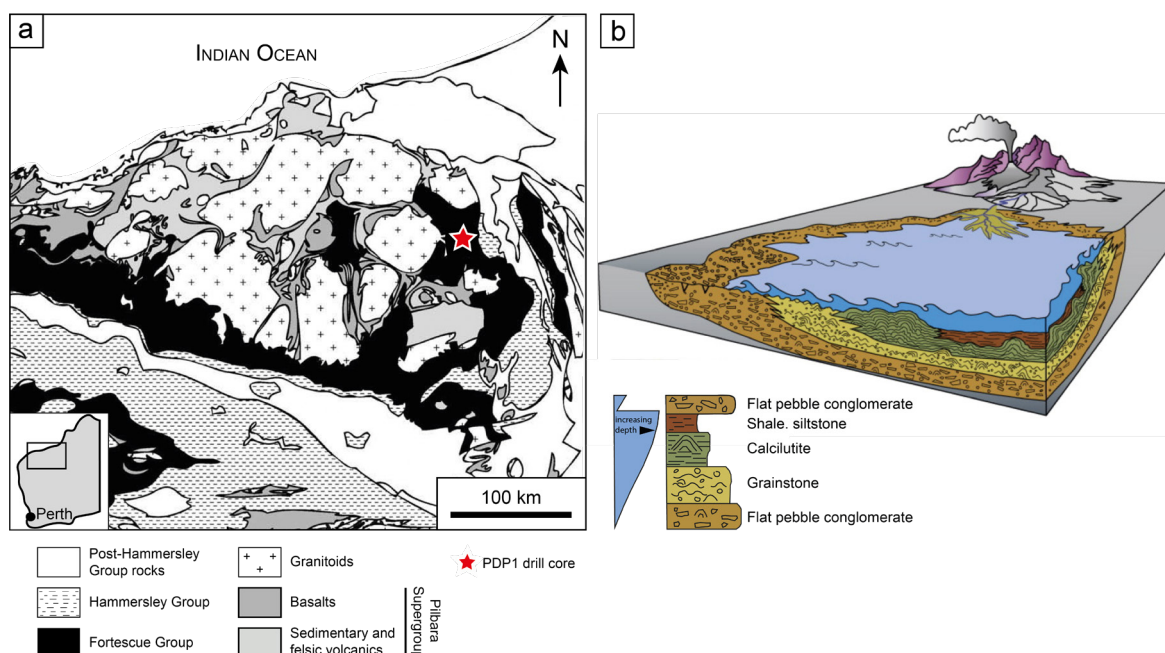


Figure 2. 2: Geological context of the Tumbiana Fm. a) Geological map of the Pilbara Craton (Western Australia) and location of the PDP1 drill core. Modified after Thomazo *et al.* (2009). b) Depositional model with lithofacies association of the Meentheena Member, from Awramik and Buchheim (2009).

with a peak of temperature lower than 300°C (Lepot *et al.*, 2008). This low-grade metamorphism was dated to about 2.2 Ga (Rasmussen *et al.*, 2001). Two members are identified in the Tumbiana Fm, the basal Mingah Member composed of volcanic tuff layers and accretionary lapilli, and the upper Meentheena Member made of carbonated stromatolite intervals, sandstones, volcanic tuff and black shales. The depositional environment of the Tumbiana Fm is interpreted as shallow marine (Packer, 1990; Sakurai *et al.*, 2005) or lacustrine (Fig. 2.2b; Buick, 1992; Awramik and Buchheim, 2009). Arguments for a marine origin include a lateral continuity of lithofacies, thickening of the formation from north to south with a typical sedimentary basin geometry, herringbone cross-stratification, and homogenous carbon isotope compositions of carbonates throughout the formation (Thorne and Trendall, 2001; Sakurai *et al.*, 2005). However, other lines of evidence support a lacustrine origin. These include presence of alluvial fan and fluvial sediments, symmetrical ripples instead of current ripples, rare occurrences of dolomite, vertical and lateral facial variations and REE patterns compatible with a lacustrine depositional environment (Buick, 1992; Bolhar and van Kranendonk, 2007; Awramik and Buchheim, 2009). My work focused on four carbonated stromatolite samples from the PDP1 drill core (Philippot *et al.*, 2009) of the Tumbiana Fm (Meentheena locality). The drill core sampled a thick stromatolite interval, representing one of the oldest undisputed Archean biogenic stromatolite deposits. Samples were chosen because of the preservation of laminated domal structures at microscale and an exceptional lamina diversity, but also because they were petrographically and geochemically characterized in previous studies ($\delta^{13}\text{C}$ on organic and carbonate, $\delta^{15}\text{N}$, $\delta^{34}\text{S}$; Lepot *et al.*, 2009, 2019; Thomazo *et al.*, 2009, 2011; Sforza *et al.*, 2014; Marin-Carbonne *et al.*, 2018). An exceptional diversity of pyrite-bearing laminae is described in these four samples as detailed in Table 2.1 and in chapter 5. Pyrite grains from these samples larger than 5 μm were analyzed for Fe isotopes by SIMS at CRPG (Nancy, France) and SwissSIMS (University of Lausanne, Switzerland; see details in section 2).

Table 2. 1: Summary of main characteristics of the Tumbiana Fm and studied samples.

Tumbiana Formation, Fortescue Group				
# sample	GIS67.8	GIS68.1	GIS68.9	GIS70.8
Pyrite observation	Disseminated	Disseminated and forming laminae (type 2)	Disseminated and forming laminae (type 2)	Disseminated
Size	[~100 nm- 20 µm]	[~100 nm- 60 µm]	[~100 nm- 20 µm]	[5 µm- 20 µm]
Morphology	Euhedral and aggregated	Euhedral and aggregated	Euhedral and aggregated	Euhedral and aggregated
Facies	Stromatolite	Stromatolite	Stromatolite	Stromatolite
Mineralogy	<p>Type 1 laminae: micrite, chlorite, pyrite</p> <p>Type 3 laminae: Sparite, micrite, pyrite</p>	<p>Type 1 laminae: micrite, chlorite, pyrite</p> <p>Type 2 laminae: organic matter, chlorite, pyrite</p> <p>Type 3 laminae: Sparite, micrite, pyrite</p>	<p>Type 1 laminae: micrite, chlorite, pyrite</p> <p>Type 2 laminae: organic matter, chlorite, pyrite</p> <p>Type 3 laminae: Sparite, micrite, pyrite</p> <p>Type 4 laminae: ooid, peloid, sparite</p>	<p>Type 1 laminae: micrite, chlorite, pyrite</p> <p>Type 3 laminae: Sparite, micrite, pyrite</p>
Age	2.72 Ga			
Location	Pilbara Craton, Western Australia			
Geological context	Shallow marine or lacustrine			

1.2. Stromatolites from the Malmani Subgroup (2.5 Ga, South Africa)

The Malmani-Campbellrand carbonate platform is a part of the lower Transvaal Supergroup, deposited on the Kaapvaal Craton. The platform is preserved in two basins, named the Transvaal basin in the eastern part and the Griqualand West basin in the western part of the craton (**Fig. 2.3a**). The Malmani Subgroup is observed in the Transvaal basin and is stratigraphically correlated with the Campbellrand Subgroup in the Griqualand West basin. A portion of the central part of the platform is exposed in the Kanye area of Botswana. The Malmani-Campbellrand carbonate platform mainly experienced a low-grade metamorphism in the greenschist facies with temperatures around 250-330°C. Yet, it was locally affected by a contact metamorphism induced by the intrusion of the Bushveld Complex at 2.06 Ga and late fluid circulations promoting the formation of ore deposits (*Button, 1973*). Five formations are preserved in the Malmani Subgroup (Oaktree, Monte Christo, Lyttleton, Eccles and Frisco) correlated to eight formations in the Campbellrand subgroup (Monteville, Reivilo, Fairfield, Klipfonteinheuwel, Papkuil, Klippan, Kogelbeen and Gamohaam), both overlain by the Penge and Kuruman iron formations, respectively. Deposition of the platform was dated by U-Pb zircons geochronology using ion microprobe between 2650 and 2500 Ma (*Altermann and Nelson, 1998*). This formation is observed from northeast to southwest over 190,000 km² of preserved outcrops but likely originally extended over the entire craton surface (~600,000 km²; *Beukes, 1987*). The northeast part of the platform represents shallow peritidal to

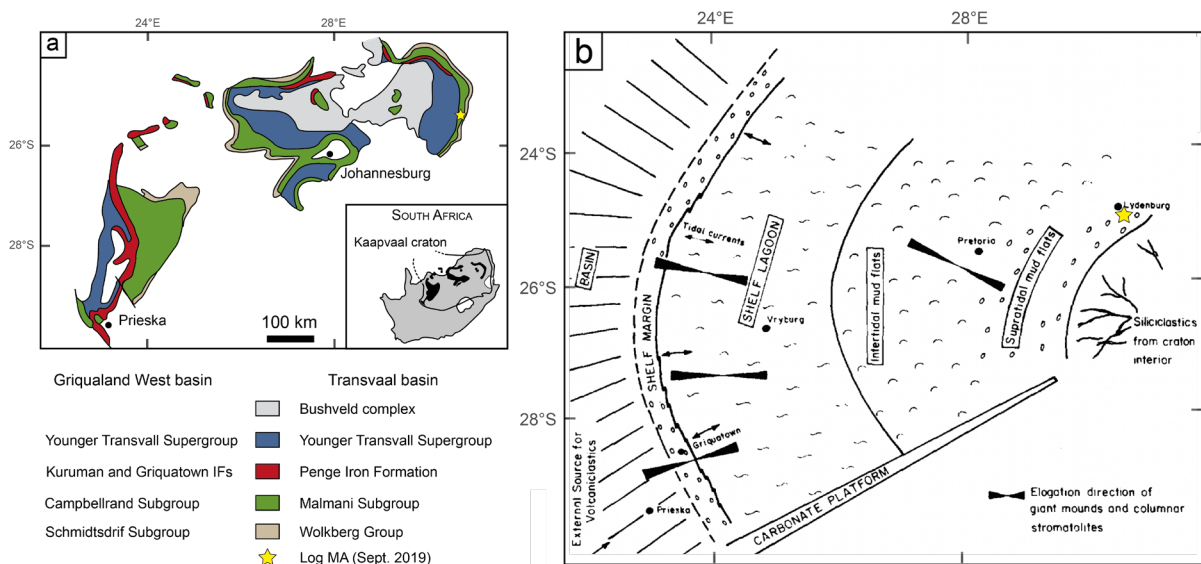


Figure 2.3: Geological context of the Malmani platform. a) Geological map of the lower Transvaal sequence (South Africa) and location of the MA stratigraphic section. Modified after Sumner and Beukes (2006). b) Paleo reconstruction map of depositional environments of the Campbellrand-Malmani Subgroups, from Beukes (1987).

subtidal facies which evolves to slope and basinal facies in the southwest (Fig. 2.3b). Although limestones are still preserved in the Malmani-Campbellrand platform, most of the primary fabric was replaced by dolomite and/or was partly silicified. Typical domal and columnar stromatolites indicating supratidal to subtidal environments are preserved (Eriksson, 1977; Beukes, 1987; Eroglu et al., 2015). The depositional environment, sea level variation and redox state of the basin were previously investigated in detail using facies analysis, stratigraphy, bulk stable isotope (Fe, S, N, C), major and trace elemental measurements (Button, 1973; Eriksson and Altermann, 1998; Kamber and Whitehouse, 2006; Sumner and Beukes, 2006; Wille et al., 2007; Godfrey and Falkowski, 2009; Ono et al., 2009; Eroglu et al., 2017, 2018). During my PhD, I focused on a shallow carbonate facies located in the northeast part of the Malmani Subgroup in the Barberton area (25° 21.561S, 30° 42.956E; Fig. 2.3). During a field trip conducted in September 2019, I collected 43 samples along a 20 m sedimentary section made of dolomitized and partially chertified stromatolites which include a 1.5 m depth drill core. A large scale lateral stratigraphic correlation was never made, thus the entire region requires detailed mapping. Based on field observations, the described section is likely a part of the Upper Monte Christo Formation (personal communication from W. Altermann), which reflects a shallow subtidal setting which contains various columnar stromatolites, wavy laminations and interbedded with rippled ooid grainstones (Tyler and Tyler, 1996). Petrographic observations and developing the syn- and post-depositional sedimentation model were parts of the Master projects of Aude Gounelle and Guillaume Lawnizack. During my PhD, I prepared samples for thin sections (cutting), major and trace element analyses (powdering). Based on observations under microscope, I selected three samples enriched in pyrite for Fe and S isotope analyses by SIMS. However, the overall sampled section has particularly low pyrite contents, making measurement of Fe and S isotope variations throughout the section (i.e. chemostratigraphy) difficult. Because of the scarcity of pyrite grains across the section, spatially resolved Fe and S isotope compositions were conducted on only three samples (Table 2.2).

Table 2. 2: Summary of main characteristics of the Malmani Subgroup and studied samples.

Upper Monte Christo Formation, Malmani Subgroup			
# sample	MA37	MA39	AmalC4
Pyrite observation	Disseminated micrometric pyrite in dolomite or quartz Partially oxidized pyrite (size~ hundreds of μm), aligned in the sample, associated with quartz	Disseminated micrometric pyrite in dolomite or quartz Partially oxidized pyrite (size~ hundreds of μm), aligned in the sample, associated with quartz	Disseminated micrometric pyrite in dolomite or quartz A few grains entirely oxidized
Size	[10 μm - 150 μm]	[10 μm - 170 μm]	[2 μm - 35 μm]
Morphology	Euhedral and aggregated	Euhedral	Euhedral and aggregated
Facies	Stromatolite	Stromatolite	Stromatolite
Mineralogy	Quartz, dolomite, phyllosilicate, pyrite	Quartz, dolomite, phyllosilicate, pyrite	Quartz, dolomite, phyllosilicate, pyrite
Age	2.55 Ga		
Location	Northeast Kaapvaal Craton		
Geological context	Marine carbonate platform		

1.3. MISS from the Thaynes Group (251 Ma, United-States)

The 251 Ma Lower Weber Canyon (LWC) is located at the northeast of the Sonoma foreland basin in Utah (USA). This sedimentary basin resulted from the Sonoma orogeny during the Permian-Triassic transition. The Sonoma basin was located on the west Pangea margin close to the equator (**Fig. 2.4a**; *Burchfiel and Davis, 1975*; *Romano et al., 2013*). The basin is now elongated in NW-SE direction, corresponding to the orientation of the basin relative to the long-term sea level rising during the Early Triassic. This sediment package corresponds to the second third-order transgressive-regressive sequence determined in the Sonoma foreland basin (*Embry, 1997*). The maximum sea level flooding was recorded at the Smithian-Spathian boundary (Early Triassic) using ammonoid beds (*Anasiberites, Brayard et al., 2013*). The LWC section is part of the Thaynes Group composed of lithologies ranging from terrigenous to marine carbonates and shales (*Grosjean et al., 2018*). The Thaynes Group overlies the Moenkopi Group which is composed of terrigenous conglomerates and sandstones. The LWC section includes the Smithian-Spathian boundary, a period of biotic loss of diversity following the most severe biotic crisis of the Phanerozoic, the end Permian mass extinction event (252 Ma). This period is of particular interest due to the occurrence of microbial deposits described as anachronistic facies (*Brayard et al., 2013*). Only non-mineralized microbial deposits, i.e. MISS, are preserved in the LWC section (*Grosjean et al., 2018*). This section consists of four stratigraphic units (*Grosjean et al., 2018*) deposited along a ramp system (**Fig. 2.4b**). Eight samples were selected for this study due to their high S content and because they represent a large range of depositional environments (**Table 2.3**).

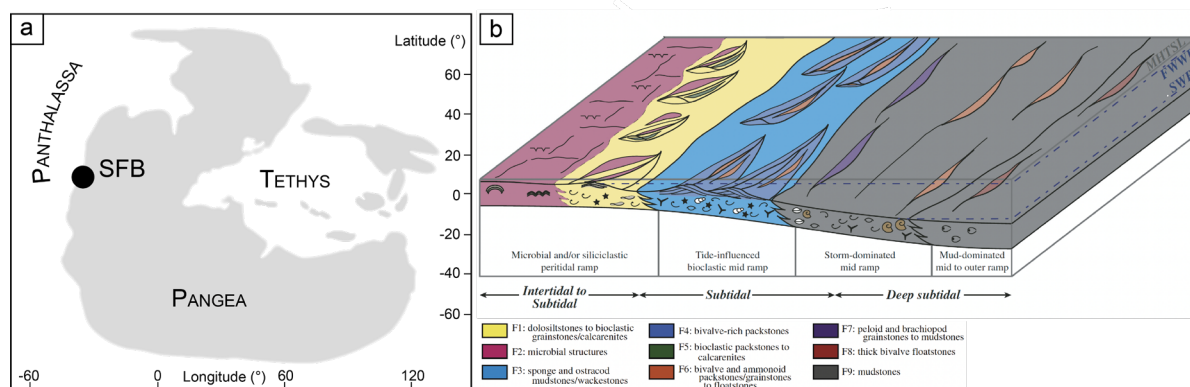


Figure 2. 4: Geological context of the LWC samples. a) Paleogeographic map of the Early Triassic with the location of the Sonoma foreland basin. Modified after (*Romano et al., 2013*). b) Depositional model of the Thaynes Group, representing a ramp system from siliciclastic peritidal to subtidal settings, and lithofacies association. From *Grosjean et al. (2018)*.

Table 2. 3: Summary of main characteristics of the Lower Weber Canyon stratigraphic section and studied samples

Thaynes Group									
# sample	LWC31	LWC39	LWC41	LWC47	LWC49	LWC55	LWC72	LWC88	
Pyrite observation	Nodule or in the nodule area	Disseminated	Forming a lamina or slightly spreading the lamina	Disseminated	Disseminated	Disseminated	Disseminated	Disseminated	
Size	[20 µm- 3 mm]	[15 µm- 60 µm]	[15 µm- 50 µm]	[5 µm- 10 µm]	[5 µm- 30 µm]	[5 µm- 35 µm]	[5 µm- 15 µm]	[5 µm- 15 µm]	
Morphology	Nodule, euhedral and aggregated	Euhedral and aggregated	Euhedral and framboid with overgrowth	Euhedral and framboid	Euhedral, framboid and aggregated	Euhedral, framboid and aggregated	Euhedral, framboid and aggregated	Euhedral, framboid and aggregated	
Facies	Carbonated siltstone	MISS	MISS	Bioclastic packstone	Bioclastic packstone	Bioclastic wackestone	Mudstone	Mudstone	
Mineralogy	Micrite, quartz, phyllosilicate, dolomite, pyrite	Micrite, quartz, phyllosilicate, dolomite, organic-rich laminae, pyrite	Micrite, quartz, phyllosilicate, dolomite, organic-rich laminae, pyrite	Micrite, quartz, phyllosilicate, sparite-filled bioclasts, pyrite	Micrite, quartz, phyllosilicate, sparite-filled bioclasts, pyrite	Micrite, quartz, phyllosilicate, sparite-filled bioclasts, pyrite	Micrite ± fine quartz layers, pyrite	Micrite ± fine quartz layers, pyrite	
Age	251 Ma								
Location	Northeast Sonoma foreland basin, Utah, United-States								
Geological context	Marine carbonated ramp								

1.4. Modern microbialite from Cayo Coco (Cuba) and Atexcac lake (Mexico)

Cayo Coco is a small island located in the North coast of Cuba, bordering the Atlantic Ocean (**Fig. 2.5**; Greater Antilles, Caribbean Sea). This island is part of a 200 km archipelago associated with a coral reef and extends over 370 km². The archipelago is separated from the mainland by a 20 km large bay, named Perros Bay, connected to the ocean by channels. However, seawater inputs and circulation were modified on the western side of the bay by the construction of a causeway crossing Perros Bay (*Bouton et al., 2016*). A lagoonal network is observed on the south part of Cayo Coco, composed of 500-m wide and ~0.8-m deep ovoid depressions formed on a Pleistocene substratum. Lagoons are fully to partially connected to Perros Bay to the west, depending on the water level, i.e. dry or wet season. This causes a progressive restriction and thus, a chemical gradient to form from west to east part of the lagoonal network. This in turn causes an increase in the carbonate saturation index accompanied by the formation of microbialites. Here, the studied sample is from a microbialite developed in the eastern lagoon, which is connected to the rest of the network by an ephemeral channel during the high water level season. In addition to the intrinsic parameters, referring to microbial processes, the role of external parameters, i.e. hydrodynamic conditions, have been demonstrated to control microbialite development and morphologies (*Bouton et al., 2016; Pace et al., 2018*). The studied sample «M2 6.8-7.1» is a mineralized microbialite (**Table 2.4**) from a 14 cm core collected on the western shore of the lagoon. This sample was already mineralogically characterized and analyzed for bulk rock $\delta^{13}\text{C}_{\text{org}}$ and $\delta^{15}\text{N}$ values (*Pace et al., 2018; Bouton et al., 2016, 2020*). Pyrite grains from these samples were previously measured for $\delta^{34}\text{S}$ values using a high spatial resolution technique (NanoSIMS; *Marin-Carbonne et al., 2022*).

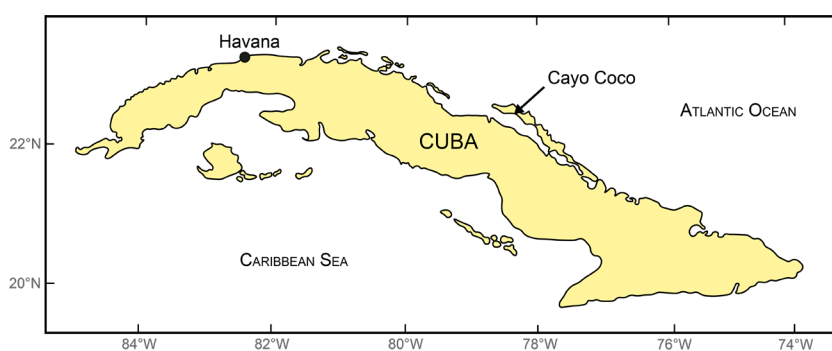


Figure 2. 5: Map of Cuba island with the location of Cayo Coco lagoon. Modified after Pardo (2009).

Atexcac lake is a maar lake, i.e. it formed after a phreato-magmatic eruption, owing to its position in the Trans-Mexican Volcanic Belt (hereafter TMVB; **Fig. 2.6**) in the Cuenca de Oriental basin (Puebla state, Mexico). The TMVB is 1000 km long and 20 to 100 km large E-W volcanic arc resulting from the subduction of Cocos and Rivera plates behind the North America plate during the Neogene (*Ferrari et al., 2012*). Atexcac lake formed, along with several other maar lakes, during the Pleistocene (0.33 Ma for Atexcac lake) on an andesitic substrate (*Carrasco-Nez et al., 2007*). This lake is located on the eastern part of the TMVB at an elevation

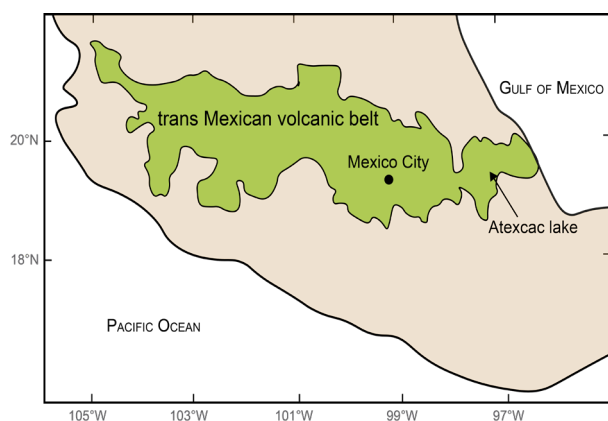


Figure 2. 6: Map of Mexico with the extent of the trans-mexican volcanic belt and the location of Atexcac lake. Modified after Ferrari et al. (2012).

of 2360 m. The water depth is around 39 m and water mixing occurs once per year between January and May. The chemocline, i.e. a chemical boundary between oxygenated and anoxic or sulfidic conditions, is located around 15 m deep. Microbialites form encrustations on the steep walls of the lake. The sample studied «ATX-2012-08» is a living microbialite (Table 2.4), i.e. covered by an active microbial mat, collected in January 2012 on the southwest shore of the lake (Zeyen et al., 2015). Similar to the Cayo Coco sample, this sample has been previously studied for its mineralogy (Zeyen et al., 2015, 2017, 2019) and spatially resolved pyrite $\delta^{34}\text{S}$ values (Marin-Carbonne et al., 2022).

Table 2. 4: Summary of main characteristics of Cayo Coco lagoon /Atexcac lake and samples studied.

Cayo Coco and Atexcac		
# sample	M2 6.8-7.1	ATX-2012-08
Pyrite observation	Within the mineralization or associated with bioclasts	Within the mineralization or at the edge of the mineralization
Size	[1 μm - 20 μm]	[1 μm - 25 μm]
Morphology	Euhedral and framboid	Euhedral and framboid
Facies	Microbialite	Microbialite
Mineralogy	Aragonite, Mg-calcite, Mg-silicate, pyrite	Aragonite, Mg-silicate, pyrite
Age	Modern	
Location	South of Cayo Coco island, Cuba	Eastern trans-Mexican volcanic belt, Mexico
Geological context	Lagoon	Maar lake

2. Methods

2.1. Sample preparation

Before detailing iron isotope analytical protocol, it is important to describe all the steps preceding the SIMS analyses. Microbialites are collected as decimeter-size samples that were sawed into a piece with dimension of 2.5x4 cm. This piece of rock was used to produce thin sections, made at ISTE-UNIL (Lausanne, Switzerland) and SIMS mounts. The preparation of a SIMS mount follows several steps. First, the sample is embedded in a transparent acrylic hot mounting resin for polishing. This type of resin is not compatible with SIMS analyses because of low polymerization and high degassing effect, however it is used for producing flat polished rock surfaces using an abrasive silicon carbide grinding paper with decreasing grain size (600, 1200, 2400 grains/cm²). The resin mounts were then polished on smooth polishing pads covered with diamond paste with grain sizes of 6, 3, 1 and 0.5 μm . Then, the zones of interest in the samples were cut using a wire-saw (slide of few millimeters) and pressed into indium contained within 1-inch aluminium sample holders. Mounting into indium allows to improve high vacuum during SIMS measurements ($<10^{-9}$ mbar) in the sample chamber. However, it is also possible to embed samples in a specific epoxy resin and polish it, yet in such case, the mount must be held under low vacuum conditions at least 2 days before the analytical session, to prevent a severe degassing effect. Once polished, sample topography was measured using a white light interferometric microscope (Bruker Contour GTK at University of Lausanne). Sample topography must be lower than 5 μm to achieve minimal analytical fractionation (Kita *et al.*, 2011; Fig. 2.7).

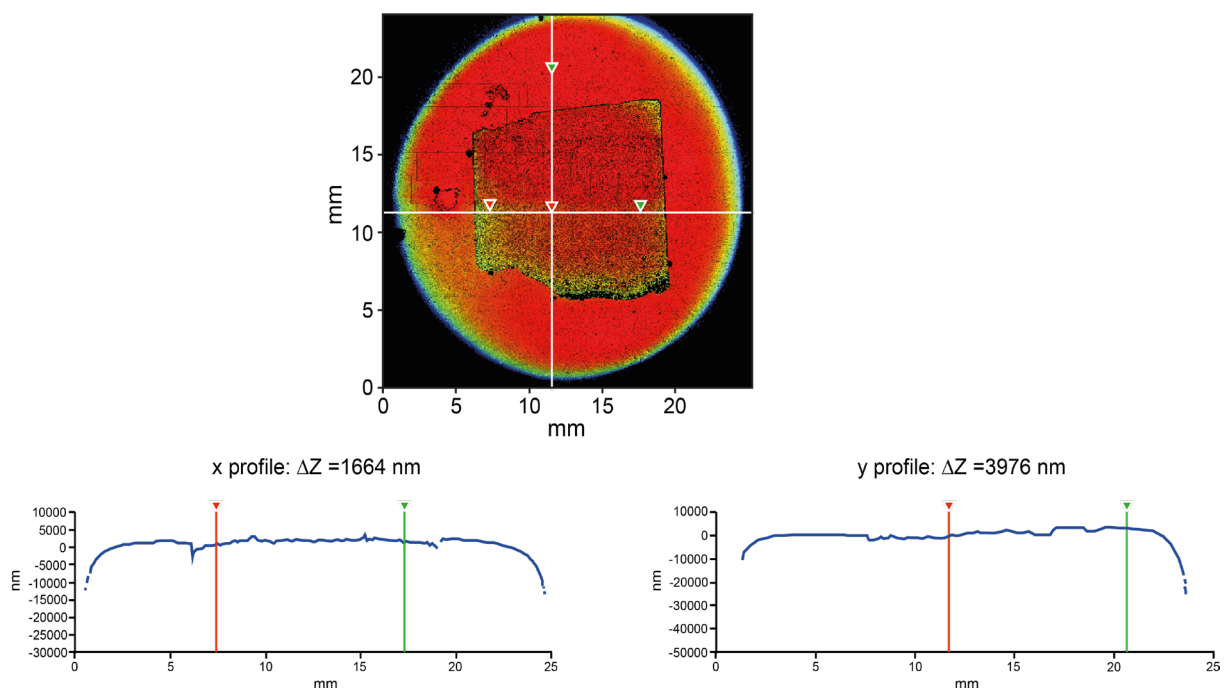


Figure 2.7: Interferometer image showing the topography of an epoxy mount along x and y profiles.

Once the topography is checked, the mounts were imaged in reflected light using a petrographic microscope. Given the small grain size of pyrites, these images were then used to guide the high spatial resolution isotope measurements (**Fig. 2.8**). Finally, mounts are carbon or gold coated to improve electron or ion conductivity on the sample surface for respective scanning electron microscopy (SEM) or secondary ion mass spectrometry (SIMS) analyses.

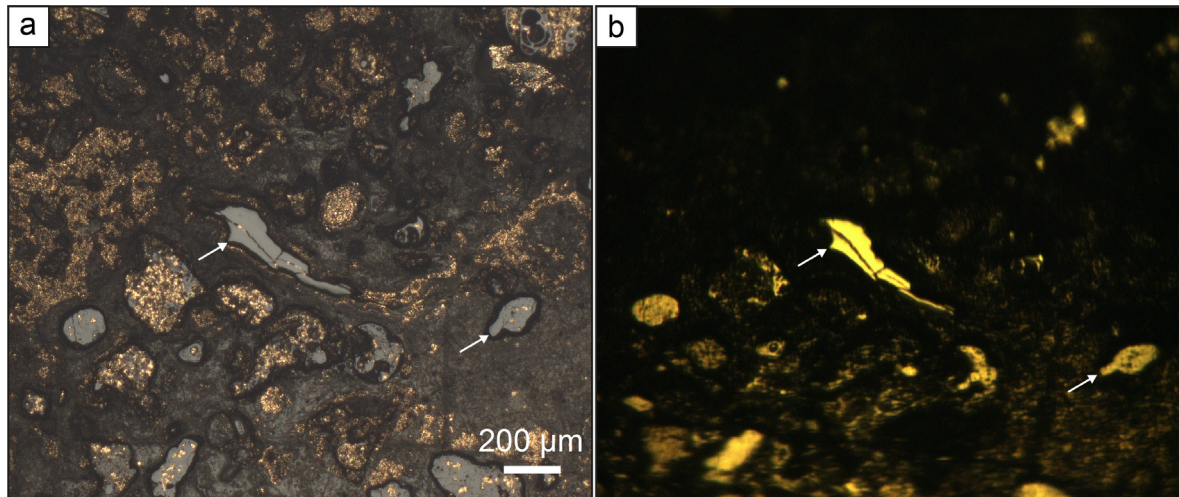


Figure 2.8: Views of a sample under the microscope and the camera of the SIMS. a) Reflected light microscopy image and b) corresponding view using the CCD camera of the ims 1280HR (SwissSIMS, Lausanne).

2.2. Scanning electron microscopy (SEM)

Because of its high reflectivity, an opaque mineral such as pyrite is easily observed by reflected light microscopy. However, due to the micrometer size of pyrite grains, determination of their shape and size is done using scanning electron microscopy (SEM). SEM allows for high spatial resolution observation down to several nm and thus, mineralogical identification of micrometric objects. This technique is based on the interaction between electrons and a solid sample surface. A primary electron beam is generated by thermo-ionization of a tungsten filament which is accelerated by a 5 to 30 keV high voltage. Interactions between the primary electron beam and the sample surface generate different type of signals as a function of primary electron penetration depth and the intensities of secondary radiation. It includes the emission of Auger, secondary and backscattered electrons and X-rays or visible light (cathodoluminescence). Secondary electrons (SE) result in the inelastic interaction between the primary ion and valence band of the atom. SE are sensitive to surface effects and inform about the sample topography. In contrast, the backscattered electrons (BSE) are deviated primary electrons by atomic nuclei. They are emitted deeper within the sample and have thus low sensibility to topography variations. BSE are dependent on the average atomic mass, providing information on the chemical composition of the targeted mineral. Energy dispersive X-ray spectroscopy (EDS) can be coupled with BSE imaging to obtain semi-quantitative chemical analyses of minerals. Analyses can be performed as point measurements ($<1 \mu\text{m}$) or area mapping (**Fig. 2.9**). X-ray radiation is produced by (1)

ionization of the inner shell electron by primary electron beam, leaving a vacancy in the atomic structure and (2) an electron from an outer shell falls back to the lower energy orbital to fill this vacancy (electron relaxation), resulting in the emission of a characteristic X-ray radiation. This radiation is characteristic of chemical elements and their detection allows to reconstruct EDS spectra for characterization elemental composition of a mineral. During this thesis, BSE imaging and EDS analyses were performed at a working distance of 21 mm with a 1.5 nA primary beam at 20 kV. Scanning electron microscopy observations were performed using a Tescan Mira LMU at ISTE-UNIL (Lausanne, Switzerland) equipped with an X-ray silicon diffusion detector (SDD; Ultim Max-Oxford Instruments).

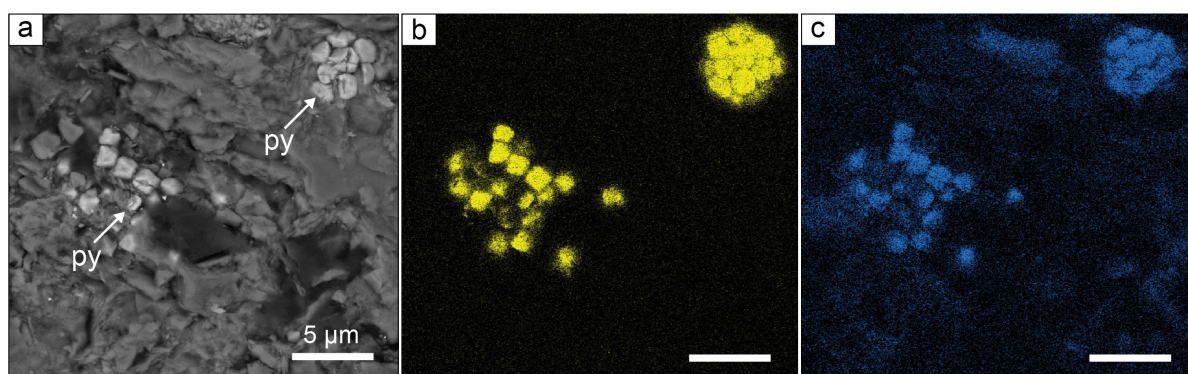


Figure 2.9: Chemical map of framboid pyrite by SEM. a) BSE image of a pyrite enriched zone; b) Sulfur mapping; and c) Iron mapping of the BSE area.

2.3. Electron probe micro-analyses (EPMA)

As a complement to the qualitative EDS-SEM analyses, EPMA is a non-destructive method for quantitative elemental analyses with a limit of detection at the level of ppm. In this study, EPMA was used to quantify major, minor and trace elements in pyrite structure. The analytical principle is similar to SEM as sample surface is bombarded by an electron beam of 5 to 30 keV. This method focuses on the collection of X-ray photons emitted during electron relaxation of various elemental species. Those X-rays have wavelengths of characteristic energies of elements excited that can be identified by Wavelength dispersive spectroscopy (WDS) spectra. Wavelength dispersive spectrometers are composed of several diffracting monochromator crystals of different inter reticular spaces in order to diffract all X-ray wavelengths to the detector. The crystal and detector move following a Rowland circle geometry to collect the entire range of angles between incident X-ray photons and the monochromatic crystal and thus to collect all wavelengths. This configuration allows analyses of all elements from boron to uranium. EPMA analyses were performed using a JEOL JXA-8530F HyperProbe equipped with a Schottky electron gun for operating high spatial resolution analyses ($\sim 2 \mu\text{m}$) at ISTE-UNIL (Lausanne, Switzerland). However, chemical zoning of few microns (typically less than $1 \mu\text{m}$) observed in pyrite were not able to be characterized.

2.4. Raman

Raman spectroscopy was used in this thesis to complete EDS analyses for mineralogical description of samples and to characterize the structure of carbonaceous material (CM) found sometimes in association with pyrite (**Fig. 2.10**). Estimation of the maximum peak metamorphic temperature experienced by the sample can be deduced from the ratio of the different band areas (i.e. D-bands D1, D2, D3, D4 representing disorder CM and G-band representing graphite) constituting the Raman spectra of the CM (*Beysac et al., 2002*). Raman spectroscopy is a non-destructive method used for characterizing nature and structure of molecules. It is also powerful to quantify concentration of a molecule by measuring the intensity of spectral lines. This technique is based on Raman scattering, which is a monochromatic light, i.e. laser, scattering phenomenon named after its finder Chandrashekhara Venkata Râman. Raman scattering corresponds to a difference between incident and scattering light frequencies. When the incident monochromatic laser interacts with electron in the sample, this electron absorbs energy from the incident photon and its energy increases to a virtual energy state. During the relaxation, electron energy drops down toward lower energy state. The relaxation can be done at the same energy than the incident photon, i.e. the electron falls back to the initial vibrational level. Therefore, the emitted photon has the same frequency as the incident photon (elastic Rayleigh scattering). However, electron can also drop down to a different vibrational level, meaning relaxation occurs at a frequency different from the excitation frequency (Raman scattering). Raman scattering is divided into inelastic Stokes lines, when the electron absorbs energy and anti-Stokes scattering when electron emits energy. Raman spectra were obtained using a Horiba Jobin Yvon LabRAM HR800 spectrometer (ISTE, UNIL) in a confocal configuration equipped with an Ar⁺ 532 nm laser and a CCD detector. Measurements were performed at room temperature on thin sections, with a laser power delivered at the sample surface <1 mW to prevent thermal damages.

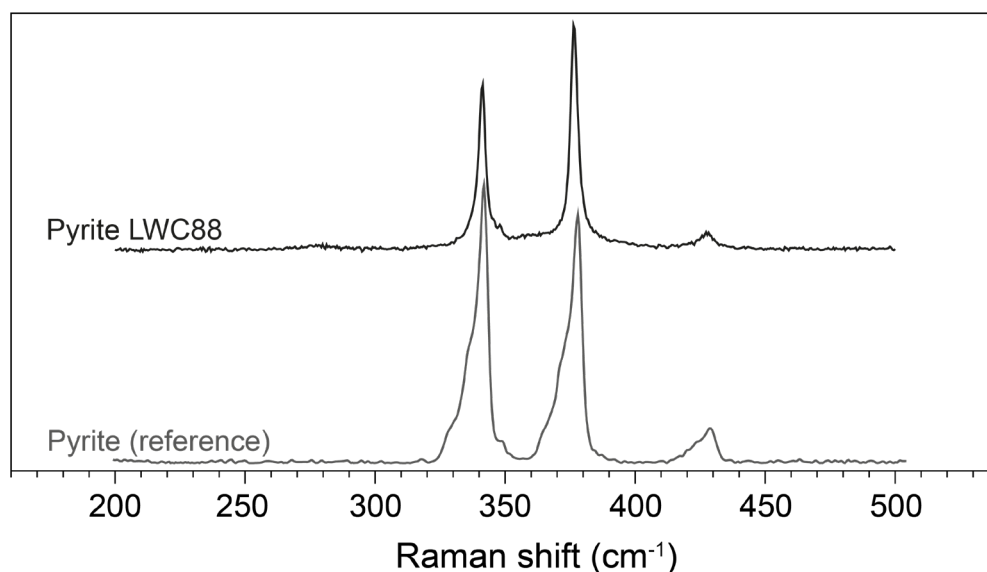


Figure 2. 10: Raman spectrum of pyrite in LWC88 compared to reference spectrum of pyrite from the Ruff database.

2.5. Major and trace elements

Concentrations of major and trace elements, including REE, were measured in samples from the Upper Monte Christo Fm (Malmani subgroup) by the Service d'Analyse de Roches et Minéraux (SARM, CRPG, Nancy, France). We selected 18 samples along the stratigraphy and sent about 8g of ground powders to complete ICP-MS analyses. The uncertainties of the major and trace element measurements were respectively between 2 and 25% and between 5 and 25%, depending on their concentrations.

2.6. Secondary ion mass spectrometry (SIMS) CAMECA ims 1280 HR

The main goal of this thesis was to perform high spatial resolution analyses of iron isotopes in micrometric ($<10\ \mu\text{m}$) pyrite. The analytical procedure published previously (*Decraene et al., 2021*) as well as the description of the instrument and basic principles are detailed in this chapter.

2.6.1. General principles

Secondary ion mass spectrometry is based on ionized compounds emitted from a sample surface during sputtering by a primary ion beam, conceived in the early 1960's by Raymond Castaing and his student Georges Slodzian. Ion microprobe instruments were developed for in situ analyses of isotope compositions and elemental concentrations at a microscopic scale. A flat surface sample is sputtered by a primary ion beam of positive (Cs^+) or negative (O^- or O_2^-) polarity and the first nano to micrometer of the sample are ejected as atoms (**Fig. 2.11**). Not all compounds will be ionized as ionization proceeds depending on the ionization potential of each element, the primary source, the extraction energy and other analytical conditions. Secondary ions are then focused to form a secondary ion beam (**Fig. 2.11**). An electric potential of 10 kV between the surface sample (10 kV) and the front plate of an immersion lens (grounded) is used to accelerate the secondary ion beam, which is focused by a set of electrostatic lenses before

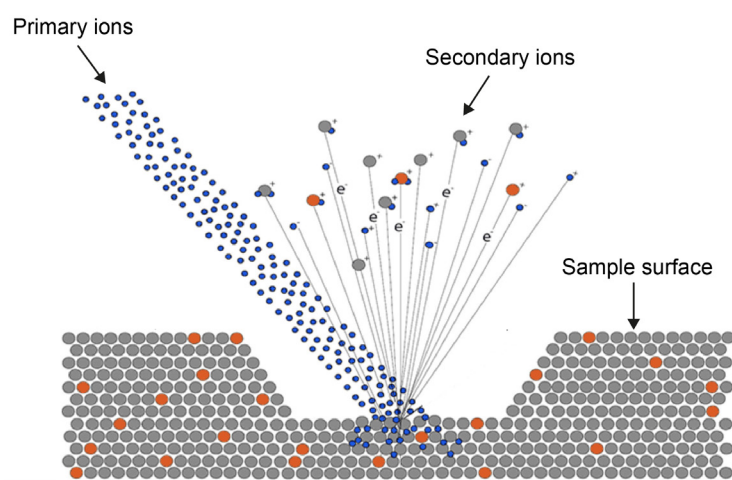


Figure 2.11: Schematic of primary ion beam sputtering on a sample surface and production of secondary ions. Modified from a Cameca document.

being sorted by an electrostatic sector and a magnet. This double focusing allows for sorting as a function of charge and mass of atoms in order to detect isotope species. Charged compounds of interest are then collected simultaneously or sequentially on electron multipliers (for low signals) or faraday cups (for high signals). Due to the large radius of the magnet, all elements from hydrogen (H) to uranium (U) can be measured with a detection limit of a few ppm.

2.6.2. Instrumental description

Although the CAMECA ims 1280 HR is composed of many components (Fig. 2.12), it can be divided in three main parts that are described below. In addition, the airlock system is designed to introduce up to six samples into the high vacuum of the sample chamber, without affecting the vacuum of the other parts of the instrument.

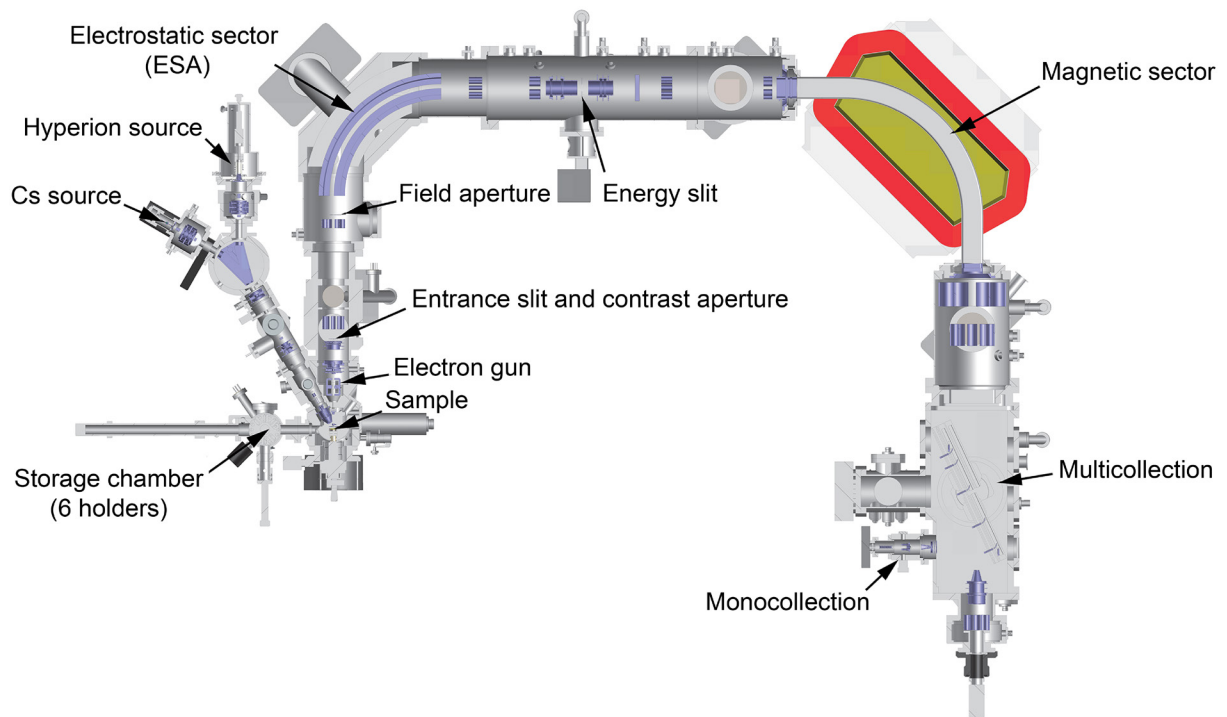


Figure 2. 12: Schematic of a CAMECA ims 1280HR ion microprobe (credits: F.Plane).

2.6.2.1. Primary column and sources

Two sources are available on ion microprobes: i) the cesium source that produces positive primary ions Cs^+ and ii) the Hyperion radio frequency source that produced negative primary ions $^{16}\text{O}^-$ or $^{16}\text{O}_2^-$. Selection of the ion source depends on ionization energy of the species of interest.

Cs source

The Cesium source is a thermal-ionization source (**Fig. 2.13**) used to extract negatively charged secondary ions, such as for example O^- , Si^- or H^- . Cesium ions are produced by heating Cs_2CO_3 to produce Cs^+ vapor (*Storms et al., 1977*). This vapor is then ionized by a hot tungsten plate (1100°C) and the generated ions are accelerated by a potential between the plate and the extraction electrode into the primary column. The primary Cs^+ ion beam expulses electrons from the sample surface and creates an accumulation of positive charges that can cause an explosion at the sample surface. This charge effect is compensated by the production of electrons by a normal incident electron gun (NEG). Electron beam position is set by two coils (horizontally by B_x and vertically by B_y) which induce a deviation of the secondary ion beam. This deviation is corrected through the B_y coil. In the specific case of pyrite, a Cs source is used for analyses of sulfur isotopes. Although pyrite is a conductive mineral, influence of insulating matrix around, such as carbonate or silicate, or holes promote charge accumulation. The use of NEG is thus mandatory to avoid such effects and to enhance the ionization.

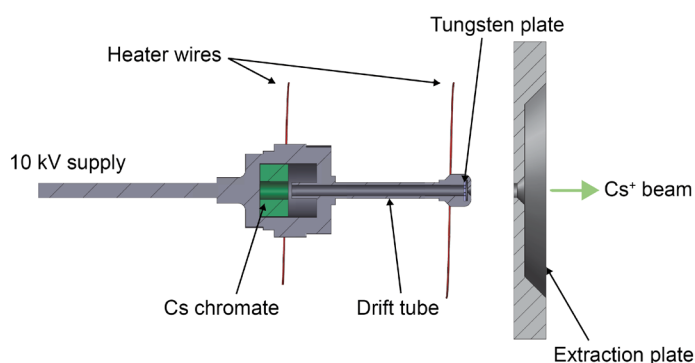


Figure 2.13: Detailed scheme of the Cesium source (credits: F. Plane).

Hyperion source

The Hyperion-II is a new generation radio frequency plasma ion source (**Fig. 2.14**) developed by Oregon Physics and replaces the older oxygen Duoplasmatron source (*Liu et al., 2018*). This source generates $^{16}\text{O}^-$ ions for measuring elements that preferentially ionize into cations, such as iron, potassium, or aluminum. Oxygen plasma is created by ionization of an oxygen gas by delivering radiofrequency currents to a coil around the plasma tube. An electromagnet located at the end of the plasma tube increases the plasma density by reducing electron diffusion before extraction of the ion beam (*Malherbe et al., 2016*). This source was designed to produce a higher primary beam density for increasing spatial resolution without decreasing analytical precision. In this thesis, the use of this source is relevant for the analyses of micrometric phases such as micropyrrite.

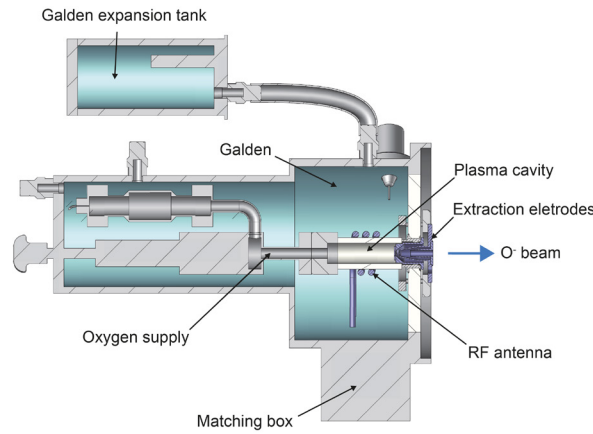


Figure 2. 14: Detailed scheme of the Hyperion-II source (credits: F.Plane).

Primary column

The focalization of extracted primary ions occurs in the primary column, by the combined effect of electrostatic lenses, stigmators and deflectors. Two primary apertures located after PBMF and before LPRIM4 lenses remove aberrations of the primary beam. Primary beam size can be mainly modulated by primary lenses L1, L2, L3 and L4 or by reflecting the projected image of a primary aperture. These two modes produce Gaussian or projected beams, respectively. The Gaussian beam is denser but less homogenous compared to the projected beam.

2.6.2.2. Secondary column

Each secondary ion is characterized by (1) a kinetic energy and (2) an extraction angle. The ion transfer optics allows for homogenization of energy and angular distribution. Secondary ions are emitted with variable angles and various kinetic energies. However, the mass spectrometer can only separate ions as a function of their mass over charge (m/q) ratio. The role of transfer optics is thus to reduce the energy dispersion of ions before entrance in the mass spectrometer. The transfer optics are composed of the immersion lens maintained at 0kV on the front side, producing a potential of 10 kV with the sample surface (-10 kV). This potential enhances the acceleration of secondary ions toward the entrance slit via transfer lenses and apertures. Contrast and field apertures eliminate extreme trajectories of secondary ions and define the ion transmission to the spectrometer. The field aperture allows the selection of ions from a defined surface area of the sample whereas the contrast aperture reduces aberrations and increases spatial resolution of the secondary ion image. At the end of the transfer optics (before reaching the spectrometer, **Fig. 2.12**), trajectory of secondary ion beam is linear, centered, spatially resolved and devoid of aberrations.

A mass spectrometer is composed of two parts: (1) the electrostatic analyzer (ESA) and (2) the magnet. ESA consists of two curved plates in which a potential is applied. Ion trajectory (R) follows equilibrium law between electrostatic energy and kinetic energy as **eq. 2.1**:

$$R = \frac{mv^2}{qE} \tag{eq. 2.1}$$

where m is ion mass, v its velocity, E electrostatic constant and q the ion charge. Behind the ESA, the energy slit filters through ions with a similar initial energy and removes most of molecular ions (having lower initial energies than atomic ions) that can interfere with atomic ion signal. A focalization of the secondary ion beam is performed by the coupling optics (coupling lenses and deflectors) before reaching the magnet.

The magnet consists of a constant magnetic field (B) circulating in a coil. The ion trajectory can be expressed as **eq. 2.2**:

$$R = \frac{1}{B} * \sqrt{\frac{2mV}{q}} \quad (\text{eq. 2.2})$$

where m is mass of ion, q its charge and V its initial energy. Because B and V are constant, the average radius of an ion trajectory is a function of the ratio m/q . Therefore, ions with similar m/q ratio are focused on the exit slit. The exit slit is used to sort the ion mass. The ratio between exit and entrance slit width corresponds to the Mass Resolving Power (MRP). The MRP defines the ability to distinguish the closely spaced masses and to separate mass interferences (**Fig. 2.15**). The MRP is measured at 10% of the peak width.

2.6.2.3. Detection

The filtered secondary ion beam are detected on a channel plate that consists of electron multipliers (EMs) coupled to a fluorescent screen (configuration: projection down and electrostatic sector associated with the detection part OFF) or can be deviated either to the monocollection detection system (configuration: projection down and electrostatic sector ON) or to the multicollection detection system (configuration: projection up and electrostatic sector OFF). Secondary ions can be detected sequentially, using the monocollection mode, or simultaneously, using the multicollection mode (**Fig. 2.12**). Several detectors are available for monocollection and multicollection modes. The monocollection is composed of two faraday cups (FCs) and one axial EM but only one detector can be chosen for analyses. Monocollection mode is used for measurement requiring mass changes, i.e. peak switching. The multicollection is composed of

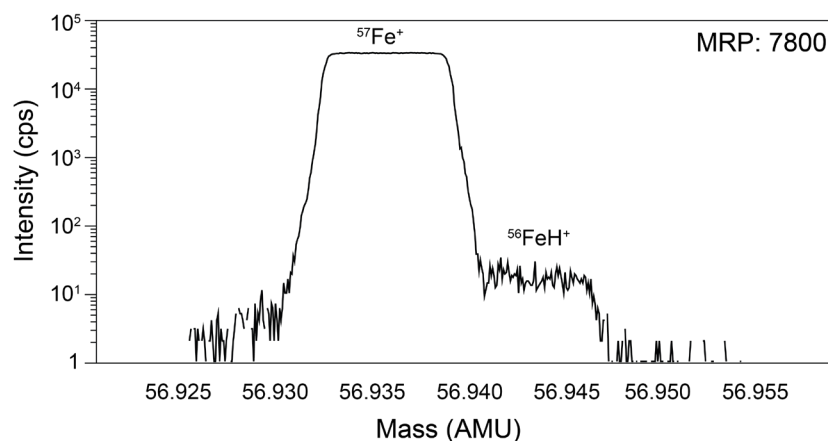


Figure 2.15: ⁵⁷Fe⁺ and ⁵⁶FeH⁺ intensity signals. A MRP of 7700 is required to separate hydride peak interfering on the ⁵⁷Fe⁺ signal.

five mobile detectors on a rail, the two extreme positions are 2 FCs (L'2 and H'2) that are coupled to 2 EMs (L2 and H2), L1 is an EM, C and H1 are FCs. For low signal intensity < 5E+5 counts/second (cps), secondary beam is detected on an EM. The EM principle consists in the conversion of each secondary ion impact into a cascade of electrons that are accelerated and multiplied on successive dynodes. This signal is then converted in an electric signal and interpreted as ionic signal. The EMs have several limitations. First, they are not adapted for secondary signal as high as 5E+5 cps. Secondly, several analytical biases must be corrected. For example, an accelerated degradation of EM is observed for high counting rate (> 2E+5 cps), causing the sensitivity drift along the analytical session. A dead time correction is also required as EM has a minimum time interval between two ion impacts during which no electric signal is produced. One EM was used for the measurement of $^{52}\text{Cr}^+$ in order to correct the interference of $^{54}\text{Cr}^+$ on $^{54}\text{Fe}^+$. However, as iron is a major element in pyrite and as we measured the two most abundant ions $^{56}\text{Fe}^+$ and $^{54}\text{Fe}^+$, the intensity of the secondary ion beam exceeds capacities of EM for signal counting. Therefore, the secondary ion acquisition was performed by using FCs. A faraday cup consists of a metal cylinder that collects ion impacts. Each ion impact on the cylinder wall produces an electron flux, trapped in the FC by a negative charged plate (Repeller). This latter is converted in an intensity by an amplifier which is then translated in a current (in cps). The FCs yields and backgrounds are measured before analytical session and are considered constant along the session. The use of multicollection is possible for ions of similar m/q ratios. The magnet is set on an axial mass value and mobile trolleys move to a specific position to detect each mass. For example, iron isotope analyses require the use of L2 for detection of $^{52}\text{Cr}^+$, H1 for $^{54}\text{Fe}^+$, C for $^{56}\text{Fe}^+$ and H'2 for $^{57}\text{Fe}^+$ that are distributed around the axial mass 54.5.

2.7. Pyrite S isotope analyses

Spatially resolved multiple sulfur isotope (^{32}S , ^{33}S and ^{34}S) analyses were specifically conducted on samples from the Upper Monte Christo Fm. Multiple S-species yield a line with a slope of 0.515 in the $\delta^{34}\text{S}$ and $\delta^{33}\text{S}$ coordinates (mass dependent fractionation line). This line was calibrated using Balmat, Maine and Ruttan pyrite standards. The instrumental mass fractionation was corrected by standard bracketing. The reproducibility of Balmat was better than 0.08‰ (2SD) over the session. The use of the cesium source combined with the electron gun is required to measure sulfur isotopes as this element better ionized in the negative polarity. A 4 nA Cs^+ primary beam was focused to form a spot of $\sim 10 \mu\text{m}$. $^{32}\text{S}^-$, $^{33}\text{S}^-$ and $^{34}\text{S}^-$ ions were simultaneously collected on faraday cups (respectively L'2, C and H1). The slit 2 of the multicollection was used to set a MRP of ~ 5000 to resolve isobaric interferences of $^{32}\text{SH}^-$ over $^{33}\text{S}^-$ and $^{33}\text{SH}^-$ over $^{34}\text{S}^-$. Data acquisition consists of 30 cycles preceded of 40s presputtering time followed by automatic centering of the beam (dtfa and dtca). A typical $^{32}\text{S}^-$ count rate of 4.70E+9 cps on pyrite.

2.8. Analytical protocol for measuring Fe isotope compositions in micrometric pyrite

2.8.1. Objectives

Spatially resolved analyses of Fe isotope composition by SIMS or laser ablation coupled to MC-ICPMS have expanded over the past decade thanks to technical improvements (*Horn et al., 2006; Whitehouse and Fedo, 2007; Nishizawa et al., 2010; Marin-Carbonne et al., 2014*). An advantage of such an approach is the possibility of assessing internal isotope variability within a grain or a population of grains and targeting several matrices in a sample. Because of the precision of in situ techniques of ± 0.1 to 0.4% , the in situ Fe isotope analyses are mostly used in samples with large ranges of Fe isotope compositions. The in situ Fe-isotope measurements are particularly useful for understanding low-temperature biogeochemical processes and are also relevant for investigating high-temperature processes (*Richter et al., 2009*). Spatially resolved Fe isotope measurements document large isotope variabilities that were previously unavailable from the bulk rock analyses and thus, have enabled more comprehensive interpretations of the Fe cycling in ancient sedimentary environments (*Czaja et al., 2010; Yoshiya et al., 2012*). However, the size of targeted mineral grains is typically limited to the size of the primary beam of about $20\ \mu\text{m}$, hampering investigations of features smaller than that size (e.g. framboidal pyrite, thin overgrowth rims). The advent of a new generation of plasma ion source for SIMS instruments, the Hyperion-II source, presents an opportunity to improve the spatial resolution of the Fe-isotope measurements. The Hyperion-II was installed on the Cameca ims 1280HR in CRPG Nancy (France) in 2017 and in SwissSIMS Lausanne (Switzerland) in 2019. This source generates a primary beam 10 times denser compared to previous source. Thus, with this analytical improvement, it is now possible to perform high precision isotope analyses using a reduced primary beam intensity and consequently a reduced spot size. Because no sedimentary pyrite as small as $5\ \mu\text{m}$ has been ever measured, the first goal of this PhD was to develop an analytical protocol for precise and accurate Fe isotope analyses. A part of the protocol, notably for chromium interference correction, was adapted from *Marin-Carbonne et al. (2011)*.







2.8.2. Article published in RCM

Published in *Rapid Communications in Mass Spectrometry*.

Decraene M-N., Marin-Carbonne J., Bouvier A-S., Villeneuve J., Bouden N., Luais B., and Deloule E. 2021

RESEARCH ARTICLE

High-spatial-resolution measurements of iron isotopes in pyrites by secondary ion mass spectrometry using the new Hyperion-II radio-frequency plasma source

Marie-Noëlle Decraene^{1,2}  | Johanna Marin-Carbone¹  |
Anne-Sophie Bouvier¹  | Johan Villeneuve²  | Nordine Bouden² |
Béatrice Luais²  | Etienne Deloule² 

¹Institut des Sciences de la Terre, Université de Lausanne, Lausanne, Switzerland

²Université de Lorraine, CNRS, CRPG, Nancy, F-54000, France

Correspondence

M.-N. Decraene, Institut des Sciences de la Terre, Université de Lausanne, Lausanne, Switzerland.

Email: marie-noelle.decraene@unil.ch

Funding information

H2020 European Research Council, Grant/Award Number: 759289

Rationale: Iron isotopic signatures in pyrites are considered as a good proxy for reconstructing paleoenvironmental and local redox conditions. However, the investigation of micro-pyrites less than 20 μm in size has been limited by the available analytical techniques. The development of a new brighter radio-frequency plasma ion source (Hyperion-II source) enhances the spatial resolution by increasing the beam density 10 times compared with the Duoplasmatron source.

Methods: Here we present high-spatial-resolution measurements of iron isotopes in pyrites using a 3 nA–3 μm primary $^{16}\text{O}^-$ beam on two Cameca IMS 1280-HR2 ion microprobe instruments equipped with Hyperion sources at CRPG-IPNT (France) and at SwissSIMS (Switzerland). We tested analytical effects, such as topography and crystal orientation, that could induce analytical biases perceptible through variations of the instrumental mass fractionation (IMF).

Results: The $\delta^{56}\text{Fe}$ reproducibility for the Balmat pyrite standard is $\pm 0.25\%$ (2 standard deviations) and the typical individual internal error is $\pm 0.10\%$ (2 standard errors). The sensitivity on $^{56}\text{Fe}^+$ was 1.2×10^7 cps/nA/ppm or better. Tests on Balmat pyrites revealed that neither the crystal orientation nor channeling effects seem to significantly influence the IMF. Different pyrite standards (Balmat and SpainCR) were used to test the accuracy of the measurements. Indium mounts must be carefully prepared with a sample topography less than 2 μm , which was checked using an interferometric microscope. Such a topography is negligible for introducing change in the IMF. This new source increases the spatial resolution while maintaining the high precision of analyses and the overall stability of the measurements compared with the previous Duoplasmatron source.

Conclusions: A reliable method was developed for performing accurate and high-resolution measurements of micrometric pyrites. The investigation of sedimentary micro-pyrites will improve our understanding of the processes and environmental conditions during pyrite precipitation, including the contribution of primary (microbial activities or abiotic reactions) and secondary (diagenesis and/or hydrothermal fluid circulation) signatures.

1 | INTRODUCTION

Iron stable isotope geochemistry has developed rapidly over the last 15 years, particularly because iron is a ubiquitous element that occurs in three oxidation states: Fe⁰, Fe²⁺ and Fe³⁺. The redox state affects the iron isotope fractionation of the four stable isotopes, ⁵⁴Fe (5.80%), ⁵⁶Fe (91.72%), ⁵⁷Fe (2.20%) and ⁵⁸Fe (0.28%), following the mass- and temperature-dependent fractionation laws.^{1–4} The iron isotopic composition is reported using the delta (δ) notation (in ‰) defined as deviations of the measured ⁵⁶Fe/⁵⁴Fe or ⁵⁷Fe/⁵⁴Fe ratios of a sample relative to the international standard IRMM-014 (⁵⁶Fe/⁵⁴Fe value of 15.6986 and ⁵⁷Fe/⁵⁴Fe value of 0.3626)^{5,6}:

$$\delta^{5x}\text{Fe} = \left[\frac{\left(\frac{{}^{5x}\text{Fe}}{{}^{54}\text{Fe}}_{\text{sample}} \right)}{\left(\frac{{}^{5x}\text{Fe}}{{}^{54}\text{Fe}}_{\text{IRMM014}} \right)} - 1 \right]$$

where x is either 6 or 7. The accuracy and precision were determined by the analysis of in-house pyrite standards, Balmat and SpainCR (detailed in section 2.1).

The difference in iron isotopic compositions between two species defines the isotopic fractionation. Iron isotope systematics is used in numerous fundamental fields, such as cosmochemistry and igneous petrology, that focus on the accretion of planetary bodies, magmatic differentiation and diffusion during crystal growth,^{5,7–11} as well as in environmental geochemistry for understanding the past and modern redox marine cycle.^{5,12–17} Iron is also a major element in numerous biological reactions leading to diagnostic isotopic fractionations and, thus, it can be a good proxy for biosignature recognition. The microbial iron cycle is controlled by dissimilatory iron reduction and bacterial iron oxidation leading to precipitation of diverse Fe(II)-bearing biominerals, including iron sulfides.^{18,19} However, pyrites can also be formed through abiotic reactions. Both biological and abiotic pathways are associated with large mass-dependent iron isotopic fractionations.^{20–33} Consequently, biologically precipitated pyrites record $\delta^{56}\text{Fe}$ variations up to 6‰,^{20,22–24} encompassing the entire range of terrestrial iron isotopic fractionation (see e.g. Johnson et al.¹³ and Beard and Johnson³⁴ for reviews). The formation of sedimentary pyrites is a complex, multi-stage process that includes dissolution of FeS_m precursors such as mackinawite (FeS) or greigite (Fe₂S₃).^{35,36} Importantly, biologically mediated sulfides are typically very small, <1 μm in size, as illustrated by FeS precipitates in microbial sulfate-reducing bacteria cultures (reviewed in Rickard³⁷). The dissolution of those FeS precursors leads to the precipitation of pyrites ranging in size from less than 1 μm to tens of micrometers (especially for sedimentary pyrite framboids),³⁸ which introduces analytical challenges for isotopic measurements in a single pyrite grain.

Investigation of iron isotope variability started with the application of thermal ionization mass spectrometry (TIMS) and was followed by multi-collection inductively coupled plasma mass

spectrometry (MC-ICPMS), which yielded higher sensitivity and higher precision measurements. As a result, the application of MC-ICPMS to igneous rocks allowed the recognition of small iron isotope variations associated with high-temperature fractionation processes.^{8,32,33} However, only a few studies have focused on microscale isotope variations in biogeochemistry. For instance, depending on the technique, strong contrasts in iron isotope compositions have been documented in pyrites from the 2.7 Ga Tumbiana Formation (Pilbara Craton, Western Australia). Bulk rock analyses produced a narrow range of $\delta^{56}\text{Fe}$ values of $-0.02 \pm 0.26\%$ (2SD, standard deviation),¹⁵ while *in situ* analyses by laser ablation MC-ICPMS yielded a wide range of $\delta^{56}\text{Fe}$ values, from -2.9% to $+1.5\%$.^{39,40} Similarly, in Archean pyrite nodules (2.7 Ga shale from Bubi Greenstone Belt, Zimbabwe), the bulk $\delta^{56}\text{Fe}$ values were around -1.4% whereas *in situ* measurements by secondary ion mass spectrometry (SIMS) described rim-to-core profiles from $+0.5\%$ to -2% .¹⁶ These two examples strongly support the importance of combining whole rocks and micrometer-scale *in situ* analysis to constrain primary and/or secondary signals recorded in a pyrite.

Available on the market since 2015, the new radio-frequency oxygen ion source on SIMS instruments, the Hyperion-II, has a primary beam current density that is 10 times greater than that of the conventional Duoplasmatron oxygen source.⁴¹ The characteristics of the primary beam and secondary transmission are documented in Liu et al.⁴¹ For a given primary beam intensity, the improved current density increases the spatial resolution while maintaining analytical precision compared with the previous ¹⁶O⁻ source performance. The improvement of secondary ion transmission, and higher precision and reproducibility measurements have been reported for Mg^{41,42} and Si⁴³ isotope systems. For example, an external reproducibility of $\pm 0.2\%$ (2SD) on $\Delta^{26}\text{Mg}^*$ (independent mass fractionation) is achieved with a primary beam size of 3–4 μm,⁴¹ much smaller than the 15 μm achievable with the Duoplasmatron source.⁴⁴ The new source has also higher sensitivity per unit area for Pb isotopes with a 10 nA primary beam, allowing the precision of U–Pb dating measurements of zircons to be enhanced.⁴¹ Therefore, one of the main advantages of the Hyperion source is the improved spatial resolution achieved without a loss in the precision required for resolving biogeochemical processes. Previously, the expected precision of $\pm 0.2\%$ (2SD) for iron isotope analysis was obtained with a 10 nA primary beam intensity delivered by the Duoplasmatron source, focused into a ca 15 μm spot to generate enough secondary ion intensity to be collected by multi-collection Faraday cups (FCs). However, such spot sizes limited the investigation of iron isotopes in micrometric grains, whereas the Hyperion source opens new possibilities for the studies of biochemical processes.

In order to explore micrometric-scale variations of iron isotopes in pyrites, we have adapted a previously described analytical procedure by using the Hyperion source, combining the reduction of the spot size for a given intensity, and maintaining a precision of 0.2‰ (2SD). This protocol has been tested on two different SIMS instruments and will open a new analytical field for the study of iron isotope microscale variabilities in sedimentary pyrites.

2 | EXPERIMENTAL

SIMS measurements were carried out using the Cameca IMS 1280-HR2 ion probes (Cameca, Gennevilliers, France) at CRPG-IPNT (Nancy, France) and SwissSIMS (University of Lausanne, Switzerland), both of which were equipped with the new Hyperion-II radio-frequency source. We performed four iron isotope sessions at CRPG-IPNT (February 2018, April 2018, July 2018 and September 2020) and four sessions at SwissSIMS (July 2019, January 2020, March 2020 and June 2020).

2.1 | Standards

The stability of both instruments was monitored by running multiple measurements of in-house pyrite standards, either Balmat or SpainCR pyrites, that were also used to correct a possible instrumental drift. The major elemental composition of Balmat pyrite is described elsewhere⁴⁵ and it contains 46.5 wt% of Fe and 53.6 wt% of S. This pyrite standard is extensively used for SIMS Fe and S isotopes analyses.^{16,45–47} The major and trace element compositions of SpainCR pyrite were determined using a JXA-8530F electron microprobe (JEOL, Tokyo, Japan) at the University of Lausanne and data are available in the supporting information (Data S1). The analytical parameters are also described in the supporting information (Data S2). SpainCR pyrite grains contain 46.6 wt% of Fe and 53.1 wt% of S. The Co, Mn, Cr, Zn and Cu contents are below the detection limit, and the Pb, Ti and Ni contents are 1112, 1003 and 354 ppm, respectively. The SpainCR standard was previously used for SIMS S isotope analysis.^{47,48} The Fe isotopic composition of SpainCR pyrite was determined at CRPG. The chemistry employed for Fe purification and the Fe isotopic analysis using the NeptunePlus MC-ICPMS instrument are detailed elsewhere.^{45,49,50} In order to evaluate the homogeneity of the Fe isotopic composition of the SpainCR pyrite standard, the core and rim samples were chemically processed and analyzed separately. The bulk Fe isotope measurement sequence follows the sample/standard bracketing method, with IRMM-014 Fe as the normalizing standard. We obtained similar $\delta^{56}\text{Fe}$ (and $\delta^{57}\text{Fe}$) values of $+0.516 \pm 0.05\text{‰}$ ($+0.804 \pm 0.03\text{‰}$) (2SD) and $+0.521 \pm 0.02\text{‰}$ ($+0.795 \pm 0.01\text{‰}$) (2SD) for the core and rim, respectively, for $n = 3$ replicates of each. This gives a $\delta^{56}\text{Fe}_{\text{mean}}$ reference value of $0.52 \pm 0.03\text{‰}$ for this highly homogeneous SpainCR pyrite standard. The data accuracy and 2SD reproducibility were evaluated by replicate analyses of geostandards, with values of $\delta^{56}\text{Fe} = +0.648 \pm 0.129\text{‰}$ and $\delta^{57}\text{Fe} = +0.960 \pm 0.163\text{‰}$ ($n = 3$) for IF-G (BIF Greenland) and $\delta^{56}\text{Fe} = +0.098 \pm 0.033\text{‰}$ and $\delta^{57}\text{Fe} = +0.143 \pm 0.057\text{‰}$ ($n = 15$) for BIR-1 (USGS Iceland basalt) during the course of this study. These values were within the range of the reported reference values.⁵ The homogeneity of the SpainCR standard was tested using SIMS by measuring three different grains prepared in the same mount (July 2018 session at CRPG-IPNT). Based on 68 measurements, the external reproducibility was $\pm 0.28\text{‰}$ (2SD) (Figure S1, supporting information (Data S2)).

As no Cr was detected in the pyrite reference materials, the Russie magnetite standard was used to evaluate the degree of ^{54}Cr interference on ^{54}Fe , which was necessary for the natural samples due to the presence of Cr. Details are given in section 2.5.

2.2 | Sample preparation

Standard grains were embedded in epoxy and polished with 0.5- μm diamond paste. Those grains were carefully removed from epoxy and pressed into a 1-inch indium mount. A white light interferometric Contour GT-K microscope (Bruker, Karlsruhe, Germany) at the University of Lausanne was used to measure the sample topography. The relief across the analyzed surface was below 5 μm .⁵¹ The samples were coated with a 35-nm thick gold film to ensure conductivity between the sample surface and the SIMS holder.

2.3 | Electron backscatter diffraction

To check for the influence of crystallographic orientations on SIMS measurements, three Balmat pyrite grains were removed from the indium mount and embedded in epoxy resin with the analyzed mineral surfaces facing upwards. To eliminate any residual surface damage, the mount was further polished for 40 min using the combined chemical and mechanical effect of an alkaline (pH = 9.8) suspension of colloidal silica (0.05 μm). The sample was not carbon-coated before electron backscatter diffraction (EBSD) analysis in order to maximize the detected signal. The crystallographic orientation patterns were acquired at the University of Lausanne, using a Mira II LMU field emission scanning electron microscope (Tescan, Brno, Czech Republic) equipped with a Symmetry detector and employing the Aztec 4.2 software package (both from Oxford Instruments, Abingdon, UK). The acquisition parameters included an acceleration voltage of 20 kV, a probe current of 1.1 nA, a working distance of 23 mm and a 70° tilt of the sample surface with respect to the horizontal. As pyrite has a cubic crystal structure, the [100], [010] and [001] axes are equivalent and orthogonal, and the maximum misorientation imposed by symmetry is 62.8°. The pyrite (m3)⁵² match unit ($a = 5.4166 \text{ \AA}$) was used as a reference file for the indexing of the EBSD patterns, the high quality of which was attested by a mean angular deviation value ranging between 0.2 and 0.6. Six to ten EBSD patterns per grain were collected and the average crystallographic orientations represented in an upper hemisphere equal area pole figure of Euler angle triplets (φ_1 , Φ , φ_2). For more information on the basics of the EBSD technique, the reader is referred to Prior et al.⁵³

2.4 | SIMS settings

The samples were stored in a vacuum chamber at 2.5×10^{-8} to 2×10^{-9} mbar, and sputtered with a 3 nA $^{16}\text{O}^-$ primary beam accelerated by a 13 kV voltage, with a corresponding spot size of 2.5

to 3 μm (Figure 2). The primary beam was mainly focused through the L3 and L4 lenses of the primary column in Gaussian mode and the aberration was reduced using a PBMF aperture of 200 μm . The L4 aperture was maintained open at 750 μm . These settings of primary beam apertures were the same for both instruments and the main SIMS settings are summarized in Table 1. The entrance slit was set to 61 μm at SwissSIMS and 85 μm at CRPG-IPNT, corresponding to a mass resolving power (MRP) of $M/\Delta M \sim 6700\text{--}7000$ (slit 3) at SwissSIMS and $M/\Delta M \sim 6100$ (slit 3) at CRPG-IPNT, resolving the interference of $^{53}\text{CrH}^+$ on $^{54}\text{Fe}^+$ ($M/\Delta M = 6088$). The interference of $^{54}\text{Cr}^+$ on $^{54}\text{Fe}^+$ (MRP $\sim 74\,000$) was monitored by measuring $^{52}\text{Cr}^+$ as described elsewhere.⁴⁵ Although pyrite standards have no detectable Cr, hundreds to thousands of counts of ^{52}Cr are measured in natural pyrites, calling the $^{54}\text{Cr}^+$ contribution at mass 54 to be estimated and then corrected for. The correction scheme for Cr was established using a magnetite standard, which has a detectable amount of Cr, resulting in a final correction of *ca* 0.15% on $\delta^{56}\text{Fe}$ per 1×10^4

counts per second (cps) of $^{52}\text{Cr}^+$. The interference of $^{56}\text{FeH}^+$ on $^{57}\text{Fe}^+$, which requires a MRP of 7700, could not be clearly resolved with the chosen slit settings. However, this high-spatial-resolution method has been developed in order to measure $\delta^{56}\text{Fe}$ values in micrometric pyrites. To obtain a maximum internal error of 0.3‰ (2SE, standard error) on $\delta^{56}\text{Fe}$, the minimum $^{56}\text{Fe}^+$ intensity on the pyrite standard should be 4×10^7 cps, which cannot be attained when the MRP is > 7000 . Pyrite, being a nominally anhydrous mineral held under a vacuum of *ca* 2×10^{-9} mbar, yields low interferences of $^{56}\text{FeH}^+$ on $^{57}\text{Fe}^+$. When the pyrites are prepared in an indium mount, iron hydride is not detected in the FC measurements (see section 2.5). The secondary ion beam was filtered by an energy slit of 50 eV. A 2000 μm square field aperture was used to clip *ca* 10% of the signal and to remove off-axis aberrations of the secondary ion beam. We used a transmission setting (maximum area (MA) 80) leading to a field of view of the sample of 20 $\mu\text{m} \times 20 \mu\text{m}$ in the field aperture. The secondary $^{54}\text{Fe}^+$, $^{56}\text{Fe}^+$, $^{57}\text{Fe}^+$ and $^{52}\text{Cr}^+$ ions were accelerated at

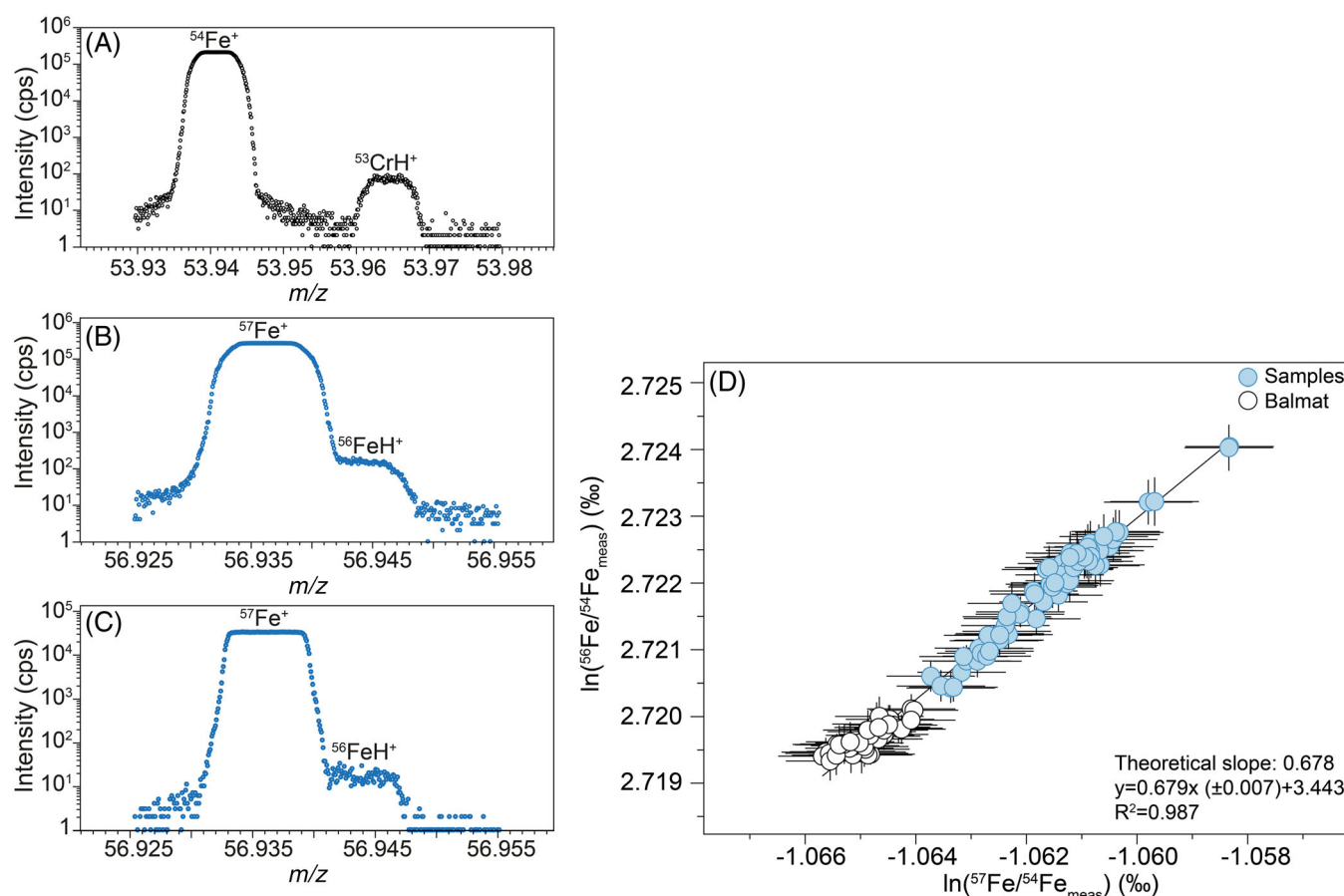


FIGURE 1 (A) Scan of the ^{54}Fe signal on the axial EM, using a mass resolution of 6800 to reveal the $^{53}\text{CrH}^+$ contribution. This scan was carried out on a Russie magnetite standard which has a detectable Cr content. (B) Scan of the ^{57}Fe signal on the axial EM, using a mass resolution of 6800 to reveal the $^{56}\text{FeH}^+$ contribution. (C) High-mass-resolution (MRP of 7800) scan of the ^{57}Fe signal, where the $^{57}\text{Fe}^+$ and $^{56}\text{FeH}^+$ peaks are separated. (D) Three-isotope plot of the logarithm of the measured Fe isotope ratios in Balmat pyrite standard (white dots) and pyrites from sedimentary rocks (blue dots), corrected for the ^{54}Cr contribution (July 2020 session at SwissSIMS). The regression line gives a slope of 0.679 ± 0.007 , which is in good agreement with the theoretical slope of 0.678 within the error bar. The theoretical value represents the mass-dependent fractionation law for Fe isotopes using a simple harmonic oscillator approximation. Data are available in Table S1 (supporting information, Data S2)

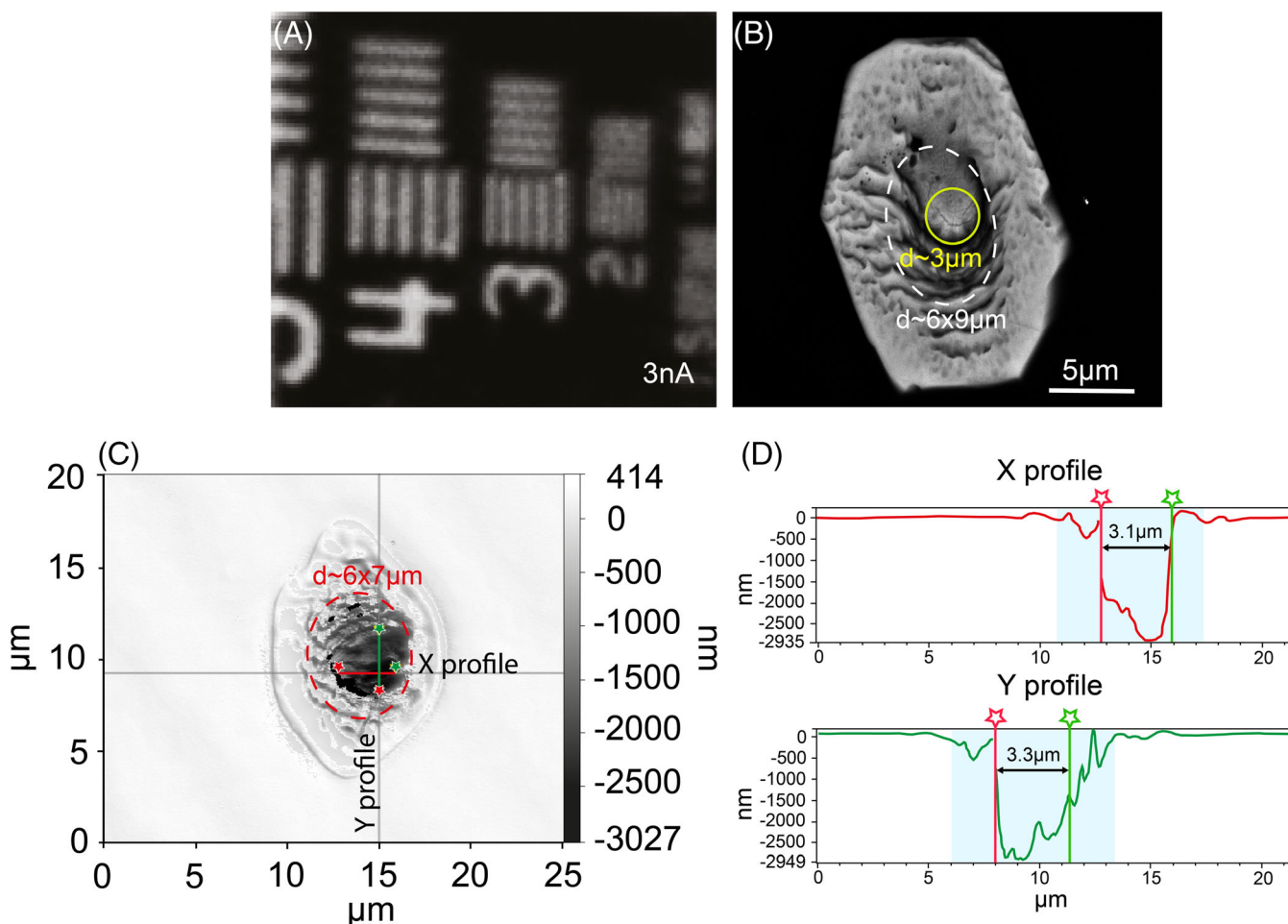


FIGURE 2 (A) $^{30}\text{Si}^+$ image of the Si grid on electron multiplier. The spatial resolution of the primary $^{16}\text{O}^-$ beam is determined according to the ability to differentiate two silicon bars on the 4, 3 or 2 μm grid. (B) SEM image of a sedimentary micro-pyrite after SIMS analyses. The shape of the spot is due to the position of the source which makes an angle with the sample surface. (C) Image from interferometric microscope of the sputtering pit. (D) X and Y topographic profiles measured by an interferometric microscope. The profiles refer to (C) and show the diameter of the pit, which corresponds to the real spot size (measured at the bottom of the pit), and the sputtered area (blue area in (D) and dashed red circle in (C), measured at the top of the pit)

10 kV and measured on three off-axis FCs and one electron multiplier (detectors C, H1, H'2 and L2, respectively). The C and H1 FCs were equipped with $10^{11} \Omega$ resistors, and the H'2 FC was equipped with a $10^{12} \Omega$ resistor at CRPG-IPNT and a $10^{11} \Omega$ resistor at SwissSIMS. The relative yields of the amplifiers of the FCs were calibrated before each session on both ion microprobes and the background noise of the FCs was measured for each analysis. The high voltage of the electron multiplier was adjusted before each session. No aging effect of the electron multiplier was observed during the session. A presputtering time is necessary to remove the 35 nm of gold and potential surface contamination, to implant primary ions in the sample surface and to obtain a stable secondary signal. The intensity of $^{56}\text{Fe}^+$ increased until it became stable after 90 s (Figure S2, supporting information (Data S2)). The intensity of the signal is then stable with a typical count rate between 4×10^7 and 5×10^7 cps when using a 3 nA primary beam intensity.

The analytical routine then consisted of 90 s of presputtering followed by 60 cycles (5 s each) of collection separated by 0.08 s waiting time, for a total of 7 min per analysis. After presputtering, automatic beam centering in the field and contrast apertures, the energy slit and transfer deflectors was performed routinely. The typical count rates of $^{54}\text{Fe}^+$, $^{56}\text{Fe}^+$ and $^{57}\text{Fe}^+$ are 3.2×10^6 , 4.8×10^7 and 1.1×10^6 cps, respectively, for the Balmat reference material measured with the SwissSIMS instrument tuned with a primary beam intensity of 3.05 nA and 4.3×10^6 , 6.4×10^7 and 1.4×10^6 cps, respectively, with the CRPG-IPNT instrument tuned with a primary beam intensity ranging from 3.2 to 3.5 nA (Table 1). The difference in ion counting intensities between the two instruments is due to the higher primary current set at CRPG-IPNT and also reflects a differential transmission because a larger entrance slit was used at CRPG-IPNT. The internal precision on the $\delta^{56}\text{Fe}$ value of the Balmat standard was $\pm 0.10\%$ (2SE); the reproducibility is reported in terms

TABLE 1. SIMS settings for each Fe isotope session at CRPG-IPNT (February 2018, April 2018 and September 2020) and SwissSIMS (July 2019, January 2020, March 2020 and June 2020) using the Hyperion-II source and resulting $^{56}\text{Fe}^+$ intensities and ion yields measured on Balmat pyrite. Comparison with settings and $^{56}\text{Fe}^+$ yields measured with the Duoplasmatron^{45,46}

	This study				Published data			
	CRPG-IPNT		SwissSIMS		CRPG-IPNT	Nord SIMS		
Session	Hyperion-II	Hyperion-II	Hyperion-II	Hyperion-II	Duoplasmatron			
Feb. 2018	Apr. 2018	Sep. 2020	Jul. 2019	Jan. 2020	Mar. 2020	Jun. 2020	Ref. 45	Ref. 46
Field aperture (μm)	2000	2400	2000	2000	2500	2500	3000	3000
Contrast aperture (μm)	400			400	400		400	
Max. area	80	80	80	80	80	80	160	160
		160						
Entrance slit (μm)	85	61	61	61	—	—	60	60
Energy slit (eV)	50			50	50	50	60	60
Slit mode	Circular		Circular		Circular			
Exit slit	150 μm (slit 3)			150 μm (slit 3)	150 μm (slit 3)	150 μm (slit 3)	250 μm (slit 2)	
MRP	6100	6800		6700–6800	ca 7000	ca 7000	<6000	
Primary intensity (nA)	3.40	3.00	3.14	3.05	2.99	2.80	10	10
$^{56}\text{Fe}^+$ count rate on Balmat (cps)	6.5×10^7	4.70×10^7	4.90×10^7	4.85×10^7	4.46×10^7	4.49×10^7	$ca 1.2 \times 10^8$	$ca 1.5 \times 10^8$
		1.51×10^7						
$^{56}\text{Fe}^+$ yield on Balmat (cps/nA)	1.87×10^7	2.01×10^7	1.56×10^7	1.59×10^7	1.49×10^7	1.61×10^7	$ca 1.2 \times 10^7$	1.5×10^7
			5.05×10^6					

of 2SD. The external reproducibility ranges between $\pm 0.24\%$ ($n = 33$) and $\pm 0.30\%$ ($n = 17$; 2SD) at CRPG-IPNT and from $\pm 0.15\%$ ($n = 10$) to $\pm 0.28\%$ ($n = 39$; 2SD) at SwissSIMS (Table 2).

2.5 | Mass interferences ($^{53}\text{CrH}^+$ and $^{56}\text{FeH}^+$)

The required MRP to resolve the isobaric interference of $^{54}\text{Cr}^+$ on $^{54}\text{Fe}^+$ is beyond the capabilities of the ion microprobe (MRP $\sim 74\,000$), and thus the interference was indirectly quantified by measuring $^{52}\text{Cr}^+$. The detailed procedure for Cr correction⁴⁵ shows that the $^{53}\text{Cr}/^{52}\text{Cr}$ ratio measured by SIMS is similar to that determined from Cr isotope natural abundances ($^{52}\text{Cr} = 83.8\%$, $^{53}\text{Cr} = 9.5\%$ and $^{54}\text{Cr} = 2.4\%$). We thus used the natural abundances of the Cr isotopes combined with the measured $^{52}\text{Cr}^+$ intensity to calculate the $^{54}\text{Cr}^+$ intensity in standards and samples and then corrected the ^{54}Cr contribution from the measured ^{54}Fe signal. The $^{53}\text{CrH}^+$ peak height was measured in the Russie magnetite standard, on the axial electron multiplier (monocollection mode), using an 800 pA primary beam intensity to obtain $ca\ 2 \times 10^5$ cps on $^{54}\text{Fe}^+$ and to not saturate the detector. Under a vacuum of 3.4×10^{-9} mbar, the $^{53}\text{CrH}^+$ peak represents less than 0.05% of the $^{54}\text{Fe}^+$ peak (Figure 1A). Tens of counts are detected for $^{52}\text{Cr}^+$ in pyrite standards using a 3 nA primary beam, meaning that this hydride contribution can be ignored.

The accuracy of analysis can also be impacted by the interference of $^{56}\text{FeH}^+$ on $^{57}\text{Fe}^+$. In this study, the MRP was set lower ($ca\ 6800$) than that required to separate these two species. Using a higher MRP to obtain accurate $\delta^{57}\text{Fe}$ data would decrease the precision of $^{56}\text{Fe}/^{54}\text{Fe}$ ratios. However, the contribution from $^{56}\text{FeH}^+$ has been measured to evaluate the reliability of $^{57}\text{Fe}/^{54}\text{Fe}$ ratios. A high-resolution scan (MRP of 7800) of mass ^{57}Fe was carried out on the axial electron multiplier using a 1 nA primary beam intensity (Figure 1C). The magnitude of the $^{56}\text{FeH}^+$ peak is 0.05% of the $^{57}\text{Fe}^+$ peak height due to good vacuum conditions in the analysis chamber ($ca\ 3.4 \times 10^{-9}$ mbar) but can be up to 0.2% of the $^{57}\text{Fe}^+$ peak height when the vacuum conditions deteriorate to 2×10^{-8} mbar. The level of $^{56}\text{FeH}^+$ formation is thus estimated as 0.01–0.04%. At MRP of 6800, the mass scan shows that the ^{57}Fe flat top is affected by the tail of the hydride peak (Figure 1B). The hydride contribution to the ^{57}Fe signal is thus insignificant for measurements made in indium mounts. The contribution of hydrides to the Fe isotopic signal, in particular the interference of $^{56}\text{FeH}^+$ with $^{57}\text{Fe}^+$, can also be evaluated by the relationship between the $^{56}\text{Fe}/^{54}\text{Fe}$ and $^{57}\text{Fe}/^{54}\text{Fe}$ ratios. Pyrites from sedimentary rocks (Sonoma Basin, USA) and standards (Balmat pyrite) measured during the July 2020 session are plotted in a three-isotope diagram using the natural logarithms of the measured $^{56}\text{Fe}/^{54}\text{Fe}$ and $^{57}\text{Fe}/^{54}\text{Fe}$ ratios (Figure 1D; data available in Table S1, supporting information (Data S2)). All the data define a slope of 0.679 (± 0.007) with a correlation coefficient r^2 of 0.987, which is consistent with the expected mass-dependent fractionation slope of 0.678. Since the measured slope is consistent with the terrestrial mass fractionation slope, the contribution of $^{56}\text{FeH}^+$ to the $^{57}\text{Fe}/^{54}\text{Fe}$ ratio is assumed to be negligible. Sample mounting using

indium rather than epoxy together with vacuum conditions below 5×10^{-9} mbar is crucial for maintaining small hydride contributions and for producing reliable $\delta^{57}\text{Fe}$ data and high-precision $\delta^{56}\text{Fe}$ values.

2.6 | Instrumental mass fractionation correction

The effect of a mass-dependent fractionation due to the instrument, or instrumental mass fractionation (IMF), is defined as:

$$\alpha_{\text{inst}} = \frac{\left(\frac{^{56}\text{Fe}}{^{54}\text{Fe}}\right)_{\text{measured}}}{\left(\frac{^{56}\text{Fe}}{^{54}\text{Fe}}\right)_{\text{true}}} \quad \text{or} \quad \Delta^{56}\text{Fe}_{\text{inst}} (\text{‰}) = \delta^{56}\text{Fe}_{\text{measured}} - \delta^{56}\text{Fe}_{\text{true}}$$

using the approximation $\Delta^{56}\text{Fe}_{\text{inst}} \approx \ln(\alpha_{\text{inst}})$.

The “measured” and “true” $\delta^{56}\text{Fe}$ values are Fe isotopic compositions measured in the same reference material by SIMS and MC-ICPMS. The typical IMF on pyrite is $ca\ -30 \pm 5\%$, measured by both Hyperion-II and Duoplasmatron sources, but the exact value depends on the instrument tuning. For example, a 4‰ shift in the IMF for Balmat pyrite was measured after retuning of the primary beam. Slight modifications of the primary beam (i.e. different high voltages on the primary lenses resulting in similar primary intensity but different beam densities) and entrance slit settings lead to a variation of the IMF on Balmat pyrite between -31.20% and -33.10% at CRPG-IPNT and highly variable, from -27.23% to -35.16% , at SwissSIMS (Table 2). We measured the IMF using the Balmat pyrite standard to monitor the stability of the ion probe during each session.

3 | RESULTS AND DISCUSSION

3.1 | Spot size

The resolution of ion images of a silicon grid on an electron multiplier is used to estimate the $^{16}\text{O}^-$ primary beam size. To find the best possible resolution of the image (i.e. getting the smallest beam) we tested different combinations of primary lenses; the best result was obtained by setting the voltage on L1 and L2 to 9800 and 9900 V, respectively, and keeping that on L3 close to 8500 V. The results of the $^{30}\text{Si}^+$ ion images are reported in Figure 2A. Using a 3 nA $^{16}\text{O}^-$ beam, the ability to differentiate two silicon bars on the 3 μm grid indicates a spot size similar to 3 μm . The 2 μm gap between the two horizontal Si bars is not completely resolved whereas the vertical bars are clearly visible, meaning that the spot size is between 2.5 and 3 μm . The spot size was verified by scanning electron microscopy (SEM) (Figure 2B) and an interferometric microscope (Figure 2C) after the SIMS measurements of a sedimentary micro-pyrite and the pyrite standard (Balmat). White light interferometric microscopy allows for the precise quantification of the beam size, by imaging the relief of the beam crater in both the X and Y directions (Figures 2C and 2D). The primary beam size is measured at the bottom of the pit and

TABLE 2 True $\delta^{56}\text{Fe}$ values of the standards (Balmat and SpainCR pyrites) and the corresponding IMF during the different sessions at CRPG-IPNT and SwissSIMS and comparison with the published IMF obtained with the Duoplasmatron.⁴³ The true $\delta^{56}\text{Fe}$ value of SpainCR standard was determined by MC-ICPMS at CRPG using a reported procedure.⁵⁰ The reproducibility is reported as 2SD. *n* = number of analyses; n.a. = data not available

IMF $\delta^{56}\text{Fe}_{\text{IMF}}$ and reproducibility (2SD, ‰)		SwissSIMS Hyperion-II		CRPG-IPNT Duoplasmatron				
Session	(no. of analyses)	Jul. 2018	Sept. 2020	Jul. 2019	Jan. 2020	Mar. 2020	Jun. 2020	Ref. 45
Balmat Py.	-33.10 ± 0.24 (<i>n</i> = 33)	n.a.	-31.20 ± 0.30 (<i>n</i> = 17)	-35.16 ± 0.28 (<i>n</i> = 41)	-27.23 ± 0.35 (<i>n</i> = 16)	-32.34 ± 0.18 (<i>n</i> = 33)	-33.06 ± 0.22 (<i>n</i> = 185)	-32.00 ± 0.20
SpainCR Py.	n.a.	-33.21 ± 0.28 (<i>n</i> = 68)	n.a.	-35.50 ± 0.32 (<i>n</i> = 2)	n.a.	n.a.	n.a.	n.a.

corresponds to a *ca* 3 μm diameter spot. This quantitative analysis is consistent with the beam size estimated through ion imaging of the Si grid. The sputtered area is extended over a diameter of 6 μm by 7–9 μm depending on the session and the pit is *ca* 3 μm deep (Figure 2D). The asymmetric shape of the crater and the larger sputtered area compared with the real primary beam size are due to the incidence angle of the beam with the sample surface, which is characteristic of the Cameca ion probes (except NanoSIMS) (Figure 2B).

3.2 | Crystal orientation and topography effects on the IMF

The IMF is the main limitation to the accuracy of SIMS analysis.^{54,55} It results from various processes occurring during secondary atom ionization, extraction, secondary ion transmission and detection.⁵⁵ The IMF is known to be highly dependent on sample characteristics (mineralogy, chemical composition and crystallographic orientation^{55–57}). This effect is corrected by measuring a reference material (same mineral, crystallography and major element chemical compositions) and the samples under the same analytical conditions. IMF variations occur in various isotopic systems; for example, the $\delta^{18}\text{O}$ measurements of garnets are strongly affected by their Ca–Fe–Mg content,^{58,59} as well as $\delta^{34}\text{S}$ measurements in Fe–Ni sulfides,^{56,60,61} and Mg and Si isotopes in silicates (e.g. olivine, glass, pyroxene) with an IMF depending on their Mg content.^{43,62} Crystal orientation may also in some cases have a strong influence on the IMF, as demonstrated for example on Fe isotopic compositions in magnetite,⁵⁷ on S isotope compositions in sphalerite and galena,⁶³ and on U–Pb dating in baddeleyite.⁶⁴

As pyrites are not affected by major element substitution, i.e. no solid solution or chemical variability, the potential variations of the IMF can only be the result of the crystal orientation and/or the topography. The EBSD pole figure shown in Figure 3B displays the crystallographic orientations of three different grains (G1, G2, G3) of the Balmat standard projected on a plane (XY) parallel to the surfaces analyzed by SIMS (and EBSD). With misorientation angles between the [100] axes in G1, G2 and G3 and the reference direction Z (i.e. the normal to the plane pointing towards the reader) of 14°, 6° and 1°, respectively, the analyzed surfaces can be considered nearly parallel to the face of the pyrite unit cell (i.e. normal to the [100] axis). The misorientation angle between the [100] axes located in the middle of the pole figure is 18° between G1 and G2, and 15° between G1 and G3. Fe isotopic measurements show respective mean $\delta^{56}\text{Fe}$ values and external reproducibility of $-0.29 \pm 0.30\text{‰}$ (2SD)/ $\pm 0.13\text{‰}$ (2SE, *n* = 5), $-0.59 \pm 0.42\text{‰}$ (2SD)/ $\pm 0.19\text{‰}$ (2SE, *n* = 5) and $-0.32 \pm 0.44\text{‰}$ (2SD)/ $\pm 0.20\text{‰}$ (2SE, *n* = 5) for G1, G2 and G3 (Figure 3A). Those $\delta^{56}\text{Fe}$ values suggest that the inter-grain variability is lower than the reproducibility (2SD) and the uncertainty on the averages (2SE). Although the EBSD measurements on a sample set of only three grains have no statistical significance, it can be said at this stage that no obvious relationship between the crystallographic orientation of pyrite and SIMS $\delta^{56}\text{Fe}$ measurements has been

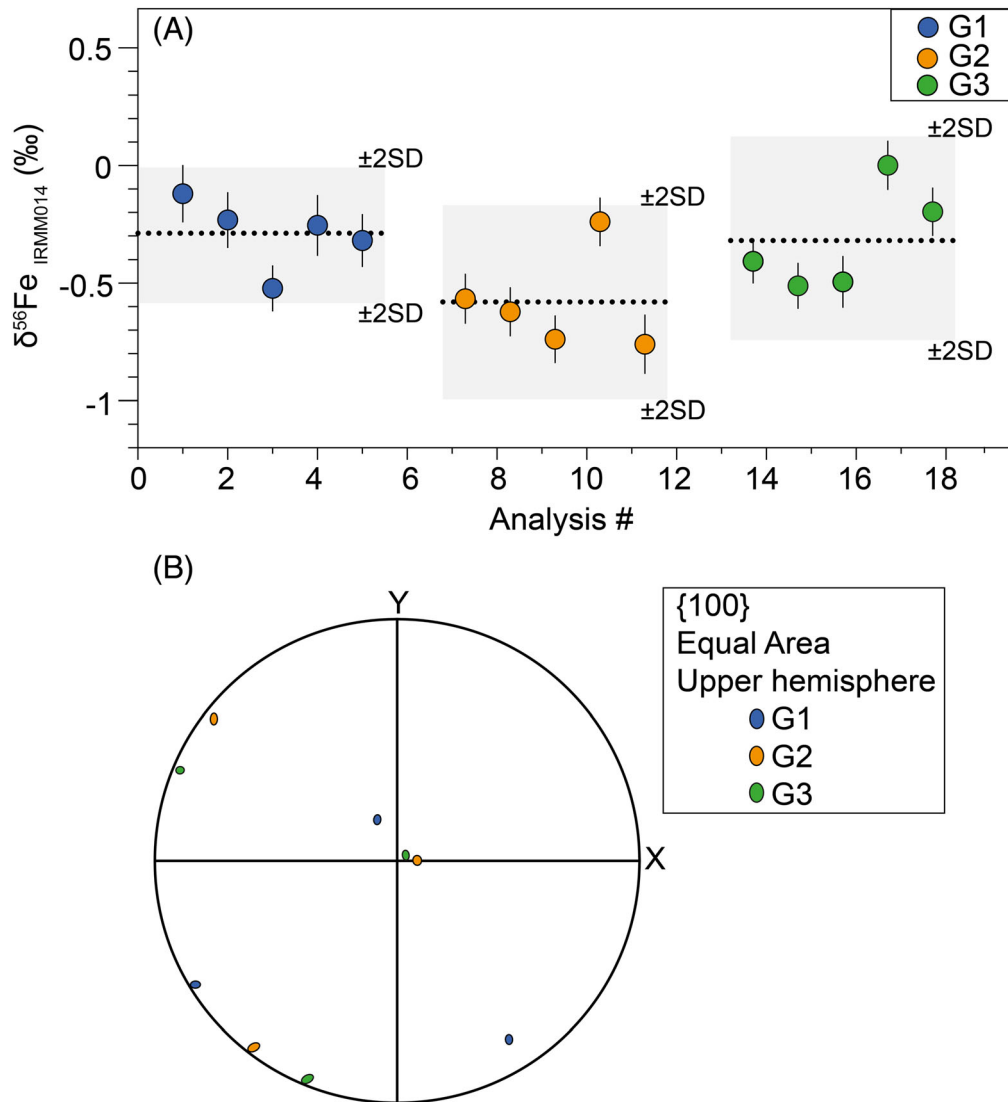


FIGURE 3 Crystal orientation (September 2020) test in the Balmat pyrite standard. (A) $\delta^{56}\text{Fe}$ value corrected from instrumental fractionation measured in three grains prepared in an indium mount. The reproducibilities are given at 2SD and show no clear difference between the grains. Data are available in Table S2 (supporting information, Data S2). (B) Upper hemisphere equal area (i.e. with Z pointing to the reader) EBSD pole figure showing the averaged crystallographic orientations of {100} for the three pyrite grains of interest. Note the strong clustering of [100] axes close to Z

observed. A thorough review (beyond the scope of this study) based on a wide range of crystallographic orientations is needed to confirm this initial statement. Our results are also consistent with the absence of crystal orientation effects on S isotopes.^{57,65}

The channeling effect of the primary ion beam as a function of atomic plane orientation has been shown to influence the secondary ion yields and thus the instrumental mass fractionation.^{66,67} Similarly to magnetite that exhibits channeling effects and plane-specific IMF for Fe and O isotopes,⁵⁷ pyrites are cubic minerals that could experience such effects. This effect was evaluated by rotating the mount in the sample holder by 90°, 180° and 270°. We ran three to six analyses per rotation (Table S2, supporting information (Data S2)). The mean IMF-corrected $\delta^{56}\text{Fe}_{\text{IRMM014}}$ values for P0, P1, P2 and P3 are $-0.38 \pm 0.31\%$

(2SD)/ $\pm 0.13\%$ (2SE, $n = 6$) for P0, $-0.49 \pm 0.37\%$ (2SD)/ $\pm 0.21\%$ (2SE, $n = 3$) for P1, $-0.38 \pm 0.12\%$ (2SD)/ $\pm 0.07\%$ (2SE, $n = 3$) for P2 and $-0.39 \pm 0.36\%$ (2SD)/ $\pm 0.16\%$ (2SE, $n = 5$) for P3 (Figure 4). Considering the external reproducibility (2SD) and the internal error (2SE) together, those data show similar mean $\delta^{56}\text{Fe}$ values across the four positions in the holder.

Surface topography could also induce artificial iron isotopic variations, especially when the pyrite grains are just slightly larger than the primary spot size. Here, a core-to-rim profile on Balmat pyrites was performed in order to examine the edge effect on the reliability of $\delta^{56}\text{Fe}$ analyses. Fe isotope analyses show similar $\delta^{56}\text{Fe}$ values for the core and the rim, of $\delta^{56}\text{Fe}_{\text{BalmatPf1@01}} = -0.27 \pm 0.11\%$ (2SE, $n = 1$, core) and $\delta^{56}\text{Fe}_{\text{BalmatPf1@8}} = -0.28 \pm 0.12\%$ (2SE, $n = 1$, rim), and an external reproducibility of $\pm 0.18\%$ (2SD) (Figure 5D; data

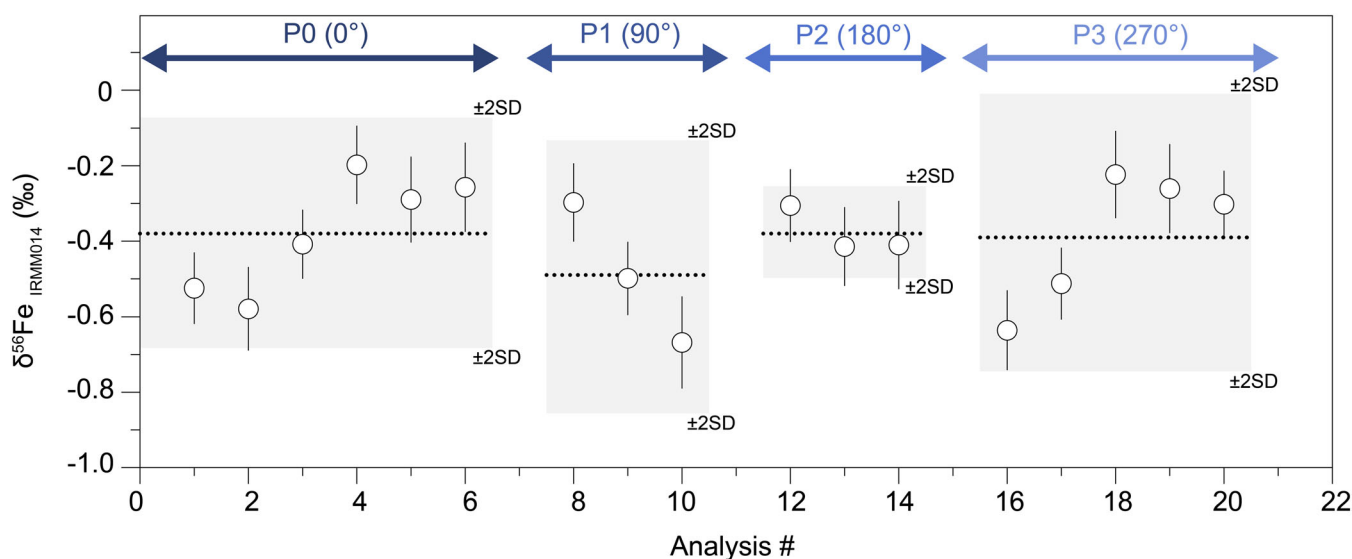


FIGURE 4 $\delta^{56}\text{Fe}$ values IMF-corrected of the Balmat pyrite standard rotated by 90° (P1), 180° (P2) and 270° (P3) compared with the initial position (P0). The external reproducibility is $\pm 0.30\text{‰}$ (2SD) and the internal variabilities are $\pm 0.10\text{‰}$ to $\pm 0.20\text{‰}$ (2SE), allowing us to rule out an orientation (channeling) effect on IMF variations. Data are available in Table S2 (supporting information, Data S2)

available in Table S2, supporting information (Data S2)). This profile (Pf1) is characterized by a topographic difference of $1.7\ \mu\text{m}$ (Figure 5C), which is not sufficiently significant to introduce a bias. However, the last analysis is located at *ca* $20\ \mu\text{m}$ from the grain edge that is *ca* $7\ \mu\text{m}$ above the enclosing indium. Thus, this value was measured in the slightly tilted shade zone on the edge of the pyrite (Figures 5A and 5B), demonstrating the reliability of the $\delta^{56}\text{Fe}$ values.

3.3 | Sensitivity

The sensitivity depends on the sputtering time, ionization, extraction of the Fe^+ ion from the matrix and secondary ion transmission until the detectors. It is defined as count rate per ppm of Fe in the analyzed phase per nA of the primary beam (cps/ppm/nA). As the Fe content is constant in pyrites, the expression of the sensitivity is approximately proportional to the ion yield:

$$^{56}\text{Fe} \text{ yield} = ^{56}\text{Fe}^+ / \text{P intensity.}$$

The sensitivity calculation is commonly used to evaluate the transmission of an ion microprobe. Table 1 presents the $^{56}\text{Fe}^+$ ion yields on Balmat pyrite, obtained over the different sessions at CRPG-IPNT and SwissSIMS using the Hyperion-II source. We compared these results with those obtained with the conventional Duoplasmatron source.^{45,46} The sensitivities determined on Balmat pyrite range from 1.56×10^7 to 2.01×10^7 cps/nA at CRPG-IPNT. Sessions performed at SwissSIMS (July 2019, January 2020, March 2020 and September 2020) show similar sensitivities, ranging from 1.49×10^7 to 1.61×10^7 cps/nA. The higher sensitivities obtained at CRPG-IPNT than at SwissSIMS are explained by the different widths of the entrance slit. The sensitivities obtained with the Duoplasmatron source vary from 1.2×10^7 cps/nA⁴⁵ to 1.5×10^7 cps/nA.⁴⁶ However, the resulting transmissions in the

two Duoplasmatron-based studies are not directly comparable as the width of the field aperture, the entrance and exit slits and the MA are different between these two studies (Table 1). In order to compare sensitivities obtained by the Hyperion and the Duoplasmatron sources, we performed two tests using (1) a MA of 80 and field aperture closed at *ca* $2500\ \mu\text{m}$ (comparable with the sensitivity obtained previously⁴⁵) and (2) a MA of 160 and an opened field aperture to transmit 100% of the signal.⁴⁶ Using a MA of 80 and similar field aperture, entrance and exit slit widths, the ^{56}Fe sensitivity is 1.56×10^7 cps/nA and better than the 1.2×10^7 cps/nA obtained with the Duoplasmatron.⁴⁵ The higher sensitivity with the Hyperion is due to the use of a smaller beam, which is less clipped in the field aperture than the Duoplasmatron beam. Using a MA of 160, we obtained a sensitivity of 5.05×10^6 cps/nA, which is lower than the 1.5×10^7 cps/nA achieved by the Duoplasmatron.⁴⁶ However, these sensitivities are not directly comparable as O_2^- and O^- primary beams were, respectively, used in Whitehouse and Fedo⁴⁶ and in the present study. The higher sensitivity obtained previously⁴⁶ can be thus attributed to the more efficient sputtering rate of the O_2^- beam. The use of smaller primary beam currents reduces the size of the crossover and off-axis aberrations of the secondary ion beam, which helps to define a sharper slit image. Therefore, for a given MRP, the entrance slit can be more opened using the Hyperion and this results in a gain of sensitivity compared with the Duoplasmatron. This test illustrates the ability of the source to provide enough secondary ion signals with a 3 nA beam focused on a $3\ \mu\text{m}$ spot and to achieve a better sensitivity than that delivered by the Duoplasmatron. The Fe secondary ion signals produced by the 3 nA primary beam can be detected by multi-collection FCs, and thus provide high-precision $\delta^{56}\text{Fe}$ measurements along with higher spatial resolution.

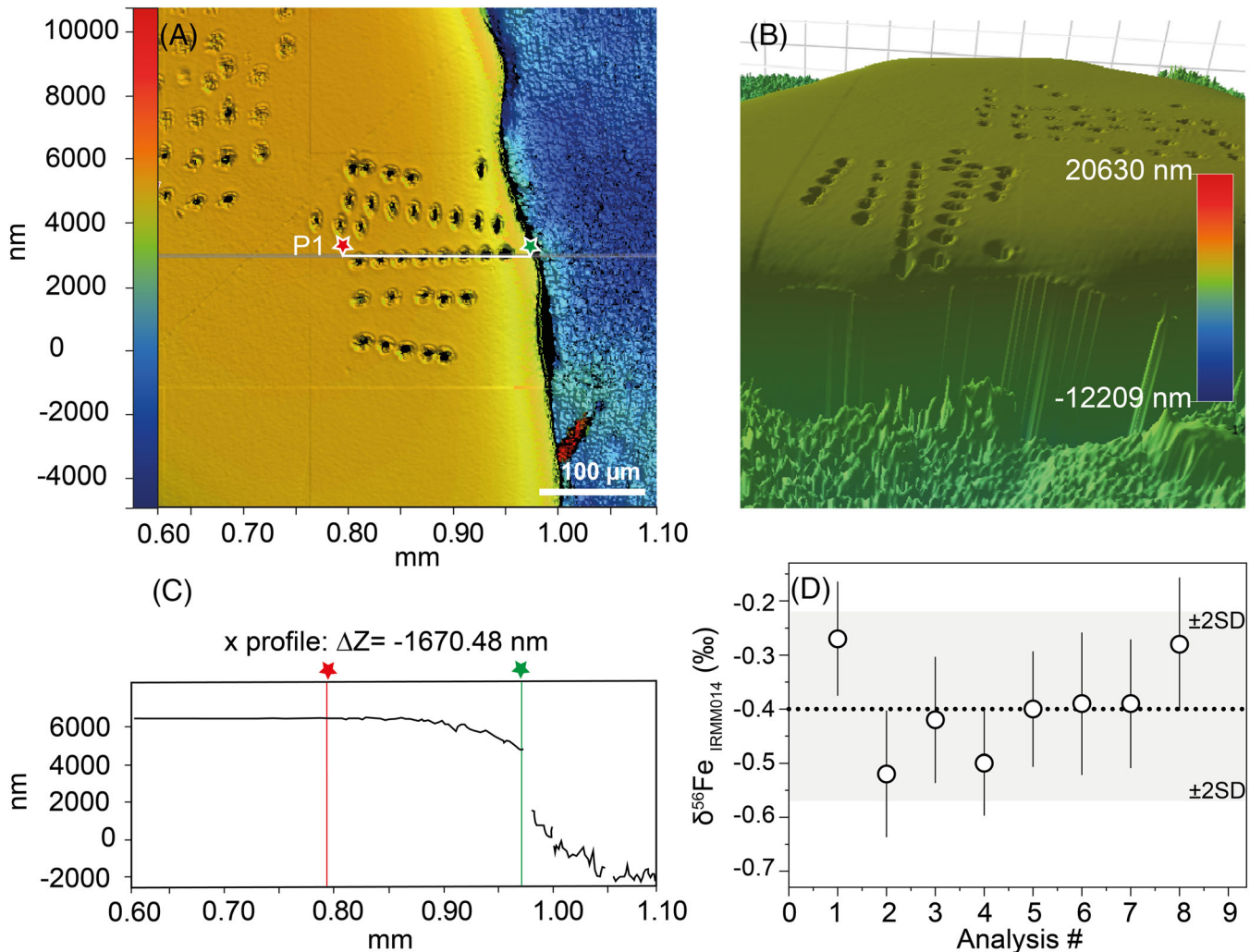


FIGURE 5 Profile in Balmat reference material. (A) Interferometric microscope image showing Pf1 profile in the pyrite grain. (B) Interferometric microscope three-dimensional image of the pyrite standard. (C) Topographic profile following Pf1 transect. This profile shows a topographic difference of *ca* 1.7 μm between the core (red star) and the rim (green star) of the grain. The gap after the green star (*ca* 7 μm) highlights the boundary between the pyrite grain and the indium. (D) $\delta^{56}\text{Fe}$ values IMF-corrected in a core-to-rim profile performed in the Balmat pyrite standard. Dashed black line is the true $\delta^{56}\text{Fe}$ value of the Balmat standard ($\delta^{56}\text{Fe} = -0.399\text{‰}$). The uncertainty on average is $\pm 0.09\text{‰}$ (2SE) and the external reproducibility is $\pm 0.18\text{‰}$ (2SD, gray area). Data are available in Table S2 (supporting information, Data S2)

3.4 | Reproducibility and accuracy

The reproducibility of the $\delta^{56}\text{Fe}$ measurements on the Balmat reference material was established over three sessions (February 2018, April 2018 and September 2020) at CRPG-IPNT and four sessions (July 2019, January 2020, March 2020 and June 2020) at SwissSIMS Lausanne (Table 2). Balmat pyrite (same grain) displays a long-term reproducibility of $\pm 0.25\text{‰}$ (2SD) for 166 measurements (Figure 6) at CRPG-IPNT and $\pm 0.22\text{‰}$ (2SD) for 185 measurements (June 2020) at the SwissSIMS ion probe facility. The short-term reproducibility on Balmat pyrite varied from $\pm 0.24\text{‰}$ (2SD, February 2018, $n = 33$; Table S3, supporting information (Data S2)) to $\pm 0.26\text{‰}$ (2SD, April 2018, $n = 133$) at CRPG-IPNT and from $\pm 0.18\text{‰}$ (2SD, March 2020, $n = 33$) to

$\pm 0.35\text{‰}$ (2SD, January 2020, $n = 16$) at SwissSIMS. The reproducibility obtained on the SpainCR standard (July 2018) is close to that measured in Balmat pyrite with a value of $\pm 0.28\text{‰}$ (2SD, $n = 61$). Published data obtained using the $^{16}\text{O}^-$ Duoplasmatron source⁶⁸ on three days of analysis show a reproducibility of $\pm 0.44\text{‰}$ (2SD, $n = 17$) on the same grain of Balmat, which highlights the better stability of the Hyperion-II source than of the Duoplasmatron.

The accuracy of the SIMS technique was tested on two pyrite standards which have different isotopic compositions. We used Balmat as a reference standard and considered SpainCR as an unknown pyrite. The $\delta^{56}\text{Fe}$ value for SpainCR was determined using the IMF calculated on the Balmat reference material. The $\delta^{56}\text{Fe}$ value for SpainCR pyrite was calculated at $+0.64 \pm 0.26\text{‰}$ (2SD, $n = 2$) in quite good agreement

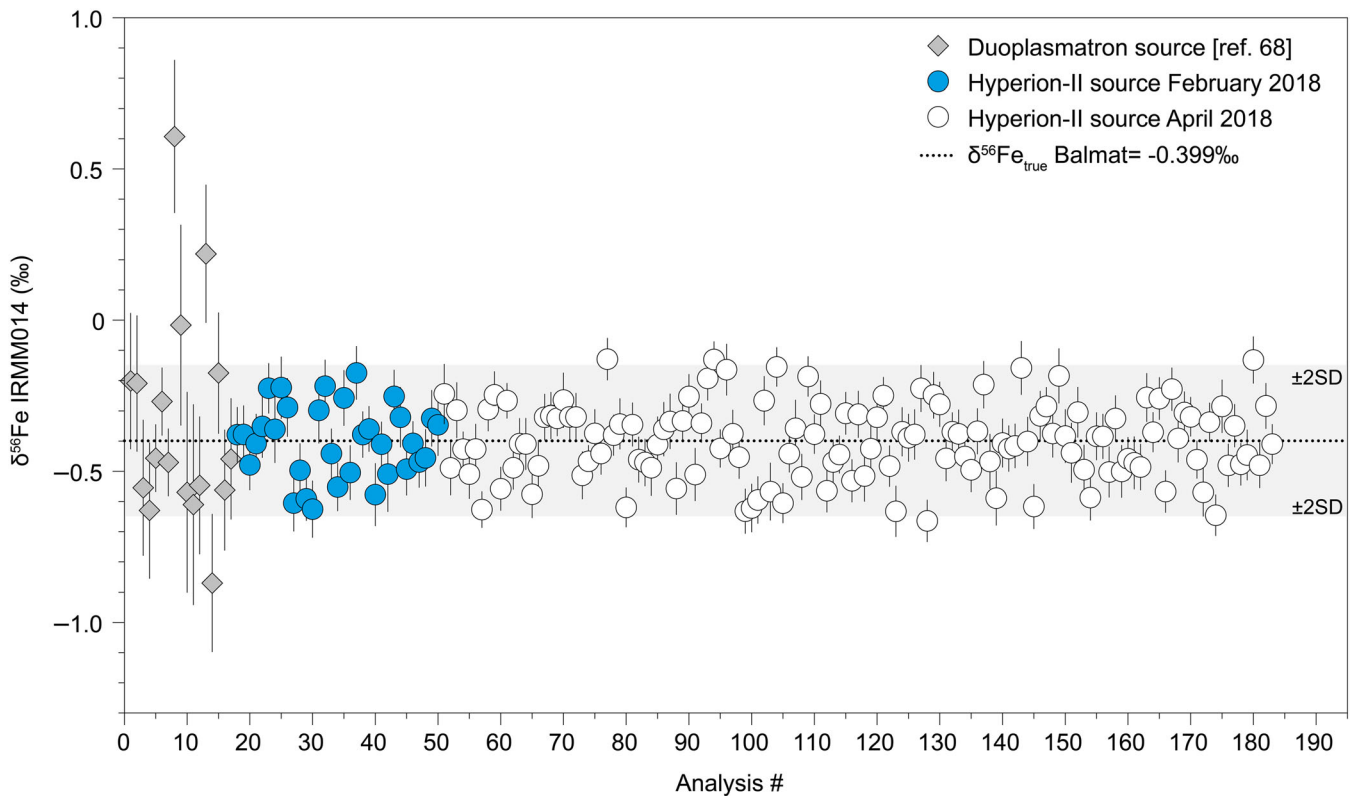


FIGURE 6 Long-term reproducibility on the Balmat pyrite reference material (0.25‰, 2SD). Dots are $\delta^{56}\text{Fe}$ values measured with the Hyperion-II radio-frequency plasma source in February 2018 (blue dots) and April 2018 (white dots) sessions. Gray diamonds are $\delta^{56}\text{Fe}$ data from the Duoplasmatron source.⁶⁸The dashed black line indicates the true $\delta^{56}\text{Fe}$ value for Balmat ($\delta^{56}\text{Fe} = -0.399\text{‰}$) and the gray area represents the long-term reproducibility of ± 0.25 at 2SD. The February 2018 data are available in Table S3 (supporting information, Data S2)

with the value of $\delta^{56}\text{Fe} = +0.52 \pm 0.03\text{‰}$ determined by MC-ICPMS, demonstrating the accuracy of the SIMS method.

4 | CONCLUSIONS

An ion microprobe equipped with the new Hyperion-II radio-frequency source is able to determine Fe isotope ratios with high accuracy, at high precision (ca 0.25‰, 2SD) and high spatial resolution (3 μm). We have detailed a procedure to achieve $\delta^{56}\text{Fe}$ measurements with a primary intensity 3 times lower than that traditionally delivered by the Duoplasmatron source, yet we achieved better precision. The MRP was intentionally set at a lower value than that required to resolve $^{56}\text{FeH}^+$ from $^{57}\text{Fe}^+$ to attain a minimum $^{56}\text{Fe}^+$ count rate of 4×10^7 cps on a pyrite reference material in order to produce high-precision $\delta^{56}\text{Fe}$ values. The level of $^{56}\text{FeH}^+$ is low compared with the intensity of $^{57}\text{Fe}^+$ under high vacuum. An MRP of ca 6700 is sufficient to limit its contribution to the ^{57}Fe signal. In our sample set, we demonstrated the absence of topography and crystal orientation effects. Currently, this new procedure is being applied to major Fe-bearing minerals to better constrain natural Fe isotopic variabilities at micrometric scale in sedimentary pyrites. The future investigation of *in situ* $\delta^{56}\text{Fe}$ signatures in minor Fe-bearing phases such as oxides, carbonates and silicates will serve as a promising tool

to answer fundamental questions in extraterrestrial and terrestrial petrology and to gain a better understanding of the biogeochemical Fe cycles.

ACKNOWLEDGEMENTS


The authors thank Caroline de Meyer and Pierre Vonlanthen for assistance with the EBSE analysis; Claire Rollion-Bard for providing the SpainCR pyrite standard; Katharina Marger for her help with the EPMA analysis; and Damien Cividini (CRPG) for help with MC-ICPMS measurements. They also thank David Zakharov for fruitful discussions that led to the improvement of the manuscript. The authors appreciate constructive reviews from Cees-Jan De Hoog and three anonymous reviewers. This research was supported by the H2020 European Research Council (STROMATA, grant agreement 759289; PI Johanna Marin-Carbonne).


PEER REVIEW

The peer review history for this article is available at <https://publons.com/publon/10.1002/rcm.8986>.

ORCID

Marie-Noëlle Decraene  <https://orcid.org/0000-0002-3929-9447>

Johanna Marin-Carbonne  <https://orcid.org/0000-0002-4265-1595>

Anne-Sophie Bouvier  <https://orcid.org/0000-0002-5202-603X>

Johan Villeneuve  <https://orcid.org/0000-0002-9892-8530>

Béatrice Luais  <https://orcid.org/0000-0002-3681-4300>

Etienne Deloule  <https://orcid.org/0000-0001-6955-1685>

REFERENCES

1. Beard BL, Johnson CM. High precision iron isotope measurements of terrestrial and lunar materials. *Geochim Cosmochim Acta*. 1999;63(11–12):1653–1660. [https://doi.org/10.1016/S0016-7037\(99\)00089-7](https://doi.org/10.1016/S0016-7037(99)00089-7)
2. Anbar AD, Roe JE, Barling J, Nealon KH. Nonbiological fractionation of iron isotopes. *Science*. 2000;288(5463):126–128. <https://doi.org/10.1126/science.288.5463.126>
3. Dauphas N, Janney PE, Mendybaev RA, et al. Chromatographic separation and multicollection-ICPMS analysis of iron. Investigating mass-dependent and independent isotope effects. *Anal Chem*. 2004;76(19):5855–5863. <https://doi.org/10.1021/ac0497095>
4. Berglund M, Wieser ME. Isotopic compositions of the elements 2009 (IUPAC technical report). *Pure Appl Chem*. 2011;83(2):397–410. <https://doi.org/10.1351/PAC-REP-10-06-02>, <https://doi.org/10.1351/PAC-REP-10-06-02>
5. Craddock PR, Dauphas N. Iron isotopic compositions of geological reference materials and chondrites. *Geostand Geoanal Res*. 2011;35(1):101–123. <https://doi.org/10.1111/j.1751-908X.2010.00085.x>
6. Taylor PDP, Maek R, De Bièvre P. Determination of the absolute isotopic composition and atomic weight of a reference sample of natural iron. *Int J Mass Spectrom Ion Processes*. 1992;121(1–2):111–125.
7. Mullane E, Russell SS, Gounelle M. Nebular and asteroidal modification of the iron isotope composition of chondritic components. *Earth Planet Sci Lett*. 2005;239(3–4):203–218. <https://doi.org/10.1016/j.epsl.2005.07.026>
8. Poitrasson F, Freyrier R. Heavy iron isotope composition of granites determined by high resolution MC-ICP-MS. *Chem Geol*. 2005;222(1–2):132–147. <https://doi.org/10.1016/j.chemgeo.2005.07.005>
9. Needham AW, Porcelli D, Russell SS. An Fe isotope study of ordinary chondrites. *Geochim Cosmochim Acta*. 2009;73(24):7399–7413. <https://doi.org/10.1016/j.gca.2009.08.034>
10. Hezel DC, Needham AW, Armitage R, et al. A nebula setting as the origin for bulk chondrule Fe isotope variations in CV chondrites. *Earth Planet Sci Lett*. 2010;296(3–4):423–433. <https://doi.org/10.1016/j.epsl.2010.05.029>
11. Dauphas N, John SG, Rouxel OJ. Iron isotope systematics. *Rev Mineral Geochem*. 2017;82(1):415–510. <https://doi.org/10.2138/rmg.2017.82.11>
12. Rouxel OJ, Bekker A, Edwards KJ. Iron isotope constraints on the Archean and Paleoproterozoic Ocean redox state. *Science*. 2005;307(5712):1088–1091. <https://doi.org/10.1126/science.1105692>
13. Johnson CM, Beard BL, Roden EE. The iron isotope fingerprints of redox and biogeochemical cycling in modern and ancient earth. *Annu Rev Earth Planet Sci*. 2008;36:457–493. <https://doi.org/10.1146/annurev.earth.36.031207.124139>
14. Severmann S, Lyons TW, Anbar A, McManus J, Gordon G. Modern iron isotope perspective on the benthic iron shuttle and the redox evolution of ancient oceans. *Geology*. 2008;36(6):487–490. <https://doi.org/10.1130/G24670A.1>
15. Czaja AD, Johnson CM, Beard BL, Eigenbrode JL, Freeman KH, Yamaguchi KE. Iron and carbon isotope evidence for ecosystem and environmental diversity in the ~2.7 to 2.5 Ga Hamersley Province, Western Australia. *Earth Planet Sci Lett*. 2010;292(1–2):170–180. <https://doi.org/10.1016/j.epsl.2010.01.032>
16. Marin-Carbonne J, Rollion-Bard C, Bekker A, et al. Coupled Fe and S isotope variations in pyrite nodules from Archean shale. *Earth Planet Sci Lett*. 2014;392:67–79. <https://doi.org/10.1016/j.epsl.2014.02.009>
17. Johnson C, Beard B, Weyer S. *Iron Geochemistry: An Isotopic Perspective*. Cham, Switzerland: Springer; 2020.
18. Johnson CM, Beard B, Roden EE, Newman DK, Nealon KH. Isotopic constraints on biogeochemical cycling of Fe. *Rev Mineral Geochem*. 2004;55:359–408. <https://doi.org/10.2138/gsrmg.55.1.359>
19. Lovley DR, Stolz JF, Nord GL, Phillips EJ. Anaerobic production of magnetite by a dissimilatory iron-reducing microorganism. *Nature*. 1987;330:252–254.
20. Bullen TD, McMahon PM. Using stable Fe isotopes to assess microbially-mediated Fe³⁺ reduction in a jet-fuel contaminated aquifer. *Mineral Mag*. 1998;62:255–256.
21. Beard BL, Johnson CM, Cox L, Sun H, Nealon KH, Aguilar C. Iron isotope biosignatures. *Science*. 1999;285(5435):1889–1892. <https://doi.org/10.1126/science.285.5435.1889>
22. Crosby HA, Johnson CM, Roden EE, Beard BL. Coupled Fe(II)–Fe(III) electron and atom exchange as a mechanism for Fe isotope fractionation during dissimilatory iron oxide reduction. *Environ Sci Technol*. 2005;39(17):6698–6704. <https://doi.org/10.1021/es0505346>
23. Crosby HA, Roden EE, Johnson CM, Beard BL. The mechanisms of iron isotope fractionation produced during dissimilatory Fe(III) reduction by *Shewanella putrefaciens* and *Geobacter sulfurreducens*. *Geobiology*. 2007;5(2):169–189. <https://doi.org/10.1111/j.1472-4669.2007.00103.x>
24. Percak-Dennett EM, Beard BL, Xu H, Konishi H, Johnson CM, Roden EE. Iron isotope fractionation during microbial dissimilatory iron oxide reduction in simulated Archean seawater. *Geobiology*. 2011;9(3):205–220. <https://doi.org/10.1111/j.1472-4669.2011.00277.x>
25. Johnson CM, Skulan JL, Beard BL, Sun H, Nealon KH, Braterman PS. Isotopic fractionation between Fe(III) and Fe(II) in aqueous solutions. *Earth Planet Sci Lett*. 2002;195(1–2):141–153. [https://doi.org/10.1016/S0012-821X\(01\)00581-7](https://doi.org/10.1016/S0012-821X(01)00581-7)
26. Welch SA, Beard BL, Johnson CM, Braterman PS. Kinetic and equilibrium Fe isotope fractionation between aqueous Fe(II) and Fe(III). *Geochim Cosmochim Acta*. 2003;67(22):4231–4250. [https://doi.org/10.1016/S0016-7037\(03\)00266-7](https://doi.org/10.1016/S0016-7037(03)00266-7)
27. Skulan JL, Beard BL, Johnson CM. Kinetic and equilibrium Fe isotope fractionation between aqueous Fe(III) and hematite. *Geochim Cosmochim Acta*. 2002;66(17):2995–3015. [https://doi.org/10.1016/S0016-7037\(02\)00902-X](https://doi.org/10.1016/S0016-7037(02)00902-X)
28. Beard BL, Handler RM, Scherer MM, et al. Iron isotope fractionation between aqueous ferrous iron and goethite. *Earth Planet Sci Lett*. 2010;295(1–2):241–250. <https://doi.org/10.1016/j.epsl.2010.04.006>
29. Wu L, Beard BL, Roden EE, Kennedy CB, Johnson CM. Stable Fe isotope fractionations produced by aqueous Fe(II)–hematite surface interactions. *Geochim Cosmochim Acta*. 2010;74(15):4249–4265. <https://doi.org/10.1016/j.gca.2010.04.060>
30. Wu L, Beard BL, Roden EE, Johnson CM. Stable iron isotope fractionation between aqueous Fe(II) and hydrous ferric oxide. *Environ Sci Technol*. 2011;45(5):1847–1852. <https://doi.org/10.1021/es103171x>
31. Frierdich AJ, Nebel O, Beard BL, Johnson CM. Iron isotope exchange and fractionation between hematite (α-Fe₂O₃) and aqueous Fe(II): A combined three-isotope and reversal-approach to equilibrium study. *Geochim Cosmochim Acta*. 2019;245:207–221. <https://doi.org/10.1016/j.gca.2018.10.033>
32. Croal LR, Johnson CM, Beard BL, Newman DK. Iron isotope fractionation by Fe(II)-oxidizing photoautotrophic bacteria. *Geochim Cosmochim Acta*. 2004;68(6):1227–1242. <https://doi.org/10.1016/j.gca.2003.09.011>

33. Bullen TD, White AF, Childs CW, Vivit DV, Schulz MS. Demonstration of significant abiotic iron isotope fractionation in nature. *Geology*. 2001;29(8):699-702. [https://doi.org/10.1130/0091-7613\(2001\)029<0699:DOSAII>2.0.CO;2](https://doi.org/10.1130/0091-7613(2001)029<0699:DOSAII>2.0.CO;2)
34. Beard BL, Johnson CM. Fe isotope variations in the modern and ancient earth and other planetary bodies. *Rev Mineral Geochem*. 2004;55(1):319-357. <https://doi.org/10.2138/gsrng.55.1.319>
35. Rickard D, Grimes S, Butler I, Oldroyd A, Davies KL. Botanical constraints on pyrite formation. *Chem Geol*. 2007;236:228-246. <https://doi.org/10.1016/j.chemgeo.2006.09.011>
36. Luther III GW. Pyrite synthesis via polysulfide compounds. *Geochim Cosmochim Acta*. 1991;55:2839-2849. [https://doi.org/10.1016/0016-7037\(91\)90449-F](https://doi.org/10.1016/0016-7037(91)90449-F)
37. Rickard D. *Sulfidic Sediments and Sedimentary Rocks*. Newnes; 2017.
38. Rickard D. Sedimentary pyrite framboid size-frequency distributions: A meta-analysis. *Palaeogeol Palaeoclim Palaeoecol*. 2019;522:62-75. <https://doi.org/10.1016/j.palaeo.2019.03.010>
39. Yoshiya K, Nishizawa M, Sawaki Y, et al. In situ iron isotope analyses of pyrite and organic carbon isotope ratios in the Fortescue group: Metabolic variations of a late Archean ecosystem. *Precambrian Res*. 2012;212:169-193. <https://doi.org/10.1016/j.precamres.2012.05.003>
40. Nishizawa M, Yamamoto H, Ueno Y, et al. Grain-scale iron isotopic distribution of pyrite from Precambrian shallow marine carbonate revealed by a femtosecond laser ablation multicollector ICP-MS technique: Possible proxy for the redox state of ancient seawater. *Geochim Cosmochim Acta*. 2010;74(9):2760-2778. <https://doi.org/10.1016/j.gca.2010.02.014>
41. Liu MC, McKeegan KD, Harrison TM, Jarzebinski G, Vltava L. The Hyperion-II radio-frequency oxygen ion source on the UCLA IMS 1290 ion microprobe: Beam characterization and applications in geochemistry and cosmochemistry. *Int J Mass Spectrom*. 2018;424:1-9. <https://doi.org/10.1016/j.ijms.2017.11.007>
42. Fukuda K, Beard BL, Dunlap DR, et al. Magnesium isotope analysis of olivine and pyroxene by SIMS: Evaluation of matrix effects. *Chem Geol*. 2020;119482. <https://doi.org/10.1016/j.chemgeo.2020.119482>
43. Villeneuve J, Chaussidon M, Marrocchi Y, Deng Z, Watson EB. High-precision in situ silicon isotopic analyses by multi-collector secondary ion mass spectrometry in olivine and low-calcium pyroxene. *Rapid Commun Mass Spectrom*. 2019;33(20):1589-1597. <https://doi.org/10.1002/rcm.8508>
44. Ushikubo T, Nakashima D, Kimura M, Tenner TJ, Kita NT. Contemporaneous formation of chondrules in distinct oxygen isotope reservoirs. *Geochim Cosmochim Acta*. 2013;109:280-295. <https://doi.org/10.1016/j.gca.2013.01.045>
45. Marin-Carbonne J, Rollion-Bard C, Luais B. In-situ measurements of iron isotopes by SIMS: MC-ICP-MS intercalibration and application to a magnetite crystal from the gunflint chert. *Chem Geol*. 2011;285(14):50-61. <https://doi.org/10.1016/j.chemgeo.2011.02.019>
46. Whitehouse MJ, Fedo CM. Microscale heterogeneity of Fe isotopes in > 3.71 Ga banded iron formation from the Isua Greenstone Belt, Southwest Greenland. *Geology*. 2007;35(8):719-722. <https://doi.org/10.1130/G23582A.1>
47. Muller É, Philippot P, Rollion-Bard C, et al. Primary sulfur isotope signatures preserved in high-grade Archean barite deposits of the Sargur group, Dharwar craton, India. *Precambrian Res*. 2017;295:38-47. <https://doi.org/10.1016/j.precamres.2017.04.029>
48. Muller É, Philippot P, Rollion-Bard C, Cartigny P. Multiple sulfur-isotope signatures in Archean sulfates and their implications for the chemistry and dynamics of the early atmosphere. *Proc Natl Acad Sci*. 2016;113(27):7432-7437. <https://doi.org/10.1073/pnas.1520522113>
49. El Korh A, Luais B, Deloule E, Cividini D. Iron isotope fractionation in subduction-related high-pressure metabasites (Ile de Groix, France). *Contrib Mineral Petrol*. 2017;172(6):41-19. <https://doi.org/10.1007/s00410-017-1357-x>
50. Liu PP, Zhou MF, Luais B, Cividini D, Rollion-Bard C. Disequilibrium Fe isotope fractionation during the high-temperature magmatic differentiation of the Baima Fe-Ti oxide-bearing mafic intrusion, SW China. *Earth Planet Sci Lett*. 2014;339:21-29. <https://doi.org/10.1016/j.epsl.2014.05.002>
51. Kita NT, Ushikubo T, Fu B, Valley JW. High precision SIMS oxygen isotope analysis and the effect of sample topography. *Chem Geol*. 2009;264(1-4):43-57. <https://doi.org/10.1016/j.chemgeo.2009.02.012>
52. Bayliss P. Crystal structure refinement of a weakly anisotropic pyrite. *Am Mineralogist*. 1977;62(11-12):1168-1172.
53. Prior DJ, Boyle AP, Brenker F, et al. The application of electron backscatter diffraction and orientation contrast imaging in the SEM to textural problems in rocks. *Am Mineralogist*. 1999;84:1741-1759. <https://doi.org/10.2138/am-1999-11-1204>
54. Shimizu N, Hart SR. Applications of the ion microprobe to geochemistry and cosmochemistry. *Annu Rev Earth Planet Sci*. 1982;10(1):483-526.
55. Eiler JM, Graham C, Valley JW. SIMS analysis of oxygen isotopes: Matrix effects in complex minerals and glasses. *Chem Geol*. 1997;138(3-4):221-244.
56. Chaussidon M, Albarede F, Sheppard SMF. Sulphur isotope heterogeneity in the mantle from ion microprobe measurements of sulphide inclusions in diamonds. *Nature*. 1987;330(6145):242-244.
57. Kita NT, Huberty JM, Kozdon R, Beard BL, Valley JW. High-precision SIMS oxygen, sulfur and iron stable isotope analyses of geological materials: Accuracy, surface topography and crystal orientation. *Surf Interface Anal*. 2011;43(1-2):427-431. <https://doi.org/10.1002/sia.3424>
58. Vielzeuf D, Champenois M, Valley JW, Brunet F, Devidal JL. SIMS analyses of oxygen isotopes: Matrix effects in Fe-Mg-Ca garnets. *Chem Geol*. 2005;223(4):208-226. <https://doi.org/10.1016/j.chemgeo.2005.07.008>
59. Vho A, Rubatto D, Putlitz B, Bouvier AS. New reference materials and assessment of matrix effects for SIMS measurements of oxygen isotopes in garnet. *Geostand Geoanal Res*. 2020;44:450-471. <https://doi.org/10.1111/ggr.12324>
60. Deloule E, Chaussidon M, Allé P. Instrumental limitations for isotope measurements with a Caméca® IMS-3f ion microprobe: Example of H, B, S and Sr. *Chem Geol Isot Geosci Sect*. 1992;101(1-2):187-192.
61. Crossley RJ, Evans KA, Jeon H, Kilburn MR. Insights into sulfur cycling at subduction zones from in-situ isotopic analysis of sulfides in high-pressure serpentinites and "hybrid" samples from Alpine Corsica. *Chem Geol*. 2018;493:359-378. <https://doi.org/10.1016/j.chemgeo.2018.06.014>
62. Chaussidon M, Deng Z, Villeneuve J, et al. In situ analysis of non-traditional isotopes by SIMS and LA-MC-ICP-MS: Key aspects and the example of mg isotopes in olivines and silicate glasses. *Rev Mineral Geochem*. 2017;82(1):127-163. <https://doi.org/10.2138/rmg.2017.82.5>
63. Kozdon R, Kita NT, Huberty JM, Fournelle JH, Johnson CA, Valley JW. In situ sulfur isotope analysis of sulfide minerals by SIMS: Precision and accuracy, with application to thermometry of ~3.5 Ga Pilbara cherts. *Chem Geol*. 2010;275(3-4):243-253. <https://doi.org/10.1016/j.chemgeo.2010.05.015>
64. Wingate MTD, Compston W. Crystal orientation effects during ion microprobe U-Pb analysis of baddeleyite. *Chem Geol*. 2000;168(1-2):75-97. [https://doi.org/10.1016/S0009-2541\(00\)00184-4](https://doi.org/10.1016/S0009-2541(00)00184-4)

65. LaFlamme C, Martin L, Jeon H, et al. In situ multiple sulfur isotope analysis by SIMS of pyrite, chalcopyrite, pyrrhotite, and pentlandite to refine magmatic ore genetic models. *Chem Geol.* 2016;444:1-15. <https://doi.org/10.1016/j.chemgeo.2016.09.032>
66. Gnaser H. Energy and angular distributions of sputtered species. In: *Sputtering by Particle Bombardment*. Berlin, Germany: Springer; 2007: 231-328.
67. Huberty JM, Kita NT, Kozdon R, et al. Crystal orientation effects in $\delta^{18}\text{O}$ for magnetite and hematite by SIMS. *Chem Geol.* 2010;276 (3-4):269-283. <https://doi.org/10.1016/j.chemgeo.2010.06.012>
68. Marin-Carbonne J, Busigny V, Miot J, et al. In situ Fe and S isotope analyses in pyrite from the 3.2 Ga Mendon formation (Barberton Greenstone Belt, South Africa): Evidence for early microbial iron reduction. *Geobiology.* 2020;18(3):306-325. <https://doi.org/10.1111/gbi.12385>

SUPPORTING INFORMATION

Additional supporting information may be found online in the Supporting Information section at the end of this article.

How to cite this article: Decraene M-N, Marin-Carbonne J, Bouvier A-S, et al. High-spatial-resolution measurements of iron isotopes in pyrites by secondary ion mass spectrometry using the new Hyperion-II radio-frequency plasma source. *Rapid Commun Mass Spectrom.* 2021;35:e8986. <https://doi.org/10.1002/rcm.8986>

3. Literature cited

- Algeo, T.J., Kuwahara, K., Sano, H., Bates, S., Lyons, T., Elswick, E., Hinnov, L., Ellwood, B., Moser, J., Maynard, J.B., 2011. Spatial variation in sediment fluxes, redox conditions, and productivity in the Permian-Triassic Panthalassic Ocean. *Palaeogeography, Palaeoclimatology, Palaeoecology* 308, 65–83. <https://doi.org/10.1016/j.palaeo.2010.07.007>
- Altermann, W., Nelson, D.R., 1998. Sedimentation rates, basin analysis and regional correlations of three Neoproterozoic and Palaeoproterozoic sub-basins of the Kaapvaal craton as inferred from precise U–Pb zircon ages from volcanoclastic sediments. *Sedimentary Geology* 120, 225–256. [https://doi.org/10.1016/S0037-0738\(98\)00034-7](https://doi.org/10.1016/S0037-0738(98)00034-7)
- Awramik, S.M., Buchheim, H.P., 2009. A giant, Late Archean lake system: The Meentheena Member (Tumbiana Formation; Fortescue Group), Western Australia. *Precambrian Research* 174, 215–240. <https://doi.org/10.1016/j.precamres.2009.07.005>
- Bekker, A., Holland, H.D., Wang, P.-L., Rumble, D., Stein, H.J., Hannah, J.L., Coetzee, L.L., Beukes, N.J., 2004. Dating the rise of atmospheric oxygen. *Nature* 427, 117–120. <https://doi.org/10.1038/nature02260>
- Beukes, N.J., 1987. Facies relations, depositional environments and diagenesis in a major early Proterozoic stromatolitic carbonate platform to basinal sequence, Campbellrand Subgroup, Southern Africa, *Sedimentary Geology*.
- Beysac, O., Goffé, B., Chopin, C., Rouzaud, J.N., 2002. Raman spectra of carbonaceous material in metasediments: a new geothermometer. *Journal of Metamorphic Geology* 20, 859–871. <https://doi.org/10.1046/j.1525-1314.2002.00408.x>
- Blake, T.S., Buick, R., Brown, S.J.A., Barley, M.E., 2004. Geochronology of a Late Archean flood basalt province in the Pilbara Craton, Australia: constraints on basin evolution, volcanic and sedimentary accumulation, and continental drift rates. *Precambrian Research* 133, 143–173. <https://doi.org/10.1016/j.precamres.2004.03.012>
- Bolhar, R., van Kranendonk, M., 2007. A non-marine depositional setting for the northern Fortescue Group, Pilbara Craton, inferred from trace element geochemistry of stromatolitic carbonates. *Precambrian Research* 155, 229–250. <https://doi.org/10.1016/j.precamres.2007.02.002>
- Bouton, A., Vennin, E., Pace, A., Bourillot, R., Dupraz, C., Thomazo, C., Brayard, A., Désaubliaux, G., Visscher, P.T., 2016. External controls on the distribution, fabrics and mineralization of modern microbial mats in a coastal hypersaline lagoon, Cayo Coco (Cuba). *Sedimentology* 63, 972–1016. <https://doi.org/10.1111/sed.12246>
- Bouton, A., Vennin, E., Thomazo, C., Mathieu, O., Garcia, F., Jaubert, M., Visscher, P.T., 2020. Microbial origin of the organic matter preserved in the cayo coco lagoonal network, Cuba. *Minerals* 10. <https://doi.org/10.3390/min10020143>
- Brayard, A., Bylund, K.G., Jenks, J.F., Stephen, D.A., Olivier, N., Escarguel, G., Fara, E., Vennin, E., 2013. Smithian ammonoid faunas from Utah: implications for Early Triassic biostratigraphy, correlation and basinal paleogeography. *Swiss Journal of Palaeontology* 132, 141–219. <https://doi.org/10.1007/s13358-013-0058-y>
- Buick, R., 1992. The Antiquity of Oxygenic Photosynthesis: Evidence from Stromatolites in Sulphate-Deficient Archean Lakes. *Science* (1979) 255, 74–77. <https://doi.org/10.1126/science.11536492>
- Burchfiel, B., Davis, G.A., 1975. Nature and controls of Cordilleran orogenesis, Western United States: extensions of an earlier synthesis. *American Journal of Science* 275, 363–396.
- Button, A., 1973. The stratigraphic history of the Malmani dolomite in the eastern and north-eastern Transvaal.
- Carrasco-Núñez, G., Ort, M.H., Romero, C., 2007. Evolution and hydrological conditions of a maar volcano (Atexcac crater, Eastern Mexico). *Journal of Volcanology and Geothermal Research* 159, 179–197. <https://doi.org/10.1016/j.jvolgeores.2006.07.001>
- Czaja, A.D., Johnson, C.M., Beard, B.L., Eigenbrode, J.L., Freeman, K.H., Yamaguchi, K.E., 2010. Iron and carbon isotope evidence for ecosystem and environmental diversity in the ~2.7 to 2.5Ga Hamersley Province, Western Australia. *Earth and Planetary Science Letters* 292, 170–180. <https://doi.org/10.1016/j.epsl.2010.01.032>

- Decraene, M.N., Marin-Carbonne, J., Bouvier, A.S., Villeneuve, J., Bouden, N., Luais, B., Deloule, E., 2021. High-spatial-resolution measurements of iron isotopes in pyrites by secondary ion mass spectrometry using the new Hyperion-II radio-frequency plasma source. *Rapid Communications in Mass Spectrometry* 35. <https://doi.org/10.1002/rcm.8986>
- Embry, A.F., 1997. Global sequence boundaries of the Triassic and their identification in the Western Canada Sedimentary Basin 1, *Bulletin of Canadian Petroleum Geology*.
- Eriksson, K.A., 1977. Tidal flat and subtidal sedimentation in the 2250 M.Y. Malmani Dolomite, Transvaal, South Africa. *Sedimentary Geology* 18, 223–244. [https://doi.org/10.1016/0037-0738\(77\)90013-6](https://doi.org/10.1016/0037-0738(77)90013-6)
- Eriksson, P.G., Altermann, W., 1998. An overview of the geology of the Transvaal Supergroup dolomites (South Africa), Cases and solutions *Environmental Geology*. Springer-Verlag.
- Eroglu, S., Schoenberg, R., Wille, M., Beukes, N., Taubald, H., 2015. Geochemical stratigraphy, sedimentology, and Mo isotope systematics of the ca. 2.58–2.50 Ga-old Transvaal Supergroup carbonate platform, South Africa. *Precambrian Research* 266, 27–46. <https://doi.org/10.1016/j.precamres.2015.04.014>
- Eroglu, S., van Zuilen, M.A., Taubald, H., Drost, K., Wille, M., Swanner, E.D., Beukes, N.J., Schoenberg, R., 2017. Depth-dependent $\delta^{13}\text{C}$ trends in platform and slope settings of the Campbellrand-Malmani carbonate platform and possible implications for Early Earth oxygenation. *Precambrian Research* 302, 122–139. <https://doi.org/10.1016/j.precamres.2017.09.018>
- Eroglu, S., Schoenberg, R., Pascarelli, S., Beukes, N.J., Kleinhanns, I.C., Swanner, E.D., 2018. Open ocean vs. continentally-derived iron cycles along the neoproterozoic campbellrand-malmani carbonate platform, South Africa. *American Journal of Science* 318, 367–408. <https://doi.org/10.2475/04.2018.01>
- Farquhar, J., Bao, H., Thiemens, M., 2000. Atmospheric Influence of Earth's Earliest Sulfur Cycle. *Science* (1979) 289, 756–758. <https://doi.org/10.1126/science.289.5480.756>
- Ferrari, L., Orozco-Esquivel, T., Manea, V., Manea, M., 2012. The dynamic history of the Trans-Mexican Volcanic Belt and the Mexico subduction zone. *Tectonophysics* 522–523, 122–149. <https://doi.org/10.1016/j.tecto.2011.09.018>
- Godfrey, L. v., Falkowski, P.G., 2009. The cycling and redox state of nitrogen in the Archaean ocean. *Nature Geoscience* 2, 725–729. <https://doi.org/10.1038/ngeo633>
- Grosjean, A.S., Vennin, E., Olivier, N., Caravaca, G., Thomazo, C., Fara, E., Escarguel, G., Bylund, K.G., Jenks, J.F., Stephen, D.A., Brayard, A., 2018. Early Triassic environmental dynamics and microbial development during the Smithian–Spathian transition (Lower Weber Canyon, Utah, USA). *Sedimentary Geology* 363, 136–151. <https://doi.org/10.1016/j.sedgeo.2017.11.009>
- Horn, I., von Blanckenburg, F., Schoenberg, R., Steinhöfel, G., Markl, G., 2006. In situ iron isotope ratio determination using UV-femtosecond laser ablation with application to hydrothermal ore formation processes. *Geochimica et Cosmochimica Acta* 70, 3677–3688. <https://doi.org/10.1016/j.gca.2006.05.002>
- Kamber, B. S., & Whitehouse, M. J. (2007). Micro-scale sulphur isotope evidence for sulphur cycling in the late Archean shallow ocean. *Geobiology*, 5(1), 5-17. <https://doi.org/10.1111/j.1472-4669.2006.00091.x>
- Kita, N. T., Huberty, J. M., Kozdon, R., Beard, B. L., & Valley, J. W., 2011. High-precision SIMS oxygen, sulfur and iron stable isotope analyses of geological materials: Accuracy, surface topography and crystal orientation. *Surface and Interface Analysis*, 43(1-2), 427-431. <https://doi.org/10.1002/sia.3424>
- Lepot, K., Benzerara, K., Brown, G.E., Philippot, P., 2008. Microbially influenced formation of 2,724-million-year-old stromatolites. *Nature Geoscience* 1, 118–121. <https://doi.org/10.1038/ngeo107>
- Lepot, K., Benzerara, K., Rividi, N., Cotte, M., Brown, G.E., Philippot, P., 2009. Organic matter heterogeneities in 2.72 Ga stromatolites: Alteration versus preservation by sulfur incorporation. *Geochimica et Cosmochimica Acta* 73, 6579–6599. <https://doi.org/10.1016/j>

gca.2009.08.014

Lepot, K., Williford, K.H., Philippot, P., Thomazo, C., Ushikubo, T., Kitajima, K., Mostefaoui, S., Valley, J.W., 2019. Extreme ^{13}C -depletions and organic sulfur content argue for S-fueled anaerobic methane oxidation in 2.72 Ga old stromatolites. *Geochimica et Cosmochimica Acta* 244, 522–547. <https://doi.org/10.1016/j.gca.2018.10.014>

Liu, M.-C., McKeegan, K.D., Harrison, T.M., Jarzebinski, G., Vltava, L., 2018. The Hyperion-II radio-frequency oxygen ion source on the UCLA ims1290 ion microprobe: Beam characterization and applications in geochemistry and cosmochemistry. *International Journal of Mass Spectrometry* 424, 1–9. <https://doi.org/10.1016/j.ijms.2017.11.007>

Malherbe, J., Penen, F., Isaure, M.-P., Frank, J., Hause, G., Dobritsch, D., Gontier, E., Horr ard, F., Hillion, F., Schauml offel, D., 2016. A New Radio Frequency Plasma Oxygen Primary Ion Source on Nano Secondary Ion Mass Spectrometry for Improved Lateral Resolution and Detection of Electropositive Elements at Single Cell Level. *Analytical Chemistry* 88, 7130–7136. <https://doi.org/10.1021/acs.analchem.6b01153>

Marin-Carbonne, J., Rollion-Bard, C., Luais, B., 2011. In-situ measurements of iron isotopes by SIMS: MC-ICP-MS intercalibration and application to a magnetite crystal from the Gunflint chert. *Chemical Geology* 285, 50–61. <https://doi.org/10.1016/j.chemgeo.2011.02.019>

Marin-Carbonne, J., Rollion-Bard, C., Bekker, A., Rouxel, O., Agangi, A., Cavalazzi, B., Wohlgemuth-Ueberwasser, C.C., Hofmann, A., McKeegan, K.D., 2014. Coupled Fe and S isotope variations in pyrite nodules from Archean shale. *Earth and Planetary Science Letters* 392, 67–79. <https://doi.org/10.1016/j.epsl.2014.02.009>

Marin-Carbonne, J., Remusat, L., Sforna, M.C., Thomazo, C., Cartigny, P., Philippot, P., 2018. Sulfur isotope’s signal of nanopyrrites enclosed in 2.7 Ga stromatolitic organic remains reveal microbial sulfate reduction. *Geobiology* 16, 121–138. <https://doi.org/10.1111/gbi.12275>

Marin-Carbonne, J., Decraene, M.-N., Havas, R., Remusat, L., Pasquier, V., All on, J., Zeyen, N., Bouton, A., Bernard, S., Escrig, S., Olivier, N., Vennin, E., Meibom, A., Benzerara, K., Thomazo, C., 2022. Early precipitated micropyrrite in microbialites: A time capsule of microbial sulfur cycling. *Geochemical Perspectives Letters* 21, 7–12. <https://doi.org/10.7185/geochemlet.2209>

Nishizawa, M., Yamamoto, H., Ueno, Y., Tsuruoka, S., Shibuya, T., Sawaki, Y., Yamamoto, S., Kon, Y., Kitajima, K., Komiya, T., Maruyama, S., Hirata, T., 2010. Grain-scale iron isotope distribution of pyrite from Precambrian shallow marine carbonate revealed by a femtosecond laser ablation multicollector ICP-MS technique: Possible proxy for the redox state of ancient seawater. *Geochimica et Cosmochimica Acta* 74, 2760–2778. <https://doi.org/10.1016/j.gca.2010.02.014>

Olivier, N., Brayard, A., Fara, E., Bylund, K.G., Jenks, J.F., Vennin, E., Stephen, D.A., Escarguel, G., 2014. Smithian shoreline migrations and depositional settings in Timpoweap Canyon (Early Triassic, Utah, USA). *Geological Magazine* 151, 938–955. <https://doi.org/10.1017/S0016756813000988>

Ono, S., Kaufman, A.J., Farquhar, J., Sumner, D.Y., Beukes, N.J., 2009. Lithofacies control on multiple-sulfur isotope records and Neoproterozoic sulfur cycles. *Precambrian Research* 169, 58–67. <https://doi.org/10.1016/j.precamres.2008.10.013>

Pace, A., Bourillot, R., Bouton, A., Vennin, E., Braissant, O., Dupraz, C., Duteil, T., Bundeleva, I., Patrier, P., Galaup, S., Yokoyama, Y., Franceschi, M., Virgone, A., Visscher, P.T., 2018. Formation of stromatolite lamina at the interface of oxygenic–anoxygenic photosynthesis. *Geobiology* 16, 378–398. <https://doi.org/10.1111/gbi.12281>

Packer, B. M. (1990). Sedimentology, paleontology, and stable isotope geochemistry of selected formations in the 2.7-billion-year-old Fortescue Group, western Australia (Doctoral dissertation, University of California, Los Angeles).

Pardo, G., 2009. The geology of Cuba, in: *The Geology of Cuba*. The American Association of Petroleum Geologists, Tulsa, Oklahoma, U.S.A., pp. 311–341. <https://doi.org/10.1306/13141064St583328>

Pavlov, A.A., Kasting, J.F., 2002. Mass-Independent Fractionation of Sulfur Isotopes in Archean Sediments: Strong Evidence for an Anoxic Archean Atmosphere. *Astrobiology* 2, 27–41. <https://doi.org/10.1089/153110702753621321>

Philippot, P., van Kranendonk, M., van Zuilen, M., Lepot, K., Rividi, N., Teitler, Y., Thomazo, C., Blanc-Valleron, M.-M., Rouchy, J.-

- M., Grosch, E., de Wit, M., 2009. Early traces of life investigations in drilling Archean hydrothermal and sedimentary rocks of the Pilbara Craton, Western Australia and Barberton Greenstone Belt, South Africa. *Comptes Rendus Palevol* 8, 649–663. <https://doi.org/10.1016/j.crpv.2009.06.006>
- Rasmussen, B., Fletcher, I.R., McNaughton, N.J., 2001. Dating low-grade metamorphic events by SHRIMP U-Pb analysis of monazite in shales. *Geology* 29, 963. [https://doi.org/10.1130/0091-7613\(2001\)029<0963:DLGMEB>2.0.CO;2](https://doi.org/10.1130/0091-7613(2001)029<0963:DLGMEB>2.0.CO;2)
- Richter, F.M., Dauphas, N., Teng, F.-Z., 2009. Non-traditional fractionation of non-traditional isotopes: Evaporation, chemical diffusion and Soret diffusion. *Chemical Geology* 258, 92–103. <https://doi.org/10.1016/j.chemgeo.2008.06.011>
- Romano, C., Goudemand, N., Vennemann, T.W., Ware, D., Schneebeil-Hermann, E., Hochuli, P.A., Brühwiler, T., Brinkmann, W., Bucher, H., 2013. Climatic and biotic upheavals following the end-Permian mass extinction. *Nature Geoscience* 6, 57–60. <https://doi.org/10.1038/ngeo1667>
- Sakurai, R., Ito, M., Ueno, Y., Kitajima, K., Maruyama, S., 2005. Facies architecture and sequence-stratigraphic features of the Tumbiana Formation in the Pilbara Craton, northwestern Australia: Implications for depositional environments of oxygenic stromatolites during the Late Archean. *Precambrian Research* 138, 255–273. <https://doi.org/10.1016/j.precamres.2005.05.008>
- Sforna, M.C., Philippot, P., Somogyi, A., van Zuilen, M.A., Medjoubi, K., Schoepp-Cothenet, B., Nitschke, W., Visscher, P.T., 2014. Evidence for arsenic metabolism and cycling by microorganisms 2.7 billion years ago. *Nature Geoscience* 7, 811–815. <https://doi.org/10.1038/ngeo2276>
- Song, H., Du, Y., Algeo, T.J., Tong, J., Owens, J.D., Song, Haijun, Tian, L., Qiu, H., Zhu, Y., Lyons, T.W., 2019. Cooling-driven oceanic anoxia across the Smithian/Spathian boundary (mid-Early Triassic). *Earth-Science Reviews*. <https://doi.org/10.1016/j.earscirev.2019.01.009>
- Storms, H. A., Brown, K. F., & Stein, J. D., 1977. Evaluation of a cesium positive ion source for secondary ion mass spectrometry. *Analytical Chemistry*, 49(13), 2023-2030.
- Sumner, D.Y., Beukes, N.J., 2006. Sequence Stratigraphic Development of the Neoproterozoic Transvaal carbonate platform, Kaapvaal Craton, South Africa. *South African Journal of Geology* 109, 11–22. <https://doi.org/10.2113/gssajg.109.1-2.11>
- Thomazo, C., Ader, M., Farquhar, J., Philippot, P., 2009. Methanotrophs regulated atmospheric sulfur isotope anomalies during the Mesoarchean (Tumbiana Formation, Western Australia). *Earth and Planetary Science Letters* 279, 65–75. <https://doi.org/10.1016/j.epsl.2008.12.036>
- Thomazo, C., Ader, M., Philippot, P., 2011. Extreme ^{15}N -enrichments in 2.72-Gyr-old sediments: evidence for a turning point in the nitrogen cycle. *Geobiology* 9, 107–120. <https://doi.org/10.1111/j.1472-4669.2011.00271.x>
- Thorne A. and Trendall A.F. (2001) Geology of the Fortescue Group, Pilbara Craton, Western Australia. *Bull. Geol. Surv. West. Aust.* 144, 1-249.
- Tyler, R., Tyler, N., 1996. Pre-Permian Research Stratigraphic and structural controls on gold mineralization in the Pilgrim's Rest goldfield, eastern Transvaal, South Africa, *Precambrian Research*.
- Whitehouse, M.J., Fedo, C.M., 2007. Microscale heterogeneity of Fe isotopes in >3.71 Ga banded iron formation from the Isua Greenstone Belt, southwest Greenland. *Geology* 35, 719. <https://doi.org/10.1130/G23582A.1>
- Wille, M., Kramers, J.D., Nägler, T.F., Beukes, N.J., Schröder, S., Meisel, Th., Lacassie, J.P., Voegelin, A.R., 2007. Evidence for a gradual rise of oxygen between 2.6 and 2.5Ga from Mo isotopes and Re-PGE signatures in shales. *Geochimica et Cosmochimica Acta* 71, 2417–2435. <https://doi.org/10.1016/j.gca.2007.02.019>
- Yoshiya, K., Nishizawa, M., Sawaki, Y., Ueno, Y., Komiya, T., Yamada, K., Yoshida, N., Hirata, T., Wada, H., Maruyama, S., 2012. In situ iron isotope analyses of pyrite and organic carbon isotope ratios in the Fortescue Group: Metabolic variations of a Late Archean ecosystem. *Precambrian Research* 212–213, 169–193. <https://doi.org/10.1016/j.precamres.2012.05.003>
- Zeyen, N., Benzerara, K., Li, J., Groleau, A., Balan, E., Robert, J.-L., Estève, I., Tavera, R., Moreira, D., López-García, P., 2015.

Formation of low-T hydrated silicates in modern microbialites from Mexico and implications for microbial fossilization. *Frontiers in Earth Science* 3. <https://doi.org/10.3389/feart.2015.00064>

Zeyen, N., Daval, D., Lopez-Garcia, P., Moreira, D., Gaillardet, J., Benzerara, K., 2017. Geochemical Conditions Allowing the Formation of Modern Lacustrine Microbialites. *Procedia Earth and Planetary Science* 17, 380–383. <https://doi.org/10.1016/j.proeps.2016.12.096>

Zeyen, N., Benzerara, K., Menguy, N., Brest, J., Templeton, A.S., Webb, S.M., Gérard, E., Moreira, D., López-García, P., Tavera, R., Morin, G., 2019. Fe-bearing phases in modern lacustrine microbialites from Mexico. *Geochimica et Cosmochimica Acta* 253, 201–230. <https://doi.org/10.1016/j.gca.2019.03.021>

CHAPTER 3.

PYRITE IRON AND SULFUR ISOTOPE SIGNATURES IN MODERN MICROBIALITES

Interpretation of sedimentary pyrite isotope signals in microbialites through time relies on the understanding of chemical and biological processes promoting modern microbialite formation (*Schidlowski, 1985; Dupraz and Visscher, 2005; Breitbart et al., 2009*). In modern microbial mats, the spatial organization of microorganisms creates steep elemental and redox gradients at a micrometric scale (*Fike et al., 2008; Gomes et al., 2022*) which may result in Fe and S isotope variabilities. Such variabilities can be preserved in pyrite, where both the Fe and S biogeochemical cycles are intertwined (*Archer and Vance, 2006; Rolison et al., 2018; Mansor and Fantle, 2019*). Although pyrite formation in modern sediments is mainly attributed to microbial processes, in particular microbial sulfate reduction (MSR), there is still a lack of documentation of the effect of S and Fe metabolizing microbial communities in mats, as well as on their mutual influences on the preserved pyrite Fe and S isotope signatures (*Fike et al., 2008; McAnena, 2011; Gomes et al., 2022*). The following question is consequently raised: To what extent is the distribution of Fe and S isotope compositions recorded in modern pyrite microbially-mediated?

Due to the rapid cycles of reduction - oxidation of the various Fe-bearing phases (Fe^{2+} , Fe^{3+} , and mixed valences), the processes preserved in pyrite are still unclear. This chapter focuses on the investigation of both Fe and S isotope systematics in modern microbially-mediated pyrite in order to answer some of these questions. Please note that the biological Fe cycle has already been detailed in **chapter 1** and the sidebar “Biological Sulfur Cycling” in this chapter details the main processes involved in the microbial S-cycle.

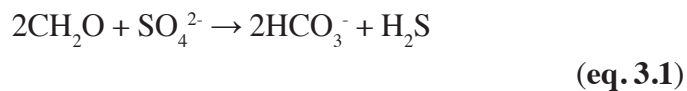
This chapter is composed of two parts focusing on the analysis of pyrite grains from two modern microbialites: first, from the Atexcac lake (Mexico) and second, from the Cayo Coco lagoon (Cuba). Samples were carefully chosen to target the comparison of two contemporaneous

microbialites yet growing in two contrasting environments (in terms of geological context and chemistry of the water column) and having experienced only weak early diagenetic processes. Although developed in different environmental settings, those microbialites contain comparable pyrite morphologies: framboids, and euhedral micrometric grains which are also termed micropyrrite. S and Fe isotope analyses were not necessarily performed on the same pyrite grains due to the necessity to re-polish the samples between analytical sessions. The first part of this chapter corresponds to a study published in *Geochemical Perspectives Letters* by *Marin-Carbonne et al. (2022)* entitled “Early precipitated micropyrrite in microbialites: A time capsule of microbial sulfur cycling”, which documents spatially resolved $\delta^{34}\text{S}$ isotope analyses by NanoSIMS in both micropyrrite and framboid grains. In this study, I contributed to petrographic observations and performed the S-isotope data acquisition. The second part of this chapter, entitled “Fe isotope biosignatures revealed in modern pyrite framboids”, is an unpublished study investigating the Fe isotope variability of framboids using SIMS (ims CAMECA 1280).

Sidebar 1: Biological Sulfur Cycling

Sulfur isotope geochemistry relies on the measurement of four stable sulfur isotopes (^{32}S , ^{33}S , ^{34}S , and ^{36}S) that can record processes producing fractionations following or not isotope mass laws, named mass dependent or independent fractionations. The finding of mass independent fractionation (S-MIF) in Archean rocks and their reproduction during photochemical dissociation experiments opened a way for understanding Earth history, including evolution of the atmosphere and oceans (*Farquhar et al., 2000; Pavlov and Kasting, 2002*). The use of multiple sulfur isotopes also provides insights into the nature of microorganisms metabolizing sulfur in modern sediments and therefore the possibility to track past microbial activity (*Jørgensen, 1977; Canfield et al., 1993; Thamdrup et al., 1993; Zerkle et al., 2009*). Biogeochemical sulfur cycling is dominated by three dissimilatory microbial processes: sulfur oxidation, sulfur disproportionation and sulfate reduction (*Johnston, 2011* for a review). Sulfur oxidation needs an oxidant (e.g. O_2 , NO_3^- , CO_2) as an electron acceptor to convert sulfide into sulfate or intermediate valence sulfur compounds (e.g. S_0 , $\text{S}_2\text{O}_3^{2-}$ or SO_3^{2-} ; *Canfield, 2001*). This process was thought to produce little fractionation, insignificant during biologically-mediated oxidation while able to reach up to 5‰ during abiotic oxidation (*Fry et al., 1988; Zerkle et al., 2009*). However, a recent study reported a fractionation up to +12‰ between sulfate and sulfur during microbial oxidation (*Pellerin et al., 2019*). Oxidative processes are responsible for the re-oxidation of 92% of sulfide produced by microbial sulfate reduction in marine settings (*Canfield and Teske, 1996; Findlay et al., 2020*). The oxidation of sulfide into intermediate valence sulfur species, such as

elemental sulfur, thiosulfate, tetrathiosulfate or sulfite, is of importance because these intermediate S-species can be used as electron donors and acceptors for disproportionating microorganisms (*Thamdrup et al., 1993; Canfield and Thamdrup, 1994, 1996; Böttcher et al., 2001; Frederiksen and Finster, 2003*). The disproportionation pathway results in the simultaneous formation of sulfide and sulfate. This metabolic pathway is achieved by diverse strains of sulfate reducers and produces highly ³⁴S-depleted sulfide, as low as -50‰ (*Canfield and Teske, 1996; Leavitt et al., 2013*), and ³⁴S-enriched sulfate (*Canfield, 2001*). The biological reduction of sulfate into sulfide by microbial sulfate reduction (MSR) is responsible of ~50% of organic matter remineralization in marine sediments (*Jørgensen, 1982; Egger et al., 2018*) by converting sulfate into sulfide at ambient temperature through the following reaction (**eq. 3.1**):



MSR is mainly supported by bacteria, but sulfate reduction is also observed in groups of organisms belonging to the Archaea domain. Sulfate reducers mainly spread in anoxic environments and are described in a large range of environments (e.g. marine and freshwater, brine; *Brandt et al., 2001; Jørgensen et al., 2019*). MSR reduces sulfate through multiple intra-cellular processes, including sulfate transport, APS (adenosine 5'-phosphosulfate enzyme) reduction and sulfite reduction (*Rees, 1973; Venceslau et al., 2014*; reviewed in *Fike et al., 2015*). Each step of intracellular reaction during sulfate reduction is associated with different S isotope fractionations (*Wing and Halevy, 2014; Bertran et al., 2018*), resulting in a final sulfide product largely depleted in ³⁴S isotope compositions, by as much as -70‰ (*Sim et al., 2011a, 2011b; Leavitt et al., 2013*). Sulfate concentration and reduction rates are parameters that strongly control the extent of sulfur isotope fractionation. For example, the maximum isotope fractionation is expressed at very low sulfate concentrations (tens to 100 μM) and low cell-specific sulfate reduction rates (*Harrison and Thode, 1958; Kaplan and Rittenberg, 1964; Leavitt et al., 2013; Wing and Halevy, 2014*). In addition, multiple sulfur isotope allow to differentiate the dynamic of sulfate reduction, i.e. open or closed system, and provide constraints on the type of metabolism involved in pyrite formation, through the measurement of slight deviation of ³³S and/or ³⁶S from the fractionation line following mass dependent laws (*Johnston, 2011*).

1. Early precipitated micropyrith in microbialites: A time capsule of microbial sulfur cycling

Published in *Geochemical Perspectives Letters*

Marin-Carbonne J., Decraene M-N., Havas R., Remusat L., Pasquier V., Alleon J., Zeyen N., Bouton A., Bernard S., Escrig S., Olivier N., Vennin E., Meibom A., Benzerara K. and Thomazo C.

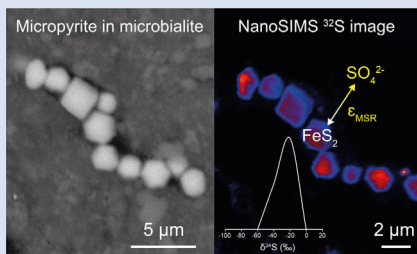
Early precipitated micropyrite in microbialites: A time capsule of microbial sulfur cycling

J. Marin-Carbonne^{1*}, M.-N. Decraene¹, R. Havas², L. Remusat³, V. Pasquier⁴,
J. Alléon¹, N. Zeyen⁵, A. Bouton², S. Bernard³, S. Escrig⁶, N. Olivier⁷,
E. Vennin², A. Meibom^{6,1}, K. Benzerara³, C. Thomazo^{2,8}



<https://doi.org/10.7185/geochemlet.2209>

Abstract



Microbialites are organosedimentary rocks that have occurred throughout the Earth's history. The relationships between diverse microbial metabolic activities and isotopic signatures in biominerals forming within these microbialites are key to understanding modern biogeochemical cycles, but also for accurate interpretation of the geologic record. Here, we performed detailed mineralogical investigations coupled with NanoSIMS (Nanoscale Secondary Ion Mass Spectrometry) analyses of pyrite S isotopes in mineralising microbial mats from two different environments, a hypersaline lagoon (Cayo Coco, Cuba) and a volcanic alkaline crater lake (Atexcac, Mexico). Both microbialite samples contain two distinct pyrite morphologies: framboids and euhedral micropyrites, which display distinct ranges of $\delta^{34}\text{S}$ values¹. Considering

the sulfate-sulfur isotopic compositions associated with both environments, micropyrites display a remarkably narrow range of Δ_{pyr} (*i.e.* $\Delta_{\text{pyr}} \equiv \delta^{34}\text{S}_{\text{SO}_4} - \delta^{34}\text{S}_{\text{pyr}}$) between 56 and 62 ‰. These measured Δ_{pyr} values agree with sulfate-sulfide equilibrium fractionation, as observed in natural settings characterised by low microbial sulfate reduction respiration rates. Moreover, the distribution of S isotope compositions recorded in the studied micropyrites suggests that sulfide oxidation also occurred at the microbialite scale. These results highlight the potential of micropyrites to capture signatures of microbial sulfur cycling and show that S isotope composition in pyrites record primarily the local micro-environments induced by the microbialite.

Received 21 October 2021 | Accepted 14 February 2022 | Published 21 March 2022

Introduction

Sulfate-reducing bacteria, *i.e.* microorganisms that use sulfate as a terminal electron acceptor, are ubiquitous in Earth environments where they play a major role both in S and C biogeochemical cycles (*e.g.*, Jørgensen *et al.*, 2019). Microbial sulfate reduction (MSR) reduces sulfate to dissolved S species, such as HS⁻ and H₂S, and discriminates against heavy sulfur isotopes. The resulting sulfide $\delta^{34}\text{S}$ values are relatively light and can be as much as -70 ‰ relative to sulfate (Jørgensen *et al.*, 2019). The fractionation induced by this metabolic activity ($^{34}\epsilon_{\text{mic}}$ hereafter) depends on the sulfate concentration, identity of the electron donor, bioavailable carbon (content and chemical form) and, perhaps most importantly, the cell-specific sulfate reduction rates (csSRR; Bradley *et al.*, 2016). In modern environments, MSR can be identified by rate measurements with radiotracers or genomic and proteomic approaches. However, since genetic markers are

not preserved in the geological record, the recognition of MSR in palaeoenvironments mostly relies on the sulfur isotopic compositions of sedimentary sulfide and sulfate minerals (Visscher *et al.*, 2000; Fike *et al.*, 2008).

MSR plays a key role in carbonate mineralisation, especially identified in microbialites and microbial mats (Visscher *et al.*, 2000). Microbial mats are stratified microbial communities whose metabolic activities produce geochemical gradients and drive elemental cycling (Canfield and Des Marais, 1993; Paerl and Pinckney, 1996). In the geological record, such deposits (often referred to as stromatolites) are considered among the oldest trace of life on Earth (Allwood *et al.*, 2009). Some Archaean stromatolites contain carbonaceous laminae that have been interpreted as fossil microbial mats or biofilms based on textural evidence (Awramik, 1992; Lepot, 2020). Interestingly, determining the precise nature of the fossil microbial community

1. Institute of Earth Sciences, Université de Lausanne, Geopolis, Mouline 1015 Lausanne, Switzerland
2. UMR CNRS/UB6282 Biogéosciences, UFR Science Vie Terre Environnement, Université de Bourgogne Franche Comté, Dijon, France
3. Muséum National d'Histoire Naturelle, Sorbonne Université, CNRS UMR7590, Institut de Minéralogie, de Physique des Matériaux et de Cosmochimie (IMPMC), Paris, France
4. Earth and Planetary Sciences, Weizmann Institute of Sciences, Rehovot, Israel
5. Department of Earth and Atmospheric Sciences, University of Alberta, T6G 2E3, Canada
6. Laboratory for Biological Geochemistry, School of Architecture, Civil and Environmental Engineering, Ecole Polytechnique Fédérale de Lausanne, CH-1015 Lausanne, Switzerland
7. Université Clermont Auvergne, CNRS, IRD, Laboratoire Magmas et Volcans, F-63000 Clermont-Ferrand, France
8. Institut Universitaire de France, Paris, France

* Corresponding author (email: johanna.marincarbonne@unil.ch)

¹ $\delta^{34}\text{S} = ((^{34}\text{S}/^{32}\text{S})_{\text{sample}} / (^{34}\text{S}/^{32}\text{S})_{\text{reference}} - 1) \times 1000$ in ‰, with Vienna Canyon Diablo Troilite as the reference.



is challenging because these organosedimentary rocks resulted from a complex balance between microbial activities, sedimentation and intermittent lithification (Reid *et al.*, 2000). In addition, the biosignatures preserved in fossil biofilms are ambiguous, especially after diagenesis and post-depositional history (Javaux, 2019; Alleon *et al.*, 2021). The oldest evidence for MSR in the Archaean geological record are sulfur isotopic signatures from deep marine sediments (Kamber and Whitehouse, 2007; Shen *et al.*, 2009) and stromatolites (Shen and Buick, 2004). In modern microbialites, numerous studies have reported dynamic MSR activity based on H₂S labelling (Visscher *et al.*, 2000; Fike *et al.*, 2008; Pace *et al.*, 2018; Gomes *et al.*, 2021), but only a few studies have investigated sulfur isotope signatures of individual pyrite grains (Gomes *et al.*, 2021).

The primary S isotopic signatures of pyrites (FeS₂) are often modified by fluid circulation during metasomatism or metamorphism (Marin-Carbonne *et al.*, 2020; Slotznick *et al.*, 2022), occurring millions or billions of years after sediment deposition. While late diagenesis can modify both pyrite crystallinity and S isotope composition (Williford *et al.*, 2011; Gomes *et al.*, 2018; Marin-Carbonne *et al.*, 2020), early diagenesis in microbial mats is thought to have a limited effect on the S isotopic composition of pyrite, meaning that microbialitic pyrites may preserve 'pristine' isotopic signatures. However, the observation of large isotopic differences of about ~30 ‰ (Raven *et al.*, 2016) between pore water sulfur species (SO₄²⁻ and H₂S) and pyrite shows that other S-bearing pools, such as organic matter, should be considered in order to quantitatively and isotopically describe sulfur cycling in microbialites. Pyrite often precipitates at the microbial mat surface

(Gomes *et al.*, 2021) and its isotopic composition is more representative of the local setting rather than global environmental conditions, *e.g.*, water column (Lang *et al.*, 2020; Pasquier *et al.*, 2021). Decoding pyrite S isotopes at the micro-scale in sedimentary rocks is required to better understand how local conditions may affect the isotopic composition of microbialite pyrites. Here, we focus our investigation on two geographically independent modern microbial mats, which have not yet undergone (complete) lithification, and/or metasomatism.

Syngenetic Microbialitic Pyrites

We studied two samples from 1) the Atexcac Lake, a monomictic volcanic crater lake (Mexico; Zeyen *et al.*, 2021) and 2) Cayo Coco Lake, a shallow hypersaline lagoon in Cuba (Pace *et al.*, 2018; Bouton *et al.*, 2020). These two depositional settings exhibit contrasting water column sulfate concentrations of 2.1 and 62 mM for Lake Atexcac and Cayo Coco, respectively (Figs. S-1 and S-2, SI). Both samples were produced by mineralising microbial mats and contained authigenic aragonite, Mg-rich calcite, dolomite, authigenic hydrated Mg-silicates/silica such as kerolite, and detrital phases such as feldspars and illite (Figs S-1 and S-2, SI). In each locality, pyrite morphologies fall into two different categories (Fig. 1): framboidal pyrites, ranging from 3 to 15 µm, and mono-crystal pyrites of a few micrometres (>3 µm), hereafter called micropyrites (Figs. 1 and 2, SI). Transmission electron microscopy analyses revealed an early origin of the micropyrite grains (SI). Considering both the

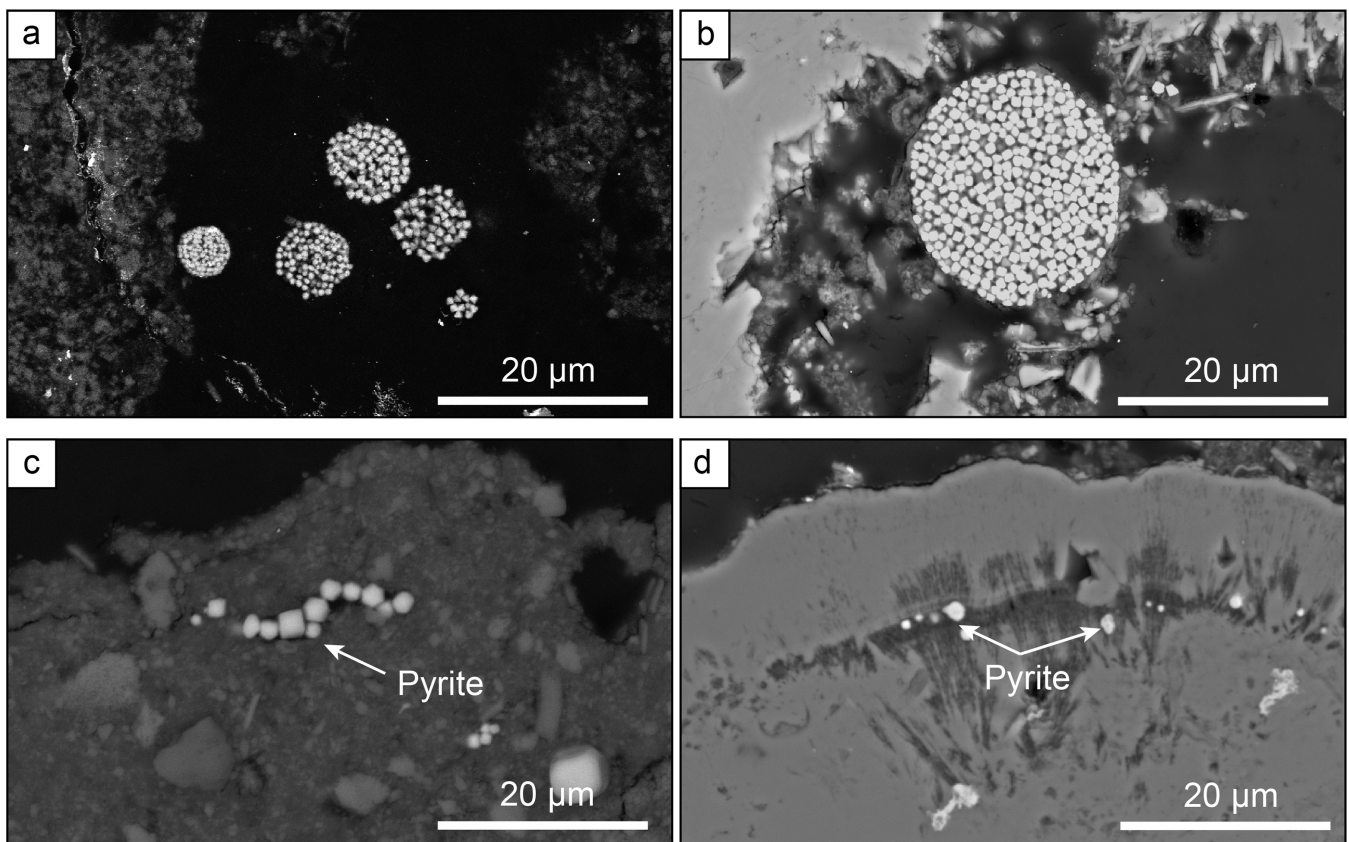


Figure 1 Secondary Electron microscopy pictures of (a, b) framboidal pyrites and (c, d) micropyrites from (a, c) Cayo Coco Lagoon and (b, d) Atexcac. Framboidal pyrites are located at the surface of the mineralised microbialite (in dark) while micropyrites are entombed within aragonite (in light grey) or Mg rich silicate (dark grey).

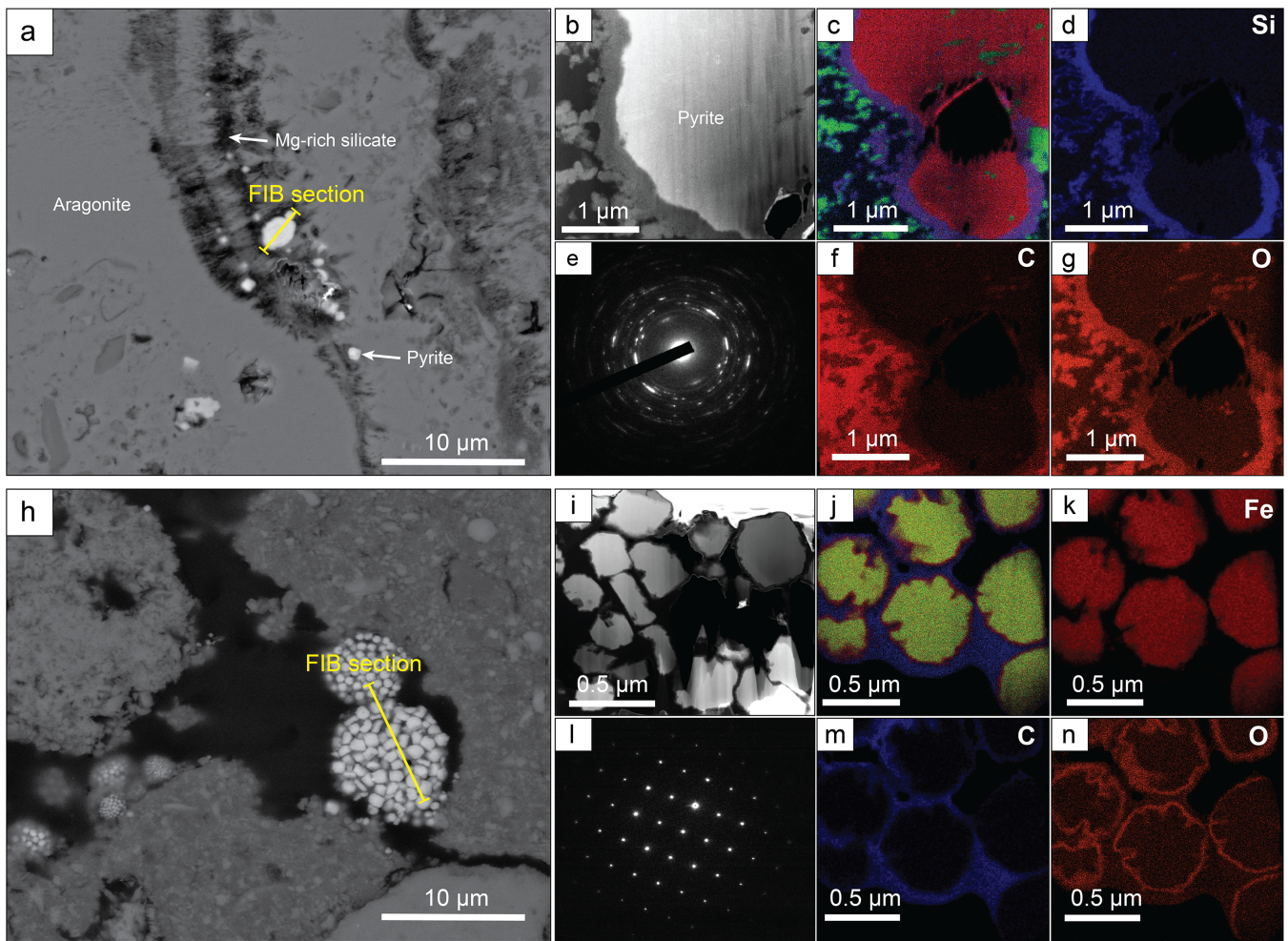


Figure 2 (a) SEM picture of micropyrates. Location where FIB section was extracted is shown by the yellow line, (b) TEM picture of the pyrite crystal and (e) its associated powder-like diffraction pattern, (c) false colour STEM EDXS image (Si in blue, Ca in green, Fe in red) and (d, f, g) Si, C and O images of the submicrometric pyrites, respectively. (h) SEM picture of framboidal pyrite with FIB section location (yellow line), (i) TEM image and (l) associated single crystal diffraction pattern along the [112] zone axis of pyrite, (j) false colour STEM EDXS image of pyrite crystallites (Fe in red, S in green, C in blue) and (k, m, n) Fe, C and O images, respectively.

alignment of the micropyrates within the organic lamination and their crystallinity, micropyrates are likely formed during an early lithification stage (SI).

NanoSIMS S Isotope Composition of Pyrites

The S isotope compositions of 66 framboidal pyrites and 55 individual micropyrates were measured by NanoSIMS with a reproducibility better than 2‰ (2 σ , see SI). Framboidal pyrites display a ~20–30‰ range in $\delta^{34}\text{S}$ values with an average of $-26.1 \pm 7\text{‰}$ and $-26.4 \pm 9\text{‰}$ (2 s.d.) for Atexcac and Cayo Coco, respectively (Figs. 3 and 4). We have extracted S isotope composition of individual crystallites from four framboids (Fig. 3, SI). All framboidal pyrites ($n = 4$) show a large internal $\delta^{34}\text{S}$ variability (~40‰, Fig. 3) characterised by a gradient from $+8.5 \pm 1.5\text{‰}$ to more ^{34}S -depleted values ranging from -42 to -69‰ . Micropyrates also show large S isotope heterogeneities with $\delta^{34}\text{S}$ values ranging from -86 to -17‰ with an average value of $-61.4 \pm 17\text{‰}$ for Atexcac, and from -53 to -21‰ with an average value of $-34.5 \pm 29\text{‰}$ in Cayo Coco (Fig. 4).

Framboidal Pyrites Record a Mixing of Reduction and Oxidation Processes

Framboidal pyrites display a large range of $\delta^{34}\text{S}$ values but also an internal isotope variation across the length scale of individual framboidal grains (Fig. 3), best explained by a combination of MSR and partial sulfide oxidation (Fig. 3; Pellerin *et al.*, 2019). As framboidal pyrites are mostly observed at the surface of the mat, S isotope variations reflect the mixing of in situ production, upward diffusion of sulfide in the mat and its subsequent reoxidation at the mat surface. The fractionation required to produce such an isotopic gradient is well above abiotic sulfide oxidation (*i.e.* $+5\text{‰}$; Fry *et al.*, 1988), yet can also be consistent with microbial sulfide oxidation in high pH environments (Pellerin *et al.*, 2019). Both sites are characterised by high pH (pH > 8, see SI), which is known to promote large isotope fractionation during sulfide oxidation (Pellerin *et al.*, 2019). Consequently, part of the observed range of $\delta^{34}\text{S}$ values may be attributed to local variation of S speciation associated with pH. As such, the internal gradient may be the result of microbially mediated surface H_2S oxidation. Alternatively, the internal isotope gradient across the framboidal pyrites (Fig. 2, SI) can be due to Rayleigh isotope fractionation, as even under

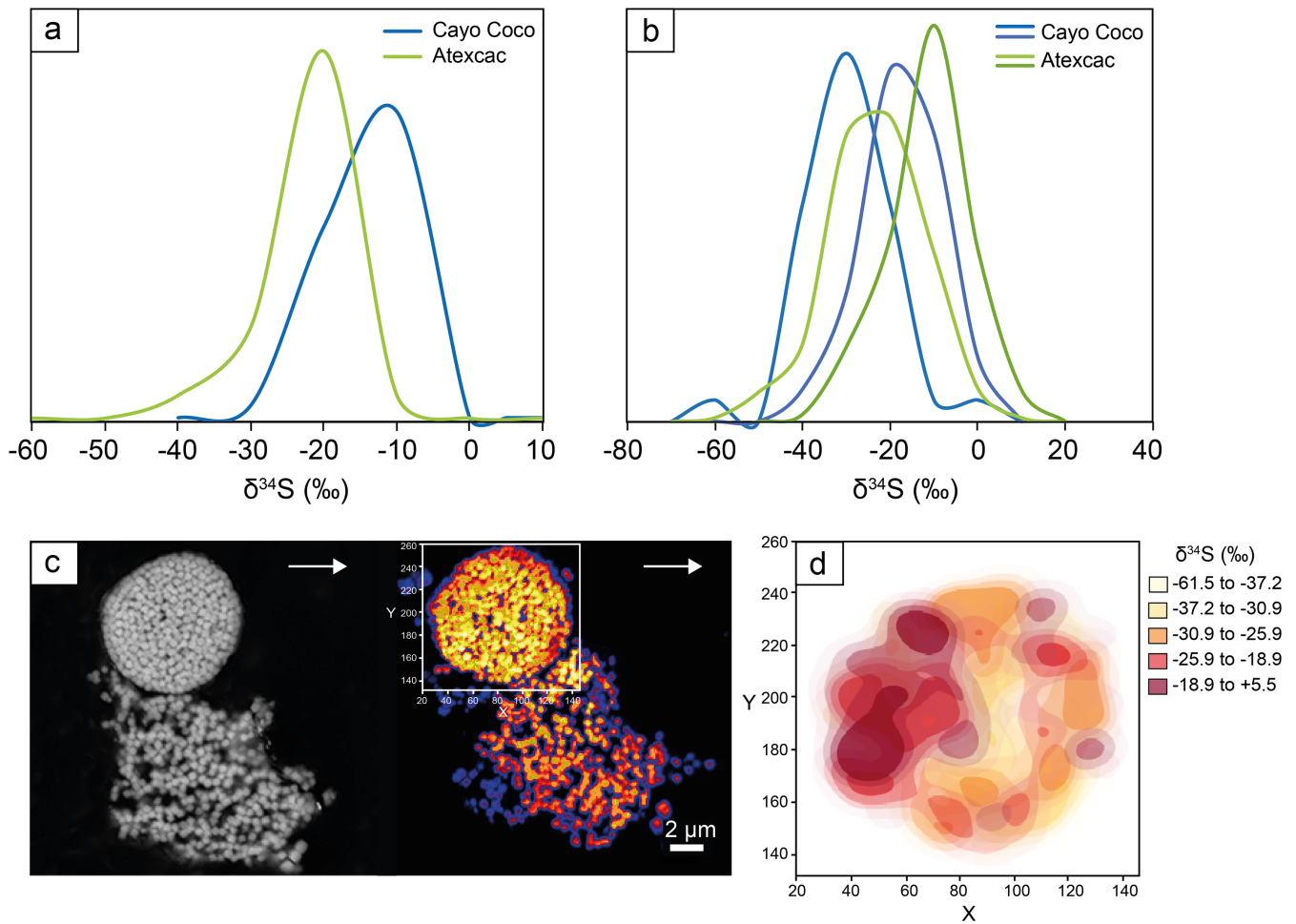


Figure 3 (a) $\delta^{34}\text{S}$ probability density function of all framboidal pyrites from Atexcac and Cayo Coco uncertainties of analyses ranges from 0.4 to 4 ‰, (b) $\delta^{34}\text{S}$ probability density function of four individual framboidal pyrites containing up to 100 pyrite crystallites, (c) SEM and corresponding NanoSIMS ^{32}S image of one framboidal pyrite; the arrow indicates the top of the mat, and (d) $\delta^{34}\text{S}$ values reconstructed for individual pyrite crystallites showing strong variations in S isotope composition across the framboidal pyrite.

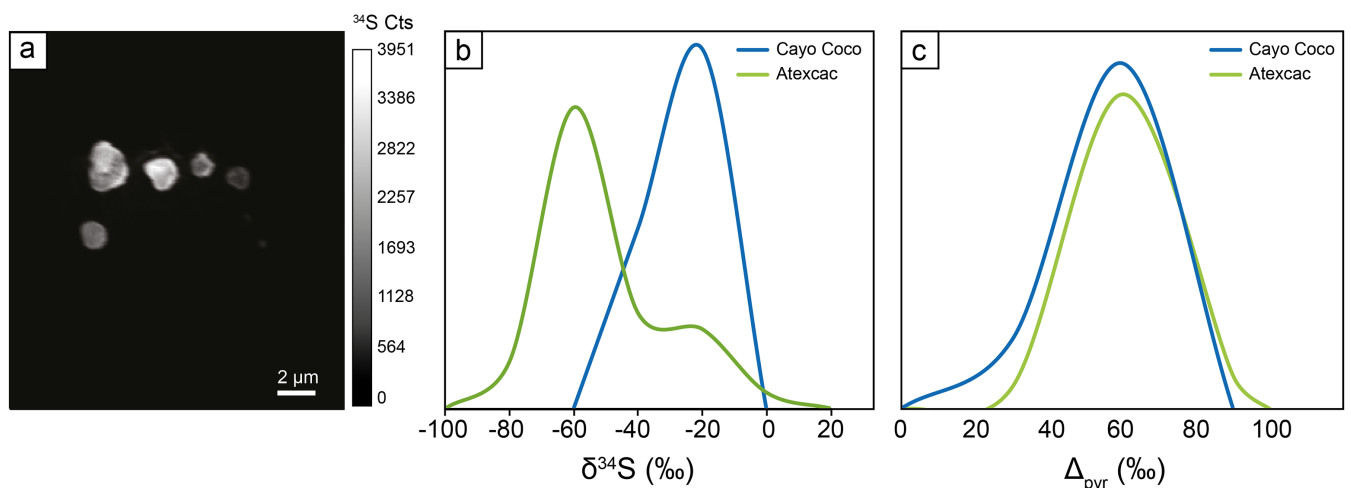


Figure 4 (a) NanoSIMS ^{32}S image of submicrometric pyrites, (b) $\delta^{34}\text{S}$ probability density function, taking account of the range of uncertainties from 1 ‰ to 8 ‰ of micropyrrites from Cayo Coco and Atexcac, (c) Δ_{pyr} distribution calculated for both environments.

oxidising (abundant sulfate) conditions, consumption can occur faster than diffusive replenishment (Goldhaber and Kaplan, 1980). Rather than reflecting water column conditions, the S

isotope composition of framboidal pyrites appears to be strongly influenced by local redox conditions (*i.e.* at the microbial mat scale).

Microbialitic Micropyrrite Preserve Primary Isotopic Microbial Fractionation Signatures

The presence of Mg silicate rich rims (SI) suggests that micropyrrites were probably formed very early during lithification (Fig. 2). Moreover, the small crystal size of micropyrrites composed of nanocrystals with different orientations has been highlighted as a possible biogenic signature (Picard *et al.*, 2018). The $\delta^{34}\text{S}$ values of dissolved sulfate are +0.52 ‰ in Atexcac and are assumed to be close to seawater composition (+21 ‰) for Cayo Coco (SI). Considering these hugely contrasting isotopic compositions of sulfate, micropyrrites display surprisingly similar Δ_{pyr} values (*i.e.* $\Delta_{\text{pyr}} = \delta^{34}\text{S}_{\text{SO}_4} - \delta^{34}\text{S}_{\text{pyr}}$) of 62 ± 17 ‰ and 56 ± 29 ‰ for Atexcac and Cayo Coco, respectively (Fig. 4). These Δ_{pyr} values are consistent with near thermodynamic equilibrium fractionation as observed in *i)* MSR batch culture experiments characterised by low growth rate and csSRR (Leavitt *et al.*, 2013; Bradley *et al.*, 2016) and *ii)* natural environments (*e.g.*, Cadagno Lake; Canfield *et al.*, 2010). High $^{34}\text{S}_{\text{mic}}$ has been observed in sulfate reducing strains only partially oxidising their carbon substrate and is sometimes associated with the degradation of carbohydrate components, including exopolymeric substances (EPS) (Sim *et al.*, 2011), which are abundant in microbialite-forming mats. Atexcac waters have a high dissolved organic carbon content (over 15 times that of the modern ocean) which can sustain MSR activity, while Cayo Coco harbours conspicuous suspended EPS-rich organic slimes (Bouton *et al.*, 2016). Despite abundant sulfate (at Cayo Coco) and organic matter, csSRR in these mats are intriguingly low and contrast with previous occurrences of high SRR in surface microbial mats (Canfield and Des Marais, 1993). Low csSRR and high S isotope fractionations in both lakes could be explained by the refractory nature of this organic matter (Bouton *et al.*, 2020; Gomes *et al.*, 2021). At the microbial mat scale, strong gradients of sulfate reduction within layered mats (Visscher *et al.*, 2000; Fike *et al.*, 2009; Pace *et al.*, 2018) have been attributed to small scale variations in csSRR and/or localised MSR micro-niches (Fike *et al.*, 2009; Gomes *et al.*, 2021). The observed laminations, which contain micropyrrites, likely reflect local high density microbe spots, which can result from a more pronounced local distillation of $\delta^{34}\text{S}$ (Pasquier *et al.*, 2021). Alternatively, the composition of microbial consortia may affect the range of csSRR at the microbial mat scale (Bradley *et al.*, 2016), with guild diversity having opposite effects on trophic group functions, thus modulating csSRR (Bell *et al.*, 2005; Peter *et al.*, 2011).

Conclusions

Here, we have shown that the S isotope composition of fram-boids and micropyrrites reflects sulfur cycling at the scale of the mat environment. While S isotope signatures in microbialite micropyrrites are primarily controlled by MSR, they can also be influenced by oxidative sulfur cycling in high pH environments. Notably, microbialites growing at different dissolved sulfate concentrations and in marine versus lacustrine environments display similar micropyrrite morphologies and comparable Δ_{pyr} . Such observations demonstrate that microbialites have the potential to record the isotopic fractionation associated with MSR irrespective of the depositional environment and sulfate level. Consequently, we propose that microbialite micropyrrites can be used as a mineral signature for reconstructing past Earth surface and microbial environments, as already suggested for Archaeal stromatolites (Marin-Carbonne *et al.*, 2018). In addition, this study clearly shows that caution should be used

in reconstructing past environmental parameters, such as water body sulfate levels, from Δ_{pyr} . Finally, the respective influence of different electron donors, sulfate concentration, and non-actualistic microbial communities on the csSRR and associated sedimentary pyrites $\delta^{34}\text{S}$ remains to be explored in order to deepen our understanding of the evolutionary trajectory of biogeochemical sulfur cycling on Earth.

Author contributions

JMC, LR, SB and CT designed the study, KB, EV, CT and AB collected samples in the field. JMC, LR, MND and SE conducted the NanoSIMS analyses, CT and RH conducted the bulk S isotope analyses. JMC, MND, JA, AB, NZ and KB conducted the microscope observations. All authors have contributed to the data interpretation. JMC wrote the manuscript with important contributions of all co-authors.

Competing interests

Authors declare no competing interests.

Data and materials availability

All data is available in the main text or the supplementary materials.

Additional Information

Supplementary Information accompanies this letter at <https://www.geochemicalperspectivesletters.org/article2209>.

Acknowledgements

This research was supported through the European Research council (ERC) under the European Union's Horizon H2020 research and innovation programme (STROMATA grant agreement 759289). The NanoSIMS facility at the Museum National d'Histoire Naturelle in Paris was established by funds from the CNRS, region ile de France, Ministère délégué à l'enseignement et à la recherche and the Museum National d'Histoire Naturelle. We thank Kevin McKeegan and Jasmine Berg for their proof-reading of the manuscript and for fruitful discussions.

Editor: Tanja Bosak



© 2022 The Authors. This work is distributed under the Creative Commons Attribution Non-Commercial No-Derivatives 4.0

License, which permits unrestricted distribution provided the original author and source are credited. The material may not be adapted (remixed, transformed or built upon) or used for commercial purposes without written permission from the author. Additional information is available at <https://www.geochemicalperspectivesletters.org/copyright-and-permissions>.

Cite this letter as: Marin-Carbonne, J., Decraene, M.-N., Havas, R., Remusat, L., Pasquier, V., Alléon, J., Zeyen, N., Bouton, A., Bernard, S., Escrig, S., Olivier, N., Vennin, E., Meibom, A., Benzerara, K., Thomazo, C. (2022) Early precipitated micropyrrite in microbialites: A time capsule of microbial sulfur cycling. *Geochem. Persp. Let.* 21, 7–12. <https://doi.org/10.7185/geochemlet.2209>

References

- ALLEON, J., BERNARD, S., OLIVIER, N., THOMAZO, C., MARIN-CARBONNE, J. (2021) Inherited geochemical diversity of 3.4 Ga organic films from the Buck Reef Chert, South Africa. *Communications Earth & Environment* 2, 6. <https://doi.org/10.1038/s43247-020-00066-7>
- ALLWOOD, A.C., GROTZINGER, J.P., KNOLL, A.H., BURCH, I.W., ANDERSON, M.S., COLEMAN, M.L., KANIK, I. (2009) Controls on development and diversity of Early Archean stromatolites. *Proceedings of the National Academy of Sciences* 106, 9548–9555. <https://doi.org/10.1073/pnas.0903323106>
- AWRAMIK, S.M. (1992) The history and significance of stromatolite. In: SCHIDLowski, M., GOLUBIC, S., KIMBERLEY, M.M., MCKIRDY, D.M., TRUDINGER, P.A. (Eds.) *Early organic evolution*. Springer, Berlin, 435–449. https://doi.org/10.1007/978-3-642-76884-2_34
- BELL, T., NEWMAN, J.A., SILVERMAN, B.W., TURNER, S.L., LILLEY, A.K. (2005) The contribution of species richness and composition to bacterial services. *Nature* 436, 1157–1160. <https://doi.org/10.1038/nature03891>
- BOUTON, A., VENNIN, E., PACE, A., BOURILLOT, R., DUPRAZ, C., THOMAZO, C., BRAYARD, A., DÉSAUBLAUX, G., VISSCHER, P.T. (2016) External controls on the distribution, fabrics and mineralization of modern microbial mats in a coastal hypersaline lagoon, Cayo Coco (Cuba). *Sedimentology* 63, 972–1016. <https://doi.org/10.1111/sed.12246>
- BOUTON, A., VENNIN, E., THOMAZO, C., MATHIEU, O., GARCIA, F., JAUBERT, M., VISSCHER, P. (2020) Microbial Origin of the Organic Matter Preserved in the Cayo Coco Lagoonal Network, Cuba. *Minerals* 10, 143. <https://doi.org/10.3390/min10020143>
- BRADLEY, A.S., LEAVITT, W.D., SCHMIDT, M., KNOLL, A.H., GIRGIS, P.R., JOHNSTON, D.T. (2016) Patterns of sulfur isotope fractionation during microbial sulfate reduction. *Geobiology* 14, 91–101. <https://doi.org/10.1111/gbi.12149>
- CANFIELD, D.E., DES MARAIS, D.J. (1993) Biogeochemical cycles of carbon, sulfur, and free oxygen in a microbial mat. *Geochimica et Cosmochimica Acta* 57, 3971–3984. [https://doi.org/10.1016/0016-7037\(93\)90347-Y](https://doi.org/10.1016/0016-7037(93)90347-Y)
- CANFIELD, D.E., FARQUHAR, J., ZERKLE, A.L. (2010) High isotope fractionations during sulfate reduction in a low-sulfate euxinic ocean analog. *Geology* 38, 415–418. <https://doi.org/10.1130/G30723.1>
- FIKE, D.A., FINKE, N., ZHA, J., BLAKE, G., HOEHLER, T.M., ORPHAN, V.J. (2009) The effect of sulfate concentration on (sub)millimeter-scale sulfide $\delta^{34}\text{S}$ in hypersaline cyanobacterial mats over the diurnal cycle. *Geochimica et Cosmochimica Acta* 73, 6187–6204. <https://doi.org/10.1016/j.gca.2009.07.006>
- FIKE, D.A., GAMMON, C.L., ZIEBIS, W., ORPHAN, V.J. (2008) Micron-scale mapping of sulfur cycling across the oxycline of a cyanobacterial mat: a paired nanoSIMS and CARD-FISH approach. *The ISME Journal* 2, 749–759. <https://doi.org/10.1038/ismej.2008.39>
- FRY, B., RUE, W., GEST, H., HAYES, J.M. (1988) Sulfur isotope effects associated with oxidation of sulfide by O_2 in aqueous solution. *Chemical Geology: Isotope Geoscience section* 73, 205–210. [https://doi.org/10.1016/0168-9622\(88\)90001-2](https://doi.org/10.1016/0168-9622(88)90001-2)
- GOLDBABER, M.B., KAPLAN, I.R. (1980) Mechanisms of sulfur incorporation and isotope fractionation during early diagenesis in sediments of the Gulf of California. *Marine Chemistry* 9, 95–143. [https://doi.org/10.1016/0304-4203\(80\)90063-8](https://doi.org/10.1016/0304-4203(80)90063-8)
- GOMES, M.L., FIKE, D.A., BERGMANN, K.D., JONES, C., KNOLL, A.H. (2018) Environmental insights from high-resolution (SIMS) sulfur isotope analyses of sulfides in Proterozoic microbialites with diverse mat textures. *Geobiology* 16, 17–34. <https://doi.org/10.1111/gbi.12265>
- GOMES, M.L., KLATT, J.M., DICK, G.J., GRIM, S.L., RICO, K.I., MEDINA, M., ZIEBIS, W., KINSMAN-COSTELLO, L., SHELDON, N.D., FIKE, D.A. (2021) Sedimentary pyrite sulfur isotope compositions preserve signatures of the surface microbial mat environment in sediments underlying low-oxygen cyanobacterial mats. *Geobiology* 20, 60–78. <https://doi.org/10.1111/gbi.12466>
- JAVAUX, E.J. (2019) Challenges in evidencing the earliest traces of life. *Nature* 572, 451–460. <https://doi.org/10.1038/s41586-019-1436-4>
- JØRGENSEN, B.B., FINDLAY, A.J., PALLERIN, A. (2019) The Biogeochemical Sulfur Cycle of Marine Sediments. *Frontiers in Microbiology* 10, 849. <https://doi.org/10.3389/fmicb.2019.00849>
- KAMBER, B.S., WHITEHOUSE, M.J. (2007) Micro-scale sulphur isotope evidence for sulphur cycling in the late Archean shallow ocean. *Geobiology* 5, 5–17. <https://doi.org/10.1111/j.1472-4669.2006.00091.x>
- LANG, X., TANG, W., MA, H., SHEN, B. (2020) Local environmental variation obscures the interpretation of pyrite sulfur isotope records. *Earth and Planetary Science Letters* 533, 116056. <https://doi.org/10.1016/j.epsl.2019.116056>
- LEAVITT, W.D., HALEVY, I., BRADLEY, A.S., JOHNSTON, D.T. (2013) Influence of sulfate reduction rates on the Phanerozoic sulfur isotope record. *Proceedings of the National Academy of Sciences* 110, 11244–11249. <https://doi.org/10.1073/pnas.1218874110>
- LEPOT, K. (2020) Signatures of early microbial life from the Archean (4 to 2.5 Ga) eon. *Earth-Science Reviews* 209, 103296. <https://doi.org/10.1016/j.earscirev.2020.103296>
- MARIN-CARBONNE, J., BUSIGNY, V., MIOT, J., ROLLION-BARD, C., MULLER, E., DRABON, N., JACOB, D., PONT, S., ROBYR, M., BONTOGNALI, T.R.R., FRANÇOIS, C., REYNAUD, S., VAN ZUILEN, M., PHILIPPOT, P. (2020) In Situ Fe and S isotope analyses in pyrite from the 3.2 Ga Mendon Formation (Barberton Greenstone Belt, South Africa): Evidence for early microbial iron reduction. *Geobiology* 18, 306–325. <https://doi.org/10.1111/gbi.12385>
- MARIN-CARBONNE, J., REMUSAT, L., SFORNA, M.C., THOMAZO, C., CARTIGNY, P., PHILIPPOT, P. (2018) Sulfur isotope's signal of nanopyrates enclosed in 2.7 Ga stromatolitic organic remains reveal microbial sulfate reduction. *Geobiology* 16, 121–138. <https://doi.org/10.1111/gbi.12275>
- PACE, A., BOURILLOT, R., BOUTON, A., VENNIN, E., BRAISSANT, O., DUPRAZ, C., DUTEIL, T., BUNDELEVA, I., PATRIER, P., GALAUP, S., YOKOYAMA, Y., FRANCESCHI, M., VIRGONE, A., VISSCHER, P.T. (2018) Formation of stromatolite lamina at the interface of oxygenic-anoxygenic photosynthesis. *Geobiology* 16, 378–398. <https://doi.org/10.1111/gbi.12281>
- PAERL, H.W., PINCKNEY, J.L. (1996) A mini-review of microbial consortia: their roles in aquatic production and biogeochemical cycling. *Microbial Ecology* 31, 225–247. <https://doi.org/10.1007/BF00171569>
- PASQUIER, V., BRYANT, R.N., FIKE, D.A., HALEVY, I. (2021) Strong local, not global, controls on marine pyrite sulfur isotopes. *Science Advances* 7, eabb7403. <https://doi.org/10.1126/sciadv.abb7403>
- PELLERIN, A., ANTLER, G., HOLM, S.A., FINDLAY, A.J., CROCKFORD, P.W., TURCHYN, A.V., JØRGENSEN, B.B., FINSTER, K. (2019) Large sulfur isotope fractionation by bacterial sulfide oxidation. *Science Advances* 5, eaaw1480. <https://doi.org/10.1126/sciadv.aaw1480>
- PETER, H., BEIER, S., BERTILSSON, S., LINDSTRÖM, E.S., LANGENHEDER, S., TRANVIK, L.J. (2011) Function-specific response to depletion of microbial diversity. *The ISME Journal* 5, 351–361. <https://doi.org/10.1038/ismej.2010.119>
- PICARD, A., GARTMAN, A., CLARKE, D.R., GIRGIS, P.R. (2018) Sulfate-reducing bacteria influence the nucleation and growth of mackinawite and greigite. *Geochimica et Cosmochimica Acta* 220, 367–384. <https://doi.org/10.1016/j.gca.2017.10.006>
- RAVEN, M.R., SESSIONS, A.L., FISCHER, W.W., ADKINS, J.F. (2016) Sedimentary pyrite $\delta^{34}\text{S}$ differs from porewater sulfide in Santa Barbara Basin: Proposed role of organic sulfur. *Geochimica et Cosmochimica Acta* 186, 120–134. <https://doi.org/10.1016/j.gca.2016.04.037>
- REID, R.P., VISSCHER, P.T., DECHO, A.W., STOLZ, J.F., BEBOUT, B.M., DUPRAZ, C., MACINTYRE, I.G., PAERL, H.W., PINCKNEY, J.L., PRUFERT-BEBOUT, J., STEPPE, T.F., DESMARAIS, D.J. (2000) The role of microbes in accretion, lamination and early lithification of modern marine stromatolites. *Nature* 406, 989–992. <https://doi.org/10.1038/35023158>
- SHEN, Y., FARQUHAR, J., MASTERTON, A., KAUFMAN, A.J., BUICK, R. (2009) Evaluating the role of microbial sulfate reduction in the early Archean using quadruple isotope systematics. *Earth and Planetary Science Letters* 279, 383–391. <https://doi.org/10.1016/j.epsl.2009.01.018>
- SHEN, Y., BUICK, R. (2004) The antiquity of microbial sulfate reduction. *Earth-Science Reviews* 64, 243–272. [https://doi.org/10.1016/S0012-8252\(03\)00054-0](https://doi.org/10.1016/S0012-8252(03)00054-0)
- SIM, M.S., ONO, S., DONOVAN, K., TEMPLER, S.P., BOSAK, T. (2011) Effect of electron donors on the fractionation of sulfur isotopes by a marine *Desulfovibrio* sp. *Geochimica et Cosmochimica Acta* 75, 4244–4259. <https://doi.org/10.1016/j.gca.2011.05.021>
- SLOTZNICK, S.P., JOHNSON, J.E., RASMUSSEN, B., RAUB, T.D., WEBB, S.M., ZI, J.-W., KIRSCHVINK, J.L., FISCHER, W.W. (2022) Reexamination of 2.5-Ga “whiff” of oxygen interval points to anoxic ocean before GOE. *Science Advances* 8, eabj7190. <https://doi.org/10.1126/sciadv.abj7190>
- VISSCHER, P.T., REID, R.P., BEBOUT, B.M. (2000) Microscale observations of sulfate reduction: Correlation of microbial activity with lithified micritic laminae in modern marine stromatolites. *Geology* 28, 919–922. [https://doi.org/10.1130/0091-7613\(2000\)28<919:MOOSRC>2.0.CO;2](https://doi.org/10.1130/0091-7613(2000)28<919:MOOSRC>2.0.CO;2)
- WILLIFORD, K.H., VAN KRANENDONK, M.J., USHIKUBO, T., KOZDON, R., VALLEY, J.W. (2011) Constraining atmospheric oxygen and seawater sulfate concentrations during Paleoproterozoic glaciation: In situ sulfur three-isotope microanalysis of pyrite from the Turee Creek Group, Western Australia. *Geochimica et Cosmochimica Acta* 75, 5686–5705. <https://doi.org/10.1016/j.gca.2011.07.010>
- ZEVEN, N., BENZERARA, K., BEYSSAC, O., DAVAL, D., MULLER, E., THOMAZO, C., TAVERA, R., LÓPEZ-GARCÍA, P., MOREIRA, D., DUPRAT, E. (2021) Integrative analysis of the mineralogical and chemical composition of modern microbialites from ten Mexican lakes: What do we learn about their formation. *Geochimica et Cosmochimica Acta* 305, 148–184. <https://doi.org/10.1016/j.gca.2021.04.030>



Early precipitated micropyrrite in microbialites: A capsule of microbial sulfur cycling

J. Marin-Carbonne, M.-N. Decraene, R. Havas, L. Remusat, V. Pasquier, J. Alleon, N. Zeyen, A. Bouton, N. Olivier, S. Escrig, E. Vennin, A. Meibom, K. Benzerara, C. Thomazo

Supplementary Information

The Supplementary Information includes:

- Sample Descriptions
- Methods
- Framboidal Pyrites
- Tables S-1 to S-5
- Figures S-1 to S-10
- Supplementary Information References

Sample Descriptions

Atexcac Microbialite

The studied sample (ATX-2012-08) consists of a microbialite collected at about 0.1 m below the lake water level (Zeyen *et al.*, 2015) in January 2012. Atexcac is a maar lake covering an area of 27 ha, located in the eastern part of the trans-Mexican volcanic belt in the Cuenca de Oriental basin (Puebla State), in the Los Llanos de San Juan region. The salinity of Lake Atexcac varies between 7 and 8 g L⁻¹, pH is around 8.5 and average temperature is 18.3 °C (Sigala *et al.*, 2017; Zeyen *et al.*, 2021). The studied sample (ATX-2012-08) was collected on the Southwestern shore of the lake (Fig. S-1). The mineralogy of the sample consists of aragonite and authigenic silicates, likely kerolite and/or stevensite.

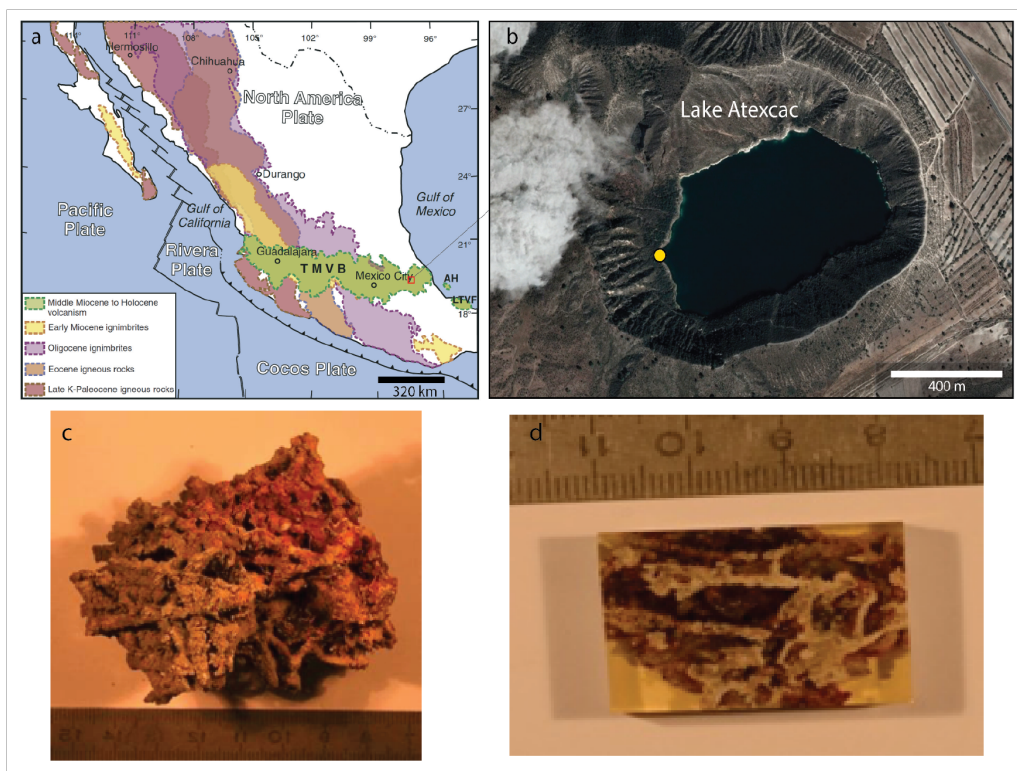


Figure S-1 Geographic location of Lake Atexcac. **(a)** Geological map representing the location of the trans-Mexican volcanic belt (TMVB, green area) from Ferrari *et al.* (2012) and the location of Lake Atexcac marked by a red square. **(b)** Google Earth image of the lake. The yellow circle corresponds to the microbialite sampling area in January 2012. **(c)** Close view of the sample and **(d)** sample included in epoxy.

Cayo Coco Microbialite

Hypersaline Cayo Coco lagoonal network is located on the south side of the island of Cayo Coco on the Atlantic coast of Cuba and consists of partially connected shallow lagoons related to the Caribbean sea through the Perros Bay. Eastern lagoon consists of wide variety of mineralising microbial mats and few microbialites (Bouton *et al.*, 2016; Pace *et al.*, 2018). This lagoon is disconnected from the rest of the network by a 50 m wide bioclastic sands and is 1 km long and 600 m wide with a maximum water depth of 75 cm. The salinity of the lagoon varying seasonably from 54 ‰ to 75 ‰, pH varying from 8 to 9, average temperature is 25.8 °C (Cepero and Lawrence, 2006; Gonzalez-De Zayas and Merino-Ibarra, 2010; Bouton *et al.*, 2020;). This lagoon is characterised by an evaporation range between 2100 and 2200 mm and limited exchange with the ocean (Gonzalez-De Zayas and Merino-Ibarra, 2010).

The sample (M2, 6.8–7.1 cm deep) studied there come from the microbial flat depositional environment from the west transect of the submersed lagoon (Fig. S-2; Bouton *et al.*, 2020). The mineralised microbial mat has been selected from the core CC2 investigated in detail by Bouton *et al.* (2020). The sample consists of microbial mat fragment embedded in a micritic mud containing bioclastic fragments (*i.e.* foraminifera, bivalves and gastropods). The fragment is similar in composition to the mineralising microbial mat observed on the shore. The mat is still composed of several lamina (an upper green indicative of ancient filamentous cyanobacterial communities and below, a brown to black lamina depicting the presence of FeS and resulting from anaerobic heterotrophic metabolism, especially sulfate-reducing bacteria (SRB) with a mm-thick carbonate crust. The presence of relics of mineralising microbial mats preserved in micritic mud is related to fluctuations in the water level over time. The mineralogy of the sample consists of high magnesium calcite, Mg silicate, aragonite, detrital grains, foraminifera tests and sulfides.

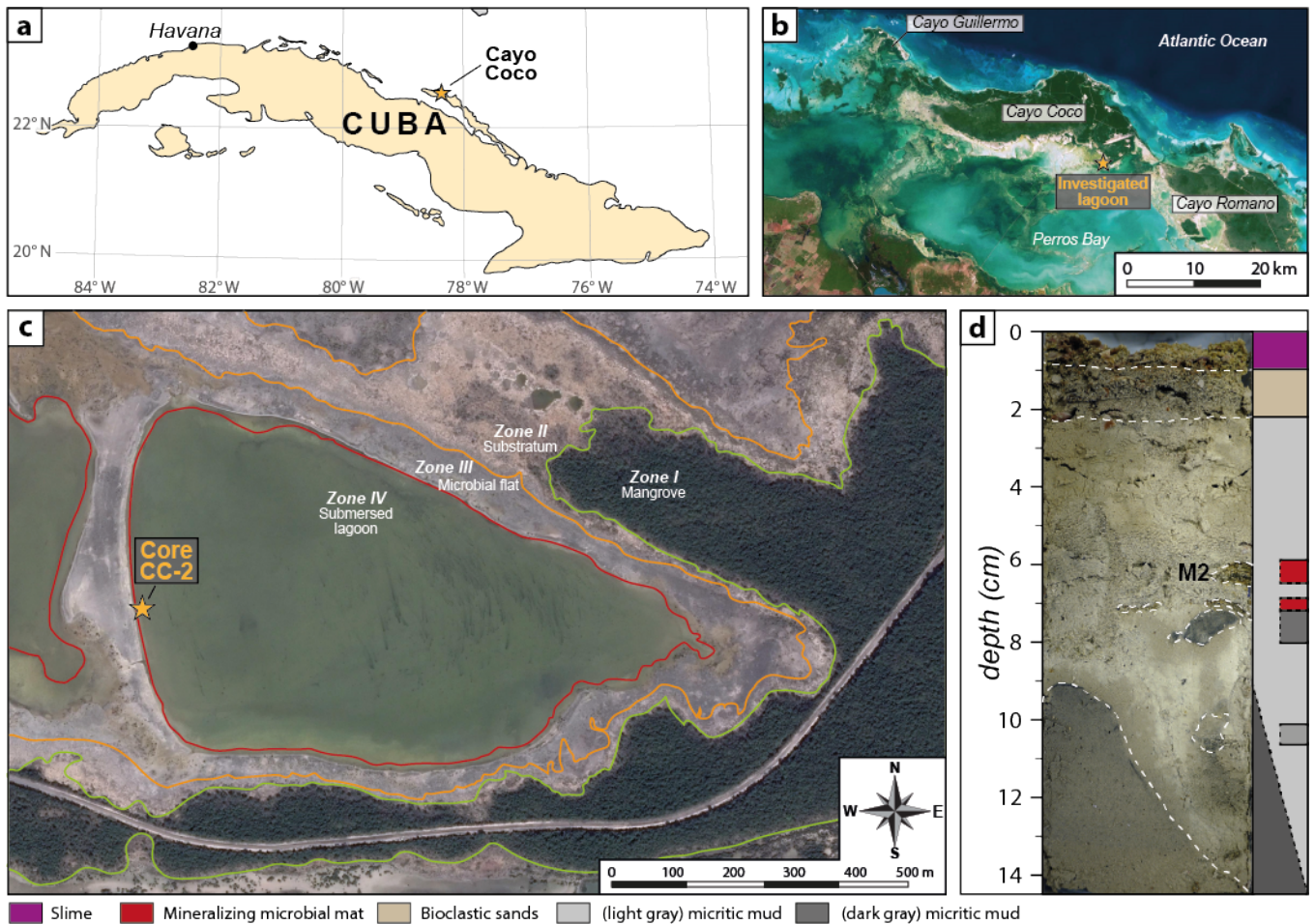


Figure S-2 Sampling location at Cayo Coco Lagoon. **(a)** Cuba map with the location of Cayo Coco Lagoon (star). **(b)** Google image of Cayo Coco Lagoon. **(c)** View of the investigated lagoon with the various zones and the location of the sample, Core CC-2. **(d)** Close view of the sample with the associated mineralogy, the two mineralising microbial mats are in red. The sample investigated here is sample M2.

Despite of the presence of calcium/magnesium carbonate in the microbial mats, they do display a high organic matter content. Different sources of organic matter (microbial mats, mangrove, soils and suspended particulate matter) were found throughout all of the depositional environment in Cayo Coco lagoon and their composition is fully described in Bouton *et al.* (2020). Sample M2 includes microbial biomass, as well as extracellular organic matter (EOM) forming an organic matrix. It is characterised by TOC (wt. %) between 0.87 ± 0.01 and 2.21 ± 0.01 depending on the studied fractions (0–200 μm and 200–2000 μm , respectively). The main contributor to the organic matter preserved within the sediment of the lagoons seem to be the slime (mostly composed of EOM) recognised in the permanently submersed zone. Nevertheless, the studied sample records $\delta^{13}\text{C}_{\text{org}} = -16.44$ to -15.53 ‰ (relative to VPDB), values comparable to the ones record in the mineralising microbial mats observed at surface all around the lagoonal networks (Bouton *et al.* 2020).

Molecular diversity studies of microbialites from Atexcac and Cayo Coco have highlighted the presence of diverse operational taxonomic units suggestive of sulfate reducing, sulfur oxidising, oxygenic and anoxygenic photosynthesising microorganisms (Pace *et al.*, 2018; Iniesto *et al.*, 2021). The floro-faunal content of these samples is both marine and continentally influenced, with foraminifera fragments, diatoms and few gastropods in Cayo Coco and predominantly diatoms in Atexcac.

Methods

SEM and TEM Analyses

Scanning Electron Microscopy (SEM) and Energy Dispersive X-ray Spectrometry (EDS) were used to characterise the microstructure and chemistry of pyrite and its inside inclusions for subsequent *in situ* extraction using focused ion beam milling (FIB). SEM observations were performed on a TESCAN VEGAII LSU at IMPMC with 15 kV accelerating voltage and a working distance of 15.4 mm according to the geometrical conditions required for EDS analyses on this microscope. SEM images were collected with both secondary (SE) and backscattered electrons (BSE) detectors. FIB ultrathin sections were extracted from different pyrite grains using an FEI Strata DB 235 at IEMN (Lille) This extraction procedure maintains textural integrity, and prevents shrinkage and deformation of microscale to nanoscale pores, even in the case of highly sensitive materials (Bassim *et al.*, 2014).

Transmission Electron Microscopy (TEM) analyses were performed on FIB sections to characterise crystallographic orientation and textures of the pyrites (Fig. S-3). TEM observations were performed with a JEOL 2100F Field Emission Gun (FEG) microscope (IMPMC, Paris, France) operating at 200 kV. Scanning Transmission Electron Microscopy (STEM) Z-contrast imaging was performed using the high-angle annular dark field (HAADF) mode. Selected-area diffraction (SAED) patterns were obtained on areas of interest (Fig. S-4).

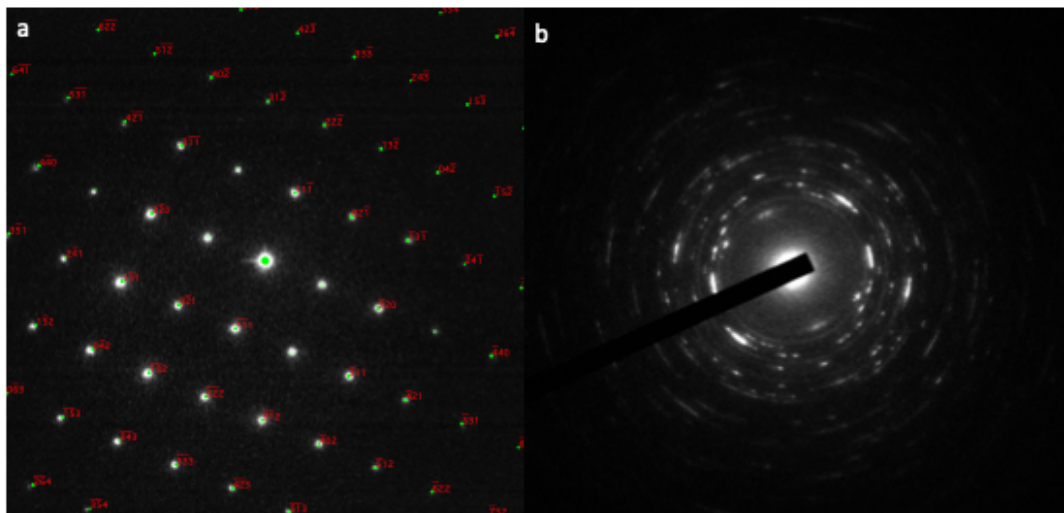
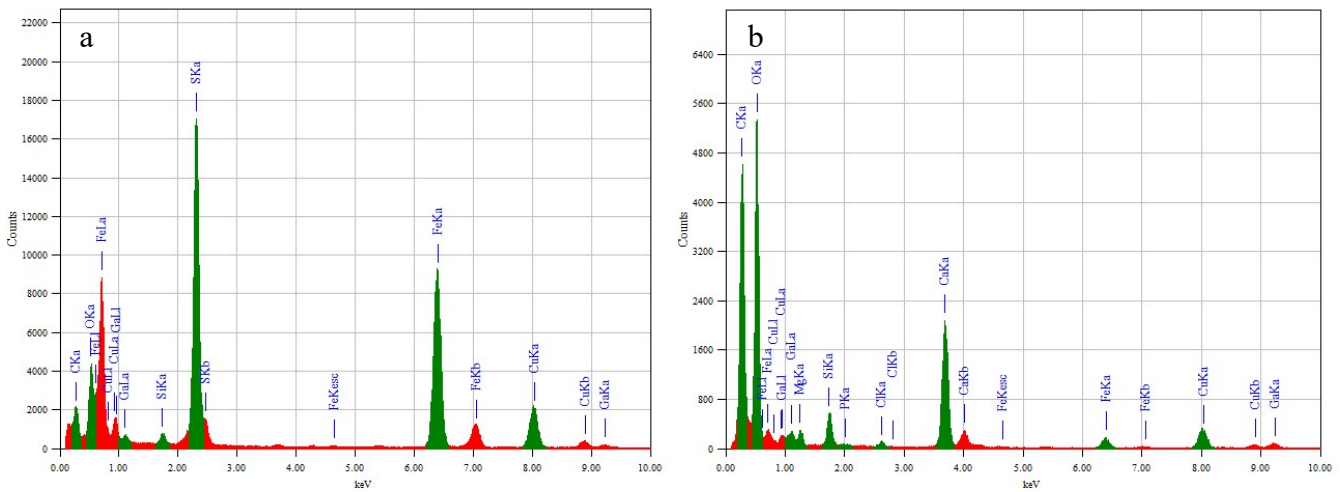


Figure S-3 (a) Indexed diffraction pattern of framboid pyrite from Cayo Coco. The diffraction pattern was indexed as pyrite seen along the $[112]$ zone axis. Based on the extinction rule of the space group of pyrite ($Pa-3$), $(1-10)$, $(3-30)$, $(20-1)$ are predicted to be extinct but can be detected because the grain was relatively thick and experienced double diffraction. (b) Selected area electron diffraction patterns of micropyrrite from Atexcac. The diffraction pattern is typical of polycrystalline nature of the micropyrrite. Different d spacings were measured and could be indexed as pyrite lattice planes as shown in Table S-1. The two rows of diffraction spots are at 90°C with d spacings at ~ 3.12 and 3.82 Å, indexed as $(11-1)$ and $(1-10)$, respectively.

Table S-1 Pyrite d spacing (\AA) and corresponding lattice planes.

d spacing (\AA)	Interpreted pyrite lattice plane
3.13	(111)
2.71	(002)
2.45	(021)
2.24	(112)
1.93	(022)
1.65	(113)
1.52	(023)
1.47	(123)
1.35	(004)

**Figure S-4** STEM EDX analyses of sample from Cayo Coco. (a) EDX spectra indicate the presence of pyrites and (b) EDX spectra show the presence of the surrounding carbonate.

Raman Spectroscopy

Raman spectroscopy was used to identify the carbonates (Fig. S-5). Raman data were collected using a Horiba Jobin Yvon LabRAM 800 HR spectrometer (UNIL, Lausanne, Switzerland) in a confocal configuration, equipped with an Ar⁺ laser (532 nm) excitation source and an electron multiplying charge-coupled device (EMCCD). Measurements were performed at constant room temperature, directly on the sample surface, by focusing the laser beam with a 200 μm confocal hole using a long working distance 50 \times objective (NA = 0.70). This configuration provided a ~ 2 μm spot size for a laser power delivered at the sample surface below 1 mW. Light was dispersed using a 1800 gr/mm diffraction grating.

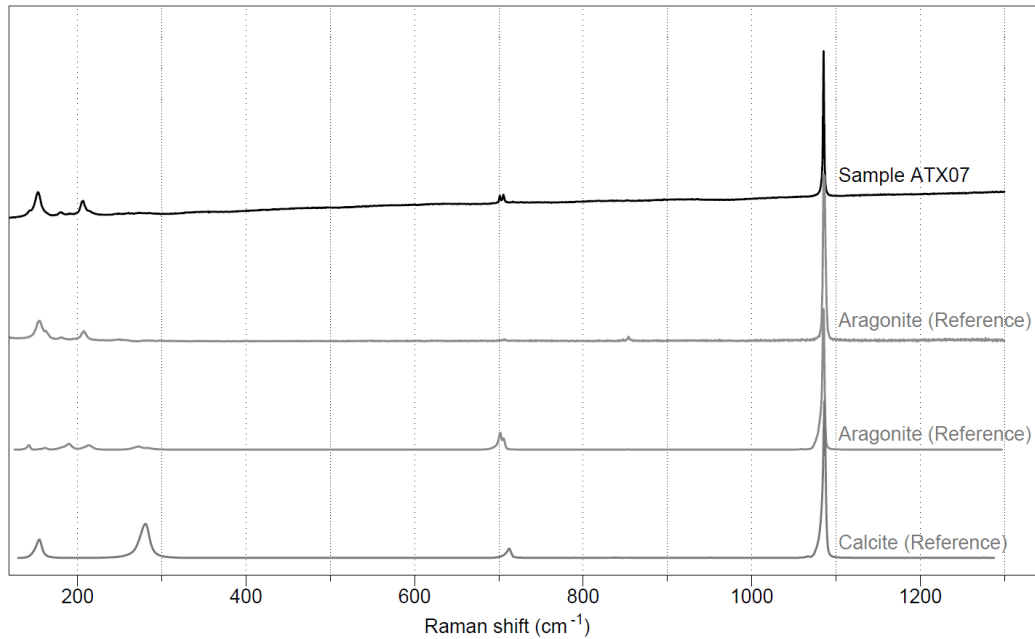


Figure S-5 Representative Raman spectrum of carbonates in sample ATX07 (Atexcac) compared with two reference spectra of aragonite with different crystal orientations and calcite. Reference data are from the RRUFF database.

Sulfur Isotope Analyses of Sulfate and Sulfide

Sulfates

Lake Atexcac sulfate sulfur isotope composition has been measured using water samples collected at various depths across the chemocline of the lake in May 2019 (Table S-2). Water samples were filtered at 0.2 μm . Dissolved sulfates were extracted after addition of a concentrated and acidic (1 M and $\text{pH} \approx 2$) barium chloride salt solution to the samples and precipitation as barium sulfate (barite). Samples were acidified to a pH between 2 and 3 and reacted with the $\text{BaCl}_2 \cdot \text{H}_2\text{O}$ solution for an hour at about 75 $^\circ\text{C}$ while being regularly agitated. Barite extracts were rinsed several times with deionised water, centrifuged and dried overnight at 50 $^\circ\text{C}$ in an oven. Sulfate recovery rates for all the samples were around 90 %, mostly due to loss of matter during scraping of BaSO_4 from the glass tubes. Purity of the precipitates was also assessed through their concentration in S that were very close to that of pure international barite standard (NBS 127).

Table S-2 Sulfate concentrations and isotope compositions of Lake Atexcac at 10 and 16 m depth.

Sample	$\delta^{34}\text{S}$		$\delta^{34}\text{S}_{\text{avg}}$ (‰)	1 σ	$[\text{SO}_4^{2-}]$ mM
ATX-10 m	0.50	0.52	0.51	0.02	2.53
ATX-16 m	0.66	0.53	0.59	0.02	2.48

Sulfate from Cayo Coco lagoon waters was not directly analysed but its isotopic composition is considered to be similar to the canonical oceanic sulfate $\delta^{34}\text{S}$, *i.e.* around +21 ‰, since the lagoon is open and connected to the ocean at the locality of sampling (Babel and Schreiber, 2004). Average water composition is given in Table S-3. Water samples were analysed in the field for conductivity, pH, temperature and alkalinity. Conductivity was determined with a WTW Cond 3110 and a TetraCon 325 probe. pH was measured using a WTW pH 3110 with a Sentix 41 electrode or a Consort C561 pH-meter with a BioBlock Scientific electrode. The total alkalinity was assessed in the field using the Gran method. The alkalinity samples were filtered using 0.22- μm polyethersulfone syringe filter. Water samples were stored

in glass vials (4-ml vials either under in situ pH conditions or acidified for analysis of major ions and 10-mL vials to determine the organic composition), kept refrigerated and transported to the laboratory. Major cation (NH_4^+ , Na^+ , K^+ , Mg^{2+} , Ca^{2+}) and anion (Cl^- , SO_4^{2-} , NO_3^- and PO_4^{3-}) concentrations were determined by ion chromatography (Dionex DX-100 or ICS-1500, with an analytical precision of 0.2 mg/L) and dissolved organic carbon (DOC) content using a Shimadzu TOC-5000A analyser. Salinity values were calculated from conductivity and temperature values, according to the Aminot and Kerouel method (Aminot and K  rouel, 2004).

Table S-3 Average water composition of Cayo Coco Lagoon.

	Conductivity (mS/cm)	pH	T (��C)	Alkalinity (mg/L) <i>in situ</i>	Na ⁺ (mg/L)	Mg ²⁺ (mg/L)	K ⁺ (mg/L)	Ca ²⁺ (mg/L)	Cl ⁻ (mg/L)	SO ₄ ²⁻ (mg/L)
July 2014 (Average)	95.25	8.9	33	132.9	23	2,341	934	801.00	41,657	6,039

Sulfides

A two-step extraction scheme was applied to retrieve both acid-volatile sulfide (AVS, mostly FeS) and chromium-reducible sulfide (CRS, mostly FeS₂) from microbialites samples following Gr  ger *et al.* (2009). In short, agitated powdered samples diluted in ethanol reacted with cold 12M HCl for 2 h in order to liberate AVS. If any, resulting hydrogen sulfide was precipitated as Ag₂S in a 0.3 M AgNO₃ solution. Then, a 1 M CrCl₂ solution (Canfield *et al.*, 1986; Gr  ger *et al.*, 2009) was added and reacted for another 2 h to liberate CRS, which in turn resulted in the precipitation of hydrogen sulfide as Ag₂S. After centrifugation, silver sulfide precipitates were rinsed several times with deionised water and dried at 50   C for 48 h in an oven.

Isotopic measurements

Both sulfides and sulfates $\delta^{34}\text{S}$ measurements were performed at the Biog  osciences Laboratory of the Universit   de Bourgogne in Dijon, France. They were analysed on SO₂ molecules via combustion of 250–500   g of Ag₂S and BaSO₄, mixed with tungsten trioxide powder in equal amount to optimise sulfur oxidation during combustion, using a Vario PYRO cube (Elementar GmbH) connected online via an open split device to an IsoPrime IRMS system. International standards (IAEA-S1/-S2/-S3 and -NBS 127 for Ag₂S and BaSO₄, respectively) were used for calibration. Results are reported in delta notation against the Vienna Canyon Diablo Troilite standard (VCDT). All measurements were duplicated. Standard and BaSO₄ samples reproducibility is better than ± 0.1 ‰ (1  ).

Waters from the surface to the chemocline in Atexcac (~20–25 m depth) show relatively homogeneous $\delta^{34}\text{S}$, around 0.6 ± 0.1 ‰ ($n = 2$). Bulk solid sulfide $\delta^{34}\text{S}$ of the Atexcac microbialite has a mean value of -28.73 ± 0.3 ‰ ($n = 2$), consisting almost exclusively of CRS.

Sulfur Isotope Analyses by NanoSIMS

Samples embedded in epoxy were polished down to 0.25 mm and gold coated. The data we report in this study were collected during three different analytical sessions, in May 2017 at IMPMC, November 2018 and October 2019 at EPFL, using the same methodology. Secondary ions of ¹²C¹⁴N⁻, ³²S⁻ and ³⁴S⁻ were simultaneously measured in multicollection mode using electron multipliers (EM) with a dead time of 44 ns. The mass resolving power was set to 18,000 (Cameca definition) to resolve potential interferences on masses 32 and 34. To avoid the build-up of positive charges over the sample's surface, an electron flood gun was used. Each analysis was preceded by a 15 min pre-sputtering phase using a 0.5 nA primary Cs⁺ beam scanned over an area slightly larger than the area of interest (25 × 25   m) to locally remove the gold coating and surface contamination, and to reach steady state sputtering regime. 20 × 20   m images of the areas of interest were collected using a 0.8 pA Cs⁺ primary beam with a 120 nm probe size, using a 256 × 256 pixels resolution, a dwell time of 1 ms/pixel and 60 cycles were stacked to get decent counting statistic.



As already described in Marin-Carbonne *et al.* (2018), S isotope analysis in sulfides is known to be biased by quasi simultaneous arrival (QSA) effect on the EM (Slodzian *et al.*, 2004). The correction of this effect was achieved by applying the method described by Nishizawa *et al.* (2010). Using different aperture slits to produce variations of the secondary ion signal over primary current ratio on the standard, we determined a QSA correcting factor of 0.54 and 0.66 for $^{34}\text{S}/^{32}\text{S}$ ratio for each sessions consistent with the value of 0.69 previously published (Slodzian *et al.*, 2004; Bontognali *et al.*, 2012; Marin-Carbonne *et al.*, 2018).

Two different pyrite standards (Maine, $\delta^{34}\text{S} = -20.62 \pm 0.01$ ‰, and CAR 123, $\delta^{34}\text{S} = +1.5 \pm 0.01$ ‰) were analysed in order to determine QSA correcting factors and instrumental mass fractionation (see Table S-4 for two sessions). Standards were analysed at the beginning and end of the sessions and every day for assessing the stability of the instruments.

NanoSIMS images were processed by LIMAGE© software from Larry Nittler (Carnegie Institution, Washington, DC). After applying regular deadtime correction (44 ns), the different frames (one frame per cycle) were aligned and region of interest (ROIs) corresponding to each framboidal pyrite were defined using the particle definition mode. The size of ROIs ranges from 1 to 270 μm^2 . Total counts were then extracted and QSA and IMF corrections were applied in Table S-5. $\delta^{34}\text{S}$ values *versus* Vienna Canyon Diablo Troilite (V-CDT) were calculated for each framboidal pyrite.

Table S-4 Measured $^{34}/^{32}\text{S}$ ratios and $\delta^{34}\text{S}$ values corrected from QSA effect in two different sessions for the Maine and UCLA pyrite standards. Instrumental mass fractionation was 1.024 in the first session and 1.0159 in the second.

Standards	$\delta^{34}\text{S}$ true (‰)	$^{34}\text{S}/^{32}\text{S}$ true	$^{34}\text{S}/^{32}\text{S}$ measured	1 σ	$\delta^{34}\text{S}$ corr QSA (‰)
<i>Session 1</i>					
UCLA	1.5	0.04423001	0.045594	1.47E-04	32.4
MAINE	-20.1	0.04327607	0.044599	7.24799E-05	9.9
<i>Session 2</i>					
UCLA	1.5	0.04423001	0.045219	6.25133E-05	23.9
MAINE	-20.1	0.04327607	0.044263	1.14E-04	2.2

Table S-5 Sulfur isotope compositions of framboidal and micropyrates.

Table S-5 is available for download (Excel) from the online version of the article at <https://doi.org/10.7185/geochemlet.2209>.

The studied framboidal pyrites consist of between 240 and 498 different pyrite grains. For four framboidal pyrites, we defined ROIs for each individual grain inside the framboidal pyrite and extracted the total counts and calculated the isotope ratios. Some of them were quite small with low total counts, therefore the associated error, influenced by counting statistics, is large. S isotope compositions are compared to framboid size or micropyrates grain size in Figures S-6 and S-7, respectively, and to C/N count rates in Figure S-8.

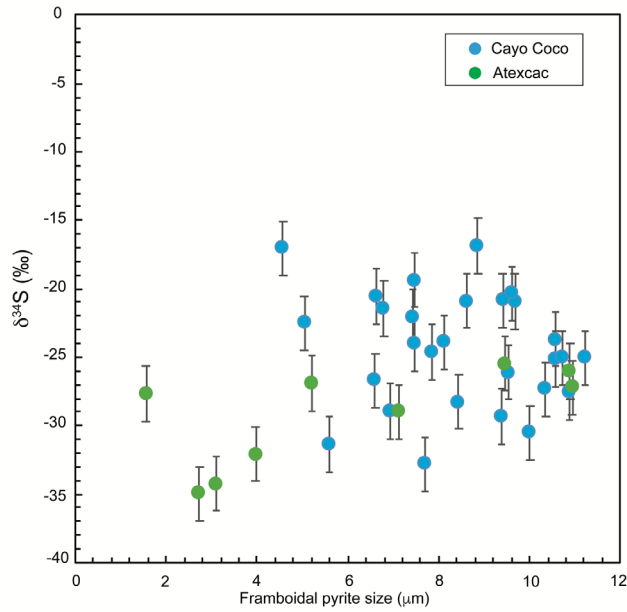


Figure S-6 Sulfur isotope composition and framboid size for Cayo Coco and Atexcac pyrites.

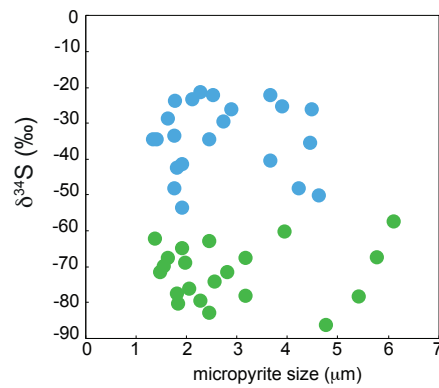


Figure S-7 $\delta^{34}\text{S}$ values *versus* size for micropyrite in Cayo Coco (blue) and Atexcac (green). Error bars on the $\delta^{34}\text{S}$ values are within the symbol size.

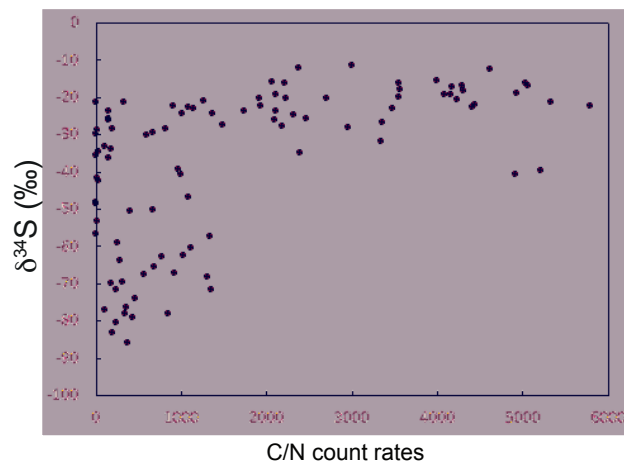


Figure S-8 $\delta^{34}\text{S}$ values *versus* C/N ratio count rates. The error bars on the $\delta^{34}\text{S}$ values are within the symbol size.

Framboidal Pyrites

Framboids are only found in surface unconsolidated sediment or enclosed within foraminifera tests. By contrast, micropyrite grains are either disseminated or aligned within microbialite laminae, in close association with aragonite and Mg-rich silicate phases (Fig. 1). Framboidal pyrites aggregate a mixture of euhedral, rounded and pyramidal pyrite grains (Fig. 1a–b), while micropyrites are predominantly euhedral (Fig. 1c–d). Transmission electron microscopy analyses show that micropyrites are composed of nanocrystals with various orientations, while framboidal pyrites are composed of micrometric pyrite crystals (Fig. 2). Framboidal pyrites are surrounded by a layer of iron oxide (Fig. 2), suggesting late oxidation (Maclean *et al.*, 2008). Micropyrites are surrounded by external layers of Fe-Mg silicate (Atexcac) or amorphous silica (Cayo Coco, Fig. 2), suggesting fluid induced reaction between pyrite and Mg authigenic silicates during or after biomineralisation and/or lithification. Previous investigations have shown that the hydrated Mg-silicate rich phase, identified as kerolite in Atexcac, is tightly linked to an early mineralisation step of microbialites (Zeyen *et al.*, 2015; Bouton *et al.*, 2016; Pace *et al.*, 2018). We suggest that the presence of the Mg-silicate rich phase associated with sulfide provide evidences for an early syngenetic origin of the micropyrite grains.

Framboidal pyrites display homogeneous sizes in both samples (Fig. S-9), consistent with a synsedimentary origin (Maclean *et al.*, 2008).

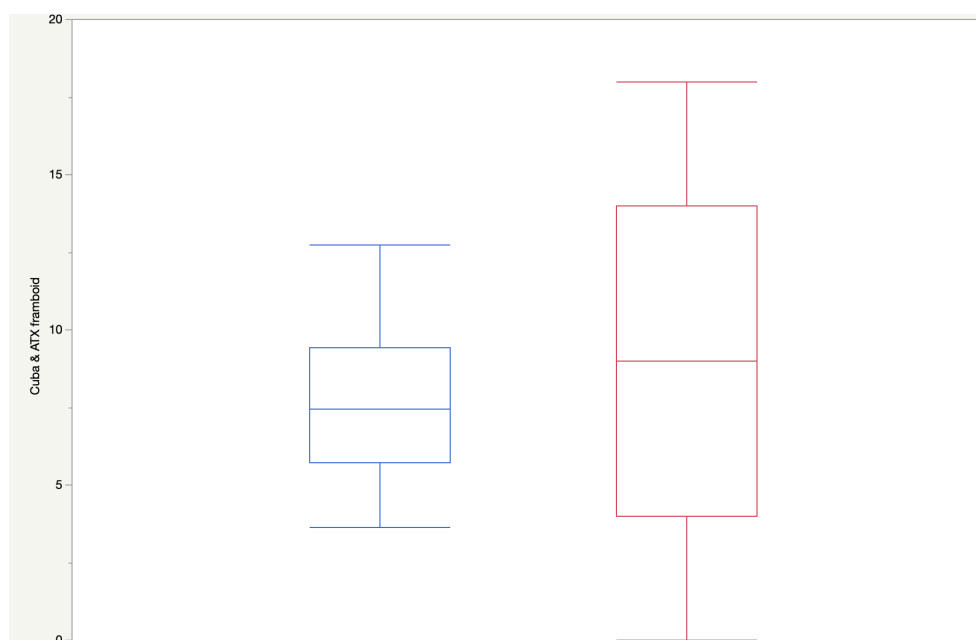


Figure S-9 Size distribution (in μm) of framboidal pyrite from Cayo Coco (blue) and Atexcac (red). The average sizes are $7.6 \pm 2.9 \mu\text{m}$ and $7.4 \pm 4.8 \mu\text{m}$ for Cayo Coco and Atexcac, respectively.

In detail, however, the number of crystallites inside each framboidal strongly varies (between 40 to more than 300) and exceeds previous reports giving an upper limit of 100 for framboidal crystallites precipitating within microbial mats (Popa *et al.*, 2004). Framboidal pyrite size has been used to infer the oxygenation state of their depositional environment, where pyrites precipitating in sediments overlain by an oxic water column display larger sizes ($>10 \mu\text{m}$) than the ones precipitated under euxinic conditions (Wilkin *et al.*, 1996). The small ($<10 \mu\text{m}$) and homogeneous size of framboidal pyrites reported here challenges the locus-size hypothesis since both samples have been formed in fully oxygenated aqueous solutions (Fig. S-10).

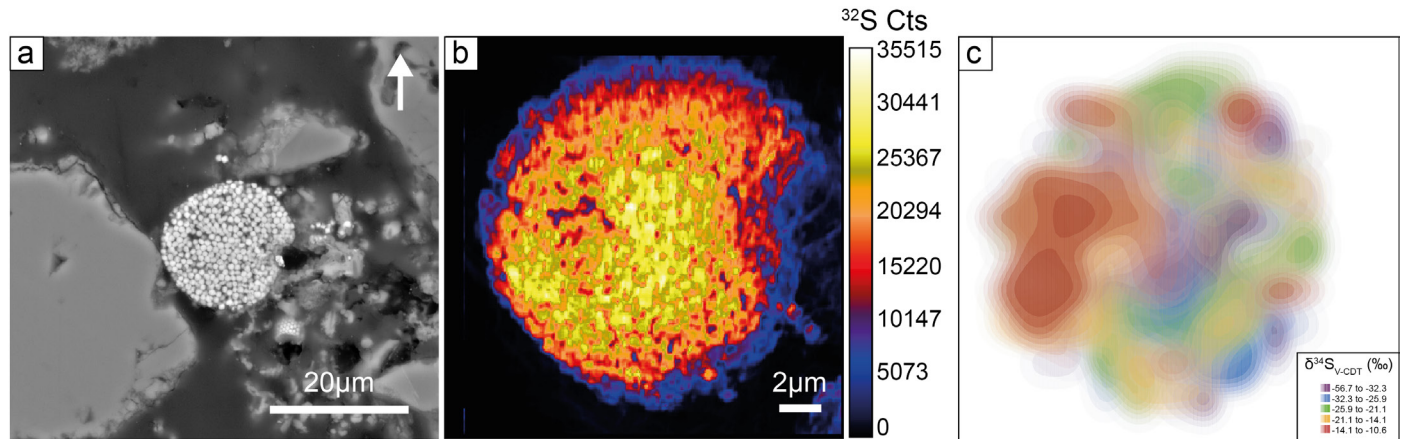


Figure S-10 SEM and NanoSIMS count rate images of framboidal pyrite from Atexcac showing heterogeneous $\delta^{34}\text{S}$ distribution. The top of the mat is indicated by the arrow. In this case, the gradient is not very visible.

Supplementary Information References

- Aminot, A., K erouel, R. (2004) Dissolved organic carbon, nitrogen and phosphorus in the NE Atlantic and the NW Mediterranean with particular reference to non-refractory fractions and degradation. *Deep Sea Research Part I: Oceanographic Research Papers* 51, 1975–1999. <https://doi.org/10.1016/j.dsr.2004.07.016>
- Bassim, N., Scott, K., Giannuzzi, L.A. (2014) Recent advances in focused ion beam technology and applications. *MRS Bulletin* 39, 317–325. <https://doi.org/10.1557/mrs.2014.52>
- Bontognali, T.R.R., Sessions, A.L., Allwood, A.C., Fischer, W.W., Grotzinger, J.P., Summons, R.E., Eiler, J.M. (2012) Sulfur isotopes of organic matter preserved in 3.45-billion-year-old stromatolites reveal microbial metabolism. *Proceedings of the National Academy of Sciences* 109, 15146–15151. <https://doi.org/10.1073/pnas.1207491109>
- Bouton, A., Vennin, E., Pace, A., Bourillot, R., Dupraz, C., Thomazo, C., Brayard, A., D esaubliaux, G., Visscher, P.T. (2016) External controls on the distribution, fabrics and mineralization of modern microbial mats in a coastal hypersaline lagoon, Cayo Coco (Cuba). *Sedimentology* 63, 972–1016. <https://doi.org/10.1111/sed.12246>
- Bouton, A., Vennin, E., Thomazo, C., Mathieu, O., Garcia, F., Jaubert, M., Visscher, P. (2020) Microbial Origin of the Organic Matter Preserved in the Cayo Coco Lagoonal Network, Cuba. *Minerals* 10, 143. <https://doi.org/10.3390/min10020143>
- Canfield, D.E., Raiswell, R., Westrich, J.T., Reaves, C.M., Berner, R.A. (1986) The use of chromium reduction in the analysis of reduced inorganic sulfur in sediments and shales. *Chemical Geology* 54, 149–155. [https://doi.org/10.1016/0009-2541\(86\)90078-1](https://doi.org/10.1016/0009-2541(86)90078-1)
- Cepero, E., Lawrence, A. (2006) Before and After the Cayo Coco Causeway, Cuba: A Critical View From Space. *Cuba in Transition* 16, 212–220.
- Ferrari, L., Orozco-Esquivel, T., Manea, V., Manea, M. (2012) The dynamic history of the Trans-Mexican Volcanic Belt and the Mexico subduction zone. *Tectonophysics* 522–523, 122–149. <https://doi.org/10.1016/j.tecto.2011.09.018>
- Gonzalez-De Zayas, R., Merino-Ibarra, M. (2010) Water, salt and nutrients budgets in Larga Lagoon, Cayo Coco, Cuba. *Land–Ocean Interactions in the Coastal Zone (LOICZ)*, 12 p, 12 p. <https://doi.org/10.13140/RG.2.1.1589.4569>
- Gr oger, J., Franke, J., Hamer, K., Schulz, H.D. (2009) Quantitative recovery of elemental sulfur and improved selectivity in a chromium-reducible sulfur distillation. *Geostandards and Geoanalytical Research* 33, 17–27. <https://doi.org/10.1111/j.1751-908X.2009.00922.x>
- Iniesto, M., Moreira, D., Reboul, G., Deschamps, P., Benzerara, K., Bertolino, P., Sagh ai, A., Tavera, R., L opez-Garc a, P. (2021) Core microbial communities of lacustrine microbialites sampled along an alkalinity gradient. *Environmental Microbiology* 23, 51–68. <https://doi.org/10.1111/1462-2920.15252>
- MacLean, L.C.W., Tyliszczak, T., Gilbert, P.U.P.A., Zhou, D., Pray, T.J., Onstott, T.C., Southam, G. (2008) A high-resolution chemical and structural study of framboidal pyrite formed within a low-temperature bacterial biofilm. *Geobiology* 6, 471–480. <https://doi.org/10.1111/j.1472-4669.2008.00174.x>
- Marin-Carbonne, J., Remusat, L., Sforza, M.C., Thomazo, C., Cartigny, P., Philippot, P. (2018) Sulfur isotope’s signal of nanopyrates enclosed in 2.7 Ga stromatolitic organic remains reveal microbial sulfate reduction. *Geobiology* 16, 121–138. <https://doi.org/10.1111/gbi.12275>
- Nishizawa, M., Maruyama, S., Urabe, T., Takahata, N., Sano, Y., (2010) Micro-scale (1.5 μm) sulphur isotope analysis of contemporary and early Archean pyrite. *Rapid Communications in Mass Spectrometry* 24, 1397–1404. <https://doi.org/10.1002/rcm.4517>

- Pace, A., Bourillot, R., Bouton, A., Vennin, E., Braissant, O., Dupraz, C., Duteil, T., Bundeleva, I., Patrier, P., Galaup, S., Yokoyama, Y., Franceschi, M., Virgone, A., Visscher, P.T. (2018) Formation of stromatolite lamina at the interface of oxygenic-anoxygenic photosynthesis. *Geobiology* 16, 378–398. <https://doi.org/10.1111/gbi.12281>
- Popa, R., Kinkle, B.K., Badescu, A. (2004) Pyrite framboids as biomarkers for iron-sulfur systems. *Geomicrobiology Journal* 21, 193–206. <https://doi.org/10.1080/01490450490275497>
- Sigala, I., Caballero, M., Correa-Metrio, A., Lozano-García, S., Vázquez, G., Pérez, L., Zawisza, E. (2017) Basic limnology of 30 continental waterbodies of the Transmexican Volcanic Belt across climatic and environmental gradients. *Boletín de la Sociedad Geológica Mexicana* 69, 313–370. <https://doi.org/10.18268/BSGM2017v69n2a3>
- Slodzian, G., Hillion, F., Stadermann, F.J., Zinner, E. (2004) QSA influences on isotopic ratio measurements. *Applied Surface Science* 231–232, 874–877. <https://doi.org/10.1016/j.apsusc.2004.03.155>
- Wilkin, R.T., Barnes, H.L., Brantley, S.L. (1996) The size distribution of framboidal pyrite in modern sediments: An indicator of redox conditions. *Geochimica et Cosmochimica Acta* 60, 3897–3912. [https://doi.org/10.1016/0016-7037\(96\)00209-8](https://doi.org/10.1016/0016-7037(96)00209-8)
- Zeyen, N., Benzerara, K., Li, J., Groleau, A., Balan, E., Robert, J.-L., Estève, I., Tavera, R., Moreira, D., López-García, P. (2015) Formation of low-T hydrated silicates in modern microbialites from Mexico and implications for microbial fossilization. *Frontiers in Earth Science* 3, 64. <https://doi.org/10.3389/feart.2015.00064>
- Zeyen, N., Benzerara, K., Beyssac, O., Daval, D., Muller, E., Thomazo, C., Tavera, R., López-García, P., Moreira, D., Duprat, E. (2021) Integrative analysis of the mineralogical and chemical composition of modern microbialites from ten Mexican lakes: What do we learn about their formation? *Geochimica et Cosmochimica Acta* 305, 148–184. <https://doi.org/10.1016/j.gca.2021.04.030>

2. Fe isotope biosignatures revealed in modern pyrite framboids

2.1. Interest of investigating framboids

Among two pyrite morphologies identified in the previous section **Chap 3.1**, only framboid pyrite grains were successfully measured. Due to the analytical precision, the euhedral pyrite grains were too small to offer a stable signal during the time of the analysis (~7 minutes). As discussed in **chapter 1**, pyrite framboids (**Fig. 3.1**) are extensively studied to reconstruct paleoredox conditions. In particular, framboid size distribution is used to constrain the locus of pyrite precipitation, either in an euxinic water column or in the sediment porewaters (*Wilkin et al., 1996; Wilkin and Barnes, 1996*).

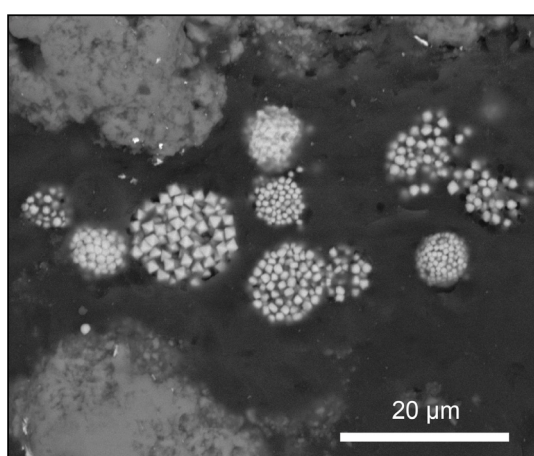


Figure 3.1: BSE image of framboid pyrite. Framboid pyrite of size ranging from 4 to 12 μm observed in a modern microbialite from Cuba (this study).

However, the analysis of framboid size proposed by *Wilkin and Barnes (1996)* relies on framboids from sediments, not from the water column itself. More recently, *Rickard (2019a)* reviewed the diameter of thousands of framboids from 104 sediment and sedimentary rock locations. This study shows that modern syngenetic and diagenetic grains yield a mean diameter of 4.7 μm and 6.7 μm respectively whereas the mean size ranges significantly overlap (2.9 to 10.9 μm for syngenetic and 3.1 to 20.9 μm for diagenetic grains). However, many counter examples warned about the extensive use of framboid size for reconstructing paleoredox conditions of the water column (*de Koff et al., 2008; Blood et al., 2015; Sun et al., 2015; Kershaw et al., 2018*). Nevertheless, this debate highlights that the formation of framboids in natural sediments is not fully understood, especially since experiments highlighted the role of oxidized species (i.e. Fe(III)-oxides, phosphates) in the acceleration of pyrite formation in microbial cultures (*Rickard, 1969; Duverger et al., 2020*). Framboids can form at ambient temperature in sedimentary environments (*Wilkin and Barnes, 1997*) through two processes: pyrite nucleation and crystal growth (*Rickard, 2019b*). Pyrite framboids form rapidly, within days or weeks, from initial monosulfide (mackinawite Fe_xS or greigite Fe_3S_4) in a supersaturated solution with respect to pyrite and precursors (*Wilkin and Barnes, 1996; Rickard and Luther, 1997*). The close association between framboid and organic matter have been interpreted as potential relic of biofilm (*Wacey*

et al., 2015), suggesting a microbial control on pyrite precipitation (*Butler and Rickard, 2000; Folk, 2005; Liu et al., 2022*). Pioneer studies even hypothesized that framboids may represent remains of microfossils (*Love, 1957; Schneiderhöhn, 1923*). On the contrary, lab experiments reproducing framboid textures at high-temperatures (similar to hydrothermal or metamorphic systems) argue for an abiotic origin via thermogenic sulfate reduction (TSR; *Scott et al., 2009*). Early diagenetic microbially-derived framboids are also frequently observed in ore deposits, bearing primary S isotope compositions despite late fluid circulations (*Large et al., 2007; Hou et al., 2016*). The formation and evolution of framboids is increasingly being documented, especially using spatially resolved techniques. For example, a recent study used NanoSIMS to explore the S isotope variability of framboids associated with gold mineralization (*Zhao et al., 2018*). This study revealed highly ^{34}S -depleted isotope signatures typical for MSR. Different pyrite generations have been interpreted as deriving from initially MSR-produced framboids which experienced fluid circulation and recrystallization to form progressively euhedral grains (*Zhao et al., 2018*). However, fluid can also transport sulfide derived from TSR and, in this case, the primary S isotope signatures are entirely reset (*Yue et al., 2020*). This illustrates the importance of differentiating the various processes leading to the preservation of pyrite in marine sediments and sedimentary rocks (e.g. water column precipitation, sedimentary early diagenesis, and/or late fluid circulation), all of which challenges the consensual view of framboid as a mirror of seawater conditions.

2.2. Sample description

The first sample studied M2 6.8-7.1 is from the CC2 drill core collected in the western part of the Cayo Coco lagoon in Cuba (**Fig. 3.2a and 3.2b**). The CC2 core was drilled at the boundary between microbial flat and submersed lagoon zones (**Fig. 3.2b**). Mineralogy, organic carbon content (TOC), carbon and nitrogen isotope signatures of this core were studied and detailed by *Bouton et al. (2020)*. The core can be divided into three parts. The upper part (first 0.8 cm) is composed of non-mineralized slime including micrite and bioclasts. The layer below (0.8 to 2.4 cm) consists of fragmented bioclast-rich micritic mud. The rest of the core is composed of micritic mud including two levels of discontinuous mineralized microbial mats (**Fig. 3.2c**). Interval 6.8-7.1cm, corresponding to a mineralized microbial mat, is composed of green and yellow to brown laminae, indicating ancient activity of filamentous cyanobacterial and anaerobic heterotroph communities, such as sulfate-reducers. Sample M2 6.8-7.1 was collected in this mineralized microbial mat interval, which has similar composition and laminated structure as the living microbial mat on the shore of the lagoon (*Bouton et al., 2020*). This sample displays TOC contents between 0.87 and 2.21 wt.%, $\delta^{15}\text{N}$ values between +4.17 and +5.15‰ and $\delta^{13}\text{C}_{\text{org}}$ values between -16.44 and -15.53‰, the latter being relatively constant within and between cores, and also matching with $\delta^{13}\text{C}_{\text{org}}$ value of microbial slime. Consequently, microbial slimes are identified as the major source of organic matter through the lagoon.

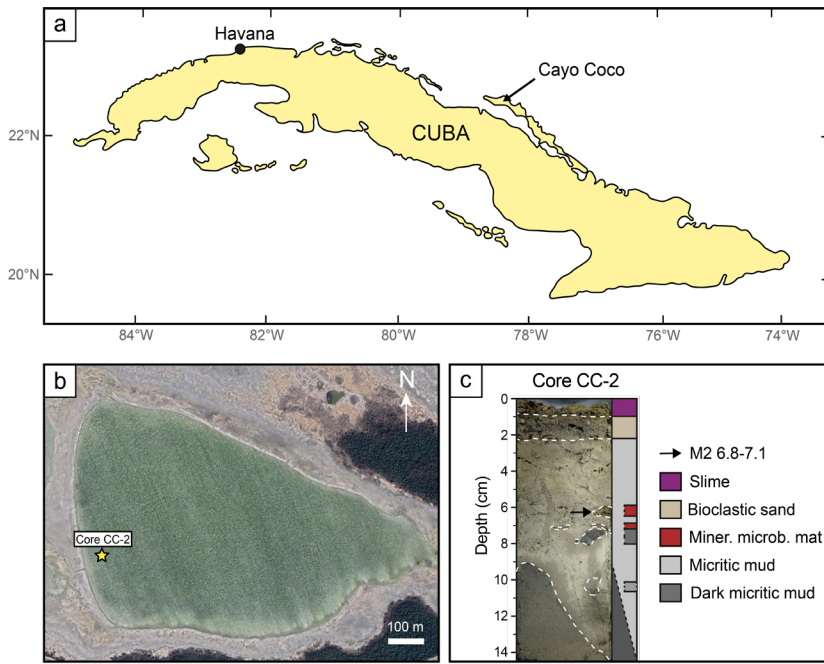


Figure 3.2: Location of the microbialite sample M2 6.8-7.1. a) Map of Cuba island with the location of Cayo Coco lagoon. Modified after Pardo (2009). b) Global view of the lagoon with the position of the CC-2 core and c) vertical section of the core with the position of the studied sample M2 6.8-7.1 (black arrow), modified after Bouton et al. (2020).

The second sample studied, ATX-2012-08, was collected in the hypersaline Atexcac lake (Mexico; **Figs. 3.3a and 3.3b**). The sample is a piece of an active microbialite, i.e. covered by a living mat, and was collected in January 2012 (**Fig. 3.3c**) on the southwestern shore of the lake, at ~0.1 m below the lake water level (Zeyen et al., 2015). Detailed petrographic characterization of this sample revealed the presence of aragonite, hydromagnesite and poorly crystalline hydrated silicate phases (Zeyen et al., 2015).

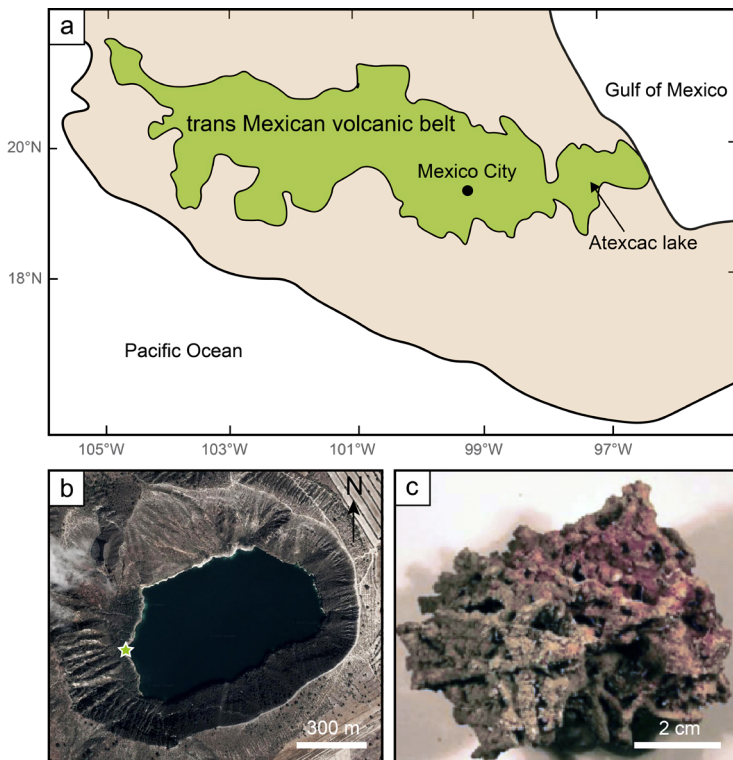


Figure 3.3: Location of the microbialite sample ATX-2012-08. a) Map of Mexico with the extent of the trans Mexican volcanic belt and the location of Atexcac lake. Modified after Ferrari et al. (2012). b) View of the Atexcac lake and position of the sampled area (green star) and c) picture of the microbialite from which sample ATX-2012-08 was made.

2.3. Results

2.3.1. Sample description

The Cayo Coco sample (hereafter M2 6.8-7.1) is an unconsolidated microbialite made of patches of Mg-silicates, Mg-calcite and aragonite. Appart from the carbonate and silicate mineralization, numerous bioclasts of bivalves, gastropods, diatoms and foraminifera are observed. Pyrite is observed as two distinct morphologies: disseminated framboids of 3 to 13 μm in size, and euhedral pyrite grains of 2 to 5 μm (Fig. 3.4a-c).

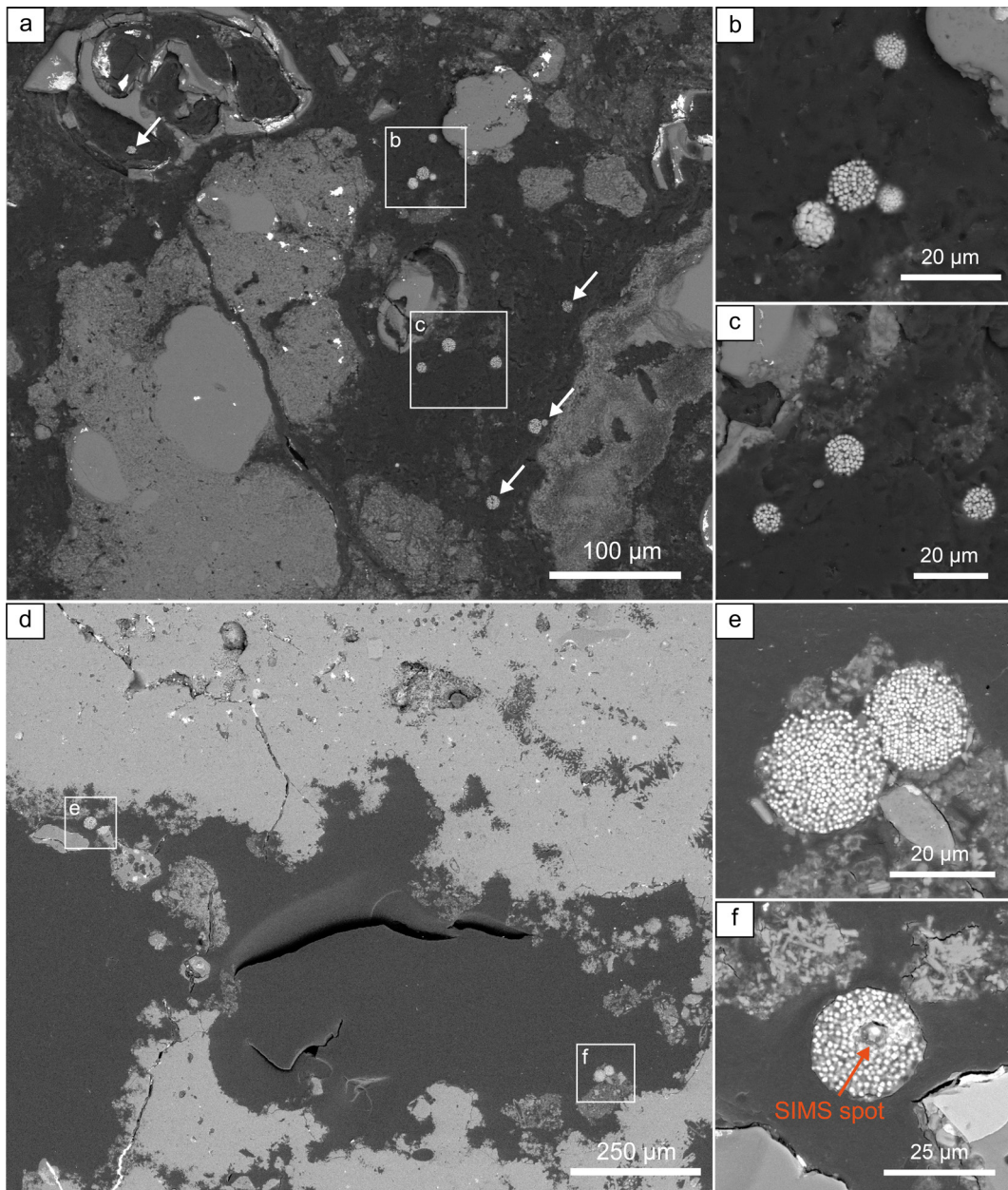


Figure 3. 4: BSE images of framboid pyrite grains measured for their $\delta^{56}\text{Fe}$ values by SIMS. a) View of sample M2 6.8-7.1 showing carbonate and silicate mineralization and bioclasts with focused areas b) and c) on framboid pyrite not enclosed in the mineralization. d) View of sample ATX-2012-08. The mineralization is mainly made of aragonite (bright grey). e) and f) BSE images of framboids at the edge of the mineralization.

The Atexcac sample (hereafter ATX-2012-08) is composed of aragonite and authigenic Mg-silicate such as kerolite and/or stevensite. Similar to M2 6.8-7.1, two morphologies of pyrite are identified: framboids with a size ranging from ~ 3 to $26 \mu\text{m}$, and euhedral pyrite of $\sim 3 \mu\text{m}$ (**Fig. 3.4d-f**). Framboid pyrite is systematically observed at the edge of the aragonite mineralization in ATX-2012-08 and either at the border of the Mg-silicate and carbonate mineralization or close by, and even sometimes, within bioclasts in M2 6.8-7.1. Those framboidal pyrites are composed of hundreds of euhedral monocrystals less than $0.5 \mu\text{m}$ in size. *Marin-Carbonne et al. (2022)* described thin Fe-oxide rims surrounding framboid crystallites in M2 6.8-7.1, likely reflecting meteoric alteration. Unlike framboids, euhedral micrometric pyrite, named micropyrrite hereafter, are included in the mineralization, i.e. enclosed in dark organic-rich and Mg-rich silicate laminae in ATX-2012-08 and in association with Mg-silicates in M2 6.8-7.1. The study of *Marin-Carbonne et al. (2022)* evidenced reaction rims of Fe-Mg silicate (in ATX-2012-08) and amorphous silica (in M2 6.8-7.1) around micropyrrite grains, arguing for syngeneity between silicate and micropyrrite.

2.3.2. $\delta^{56}\text{Fe}$ values of framboids

We measured a total of 42 framboids by CAMECA ims 1280 HR secondary ion mass spectroscopy (SIMS) with an average reproducibility of $\pm 0.3\text{‰}$. As primary beam sputtering depth ($3 \mu\text{m}$) was sometimes higher than the thickness of the pyrite grains, a few framboids were measured using a $10 \times 10 \mu\text{m}$ raster. All pyrite $\delta^{56}\text{Fe}$ values range from -3.61 to $+8.46\text{‰}$ ($n=42$; **Fig. 3.5**). Thirty analyses were performed in M2 6.8-7.1, which displays $\delta^{56}\text{Fe}$ values ranging from -3.61 to $+3.54\text{‰}$ and an average $\delta^{56}\text{Fe}$ value of $+0.30\text{‰}$. Until now, as only 12 analyses document the $\delta^{56}\text{Fe}$ variability in ATX-2012-08, I plan to perform more analyses prior to the publication of this study. This sample shows heavier Fe isotope compositions and larger isotope variability, with $\delta^{56}\text{Fe}$ values from -1.87 to $+8.48\text{‰}$ and an average $\delta^{56}\text{Fe}$ value of $+3.28\text{‰}$ (**Fig. 3.5**).

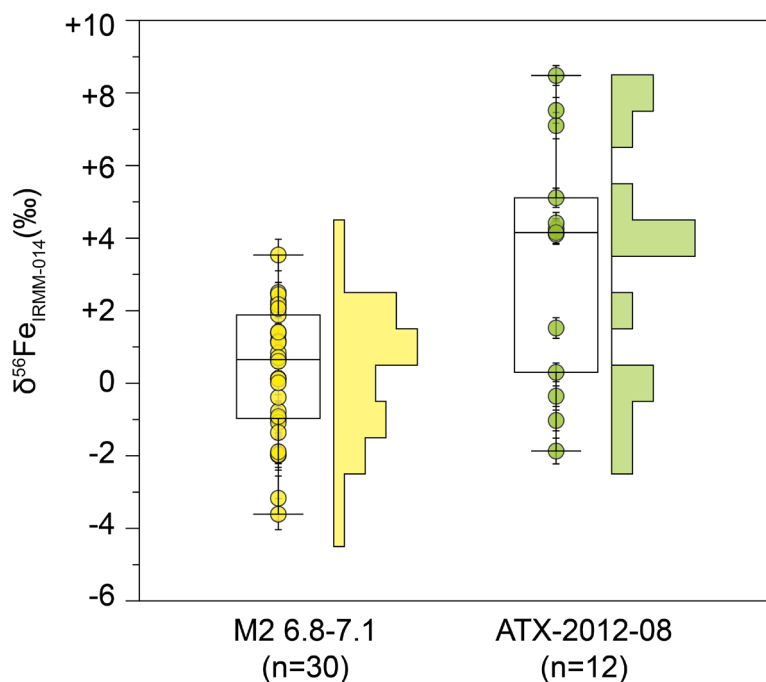


Figure 3.5: Fe isotope compositions measured in M2 6.8-7.1 (yellow dots) and ATX-2012-08 (green dots) represented as histograms and whisker plots. Black horizontal line in the box corresponds to the median $\delta^{56}\text{Fe}$ value. The lower and upper boundaries represent respectively the 25th and 75th percentiles of the dataset and smaller lines denote the maximum and minimum values.

Several analytical biases should be considered for interpretation of the dataset. First, the oxidation rims described around framboid crystallites in M2 6.8-7.1 were involuntarily measured. These rims can affect the Fe isotope compositions through a matrix effect, referring to a part of the fractionation which depends on the mineral composition which implies variation of the ionization potential and different sputtering rates (Kozdon *et al.*, 2010) between pyrite and Fe(III)-oxides. The difference of ionization potential is expressed as a variation of about one order of magnitude variation in the $^{56}\text{Fe}^+$ intensity between Fe-oxide and pyrite (Marin-Carbonne *et al.*, 2011). Therefore, high contribution of Fe-oxides in pyrite $\delta^{56}\text{Fe}$ values can be sorted by $^{56}\text{Fe}^+$ ion signal. However, the lack of correlation between the yield (ratio of the count rate of $^{56}\text{Fe}^+$ ion over the primary ion beam intensity) and $\delta^{56}\text{Fe}$ values suggest that secondary oxidation does not largely impact the measured Fe isotope signatures (Fig. 3.6a). This is consistent with the spatially limited extent of those rims (~ 25 nm) on a single framboid crystallite (~ 0.5 - 1 μm large).

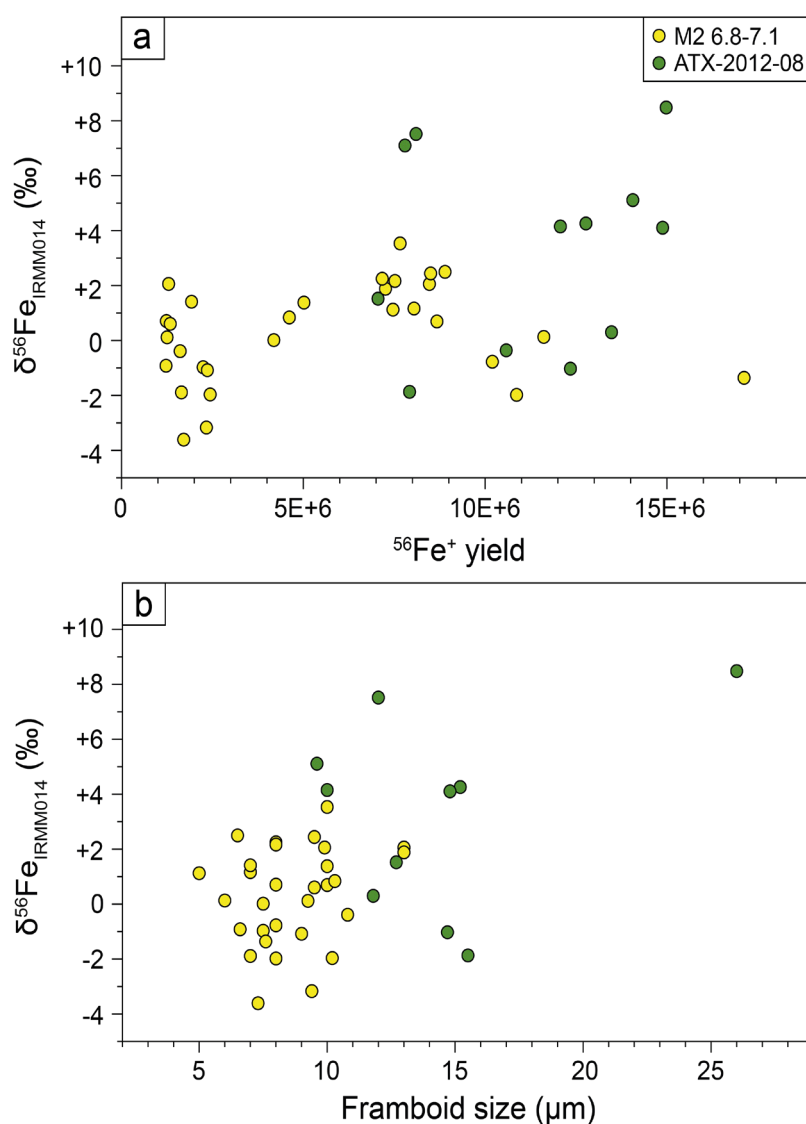


Figure 3. 6: Relationship between $\delta^{56}\text{Fe}$ values and a) the $^{56}\text{Fe}^+$ ion yield, i.e. the ratio of $^{56}\text{Fe}^+$ ion intensity (in counts per second) over the primary beam intensity, and b) the framboid grain size in M2 6.8-7.1 (yellow dots) and ATX-2012-08 (green dots).

Moreover, the lack of correlation between framboid size and $\delta^{56}\text{Fe}$ values excludes analytical effect influencing Fe isotope compositions (**Fig. 3.6b**). Second, the difficulty in locating pyrite in the dark matrix and their low thickness compared to the SIMS primary beam was a challenge for data acquisition. The number of analyses is therefore limited and the distribution of $\delta^{56}\text{Fe}$ values is probably under representative. In addition to this, the effect of repolishing between sessions resulted in the loss of many pyrite grains. Those two technical problems are jointly responsible for the small number of analyses available for ATX-2012-08, (n=12). Third, related to the second, most of the measured framboids are larger than $8\ \mu\text{m}$, with an average size of $8.6\ \mu\text{m}$ in M2 6.8-7.1 and $14.2\ \mu\text{m}$ in ATX-2012-08 (**Fig. 3.6b**). We are aware of the non-analyzed Fe pools represented by micrometric euhedral pyrite grains that could have different Fe isotope compositions and change the distribution histogram and the average $\delta^{56}\text{Fe}$ value. Since the best representation of the processes affecting Fe cycling is given in sample M2 6.8-7.1, the following model is mainly based on data from this sample.

2.4. Discussion

2.4.1. Origin of $\delta^{56}\text{Fe}$ variability under oxic conditions

Atexcac water column contains 41 ppb ($\sim 734\ \text{nM}$) of dissolved iron measured at 5 m depth and a similar concentration of 45 ppb ($\sim 805\ \text{nM}$) for particulate iron including Fe-oxides, Fe associated with organic matter and Fe in the terrigenous fraction (personal communication from C. Thomazo and E. Vennin). Dissolved Fe concentration profiles through the lake show higher concentrations in the oxic layer (0-15 m) of the water column than in the anoxic zone, arguing against hydrothermal Fe inputs (personal communication from C. Thomazo). In Cayo Coco, dissolved Fe concentrations range between 25 and 50 ppb (~ 447 to $895\ \text{nM}$; personal communication from E. Vennin). Such values are far higher than dissolved iron concentrations of the modern ocean, typically lower than $<1\ \text{nM}$ ($\sim 0.06\ \text{ppb}$), and quite unexpected under oxygenated water column (*Archer and Johnson, 2000*) but still much lower than dissolved iron concentrations in modern euxinic environments such as Lac Pavin (up to $1200\ \mu\text{M}$, $\sim 72,000\ \text{ppb}$, below the chemocline), Lake Nyos ($\sim 3\ \mu\text{M}$, $\sim 180\ \text{ppb}$) or the Black Sea ($0.3\ \mu\text{M}$, $\sim 18\ \text{ppb}$; *Lewis and Landing, 1991*; *Teutsch et al., 2009*; *Busigny et al., 2014*). Nevertheless, the presence of pyrite grains within bioclasts, not included in the microbialite, or at the surface of the microbialite, demonstrates a rapid redox gradient at the microbialite-water interface. Suboxic to anoxic conditions at the water column-sediment interface can explain the preservation of a non-negligible amount of organic matter (OM), typically $>1\ \text{wt.}\%$ in both environments (*Bouton et al., 2020*; *Zeyen et al., 2021*). This organic matter is thus available to fuel heterotrophic communities. In modern oxygenated systems, global iron cycling is controlled by complete oxidation of mobile ferrous iron Fe^{2+} into insoluble ferric Fe^{3+} under the form of ferrihydroxides or Fe-oxides, resulting in little Fe isotope variations around the average $\delta^{56}\text{Fe}$ values for igneous

rocks and hydrothermal sources. However, a part of Fe isotope variability recorded in pyrite may be inherited from different Fe sources. In modern semi-closed to closed environments, dissolved Fe²⁺ and Fe-oxides can be supplied by continental weathering of Fe-enriched substrate (clays, carbonates, ultramafic and mafic rocks, laterites; *Merrot et al., 2019; Sheppard et al., 2019*) or hydrothermal vents. $\delta^{56}\text{Fe}$ of Fe hydrothermal flux show little variation around typical values of 0 to -0.5‰ (*Beard et al., 2003*). The Fe flux associated with rivers displays more negative and variable $\delta^{56}\text{Fe}$ values, between -1 and 0‰ (*Fantle and DePaolo, 2004*). In Cayo Coco, iron can be leached from ultramafic and mafic minerals contained in peridotite, dunite or gabbro (*Siever and Woodford, 1979*). Alteration of chromite deposits associated with peridotite is also a likely source of iron in the system. In addition, a large supply of Fe-oxides can be provided by the erosion of Fe(III)-rich lateritic horizons (*Flint et al., 1948; Iturralde-Vinent et al., 2016*) or Fe in association with organic matter from the mangrove bordering the lagoon (*Bouton et al., 2020*). The Atexcac lake area in the eastern part of the TMVB has experienced frequent and diverse episodes of volcanism during the Quaternary. The source of iron in Atexcac is likely to be the weathering of mafic minerals contained in basaltic to andesitic lavas, tuffs, volcanoclastic and/or pyroclastic deposits (*Carrasco-Núñez et al., 2007*). Except fractionation > 1.5‰ reported in olivine due to Fe-Mg diffusion during crystallization (*Teng et al., 2011*) or during hydrothermal alteration of basalt, which is unlikely in this study, very limited Fe isotope fractionation is expected during magmatic processes and crystallization of mafic minerals. Therefore, the large Fe isotope range measured in M2 6.8-7.1 and ATX-2012-08 cannot be solely attributed to inherited fractionation of Fe source. This hypothesis must be confirmed by the measurement of Fe isotope compositions of dissolved Fe²⁺ and Fe-oxides from the water column in the near future. Alternatively, the production of high variation of Fe isotope signatures in framboid pyrite may reflect local Fe cycling at the water column-microbialite interface or within the microbialite, resulting from abiotic or biotic Fe oxide reduction and/or partial pyritization processes.

2.4.2. Microbial Fe oxide reduction dominate the Fe isotope record in Cuba

Sample M2 6.8-7.1 displays a wide range of $\delta^{56}\text{Fe}$ values with an average value of +0.30‰ (**Fig. 3.7**). The dataset is asymmetrical as commonly observed for a Rayleigh type distillation following **eq. 3.1** to **3.3**:

$$\delta^{56}\text{Fe}_{\text{substrate}} = \delta^{56}\text{Fe}_{\text{in}} + 1000 * f^{\alpha-1} - 1000 \quad (\text{eq. 3.1})$$

$$\delta^{56}\text{Fe}_{\text{product}} = \alpha * (\delta^{56}\text{Fe}_{\text{substrate}} + 1000) - 1000 \quad (\text{eq. 3.2})$$

$$\delta^{56}\text{Fe}_{\text{cumulate}} = f * \delta^{56}\text{Fe}_{\text{substrate}} + (1-f) * \delta^{56}\text{Fe}_{\text{product}} \quad (\text{eq. 3.3})$$

Where α is the fractionation factor, f the fraction of remaining substrate (i.e. Fe oxides), $\delta^{56}\text{Fe}_{\text{in}}$ the isotope composition of the initial Fe oxide, $\delta^{56}\text{Fe}_{\text{substrate}}$ the isotope composition of the remaining substrate, $\delta^{56}\text{Fe}_{\text{product}}$ the isotope composition of the instantaneous product and

$\delta^{56}\text{Fe}_{\text{cumulate}}$ the isotope composition of the cumulative product.

Considering initial Fe isotope compositions of Fe oxides of +0.5‰ and a DIR fractionation of -2.9‰, a peak around +0.5‰ is better described by the cumulative product. However, large isotope ranges observed both in Fe and S are unexpected in environments where dissolved ferrous iron, Fe oxides, sulfate (similar to oceanic sulfate concentration), organic matter and oxygen are not restricted. Therefore, these isotope fluctuations are necessarily attributed to local effects due to microbial activity and/or early diagenetic processes (**Fig. 3.7**). This agrees with large variations in $\delta^{34}\text{S}$ measured in framboids from the same sample and globally interpreted as microbial sulfate reduction influence. Fe isotope compositions in framboids display very negative values as low as -3.6‰ and extend to +3.5‰ (**Fig. 3.5**). A previous study by *Virtasalo et al. (2013)* reported a similar Fe isotope range from -3.1 to +4.1‰ in Holocene lacustrine pyrite concretions. Such a range has been interpreted as a sequential formation of pyrite in sediments under closed-system conditions, without differentiating biotic or abiotic pathways for Fe-oxides reduction.

The measurement of such negative values is rare in the Phanerozoic record. In the present study, the range and distribution suggest a distillation of the Fe-oxide reservoir which almost experienced a complete reduction. This is supported by the mode of $\delta^{56}\text{Fe}$ values around +0.5‰, a value matching the range of Fe oxide source (*Dauphas and Rouxel, 2006*; **Fig. 3.5**). Pyrite ^{56}Fe -depleted values in the geological record can be explain by three pathways:

- (p1) a biotic pathway corresponds to the microbial reduction of Fe-oxides associated with organic matter oxidation, named DIR, and producing Fe^{2+} fractionated up to -2.9‰.
- (p2) an abiotic pathway, consisting in reduction of Fe-oxide by H_2S (producing ^{56}Fe -depleted Fe^{2+} by up to -0.8‰), named sulfidation, and subsequent partial pyritization allowing the expression of a kinetic fractionation of -2.2‰ (*Guilbaud et al., 2011*).
- (p3) another abiotic pathway, where progressive removal of ^{56}Fe -enriched Fe-oxides leave a ^{56}Fe -depleted Fe^{2+} pool. The third hypothesis is relevant for an anoxic environment with a limited supply of oxygen in order to express the effect of partial oxidation.

Depending on the quantity of oxidized species introduced in the system, ferrous iron may be partially or totally re-oxidized and later re-reduced when anoxic conditions dominate in the mat or at its interface. Because of oxygenated conditions in the water column, the Fe source is necessarily under the form of Fe-oxides. The hypothesis p3 implies that the Fe-oxide source is first entirely reduced into Fe^{2+} and then partially oxidized to produce (1) a ^{56}Fe -depleted Fe^{2+} pool and (2) a ^{56}Fe -enriched residual Fe-oxide pool. This residual Fe-oxide pool can later undergo either total or partial reduction. Although redox fluctuations are compatible in a microbial mat, such complex oxidation-reduction cycling would produce highly positive and negative $\delta^{56}\text{Fe}$ values which do not fit a Rayleigh type distribution. Moreover, such conditions are not compatible with the development of supersaturation with respect to pyrite to form framboids. Therefore, pathway p3 is likely not the process generating the $\delta^{56}\text{Fe}$ values preserved in M2 6.8-7.1.

In this study, the most negative $\delta^{56}\text{Fe}$ value is -3.6‰ (**Fig. 3.5**). If the combination of

sulfidation and partial pyritization induces $\delta^{56}\text{Fe}$ values of around -3‰ ($\Delta_{\text{Fe(II)-Fe-ox}} = -0.8\text{‰}$ and $\Delta_{\text{FeS}_2\text{-Fe(II)}} = -2.2\text{‰}$; *Guilbaud et al., 2011; McAnena, 2011*), DIR coupled to partial pyritization is the only way to produce $\delta^{56}\text{Fe}$ values as low as -3.5‰ , considering a slightly positive $\delta^{56}\text{Fe}$ value for the Fe source. The latter needs to be confirmed. The main process described by $\delta^{56}\text{Fe}$ values is a complete reduction of Fe-oxides. Spatially resolved analyses of framboids allowed to identify the process behind this reduction. Our distribution records the complete Rayleigh distillation, starting from the first stage of distillation, characterized by highly negative $\delta^{56}\text{Fe}$, to an advanced degree of the distillation illustrated by $\delta^{56}\text{Fe}$ values $> +3\text{‰}$.

2.4.3. Iron cycling model and implication for the sulfur cycling

The production of Fe^{2+} by DIR in a microbial mat to precipitate framboids has several implications. First, because of the oxygenated conditions of the water column, the Fe^{2+} and H_2S pools required for the precipitation of pyrite are produced in the mat. Second, because framboids are not enclosed in the mineral (**Fig. 3.4**), Fe^{2+} and H_2S necessarily diffuse from their site of production (**Fig. 3.7**). In modern sediments, microbial iron and sulfate reduction preferentially occur at different depths, MSR favoring more anoxic conditions (*Jørgensen and Kasten, 2006*). However, it has been demonstrated that microorganisms performing MSR or DIR can coexist but, in this case, both metabolisms compete for organic matter (*Canfield et al., 1993; Thamdrup and Canfield, 1996; Johnson et al., 2008*). The expression of DIR in this sample may suggest that (1) DIR is more competitive than MSR in this environment, or (2) DIR and MSR are not active in the same area of the biofilm (**Fig. 3.7**). Two zones of sulfate reduction were identified in the mat, at 5 mm and 10 mm, and free HS^- concentrates deep in the mat, at around 12 mm from the mat surface during daytime, while diffusing toward the mat surface (~ 3 mm) during nighttime (*Pace et al., 2018*). The occurrence of DIR in the top of the mat suggests that the produced ferrous iron Fe^{2+} cannot react with sulfides as they are produced in a deeper location in the mat by MSR.

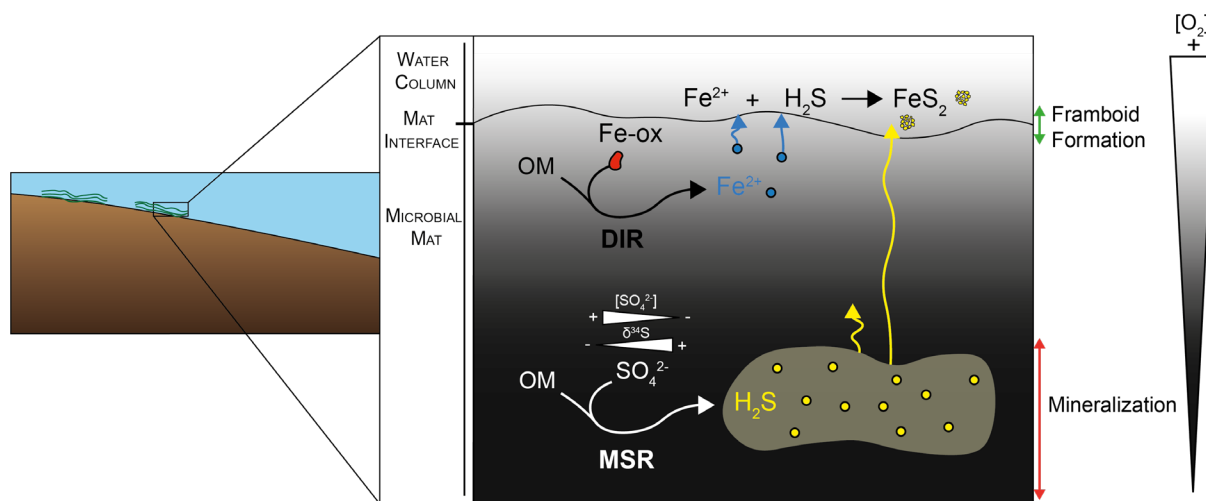
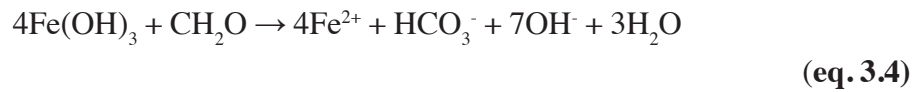


Figure 3. 7: Model of Fe and S cycling in microbial mat at Cayo Coco. This model includes the reduction of Fe oxides and sulfate which lead to the precipitation of pyrite at different locations in the mat. The formation of framboids out of the mineralization (carbonate precipitation) occurs through the reaction of Fe^{2+} derived from DIR, produced in the top of the mat, and a flux of H_2S diffusing from the mat.

Therefore, as a mobile ion, DIR-derived Fe^{2+} will diffuse out of its zone of production and can reach the top of the mat.

The recording of a distillation means that one of the reactant, either Fe-oxides or OM, was temporally limited to fuel the DIR reaction (**eq. 3.4**):



However, neither Fe-oxides seem to be restricted nor OM as high organic carbon content (TOC) at Cayo Coco (average TOC value in CC-2 core of 2.2 wt.% which locally reaches 16 wt.% in slime) are described (*Bouton et al., 2020*). Because Fe-oxides are not instantaneously entirely converted into Fe^{2+} and their potential of reduction depends on the nature of the oxide (*Canfield, 1989*), the distillation is suggested to be modulated by the diverse reactivity of Fe-oxides to microbes and/or H_2S availability. Moreover, the position of Fe-oxide in the mat determines the process of reduction (DIR versus sulfidation). A less labile organic matter may also influence the kinetic of reduction.

The increase of $\delta^{34}\text{S}$ in framboids has been interpreted either as reflecting oxidation processes by fluctuating redox conditions at the mat interface or an isotope distillation of the sulfate reservoir (*Marin-Carbonne et al., 2022*). Because Fe isotope compositions do not reflect partial oxidation processes at the mat interface, we suggest that the ^{34}S enrichment in framboids express a local distillation. Here again, a distillation of the sulfate reservoir is not compatible with abundant sulfate and OM supplied in the system. Despite high sulfate and organic matter concentrations in the Cayo Coco lagoon, the steep redox gradient within a microbial mat suggests water column and porewaters are not at equilibrium and the system likely evolves in closed conditions. Therefore, ^{34}S -enriched $\delta^{34}\text{S}$ values measured in framboids reflect a local isotopically distilled residual sulfate reservoir. The absence of Fe-oxides or ferrous iron to react with MSR-derived sulfide and/or an important sulfide production (*Pasquier et al., 2021*), enhances the diffusion of sulfide out of its zone of production (**Fig. 3.7**). This H_2S flux then reaches the top of the mat and can react with DIR-derived Fe^{2+} , forming pyrite with ^{34}S -enriched $\delta^{34}\text{S}$ values and positive $\delta^{56}\text{Fe}$ values which mostly reflect complete Fe-oxide reduction.

In the case of ATX-2012-08, the lowest $\delta^{56}\text{Fe}$ value of -1.87‰ (**Fig. 3.7**) does not support, but not exclude, microbial reduction of iron oxides. The isotope range measured in this sample could only reflect sulfidation of Fe oxides coupled to partial pyritization or microbial reduction of isotopically heavier Fe oxide sources. Isotope values of a Fe source are unknown but is unlikely to be highly fractionated. However, it remains difficult to draw conclusions about processes controlling Fe cycling in Atexcac without a good statistical representation of the isotope dataset.

3. Conclusions and perspectives

3.1. Main conclusions

Using spatially resolved S and Fe isotope analyses by NanoSIMS and SIMS, respectively, we studied framboidal pyrites from two modern mineralizing microbial mats in Cayo Coco (M2 6.8-7.1; Cuba) and Atexcac lake (ATX-2012-08; Mexico). Two relevant results emerge from the study based on pyrite S isotope signatures (*Marin-Carbonne et al., 2022*).

First, fractionation between sulfate and pyrite belonging to the same pyrite morphology is comparable in both studied localities, showing a limited influence of the depositional environment, including sulfate concentration, on pyrite S isotope compositions.

Second, the two pyrite morphologies display contrasting $\delta^{34}\text{S}$ signatures. Micropyrates display variable $\delta^{34}\text{S}$ values with averages of $-61.4 \pm 17\text{‰}$ and $-34.5 \pm 29\text{‰}$ for Atexcac and Cayo Coco, respectively. Resulting sulfate-pyrite isotope fractionation (Δ_{pyr}) is close to equilibrium fractionation during MSR characterized by low sulfate cell specific reduction rate. On the other hand, the higher $\delta^{34}\text{S}$ average value of $\sim -26\text{‰}$ and variable sulfur isotope compositions measured in micrometric framboid pyrite are either explained by (1) diffusion of MSR-derived sulfide from its zone of production in the mat to the mat/water column interface or (2) a mixing process of MSR-derived sulfide production and sulfide oxidation. Therefore, this study evidenced that the expression of MSR is directly linked to the pyrite position in the mat. Micropyrates is identified as a biomineral bearing an unequivocal signature of MSR, while more complex signatures characterize framboid pyrites which may result from a complex history of microbially-mediated sulfide (e.g. diffusion). The question raised by this study is to determine whether the Fe isotope signatures in pyrite framboids also reflect microbial processes.

This led us to the second part of the chapter focusing on Fe isotopes. The measurement of both pyrite morphologies was challenged by analytical issues and only framboidal pyrite was able to be analyzed in the frame of this thesis. Framboidal pyrite grains are located at the edge of the microbialite or are associated with foraminifera and bivalve bioclasts not included in the mineralization. This suggests that they formed at the sediment-water interface. Large Fe isotope ranges have been evidenced in both environments. For statistical relevance, the Fe cycling model is based on isotope analyses of M2 6.8-7.1 (n= 30). The average $\delta^{56}\text{Fe}$ value of $\sim +0.5\text{‰}$ is consistent with a total reduction of Fe(III)-oxides and the isotope range (-3.5 to $+3.5\text{‰}$), suggesting a microbially-mediated reduction by Fe reducing bacteria. The lower $\delta^{56}\text{Fe}$ values around -3.6‰ represent the beginning of the reduction, whereas pyrite associated with positive $\delta^{56}\text{Fe}$ values ($+3.5\text{‰}$) formed during near complete reduction. Most of the pyrite framboids formed through a complete reduction of Fe-oxides as attested by their $\delta^{56}\text{Fe}$ values that are typical $\delta^{56}\text{Fe}$ value of a Fe-oxide source. These signatures are not correlated to the size (**Fig. 3.6b**) or the location of framboids in the sample. Fe isotope signatures do not support

partial oxidation processes and define ^{34}S -enriched sulfide diffusion as controlling framboidal pyrite formation in this sample. This study shows that large Fe isotope ranges in pyrite preserved in oxygenated environments reflect the influence of local microbial processes and the effect of early burial diagenetic processes (e.g. diffusion away from the production site). Therefore, we conclude that Fe isotopes in pyrite may serve as a proxy to track early diagenetic processes rather than water column influences in modern microbialites.

3.2. Relationship between framboid and micropyrrite formation

Fe isotope compositions of micropyrrite were not successfully measured but can be hypothesized through this model. Micropyrrite $\delta^{34}\text{S}$ values are highly ^{34}S -depleted, and the calculation of S isotope fractionation ($\Delta_{\text{pyrite-sulfate}}$) revealed MSR fractionation close to equilibrium, implying low microbial sulfate reduction rates. This means that the kinetics of sulfate consumption, i.e. sulfate reduction rate followed by reactions with iron, corresponds to the rate of sulfate replenishment. Indeed, in a closed system, equilibrium S fractionation in micropyrrite reflects early stages of the MSR process. In contrast, ^{34}S -enriched $\delta^{34}\text{S}$ values and narrow S fractionation reflect advanced stages of the reaction. The occurrence of micropyrrite enclosed in the mineralization reflects that H_2S and Fe^{2+} produced in the mat are in situ consumed through the precipitation of pyrite. Because MSR inhibits DIR and Fe-oxides are not only restricted in the DIR zone, sulfide produced by MSR should promote reductive dissolution of Fe oxides. Therefore, the formation of diffusion ^{34}S -enriched H_2S flux for framboid precipitation requires the absence of reactive iron, i.e. a complete sulfidation of Fe-oxides in the MSR zone. A complete sulfidation of Fe oxide would produce pyrite with similar Fe isotope compositions than that of a Fe source ($\delta^{56}\text{Fe} \sim [0 - +1\text{‰}]$). Therefore, Fe-oxide sulfidation is mediated by ^{34}S -depleted H_2S produced in the early stages of MSR, leading to the precipitation of micropyrrite with highly negative $\delta^{34}\text{S}$ values. When complete sulfidation is achieved, favorable conditions develop for precipitation of framboid pyrite at the mat interface. I therefore suggest that variation of S isotope compositions between micropyrrite and framboidal grains is linked to the availability of iron oxides to precipitate pyrite.

This work is part of a larger project which aims to understand mechanisms involved in the formation and preservation of microbialites. These include influences of the external (environment and physico-chemical conditions) and internal (nature and diversity of microorganisms) factors on mineralization processes, in order to better understand (and interpret) geochemical informations preserved in ancient microbialites. My contribution to this project was to determine the impact of local conditions, including microbial activity, on pyrite isotope compositions through spatially resolved measurement. This work raised two main perspectives that will be tested in the near future.

First, more efforts will be invested in the acquisition of new data, particularly on sample ATX-2012-08 which presents exceptional heavy $\delta^{56}\text{Fe}$ signatures. If these values are confirmed,

this study will report the widest range of in situ Fe isotope compositions through the geological record and the heaviest $\delta^{56}\text{Fe}$ values compared to those published. This will have a major impact on the vision of the iron cycle in modern oxygenated environments, even though this cycling is associated with “micro-environment” such as microbial mats.

Second, because interpretations of Fe isotope compositions importantly rely on the initial $\delta^{56}\text{Fe}$ value of the Fe source, it is crucial to constrain it. For this, field work will be conducted at Atexcac lake in the next few months. Water sampling at the same depth than the studied microbialite as well as porewaters from the microbialite will be used to extract dissolved Fe^{2+} and particulate iron, and measure their $\delta^{56}\text{Fe}$ values. Finally, a challenging project would be to adapt the Fe isotopes analytical protocol to measure micropyrith preserved in those microbialites. This task is difficult because the primary beam is too abrasive, implying that we observe a systematic decrease of the secondary ion intensity during the 7 minutes required to complete a single $\delta^{56}\text{Fe}$ analysis period, I plan to test different analytical conditions this fall in order to find the good balance between decreasing the primary beam size and maintaining the analytical precision.

3.3. Literature cited

- Archer, D.E., Johnson, K., 2000. A model of the iron cycle in the ocean. *Global Biogeochemical Cycles* 14, 269–279. <https://doi.org/10.1029/1999GB900053>
- Archer, C., Vance, D., 2006. Coupled Fe and S isotope evidence for Archean microbial Fe(III) and sulfate reduction. *Geology* 34, 153. <https://doi.org/10.1130/G22067.1>
- Beard, B.L., Johnson, C.M., von Damm, K.L., Poulson, R.L., 2003. Iron isotope constraints on Fe cycling and mass balance in oxygenated Earth oceans. *Geology* 31, 629. [https://doi.org/10.1130/0091-7613\(2003\)031<0629:IICOFC>2.0.CO;2](https://doi.org/10.1130/0091-7613(2003)031<0629:IICOFC>2.0.CO;2)
- Bertran, E., Leavitt, W.D., Pellerin, A., Zane, G.M., Wall, J.D., Halevy, I., Wing, B.A., Johnston, D.T., 2018. Deconstructing the Dissimilatory Sulfate Reduction Pathway: Isotope Fractionation of a Mutant Unable of Growth on Sulfate. *Frontiers in Microbiology* 9. <https://doi.org/10.3389/fmicb.2018.03110>
- Blood, D.R., Lash, G.G., Larsen, D., Egenhoff, S.O., Fishman, N.S., 2015. Dynamic redox conditions in the Marcellus Shale as recorded by pyrite framboid size distributions. *The Geological Society of America Special Papers* 515, 153–168.
- Böttcher, M.E., Thamdrup, B., Vennemann, T.W., 2001. Oxygen and sulfur isotope fractionation during anaerobic bacterial disproportionation of elemental sulfur. *Geochimica et Cosmochimica Acta* 65, 1601–1609. [https://doi.org/10.1016/S0016-7037\(00\)00628-1](https://doi.org/10.1016/S0016-7037(00)00628-1)
- Bouton, A., Vennin, E., Thomazo, C., Mathieu, O., Garcia, F., Jaubert, M., Visscher, P.T., 2020. Microbial origin of the organic matter preserved in the cayo coco lagoonal network, Cuba. *Minerals* 10. <https://doi.org/10.3390/min10020143>
- Brandt, K.K., Vester, F., Jensen, A.N., Ingvorsen, K., 2001. Sulfate Reduction Dynamics and Enumeration of Sulfate-Reducing Bacteria in Hypersaline Sediments of the Great Salt Lake (Utah, USA). *Microbial Ecology* 41, 1–11. <https://doi.org/10.1007/s002480000059>
- Breitbart, M., Hoare, A., Nitti, A., Siefert, J., Haynes, M., Dinsdale, E., Edwards, R., Souza, V., Rohwer, F., Hollander, D., 2009. Metagenomic and stable isotope analyses of modern freshwater microbialites in Cuatro Ciénegas, Mexico. *Environmental Microbiology* 11, 16–34. <https://doi.org/10.1111/j.1462-2920.2008.01725.x>
- Busigny, V., Planavsky, N.J., Jézéquel, D., Crowe, S., Louvat, P., Moureau, J., Viollier, E., Lyons, T.W., 2014. Iron isotopes in an Archean ocean analogue. *Geochimica et Cosmochimica Acta* 133, 443–462. <https://doi.org/10.1016/j.gca.2014.03.004>
- Butler, I.B., Rickard, D., 2000. Framboidal pyrite formation via the oxidation of iron (II) monosulfide by hydrogen sulphide. *Geochimica et Cosmochimica Acta* 64, 2665–2672. [https://doi.org/10.1016/S0016-7037\(00\)00387-2](https://doi.org/10.1016/S0016-7037(00)00387-2)
- Canfield, D.E., 1989. Reactive iron in marine sediments. *Geochimica et Cosmochimica Acta* 53, 619–632. [https://doi.org/10.1016/0016-7037\(89\)90005-7](https://doi.org/10.1016/0016-7037(89)90005-7)
- Canfield, D.E., Jørgensen, B.B., Fossing, H., Glud, R., Gundersen, J., Ramsing, N.B., Thamdrup, B., Hansen, J.W., Nielsen, L.P., Hall, P.O.J., 1993. Pathways of organic carbon oxidation in three continental margin sediments. *Marine Geology* 113, 27–40. [https://doi.org/10.1016/0025-3227\(93\)90147-N](https://doi.org/10.1016/0025-3227(93)90147-N)
- Canfield, D.E., Thamdrup, B., 1994. The Production of ³⁴S-Depleted Sulfide During Bacterial Disproportionation of Elemental Sulfur. *Science* (1979) 266, 1973–1975. <https://doi.org/10.1126/science.11540246>
- Canfield, D.E., Teske, A., 1996. Late Proterozoic rise in atmospheric oxygen concentration inferred from phylogenetic and sulphur-isotope studies. *Nature* 382, 127–132. <https://doi.org/10.1038/382127a0>
- Canfield, D.E., Thamdrup, B., 1996. Fate of elemental sulfur in an intertidal sediment. *FEMS Microbiology Ecology* 19, 95–103. <https://doi.org/10.1111/j.1574-6941.1996.tb00202.x>
- Canfield, D.E., 2001. Biogeochemistry of Sulfur Isotopes. *Reviews in Mineralogy and Geochemistry* 43, 607–636. <https://doi.org/10.2138/gsrmg.43.1.607>

- Carrasco-Núñez, G., Ort, M.H., Romero, C., 2007. Evolution and hydrological conditions of a maar volcano (Atexcac crater, Eastern Mexico). *Journal of Volcanology and Geothermal Research* 159, 179–197. <https://doi.org/10.1016/j.jvolgeores.2006.07.001>
- Dauphas, N., Rouxel, O., 2006. Mass spectrometry and natural variations of iron isotopes. *Mass Spectrometry Reviews* 25, 515–550. <https://doi.org/10.1002/mas.20078>
- de Koff, J.P., Anderson, M.A., Amrhein, C., 2008. Geochemistry of iron in the Salton Sea, California. *Hydrobiologia* 604, 111–121. <https://doi.org/10.1007/s10750-008-9322-3>
- Dupraz, C., Visscher, P.T., 2005. Microbial lithification in marine stromatolites and hypersaline mats. *Trends in Microbiology* 13, 429–438. <https://doi.org/10.1016/j.tim.2005.07.008>
- Duverger, A., Berg, J. S., Busigny, V., Guyot, F., Bernard, S., Miot, J., 2020. Mechanisms of pyrite formation promoted by sulfate-reducing bacteria in pure culture. *Frontiers in Earth Science*, 8, 588310. [10.3389/feart.2020.588310](https://doi.org/10.3389/feart.2020.588310)
- Egger, M., Riedinger, N., Mogollón, J.M., Jørgensen, B.B., 2018. Global diffusive fluxes of methane in marine sediments. *Nature Geoscience* 11, 421–425. <https://doi.org/10.1038/s41561-018-0122-8>
- Fantle, M.S., DePaolo, D.J., 2004. Iron isotope fractionation during continental weathering. *Earth and Planetary Science Letters* 228, 547–562. <https://doi.org/10.1016/j.epsl.2004.10.013>
- Farquhar, J., Bao, H., Thiemens, M., 2000. Atmospheric Influence of Earth's Earliest Sulfur Cycle. *Science* (1979) 289, 756–758. <https://doi.org/10.1126/science.289.5480.756>
- Ferrari, L., Orozco-Esquivel, T., Manea, V., Manea, M., 2012. The dynamic history of the Trans-Mexican Volcanic Belt and the Mexico subduction zone. *Tectonophysics* 522–523, 122–149. <https://doi.org/10.1016/j.tecto.2011.09.018>
- Fike, D.A., Gammon, C.L., Ziebis, W., Orphan, V.J., 2008. Micron-scale mapping of sulfur cycling across the oxycline of a cyanobacterial mat: a paired nanoSIMS and CARD-FISH approach. *The ISME Journal* 2, 749–759. <https://doi.org/10.1038/ismej.2008.39>
- Fike, D.A., Bradley, A.S., Rose, C. v., 2015. Rethinking the Ancient Sulfur Cycle. *Annual Review of Earth and Planetary Sciences* 43, 593–622. <https://doi.org/10.1146/annurev-earth-060313-054802>
- Findlay, A.J., Pellerin, A., Laufer, K., Jørgensen, B.B., 2020. Quantification of sulphide oxidation rates in marine sediment. *Geochimica et Cosmochimica Acta* 280, 441–452. <https://doi.org/10.1016/j.gca.2020.04.007>
- Flint, D.E., de Albear, J.F., Guild, P.W., 1948. *Geology and chromite deposits of the Camagüey district, Camagüey Province, Cuba*. US Government Printing Office.
- Folk, R.L., 2005. Nannobacteria and the formation of framboidal pyrite: Textural evidence. *Journal of Earth System Science* 114, 369–374. <https://doi.org/10.1007/BF02702955>
- Frederiksen, T.-M., Finster, K., 2003. Sulfite-oxido-reductase is involved in the oxidation of sulfite in *Desulfocapsa sulfoexigens* during disproportionation of thiosulfate and elemental sulfur. *Biodegradation* 14, 189–198. <https://doi.org/10.1023/A:1024255830925>
- Fry, B., Ruf, W., Gest, H., Hayes, J.M., 1988. Sulfur isotope effects associated with oxidation of sulfide by O₂ in aqueous solution. *Chemical Geology: Isotope Geoscience section* 73, 205–210. [https://doi.org/10.1016/0168-9622\(88\)90001-2](https://doi.org/10.1016/0168-9622(88)90001-2)
- Gomes, M.L., Klatt, J.M., Dick, G.J., Grim, S.L., Rico, K.I., Medina, M., Ziebis, W., Kinsman-Costello, L., Sheldon, N.D., Fike, D.A., 2022. Sedimentary pyrite sulfur isotope compositions preserve signatures of the surface microbial mat environment in sediments underlying low-oxygen cyanobacterial mats. *Geobiology* 20, 60–78. <https://doi.org/10.1111/gbi.12466>
- Guilbaud, R., Butler, I.B., Ellam, R.M., 2011. Abiotic Pyrite Formation Produces a Large Fe Isotope Fractionation. *Science* (1979) 332, 1548–1551. <https://doi.org/10.1126/science.1202924>
- Harrison, A.G., Thode, H.G., 1958. Mechanism of the bacterial reduction of sulphate from isotope fractionation studies. *Transactions of the Faraday Society* 54, 84. <https://doi.org/10.1039/tf9585400084>

- Hou, L., Peng, H., Ding, J., Zhang, J., Zhu, S., Wu, S., Wu, Y., Ouyang, H., 2016. Textures and In Situ Chemical and Isotope Analyses of Pyrite, Huijiabao Trend, Youjiang Basin, China: Implications for Paragenesis and Source of Sulfur. *Economic Geology* 111, 331–353. <https://doi.org/10.2113/econgeo.111.2.331>
- Iturralde-Vinent, M.A., García-Casco, A., Rojas-Agramonte, Y., Proenza, J.A., Murphy, J.B., Stern, R.J., 2016. The geology of Cuba: A brief overview and synthesis. *GSA Today* 4–10. <https://doi.org/10.1130/GSATG296A.1>
- Johnson, C.M., Beard, B.L., Roden, E.E., 2008. The Iron Isotope Fingerprints of Redox and Biogeochemical Cycling in Modern and Ancient Earth. *Annual Review of Earth and Planetary Sciences* 36, 457–493. <https://doi.org/10.1146/annurev.earth.36.031207.124139>
- Johnston, D.T., 2011. Multiple sulfur isotopes and the evolution of Earth's surface sulfur cycle. *Earth-Science Reviews* 106, 161–183. <https://doi.org/10.1016/j.earscirev.2011.02.003>
- Jørgensen, B.B., 1977. The sulfur cycle of a coastal marine sediment (Limfjorden, Denmark)1. *Limnology and Oceanography* 22, 814–832. <https://doi.org/10.4319/lo.1977.22.5.0814>
- Jørgensen, B.B., 1982. Mineralization of organic matter in the sea bed—the role of sulphate reduction. *Nature* 296, 643–645. <https://doi.org/10.1038/296643a0>
- Jørgensen, B.B., Kasten, S., 2006. Sulfur cycling and methane oxidation, in: *Marine Geochemistry*. Springer Berlin Heidelberg, pp. 271–309. https://doi.org/10.1007/3-540-32144-6_8
- Jørgensen, B.B., Findlay, A.J., Pellerin, A., 2019. The Biogeochemical Sulfur Cycle of Marine Sediments. *Frontiers in Microbiology* 10. <https://doi.org/10.3389/fmicb.2019.00849>
- Kaplan, I.R., Rittenberg, S.C., 1964. Microbiological Fractionation of Sulphur Isotopes. *Journal of General Microbiology* 34, 195–212. <https://doi.org/10.1099/00221287-34-2-195>
- Kershaw, S., Tang, H., Li, Y., Guo, L., 2018. Oxygenation in carbonate microbialites and associated facies after the end-Permian mass extinction: Problems and potential solutions. *Journal of Palaeogeography* 7, 32–47. <https://doi.org/10.1016/j.jop.2017.10.001>
- Kozdon, R., Kita, N.T., Huberty, J.M., Fournelle, J.H., Johnson, C.A., Valley, J.W., 2010. In situ sulfur isotope analysis of sulfide minerals by SIMS: Precision and accuracy, with application to thermometry of ~3.5Ga Pilbara cherts. *Chemical Geology* 275, 243–253. <https://doi.org/10.1016/j.chemgeo.2010.05.015>
- Large, R.R., Maslennikov, V. v., Robert, F., Danyushevsky, L. v., Chang, Z., 2007. Multistage Sedimentary and Metamorphic Origin of Pyrite and Gold in the Giant Sukhoi Log Deposit, Lena Gold Province, Russia. *Economic Geology* 102, 1233–1267. <https://doi.org/10.2113/gsecongeo.102.7.1233>
- Leavitt, W.D., Halevy, I., Bradley, A.S., Johnston, D.T., 2013. Influence of sulfate reduction rates on the Phanerozoic sulfur isotope record. *Proceedings of the National Academy of Sciences* 110, 11244–11249. <https://doi.org/10.1073/pnas.1218874110>
- Lewis, B.L., Landing, W.M., 1991. The biogeochemistry of manganese and iron in the Black Sea. *Deep Sea Research Part A. Oceanographic Research Papers* 38, S773–S803. [https://doi.org/10.1016/S0198-0149\(10\)80009-3](https://doi.org/10.1016/S0198-0149(10)80009-3)
- Liu, J., Pellerin, A., Wang, J., Rickard, D., Antler, G., Zhao, J., Wang, Z., Jørgensen, B.B., Ono, S., 2022. Multiple sulfur isotopes discriminate organoclastic and methane-based sulfate reduction by sub-seafloor pyrite formation. *Geochimica et Cosmochimica Acta* 316, 309–330. <https://doi.org/10.1016/j.gca.2021.09.026>
- Love, L.G., 1957. Micro-organisms and the presence of syngenetic pyrite. *Quarterly Journal of the Geological Society* 113, 429–440. <https://doi.org/10.1144/GSL.JGS.1957.113.01-04.18>
- Mansor, M., Fantle, M.S., 2019. A novel framework for interpreting pyrite-based Fe isotope records of the past. *Geochimica et Cosmochimica Acta* 253, 39–62. <https://doi.org/10.1016/j.gca.2019.03.017>
- Marin-Carbonne, J., Rollion-Bard, C., Luais, B., 2011. In-situ measurements of iron isotopes by SIMS: MC-ICP-MS intercalibration

- and application to a magnetite crystal from the Gunflint chert. *Chemical Geology* 285, 50–61. <https://doi.org/10.1016/j.chemgeo.2011.02.019>
- Marin-Carbonne, J., Decraene, M.-N., Havas, R., Remusat, L., Pasquier, V., Alléon, J., Zeyen, N., Bouton, A., Bernard, S., Escrig, S., Olivier, N., Vennin, E., Meibom, A., Benzerara, K., Thomazo, C., 2022. Early precipitated micropyrite in microbialites: A time capsule of microbial sulfur cycling. *Geochemical Perspectives Letters* 21, 7–12. <https://doi.org/10.7185/geochemlet.2209>
- McAnena, A., 2011. The reactivity and isotope fractionation of Fe-bearing minerals during sulfidation: an experimental approach. (Doctoral dissertation, Newcastle University).
- Merrot, P., Juillot, F., Noël, V., Lefebvre, P., Brest, J., Menguy, N., Guigner, J.-M., Blondeau, M., Viollier, E., Fernandez, J.-M., Moreton, B., Bargar, J.R., Morin, G., 2019. Nickel and iron partitioning between clay minerals, Fe-oxides and Fe-sulfides in lagoon sediments from New Caledonia. *Science of The Total Environment* 689, 1212–1227. <https://doi.org/10.1016/j.scitotenv.2019.06.274>
- Pace, A., Bourillot, R., Bouton, A., Vennin, E., Braissant, O., Dupraz, C., Duteil, T., Bundeleva, I., Patrier, P., Galaup, S., Yokoyama, Y., Franceschi, M., Virgone, A., Visscher, P.T., 2018. Formation of stromatolite lamina at the interface of oxygenic–anoxygenic photosynthesis. *Geobiology* 16, 378–398. <https://doi.org/10.1111/gbi.12281>
- Pardo, G., 2009. The geology of Cuba, in: *The Geology of Cuba*. The American Association of Petroleum Geologists, Tulsa, Oklahoma, U.S.A., pp. 311–341. <https://doi.org/10.1306/13141064St583328>
- Pasquier, V., Fike, D.A., Halevy, I., 2021. Sedimentary pyrite sulfur isotopes track the local dynamics of the Peruvian oxygen minimum zone. *Nature Communications* 12. <https://doi.org/10.1038/s41467-021-24753-x>
- Pavlov, A.A., Kasting, J.F., 2002. Mass-Independent Fractionation of Sulfur Isotopes in Archean Sediments: Strong Evidence for an Anoxic Archean Atmosphere. *Astrobiology* 2, 27–41. <https://doi.org/10.1089/153110702753621321>
- Pellerin, A., Antler, G., Holm, S.A., Findlay, A.J., Crockford, P.W., Turchyn, A. v., Jørgensen, B.B., Finster, K., 2019. Large sulfur isotope fractionation by bacterial sulfide oxidation. *Science Advances* 5. <https://doi.org/10.1126/sciadv.aaw1480>
- Rees, C.E., 1973. A steady-state model for sulphur isotope fractionation in bacterial reduction processes. *Geochimica et Cosmochimica Acta* 37, 1141–1162. [https://doi.org/10.1016/0016-7037\(73\)90052-5](https://doi.org/10.1016/0016-7037(73)90052-5)
- Rickard, D., 1969. The microbiological formation of iron sulphides. *Stockholm Contributions to Geology*, 20, 49–66.
- Rickard, D., Luther, G.W., 1997. Kinetics of pyrite formation by the H₂S oxidation of iron (II) monosulfide in aqueous solutions between 25 and 125°C: The mechanism. *Geochimica et Cosmochimica Acta* 61, 135–147. [https://doi.org/10.1016/S0016-7037\(96\)00322-5](https://doi.org/10.1016/S0016-7037(96)00322-5)
- Rickard, D., 2019a. Sedimentary pyrite framboid size-frequency distributions: A meta-analysis. *Palaeogeography, Palaeoclimatology, Palaeoecology* 522, 62–75. <https://doi.org/10.1016/j.palaeo.2019.03.010>
- Rickard, D., 2019b. How long does it take a pyrite framboid to form? *Earth and Planetary Science Letters* 513, 64–68. <https://doi.org/10.1016/j.epsl.2019.02.019>
- Rolison, J.M., Stirling, C.H., Middag, R., Gault-Ringold, M., George, E., Rijkenberg, M.J.A., 2018. Iron isotope fractionation during pyrite formation in a sulfidic Precambrian ocean analogue. *Earth and Planetary Science Letters* 488, 1–13. <https://doi.org/10.1016/j.epsl.2018.02.006>
- Schidlowski, M., 1985. Carbon isotope discrepancy between precambrian stromatolites and their modern analogs: Inferences from hypersaline microbial mats of the Sinai coast. *Origins of Life and Evolution of the Biosphere* 15, 263–277. <https://doi.org/10.1007/BF01808173>
- Schneiderhöhn, H., 1923. Chalkographische untersuchung des mansfelder kupferschiefers. *Neues Jahrbuch für Mineralogie, Geologie und Paläontologie* 47, 1–38.
- Scott, R.J., Meffre, S., Woodhead, J., Gilbert, S.E., Berry, R.F., Emsbo, P., 2009. Development of Framboidal Pyrite During Diagenesis, Low-Grade Regional Metamorphism, and Hydrothermal Alteration. *Economic Geology* 104, 1143–1168. <https://doi.org/10.2113/gsecongeo.104.8.1143>

- Sheppard, R.Y., Milliken, R.E., Russell, J.M., Dyar, M.D., Sklute, E.C., Vogel, H., Melles, M., Bijaksana, S., Morlock, M.A., Hasberg, A.K.M., 2019. Characterization of Iron in Lake Towuti sediment. *Chemical Geology* 512, 11–30. <https://doi.org/10.1016/j.chemgeo.2019.02.029>
- Siever, R., Woodford, N., 1979. Dissolution kinetics and the weathering of mafic minerals. *Geochimica et Cosmochimica Acta* 43, 717–724. [https://doi.org/10.1016/0016-7037\(79\)90255-2](https://doi.org/10.1016/0016-7037(79)90255-2)
- Sim, M.S., Bosak, T., Ono, S., 2011a. Large Sulfur Isotope Fractionation Does Not Require Disproportionation. *Science* (1979) 333, 74–77. <https://doi.org/10.1126/science.1205103>
- Sim, M. S., Ono, S., Donovan, K., Templer, S. P., & Bosak, T., 2011b. Effect of electron donors on the fractionation of sulfur isotopes by a marine *Desulfovibrio* sp. *Geochimica et Cosmochimica Acta*, 75(15), 4244–4259. <https://doi.org/10.1016/j.gca.2011.05.021>
- Sun, Y.D., Wignall, P.B., Joachimski, M.M., Bond, D.P.G., Grasby, S.E., Sun, S., Yan, C.B., Wang, L.N., Chen, Y.L., Lai, X.L., 2015. High amplitude redox changes in the late Early Triassic of South China and the Smithian–Spathian extinction. *Palaeogeography, Palaeoclimatology, Palaeoecology* 427, 62–78. <https://doi.org/10.1016/j.palaeo.2015.03.038>
- Teng, F.-Z., Dauphas, N., Helz, R.T., Gao, S., Huang, S., 2011. Diffusion-driven magnesium and iron isotope fractionation in Hawaiian olivine. *Earth and Planetary Science Letters* 308, 317–324. <https://doi.org/10.1016/j.epsl.2011.06.003>
- Teutsch, N., Schmid, M., Müller, B., Halliday, A.N., Bürgmann, H., Wehrli, B., 2009. Large iron isotope fractionation at the oxic–anoxic boundary in Lake Nyos. *Earth and Planetary Science Letters* 285, 52–60. <https://doi.org/10.1016/j.epsl.2009.05.044>
- Thamdrup, B., Finster, K., Hansen, J.W., Bak, F., 1993. Bacterial Disproportionation of Elemental Sulfur Coupled to Chemical Reduction of Iron or Manganese. *Applied and Environmental Microbiology* 59, 101–108. <https://doi.org/10.1128/aem.59.1.101-108.1993>
- Thamdrup, B., Canfield, D.E., 1996. Pathways of carbon oxidation in continental margin sediments off central Chile. *Limnology and Oceanography* 41, 1629–1650. <https://doi.org/10.4319/lo.1996.41.8.1629>
- Venceslau, S.S., Stockdreher, Y., Dahl, C., Pereira, I.A.C., 2014. The “bacterial heterodisulfide” DsrC is a key protein in dissimilatory sulfur metabolism. *Biochimica et Biophysica Acta (BBA) - Bioenergetics* 1837, 1148–1164. <https://doi.org/10.1016/j.bbabi.2014.03.007>
- Virtasalo, J.J., Whitehouse, M.J., Kotilainen, A.T., 2013. Iron isotope heterogeneity in pyrite fillings of Holocene worm burrows. *Geology* 41, 39–42. <https://doi.org/10.1130/G33556.1>
- Wacey, D., Kilburn, M.R., Saunders, M., Cliff, J.B., Kong, C., Liu, A.G., Matthews, J.J., Brasier, M.D., 2015. Uncovering framboidal pyrite biogenicity using nano-scale CNorg mapping. *Geology* 43, 27–30. <https://doi.org/10.1130/G36048.1>
- Wilkin, R.T., Barnes, H.L., 1996. Pyrite formation by reactions of iron monosulfides with dissolved inorganic and organic sulfur species. *Geochimica et Cosmochimica Acta* 60, 4167–4179. [https://doi.org/10.1016/S0016-7037\(97\)81466-4](https://doi.org/10.1016/S0016-7037(97)81466-4)
- Wilkin, R.T., Barnes, H.L., Brantley, S.L., 1996. The size distribution of framboidal pyrite in modern sediments: An indicator of redox conditions. *Geochimica et Cosmochimica Acta* 60, 3897–3912. [https://doi.org/10.1016/0016-7037\(96\)00209-8](https://doi.org/10.1016/0016-7037(96)00209-8)
- Wilkin, R.T., Barnes, H.L., 1997. Pyrite formation in an anoxic estuarine basin. *American Journal of Science* 297, 620–650. <https://doi.org/10.2475/ajs.297.6.620>
- Wing, B.A., Halevy, I., 2014. Intracellular metabolite levels shape sulfur isotope fractionation during microbial sulfate respiration. *Proceedings of the National Academy of Sciences* 111, 18116–18125. <https://doi.org/10.1073/pnas.1407502111>
- Yue, L., Jiao, Y., Wu, L., Rong, H., Fayek, M., Xie, H., 2020. Evolution and origins of pyrite in sandstone-type uranium deposits, northern Ordos Basin, north-central China, based on micromorphological and compositional analysis. *Ore Geology Reviews* 118, 103334. <https://doi.org/10.1016/j.oregeorev.2020.103334>
- Zerle, A.L., Farquhar, J., Johnston, D.T., Cox, R.P., Canfield, D.E., 2009. Fractionation of multiple sulfur isotopes during phototrophic oxidation of sulfide and elemental sulfur by a green sulfur bacterium. *Geochimica et Cosmochimica Acta* 73, 291–306. <https://doi.org/10.1016/j.gca.2008.10.027>

Zeyen, N., Benzerara, K., Li, J., Groleau, A., Balan, E., Robert, J. L., Estève, I., Tavera, R., Moreira, D., López-García, P., 2015. Formation of low-T hydrated silicates in modern microbialites from Mexico and implications for microbial fossilization. *Frontiers in Earth Science*, 3, 64. <https://doi.org/10.3389/feart.2015.00064>

Zeyen, N., Benzerara, K., Beyssac, O., Daval, D., Muller, E., Thomazo, C., Tavera, R., López-García, P., Moreira, D., Duprat, E., 2021. Integrative analysis of the mineralogical and chemical composition of modern microbialites from ten Mexican lakes: What do we learn about their formation? *Geochimica et Cosmochimica Acta* 305, 148–184. <https://doi.org/10.1016/j.gca.2021.04.030>

Zhao, J., Liang, J., Long, X., Li, J., Xiang, Q., Zhang, J., Hao, J., 2018. Genesis and evolution of framboidal pyrite and its implications for the ore-forming process of Carlin-style gold deposits, southwestern China. *Ore Geology Reviews* 102, 426–436. <https://doi.org/10.1016/j.oregeorev.2018.09.022>

CHAPTER 4.

PYRITE Fe CYCLING DURING BIOTIC RECOVERY: EXAMPLE WITH THE SMITHIAN-SPATHIAN BOUNDARY EVENT

Chapter 4 is dedicated to an interval of time characterized by major environmental disturbances just after the end-Permian mass extinction: the Smithian-Spathian boundary (SSB). Numerous studies documented a worldwide anoxia and rapid temperature changes which contributed to a severe diversity drop among conodonts and ammonoids (*Brayard et al., 2006; Horacek et al., 2007; Algeo et al., 2011; Song et al., 2013, 2019*). This study focused on the Lower Weber Canyon sedimentary section deposited in the Sonoma Foreland Basin (USA), which includes a variety of mineralizing and non-mineralizing microbial deposits (*Grosjean et al., 2018*). Through spatially resolved $\delta^{56}\text{Fe}$ and bulk rock $\delta^{34}\text{S}$ analyses, this chapter aims to assess the impact of potential anoxia on pyrite formed during the SSB, and to identify Fe isotope signatures associated with (1) different depositional settings and (2) microbial deposits. This work has been submitted at *Palaeogeography, Palaeoclimatology, Palaeoecology*.

PYRITE IRON ISOTOPE COMPOSITIONS TRACK LOCAL SEDIMENTATION CONDITIONS THROUGH THE SMITHIAN-SPATHIAN TRANSITION (EARLY TRIASSIC, UTAH, USA)

Marie-Noëlle Decraene^{1*}, Johanna Marin-Carbonne¹, Christophe Thomazo^{2,3}, Arnaud Brayard², Anne-Sophie Bouvier¹, Brahimsamba Bomou¹, Thierry Adate¹ and Nicolas Olivier⁴

¹Institut des Sciences de la Terre, Université de Lausanne, Lausanne, Suisse.

²Biogéosciences, UMR6282, CNRS, Université Bourgogne Franche-Comté, 6 Boulevard Gabriel, 21000 Dijon, France.

³Institut Universitaire de France.

⁴Université Clermont Auvergne, CNRS, IRD, Laboratoire Magmas et Volcans, F-63000 Clermont-Ferrand, France.

*Corresponding author contact: marie-noelle.dekraene@unil.ch

Keywords: Fe-isotope, pyrite, Early Triassic, Lower Weber Canyon

Abbreviations: Smithian/Spathian Boundary (SSB), Secondary Ion Mass Spectrometer (SIMS), Scanning Electron Microscope (SEM), Microbial Sulfate Reduction (MSR), Dissimilatory Iron Reduction (DIR)

Abstract

The late Smithian and the Smithian-Spathian boundary (SSB) are associated with harsh environmental conditions, including abrupt temperature changes, oceanic acidification and oxygen deficiency causing an additional marked loss of biotic diversity in the aftermath of the end-Permian mass extinction. Such environmental disturbances are documented worldwide through large fluctuations of the C, O, S and N biogeochemical cycles. This study presents secondary ion mass spectrometry Fe isotope analyses of sedimentary pyrites from the Lower Weber Canyon (LWC) section (Utah, USA) combined with bulk rock $\delta^{34}\text{S}_{\text{py}}$ and $\delta^{34}\text{S}_{\text{CAS}}$ analyses in order to better understand the redox changes in different environmental settings along a ramp depositional system through the SSB. $\delta^{56}\text{Fe}$ analyses show a large variability along the studied ramp system of $\sim 7\text{‰}$ (from -1.99 to $+5.39\text{‰}$), over a set of 350 analyses. Bulk sulfide sulfur isotope analyses, performed on 29 samples, show $\delta^{34}\text{S}_{\text{py}}$ varying from -20.52 to $+16.27\text{‰}$. The inner ramp domain is characterized by a mean negative $\delta^{34}\text{S}_{\text{py}}$ values of -11.41‰ . A progressive ^{34}S -enrichment (up to $+16.27\text{‰}$) is recorded in pyrites from mid and outer ramp settings. Carbonate associated sulfate (CAS) sulfur isotope analyses, performed on 5 samples, show steady $\delta^{34}\text{S}_{\text{CAS}}$ ($+30.19 \pm 2.19\text{‰}$). Variations in $\delta^{34}\text{S}_{\text{py}}$ are interpreted as reflecting the degree of connection between porewaters and the overlying water column. Multiple lines of evidence point to a fully oxygenated water column and thus restricts pyrite formation in the sediment. Both the sedimentary environment and the nature of deposits seem to control $\delta^{56}\text{Fe}_{\text{py}}$. In the inner ramp, heavy average $\delta^{56}\text{Fe}_{\text{py}}$ values of $+2.05\text{‰}$ are only observed in microbially induced sedimentary structures (MISS), which record partial Fe-oxide reduction and oxidation reactions occurring at the biofilm scale. In the absence of MISS, $\delta^{56}\text{Fe}_{\text{py}}$ inner ramp values are lighter ($\delta^{56}\text{Fe}_{\text{mean}} = +0.90\text{‰}$) and reflect total reduction of Fe-oxides. In more distal and deeper mid and outer ramp settings, Fe isotope compositions are controlled by microbially-produced H_2S that scavenged iron into sulfides. This study unravels local redox state changes in the upper part of some marine sediments by coupling Fe and S isotope systematics. It demonstrates that pyrite grains, and their sulfur and iron isotope compositions, formed throughout the SSB should be used with caution to infer the redox state of the ocean after the Permian-Triassic biotic crisis.

1. Introduction

Only ~2 Myr after the devastating end-Permian mass extinction (~252 Ma), the Smithian-Spathian Boundary (SSB) has undergone successive and abrupt environmental and biotic changes (e.g. *Galfetti et al., 2007*). Significant disturbances of the global carbon, sulfur, oxygen, and nitrogen biogeochemical cycles underline sustained environmental stresses. These include climate warming up to the beginning of the late Smithian, followed by a rapid cooling across the latest Smithian and the SSB (*Goudemand et al., 2019; Zhang et al., 2019*), the spread of anoxia through ocean stratification (*Song et al., 2019*) or development of oxygen minimum zones (*Algeo et al., 2011*), and ocean acidification potentially linked with greenhouse gases released by large igneous province eruption (*Grasby et al., 2013; Zhao et al., 2020*). All combined, these deleterious conditions led to a marked loss in ecosystem diversity and a severe extinction of several nekton-pelagic organisms during the late Smithian (*Orchard, 2007; Brayard et al., 2006; Jattiot et al., 2016*). Several proxies such as sulfate and sulfide $\delta^{34}\text{S}$, paired carbonate and organic matter $\delta^{13}\text{C}$, Ce anomalies, trace elements (e.g. Mn, V, U, Mo, Mo/Al ratio), iron speciation and size of framboid pyrites suggest occurrences of transient anoxia in the water column that could have spread on continental shelves (*Grasby et al., 2013; Song et al., 2013; Zhang et al., 2015, 2019; Elrick et al., 2017; Song et al., 2019*). Although anoxic and/or euxinic conditions seem to be dominant in the Early Triassic deep ocean, well-oxygenated shallow marine environments and diversified and complex ecosystems are also documented (*Beatty et al., 2008; Hautmann et al., 2011; Collin et al., 2015; Brayard et al., 2017; Olivier et al., 2018; Smith et al., 2021*). Reconstructing the redox state of the water column together with the sediment porewater is therefore key to better understand the evolution of the environmental conditions in space and time that prevailed through the late Smithian and the SSB, and that may have markedly influenced (spatially and temporally) the post-SSB biotic recovery.

As a mineral made of redox sensitive elements, pyrite (FeS_2) is used to infer the oxygenation state of the ocean through the study of its morphology, size, trace element content and isotope (S and/or Fe) compositions (*Wilkin et al., 1996; Wilkin and Barnes, 1997; Shen et al., 2003; Bond and Wignall, 2010; Gregory et al., 2015*). Oxidation of Fe(II) into Fe(III) is associated with a large equilibrium fractionation producing ^{56}Fe -depleted dissolved Fe(II) (*Welch et al., 2003*), which can be later recorded in Fe-bearing minerals such as pyrite. Large ^{56}Fe -depletion during redox processes is however only expressed for the partial reaction of the dissolved iron reservoir, i.e., during partial oxidation of aqueous Fe^{2+} (*Rouxel et al., 2005*). Therefore, assuming that redox reaction occurred through Earth history and that $\delta^{56}\text{Fe}$ values reflect primary processes, secular variations of Fe isotope compositions can be interpreted in terms of global oxygenation state changes. Other studies propose that light $\delta^{56}\text{Fe}$ values reflect transport along the chemocline of microbially reduced dissolved Fe(II) from the shelf to the basin (*Johnson et al., 2005; Severmann et al., 2008*). Alternatively, another scenario, which does not require Fe redox cycling, suggests that $\delta^{56}\text{Fe}$ values reflect primarily the rate of pyrite precipitation (kinetic or equilibrium) that is

highly dependent of the sulfur availability (Guilbaud *et al.*, 2011; Mansor and Fantle, 2019). Therefore, the interpretation of pyrite iron isotope compositions in terms of water oxygenation state can be obscured by the involvement of redox and non-redox processes, inheritance of isotope fractionation of the Fe source, size of the sulfide reservoir, and early diagenetic processes (Severmann *et al.*, 2008; Virtasalo *et al.*, 2013; Busigny *et al.*, 2014; Marin-Carbonne *et al.*, 2020). Further, on a more local scale, processes occurring within the upper part of the sedimentary column (from the upper centimeters to meter depth), can produce large Fe isotope composition ranges. Such variations are partially to entirely decoupled from global biogeochemical cycling in the water column, resulting from the isotope distillation of Fe(II) or Fe-oxides reservoir in the sediment (Archer and Vance, 2006; Lin *et al.*, 2020). Some ambiguities in the interpretation of the pyrite $\delta^{56}\text{Fe}$ can be lifted by pairing this measurement to the $\delta^{34}\text{S}$ signal. For instance, positive covariation between pyrite $\delta^{56}\text{Fe}$ and $\delta^{34}\text{S}$ signals through Archean-Paleoproterozoic transition suggests an expansion of the sulfidic Fe sink (Heard and Dauphas, 2020). Such positive covariations have also been evidenced in 2.7 Ga sedimentary pyrite from the Belingwe greenstone belt and interpreted as early diagenetic signatures of coexisting microbial Fe and S reduction (Archer and Vance, 2006).

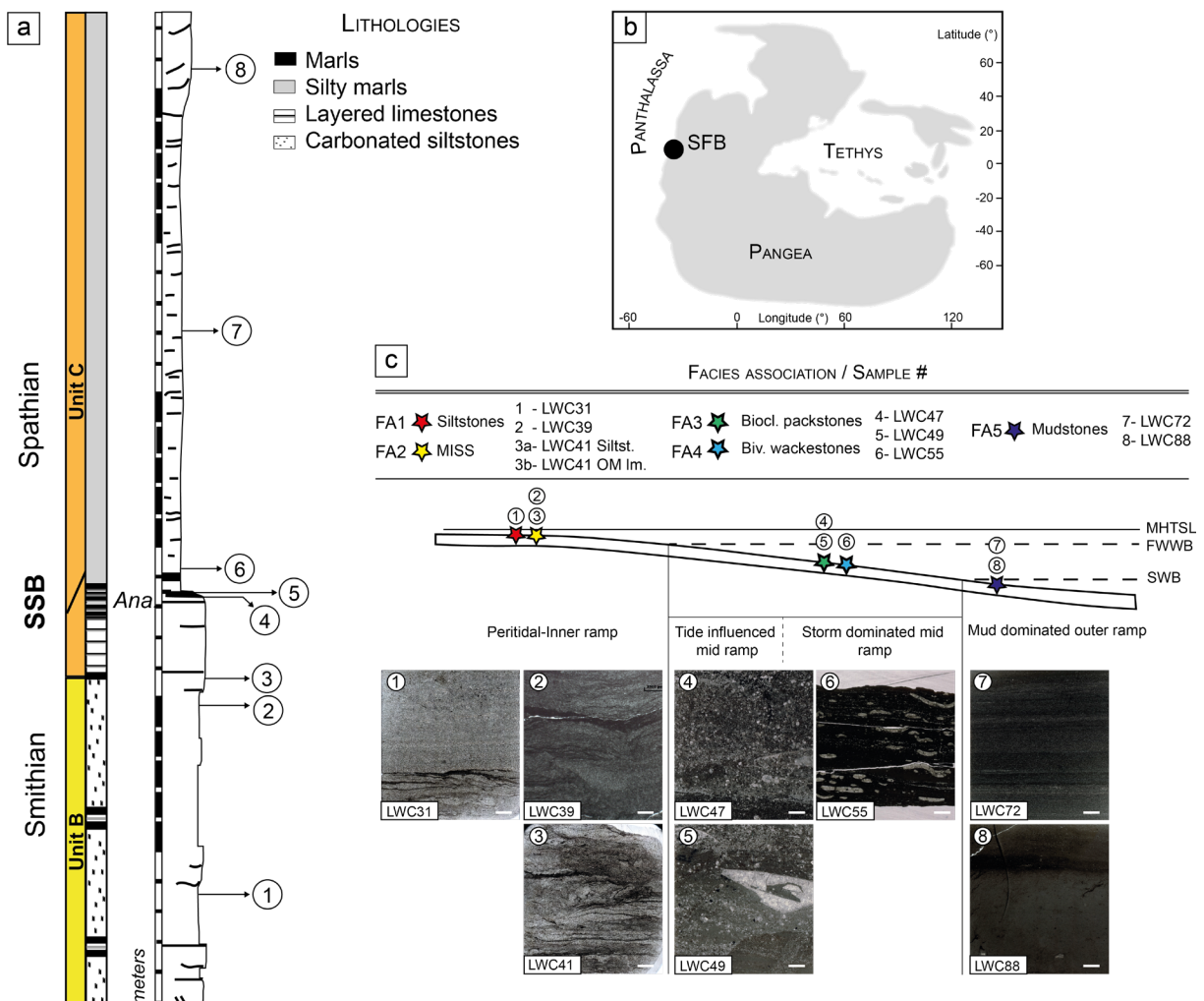
The aim of this study is to distinguish in the context of the SSB whether pyrite paired Fe-S isotope signatures (1) record redox condition variations of the seawater, (2) reflect variations of the Fe/S availability or (3) are controlled by early diagenesis and/or microbial processes within the sediment or at the seawater/sediment interface. For that, we present spatially resolved $\delta^{56}\text{Fe}$ associated with chemostratigraphic $\delta^{34}\text{S}$ records along the Lower Weber Canyon sedimentary succession (Fig. 1a; Utah, USA), which is characterized by various sediments deposited between shallow inner to deeper outer ramp settings. The combination of petrological observations, in situ $\delta^{56}\text{Fe}_{\text{py}}$ by SIMS, bulk rock $\delta^{34}\text{S}$ and total organic carbon concentrations allows to unravel pyrite formation pathways within the sediment from different facies.

2. Materials and methods

2.1. Geological context, studied section and samples

During the Permian-Triassic interval, the near equatorial region of western Pangea was an active tectonic compression zone, leading to the formation of the Sonoma orogeny and the associated Sonoma Foreland Basin (SFB; Fig. 4.1; Burchfiel and Davis, 1975; Ingersoll, 2008; Dickinson, 2013). Lower Triassic sediments of the SFB mainly cover present-day eastern Idaho, eastern Nevada and Utah (USA; Caravaca *et al.*, 2018). The Early Triassic sea-level rise resulted in a sedimentary succession exhibiting continental terrigenous conglomerates and sandstones of the Moenkopi Group on the south and eastern sides of the basin, interfingering with marine carbonates of the Thaynes Group towards the north and western sides (Paull and Paull, 1993;

Lucas et al., 2007; Brayard et al., 2013). In the SFB, a transgression that corresponds to the second 3rd order T-R (transgressive-regressive) sequence of the Smithian is recorded (Haq et al., 1987; Embry, 1997), which was controlled by regional tectonics and climate (Olivier et al., 2014; Caravaca et al., 2018; Brayard et al., 2020). Calibrations of late Smithian to early Spathian sedimentary sections within the basin are based on ammonoid biostratigraphy (Guex et al., 2010; Brayard et al., 2013, 2021). The late Smithian Anasibirites beds represent the maximum flooding at the scale of the basin (Brayard et al., 2013, 2020). The SFB is also characterized by occurrence of morphologically various, mineralized or not, microbial deposits, mainly in the southern part of the SFB (Schubert and Bottjer, 1992; Pruss et al., 2004; Brayard et al., 2011; Olivier et al., 2014, 2016, 2018; Woods, 2014; Vennin et al., 2015; Grosjean et al., 2018; Kirton and Woods, 2021). This study focuses on the Lower Weber Canyon (LWC) section, for which petrographic descriptions and interpretation in terms of depositional environments are detailed in Grosjean et al. (2018).



According to these authors, the LWC section is divided in four lithologic units (A-D), but this study concentrates on the two units (B and C) preceding and including the SSB (**Fig. 4.1**). Unit B is 111 m thick and mainly made of carbonated siltstones, including organic-rich laminae described as microbially induced sedimentary structures (MISS), and few levels of bioclastic calcarenites. Siltstone-rich sediments of the Unit B reflect a peritidal depositional environment in an inner ramp system. Sediments of this unit are of middle Smithian age as they belong to the Meekoceras ammonoid assemblage (*Grosjean et al., 2018; Brayard et al., 2021*). The 36 m-thick Unit C consists of silty mudstones that are intercalated with bioclastic limestones. The lower part of this unit includes the late Smithian Anasibirites ammonoid assemblage (*Brayard et al., 2021*) and the SSB. The mudstone-rich deposits of the Unit C reflect a mid to outer ramp setting that occasionally to rarely recorded storm events. Eight rock samples were collected in the Units B and C, thus representing different depositional environments distributed along an inner to outer ramp system (**Fig. 4.1**). Their deposition during the SSB, the diversity of depositional environments (from peritidal siltstones to deeper outer ramp mudstones), and associated facies including occurrences of MISS in a shallow and proximal environment, are relevant parameters to decipher controlling parameters on Fe isotope signatures of pyrite. A description of facies associations and corresponding depositional environments is detailed in the **section 3.1**.

2.2. Methods

2.2.1. Petrographic observations

Petrographic descriptions were carried out on polished thick sections using a Scanning Electron Microscope (SEM) at ISTE Lausanne (Tescan Mira LMU). Backscattered electron images were performed at a working distance of 21 mm using a voltage of 20 kV and a current of 1.5 nA. Semi quantitative spot analyses were done by energy dispersive X ray spectrometry to determine elemental composition of the sulfides. Mineralogy analyses of all samples were performed at ISTE Lausanne using a X-TRA Thermo-ARL diffractometer following the procedure of *Kübler (1983)* and *Adatte et al. (1996)*.

The chemical composition of pyrite was investigated by Electron Probe Micro-Analyzer (EPMA) using a JEOL JXA-8530F at ISTE Lausanne in order to quantify the trace content of zoning pyrite. The acceleration voltage was 15 kV and beam current was 15 nA focused in 3 μm . Reference materials, including sulfides, oxides, and silicates, were tested before the analysis of S, Fe, Co, Mn, Pb, Ti, Cr, Zn, Cu and Ni. Detection limits were 133 ppm for S, 130 ppm for Fe, 141 ppm for Co, 129 ppm for Mn, 327 ppm for Pb, 79 ppm for Ti, 145 ppm for Cr, 238 ppm for Zn, 199 ppm for Cu and 150 ppm for Ni.

Carbonaceous matter has been characterized by Raman spectroscopy. Raman data were obtained using a Horiba Jobin Yvon LabRAM HR800 spectrometer (ISTE, UNIL) in a confocal configuration equipped with an Ar⁺ 532 nm laser and a CCD detector. Measurements

were performed at room temperature on thin sections, with a laser power delivered at the sample surface <1 mW to prevent thermal damages. This technique allows to document the structural organization of the aromatic skeleton of carbonaceous matter, and to estimate the peak metamorphic temperature experienced by the carbonaceous matter (*Beyssac et al., 2002*). Peak temperature estimations were done following the methodology proposed by (*Kouketsu et al., 2014*).

2.2.2. Hg concentrations and TOC contents

Mercury concentrations were conducted using a Zeeman R-915F (Lumex, Saint-Petersburg, Russia) high-frequency atomic absorption spectrometer at the University of Lausanne. Hg was extracted by thermal evaporation at 700°C from solid samples that were previously powdered. Analyses were bracketed by the measurement of a certified external standard (GSD-11, Chinese alluvium, Hg concentration: 72 ±6 ppb) and two aliquots were systematically analyzed. To be exempt of biased Hg peaks due to affinity of Hg with organic carbon and sulfide, measured Hg concentrations were normalized to TOC and sulfur concentrations.

Total organic carbon (TOC in wt.%) contents were obtained through Rock-Eval 6 analyses at University of Lausanne following the procedure of *Espitalie et al. (1985)* and *Behar et al. (2001)*. The reference material IFP 160000 (French Institute of Petroleum) was used to calibrate the measurements and the precision was <0.1%. Analyses consist of a combined pyrolysis of ~60 mg of powdered samples followed by oxidation of the residue.

2.2.3. Bulk rock $\delta^{34}\text{S}$

Sulfide sulfur was retrieved using a conventional wet chemical extraction at the Biogéosciences Laboratory, Dijon, France. Acid volatile sulfide (AVS), representing monosulfides, and chromium reducible sulfur (CRS) consisting primarily of pyrite were extracted sequentially. First, AVS was liberated using cold concentrated HCl for 2 hours. If any, resulting hydrogen sulfide was precipitated as Ag_2S with a 0.3 M AgNO_3 solution. Subsequently, CRS was released using a hot and acidic 1.0 M CrCl_2 solution following the method described in *Gröger et al (2009)*. The resulting H_2S was precipitated as Ag_2S . After centrifugation, the silver sulfide precipitate was washed several times with deionized distilled water and dried at 50°C for 48 hours in an oven and weighted. Mass balance was used to calculate the amount of AVS and CRS. Concentrations in ppm are reported individually in **Table S1** (note that monosulfides were below the detection limit in all samples).

CAS sulfur was retrieved using a wet chemical extraction. Fifty grams of carbonate samples (with carbonate contents typically >70 wt.% of the total rock) were powdered, soluble sulfates being leached by a 1.7 M NaCl solution for 4 hours, followed by four rinses in deionized water. This step was repeated five times and the powder was then dissolved in 4N HCl (12h). The acidified samples were then filtered, on a 0.45- μm nitrocellulose paper and an excess of 250 g.l-1 of BaCl_2 solution was added to the filtrate to precipitate BaSO_4 . After centrifugation,

the barium sulfate precipitate was washed several times with deionized distilled water and dried at 60°C for 24 hours in an oven.

The $\delta^{34}\text{S}$ measurements were performed at the Biogéosciences Laboratory, Dijon, France, on SO_2 molecules via combustion of $\sim 500 \mu\text{g}$ of samples (silver sulfide and barium sulfate) homogeneously mixed with an equal amount of tungsten trioxide using a Vario PYRO cube (Elementar GmbH) connected online via an open split device to an IsoPrime IRMS system (IsoPrime, Manchester, UK). International standards IAEA-S-1, IAEA-S-2, IAEA-S-3 and NBS-127 were used for calibration assuming $\delta^{34}\text{S}$ values of -0.3, +22.7, -32.3 and 20.3‰ (VCDT), respectively. Analytical reproducibility was better than $\pm 0.4\%$ (1σ) based on replicates for standard materials and samples.

2.2.4. Fe isotope analyses by SIMS

Iron isotope compositions were measured over four SIMS sessions (March 2020, June 2020, November 2020, September 2021) using the Cameca ims 1280 HR2 at the SwissSIMS (University of Lausanne). Iron isotope compositions are expressed in delta notation, reporting permil variations of the $^{56}\text{Fe}/^{54}\text{Fe}$ ratios normalized to IRMM-014 as the following:

$$\delta^{56}\text{Fe} = \left[\frac{\left(\frac{^{56}\text{Fe}}{^{54}\text{Fe}} \right)_{\text{sample}}}{\left(\frac{^{56}\text{Fe}}{^{54}\text{Fe}} \right)_{\text{IRMM014}}} - 1 \right] * 1000$$

In order to preserve high vacuum conditions of $\sim 10^{-9}$ mbar in the analytical chamber and avoid hydride formations, thick sections were polished and pressed into one-inch indium mounts. Balmat pyrite standard was used over the sessions to assess the stability of the instrument ($\delta^{56}\text{Fe} = -0.40 \pm 0.01\%$) and was included in each sample mount. The conductivity of the sample surface was ensured by a 35 nm-thick gold coating. A total of 350 analyses of pyrite was performed in 8 different samples following the method described in *Decraene et al. (2021)*. Briefly, a 10 kV, 3 nA Gaussian $^{16}\text{O}^-$ primary beam was focused into a 2.5 to 3 μm spot. $^{52}\text{Cr}^+$, $^{54}\text{Fe}^+$, $^{56}\text{Fe}^+$ and $^{57}\text{Fe}^+$ secondary ions were collected simultaneously by electron multipliers (L2 for $^{52}\text{Cr}^+$) and off-set faraday cups (C for $^{54}\text{Fe}^+$, H1 for $^{56}\text{Fe}^+$ and H'2 for $^{57}\text{Fe}^+$). We used an entrance slit width of 61 μm and the slit 3 of the multicollection to obtain a Mass Resolving Power at ~ 7000 (interference of $^{53}\text{CrH}^+$ on $^{54}\text{Fe}^+$). The field aperture was set at 2000 μm and the energy slit at 50 eV. A 90 s presputtering time was applied to remove the surface contamination, followed by secondary ion beam centering and background detector measurements. Then, data acquisition is conducted for 300 seconds. Typical count rate for $^{56}\text{Fe}^+$ on Balmat standard was $4.50\text{E}+7$ counts per second (cps) and the mean reproducibility was $\pm 0.21\%$ (2SD). Instrumental mass fractionation (IMF) was corrected by standard bracketing.

3. Results

3.1. Facies description

According to *Grosjean et al. (2018)*, the eight studied samples belong to five different facies associations. These facies are distributed along a ramp depositional profile from proximal and shallow siliciclastic dominated deposits to more distal and deeper mud-dominated sediments (**Fig. 4.1**). The inner peritidal ramp setting is dominated by two facies associations, carbonated-siltstones (FA1) and organic-rich laminae (FA2). FA1 consists of micrite, quartz, phyllosilicates and dolomite (see supplementary materials; **Fig. S1**). Small fragmented bioclasts are observed as well as accessory minerals such as apatite, zircon and anatase. This facies association corresponds to samples LWC31 and LWC41-3a. FA2 is composed of undulated organic-matter laminae that are laterally discontinuous and locally reworked in a carbonated and silty matrix. These organic laminae and chips are interpreted by *Grosjean et al. (2018)* as MISS. Samples LWC39 and LWC41-3b are attributed to FA2.

Samples from the mid ramp setting reflect two facies associations, bioclastic packstones to wackestones (FA3; LWC47 and LWC49) and bioclastic wackestones (FA4; LWC55). FA3 consists of micrite, phyllosilicates and quartz. Few apatites and oxides are also observed (**Fig. S1**). Bivalves and ammonoids shells are recrystallized by sparite. FA4 is made of sparite-filled bivalves following a planar distribution in a micritic dominated matrix with common small quartz grains. Apatite and zircon grains are present as accessory minerals.

Samples from the mud-dominated outer ramp correspond to a mudstone facies association (FA5; LWC72 and LWC88). These sediments deposited closed to the mid to outer ramp transition as they consist of mudstone sometimes interbedded with rare thin layers made of small quartz grains. Apatite, zircon, anatase and chalcopyrite are present as accessory mineral phases.

3.2. Carbon, sulfur and mercury contents

Total organic contents vary from 0.04 to 0.49 wt.% and show an enrichment across the SSB, with a maximum TOC content recorded in LWC55 (**Fig. 4.2**). TOC concentrations for samples LWC39 and LWC41 are biased due to the heterogeneous distribution of organic-rich laminae in the analyzed samples. Sulfur contents of 29 LWC samples (from LWC31 to LWC70) vary between 21 and 12357 ppm with a mean value of 2585 ppm (**Fig. 4.2** and **Table S1**). Sulfur content is highly variable with highest concentrations recorded in samples deposited during and immediately after the SSB. Inner ramp samples (LWC31 to LWC42) show S concentrations between 21 and 3780 ppm, with an average of 1222 ppm (**Table S1**). There is no difference in sulfide content between samples from siltstone facies (FA1) and MISS facies (FA2). Sulfur concentrations in samples from mid ramp setting range from 296 to 11472 ppm and show the highest average value (4232 ppm). Samples from the outer ramp system exhibit the larger

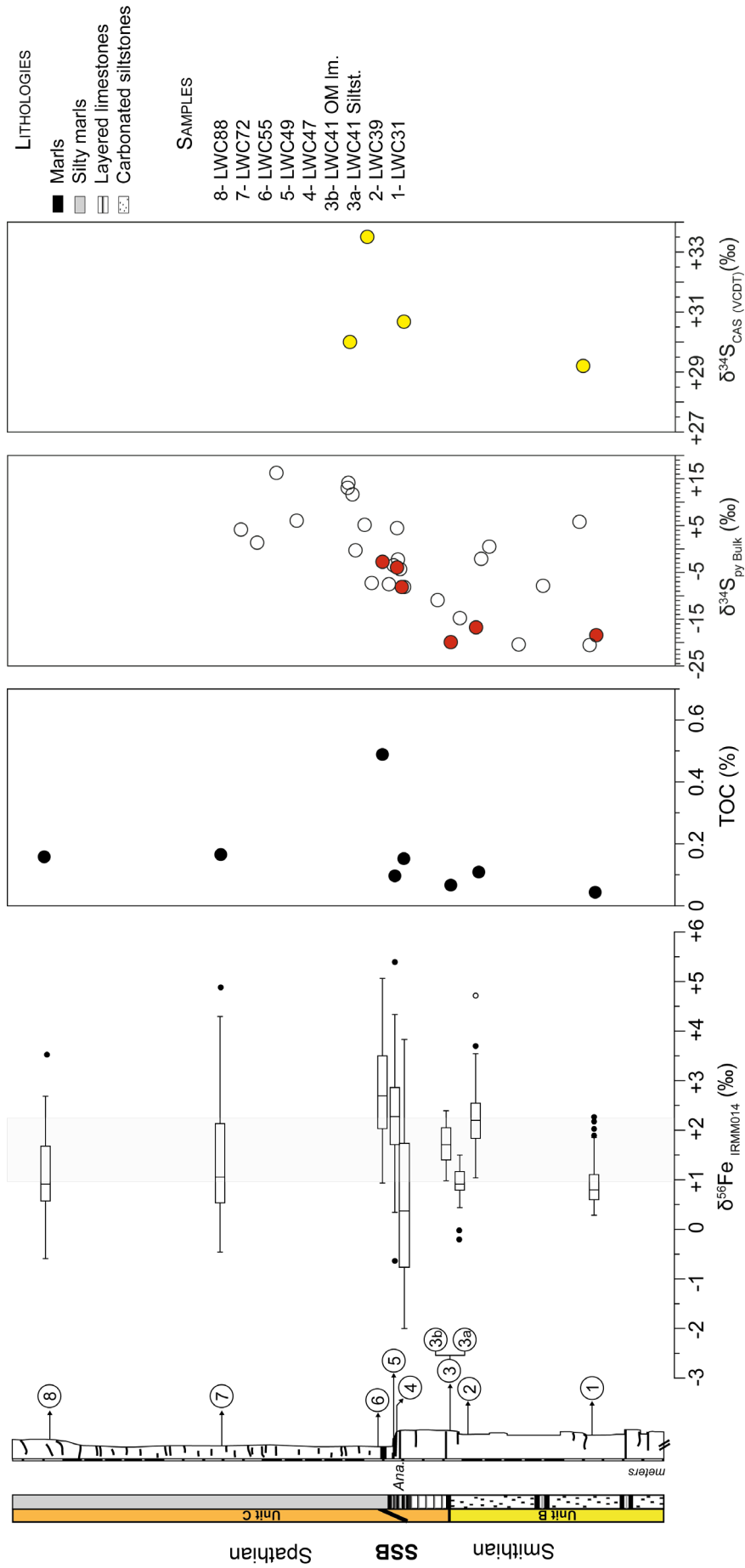


Figure 4. 2: Evolution of Fe isotope compositions measured by SIMS on 8 LWC samples with corresponding total organic carbon concentrations (in %), pyrite $\delta^{34}\text{S}$ values on 29 samples (LWC31 to LWC70) and carbonate associated sulfate (CAS) $\delta^{34}\text{S}$ values on 4 samples of the section. The simplified log reports lithologies and positions of samples measured by SIMS.

variation, from 61 to 12358 ppm. Mercury concentrations vary between 2.70 and 25.55 ppb (Table S2, Fig. S3). Normalization with TOC and S contents does not show any Hg enrichment in the studied samples.

3.3. Bulk pyrite and CAS $\delta^{34}\text{S}$

The $\delta^{34}\text{S}_{\text{py}}$ shows large variations from -20.52 to $+16.27\text{‰}$ (Fig. 4.2, Table S1). Except for three samples, only negative $\delta^{34}\text{S}$ values are recorded in the inner and the mid ramp systems, while the majority of $\delta^{34}\text{S}$ values in the outer ramp are positive. The inner ramp setting shows highly variable $\delta^{34}\text{S}$ values, ranging from -20.52 to $+5.82\text{‰}$, with an average value of $-11.41 \pm 9.31\text{‰}$ (1SD). The mid ramp setting documents small variations with a $\delta^{34}\text{S}$ average of $-4.04 \pm 3.97\text{‰}$ (1SD). The outer ramp system displays the highest S isotope compositions, ranging from -7.26 to $+16.27\text{‰}$, and an average value of $+6.44 \pm 7.40\text{‰}$ (1SD). The $\delta^{34}\text{S}$ signal of sedimentary sulfide shows an ^{34}S enrichment tendency from the base to the top of the LWC section. The $\delta^{34}\text{S}_{\text{CAS}}$ signal measured on five samples across the section does not exhibit noticeable secular variations (Fig. 4.2). Indeed, $\delta^{34}\text{S}_{\text{CAS}}$ values range from 29.20 to 33.51‰ , with a mean value of $30.19 \pm 2.19\text{‰}$ (1SD).

3.4. Pyrite and organic matter description

In the eight studied samples, pyrite grains display various morphologies, categorized as euhedral, framboid, aggregate and framboid with secondary overgrowth (Fig. 4.3 and Fig. S4) and range in size between 5 to $\sim 100 \mu\text{m}$ (Fig. S5). Only LWC31 displays a large pyrite nodule of $\sim 3 \text{ mm}$ wide. The absence of large euhedral pyrite following a linear pattern suggests that

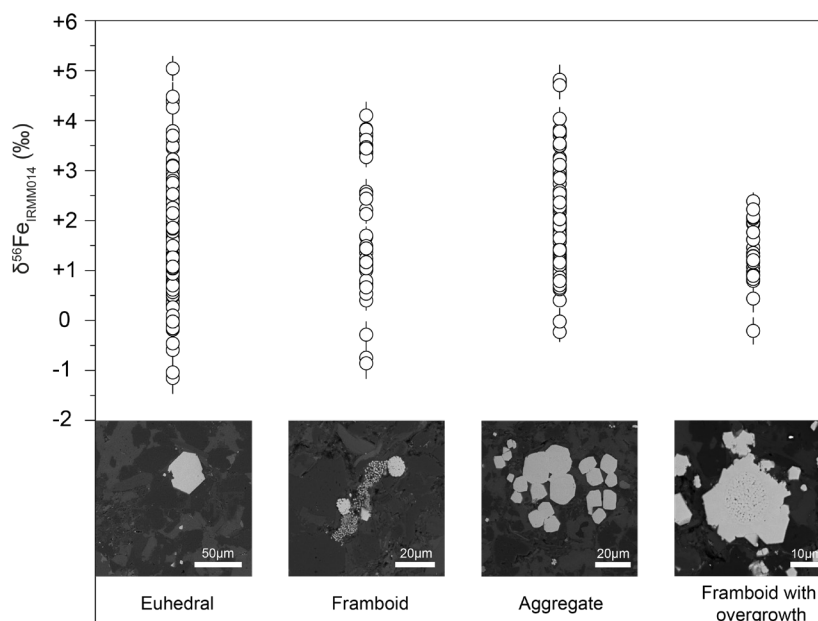


Figure 4. 3: $\delta^{56}\text{Fe}_{\text{py}}$ as a function of pyrite morphologies: euhedral, framboid, aggregate and secondary overgrowth. No clear difference is observed between each morphology.

their growth do not depend on fluid circulation system. Electronic microprobe analyses revealed chemical zoning in aggregated pyrite from LWC49 (**Fig. S6**). These zonations are Ni-enriched but due to the size of this pyrite and the spatial resolution of electron beam, Ni concentrations were not always precisely quantified. A close association between pyrite and organic matter is shown in samples LWC31, LWC39, LWC41 and LWC88 (**Fig. S7**). All Raman spectra obtained on these laminae show characteristics of poorly ordered carbonaceous material (**Fig. S8**), corresponding to maximum temperature of 150°C consistent with burial diagenesis (*Heydari and Moore, 1989*).

3.5. In situ iron isotope compositions

Large variations of pyrite $\delta^{56}\text{Fe}$ values, from -1.99 to +5.39‰, are evidenced over 350 analyses through the studied section (**Fig. 4.2; Table S3**). In the inner ramp deposits (FA1 and FA2), 143 pyrite analyses show $\delta^{56}\text{Fe}$ values ranging from -0.21 to +4.72‰, and an average $\delta^{56}\text{Fe}_{\text{py}}$ value of +1.32‰ (**Fig. 4.4**). In the mid ramp sediments (FA3 and FA4), the 125 $\delta^{56}\text{Fe}_{\text{py}}$ values display the largest range from -1.99 to +5.39‰, and an average $\delta^{56}\text{Fe}_{\text{py}}$ value of +2.10‰. In the outer ramp deposits (FA5), $\delta^{56}\text{Fe}_{\text{py}}$ values (n=82) range from -0.59 to +4.88‰, with an average $\delta^{56}\text{Fe}_{\text{py}}$ value of +1.28‰ (**Fig. 4.4**). In details, the inner ramp FA1 includes samples LWC31 (n=77) and LWC41-3a (n=13), showing respective $\delta^{56}\text{Fe}_{\text{py}}$ values from +0.28 to +2.27‰ ($\delta^{56}\text{Fe}_{\text{mean}}=+0.91‰$) and from -0.21 to +1.50‰ ($\delta^{56}\text{Fe}_{\text{mean}}=+0.84‰$) (**Fig. 4.4**). The inner ramp FA2 includes samples LWC39 (n=30) and LWC41-3b (n=23) with isotopically heavier $\delta^{56}\text{Fe}$ values, varying respectively from +1.04 to +4.72‰ ($\delta^{56}\text{Fe}_{\text{mean}}=+2.29‰$) and from +0.98 to +2.39‰ ($\delta^{56}\text{Fe}_{\text{mean}}=+1.71‰$). Fe isotope compositions of mid ramp FA3, including samples LWC47 (n=25) and LWC49 (n=52), range from -1.99 to +3.83‰ ($\delta^{56}\text{Fe}_{\text{mean}}=+0.46‰$) and from -0.63 to +5.39‰ ($\delta^{56}\text{Fe}_{\text{mean}}=+2.30‰$), respectively. Mid ramp FA4 corresponds to sample LWC55 (n=48), which shows $\delta^{56}\text{Fe}$ values ranging from +0.93 to +5.06‰, with the heaviest $\delta^{56}\text{Fe}_{\text{mean}}$ value of +2.73‰. Outer ramp FA5 is represented by samples LWC72 (n=35) and LWC88 (n=47) that have respective $\delta^{56}\text{Fe}$ values ranging between -0.46 and +4.88‰ ($\delta^{56}\text{Fe}_{\text{mean}}=+1.55‰$) and from -0.59 to +3.52‰ ($\delta^{56}\text{Fe}_{\text{mean}}=+1.08‰$). No correlation between $\delta^{56}\text{Fe}$ values and S content has been observed (**Fig. S2**).

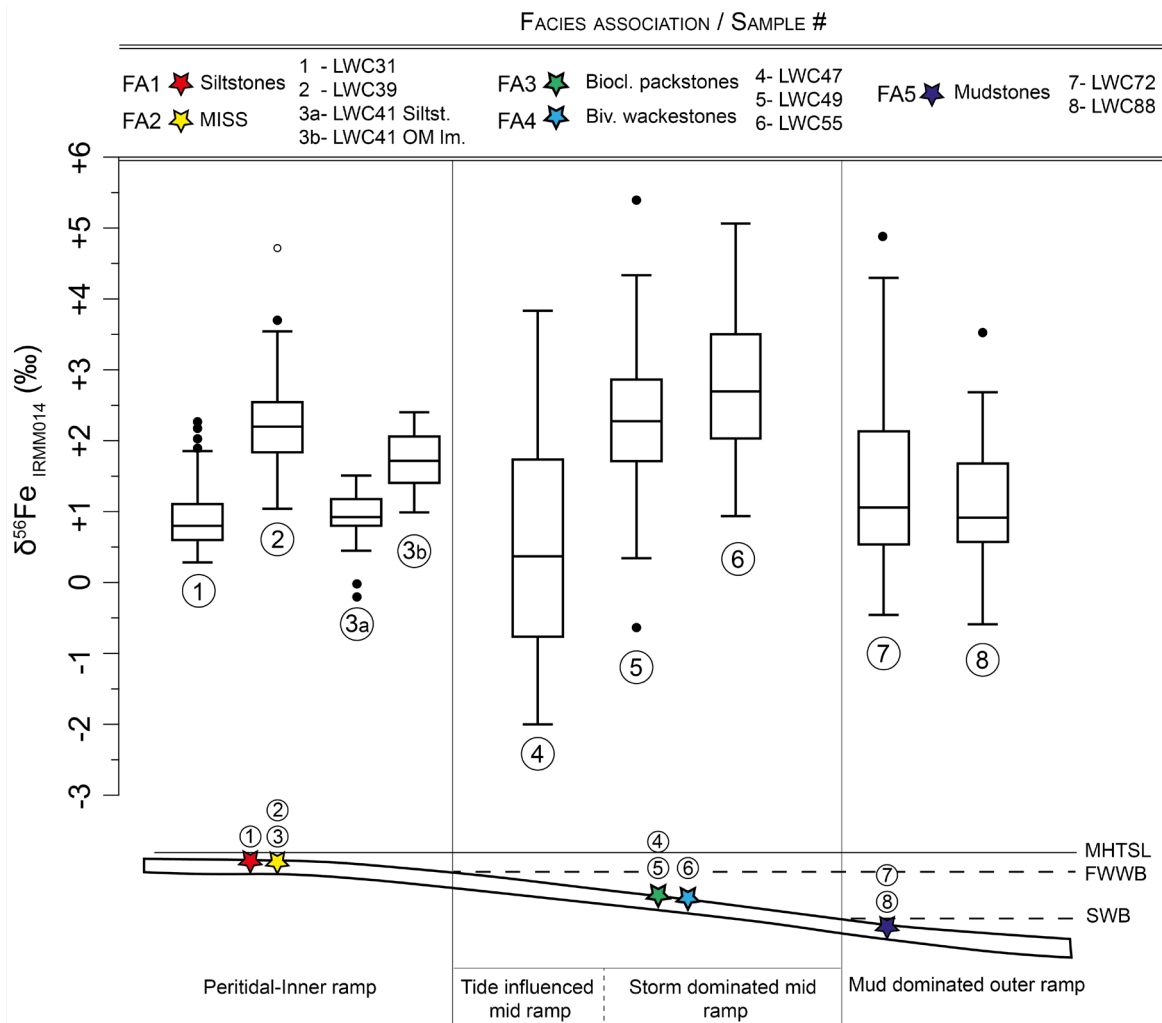


Figure 4. 4: Fe isotope compositions of pyrite from the Lower Weber Canyon section as a function of depositional environments along a ramp system. The different star colors refer to the corresponding facies association. Fe isotope compositions are reported using outlier box plot representation. Line through the box is the median and the edges of the box represent the quartiles (lower line is the 1st quartile Q1, i.e. the 25th percentile, and upper line is the 3rd quartile Q3, i.e. the 75th percentile). Lower and upper whiskers represent 1.5*IQR (interquartile range, i.e. the range between Q1 and Q3). The minimum and maximum are marked by small lines at the end of whiskers and represent respectively the lowest and highest values of the distribution, excluding outlier values of the dataset (filled and unfilled dots below and above whiskers). See Fig. 1 for abbreviations.

4. Discussion

4.1. Pyrite precipitation locus and environmental redox conditions

Abiotic or biogenic reduction of sulfate and Fe-oxide enhances accumulation of iron and sulfide that lead to pyrite formation either in the water column, named syngenetic pyrite, or in the sediment porewaters, named sedimentary pyrite (*Raiswell et al., 2011*). To determine if the studied pyrite grains have a syngenetic (water column) or a sedimentary (early diagenetic) origin, it is essential to examine whether the redox state of the Early Triassic ocean was consistent with water column sulfide accumulation. Indeed, precipitation of pyrite in the water column only occur under stratified or pervasive euxinic (sulfidic and anoxic) conditions (*Raiswell and Berner, 1986; Wilkin and Barnes, 1997*). Carbon isotope chemostratigraphy in carbonate and organic matter and multiple sulfur isotopes in pyrite suggest euxinia or anoxia affecting shallow marine environments in South China and Spitsbergen (*Horacek et al., 2007; Takahashi et al., 2015; Zhang et al., 2015; Wignall et al., 2016*). In contrast, a study reporting elemental concentrations and pyrite $\delta^{34}\text{S}$ values of the Mineral Mountains section (Utah, USA) suggests sediment deposition under oxic to suboxic conditions in shallow inner to outer ramp settings (*Thomazo et al., 2016*). The Mineral Mountains section being part of the same sedimentary basin than LWC, water column conditions can reasonably be considered similar. Well-oxygenated water column at LWC is further supported by tide and storm sediment reworking, coupled to a relatively low S content (mean S content= 2585 ppm) and a low TOC content (mean TOC= 1477 ppm) which are not expected under euxinic conditions. Importantly, the constant S isotope value of sulfate reservoir, represented by CAS, around +30.19‰ proves that pyrite S isotope composition variations are not driven by global change of the oceanic sulfate reservoir. Therefore, precipitation of syngenetic pyrite within the water column is not supported here. In this study, the homogeneity of CAS $\delta^{34}\text{S}$ signatures, the close association between pyrite and OM, and the large range of pyrite morphology, with various degree of complexity (i.e. framboids with overgrowth) suggest that sulfide formed in the sediment porewaters. Two sedimentary pyrite generations can be distinguished as (1) synsedimentary pyrite associated with MISS, which likely formed during the activity of the biofilm close to the water column/sediment interface and (2) early diagenetic pyrite, still controlled by a microbial activity spreading over the upper tens of centimeters of the sediment. Both are largely dependent of the degree of connectivity of the sediment porewaters with the overlying water column (cf. **section 4.3**).

Pyrite formation may also result from fluid circulation during late diagenesis (*Raymond, 1996; Slotznick et al., 2022*). Nevertheless, the absence of large euhedral pyrite veins, extended recrystallization features, and the preservation of framboid pyrite associated with poorly crystalline carbonaceous material is consistent with a limited fluid circulation contribution. Thus, synsedimentary to early diagenetic processes likely largely controlled Fe isotope signatures of

pyrites in the studied samples during the late Smithian and across the SSB.

4.2. Iron isotope kinetic and equilibrium isotope effects

Pyrite precipitation associated with various degree of kinetic and equilibrium fractionation is a possible hypothesis to explain large Fe isotope range of isotope composition (*Mansor and Fantle, 2019*). This hypothesis links Fe/S ratio changes with highly variable Fe pyrite isotope signatures. Indeed, an elevated Fe/S ratio enhances the expression of kinetic fractionation, i.e. formation of pyrite with negative $\delta^{56}\text{Fe}$ values, in a sulfate (and thus sulfide) poor environment. In contrast, pyrite expressing the equilibrium isotope fractionation, i.e. positive $\delta^{56}\text{Fe}$ values, reflects low Fe/S ratio and thus an environment with higher sulfate concentrations. Therefore, the increase of $\delta^{56}\text{Fe}$ values through the SSB can reflect variations in the supply of sulfate to the ocean, for example by volcanic degassing as already suggested during the SSB interval (*Bond and Grasby, 2017*). However, the absence of high Hg concentrations through the SSB does not support sulfate concentration variations driven by volcanism. Moreover, CAS isotope compositions do not suggest variation in sulfate concentrations. Finally, the absence of covariation between sulfur content and bulk $\delta^{34}\text{S}$ values further indicates that sulfur availability during pyritization contents did not primarily control the $\delta^{56}\text{Fe}$ signal observed in the studied samples through the SSB in the LWC section.

4.3. Pyrite $\delta^{56}\text{Fe}$ values controlled by sedimentary depositional settings and microbial communities

We suggest that $\delta^{56}\text{Fe}$ variability is driven by redox cycling proceeding within the sediment, including biotic Fe-oxide reduction by DIR and reductive dissolution of Fe-oxides by sulfides. Based on petrographic observations, $\delta^{56}\text{Fe}$ and $\delta^{34}\text{S}$ results, two models are proposed below to account for the $\delta^{56}\text{Fe}$ variations observed within the LWC ramp system deposits: (1) an “inner ramp” model, functioning in an open sedimentary environment and (2) a “mid and outer ramp” model, describing operating in a closed sedimentary environment controlled by the buildup of Fe-oxide pools within the sediment.

4.3.1. Inner ramp model: $\delta^{56}\text{Fe}$ values controlled by the nature of deposit

The LWC inner ramp is characterized by frequent remobilization of sediment by tidal currents or waves that facilitated the connection between sediment porewaters and the water column. Therefore, sulfate, Fe-oxides and organic matter that fuel metabolic reactions related to sedimentary sulfides precipitation are assumed to be non-limiting. An open system is consistent with obtained negative $\delta^{34}\text{S}$ values in average ($\delta^{34}\text{S} = -11.41 \pm 9.31\text{‰}$, 1SD) and specifically in samples LWC31, LWC39 and LWC41 also measured for their Fe isotope compositions (average $\delta^{34}\text{S}$ value = $-18.43 \pm 1.59\text{‰}$, 1SD). Consequently, high $\delta^{56}\text{Fe}$ values of $+2.04 \pm 0.72\text{‰}$ (1SD) associated with MISS samples (FA2; LWC39 and LWC41-3b) (**Fig.**

4.5a and 4.5c) suggest that a strong redox gradient developed in these microbial mats where iron reduction and oxidation can occur cyclically or even simultaneously (Byrne *et al.*, 2015; Berg *et al.*, 2016) due to the co-localized presence of aerobic and anaerobic metabolisms (e.g. O₂ respiration, H₂S oxidizers and sulfate reducers; Kühl and Jørgensen, 1992), fostered by potential sediment reworking (Fike *et al.*, 2015). In this case, a partial reduction of the Fe-oxide reservoir is suggested (Fig. 4.5a), owing strong redox fluctuations within a biofilm that can occur rapidly within restricted areas (Fike *et al.*, 2008; Dupraz *et al.*, 2009). This process should produce (1) a ⁵⁶Fe-depleted Fe(II) pool available for pyrite precipitation, and (2) a ⁵⁶Fe-enriched residual Fe-oxide pool. Depending on the redox gradient, the reduction of the residual heavy Fe-oxide reservoir can also occur, as well as a complete or partial re-oxidation of the newly formed pyrite. This cryptic Fe cycle can produce heavy pyrite δ⁵⁶Fe values associated with a large isotope range, comparable to those observed in FA2.

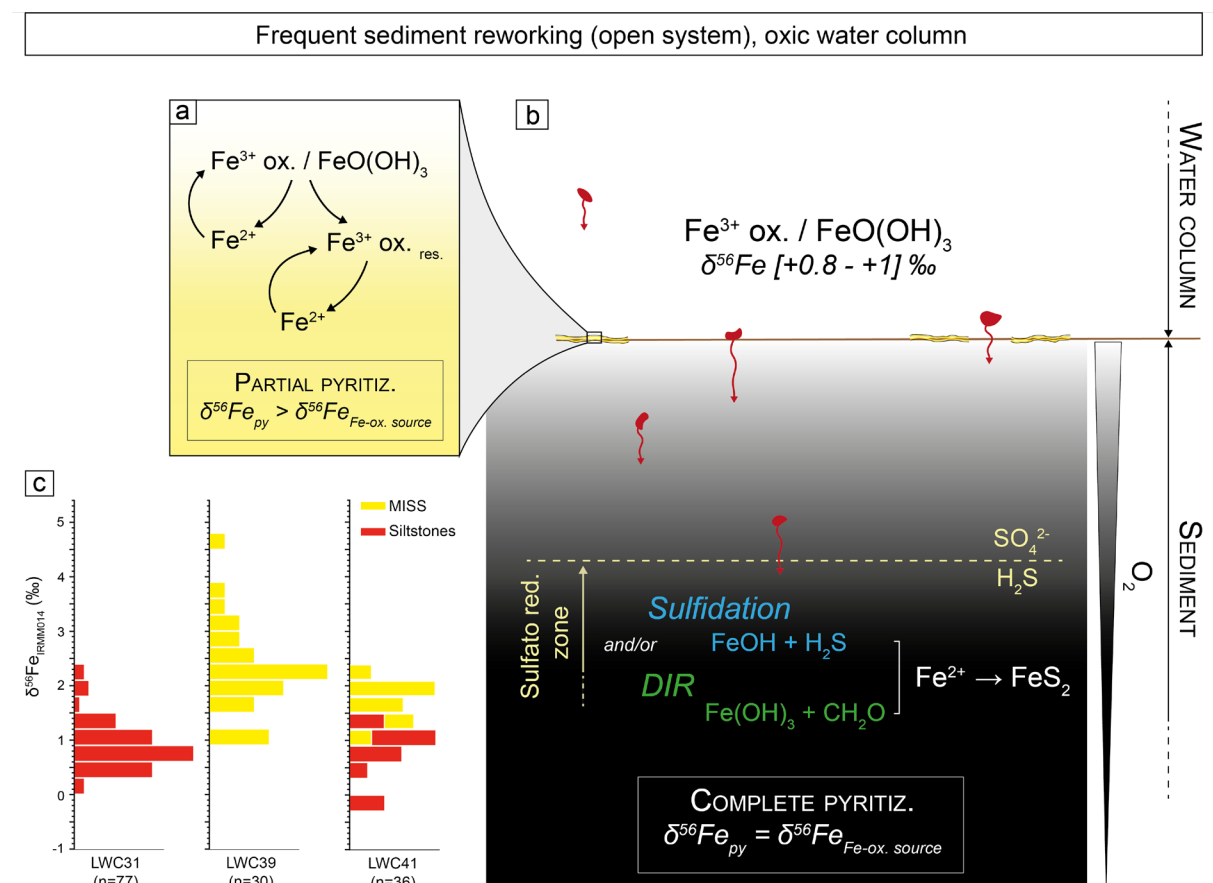


Figure 4. 5: Iron cycling model in the sediment from inner ramp samples. a) Model of Fe reduction for MISS samples (FA2), where a strong redox gradient occurs due to the variety of microbial metabolisms. In this case, Fe-oxides are partially reduced, and recycling can generate higher δ⁵⁶Fe values. b) Model of Fe reduction for siltstone samples (FA1). In this model, Fe-oxides are converted into Fe²⁺ or FeS and subsequently pyrite by reaction with H₂S. Sulfide is produced by microbial sulfate reduction (blue pathway: Sulfidation) combined with the possible effect of iron reducing bacteria (green pathway: Dissimilatory Iron Reduction). c) Histograms of δ⁵⁶Fe_{py} measured in facies associations FA1 (siltstone) and FA2 (MISS).

On the other side, pyrites from inner ramp siltstones (FA1; LWC31 and LWC41-3a) do not seem to record redox fluctuation as the average pyrite δ⁵⁶Fe_{mean} of +0.90‰ matches with the canonical Fe isotope compositions known for Fe-oxides through Earth history (Rouxel *et*

al., 2005; Wu *et al.*, 2011; **Fig. 4.5b and 4.5c**). In well-ventilated sediments devoid of biofilms, microbial sulfate reduction (MSR) occurs deeper in the sediment where the quantity and reactivity of organic matter decrease as a function of the sediment depth and redox potential (Middelburg, 1989; Dauwe *et al.*, 1999; Meister *et al.*, 2013). Moreover, due to its low mobility, Fe-oxide quantity decreases as a function of the sediment depth. In this case, even limited by the low reactivity of organic matter (i.e. at a lower rate of sulfate reduction), the production of H₂S through MSR corresponds to the rate of Fe-oxide consumption. Therefore, a total reduction of Fe-oxide is expected to account for the observed iron isotope signatures. Dissimilatory iron reduction (DIR) is however not suggested here because $\delta^{56}\text{Fe}_{\text{py}}$ values are not negative enough to support this process (Crosby *et al.*, 2005; **Fig. 4.5b**).

4.3.2. Mid and outer ramp model: $\delta^{56}\text{Fe}_{\text{py}}$ controlled by H₂S production in a closed system

Samples from the mid ramp system record a progressive increase in $\delta^{56}\text{Fe}$ values, from +0.46 to +2.73‰, that is also recorded in S isotope compositions with an increase from -8.20 to -2.76‰ (**Fig. 4.2**). A concurrent increase of $\delta^{56}\text{Fe}$ and $\delta^{34}\text{S}$ values for mid ramp samples can reflect a distillation of the Fe-oxide and sulfate reservoirs within the sediment under closed system conditions (**Fig. 4.6**). Samples LWC47 and LWC49 show disarticulated bioclasts of bivalves and ammonoids, reflecting rare storm events and limited transport (Seilacher *et al.*, 1985; Kidwell *et al.*, 1986; Grosjean *et al.*, 2018). LWC55 also shows fragmented bivalves and thin layers of silty beds (**Fig. 4.1**), but the higher proportion of micritic matrix compared to LWC47 and LWC49 suggests a slightly deeper depositional environment (**Fig. 4.1**). In such environments, episodic storms resulted in rapid sediment accumulations that promoted, disconnections between porewater and the water column is expected. In this environmental context replenishment of solute oxidized species is restricted (**Fig. 4.6a**). Consequently, a closed system sulfate reduction developed and may have driven the partial reduction of Fe-oxides, leading to the buildup of a residual Fe-oxide pools in the sediment that are progressively ^{56}Fe and ^{34}S -enriched (**Fig. 4.6a and 4.6b**). The large range and non-Rayleigh-type distribution of $\delta^{56}\text{Fe}$ values in LWC47 (**Fig. 4.6c**) support that (1) pyrite recorded multiple steps of partial reduction of a residual Fe-oxide pool, and (2) a possible recycling (reoxidation-reduction) of the produced Fe²⁺. The average $\delta^{56}\text{Fe}$ value of outer ramp samples LWC72 and LWC88 is of +1.28‰, i.e. ~1‰ lower than that of the mid ramp samples (mean $\delta^{56}\text{Fe}_{\text{Mid}} = +2.10‰$). The large variability of $\pm 1.14‰$ observed in these outer ramp samples is not distributed along a Rayleigh-type distillation. In contrast, S isotope signal increases, from -4.04‰ in the mid ramp to +6.44‰ in the outer ramp setting. LWC72 and LWC88 pertained to FA5 (**Fig. 4.4**), which is dominated by sediment decantation and very low hydrodynamic regime. Deposition of FA5 occurred in a more distal position along the ramp where sediment reworking is very rare, meaning that the sediments likely evolved under closed system conditions. In such setting, sulfides generated in sediments by sulfate reduction may promote the partial reduction of reactive Fe-oxides (**Fig. 4.6**) in outer

ramp sediments. This partial reduction produces Fe^{2+} that can be then converted into pyrite. Due to the activity of sulfate reducing metabolisms and the progressive buildup of residual Fe-oxide pools from an initial reservoir, reactive Fe-oxides tend to be rare. Therefore, sulfides produced deeper in the sediment is not consumed in situ by reaction with Fe^{2+} and accumulates, leading to a diffusion upward its zone of production (Riedinger *et al.*, 2017; Liu *et al.*, 2020). This diffusion process results in the successive sulfidation of the (more) reactive residual and initial Fe-oxides pools (Fig. 4.6), converting them to pyrite characterized by ^{34}S -enriched S isotope signatures, a large $\delta^{56}\text{Fe}$ range of values and an average $\delta^{56}\text{Fe}$ signal close to the signatures of the Fe-oxide source.

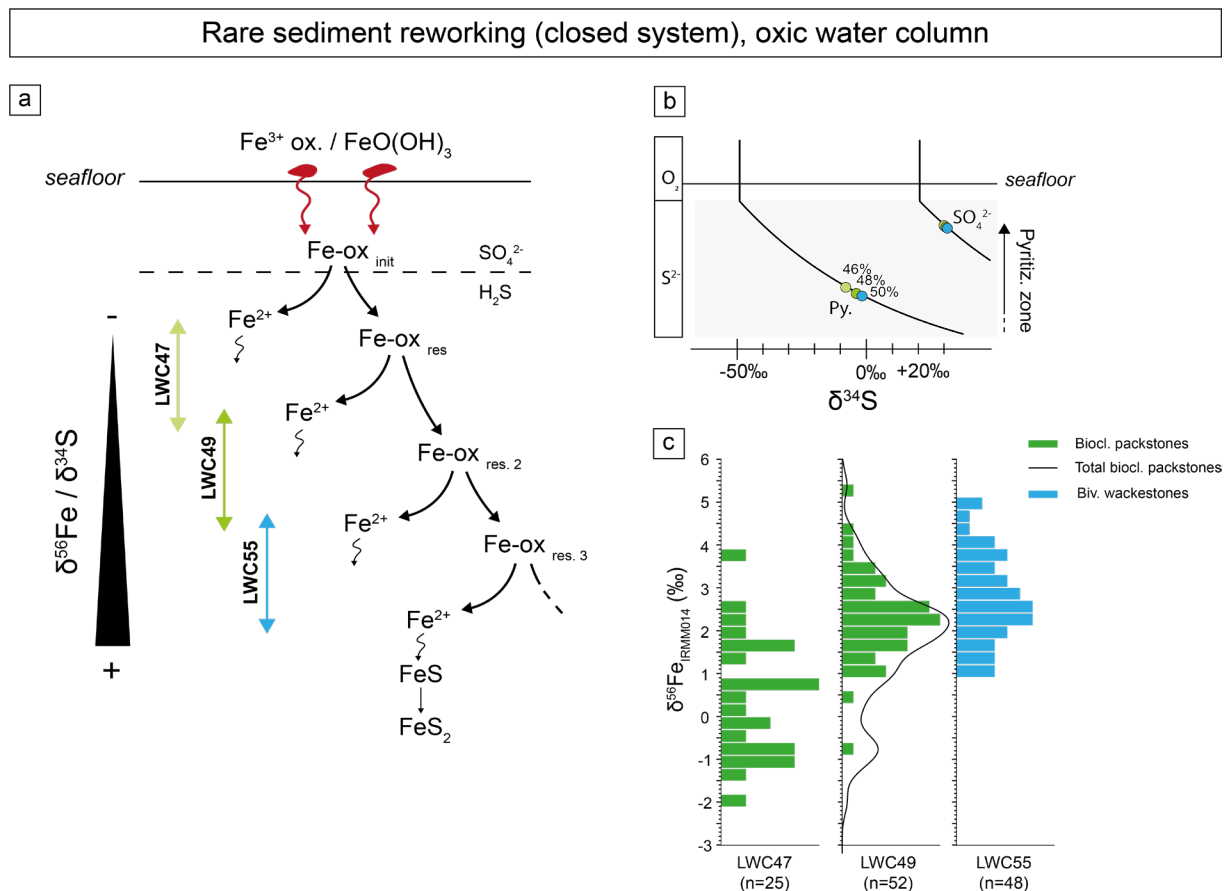


Figure 4.6: Iron cycling model in the sediment from mid and outer ramp samples. a) Model for Fe-oxide reduction in closed-system, where Fe-oxides are partially reduced by reaction with limiting H_2S (as sulfate reservoir also evolves in a closed-system), leading to the buildup of different residual Fe-oxide pools. b) Evolution of newly formed pyrite and sulfate in a closed sediment. Percentage of newly formed pyrite during the Rayleigh distillation is reported for LWC 47 (light green), LWC49 (green) and LWC55 (blue). c) Histograms of $\delta^{56}\text{Fe}_{\text{py}}$. Green and blue colors correspond to facies associations FA3 (bioclastic packstones) and FA4 (bivalve wackestones) respectively. Black line represents probability density for both LWC47 and LWC49.

4.4. Pyrite formation during an interval of biotic diversity loss: a depositional environment control rather the deleterious anoxic conditions

The oceanic redox condition through the SSB was highly documented by studying pyrite. Indeed, many studies focused on the occurrence and size distribution of pyrite framboids, Fe speciation and multiple sulfur isotope signals to assess euxinia, anoxia or ferruginous conditions of the water column (e.g. *Shen et al., 2011; Sun et al., 2015; Clarkson et al., 2016; Song et al., 2019*). However, there have been no studies using iron isotopes to document this biotic crisis, although iron is also a redox-sensitive element. Here we evidence that depositional environment and more specifically varying degree of sediment connection with the water column, modulated by sediment reworking and accumulation, control the S and Fe isotope compositions through variations of Fe-oxide and sulfate supply in the sediment microbial active zones. When sediment is well-connected to the water column, pyrite displays negative $\delta^{34}\text{S}$ values and Fe isotope compositions reflect the complete reduction of Fe-oxides. On the other hand, the disconnection between the water column and the sediment leads to the isotope distillation of sulfate and Fe-oxide reservoirs.

The control of the sediment-seawater connectivity between each depositional environment is direct on S isotope signatures, while Fe isotopes show the additional influence of the nature of deposit (presence of MISS) in the inner ramp system and the reactivity of Fe-oxides with H_2S fluxes in the outer ramp system. This suggests that both Fe and S isotope variations through the SSB at LWC are driven by local processes within the sediment rather than the water column redox structure. In this study, no direct causality can be established between Fe isotope signal and interval of biotic crisis as already demonstrated through the SSB using multiple sulfur isotope signals (*Thomazo et al., 2019*). Finally, the message to learn with Fe isotope compositions along with S isotopes and petrographic observations is consistent with local microbial and sedimentological processes as the primary driver of sedimentary geochemical signals within the studied biotic diversity loss interval.

5. Conclusions

Pyrite Fe isotope compositions obtained from LWC section through the Smithian-Spathian transition indicate a sedimentary depositional system control, locally coupled with an influence of the nature of deposits (i.e. presence or absence of MISS) on pyrite formation. LWC sediments deposited along a tide and wave influenced ramp system, ranging from shallow inner ramp to deeper outer ramp settings, was overlaid by an oxygenated water column. In these environments, the intensity of biological and physical induced sediment reworking produces two regimes of water column-sediment exchanges, an open system characterized by well-ventilated sediment and a closed system govern by diffusion within the porewater sediment. We propose two iron cycling models both influenced by the position along the ramp and nature of the deposits. The

first model is relevant to reworked sediments from inner ramp settings, where lighter $\delta^{56}\text{Fe}_{\text{py}}$ ($\delta^{56}\text{Fe}_{\text{mean}} \sim +1\text{‰}$) reflect the complete reduction of Fe-oxides and heavy $\delta^{56}\text{Fe}_{\text{py}}$ values ($\delta^{56}\text{Fe}_{\text{mean}} \sim +2\text{‰}$) in MISS are attributed to a complex microbial oxidation-reduction cycling. The second model is relevant for sediments deposited in the mid and outer ramp zones that were rarely affected by reworking. In these settings, there is no facies control on $\delta^{56}\text{Fe}_{\text{py}}$ values. Rather, the concurrent increase of Fe and S isotope compositions suggests that the disconnection between porewaters and water column drives the distillation of the Fe-oxide and sulfate sedimentary reservoirs.

This study highlights the importance of using different isotope systematics the sedimentary depositional/nature of sediments to unravel local versus global control on geochemical signatures and call for caution in the “redox” interpretation of Fe and S isotope signals, especially digging into geological intervals associated with oceanic anoxia in the aftermath of mass extinction events.

6. Acknowledgements

K.G. Bylund, J.F. Jenks, D.A. Stephen, E. Fara, G. Escarguel, E. Vennin, G. Caravaca and A.S. Grosjean are thanked for their work in the field, and notably for their participation to the sample collection. V. Pasquier is thanked for fruitful discussions. We thank J. Alleon for his assistance during Raman analyses. M. Robyr is thanked for his help during EPMA analyses. We thank private landowners (Scott Rees – south side of Weber River and Mrs. Monte Brough – north side of Weber River) for allowing access to their lands. This research was supported by the European Union’s Horizon H2020 research and innovation program ERC (STROMATA, grant agreement 759289). This work is also a contribution to the ANR project AFTER (ANR-13-JS06-0001-01) and was also supported by the French “Investissements d’Avenir” program, project ISITE-BFC (ANR-15-IDEX-03) and received funding from the programme TelluS of the Institut National des Sciences de l’Univers, CNRS.

7. Literature cited

- Aadte, T., Stinnesbeck, W., Keller, G., 1996. Lithostratigraphic and mineralogic correlations of near K/T boundary clastic sediments in northeastern Mexico: Implications for origin and nature of deposition, in: *The Cretaceous-Tertiary Event and Other Catastrophes in Earth History*. Geological Society of America. <https://doi.org/10.1130/0-8137-2307-8.211>
- Algeo, T.J., Kuwahara, K., Sano, H., Bates, S., Lyons, T., Elswick, E., Hinnov, L., Ellwood, B., Moser, J., Maynard, J.B., 2011. Spatial variation in sediment fluxes, redox conditions, and productivity in the Permian-Triassic Panthalassic Ocean. *Palaeogeography, Palaeoclimatology, Palaeoecology* 308, 65–83. <https://doi.org/10.1016/j.palaeo.2010.07.007>
- Beatty, T.W., Zonneveld, J.P., Henderson, C.M., 2008. Anomalously diverse Early Triassic ichnofossil assemblages in northwest Pangea: A case for a shallow-marine habitable zone. *Geology* 36, 771–774. <https://doi.org/10.1130/G24952A.1>
- Behar, F., Beaumont, V., de B. Pentead, H.L., 2001. Rock-Eval 6 Technology: Performances and Developments. *Oil & Gas Science and Technology* 56, 111–134. <https://doi.org/10.2516/ogst:2001013>
- Berg, J.S., Michellod, D., Pjevac, P., Martinez-Perez, C., Buckner, C.R.T., Hach, P.F., Schubert, C.J., Milucka, J., Kuypers, M.M.M., 2016. Intensive cryptic microbial iron cycling in the low iron water column of the meromictic Lake Cadagno. *Environmental Microbiology* 18, 5288–5302. <https://doi.org/10.1111/1462-2920.13587>
- Beysac, O., Goffé, B., Chopin, C., Rouzaud, J.N., 2002. Raman spectra of carbonaceous material in metasediments: a new geothermometer. *Journal of Metamorphic Geology* 20, 859–871. <https://doi.org/10.1046/j.1525-1314.2002.00408.x>
- Bond, D.P.G., Wignall, P.B., 2010. Pyrite framboid study of marine Permian-Triassic boundary sections: A complex anoxic event and its relationship to contemporaneous mass extinction. *Bulletin of the Geological Society of America* 122, 1265–1279. <https://doi.org/10.1130/B30042.1>
- Bond, D.P.G., Grasby, S.E., 2017. On the causes of mass extinctions. *Palaeogeography, Palaeoclimatology, Palaeoecology* 478, 3–29. <https://doi.org/10.1016/j.palaeo.2016.11.005>
- Brayard, A., Bucher, H., Escarguel, G., Fluteau, F., Bourquin, S., Galfetti, T., 2006. The Early Triassic ammonoid recovery: Paleoclimatic significance of diversity gradients. *Palaeogeography, Palaeoclimatology, Palaeoecology* 239, 374–395. <https://doi.org/10.1016/j.palaeo.2006.02.003>
- Brayard, A., Vennin, E., Olivier, N., Bylund, K.G., Jenks, J., Stephen, D.A., Bucher, H., Hofmann, R., Goudemand, N., Escarguel, G., 2011. Transient metazoan reefs in the aftermath of the end-Permian mass extinction. *Nature Geoscience* 4, 693–697. <https://doi.org/10.1038/ngeo1264>
- Brayard, A., Bylund, K.G., Jenks, J.F., Stephen, D.A., Olivier, N., Escarguel, G., Fara, E., Vennin, E., 2013. Smithian ammonoid faunas from Utah: implications for Early Triassic biostratigraphy, correlation and basinal paleogeography. *Swiss Journal of Palaeontology* 132, 141–219. <https://doi.org/10.1007/s13358-013-0058-y>
- Brayard, A., Krumenacker, L.J., Botting, J.P., Jenks, J.F., Bylund, K.G., Fara, E., Vennin, E., Olivier, N., Goudemand, N., Saucède, T., Charbonnier, S., Romano, C., Doguzhaeva, L., Thuy, B., Hautmann, M., Stephen, D.A., Thomazo, C., Escarguel, G., 2017. Unexpected Early Triassic marine ecosystem and the rise of the Modern evolutionary fauna. *Science Advances* 3. <https://doi.org/10.1126/sciadv.1602159>
- Brayard, A., Olivier, N., Vennin, E., Jenks, J.F., Bylund, K.G., Stephen, D.A., McShinsky, D., Goudemand, N., Fara, E., Escarguel, G., 2020. New middle and late Smithian ammonoid faunas from the Utah/Arizona border: New evidence for calibrating Early Triassic transgressive-regressive trends and paleobiogeographical signals in the western USA basin. *Global and Planetary Change* 192, 103251. <https://doi.org/10.1016/j.gloplacha.2020.103251>
- Brayard, A., Jenks, J.F., Bylund, K.G., Olivier, N., Vennin, E., Stephen, D.A., Escarguel, G., Fara, E., 2021. Latest Smithian (Early

Triassic) ammonoid assemblages in Utah (western USA basin) and their implications for regional biostratigraphy, biogeography and placement of the Smithian/Spathian boundary. *Geobios* 69, 1–23. <https://doi.org/10.1016/j.geobios.2021.05.003>

Burchfiel, B., Davis, G.A., 1975. Nature and controls of Cordilleran orogenesis, Western United States: extensions of an earlier synthesis. *American Journal of Science* 275, 363–396.

Busigny, V., Planavsky, N.J., Jézéquel, D., Crowe, S., Louvat, P., Moureau, J., Viollier, E., Lyons, T.W., 2014. Iron isotopes in an Archean ocean analogue. *Geochimica et Cosmochimica Acta* 133, 443–462. <https://doi.org/10.1016/j.gca.2014.03.004>

Byrne, J.M., Klueglein, N., Pearce, C., Rosso, K.M., Appel, E., Kappler, A., 2015. Redox cycling of Fe(II) and Fe(III) in magnetite by Fe-metabolizing bacteria. *Science* (1979) 347, 1473–1476. <https://doi.org/10.1126/science.aaa4834>

Caravaca, G., Thomazo, C., Vennin, E., Olivier, N., Cocquerez, T., Escarguel, G., Fara, E., Jenks, J.F., Bylund, K.G., Stephen, D.A., Brayard, A., 2017. Early Triassic fluctuations of the global carbon cycle: New evidence from paired carbon isotopes in the western USA basin. *Global and Planetary Change* 154, 10–22. <https://doi.org/10.1016/j.gloplacha.2017.05.005>

Caravaca, G., Brayard, A., Vennin, E., Guiraud, M., le Pourhiet, L., Grojean, A.-S., Thomazo, C., Olivier, N., Fara, E., Escarguel, G., Bylund, K.G., Jenks, J.F., Stephen, D.A., 2018. Controlling factors for differential subsidence in the Sonoma Foreland Basin (Early Triassic, western USA). *Geological Magazine* 155, 1305–1329. <https://doi.org/10.1017/S0016756817000164>

Clarkson, M.O., Wood, R.A., Poulton, S.W., Richoz, S., Newton, R.J., Kasemann, S.A., Bowyer, F., Krystyn, L., 2016. Dynamic anoxic ferruginous conditions during the end-Permian mass extinction and recovery. *Nature Communications* 7, 12236. <https://doi.org/10.1038/ncomms12236>

Dauphas, N., Rouxel, O., 2006. Mass spectrometry and natural variations of iron isotopes. *Mass Spectrometry Reviews* 25, 515–550. <https://doi.org/10.1002/mas.20078>

Dauwe, B., Middelburg, J.J., Herman, P.M., Heip, C.H., 1999. Linking diagenetic alteration of amino acids and bulk organic matter reactivity. *Limnology and Oceanography*.

Decraene, M.N., Marin-Carbonne, J., Bouvier, A.S., Villeneuve, J., Bouden, N., Luais, B., Deloule, E., 2021. High-spatial-resolution measurements of iron isotopes in pyrites by secondary ion mass spectrometry using the new Hyperion-II radio-frequency plasma source. *Rapid Communications in Mass Spectrometry* 35. <https://doi.org/10.1002/rcm.8986>

Dickinson, W.R., 2013. Phanerozoic palinspastic reconstructions of Great Basin geotectonics (Nevada-Utah, USA). *Geosphere* 9, 1384–1396. <https://doi.org/10.1130/GES00888.1>

Dupraz, C., Reid, R.P., Braissant, O., Decho, A.W., Norman, R.S., Visscher, P.T., 2009. Processes of carbonate precipitation in modern microbial mats. *Earth-Science Reviews*. <https://doi.org/10.1016/j.earscirev.2008.10.005>

Elrick, M., Polyak, V., Algeo, T.J., Romaniello, S., Asmerom, Y., Herrmann, A.D., Anbar, A.D., Zhao, L., Chen, Z.Q., 2017. Global-ocean redox variation during the middle-late Permian through Early Triassic based on uranium isotope and Th/U trends of marine carbonates. *Geology* 45, 163–166. <https://doi.org/10.1130/G38585.1>

Embry, A.F., 1997. Global sequence boundaries of the Triassic and their identification in the Western Canada Sedimentary Basin 1, *Bulletin of Canadian Petroleum Geology*.

Espitalie, J., Deroo, G., Marquis, F., 1985. La pyrolyse Rock-Eval et ses applications. Deuxième partie. *Revue de l'Institut Français du Pétrole* 40, 755–784. <https://doi.org/10.2516/ogst:1985045>

Fike, D.A., Gammon, C.L., Ziebis, W., Orphan, V.J., 2008. Micron-scale mapping of sulfur cycling across the oxycline of a cyanobacterial mat: a paired nanoSIMS and CARD-FISH approach. *The ISME Journal* 2, 749–759. <https://doi.org/10.1038/ismej.2008.39>

Galfetti, T., Bucher, H., Ovtcharova, M., Schaltegger, U., Brayard, A., Brühwiler, T., Goudemand, N., Weissert, H., Hochuli, P.A., Cordey, F., Guodun, K., 2007. Timing of the Early Triassic carbon cycle perturbations inferred from new U–Pb ages and ammonoid biochronozones.

Earth and Planetary Science Letters 258, 593–604. <https://doi.org/10.1016/j.epsl.2007.04.023>

Goudemand, N., Romano, C., Leu, M., Bucher, H., Trotter, J.A., Williams, I.S., 2019. Dynamic interplay between climate and marine biodiversity upheavals during the early Triassic Smithian–Spathian biotic crisis. *Earth-Science Reviews*. <https://doi.org/10.1016/j.earscirev.2019.01.013>

Grasby, S.E., Beauchamp, B., Embry, A., Sanei, H., 2013. Recurrent Early Triassic ocean anoxia. *Geology* 41, 175–178. <https://doi.org/10.1130/G33599.1>

Grosjean, A.S., Vennin, E., Olivier, N., Caravaca, G., Thomazo, C., Fara, E., Escarguel, G., Bylund, K.G., Jenks, J.F., Stephen, D.A., Brayard, A., 2018. Early Triassic environmental dynamics and microbial development during the Smithian–Spathian transition (Lower Weber Canyon, Utah, USA). *Sedimentary Geology* 363, 136–151. <https://doi.org/10.1016/j.sedgeo.2017.11.009>

Guex, J., Hungerbühler, A., O'Dogherty, L., Atudorei, V., Taylor, D. G., Bucher, H., & Bartolini, A. (2010). Spathian (Lower Triassic) ammonoids from western USA (Idaho, California, Utah and Nevada). *Mémoires de Géologie (Lausanne)*, 49.

Guilbaud, R., Butler, I.B., Ellam, R.M., 2011. Abiotic Pyrite Formation Produces a Large Fe Isotope Fractionation. *Science* (1979) 332, 1548–1551. <https://doi.org/10.1126/science.1202924>

Haq, B.U., Hardenbol, J., Vail, P.R., 1987. Chronology of Fluctuating Sea Levels Since the Triassic. *Science* (1979) 235, 1156–1167. <https://doi.org/10.1126/science.235.4793.1156>

Heard, A.W., Dauphas, N., 2020. Constraints on the coevolution of oxic and sulfidic ocean iron sinks from archean-paleoproterozoic iron isotope records. *Geology* 48, 358–362. <https://doi.org/10.1130/G46951.1>

Heydari, E., Moore, C.H., 1989. Burial diagenesis and thermochemical sulfate reduction, Smackover Formation, southeastern Mississippi salt basin.

Horacek, M., Richo, S., Brandner, R., Krystyn, L., Spötl, C., 2007. Evidence for recurrent changes in Lower Triassic oceanic circulation of the Tethys: The $\delta^{13}\text{C}$ record from marine sections in Iran. *Palaeogeography, Palaeoclimatology, Palaeoecology* 252, 355–369. <https://doi.org/10.1016/j.palaeo.2006.11.052>

Ingersoll, R. v., 2008. Chapter 11 Subduction-Related Sedimentary Basins of the USA Cordillera. pp. 395–428. [https://doi.org/10.1016/S1874-5997\(08\)00011-7](https://doi.org/10.1016/S1874-5997(08)00011-7)

Jattiot, R., Bucher, H., Brayard, A., Monnet, C., Jenks, J.F., Hautmann, M., 2016. Revision of the genus *Anasibirites* Mojsisovics (Ammonoidea): An iconic and cosmopolitan taxon of the late Smithian (Early Triassic) extinction. *Papers in Palaeontology* 2, 155–188. <https://doi.org/10.1002/spp2.1036>

Johnson, C.M., Beard, B.L., 2005. Biogeochemical Cycling of Iron Isotopes. *Science* (1979) 309, 1025–1027. <https://doi.org/10.1126/science.1112552>

Jørgensen, B.B., Kasten, S., 2006. Sulfur cycling and methane oxidation, in: *Marine Geochemistry*. Springer Berlin Heidelberg, pp. 271–309. https://doi.org/10.1007/3-540-32144-6_8

Kidwell, S.M., Fursich, F.T., Aigner, T., 1986. Conceptual Framework for the Analysis and Classification of Fossil Concentrations. *PALAIOS* 1, 228. <https://doi.org/10.2307/3514687>

Kirton, J.M.C., Woods, A.D., 2021. Stromatolites from the Lower Triassic Virgin Limestone at Blue Diamond, NV USA: The role of dysoxia, enhanced calcification and nutrient availability in the growth of post-extinction microbialites. *Global and Planetary Change* 198. <https://doi.org/10.1016/j.gloplacha.2021.103429>

Kouketsu, Y., Nishiyama, T., Ikeda, T., Enami, M., 2014. Evaluation of residual pressure in an inclusion-host system using negative frequency shift of quartz Raman spectra. *American Mineralogist* 99, 433–442. <https://doi.org/10.2138/am.2014.4427>

Kübler, B., 1983. Cristallinité de l'illite, méthodes normalisées de préparations, méthodes normalisées de mesures. *Cahiers Institut*

- Kühl, M., Jørgensen, B.B., 1992. Microsensor Measurements of Sulfate Reduction and Sulfide Oxidation in Compact Microbial Communities of Aerobic Biofilms. *Applied and Environmental Microbiology* 58, 1164–1174. <https://doi.org/10.1128/aem.58.4.1164-1174.1992>
- Kunzmann, M., Gibson, T.M., Halverson, G.P., Hodgskiss, M.S.W., Bui, T.H., Carozza, D.A., Sperling, E.A., Poirier, A., Cox, G.M., Wing, B.A., 2017. Iron isotope biogeochemistry of Neoproterozoic marine shales. *Geochimica et Cosmochimica Acta* 209, 85–105. <https://doi.org/10.1016/j.gca.2017.04.003>
- Liu, J., Pellerin, A., Izon, G., Wang, J., Antler, G., Liang, J., Su, P., Jørgensen, B.B., Ono, S., 2020. The multiple sulphur isotope fingerprint of a sub-seafloor oxidative sulphur cycle driven by iron. *Earth and Planetary Science Letters* 536. <https://doi.org/10.1016/j.epsl.2020.116165>
- Mansor, M., Fantle, M.S., 2019. A novel framework for interpreting pyrite-based Fe isotope records of the past. *Geochimica et Cosmochimica Acta* 253, 39–62. <https://doi.org/10.1016/j.gca.2019.03.017>
- Matthews, A., Zhu, X.-K., O’Nions, K., 2001. Kinetic iron stable isotope fractionation between iron (-II) and (-III) complexes in solution. *Earth and Planetary Science Letters* 192, 81–92. [https://doi.org/10.1016/S0012-821X\(01\)00432-0](https://doi.org/10.1016/S0012-821X(01)00432-0)
- Meister, P., Liu, B., Ferdelman, T.G., Jørgensen, B.B., Khalili, A., 2013. Control of sulphate and methane distributions in marine sediments by organic matter reactivity. *Geochimica et Cosmochimica Acta* 104, 183–193. <https://doi.org/10.1016/j.gca.2012.11.011>
- Middelburg, J.J., 1989. A simple rate model for organic matter decomposition in marine sediments. *Geochimica et Cosmochimica Acta* 53, 1577–1581. [https://doi.org/10.1016/0016-7037\(89\)90239-1](https://doi.org/10.1016/0016-7037(89)90239-1)
- Olivier, N., Brayard, A., Fara, E., Bylund, K.G., Jenks, J.F., Vennin, E., Stephen, D.A., Escarguel, G., 2014. Smithian shoreline migrations and depositional settings in Timpoweap Canyon (Early Triassic, Utah, USA). *Geological Magazine* 151, 938–955. <https://doi.org/10.1017/S0016756813000988>
- Olivier, N., Brayard, A., Vennin, E., Escarguel, G., Fara, E., Bylund, K.G., Jenks, J.F., Caravaca, G., Stephen, D.A., 2016. Evolution of depositional settings in the Torrey area during the Smithian (Early Triassic, Utah, USA) and their significance for the biotic recovery. *Geological Journal* 51, 600–626. <https://doi.org/10.1002/gj.2663>
- Olivier N., Fara E., Vennin E., Bylund K.G., Jenks J.F., Escarguel G., Stephen D.A., Goudemand N., Snyder D., Thomazo C., Brayard A., 2018. Late Smithian microbial deposits and their lateral marine fossiliferous limestones (Early Triassic, Hurricane Cliffs, Utah, USA). *Facies* 64:13, <https://doi.org/10.1007/s10347-018-0526-3>
- Orchard, M.J., 2007. Conodont diversity and evolution through the latest Permian and Early Triassic upheavals. *Palaeogeography, Palaeoclimatology, Palaeoecology* 252, 93–117. <https://doi.org/10.1016/j.palaeo.2006.11.037>
- Paull, R.A., Paull, R.K., 1993. Interpretation of Early Triassic nonmarine-marine relations, Utah, USA. In: Lucas, S.G., Morales, M. (Eds.), *The Nonmarine Triassic*. New Mexico Museum of Natural History and Science Bulletin vol. 3, pp. 403–409
- Polyakov, V.B., Clayton, R.N., Horita, J., Mineev, S.D., 2007. Equilibrium iron isotope fractionation factors of minerals: Reevaluation from the data of nuclear inelastic resonant X-ray scattering and Mössbauer spectroscopy. *Geochimica et Cosmochimica Acta* 71, 3833–3846. <https://doi.org/10.1016/j.gca.2007.05.019>
- Pruss, S., Fraiser, M., Bottjer, D.J., 2004. Proliferation of Early Triassic wrinkle structures: Implications for environmental stress following the end-Permian mass extinction. *Geology* 32, 461. <https://doi.org/10.1130/G20354.1>
- Raiswell, R., Berner, R.A., 1986. Pyrite and organic matter in Phanerozoic normal marine shales. *Geochimica et Cosmochimica Acta* 50, 1967–1976. [https://doi.org/10.1016/0016-7037\(86\)90252-8](https://doi.org/10.1016/0016-7037(86)90252-8)
- Raiswell, R., Reinhard, C.T., Derkowski, A., Owens, J., Bottrell, S.H., Anbar, A.D., Lyons, T.W., 2011. Formation of syngenetic and early diagenetic iron minerals in the late Archean Mt. McRae Shale, Hamersley Basin, Australia: New insights on the patterns, controls and paleoenvironmental implications of authigenic mineral formation. *Geochimica et Cosmochimica Acta* 75, 1072–1087. <https://doi.org/10.1016/j.gca.2011.03.011>

gca.2010.11.013

Riedinger, N., Brunner, B., Krastel, S., Arnold, G.L., Wehrmann, L.M., Formolo, M.J., Beck, A., Bates, S.M., Henkel, S., Kasten, S., Lyons, T.W., 2017. Sulfur Cycling in an Iron Oxide-Dominated, Dynamic Marine Depositional System: The Argentine Continental Margin. *Frontiers in Earth Science* 5. <https://doi.org/10.3389/feart.2017.00033>

Rolison, J.M., Stirling, C.H., Middag, R., Gault-Ringold, M., George, E., Rijkenberg, M.J.A., 2018. Iron isotope fractionation during pyrite formation in a sulfidic Precambrian ocean analogue. *Earth and Planetary Science Letters* 488, 1–13. <https://doi.org/10.1016/j.epsl.2018.02.006>

Rouxel, O.J., Bekker, A., Edwards, K.J., 2005. Iron Isotope Constraints on the Archean and Paleoproterozoic Ocean Redox State. *Science* (1979) 307, 1088–1091. <https://doi.org/10.1126/science.1105692>

Schubert, J.K., Bottjer, D.J., 1992. Early Triassic stromatolites as post-mass extinction disaster forms. *Geology* 20, 883. [https://doi.org/10.1130/0091-7613\(1992\)020<0883:ETSAPM>2.3.CO;2](https://doi.org/10.1130/0091-7613(1992)020<0883:ETSAPM>2.3.CO;2)

Seilacher, A., Reif, W.-E., Westphal, F., Riding, R., Clarkson, E.N.K., Whittington, H.B., 1985. Sedimentological, ecological and temporal patterns of fossil Lagerstätten. *Philosophical Transactions of the Royal Society of London B* 311, 5–23.

Severmann, S., Lyons, T.W., Anbar, A., McManus, J., Gordon, G., 2008. Modern iron isotope perspective on the benthic iron shuttle and the redox evolution of ancient oceans. *Geology* 36, 487–490. <https://doi.org/10.1130/G24670A.1>

Shen, Y., Knoll, A.H., Walter, M.R., 2003. Evidence for low sulphate and anoxia in a mid-Proterozoic marine basin. *Nature* 423, 632–635. <https://doi.org/10.1038/nature01651>

Shen, Y., Farquhar, J., Zhang, H., Masterson, A., Zhang, T., Wing, B.A., 2011. Multiple S-isotope evidence for episodic shoaling of anoxic water during Late Permian mass extinction. *Nature Communications* 2, 210. <https://doi.org/10.1038/ncomms1217>

Smith, C.P.A., Laville, T., Fara, E., Escarguel, G., Olivier, N., Vennin, E., Goudemand, N., Bylund, K.G., Jenks, J.F., Stephen, D.A., Hautmann, M., Charbonnier, S., Krumenacker, L.J., Brayard, A., 2021. Exceptional fossil assemblages confirm the existence of complex Early Triassic ecosystems during the early Spathian. *Scientific Reports* 11. <https://doi.org/10.1038/s41598-021-99056-8>

Song, H., Wignall, P.B., Tong, J., Yin, H., 2013. Two pulses of extinction during the Permian-Triassic crisis. *Nature Geoscience* 6, 52–56. <https://doi.org/10.1038/ngeo1649>

Song, H., Du, Y., Algeo, T.J., Tong, J., Owens, J.D., Song, H., Tian, L., Qiu, H., Zhu, Y., Lyons, T.W., 2019. Cooling-driven oceanic anoxia across the Smithian/Spathian boundary (mid-Early Triassic). *Earth-Science Reviews* 195, 133–146. <https://doi.org/10.1016/j.earscirev.2019.01.009>

Sun, Y.D., Wignall, P.B., Joachimski, M.M., Bond, D.P.G., Grasby, S.E., Sun, S., Yan, C.B., Wang, L.N., Chen, Y.L., Lai, X.L., 2015. High amplitude redox changes in the late Early Triassic of South China and the Smithian–Spathian extinction. *Palaeogeography, Palaeoclimatology, Palaeoecology* 427, 62–78. <https://doi.org/10.1016/j.palaeo.2015.03.038>

Takahashi, S., Yamasaki, S., Ogawa, K., Kaiho, K., Tsuchiya, N., 2015. Redox conditions in the end-Early Triassic Panthalassa. *Palaeogeography, Palaeoclimatology, Palaeoecology* 432, 15–28. <https://doi.org/10.1016/j.palaeo.2015.04.018>

Teutsch, N., von Gunten, U., Porcelli, D., Cirpka, O.A., Halliday, A.N., 2005. Adsorption as a cause for iron isotope fractionation in reduced groundwater. *Geochimica et Cosmochimica Acta* 69, 4175–4185. <https://doi.org/10.1016/j.gca.2005.04.007>

Thomazo, C., Brayard, A., Elmeknassi, S., Vennin, E., Olivier, N., Caravaca, G., Escarguel, G., Fara, E., Bylund, K.G., Jenks, J.F., Stephen, D.A., Killingsworth, B., Sansjofre, P., Cartigny, P., 2019. Multiple sulfur isotope signals associated with the late Smithian event and the Smithian/Spathian boundary. *Earth-Science Reviews*. <https://doi.org/10.1016/j.earscirev.2018.06.019>

Vennin, E., Olivier, N., Brayard, A., Bour, I., Thomazo, C., Escarguel, G., Fara, E., Bylund, K.G., Jenks, J.F., Stephen, D.A., Hofmann, R., 2015. Microbial deposits in the aftermath of the end-Permian mass extinction: A diverging case from the Mineral Mountains (Utah, USA).

Sedimentology 62, 753–792. <https://doi.org/10.1111/sed.12166>

Welch, S.A., Beard, B.L., Johnson, C.M., Braterman, P.S., 2003. Kinetic and equilibrium Fe isotope fractionation between aqueous Fe(II) and Fe(III). *Geochimica et Cosmochimica Acta* 67, 4231–4250. [https://doi.org/10.1016/S0016-7037\(03\)00266-7](https://doi.org/10.1016/S0016-7037(03)00266-7)

Wignall, P.B., Bond, D.P.G., Sun, Y., Grasby, S.E., Beauchamp, B., Joachimski, M.M., Blomeier, D.P.G., 2016. Ultra-shallow-marine anoxia in an Early Triassic shallow-marine clastic ramp (Spitsbergen) and the suppression of benthic radiation. *Geological Magazine* 153, 316–331. <https://doi.org/10.1017/S0016756815000588>

Wilkin, R.T., Barnes, H.L., Brantley, S.L., 1996. The size distribution of framboidal pyrite in modern sediments: An indicator of redox conditions. *Geochimica et Cosmochimica Acta* 60, 3897–3912. [https://doi.org/10.1016/0016-7037\(96\)00209-8](https://doi.org/10.1016/0016-7037(96)00209-8)

Wilkin, R.T., Barnes, H.L., 1997. Pyrite formation in an anoxic estuarine basin. *American Journal of Science* 297, 620–650. <https://doi.org/10.2475/ajs.297.6.620>

Woods, A.D., 2014. Assessing Early Triassic paleoceanographic conditions via unusual sedimentary fabrics and features. *Earth-Science Reviews* 137, 6–18. <https://doi.org/10.1016/j.earscirev.2013.08.015>

Wu, L., Beard, B.L., Roden, E.E., Johnson, C.M., 2011. Stable Iron Isotope Fractionation Between Aqueous Fe(II) and Hydrated Ferric Oxide. *Environmental Science & Technology* 45, 1847–1852. <https://doi.org/10.1021/es103171x>

Zhang, G., Zhang, X., Li, D., Farquhar, J., Shen, S., Chen, X., Shen, Y., 2015. Widespread shoaling of sulfidic waters linked to the end-Guadalupian (Permian) mass extinction. *Geology* 43, 1091–1094. <https://doi.org/10.1130/G37284.1>

Zhang, L., Orchard, M.J., Brayard, A., Algeo, T.J., Zhao, L., Chen, Z.Q., Lyu, Z., 2019. The Smithian/Spathian boundary (late Early Triassic): A review of ammonoid, conodont, and carbon-isotope criteria. *Earth-Science Reviews*. <https://doi.org/10.1016/j.earscirev.2019.02.014>

Zhao, H., Dahl, T.W., Chen, Z.Q., Algeo, T.J., Zhang, L., Liu, Y., Hu, Zhaochu, Hu, Zihao, 2020. Anomalous marine calcium cycle linked to carbonate factory change after the Smithian Thermal Maximum (Early Triassic). *Earth-Science Reviews*. <https://doi.org/10.1016/j.earscirev.2020.103418>

Supplementary material

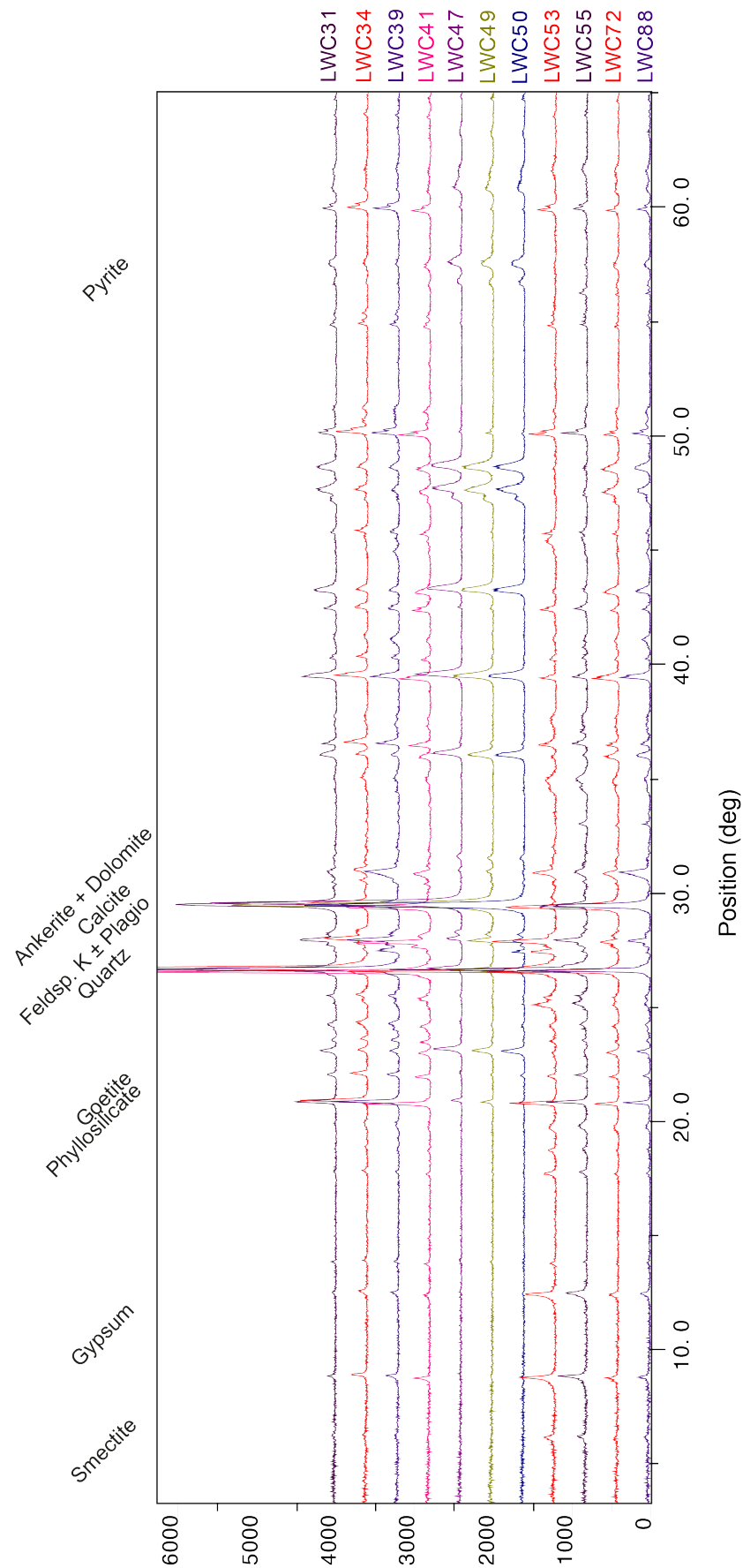


Figure S1: XRD spectra from LWC samples

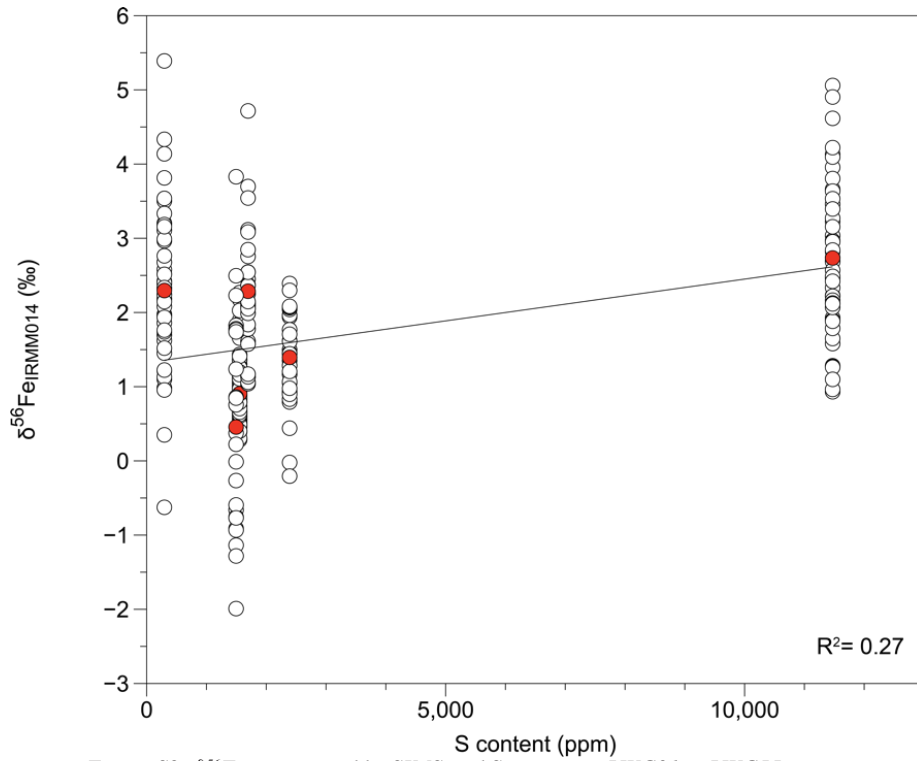


Figure S2: $\delta^{56}Fe_{py}$ measured by SIMS and S content in LWC31 to LWC55

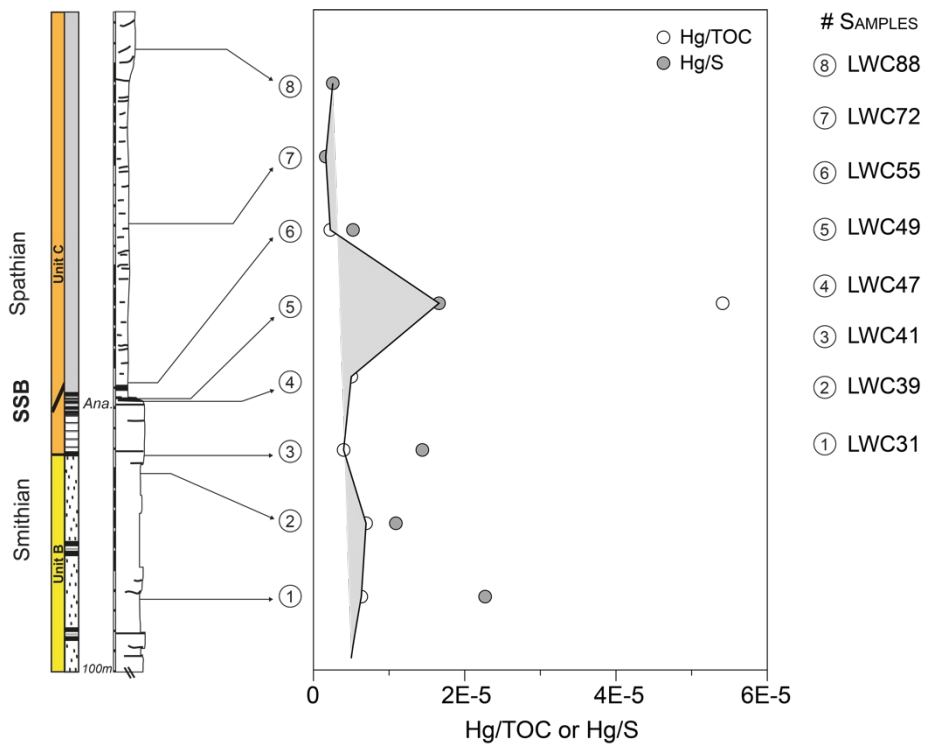


Figure S3: Hg concentrations normalized to TOC or S concentrations along the LWC stratigraphy. Normalization helps to remove biases due to affinity between mercury and organic matter or sulfide phases.

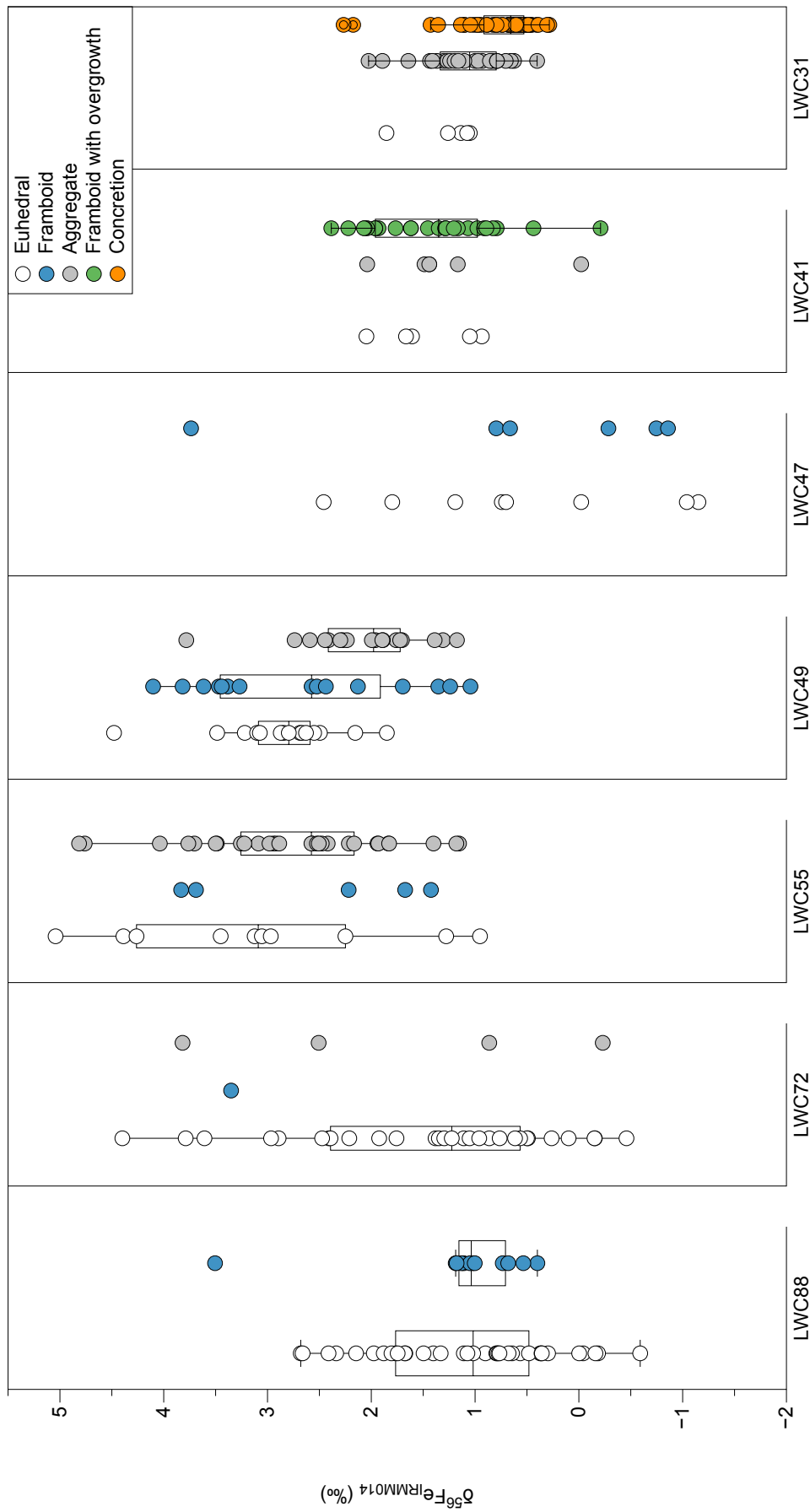


Figure S4: $\delta^{56}\text{Fe}_{\text{py}}$ values in all samples from LWC as a function of pyrite morphologies.

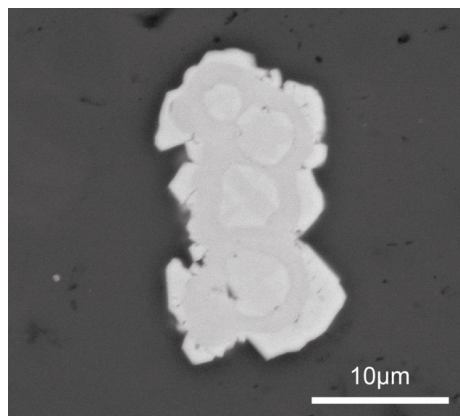
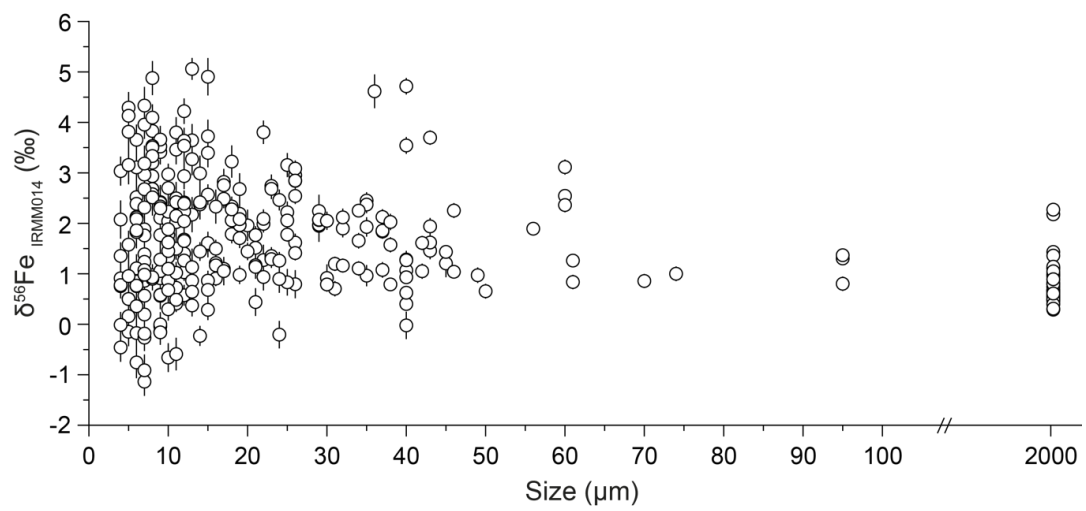


Figure S6: Backscattered electron image of pyrite in LWC49. Zonings are Ni-enriched.

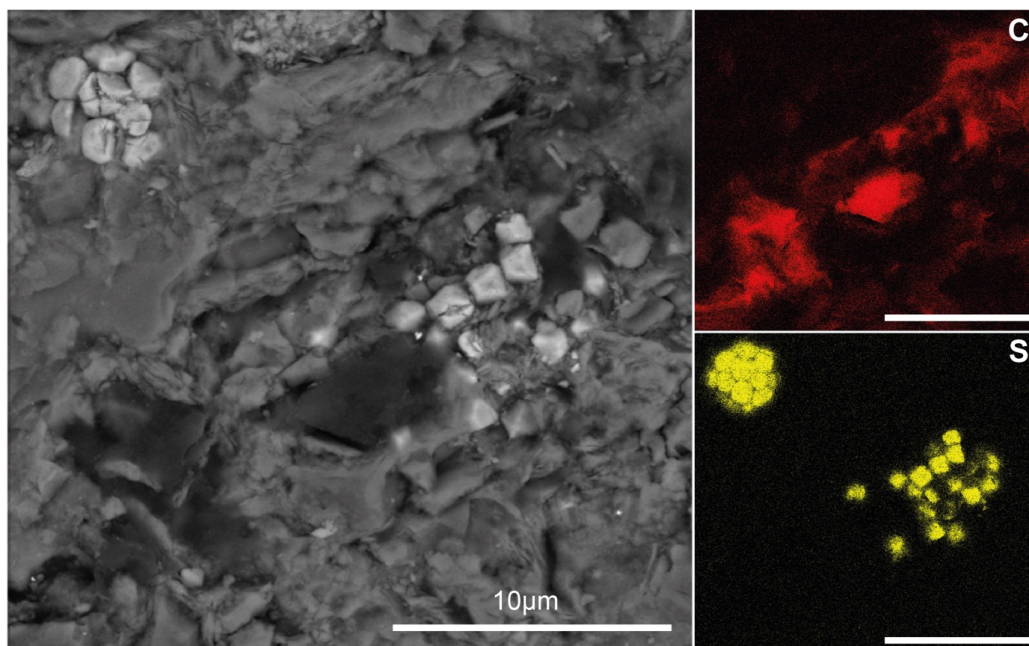


Figure S7: Backscattered electron image of pyrite associated with organic matter in LWC88. On the right part, maps of carbon (in red) and sulfur (in yellow). Scale bars = 10 μm .

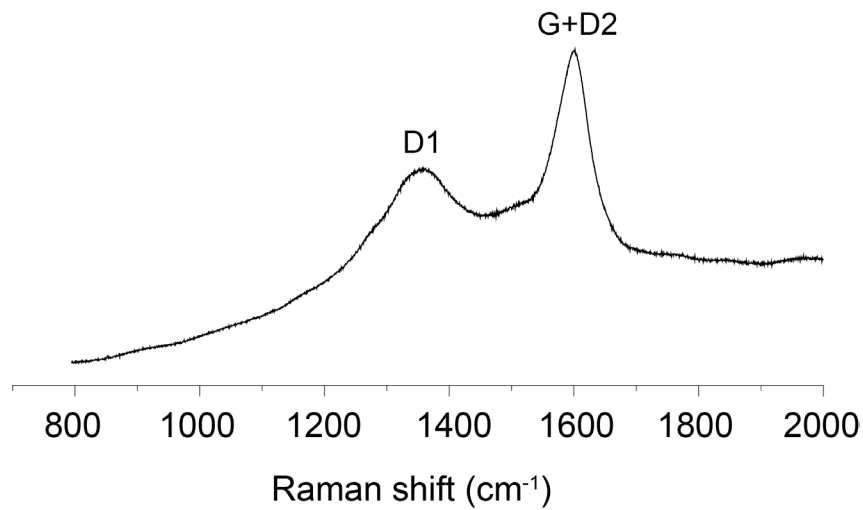


Figure S8: Raman spectra of organic matter in LWC41 and LWC88. Graphite (G) and defect (D) bands provide information on the structural organization of the aromatic skeleton (Beysac et al., 2002).

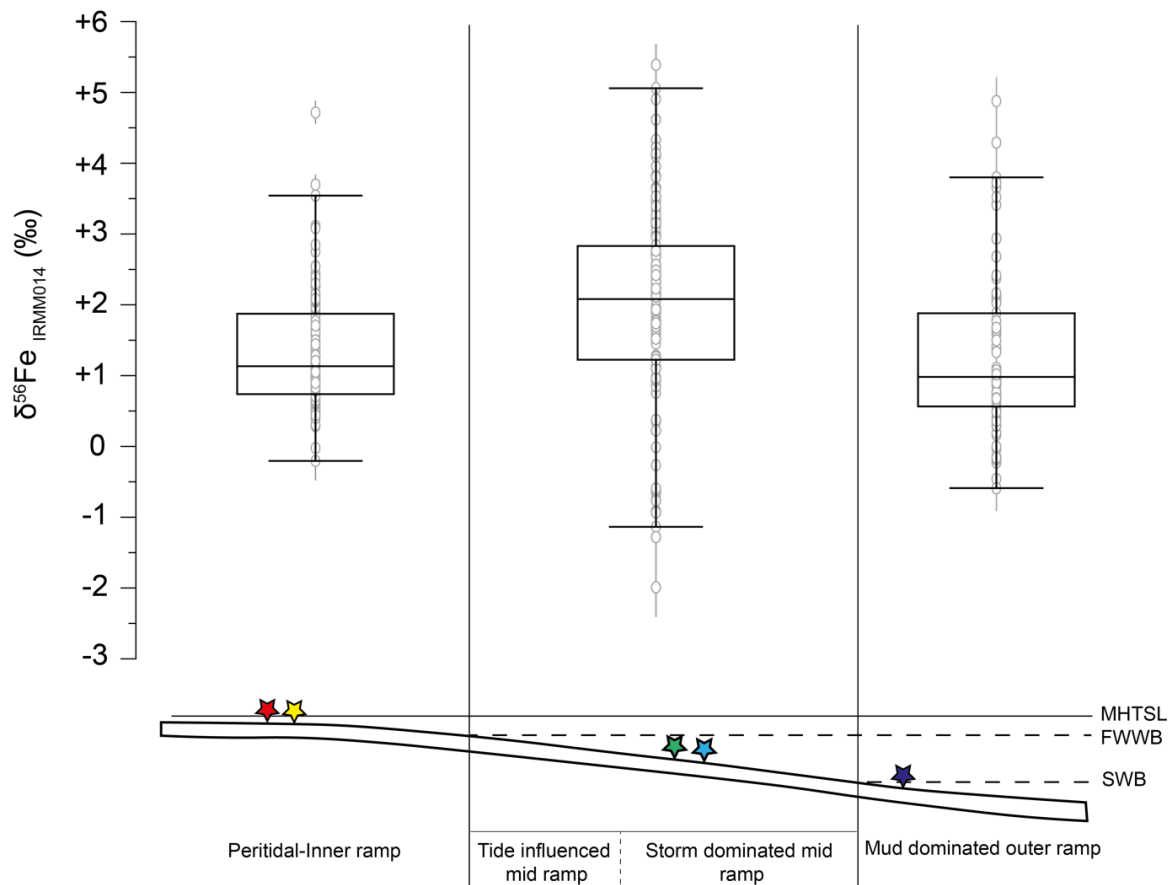


Figure S9: Fe isotope compositions of pyrite under box plot representation as a function of depositional environments along a ramp system. Stars correspond to position of samples. Inner ramp system includes LWC31, LWC39 and LWC41. Mid ramp system includes LWC47, LWC49 and LWC55. Outer ramp system includes LWC72 and LWC88. MHTSL: Mean High Tide Sea Level; FWWB: Fair Weather Wave Base; SWB: Storm Wave Base.

Table S1: S content (ppm), $\delta^{34}\text{S}$ values for pyrite and CAS in LWC samples

Sample #	S content (ppm)	$\delta^{34}\text{S}$ (S1 norm.)	SD	$\delta^{34}\text{S}_{\text{CAS}}$ (NBS-127 norm.)	Setting
LWC70	<i>n.d.</i>	4.16	0.38		Outer ramp
LWC69	126	1.36	0.01		
LWC68	75	16.27	0.23		
LWC67	61	6.07	0.16		Average 6.44
LWC64	661	13.08	0.06	30.00	Stdv 7.40
LWC63	71	14.15	0.07		Min -7.26
LWC61	82	11.70	0.11		Max 16.27
LWC60	781	-0.27	0.95		
LWC59	12358	5.17	0.03	33.51	
LWC57	9226	-7.26	0.88		
LWC55	11472	-2.76	0.91		Mid ramp
LWC54	11267	-7.52	0.89		
LWC53	1621	-3.49	0.00		Average -4.04
LWC52	5298	4.47	0.26		Stdv 3.97
LWC50	1409	-2.24	0.42		Min -8.38
LWC49	296	-3.94	0.02		Max 4.47
LWC48	3811	-4.29	0.50		
LWC47	1496	-8.38	0.21	30.68	
LWC46	1422	-8.20	0.07		
LWC42	59	-10.92	0.06		Inner ramp
LWC41	2391	-19.91	0.03		
LWC40	1548	-14.76	0.11		
LWC39	1695	-16.75	0.06		Average -11.41
LWC38	62	-2.10	0.03	27.56	Stdv 9.31
LWC37	21	0.52	ND		Min -20.52
LWC35	1318	-20.39	0.06		Max 5.82
LWC34	3780	-7.85	0.04		
LWC32	68	5.82	0.04	29.20	
LWC30	956	-20.52	0.09		
LWC31	1555	-18.63	0.34		

Table S2: Hg content (in ppb), TOC and S contents in LWC samples

# Sample	Hg content (ppb)	TOC (%)	TOC (ppb)	Hg/TOC	S content (%)	S content (ppb)	Hg/S
LWC31	9.85	0.04	4.34E+05	2.27E-05	0.16	1.55E+06	6.33E-06
LWC39	11.80	0.11	1.09E+06	1.09E-05	0.17	1.70E+06	6.96E-06
LWC41	9.55	0.07	6.65E+05	1.44E-05	0.24	2.39E+06	3.99E-06
LWC47	7.50	0.15	1.52E+06	4.93E-06	0.15	1.50E+06	5.01E-06
LWC49	16.00	0.10	9.64E+05	1.66E-05	0.03	2.96E+05	5.41E-05
LWC55	25.55	0.49	4.88E+06	5.23E-06	1.15	1.15E+07	2.23E-06
LWC72	2.70	0.17	1.65E+06	1.63E-06	<i>Not meas.</i>	-	-
LWC88	4.05	0.16	1.58E+06	2.56E-06	<i>Not meas.</i>	-	-

Table S3: $\delta^{56}\text{Fe}$ values measured in 8 samples of the LWC section

Analyses #	$\delta^{56}\text{Fe}$ (‰)	2σ	Analyses #	$\delta^{56}\text{Fe}$ (‰)	2σ
P1@01	0.41	0.14	P2@10	0.59	0.14
P1@02	0.68	0.15	P2@11	0.48	0.16
P1@03	0.97	0.13	P2@12	0.49	0.14
P1@04	0.51	0.13	P2@13	0.79	0.12
P1@05	0.66	0.12	P2@14	0.89	0.14
P1@06	0.58	0.14	P2@15	0.39	0.15
P1@07	0.63	0.13	P2@16	2.27	0.14
P1@08	1.43	0.13	P2@17	0.31	0.12
P1@09	0.67	0.13	P2@18	0.61	0.14
P1@10	0.94	0.13	LWC31@01	0.40	0.12
P1@11	0.55	0.14	LWC31@02	1.43	0.13
P1@12	0.67	0.15	LWC31@03	1.30	0.12
P1@13	0.83	0.14	LWC31@04	1.37	0.13
P1@14	0.29	0.15	LWC31@05	0.80	0.14
P1@15	1.01	0.14	LWC31@06	1.00	0.15
P1@16	0.56	0.12	LWC31@07	1.89	0.12
P1@17	0.65	0.13	LWC31@08	1.14	0.16
P1@18	0.60	0.13	LWC31@09	0.84	0.14
P1@19	0.79	0.21	LWC31@10	1.26	0.13
P1@20	1.10	0.13	LWC31@11	1.85	0.14
P1@21	1.10	0.13	LWC31@12	0.63	0.13
P1@22	0.45	0.14	LWC31@13	0.93	0.13
P1@23	1.36	0.14	LWC31@14	1.05	0.15
P1@24	0.66	0.13	LWC31@15	1.08	0.16
P1@25	1.14	0.12	LWC31@16	0.97	0.15
P1@26	0.48	0.14	LWC31@17	1.27	0.12
P1@27	0.63	0.15	LWC31@18	0.66	0.15
P1@28	0.54	0.13	LWC31@19	2.03	0.16
P1@29	0.52	0.15	LWC31@20	1.66	0.16
P1@30	0.98	0.14	LWC31@21	1.11	0.14
P2@01	1.05	0.15	LWC31@22	0.86	0.14
P2@02	0.88	0.13	LWC31@23	1.26	0.17
P2@03	0.47	0.12	LWC31@24	0.71	0.15
P2@04	0.80	0.15	LWC31@25	1.20	0.14
P2@05	0.74	0.13	LWC31@26	1.16	0.14
P2@06	0.74	0.12	LWC31@27	0.79	0.13
P2@07	0.56	0.14	LWC31@28	1.41	0.15
P2@08	2.17	0.14	LWC31@29	0.79	0.13
P2@09	0.28	0.14	LWC39@01	1.61	0.14

(Continued)

Analyses #	$\delta^{56}\text{Fe}$ (‰)	2σ	Analyses #	$\delta^{56}\text{Fe}$ (‰)	2σ
LWC39@3	1.78	0.14	LWC41@13	1.07	0.17
LWC39@7	2.28	0.14	LWC41@14	1.28	0.17
LWC39@8	2.76	0.14	LWC41@15	2.04	0.25
LWC39@9	2.45	0.17	LWC41@16	2.06	0.16
LWC39@10	2.37	0.17	LWC41@17	2.07	0.17
LWC39@12	2.25	0.15	LWC41@18	1.77	0.18
LWC39@13	1.04	0.13	LWC41@19	2.39	0.18
LWC39@14	2.25	0.14	LWC41@21	2.08	0.20
LWC39@15	3.11	0.15	LWC41@22	1.71	0.20
LWC39@16	2.54	0.13	LWC41@23	0.98	0.18
LWC39@17	2.36	0.14	LWC41@25	2.30	0.18
LWC39@18	1.57	0.15	LWC41@26	1.44	0.18
LWC39@19	1.84	0.14	LWC41@27	1.50	0.18
LWC39@20	2.13	0.15	LWC41@28	1.17	0.17
LWC39@21	3.70	0.14	LWC41@29	1.44	0.17
LWC39@23	2.54	0.16	LWC41@30	-0.02	0.27
LWC39@24	1.99	0.17	LWC41@36	0.79	0.28
LWC39@25	2.09	0.19	LWC41@37	0.92	0.27
LWC39@26	3.08	0.16	LWC41@38	0.83	0.26
LWC39@27	2.12	0.17	LWC41@39	0.94	0.27
LWC39@28	2.85	0.17	LWC41@41	0.90	0.27
LWC39@29	3.54	0.17	LWC41@42	-0.21	0.27
LWC39@30	4.72	0.16	LWC41@43	1.17	0.27
LWC39@31	2.06	0.17	LWC41@44	1.05	0.28
LWC39@35	2.05	0.18	LWC41@45	0.44	0.28
LWC49@41	2.15	0.25	LWC41@46	1.21	0.27
LWC49@42	1.06	0.25	LWC47@01	-1.14	0.28
LWC49@46	1.13	0.25	LWC47@2	0.76	0.24
LWC49@49	1.17	0.24	LWC47@5	-0.01	0.26
LWC41@01	1.62	0.18	LWC47@22	-0.27	0.27
LWC41@2	1.46	0.17	LWC47@23	1.83	0.25
LWC41@3	1.62	0.16	LWC47@24	2.50	0.32
LWC41@4	1.94	0.17	LWC47@25	1.24	0.35
LWC41@5	1.35	0.18	LWC47@27	0.86	0.21
LWC41@6	1.29	0.17	LWC47@28	3.83	0.36
LWC41@9	1.96	0.17	LWC47@29	-0.66	0.29
LWC41@10	1.96	0.16	LWC47@30	0.76	0.25
LWC41@11	2.06	0.24	LWC47@31	-0.76	0.31
LWC41@12	1.61	0.17	LWC47@34	-0.91	0.31

(Continued)

Analyses #	$\delta^{56}\text{Fe}$ (‰)	2σ	Analyses #	$\delta^{56}\text{Fe}$ (‰)	2σ
LWC47@36	0.85	0.28	LWC49@56	2.15	0.35
LWC49@01	1.95	0.32	LWC49@57	2.33	0.35
LWC49@2	1.97	0.32	LWC49@59	1.86	0.36
LWC49@3	2.24	0.32	LWC55@2	3.22	0.32
LWC49@4	2.19	0.34	LWC55@3	2.23	0.29
LWC49@5	2.68	0.32	LWC55@4	3.64	0.32
LWC49@6	2.52	0.34	LWC55@5	3.04	0.29
LWC49@7	2.33	0.34	LWC55@7	2.82	0.26
LWC49@8	1.21	0.32	LWC55@8	1.28	0.24
LWC49@9	2.39	0.34	LWC55@10	3.66	0.27
LWC49@11	2.42	0.33	LWC55@11	3.96	0.28
LWC49@12	4.33	0.37	LWC55@12	3.27	0.32
LWC49@14	1.96	0.31	LWC55@13	3.81	0.23
LWC49@15	1.52	0.32	LWC55@16	4.13	0.37
LWC49@16	0.98	0.37	LWC55@17	3.46	0.29
LWC49@18	2.08	0.36	LWC55@18	1.58	0.25
LWC49@21	1.45	0.36	LWC55@19	2.74	0.23
LWC49@22	1.10	0.35	LWC55@20	2.70	0.35
LWC49@26	1.13	0.37	LWC55@21	0.93	0.26
LWC49@30	2.31	0.39	LWC55@22	5.06	0.22
LWC49@31	2.97	0.36	LWC55@23	3.64	0.26
LWC49@33	2.58	0.36	LWC55@24	2.33	0.20
LWC49@36	2.42	0.34	LWC55@25	2.46	0.21
LWC49@37	2.40	0.36	LWC55@26	1.27	0.30
LWC49@38	1.62	0.36	LWC55@27	4.62	0.33
LWC49@39	2.17	0.35	LWC55@28	4.09	0.26
LWC49@40	3.11	0.35	LWC55@29	0.96	0.21
LWC49@43	2.68	0.37	LWC55@30	4.90	0.37
LWC49@44	3.50	0.35	LWC55@31	2.68	0.20
LWC49@45	2.99	0.35	LWC55@32	2.22	0.21
LWC49@46	3.54	0.34	LWC55@33	2.97	0.21
LWC49@47	3.20	0.35	LWC55@34	2.57	0.20
LWC49@48	2.51	0.36	LWC55@35	1.93	0.19
LWC49@49	3.33	0.37	LWC55@36	1.26	0.19
LWC49@50	3.18	0.36	LWC55@38	1.65	0.18
LWC49@51	3.16	0.38	LWC55@39	2.95	0.26
LWC49@53	3.81	0.39	LWC55@40	1.90	0.18
LWC49@54	2.24	0.33	LWC55@41	2.49	0.19
LWC49@55	0.96	0.37	LWC55@42	1.79	0.18

(Continued)

Analyses #	$\delta^{56}\text{Fe}$ (‰)	2σ	Analyses #	$\delta^{56}\text{Fe}$ (‰)	2σ
LWC55@43	2.84	0.21	LWC72@44	1.64	0.31
LWC55@44	1.88	0.23	LWC72@45	2.11	0.34
LWC55@46	4.22	0.25	LWC72@47	2.04	0.39
LWC55@48	3.15	0.24	LWC72@48	0.86	0.27
LWC55@50	3.53	0.26	LWC72@49	2.13	0.30
LWC55@51	1.10	0.18	LWC72@50	4.88	0.34
LWC55@52	2.17	0.26	LWC72@51	2.08	0.38
LWC55@53	2.42	0.23	LWC72@52	0.19	0.30
LWC55@54	2.13	0.22	LWC88@02	0.56	0.27
LWC55@55	2.07	0.18	LWC88@06	1.88	0.26
LWC55@56	2.12	0.28	LWC88@20	1.76	0.22
LWC55@58	3.40	0.29	LWC88@22	0.96	0.18
LWC72@01	0.86	0.22	LWC88@23	1.11	0.14
LWC72@2	2.93	0.32	LWC88@24	1.02	0.19
LWC72@3	3.41	0.25	LWC88@25	1.03	0.17
LWC72@5	3.65	0.30	LWC88@26	0.29	0.20
LWC72@7	-0.46	0.28	LWC88@27	0.41	0.17
LWC72@8	1.35	0.27	LWC88@28	0.91	0.19
LWC72@9	0.50	0.25	LWC88@29	0.86	0.18
LWC72@10	-0.15	0.29	LWC88@30	0.57	0.21
LWC72@11	0.50	0.27	LWC88@38	0.59	0.15
LWC72@12	0.97	0.20	LWC88@37	0.58	0.19
LWC72@13	0.57	0.23	LWC88@54	0.91	0.15
LWC72@14	-0.15	0.22	LWC88@2	1.11	0.28
LWC72@16	0.86	0.20	LWC88@3	2.02	0.35
LWC72@17	1.39	0.23	LWC88@4	2.37	0.26
LWC72@18	-0.23	0.20	LWC88@5	0.37	0.22
LWC72@22	2.94	0.26	LWC88@7	0.64	0.22
LWC72@23	0.72	0.25	LWC88@8	2.68	0.27
LWC72@24	3.80	0.30	LWC88@9	0.78	0.24
LWC72@27	3.72	0.33	LWC88@10	1.77	0.30
LWC72@29	2.13	0.25	LWC88@11	2.16	0.22
LWC72@30	0.16	0.29	LWC88@14	0.77	0.29
LWC72@31	0.99	0.27	LWC88@15	0.68	0.21
LWC72@32	4.29	0.31	LWC88@16	0.30	0.23
LWC72@33	0.91	0.32	LWC88@17	1.07	0.23
LWC72@36	1.58	0.28	LWC88@18	-0.04	0.24
LWC72@41	1.05	0.30	LWC88@20	0.90	0.23
LWC72@42	-0.17	0.30	LWC88@22	0.00	0.24

(Continued)

Analyses #	$\delta^{56}\text{Fe}$ (‰)	2σ
LWC88@23	1.40	0.22
LWC88@24	1.68	0.21
LWC88@25	1.33	0.21
LWC88@26	2.41	0.24
LWC88@27	3.52	0.23
LWC88@31	1.02	0.21
LWC88@32	0.68	0.24
LWC88@33	1.50	0.22
LWC88@34	-0.18	0.31
LWC88@35	1.77	0.26
LWC88@36	-0.16	0.25
LWC88@37	-0.59	0.32
LWC88@38	0.36	0.29
LWC88@39	1.68	0.21
LWC88@40	0.49	0.22
LWC88@41	2.68	0.22

CHAPTER 5.

MICROBIAALLY INFLUENCED Fe CYCLING IN ARCHEAN STROMATOLITES

This chapter focuses on one of the most emblematic stromatolite formation, in term of diversity of morphologies and preservation, of the Neoproterozoic: the 2.72 Ga Tumbiana Formation (Fortescue Group, Pilbara, western Australia). This well-preserved feature has resulted in many works dedicated to the search of early metabolic pathways, including for example sulfur respiration and microbial CH₄ oxidation (Hayes, 1994; Thomazo et al., 2009; Marin-Carbonne et al., 2018). Therefore, the Tumbiana stromatolites are recognized as one of the oldest consensual biogenic stromatolites, characterized by a large diversity of microorganisms active during their formation (Buick, 1992; Thomazo et al., 2009; Coffey et al., 2013; Sforza et al., 2014; Stüeken et al., 2017; Marin-Carbonne et al., 2018; Lepot et al., 2019). However, although highly suggested (Yoshiya et al., 2012), the presence of iron respiration has never been demonstrated. I investigated the Fe redox cycling in different laminae of four stromatolite samples using spatially resolved pyrite $\delta^{56}\text{Fe}$ values in order to assess the role of iron reducing organisms in pyrite formation. This chapter is under the form of a published manuscript at *Geochimica et Cosmochimica Acta*, entitled “Intense biogeochemical iron cycling revealed in Neoproterozoic micropyrates from stromatolites”.



Intense biogeochemical iron cycling revealed in Neoproterozoic micropyrates from stromatolites

Marie-Noëlle Decraene^{a,b,*}, Johanna Marin-Carbonne^a, Christophe Thomazo^{c,d},
Nicolas Olivier^e, Pascal Philippot^{f,g}, Harald Strauss^h, Etienne Deloule^b

^a Institut des Sciences de la Terre, Université de Lausanne, Lausanne, Switzerland

^b Université de Lorraine, CNRS, CRPG, 54500 Vandoeuvre les Nancy, France

^c UMR CNRS 5561 Biogéosciences, Université de Bourgogne Franche Comté, Dijon, France

^d Institut Universitaire de France

^e Université Clermont Auvergne, CNRS, IRD, Laboratoire Magmas et Volcans, F-63000 Clermont-Ferrand, France

^f Géosciences Montpellier, CNRS UMR 5243, Université de Montpellier, 34000 Montpellier, France

^g Institute of Astronomy, Geophysics and Atmospheric Sciences, University of São Paulo, Rua do Matão 1226, Cidade Universitária, 05508-090 São Paulo, Brazil

^h Westfälische Wilhelms-Universität, Institut für Geologie und Paläontologie, Corrensstr. 24, 48149 Münster, Germany

Received 22 March 2021; accepted in revised form 19 July 2021; available online 29 July 2021

Abstract

Iron isotope compositions of sedimentary pyrites (FeS₂) are used to constrain the redox evolution of the Precambrian ocean and early Fe-based metabolisms such as Dissimilatory Iron Reduction (DIR). Sedimentary pyrites can record biotic and abiotic iron reduction, which have similar ranges of Fe isotopic fractionation, as well as post-depositional histories and metamorphic overprints that can modify Fe isotope compositions. However, some exceptionally well-preserved sedimentary records, such as the stromatolite-bearing Tumbiana Formation (ca. 2.7 Ga, Western Australia) have been proven to retain primary information on Early Neoproterozoic microbial ecosystems and associated metabolic pathways. Here, we present *in situ* Fe isotope measurements of micropyrates included in four stromatolites from the Tumbiana Formation in order to assess iron respiration metabolism using Fe isotope signatures. A set of 142 micropyrates has been analyzed in three lamina types, *i.e.* micritic, organic-rich and fenestral laminae, by Secondary Ion Mass Spectrometry (SIMS), using a Hyperion radio-frequency plasma source. The diversity of laminae is attributed to specific depositional environments, leading to the formation of Type 1 (micritic laminae) and Type 2 (organic-rich laminae) and early diagenetic effects (Type 3, fenestral laminae). Type 1 and 2 laminae preserved comparable $\delta^{56}\text{Fe}$ ranges, respectively from -1.76‰ to $+4.15\text{‰}$ and from -1.54‰ to $+4.44\text{‰}$. Type 3 laminae recorded a similar range, although slightly more negative $\delta^{56}\text{Fe}$ values between -2.20‰ and $+2.65\text{‰}$. Globally, our data show a large range of $\delta^{56}\text{Fe}$ values, from -2.20‰ to $+4.44\text{‰}$, with a unimodal distribution that differs from the bimodal distribution previously reported in the Tumbiana stromatolites. Such a large range and unimodal distribution cannot be explained by a unique process (*e.g.*, biotic/abiotic Fe reduction or pyrite formation only controlled by the precipitation rate). It rather could reflect a two-step iron cycling process in the sediment pore water including i) partial Fe oxidation forming Fe(OH)₃ with positive $\delta^{56}\text{Fe}$ values followed by ii) partial, possibly microbially induced, Fe reduction leading to Fe²⁺ availability for pyrite formation by sulfate reducers carrying both negative $\delta^{56}\text{Fe}$ and $\delta^{34}\text{S}$ signatures. In this model, the buildup and subsequent reduction through time of a residual Fe(OH)₃ reservoir arising from the activity of methanotrophs, can explain the

Abbreviations: DIR, Dissimilatory Iron Reduction; MSR, Microbial Sulfate Reduction; AOM, Anaerobic Oxidation of Methane; SEM, Scanning Electron Microscopy; SIMS, Secondary Ion Mass Spectrometry

* Corresponding author at: Institut des Sciences de la Terre, Université de Lausanne, Lausanne, Suisse.

E-mail address: marie-noelle.decraene@unil.ch (M.-N. Decraene).

<https://doi.org/10.1016/j.gca.2021.07.020>

0016-7037/© 2021 The Author(s). Published by Elsevier Ltd.

This is an open access article under the CC BY license (<http://creativecommons.org/licenses/by/4.0/>).

strongly positive $\delta^{56}\text{Fe}_{\text{Fe}(\text{OH})_3}$ values up to 4‰. These results indicate that Archean microbial mats have been the site of the interaction of several closely linked biogeochemical cycles involving Fe, S and C.

© 2021 The Author(s). Published by Elsevier Ltd. This is an open access article under the CC BY license (<http://creativecommons.org/licenses/by/4.0/>).

Keywords: Early life; Stromatolites; Tumbiana Formation; Iron isotopes; Ion microprobe; Iron respiration

1. INTRODUCTION

Stromatolites are laminated organo-sedimentary structures, formed by microbial activities in response to environmental and sediment dynamics, and are considered to be the most undisputable evidence of early life on Earth (Allwood et al., 2006; Awramik, 2006; Schopf et al., 2007). The 2.724 Ga old Tumbiana Formation, Western Australia, contains some of the best preserved and most diverse Archean stromatolitic carbonate structures (Buick, 1992; Sakurai et al., 2005; Awramik and Buchheim, 2009; Coffey et al., 2013), including domal, conical, ridged and tufted mm- to m-scale morphologies (Buick, 1992; Flannery and Walter, 2012). A variety of isotopic proxies such as $\delta^{13}\text{C}_{\text{org}}$, $\delta^{98/95}\text{Mo}$ and $\delta^{82/78}\text{Se}$ have been interpreted to reflect the buildup of oxidized dissolved species that could result from the activity of oxygenic photosynthesizers (Coffey et al., 2013; Stüeken et al., 2015a; Williford et al., 2016; Stüeken et al., 2017). The record of one of the largest organic carbon isotope excursions on Earth, the Fortescue Excursion, with $\delta^{13}\text{C}_{\text{org}}$ values as low as -60‰ (Hayes, 1994; Hinrichs, 2002) has been interpreted to represent either the incorporation of ^{12}C in organic matter during oxidation of methane through methanotrophy (Schidlowski, 1982; Hayes, 1994; Eigenbrode and Freeman, 2006; Thomazo et al., 2009; Lepot et al., 2019) or linked to acetogenesis using Acetyl-coA metabolisms (Slotznick and Fischer, 2016), although this latter pathway has been considered unlikely in the Tumbiana stromatolites by other workers (Lepot et al., 2019). Other biological pathways reported in these stromatolites include Microbial Sulfate Reduction (Thomazo et al., 2009; Marin-Carbonne et al., 2018), Dissimilatory Iron Reduction (Yoshiya et al., 2012), arsenic cycling involving both As(III) oxidation and As(V) reduction (Sforna et al., 2014), microbially-induced ammonia oxidation leading to one of the most extreme isotopic ^{15}N enrichment ($\delta^{15}\text{N}$ up to $+50\text{‰}$) ever recorded on Earth (Thomazo et al., 2011; Stüeken et al., 2015b), and microbially-derived nano-aragonite precipitates associated with organic globules containing aromatic, aliphatic and carboxyl groups (Lepot et al., 2008; Lepot et al., 2009).

The presence of sulfate and Fe-oxides at the time of deposition and/or early diagenesis may have fueled the reaction of anaerobic oxidation of methane (AOM) in the Tumbiana Formation (Marin-Carbonne et al., 2018; Lepot et al., 2019). Sulfate-reducing metabolizers reduce sulfate into dissolved S species (e.g., H_2S , HS^- , S_0), a process accompanied by a large fractionation of sulfur isotopes between sulfide and sulfate of $\sim 70\text{‰}$ (e.g., Johnston, 2011; Sim et al., 2011). This metabolic effect has been identified in the Tumbiana Formation by bulk rock (Thomazo

et al., 2009) and *in situ* (Marin-Carbonne et al., 2018) S-isotope analyses, although the extent of the measured isotopic fractionation differed from one technique to another. The reduced $\delta^{34}\text{S}$ range of $\sim 8\text{‰}$ measured by bulk analyses has been interpreted as MSR completed under low sulfate concentrations, as expected during the Archean (Crowe et al., 2014). In contrast, the larger $\delta^{34}\text{S}$ range of $\sim 84\text{‰}$ recorded at the lamina scale confirms the activity of MSR associated with locally high sulfate concentrations (Marin-Carbonne et al., 2018). DIR reduces Fe-oxides into dissolved Fe^{2+} and is associated with Fe isotopic fractionation of -2.9‰ between ferrous iron and Fe-oxides (Crosby et al., 2005; Crosby et al., 2007). Although a bulk rock study reported a limited $\delta^{56}\text{Fe}$ range in the Tumbiana Formation interpreted to reflect a limited Fe cycle (Czaja et al., 2010), *in situ* laser ablation analyses evidenced a larger Fe isotopic range of both negative and positive $\delta^{56}\text{Fe}$ values between -4.2‰ and $+2.1\text{‰}$, interpreted as reflecting an active Fe cycling (Nishizawa et al., 2010; Yoshiya et al., 2012). Ideally, coupled analyses of Fe and S isotopes of pyrites can provide informations on the intimate link between Fe and S cycling in microbial mats (Archer and Vance, 2006; Marin-Carbonne et al., 2014). While $\delta^{34}\text{S}$ analyses at the scale of individual microscopic pyrites have been performed in stromatolitic laminae of the Tumbiana Formation (Marin-Carbonne et al., 2018), this approach was not available until recently for Fe isotopes.

Here we use the new procedure developed for micrometric scale analyses of Fe isotopes by SIMS (Decraene et al., 2021) to the same micropyrrite-bearing laminae present in Tumbiana stromatolites previously investigated by Marin-Carbonne et al. (2018). Results show that a large range of positive and negative $\delta^{56}\text{Fe}$ recorded in these micropyrrites is best attributed to an intense oxidative and reductive Fe cycling, parsimoniously interpreted as resulting from DIR activity, coupled with methanotrophy and MSR.

2. MATERIAL AND METHODS

2.1. Geological setting and sample collection for SIMS analyses and Fe speciation

The Tumbiana Formation is a sedimentary succession of about 200 m thick, 680 km wide, with an WNW-ESE extension through the Pilbara Craton (Thorne and Trendall, 2001). The Tumbiana Formation is part of the Neoproterozoic Fortescue Group (Hamersley Basin, Western Australia) and consists of alternating low-metamorphic grade volcanic and sedimentary rocks deposited during a period of continental extension and rifting (Blake and Barley, 1992; Blake, 1993). It has been subdivided in two main members, the Mingah Member, composed of volcanic tuffs, accre-

tionary lapillis, conglomerates and sandstones, and the Meentheena Member, composed of several horizons of stromatolitic limestones, sandstones and mudstones (Thorne and Trendall, 2001; Sakurai et al., 2005; Flament et al., 2011; Flannery et al., 2014). U-Pb dating on zircons and volcanic rocks yielded depositional ages between 2724 ± 5 Ma and 2715 ± 6 Ma (Arndt et al., 1991; Blake et al., 2004). The Tumbiana Formation overprinted low-grade metamorphism < 300 °C, allowing the preservation of cell-like organic globules in micrites (Lepot et al., 2008). The depositional environment has been interpreted either as a giant lake system (Buick, 1992; Bolhar and Van Kranendonk, 2007; Awramik and Buchheim, 2009; Coffey et al., 2013; Stüeken et al., 2015b) or a shallow marine setting (Thorne and Trendall, 2001; Sakurai et al., 2005).

Our samples are from the PDP1 drill core of the Pilbara Drilling Project, which intercepts the base of the Maddina basalt, the Meentheena Member and the top of the Mingah Member (Philippot et al., 2009). This drill core has been extensively studied over the past decade for its mineralogy and S, C, N isotopic compositions and represents a unique time capsule in the search for Earth's earliest metabolic activities (Thomazo et al., 2007; Lepot et al., 2008; Lepot et al., 2009; Philippot et al., 2009; Thomazo et al., 2011; Marin-Carbonne et al., 2018; Lepot et al., 2019). This SIMS study focuses on four stromatolites from the Meentheena Member, sampled at 67.8 m (GIS67.8), 68.1 m (GIS68.1), 68.9 m (GIS68.9) and 70.8 m (GIS70.8) depth in stromatolite-rich intervals of the PDP1 drill core (Fig. 1). Samples GIS67.8 and GIS68.9 have been previously investigated for their C_{organic} and S_{pyrite} isotopes compositions of carbonaceous matter and nano-scale sulfides at high spatial resolution (Marin-Carbonne et al., 2018; Lepot et al., 2019). A detailed sample description is further provided in Section 3.1.

2.2. Optical and SEM observations

The samples were first described by optical microscopy. Scanning Electron Microscopes (SEM) were used at CRPG Nancy (JEOL JSM 6510) and at ISTE Lausanne (Tescan Mira LMU) to produce backscattered electron images at a working distance of 21 mm. Analysis were performed with a 1.5nA primary beam at 20 kV. Energy dispersive X ray spectrometry was used for semi quantitative punctual analysis and mapping to determine elemental composition of the sulfides and to select pyrite rich areas for subsequent SIMS analysis.

2.3. Iron speciation

Identification of Fe-mineral species follows the sequential iron extraction procedure proposed by Poulton and Canfield (2005). Four different mineral phases were extracted: (1) carbonate-associated Fe (Fe_{carb}) present in calcite, siderite and ankerite; (2) Fe contained in oxides, hydroxides and oxyhydroxides (Fe_{ox}) including hematite, goethite, akaganeite, lepidocrocite and ferrihydrite; (3) magnetite (Fe_{mag}) and (4) Fe bound to poorly reactive sheet silicates (Fe_{PRS}) including biotite, chlorite and glauconite. Furthermore, in order to evaluate total iron contents

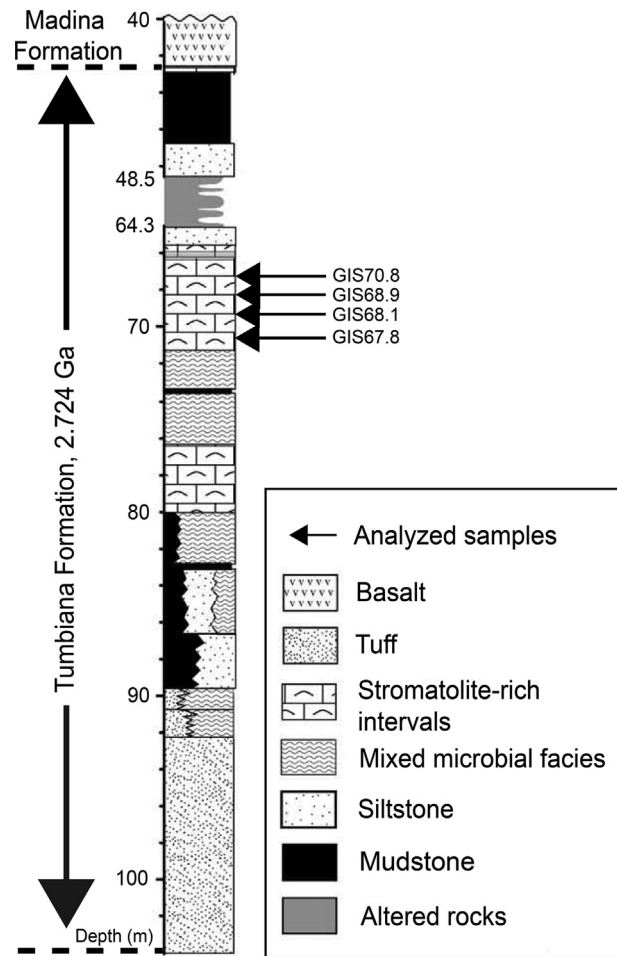


Fig. 1. Simplified log of the PDP1 drill core modified after Thomazo et al. (2009). Black arrows represent the location of the studied samples.

(Fe_T) the technique developed by Aller et al. (1986); see Poulton and Canfield (2005) was applied. Around 200 mg of each sample were ashed (at 450 °C for 8 h) in ceramic crucibles and reacted with 10 mL 6 N HCl. This extraction was conducted at 80 °C for 24 h. Each extracted species of iron described above was reacted with phenantroline and the concentration of the resulting Fe^{2+} -phenantroline complex was measured using a Genesys spectral photometer Series 10 at 515 nm, at the Institut für Geologie und Paläontologie, Westfälische Wilhelms-Universität Münster, Germany, following the method proposed in Reuschel et al. (2012) and described in detail in Sauvage et al. (2013). The concentration of S associated with pyrite (S_{py}) was evaluated using gravimetric quantification after chromium reducible sulfur extraction (Canfield et al., 1986). Iron associated with pyrite (Fe_{py}) was calculated from the S_{py} assuming a stoichiometric ratio. The total iron concentrations (Fe_T) measured during the course of this study using the sequential extraction method were also compared to previous ICPMS measurements reported in Thomazo et al. (2010). The intercalibration between both methods displays a good correlation ($R^2 = 0.97$, Table 1, Electronic Annex (EA); Fig. EA-1).

Table 1
Iron speciation data for stromatolite samples, from 42.7 m to 85.7 m depth of the drill core PDPI.

Sample	Lithology	Al (ppm)	Fe _T (ppm)	Fe _{ICPMS} (ppm)	Fe _{py} (ppm)	Fe _{carb} (ppm)	Fe _{ox} (ppm)	Fe _{mag} (ppm)	Fe _{prps} (ppm)	Fe _U + Fe _{prgs} (ppm)	Fe _{HR} (ppm)	Fe _{HR} /Fe _T	Fe _{py} /Fe _{HR}
GIS42.7	Stromatolite	3963.11	10,260.00	11,354	348	3640	178	522	1100	5572.00	4688	0.46	0.07
GIS68.0	Stromatolite	14,257.09	21,443.36	21,707	958	3887	90	316	1194	16,192.36	5251	0.24	0.18
GIS68.2	Stromatolite	22,435.73	<i>n.a.</i>	25,459	1655	2530	193	464	4109	<i>n.a.</i>	4842	0.19	0.34
GIS68.9	Stromatolite	55,316.89	<i>n.a.</i>	42,581	3745	<i>n.a.</i>	<i>n.a.</i>	<i>n.a.</i>	<i>n.a.</i>	<i>n.a.</i>	<i>n.a.</i>	<i>n.a.</i>	<i>n.a.</i>
GIS69.2	Stromatolite	17,074.17	26,845.63	27,440	3745	4207	120	826	1104	17,947.63	8898	0.33	0.42
GIS70.4	Stromatolite	15,332.43	18,687.26	18,949	1742	3967	41	312	755	12,625.26	6062	0.32	0.29
GIS70.8	Stromatolite	18,578.64	22,503.36	22,960	87	3642	204	813	1306	17,757.36	4746	0.21	0.02
GIS72.1	Stromatolite	8976.31	12,697.44	12,446	523	2794	12	149	284	9219.44	3478	0.27	0.15
GIS77.1	Stromatolite	4483.11	<i>n.a.</i>	12,628	1045	3860	324	<i>n.a.</i>	509	<i>n.a.</i>	<i>n.a.</i>	<i>n.a.</i>	<i>n.a.</i>
GIS77.2	Stromatolite	51,989.90	<i>n.a.</i>	57,246	958	1391	325	571	2741	<i>n.a.</i>	3245	0.06	<i>n.a.</i>
GIS78.1	Stromatolite	6275.34	10,370.15	15,330	1132	4018	114	171	510	4935.15	5435	0.52	0.21
GIS78.4	Stromatolite	7123.50	17,622.55	16,177	697	3649	82	371	659	12,823.55	4799	0.27	0.15
GIS83.2	Stromatolite	21,143.30	46,724.23	43,029	958	4765	188	1605	2277	39,208.23	7516	0.16	0.13
GIS85.7	Stromatolite	<i>n.a.</i>	34,037.77	<i>n.a.</i>	2003	4947	277	1620	2959	25,190.77	8847	0.26	0.23

Because of their high reactivity toward hydrogen sulfide (Canfield et al., 1992; Poulton and Canfield, 2005), the sum of Fe_{carb}, Fe_{ox}, Fe_{mag} and Fe_{py} are referred to as ‘Highly Reactive’ Fe fraction (Fe_{HR}) of the total iron. Fe_{HR}/Fe_T ratio is commonly used to scale anoxic conditions when values are above a threshold of 0.38 (Raiswell and Canfield, 1998). Fe_{HR} enrichment, in excess toward this maximal detrital background, indicates an external source of reactive Fe decoupled from the siliciclastic flux. Euxinic conditions can also be recognized when both Fe_{HR}/Fe_T and Fe_{py}/Fe_{HR} exceed thresholds of 0.38 and 0.80, respectively. However, in lacustrine environment, bias due to high sedimentation rates makes threshold based on Fe_{HR}/Fe_T questionable (Lyons and Severmann, 2006) and Tumbiana Fe speciation data should be interpreted with caution.

2.4. *In situ* Fe isotope analyses of micropyrates by SIMS

142 micropyrates were analyzed over three SIMS sessions (April 2018, July 2018 and October 2018). One reference standard grain was included in each sample mount, and the mounts were carbon-coated before analysis. *In situ* iron isotope analyses were performed with the CAMECA ims 1280HR2 equipped with the new Hyperion radio-frequency source at CRPG-IPNT in Nancy (France). Using the procedure detailed in Decraene et al. (2021), this source allows measurement of micrometric targets (less than 20 microns) with a current density 10 times greater than that of a standard duoplasmatron source (Liu et al., 2018). A 3nA Gaussian ¹⁶O⁻ primary beam was focused into a 2.5 to 3 μm spot. Typical ⁵⁶Fe intensities ranged between 1.2x10⁷ and 8.2x10⁷ counts per second. The mass resolution power was set at ~6800 to resolve interferences on ⁵⁴Fe⁺ (⁵³CrH⁺) and on ⁵⁶Fe⁺ (⁵⁵MnH⁺). The measurement of ⁵²Cr allow to monitor the ⁵⁴Cr⁺ isobaric interference on ⁵⁴Fe⁺ according to the method described in Marin-Carbonne et al. (2011). Simultaneous measurement of ⁵²Cr, ⁵⁴Fe, ⁵⁶Fe and ⁵⁷Fe was performed in multicollection mode with three off-axis Faraday cups and one electron multiplier for ⁵²Cr. Finally, iron isotope compositions are reported as permil variations of ⁵⁶Fe/⁵⁴Fe ratios measured in the samples normalized to that of the international reference material IRMM-014 as the following:

$$\delta^{56}\text{Fe} = \left[\frac{\left(\frac{^{56}\text{Fe}}{^{54}\text{Fe}} \right)_{\text{sample}}}{\left(\frac{^{56}\text{Fe}}{^{54}\text{Fe}} \right)_{\text{IRMM-014}}} - 1 \right] * 1000$$

Before running analyses, ³²S⁺ isotope images were collected via electron multiplier, in order to record the exact location of the micropyrates (Electronic Annex (EA); Fig. EA-2). Afterward, a 90 s presputtering time was applied, followed by data acquisition in multicollection mode for 300 seconds. Backgrounds of the detectors were measured during presputtering and were subtracted from each analysis. Balmat and Spain pyrites (respectively δ⁵⁶-Fe_{true} = -0.40 ± 0.01‰ Whitehouse and Fedo, 2007 and δ⁵⁶-Fe_{true} = +0.52 ± 0.03‰ Decraene et al., 2021) were used as standards to correct the instrumental mass fractionation

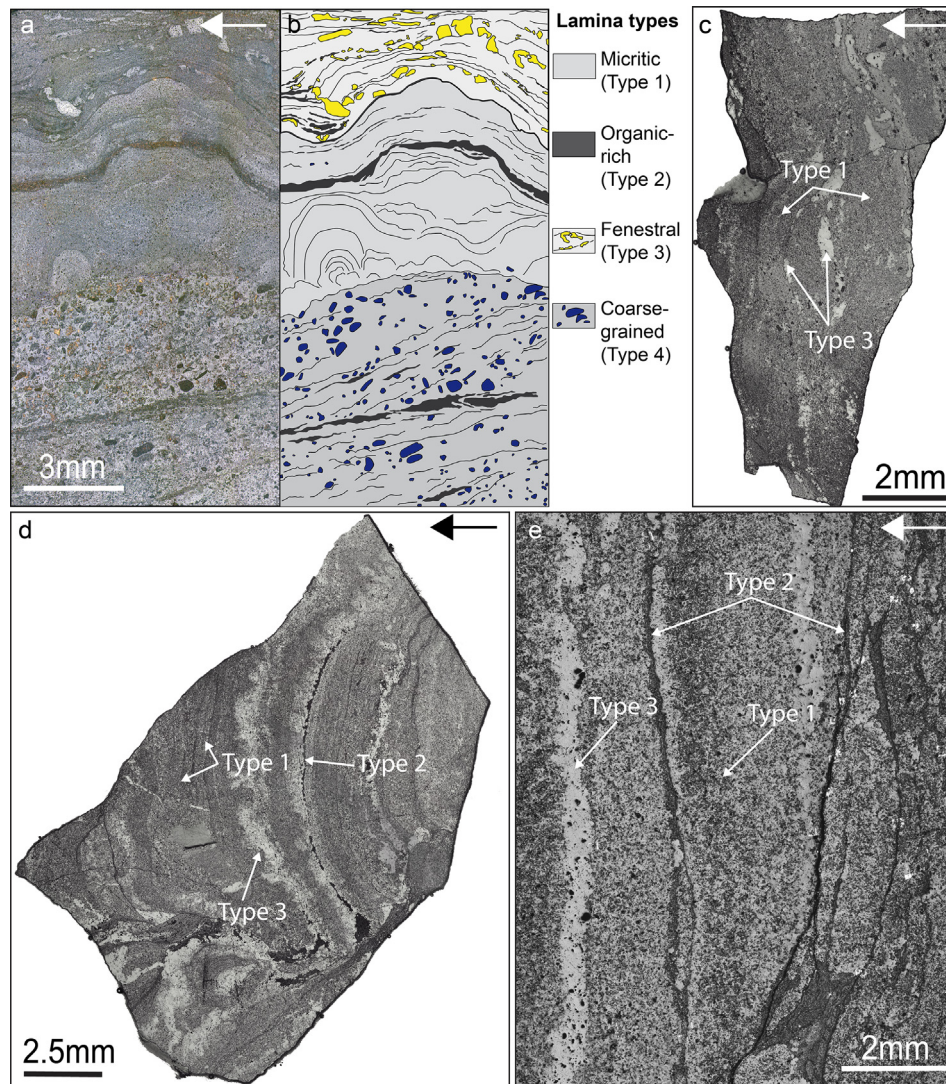


Fig. 2. Optical microscope large views of the four analyzed samples. (a) GIS68.9; (b) Schematic view of the four different laminae (Type 1: Micritic lamina; Type 2: Organic-rich lamina; Type 3: Fenestral lamina and Type 4: coarse-grained lamina) in GIS68.9; (c) GIS70.8; (d) GIS67.8 and (e) GIS68.1. The different types of laminae are indicated by white arrows. The mineralogy of the different laminae is detailed in Fig. 3. Arrows on the top right give the orientation of the samples. (For interpretation of the references to colour in this figure legend, the reader is referred to the web version of this article.)

$\alpha = (^{56}\text{Fe}/^{54}\text{Fe})_{\text{meas}} / (^{56}\text{Fe}/^{54}\text{Fe})_{\text{true}}$, defined as the ratio between iron isotopic ratio measured by SIMS and the true ratio determined by MC-ICP-MS (for Multi Collector Inductively Coupled Plasma Mass Spectrometry). The reproducibility was $\pm 0.24\%$ for Balmat pyrite (2SD, standard deviation, April 2018 session; Electronic Annex (EA); Fig. EA-3) and $\pm 0.28\%$ for Spain pyrite (July 2018 session; Electronic Annex (EA); Fig. EA-4; Table EA-1).

3. RESULTS

3.1. Petrographic investigations

The four studied samples are part of a well-developed stromatolite facies and belong to the stromatolite-rich interval described between ~66 to ~71.5 m depth of the

PDP1 drill core (Fig. 1, Philippot et al., 2009). The four investigated samples (GIS67.8, GIS68.1, GIS68.9, GIS70.8) show an internal variability in the stromatolite fabric, leading to the recognition of four main types of laminae (Fig. 2):

- Type 1: Micritic laminae, where a cement of micrite represents the major mineral phase, associated with scarce automorphic chlorites and micropyrates. Few micrometric (10 μm to 20 μm) detrital zircons were also observed. This stromatolitic fabric is characterized by well-marked laminated domal structures.
- Type 2: Organic-rich laminae, which are composed of nano to micropyrates and automorphic chlorites. Accessory mineral phases such as sphalerite, zircon and anatase are rare. This type of lamina is often laterally

discontinuous and is observed between different types of laminae.

- Type 3: Fenestral laminae, which are composed of micritic and sparitic cements, and micropyrates. This laminoid-fenestral fabric is characterized by spar-filled cavities that are arranged along the lamination. These cavities can be either by irregular or elongated horizontal fenestrae, which are embedded in a micritic cement.
- Type 4: coarse-grained laminae, composed of various sedimentary grains such as peloids and ooids, with a sparse and non-continuous internal lamination. These do not contain any pyrite and therefore are not considered in the following geochemical ($\delta^{56}\text{Fe}$) comparisons.

Type 1 and 3 laminae have a pluri-millimeter to centimeter thickness whereas Type 2 are sub-millimetric to millimetric. Microcrystalline quartz cement is identified in all samples, independently of the type of laminae, which indicates a post-depositional silicification process (Lepot et al., 2009; Philippot et al., 2009). Pyrites are identified in Type 1, 2 and 3 laminae (Fig. 3) in various proportions (more abundant in organic-rich laminae relative to the others) and exhibit euhedral morphologies, as single grains or aggregates. The size of the pyrites ranges from ~ 100 nm–20 μm , except for GIS68.1, which present some larger pyrites up to 60 μm . Pyrites associated with organic-rich laminae (Type 2) are mainly between 5 to 10 μm in size and in average ~ 10 μm in micritic and fenestral laminae (Types 1 and 3). The measured micropyrates have similar size ranges (5 to 15 μm) whatever the lamina type, but the smallest pyrites ($< 5\mu\text{m}$ to hundreds nm) are preferentially located in organic-rich (Type 2) laminae (Fig. 3).

3.2. Iron species

Iron speciation was used to evaluate the relative contribution of carbonate, oxide, silicate and sulfide as iron-bearing minerals compared to the total iron content. Iron speciation has been measured in 41 samples from 42.7 m to 90.4 m depth of the PDP1 drill core. Total iron (Fe_T) content in three different lithologies (stromatolites, mudstones and siltstones) vary between 0.64 and 5.69wt.% with a mean value of 2.99wt.%. Results for Fe speciation in the stromatolite facies are shown in Table 1.

Fe_T in stromatolites range between 1.03 and 4.67wt.% with a mean value of 2.22wt.%. Among the different Fe-bearing phases, Fe content was subdivided into three main categories. These include extractable iron (Fe_{ext}) clumped iron in pyrites, oxides, magnetites and carbonates (Fe_{py} , Fe_{ox} , Fe_{mag} and Fe_{carb}); iron in poorly reactive sheet silicates (mainly chlorite, Fe_{PRS}); and unreactive iron (Fe_U), defined as the difference between extractable iron and the total iron contents. The extraction of Fe from poorly reactive sheet silicates is however often incomplete and part of Fe contained in chlorites may participate to the fraction of unreactive iron. Iron oxides display low Fe content between 12 to 325 ppm with an average value of 165 ppm. Fe content in magnetites ranges between 149 to 1620 ppm with an average value of 645 ppm. Except for GIS68.9 and GIS69.2, which display Fe concentrations in pyrites close to 0.37wt.%, the average pyrite Fe content is around 0.10wt.%. Fe content in carbonates varies between 0.14 and 0.49wt.% with a mean value of 0.36wt.%. Fe content associated with poorly reactive silicates displays a range between 0.02 and 0.41wt.%, with an average of 0.15wt.%. We observe that Fe is mostly concentrated in carbonate and in sheet silicates as chlorites. Moreover, the difference between Fe_T and Fe_{ext} shows that a large fraction ($\sim 25\%$) of iron is concentrated in unreactive phases.

3.3. SIMS analyses

3.3.1. Iron isotope compositions

Iron isotope compositions of the 142 micropyrates analyzed in GIS67.8, GIS68.1, GIS68.9 and GIS70.8 are summarized in Table 2. These micropyrates show a large range in iron isotope compositions, between -2.20‰ and $+4.44\text{‰} \pm 0.24\text{‰}$ ($2\sigma, \text{SD}$) (Fig. 4a), encompassing the entire terrestrial iron isotope range of values reported in the literature (Dauphas et al., 2017). Stromatolites GIS67.8 and GIS68.9 show a similar large range of $\delta^{56}\text{Fe}$ between -2.20‰ and $+4.15\text{‰}$ ($n = 70$) and between -1.44‰ and $+4.44\text{‰}$ ($n = 60$) respectively, while GIS68.1 and GIS70.8 display mostly positive values and smaller ranges of $\delta^{56}\text{Fe}$ values from -0.01‰ to $+3.79\text{‰}$ ($n = 8$) and from $+0.49\text{‰}$ to $+2.41\text{‰}$ ($n = 4$) respectively (Fig. 4a). In addition, we observe that iron isotope compositions of analyzed micropyrates might be dependent on the

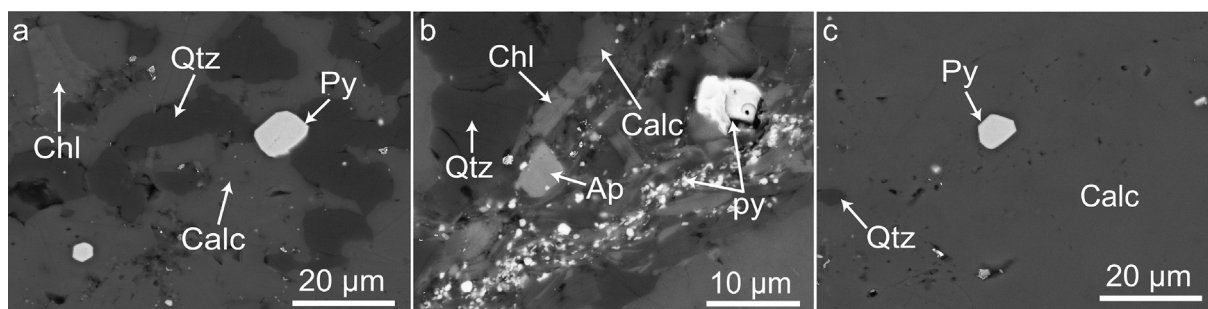


Fig. 3. SEM images of the different types of laminae in which micropyrates were measured. (a) Micropyrates in a micritic lamina (Type 1); (b) Micropyrates in an organic-rich lamina (Type 2); (c) Micropyrates in a fenestra (Type 3). Chl: Chlorite; Qtz: Quartz; Py: Pyrite; Calc: Calcite; Ap: Apatite.

Table 2

Iron isotope compositions of 142 micropyrates from GIS67.8, GIS68.1, GIS68.9 and GIS70.8 samples of the Tumbiana Formation. The type of lamina refers to micritic laminae (Type 1), organic-rich laminae (Type 2) and fenestral laminae (Type 3).

# Sample	Analyses	$^{56}\text{Fe}^+$ intensity (cps)	$\delta^{56}\text{Fe}$ (‰)	2σ (‰)	Type of lamina
GIS67.8	PDP1-G1Z8a	3.63E+07	-1.86	0.21	3
	PDP1-G1Z16b	1.58E+07	1.39	0.30	3
	PDP1-G1Z14c	7.34E+07	1.13	0.18	2
	PDP1-G1Z13d	8.23E+07	-0.87	0.16	2
	PDP1-G1Z11k	3.37E+07	-0.93	0.19	3
	PDP1-G1Z11j	3.40E+07	-1.17	0.19	3
	PDP1-G1Z11i	3.98E+07	-0.54	0.19	3
	PDP1-G1Z11f	4.40E+07	0.90	0.19	3
	PDP1-G1Z11b	5.60E+07	-0.77	0.16	3
	PDP1-G1-Z33i	3.07E+07	0.81	0.19	1
	PDP1-G1-Z33h	2.15E+07	-0.36	0.22	1
	PDP1-G1-Z33e	2.67E+07	0.53	0.20	1
	PDP1-G1-Z33c	1.50E+07	-0.30	0.32	1
	PDP1-G1-Z33d	1.55E+07	-0.22	0.31	1
	PDP1-G1-Z25e	2.63E+07	2.67	0.23	1
	PDP1-G1-Z33b	2.00E+07	0.52	0.25	1
	PDP1-Z18e	3.51E+07	-0.54	0.21	3
	PDP1-Z19a	4.62E+07	-1.14	0.19	3
	PDP1-Z18b	2.94E+07	-1.00	0.21	3
	PDP1-Z18c	2.75E+07	0.32	0.18	3
	PDP1-Z19b	2.72E+07	-2.20	0.21	3
	PDP1-Z19c	5.68E+07	-0.57	0.16	3
	PDP1-Z19d	2.19E+07	-1.96	0.23	3
	PDP1-Z19e	1.54E+07	1.73	0.34	3
	PDP1-Z19f	4.69E+07	-1.35	0.17	3
	PDP1-Z19g	2.92E+07	2.65	0.22	3
	PDP1-Z20d	3.05E+07	-0.11	0.21	3
	PDP1-Z20e	4.64E+07	-0.81	0.17	3
	PDP1-Z20g	4.77E+07	0.24	0.18	3
	PDP1-Z27a	4.32E+07	-0.54	0.16	2
	PDP1-Z27b	1.45E+07	0.74	0.31	2
	PDP1-Z22a	5.63E+07	0.45	0.17	3
	PDP1-Z31a	2.90E+07	0.09	0.17	2
	PDP1-Z31b	2.39E+07	-0.28	0.26	2
	PDP1-Z31c	5.43E+07	0.63	0.14	2
	PDP1-Z31d	2.34E+07	1.78	0.22	2
	PDP1-Z31e	3.27E+07	-1.54	0.19	2
	PDP1-Z31f	3.59E+07	1.79	0.16	2
	PDP1-Z36a	3.82E+07	-0.38	0.16	2
	PDP1-Z37a	5.87E+07	1.91	0.13	1
	PDP1-Z37b	3.43E+07	0.81	0.22	1
	PDP1_Z1a	2.14E+07	2.36	0.18	1
	PDP1_Z1b	5.49E+07	2.77	0.11	1
	PDP1_Z1c	5.08E+07	1.92	0.14	1
	PDP1_Z1d	2.10E+07	1.37	0.22	1
	PDP1_Z2a	2.67E+07	0.35	0.23	3
	PDP1_Z2b	2.61E+07	0.98	0.18	3
	PDP1_Z2d	2.42E+07	-0.63	0.19	3
	PDP1_Z2e	1.91E+07	0.18	0.26	3
	PDP1_Z2f	5.23E+07	1.54	0.16	3
	PDP1_Z2g	2.94E+07	1.04	0.16	3
	PDP1_Z2h	3.35E+07	1.21	0.14	3
	PDP1-IV-Z9a	2.48E+07	4.15	0.26	1
	PDP1-IV-Z21	2.65E+07	-1.03	0.20	3
	PDP1-IV-Z19a	2.52E+07	-1.27	0.20	3
	PDP1-IV-Z19c	1.76E+07	-0.88	0.24	3
	PDP1-IV-Z19d	1.99E+07	-0.26	0.25	3
	PDP1-IV-Z19e	1.50E+07	2.15	0.33	3
	PDP1-IV-Z19f	1.94E+07	-0.92	0.29	3
	PDP1-IV-Z20	2.68E+07	-0.15	0.22	1

Table 2 (continued)

# Sample	Analyses	$^{56}\text{Fe}^+$ intensity (cps)	$\delta^{56}\text{Fe}$ (‰)	2σ (‰)	Type of lamina
	PDP1-IV-Z18a	3.32E+07	1.17	0.18	3
	PDP1-IV-Z18b	2.11E+07	-2.06	0.25	3
	PDP1-IV-Z12a	3.66E+07	0.84	0.17	1
	PDP1-IV-Z11a	2.46E+07	2.33	0.22	1
	PDP1-IV-Z11b	2.77E+07	-1.40	0.21	1
	PDP1-IV-Z6a	2.09E+07	3.43	0.36	1
	PDP1-IV-Z6b	2.08E+07	0.71	0.23	1
	PDP1-IV-Z4a	2.68E+07	-0.27	0.18	1
	PDP1-IV-Z5a	1.24E+07	-1.76	0.37	1
	PDP1-IV-Z5b	1.54E+07	2.43	0.28	2
GIS68.1	PDP1-III-Z1b	3.49E+07	3.48	0.16	1
	PDP1-III-Z15e	2.70E+07	3.30	0.19	1
	PDP1-III-Z15d	2.41E+07	3.79	0.29	1
	PDP1-III-Z20c	3.62E+07	2.20	0.17	1
	PDP1-III-Z23a	3.42E+07	-0.01	0.20	1
	PDP1-III-Z13a	3.07E+07	0.44	0.17	1
	PDP1-III-Z13b	2.62E+07	1.20	0.18	1
	PDP1-III-Z10b	3.17E+07	2.42	0.23	1
GIS68.9	PDP1-G3Z4a	6.32E+07	-0.21	0.15	1
	PDP1-G3Z4b	4.33E+07	3.81	0.50	1
	PDP1-G3Z4e	5.57E+07	1.34	0.15	1
	PDP1-G3Z4f	6.63E+07	0.81	0.16	1
	PDP1-G3Z4g	3.72E+07	3.41	0.18	1
	PDP1-G3Z4h	6.43E+07	0.10	0.18	1
	PDP1-G3Z4i	5.61E+07	0.45	0.16	1
	TumbianaZ25b	4.62E+07	2.18	0.29	2
	TumbianaZ30a	5.28E+07	-0.33	0.14	1
	TumbianaZ31a	5.98E+07	-0.58	0.16	1
	TumbianaZ31b	6.30E+07	0.17	0.15	1
	TumbianaZ17a	7.06E+07	-0.75	0.14	1
	TumbianaZ17b	7.10E+07	0.07	0.13	1
	TumbianaZ18a	7.65E+07	-1.44	0.13	1
	TumbianaZ16a	7.35E+07	-0.68	0.12	1
	Tumbiana-Z19	7.37E+07	0.45	0.14	1
	Tumbiana-Z15	7.99E+07	-0.36	0.15	1
	Tumbiana-Z23a	2.92E+07	0.02	0.17	2
	Tumbiana-Z23b	6.56E+07	-0.27	0.15	2
	Tumbiana-Z23c	1.86E+07	-1.12	0.45	2
	Tumbiana-Z23f	5.37E+07	1.73	0.17	2
	Tumbiana-Z24b	5.11E+07	2.23	0.24	2
	LE_Z1	6.48E+07	0.91	0.15	2
	LE-Z2e	5.89E+07	4.44	0.16	2
	LE-Z2c	4.42E+07	3.80	0.21	2
	LE-Z4b	5.47E+07	4.02	0.22	2
	LE-Z4a	5.50E+07	0.08	0.17	2
	LE-Z8a	5.72E+07	2.09	0.23	2
	LE-Z12b	5.97E+07	1.42	0.15	2
	LE-Z12a	4.77E+07	2.80	0.17	2
	LE-Z13b	3.20E+07	3.62	0.21	2
	L1_Z2a	4.68E+07	2.05	0.20	2
	L3_Z3	5.48E+07	1.59	0.16	2
	Matrix_Z1b	2.78E+07	1.94	0.19	1
	Matrix_Z1c	5.06E+07	3.06	0.13	1
	Matrix_Z1f	4.73E+07	1.92	0.14	1
	Matrix_Z1e	4.77E+07	3.34	0.15	1
	Matrix_Z1d	5.39E+07	0.55	0.15	1
	Matrix_Z2a	4.60E+07	1.75	0.16	1
	Matrix_Z2b	3.64E+07	1.33	0.15	1
	Matrix_Z2c	2.72E+07	1.65	0.17	1
	Matrix_Z2d	3.03E+07	1.87	0.19	1
	Matrix_Z2e	3.86E+07	0.19	0.14	1
	Matrix_Z3a	4.57E+07	1.02	0.12	1

Table 2 (continued)

# Sample	Analyses	$^{56}\text{Fe}^+$ intensity (cps)	$\delta^{56}\text{Fe}$ (‰)	2σ (‰)	Type of lamina
	Matrix_Z3d	1.68E+07	-1.34	0.27	1
	Matrix_Z3e	4.05E+07	0.78	0.14	1
	Matrix_Z3f	2.78E+07	2.93	0.24	1
	Matrix_Z3g	5.56E+07	1.06	0.13	1
	Matrix_Z3h	4.39E+07	1.25	0.13	1
	Matrix_Z3i	2.21E+07	1.27	0.24	1
	Matrix_Z4a	3.46E+07	1.08	0.18	1
	Matrix_Z4b	1.95E+07	-0.61	0.23	1
	Matrix_Z4c	3.41E+07	1.36	0.15	1
	Matrix_Z4d	4.71E+07	0.45	0.12	1
	Matrix_Z5a	6.67E+07	0.41	0.11	1
	Matrix_Z5b	4.64E+07	1.34	0.13	1
	Matrix_Z5c	3.42E+07	1.09	0.18	1
	Matrix_Z5d	2.98E+07	1.01	0.18	1
	Matrix_Z6b	5.75E+07	0.72	0.12	1
	Matrix_Z6c	5.81E+07	0.96	0.12	1
GIS70.8	PDP1-G2-Z9a	4.28E+07	2.04	0.29	1
	PDP1-G2-Z9b	5.60E+07	0.49	0.14	1
	PDP1-G2-Z9d	5.24E+07	1.72	0.15	1
	PDP1-G2-Z9e	5.69E+07	2.41	0.15	1

type of their hosting lamina (Fig. 4b). Pyrites measured in micritic laminae show large isotopic variations ($\delta^{56}\text{Fe}$ from -1.76‰ to $+4.15\text{‰}$, $n = 77$), comparable with those recorded in pyrites hosted in organic-rich laminae ($\delta^{56}\text{Fe}$ from -1.54‰ to $+4.44\text{‰}$, $n = 29$). In comparison, fenestral laminae yield a smaller Fe isotope signal from -2.20‰ to $+2.65\text{‰}$ ($n = 36$). The median $\delta^{56}\text{Fe}$ value is $+1.01\text{‰}$ in micritic type laminae, $+1.42\text{‰}$ in organic-rich laminae and -0.54‰ in fenestral laminae (Fig. 4c).

Iron isotopic compositions can also be correlated with the pyrite sizes (Fig. 5). Fe isotopic compositions range between -0.54‰ and $+2.67\text{‰}$ for pyrites below $5\ \mu\text{m}$ in size ($n = 9$, mean $\delta^{56}\text{Fe} = 0.69\text{‰}$), between -1.76‰ and $+3.94\text{‰}$ for the $5\text{--}10\ \mu\text{m}$ category ($n = 64$, mean $\delta^{56}\text{Fe} = 0.68\text{‰}$), -2.20‰ and $+4.44\text{‰}$ for pyrites of $[10\text{--}15]\ \mu\text{m}$ ($n = 53$, mean $\delta^{56}\text{Fe} = 0.92\text{‰}$) and between -1.44‰ and $+3.48\text{‰}$ for pyrites bigger than $15\ \mu\text{m}$ ($n = 16$, mean $\delta^{56}\text{Fe} = 1.07\text{‰}$). Pyrites $> 10\ \mu\text{m}$ in size seem to record ^{56}Fe -enriched isotopic compositions. However, due to the difference in the population size of each categories, we cannot conclude on a clear influence of the size of the pyrites on their respective Fe isotopic compositions. Furthermore, pyrites with similar size can record a large Fe isotopic range (Fig. 6a and b; pyrites of $8\text{--}9\ \mu\text{m}$ size have $\delta^{56}\text{Fe}$ values between -0.61‰ and $+4.02\text{‰}$). Finally, individual pyrite grain observations after SIMS analysis support that there is no correlation between the $\delta^{56}\text{Fe}$ values and the pyrite shapes (Fig. 6c; Electronic Annex (EA); Fig. EA-5).

3.3.2. Probability density and comparison with previous *in situ* studies

Iron isotopic compositions are presented using probability densities, which calculate a Gaussian function for

each analysis considering the associated error (Marin-Carbonne et al., 2012). Because probability density distribution strongly depends on bin size and bin boundary, we chose a bin size of 0.1 in order to reduce the bin boundary effects, *i.e.* the distribution has the same shape whatever the starting $\delta^{56}\text{Fe}$ value of the probability density, even if artificial secondary peaks are produced (Fig. 7a). We also report cumulative functions which allow us to clearly identify bimodal and modal distributions (Fig. 7). In previous works from the Redmont area, Nishizawa et al. (2010) and Yoshiya et al. (2012) reported a bimodal distribution (Fig. 7b) with a positive mode around $+1\text{‰}$ and a negative mode around -1.8‰ . In this study we observe a monomodal $\delta^{56}\text{Fe}$ distribution with mode around $+1\text{‰}$ (Fig. 7a). The cumulative probability functions provide an alternative dataset representation (Fig. 7c and d) and show a stair shape distribution, which highlights the two modes observed in the previous studies (Fig. 7d). In this study, probability density and cumulative functions are in good agreement with a theoretical gaussian curve, showing a progressive increasing ramp for the cumulative representation (Fig. 7c). The whole dataset thus follows a gaussian distribution centered at $+1\text{‰}$ (Fig. 7a). The difference between our distribution and previously published distributions is likely due to different grade of metasomatism that affected variously the Redmont and Meentheena localities (White et al., 2014). Moreover, most of the pyrite grains in this study range from 5 to 10 μm when pyrites previously measured by Nishizawa et al. (2010) and Yoshiya et al. (2012) were tens to hundreds of μm . Micropyrites from this study likely recorded more discreet processes that are not evident in larger pyrite grains from the Redmont locality.

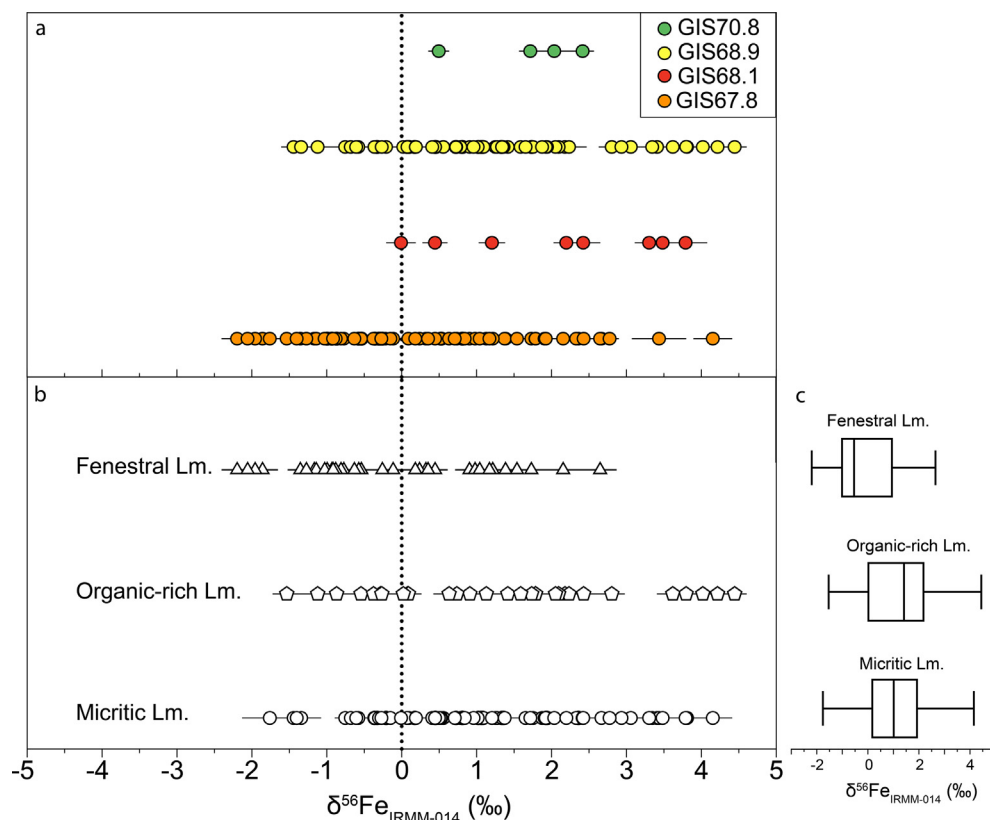


Fig. 4. Iron isotopic compositions measured (a) in the different samples GIS67.8 (orange dots, $n = 70$), GIS68.1 (red dots, $n = 8$), GIS68.9 (yellow dots, $n = 60$) and GIS70.8 (green dots, $n = 4$); (b) in the different laminae: micritic (Type 1, $n = 77$), organic-rich (Type 2, $n = 29$) and fenestrae (Type 3, $n = 36$). GIS67.8 displays large $\delta^{56}\text{Fe}$ isotopic range between -2.20‰ and $+4.15\text{‰}$, similar to GIS68.9 isotopic range. Amplitude of isotopic ranges for GIS68.1 and GIS70.8 are less wide and probably un-representative of the whole isotopic variability. In general, more ^{56}Fe -depleted values are observed in fenestrae whereas organic-rich laminae are characterized by ^{56}Fe -enriched isotopic values. Error bars yield the 2SE (standard error); (c) Box plots using $\delta^{56}\text{Fe}$ values of the different laminae types. (For interpretation of the references to colour in this figure legend, the reader is referred to the web version of this article.)

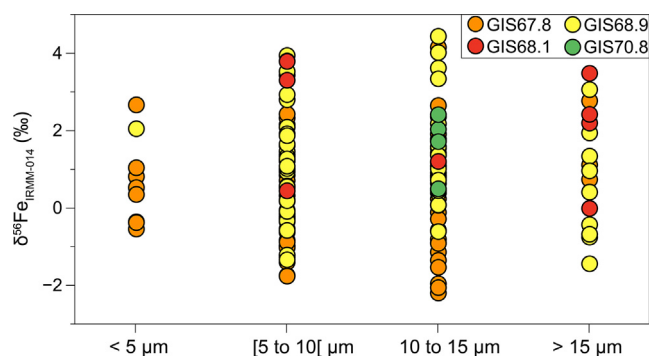


Fig. 5. Iron isotopic compositions as a function of the size of micropyrates. We considered 4 categories of size: less than $5\ \mu\text{m}$, $5\ \mu\text{m}$ to $10\ \mu\text{m}$, $10\ \mu\text{m}$ to $15\ \mu\text{m}$ and $> 15\ \mu\text{m}$. (For interpretation of the references to colour in this figure legend, the reader is referred to the web version of this article.)

4. DISCUSSION

The large range of $\delta^{56}\text{Fe}$ values measured in micropyrates of the Tumbiana Formation could reflect several biotic or abiotic processes. In the following section, we discuss the possible iron sources involved in pyrite precipitation and processes able to explain the range of $\delta^{56}\text{Fe}$ value recorded in the studied stromatolitic laminae.

4.1. Context of micropyrates precipitation

4.1.1. Pyrite as a minor sink of iron in Tumbiana stromatolites

Although iron speciation proxy is not calibrated for lacustrine environment, important features can be drawn from these analyses. In Tumbiana stromatolites, Fe speciation data show that Fe_{PRS} and Fe_{U} , mostly represented by

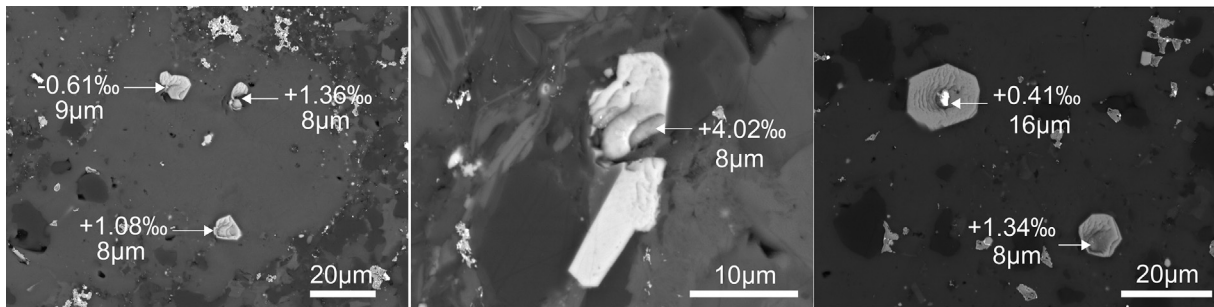


Fig. 6. SEM pictures of micropyrrites in GIS68.9. (a) and (b) Fe isotopic compositions measured in pyrites of 8 to 9 μm size. This size category shows an isotopic range up to 4‰, showing the absence of correlation between $\delta^{56}\text{Fe}$ and the size of the pyrite; c) Fe isotopic compositions of two hexagonal pyrites of 16 μm and 8 μm in size. These pyrites recorded an isotopic difference of 1‰, located at 30 μm from each other, meaning that iron isotopic compositions are not controlled by the shape of the pyrite.

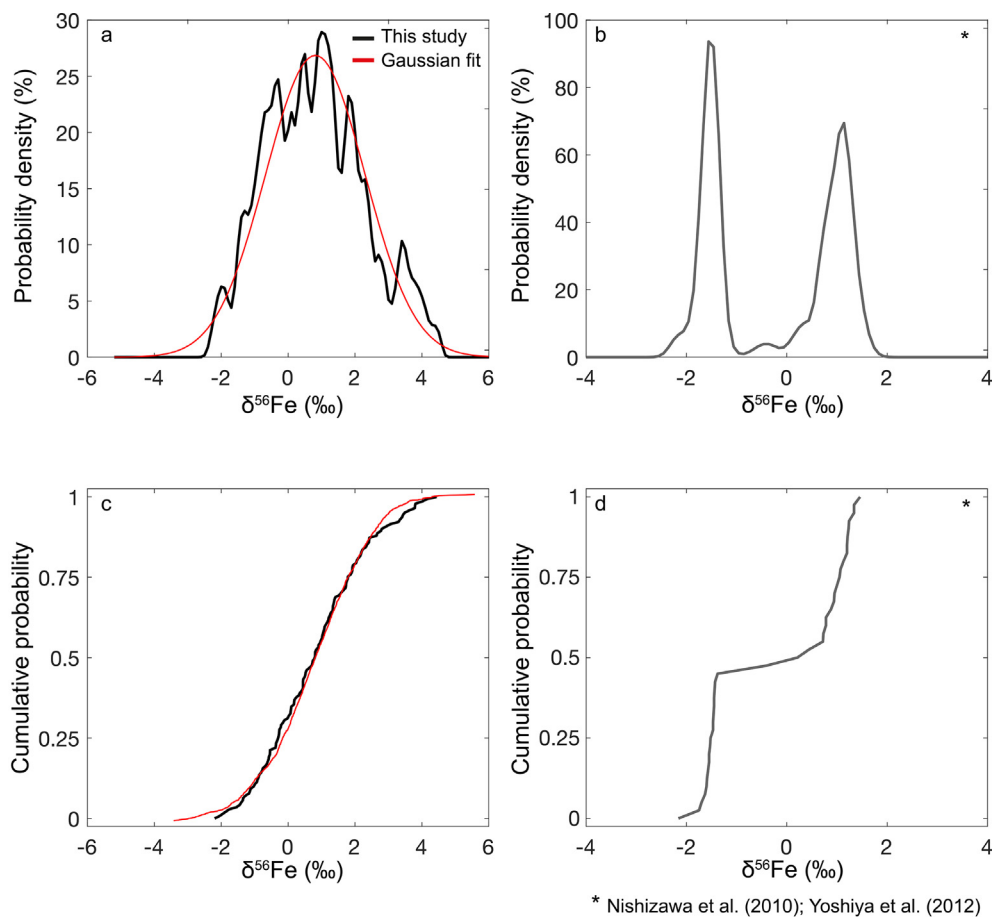


Fig. 7. Probability density distributions calculated for a) the entire $\delta^{56}\text{Fe}$ dataset (black curve, this study) showing a continuous, gaussian shape distribution centered on +1‰. The red curve represents the theoretical Gaussian function given by $f(x) = \frac{1}{\sigma\sqrt{2\pi}} * e^{-\frac{(x-\mu)^2}{2\sigma^2}}$ with μ the dataset mean value and σ the standard deviation; b) Previous published $\delta^{56}\text{Fe}$ values for stromatolite samples describing a bimodal distribution (grey curve, data from Nishizawa et al., 2010; Yoshiya et al., 2012); c) Cumulative function of the entire dataset (black curve, this study) and Gaussian fit (red curve) and d) Cumulative function associated with Nishizawa et al. (2010) and Yoshiya et al. (2012) data. (For interpretation of the references to colour in this figure legend, the reader is referred to the web version of this article.)

chlorites, represent in average 73% of the total iron content (Fe_T). The occurrence of few detrital minerals like zircon and anatase suggests that continental weathering and riverine transport were active during deposition of the Tumbiana sediments. Moreover, in situ weathering and

devitrification of the mafic substrate, including volcanic ashes, likely drove the formation of chlorites that are abundant in the samples. As aluminium is a conservative element during weathering and is not remobilized by low temperature hydrothermal fluids, the positive correlation between

Fe_T and Al contents within stromatolite layers ([Electronic Annex \(EA\); Fig. EA-6](#)) suggests that Fe is mostly inherited from Fe-rich mafic lithologies ([Sugisaki, 1978; Wintsch and Kvale, 1994; Sugitani et al., 1996](#)). The input of Fe-rich detritus can explain the low abundance of highly reactive iron (Fe_{HR}) compare to Fe_T ([Table 1](#)). The low pyrite content (4% relative to Fe_T) coupled with low Fe_{pyr}/Fe_{HR} ratio (~0.11 on average) argue for non-sulfidic conditions in the Tumbiana water column. However, as organic-matter is sulfidized in the Tumbiana stromatolites ([Lepot et al., 2009](#)), variable local sulfidic conditions could have occurred in the sediment pore water. Finally, the micropyrates studied here only reflect a small fraction of the Fe budget in the Tumbiana environment and therefore cannot be considered to account for the whole Tumbiana basin Fe cycling.

4.1.2. Origin of the laminae diversity

The observed fabric variability in our samples underlines the existence of four different types of laminae reflecting diverse mineralization processes leading to the formation of stromatolites ([Fig. 2a](#)). The micritic laminae (Type 1), which are mainly made of microcrystalline calcite, reflect a microbial cement precipitation commonly observed in stromatolites through Earth history ([Visscher et al., 1998](#)). The organic-rich laminae (Type 2) are chlorite-rich suggesting a terrigenous input in the system. The spatial distribution of these laminae along the domal structure of the stromatolite, their morphology and the lateral variability in thickness argue against a stylolitic origin. Process of trapping of detrital material is highlighted and illustrated by the presence of chlorite, zircon and anatase. The formation of organic matter is associated with the activity of microbial mats. Fenestral laminae (Type 3) are laterally more or less continuous. These sparitic fenestrae indicate a syngenetic or early diagenetic filling of a primary porosity that can be formed by gas released after organic matter or mat breakdown ([Tebbutt et al., 1965; Choquette and Pray, 1970; Mata et al., 2012](#)). Finally, the coarse-grained laminae (Type 4), that are devoid of pyrite, highlight an intense trapping and binding of peloids and ooids from adjacent sedimentary bodies. The depositional model of [Awramik and Buchheim \(2009\)](#) for the Meentheena Member positioned the studied stromatolites between shallow and high-energy ooidal grainstones and deeper siltstones and shales. In such a depositional environment, micritic laminae (Type 1) reflect optimal conditions for stromatolite development associated with increased carbonate precipitation. However, the thickness of these micritic laminae does not exceed few millimeters, indicating that their growth was frequently disrupted. Indeed, the Meentheena sedimentary system was relatively dynamic, notably disturbed by rapid lateral facies changes due to frequent storm events ([Awramik and Buchheim, 2009](#)). Stromatolite growth was thereby interrupted by recurrent ooidal sand body migration leading to the formation of the coarse-grained laminae (Type 4), or by periods of increased terrigenous runoff to form organic-rich laminae (Type 2). The presence of nutrients associated with river discharges is also consistent with higher rates of organic matter production recorded in these Type 2 laminae. The presence of chlorites also promoted a

best post-deposit preservation of organic compounds in this lamina type ([Jardine et al., 1989](#)).

Differences in stromatolite growth rates are generally assumed to be controlled by an interplay between internal (microbial communities) and external (*i.e.* environmental) factors ([Reid et al., 2000; Dupraz et al., 2009; Bowlin et al., 2012; Bouton et al., 2016](#)). Intrinsic parameters relate to the metabolic activities in the microbial mat or the biofilm, that is the dynamism and diversity of the microbial community. These parameters strongly act on the mineralization of laminae by controlling the availability of HCO₃³⁻ (the alkalinity) and Ca²⁺ ions ([Aloisi, 2008; Dupraz et al., 2009](#)). Extrinsic factors relate to variations in environmental factors, which can influence both the microbial activity and ions availability. These variables include for example, temperature, chemical composition of water (*e.g.*, salinity, pH, alkalinity), solar irradiance, supply (*i.e.* source material and flux) of sedimentary material ([Reid et al., 2000; Arp et al., 2003; Andres and Pamela Reid, 2006; Planavsky and Grey, 2008; Jahnert et al., 2013; Bouton et al., 2016; Bouton et al., 2020](#)). Among the different factors that can influence the stromatolite growth and the microbial mineralization potential, physical parameters such as trapping and binding also directly influence stromatolite growth and carbonate precipitation rates ([Awramik et al., 1976; Reid et al., 2000; Awramik and Grey, 2005](#)). The diversity of laminae recorded in the Tumbiana stromatolites is a clear illustration of the different processes (mineralization, trapping, terrigenous influence) that can be involved in stromatolite fabric and growth. It also illustrates how the depositional environment and early diagenesis may have influenced the micropyrates distribution and Fe isotopic compositions.

4.1.3. A syngenetic origin of the micropyrates

In the four analyzed samples, the absence of rounded grains argues against a detrital origin of the pyrites. Similarly, the absence of hydrothermal veins and secondary veins of pyrites argue against a late stage hydrothermal overprint. A limited metamorphic imprint is further supported by δ¹³C analyses in carbonate and organic matter, where the range of equilibrium fractionation (Δ¹³C_{carb-org}) expected for an isotopic re-equilibration during high-grade metamorphism is inconsistent with the one determined in the Tumbiana samples ([Thomazo et al., 2009](#)). The absence of major secondary overprint and preservation of primary features have been likely favored by the pervasive silicification affecting the different samples studied here. Petrographic investigations show that the size, morphology and distribution of the pyrites recorded in the different laminae cannot be used to identify a relative chronology of formation. The smallest pyrites (<5 μm to hundreds nm) occur preferentially in intimate association with organic matter in Type 2 laminae and are more concentrated in this lamina type ([Fig. 3; Electronic Annex \(EA\); Fig. EA-7](#)). This indicates a causal relationship between organic matter availability on the abundance of pyrite formed ([Rickard et al., 2017](#)). Because micropyrates are enclosed in subparallel stromatolitic laminae, associated with pristine organic matter ([Lepot et al., 2009; Marin-Carbonne et al., 2018](#)), and

display a unimodal Fe isotopic distribution, we interpreted these micropyrates to be precipitated during stromatolite growth or during early diagenesis.

4.2. Large $\delta^{56}\text{Fe}$ range of micropyrates reflects a kinetic effect

Different processes can account for the large Fe isotope range of values recorded in the studied micropyrates. These include: i) $\delta^{56}\text{Fe}$ values inherited from Fe sources, ii) Rayleigh distillation process during precipitation of pyrites from monosulfides, iii) variable pyrite precipitation rate (Mansor and Fantle, 2019), iv) H_2S reduction of Fe(III)-oxides and v) Dissimilatory Iron Reduction (DIR) (Yoshiya et al., 2012). All Fe isotope fractionations considered in the following discussion are summarized in Fig. 8.

4.2.1. Iron isotope compositions inherited from Fe sources

Iron isotope compositions of sedimentary micropyrates could be inherited from various sources of Fe to the system. Fe^{2+} may have been delivered from mafic mineral dissolution, the incorporation into authigenic carbonates or magmatic magnetites. Fe isotope fractionation in magmatic rocks are partially attributed to magma evolution processes, such as fractional crystallization or fluid exsolution. The largest range of Fe isotope compositions of $\sim 1.6\text{‰}$ has been measured in olivine and assigned to Fe-Mg exchange diffusion between olivine and melt (Teng et al., 2011). Except this large isotope range, small fractionations in the order of 0.1‰ to 0.3‰ are typical for magmatic processes (Dauphas et al., 2017 for a review). For example, an

equilibrium fractionation of $+0.2 \pm 0.016\text{‰}$ has been described between fayalite and magnetite at temperatures ranging between 600 and 800 °C (Shahar et al., 2008). Furthermore, several studies have assessed Fe isotope fractionations that occur during abiotic mafic rock and mineral dissolution. A large Fe isotope fractionation of $\sim -1.5\text{‰}$ has been measured for the weathering of a tholeiitic basalt between aqueous Fe released after few hours of experiment and the basalt. Nonetheless, the extend of this fractionation tends to decrease ($\Delta^{56}\text{Fe}_{\text{solution-rock}} = -0.5\text{‰}$) as a function of leaching time (Chapman et al., 2009). Only few studies have investigated Fe isotope fractionation during dissolution of silicates. The dissolution of hornblende in the presence of different organic ligands produces dissolved iron slightly enriched in light isotopes, with a maximum fractionation of -0.6‰ between Fe in solution and the mineral (Brantley et al., 2001; Brantley et al., 2004). Similar fractionations were determined during the dissolution of biotite and chlorite from granite (Kiczka et al., 2010). Experiments measuring Fe isotope fractionations between aqueous Fe and siderite have shown $\Delta^{56}\text{Fe}_{\text{Fe(II)aq-siderite}}$ of 0‰ and $+0.5\text{‰}$, respectively under biotic and abiotic influences (Wiesli et al., 2004; Johnson et al., 2005). An equilibrium Fe fractionation factor of $+0.9\text{‰}$ has been reported for ankerite formation during microbial DIR (Johnson et al., 2005). Finally, Sossi et al. (2012) reported Fe isotope fractionation of $\sim +0.1\text{‰}$ between magnetite and melt at temperature of 900–1000 °C. Thus the Fe isotope range inherited from magmatic processes and/or mineral precipitation is limited and it seems difficult to explain

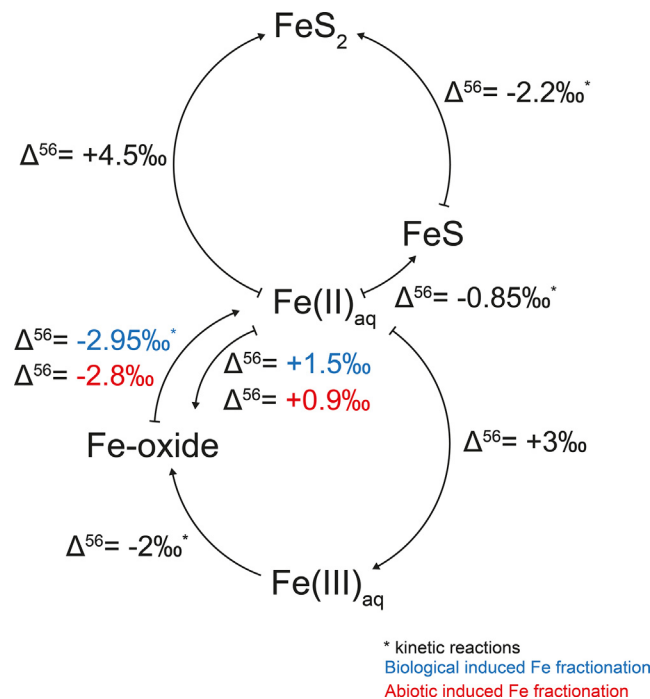


Fig. 8. Theoretical Fe isotopic fractionations between oxidized Fe species, ferrous Fe, monosulfide and pyrite. Data from Welch et al. (2003); Bullen et al. (2001); Croal et al. (2004); Guilhaud et al. (2011); Polyakov et al. (2007); Butler et al. (2005); Crosby et al. (2007). Blue and red colors indicate respectively Fe fractionations due to biological and abiotic reactions. (For interpretation of the references to colour in this figure legend, the reader is referred to the web version of this article.)

the $\sim 6\text{‰}$ range in Fe isotope compositions measured in micropyrates by one or several of the fractionation processes described above.

4.2.2. Rayleigh distillation during precipitation of pyrites from monosulfides

Considering that the pyrites studied here have a synsedimentary origin, micropyrates Fe isotope signatures can result from a Rayleigh distillation process during conversion of pyrite precursors attending stromatolite growth or during early stages of diagenesis. Assuming Fe isotope composition of 0‰ for the overlying water column (Sharma et al., 2001; Beard et al., 2003; Severmann et al., 2004; Johnson et al., 2008), monosulfide pyrite precursor, most likely mackinawite, should in average carry a $\delta^{56}\text{Fe}$ value of about -0.85‰ (Butler et al., 2005). Using a fractionation factor between pyrite and mackinawite of $\Delta_{\text{FeS}_2\text{-FeS}} = -2.2\text{‰}$ (Guilbaud et al., 2011), we can model the theoretical evolution of precipitated pyrite iron isotopes signature during a Rayleigh distillation process. Results of this isotopic evolution reported as a cumulative probability plot in Fig. 9 show a large isotopic range with values as high as 8‰ . The observed range of values obtained in this study between -2.20‰ and $+4.44\text{‰}$ is completed for 98% of the Fe fraction precipitated as pyrites in the Rayleigh process. However, in the case of Rayleigh fractionation during the conversion of mackinawite to pyrite, a much higher abundance of isotopically light values would be expected, in contrast to what is observed in the micropyrates (Fig. 9). Additionally, a gradual increase of Fe isotopic compositions due to Rayleigh distillation may generate a specific spatial distribution, from low to progressively higher $\delta^{56}\text{Fe}$ values from the lamina to the sample scale. The random distribution of $\delta^{56}\text{Fe}$ values of the micropyrates

within a single lamina (e.g., GIS68.9; $\delta^{56}\text{Fe}$ from $+0.08 \pm 0.17\text{‰}$ to $+4.44 \pm 0.16\text{‰}$), which is observed in the whole sample, does not support the spatial distribution that might be expected during a Rayleigh distillation (Electronic Annex (EA); Fig. EA-8). Hence, we suggest that a single stage of pyrite precipitation associated with Rayleigh distillation is not supported here.

4.2.3. Variable pyrite precipitation rate

A recent study proposed that a combination of both kinetic and equilibrium isotopic effects could explain the whole Fe isotopic range in sedimentary pyrites recorded through geological history (Mansor and Fantle, 2019). Pyrites with positive $\delta^{56}\text{Fe}$ values can be formed under equilibrium considering a fractionation factor between pyrite and the initial $\text{Fe(II)}_{\text{aq}}$ of about $+4.5\text{‰}$ (Polyakov et al., 2007). Alternatively, pyrites with negative $\delta^{56}\text{Fe}$ values reflect kinetic effect between pyrite and mackinawite ($\Delta_{\text{FeS}_2\text{-FeS}} = -2.2\text{‰}$, Guilbaud et al., 2011). Hence, to account for the large Fe isotopic range recorded in sedimentary pyrite, Mansor and Fantle (2019) proposed a variable expression of the kinetic (KIE) and equilibrium isotope effect (EIE) as a function of the rate of pyrite precipitation (RPP) and isotopic exchange between pyrite and $\text{Fe(II)}_{\text{aq}}$, the latter being controlled by the particle size and the concentrations of Fe(II) and H_2S in the system. For example, heavy Fe isotope pyrites are expected when EIE is expressed in association with low RPP. Consequently, pyrite showing $\delta^{56}\text{Fe}$ signatures close to 0‰ can reflect a growing influence of the KIE and an increase in RPP (Guilbaud et al., 2011; Mansor and Fantle, 2019). This hypothesis of a first order control on the $\delta^{56}\text{Fe}$ signal of pyrite precipitation on the long-time range (Guilbaud et al., 2011; Rolison et al., 2018) is further supported by the positive correlation

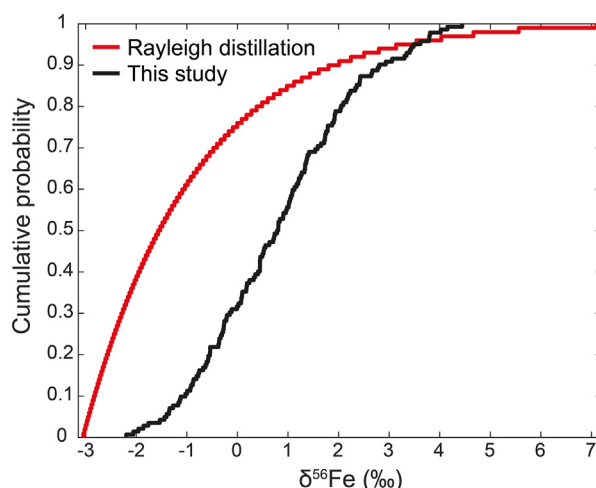


Fig. 9. Rayleigh distillation model. Cumulative function calculated for a near complete (98%) Rayleigh distillation (in red) using a fractionation factor of -2.2‰ between FeS_2 and FeS , and an initial $\delta^{56}\text{Fe}_{\text{FeS}}$ of -0.85‰ (Guilbaud et al., 2011; Butler et al., 2005). The black curve represents our dataset. $\delta^{56}\text{Fe}$ values for Rayleigh Distillation is given by $\delta^{56}\text{Fe}_{\text{prod}} = \alpha_{\text{FeS}_2\text{-FeS}} * (\delta^{56}\text{Fe}_{\text{res}} + 1000) - 1000$ and $\delta^{56}\text{Fe}_{\text{res}} = (\delta^{56}\text{Fe}_{\text{init}} + 1000) * f^{(\alpha_{\text{FeS}_2\text{-FeS}} - 1)} - 1000$, where “prod” refers to the product, “res” to the residue and f is the remaining fraction of reactant. The comparison suggests that a process of pyrite recrystallisation from monosulfides controlled by a Rayleigh distillation do not fit our measurements. (For interpretation of the references to colour in this figure legend, the reader is referred to the web version of this article.)

revealed between $\delta^{56}\text{Fe}$ and $\delta^{34}\text{S}$ values recorded in sedimentary pyrites (Heard et al., 2020). At the scale of a single pyrite grain, we can assume that RPP is faster in the initial stage relative to the final stage of precipitation due to either $\text{Fe(II)}_{\text{aq}}$ and S pool availability or surface area to volume ratio variations. Accordingly, a single pyrite grain should show evolving isotope signal toward more positive $\delta^{56}\text{Fe}$ values from core to rim. Because of the size of the micropyrates and the low image resolution of the SIMS, profiles along pyrite grain were not completed here. Nonetheless, the exhaustive comparison between $\delta^{56}\text{Fe}$ values and the size of micropyrates does not show a specific trend (Fig. 5). The different concentrations of pyrites between the Type 1, 2 and 3 laminae may reflect variable Fe/S ratios or variable organic matter availability among these laminae, which should influence the RPP. Although micritic and organic-rich laminae include variable concentration of pyrites, comparison of Fe isotopic compositions between these two lamina types shows similar ranges, with $\delta^{56}\text{Fe}$ between -1.76‰ and $+4.15\text{‰}$ in the micritic laminae (Type 1) compared to -1.54‰ and $+4.44\text{‰}$ in the organic-rich laminae (Type 2). Comparable Fe isotopic ranges in both types of lamina suggests that the micropyrates Fe isotopic compositions are not controlled by the availability of organic matter between the lamina types. In a previous study focused on S isotope compositions of nanopyrites preserved in Type 2 organic-rich laminae, Marin-Carbonne et al. (2018) concluded that sulfate was a limiting reactant but may have been locally concentrated in micro-

metric scale niches. In our samples, the different laminae record variable amounts of detrital material that can account for varying Fe/S ratios at the micro-scale. The higher terrigenous fraction recognized in organic-rich laminae (see Section 4.1.2) should reflect a different Fe/ H_2S ratio compare to micritic and fenestral laminae. However, micropyrates from organic-rich and micritic laminae seem to record random $\delta^{56}\text{Fe}$ ranges over a distance of one to several hundreds of microns ($\sim 4.2\text{‰}$ in Fig. 10a, $\sim 1.4\text{‰}$ in Fig. 10b, $\sim 2.7\text{‰}$ in Fig. 10d and $\sim 4\text{‰}$ in Fig. 10e).

Progressive distillation of the ambient sulfate reservoir seems consistent with measurements performed in fenestral laminae, where we observed micropyrates in GIS68.1 distributed along a profile of $\sim 400\ \mu\text{m}$ displaying $\delta^{56}\text{Fe}$ values of $+2.15\text{‰}$, -0.92‰ , -0.26‰ , -0.88‰ and -1.27‰ , respectively from the bottom to the top of the profile (Fig. 10c). This type of distribution is not systematic in fenestral laminae however, as shown by the randomly distributed $\delta^{56}\text{Fe}$ values (Fig. 10f). Therefore, this study does not fully support nor exclude that intra-facies $\delta^{56}\text{Fe}$ variability, recorded in micropyrates of the Tumbiana Formation, can reflect variation of the RPP during pyrite formation.

4.2.4. Sulfidation of highly-reactive Fe phases

The subsequent formation of monosulfide precursors (FeS) and pyrites can be promoted by sulfide mediated reductive dissolution of Fe(III)-oxides (Berner, 1984; Dos Santos Afonso and Stumm, 1992). The experimental

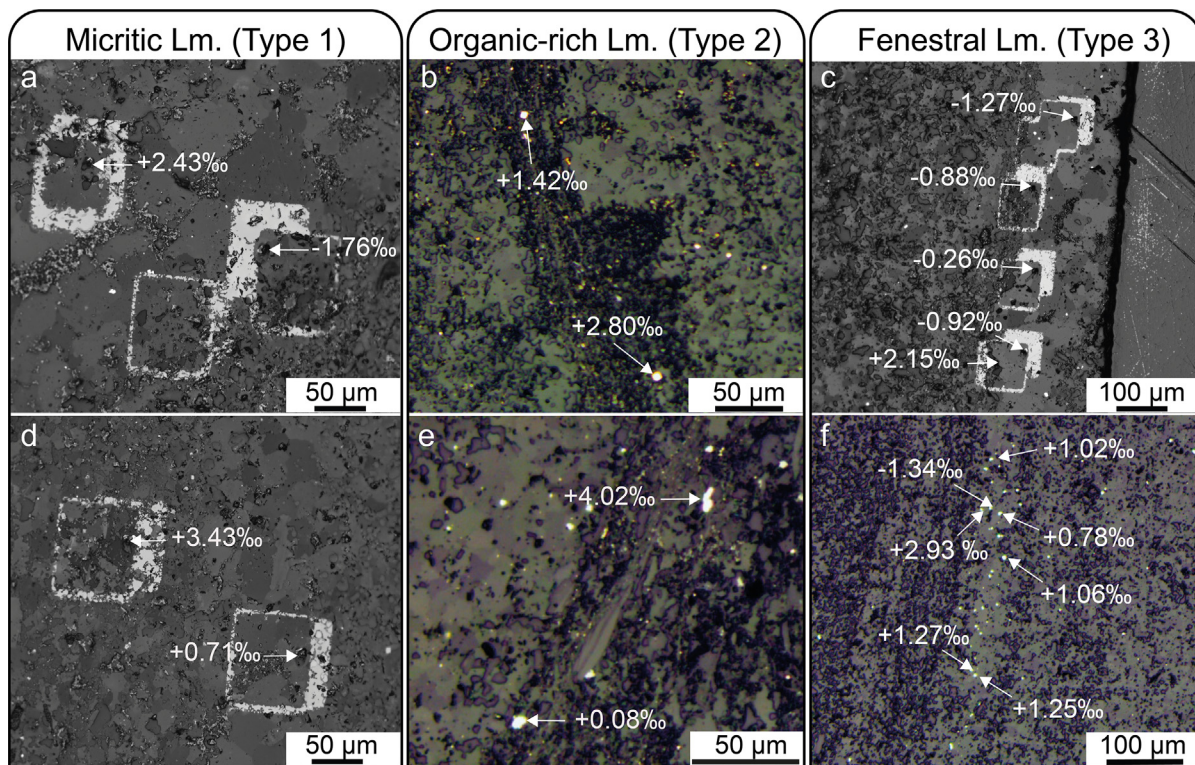


Fig. 10. SEM images of micropyrates and their corresponding $\delta^{56}\text{Fe}$ values in the different lamina types. (a) and (d) Fe isotopic compositions measured in micropyrates from micritic laminae (Type 1) in GIS68.1; (b) and (e) Fe isotopic compositions measured in micropyrates from organic-rich laminae (Type 2) in GIS68.9; (c) and (f) Fe isotopic compositions measured in micropyrates from fenestral laminae (Type 3) in GIS68.1 and GIS68.9.

sulfidation of a variety of Fe(III)-bearing phases, such as ferrihydrite, goethite, hematite and lepidocrocite produces a significant Fe isotope fractionation of -0.85‰ ($\Delta^{56}\text{Fe}_{\text{Fe2+aq-Fe(III)solid}}$) and should be considered for cycling Fe in the sediment porewater (McAnena, 2011). If we cannot fully exclude abiotic sulfidation as an efficient reduction pathway of Fe(III)-oxides, this process alone is not likely to explain $\delta^{56}\text{Fe}$ values as low as -2.2‰ .

4.2.5. Dissimilatory Iron Reduction (DIR)

A previous study has proposed that the Fe isotope composition of pyrites from the Tumbiana Formation can account for Dissimilatory Iron Reduction process (Yoshiya et al., 2012). Positive $\delta^{56}\text{Fe}$ values of pyrites can reflect the total reduction of preexisting Fe-oxides, while negative $\delta^{56}\text{Fe}$ values can be explained by partial reduction (Yoshiya et al., 2012). However, the recent discovery of negative Fe isotopic fractionation during abiotic Fe-oxides reduction that mimics DIR isotopic signatures (Friedrich et al., 2019) has changed the interpretation of the $\delta^{56}\text{Fe}$ signal. Knowing that abiotic Fe reduction can occur at similar rate than DIR in the presence of Fe-oxides and amorphous FeS (Mortimer et al., 2011), it seems difficult to firmly infer which one controlled pyrite precipitation and ensuing iron isotope signal. In the four analyzed samples, no Fe-oxide has been observed but the Fe speciation data support the presence of a non-negligible amount of Fe-oxides (between 90 ppm and 204 ppm, Table 1). The difference between partial and total iron reduction should therefore be due to organic matter availability. Indeed, the preservation of organic-matter in Type 2 laminae could be the result of partial reduction, whereas in Type 1 micritic laminae, the absence or discrete occurrence of organic matter, could reflect near-complete reduction. However, the rather comparable Fe isotopic ranges recorded in pyrites do not support the hypothesis of varying Fe reduction rate between Type 1 and 2 laminae. Thus, the preservation of organic-matter in Type 2 laminae is likely due to the ability of clays to adsorb organic-matter compared to micrite in Type 1 laminae.

Covariation between Fe and S isotopes could provide evidence for paired microbial Fe and sulfate reduction (Archer and Vance, 2006). A large S isotopic range measured in nanopyrates from organic-rich laminae (Type 2) has been previously interpreted as diagnostic for MSR (Marin-Carbonne et al., 2018). However, the Fe-S covariation proposed by Archer and Vance (2006) has not been tested at the micropyrates scale, although large isotopic ranges have been evidenced for both Fe ($\delta^{56}\text{Fe}$ from -1.5‰ to $+4.4\text{‰}$) and S ($\delta^{34}\text{S}$ from -33.7‰ to $+50.4\text{‰}$) for organic-rich laminae. The presence of iron enriched micrite (Fe > 0.5wt.%) in Type 1 laminae and magnetite, as indicated by iron speciation, can be either interpreted as a direct incorporation of Fe(II) provided by the dissolution of mafic minerals, or as an end-product of DIR. Hence, if a microbial iron reduction seems plausible, it cannot solely explain the whole Fe isotopic distribution recorded in the four samples.

4.3. An emerging view of the biogeochemical Fe cycling recorded in Archean stromatolites

4.3.1. Pyrite Fe isotopes and microbial activity

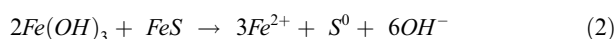
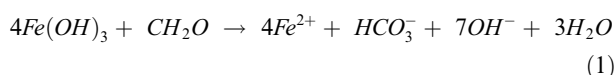
In situ analyses applied to stromatolites from the Tumbiana Formation allowed the identification of S, C and Fe isotopic variations (Nishizawa et al., 2010; Yoshiya et al., 2012; Marin-Carbonne et al., 2018; Lepot et al., 2019) significantly different than those obtained so far by bulk-rock analyses (Thomazo et al., 2009; Czaja et al., 2010). These micro-scale heterogeneities in both organics and pyrites promote a microenvironmental, *i.e.* local, control on $\delta^{34}\text{S}_{\text{py}}$, $\delta^{13}\text{C}_{\text{org}}$ and $\delta^{56}\text{Fe}_{\text{py}}$ (Thomazo et al., 2009; Fike et al., 2015; Marin-Carbonne et al., 2018; Lepot et al., 2019). MSR has been previously called upon to explain S isotope heterogeneities and to be a major driver for micro- to nanometric pyrite precipitation on a local scale (Marin-Carbonne et al., 2018). Methanotroph metabolic activity, that can be aerobically mediated using oxygen (Hayes, 1994) or anaerobically (AOM for Anaerobic oxidation of Methane) using sulfates (Hinrichs, 2002), nitrates (Haroon et al., 2013) or even Fe-oxides (Beal et al., 2009), was likely active to create the large negative $\delta^{13}\text{C}$ excursion recorded in organic matter (Hayes, 1994; Thomazo et al., 2009; Lepot et al., 2019). C-isotope analyses of organic matter from another Tumbiana stromatolite samples (Lepot et al., 2019), equivalent to our Type 1 (micritic) laminae and Type 2 (organic-rich) laminae, revealed highly ^{13}C -depleted signatures as low as $-58.8 \pm 3.6\text{‰}$ (SD) in micrite and $-53.5 \pm 1.8\text{‰}$ (SD) in organic rich horizons. Extremely ^{13}C -depleted values of organic matter from micritic laminae associated with high abundance of organic sulfur have been interpreted as the result of sulfate-thriving AOM. The less negative $\delta^{13}\text{C}_{\text{org}}$ values recorded in organic matter from Type 2 laminae is interpreted to reflect a competition between sulfate and Fe-oxides during AOM (Lepot et al., 2019).

The three lamina types illustrate various concentration of organic-matter, terrigenous material and the effect of early diagenesis that can account for pyrite precipitation. The lower $\delta^{56}\text{Fe}$ values ($\delta^{56}\text{Fe}$ from -2.2‰ to $+2.65\text{‰}$) measured in micropyrates from fenestral laminae (Type 3), which are formed later compared to micritic and organic-rich laminae, can be related to the sparite filling that occurred during early diagenesis. We can thus conclude that diagenetic processes affect the mean Fe isotopic composition recorded in micropyrates but the heterogeneity of $\delta^{56}\text{Fe}$ values is still preserved. The Fe isotopic record shows similar $\delta^{56}\text{Fe}$ variations and ranges between micritic and organic-rich laminae. Based on these two lamina types, the absence of variability rules out either a control of organic-matter, sulfate and Fe-oxides availability or a control of the biomineralization (higher in micritic laminae compared to organic-rich laminae) of the stromatolite on the Fe isotopic signatures. Therefore, the heterogeneity of $\delta^{56}\text{Fe}$ signatures seems to be primarily inherited from metabolic activities.

4.3.2. A complex interplay of Fe redox reactions

Based on previous knowledge on microbial processes operating in the Tumbiana environment, we propose a multi-step model of iron cycling than can account for the $\delta^{56}\text{Fe}$ distribution attributed to the micropyrates. This model includes metabolisms previously proposed to be active in these stromatolites, such as MSR and AOM. While consistent with $\delta^{56}\text{Fe}$ measured in micropyrates and previous geochemical studies performed in the Tumbiana Formation, some uncertainties due to processes that could significantly contribute to Fe isotope signatures must be considered in the model. These include the influence of EIE/KIE, potential isotopic fractionation during the conversion of mackinawite into pyrites or isotopic variability inherited from the Fe source. The detrital $\text{Fe}_{\text{aq}}^{2+}$ supplied by weathering of the mafic substrate (pathway 1, Fig. 11) was partially oxidized into Fe^{3+} , and precipitated as ferric oxide/hydroxides (pathway 2, Fig. 11). Whereas the question of the oxidant used for the $\text{Fe(II)}_{\text{aq}}$ oxidation remains open, Fe isotopic fractionations during partial oxidation mediated by O_2 , anoxygenic photosynthesis or UV photo-oxidation are similar ranging from +0.9‰ to +1.5‰

(Bullen et al., 2001; Croal et al., 2004; Nie et al., 2017). We thus considered in the following section a mean isotopic fractionation between dissolved Fe^{2+} and $\text{Fe(III)-oxides/hydroxides}$ Fe(OH)_3 of +1‰. $\text{Fe(III)-oxides/hydroxides}$ are then used as electron acceptors during the microbial reduction mediated by DIR bacteria (1) (Czaja et al., 2010) or abiotically (2) (Mortimer et al., 2011) (pathway 3, Fig. 11).



On one hand, the biotic or abiotic Fe reduction is partial in order to generate Fe^{2+} depleted in ^{56}Fe with $\delta^{56}\text{Fe}$ values between -2‰ to -0.5‰ . This ^{56}Fe -depleted iron source can be used in turn to react with reduced sulfur species (e.g., H_2S , S_0) produced by MSR and hence precipitate successively as iron monosulfides and sedimentary pyrites (pathway 3a, Fig. 11). On the other hand, the partial reduction pathway allows the buildup of a residual Fe^{3+} -oxides/hydroxides pool which are experimentally shown to be

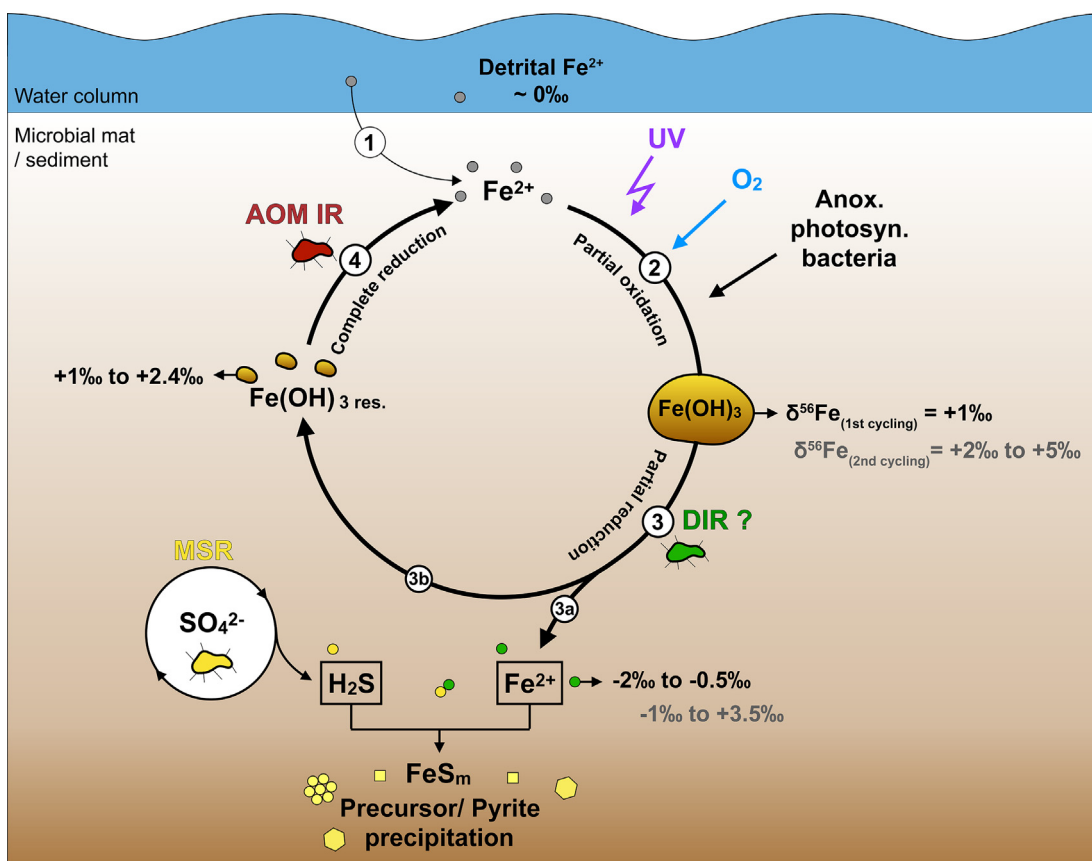
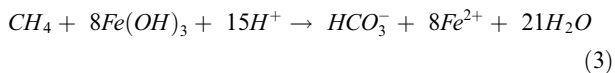


Fig. 11. Schematic view of microbial reactions discussed at local scale. Iron from water column is cycled several times by oxidation and reduction processes in the sediment. DIR: Dissimilatory Iron Reduction. MSR: Microbial Sulfate reduction. AOM IR: Anaerobic oxidation of methane coupled to iron reduction. Black numbers correspond to iron isotopic compositions of the different species at the first cycling. Grey numbers referred to iron isotopic compositions obtained after the second cycling. Probability density functions of the $\delta^{56}\text{Fe}$ distribution calculated for 4 cumulative Fe cycling (bin size of 0.1) and the comparison with probability density function of the $\delta^{56}\text{Fe}$ distribution of the 142 micropyrates are available in [Electronic annex \(Fig. EA-9\)](#). (For interpretation of the references to colour in this figure legend, the reader is referred to the web version of this article.)

enriched in heavy iron isotope (Welch et al., 2003). The Fe isotopic compositions of the residual Fe(OH)₃ is estimated to range between +1‰ and +2.4‰ (pathway 3b, Fig. 11). This residual Fe(III)-oxides pool can later be fully converted back to Fe²⁺, coupled for example with the activity of anaerobic methanotroph bacteria following the equation (3) (Czaja et al., 2010):



The involvement of this step of complete reduction, possibly conducted by AOM-IR, allows to the preservation of the Fe isotopic range recorded by the residual Fe(III)-oxides. The conjoint activity of methanotrophs and potentially Fe reducing bacteria, leading to the formation of bicarbonate and ferrous iron, could participate to the precipitation of micrite observed in Type 2 laminae slightly enriched in iron. After reduction of Fe(III)-oxides into Fe²⁺, possibly by methanotrophs, a re-cycling of this isotopically heavy dissolved Fe²⁺ could produced:

- δ⁵⁶Fe values of Fe-oxi/hydroxides from +2‰ to +5‰ after partial oxidation (pathway 2, 2nd cycling, Fig. 11).
- δ⁵⁶Fe values of Fe²⁺ from −1‰ to +3.5‰ after iron reduction (pathway 3a, 2nd cycling, Fig. 11). Isotopically heavier Fe²⁺ is available for pyrite precursor precipitations.

The model includes episodic supplies of detrital Fe²⁺ in the sediment pore water, likely generated by the weathering of mafic volcanoclastic substrate. The distribution of δ⁵⁶Fe values measured in Tumbiana micropyrates is best modeled after four successive cycles with a partial reduction rate of 30% (Electronic Annex (EA); Fig. EA-9), which is in the range of the reduction rate reported for Dissimilatory Iron Reduction in batch experiments (Benner et al., 2002; Hansel et al., 2004). Such an intensive Fe oxido-reduction iron cycling echoes Fe and S cryptic cycles, which can occur in modern stratified lacustrine environments (e.g., Pavin lake, Cadagno lake; Berg et al., 2016; Berg et al., 2019) and oxygen minimum zone (e.g., Chilean coast; Canfield et al., 2010; Teske, 2010). Independently of the Fe concentration of the water column, the subsequent Fe(II) oxidation and Fe-oxide reduction are the result of a prevalent microbial iron cycling in the water column chemocline (Berg et al., 2016; Berg et al., 2019). Although the origin of the oxidation is still questionable for Archean stromatolites such as those from the Tumbiana Formation, this study demonstrates the importance of local redox processes controlling the multiple step Fe cycling associated with coeval microbial metabolisms that promoted pyrite precipitation.

5. CONCLUSIONS

Iron isotope compositions of micropyrates from the 2.724 Ga Tumbiana Formation provide a unique view of the possible iron cycle during the Archean. Based on the study of stromatolite samples, four types of laminae have been evidenced: micritic (Type 1), organic-rich (Type 2),

fenestral (Type 3) and coarse-grained (Type 4) laminae. These laminae reflect the different processes typically recognized in a stromatolite, such as carbonate precipitation (Type 1), terrigenous influence (Type 2), trapping and binding (Type 4) and cementation during early diagenesis (Type 3). Micropyrates recorded a local microenvironment and a limited impact of diagenesis. In addition to reflect a combined activity of AOM, MSR and possibly DIR, micropyrates recorded multiple stages of Fe oxidation and reduction. This study helps to better understand the iron isotopic signatures that result from multiple redox fluctuations in microbial mats. Therefore, stromatolites of the Tumbiana Formation can be considered to reflect a fossil microbial ecosystem that has recorded an exceptional diversity of microbial metabolisms. Future investigations should focus on the coupled Fe, S and C isotope evolution at the local scale in order to assess the effect of metabolism interactions on Fe isotope signatures.

Declaration of Competing Interest

The authors declare that they have no known competing financial interests or personal relationships that could have appeared to influence the work reported in this paper.

ACKNOWLEDGEMENTS

Johan Villeneuve and Nordine Bouden are thanked for their help during SIMS sessions. Colette Guilbaud is thanked for her help with sample preparation. Virgil Pasquier, Elias Bloch and Mathieu Gravey are thanked for fruitful discussions. Béatrice Luais is acknowledged for providing us standard material. This research was supported by the European Union's Horizon H2020 research and innovation program ERC (STROMATA, grant agreement 759289). Pascal Philippot acknowledges support from the São Paulo Research Foundation (FAPESP grant 2015/16235-2).

APPENDIX A. SUPPLEMENTARY DATA

Supplementary data to this article can be found online at <https://doi.org/10.1016/j.gca.2021.07.020>.

REFERENCES

- Aller R. C., Mackin J. E. and Cox R. T. (1986) Diagenesis of Fe and S in Amazon inner shelf muds: apparent dominance of Fe reduction and implications for the genesis of ironstones. *Cont. Shelf Res.* 6(1-2), 263–289.
- Allwood A. C., Walter M. R., Kamber B. S., Marshall C. P. and Burch I. W. (2006) Stromatolite reef from the Early Archaean era of Australia. *Nature* 441(7094), 714–718.
- Aloisi G. (2008) The calcium carbonate saturation state in cyanobacterial mats throughout Earth's history. *Geochim. Cosmochim. Acta* 72, 6037–6060.
- Andres M. S. and Pamela Reid R. (2006) Growth morphologies of modern marine stromatolites: a case study from Highborne Cay Bahamas. *Sed. Geol.* 185(3-4), 319–328.
- Archer C. and Vance D. (2006) Coupled Fe and S isotope evidence for Archean microbial Fe(III) and sulfate reduction. *Geology* 34(3), 153.

- Arndt N., Nelson D., Compston W., Trendall A. and Thorne A. (1991) The age of the Fortescue Group, Hamersley Basin, Western Australia, from ion microprobe zircon U-Pb results. *Aust. J. Earth Sci.* **38**, 261–281.
- Arp G., Reimer A. and Reitner J. (2003) Microbialite formation in seawater of increased alkalinity, Satonda Crater Lake. *Indonesia. J. Sed. Res.* **73**, 105–127.
- Awramik S., Margulis L. and Barghoorn E. (1976) Evolutionary processes in the formation of stromatolites. *Devel. Sed.*, 149–162.
- Awramik S. M. (2006) Palaeontology: respect for stromatolites. *Nature* **441**(7094), 700–701.
- Awramik S. M. and Buchheim H. P. (2009) A giant, Late Archean lake system: The Meentheena Member (Tumbiana Formation; Fortescue Group), Western Australia. *Precambrian Res.* **174**(3–4), 215–240.
- Awramik S. M. and Grey K. (2005) Stromatolites: biogenicity, biosignatures, and bioconfusion. *Astro. Planet. Miss.* **5906**, 59060P.
- Beal E. J., House C. H. and Orphan V. J. (2009) Manganese- and iron-dependent marine methane oxidation. *Science* **325**(5937), 184–187.
- Beard B. L., Johnson C. M., Von Damm K. L. and Poulson R. L. (2003) Iron isotope constraints on Fe cycling and mass balance in oxygenated Earth oceans. *Geology* **31**(7), 629.
- Benner S. G., Hansel C. M., Wielinga B. W., Barber T. M. and Fendorf S. (2002) Reductive dissolution and biomineralization of iron hydroxide under dynamic flow conditions. *Envir. Sci. Tech.* **36**(8), 1705–1711.
- Berner R. A. (1984) Sedimentary pyrite formation: an update. *Geochim. Cosmochim. Acta* **48**, 605–615.
- Berg J. S., Michellod D., Pjevac P., Martinez-Perez C., Buckner C. R., Hach P. F., Schubert C. J., Milucka J. and Kuypers M. M. (2016) Intensive cryptic microbial iron cycling in the low iron water column of the meromictic Lake Cadagno. *Environ. Microbiol.* **18**, 5288–5302.
- Berg J. S., Jézéquel D., Duverger A., Lamy D., Laberty-Robert C., Miot J. and Senko J. M. (2019) Microbial diversity involved in iron and cryptic sulfur cycling in the ferruginous, low-sulfate waters of Lake Pavin. *PLoS One* **14**(2), e0212787.
- Blake T. S. (1993) Late Archaean crustal extension, sedimentary basin formation, flood basalt volcanism and continental rifting: the Nullagine and Mount Jope Supersequences, Western Australia. *Precambrian Res.* **60**(1–4), 185–241.
- Blake T. S. and Barley M. E. (1992) Tectonic evolution of the Late Archaean to Early Proterozoic Mount Bruce Megasequence Set, Western Australia. *Tectonics* **11**(6), 1415–1425.
- Blake T. S., Buick R., Brown S. J. A. and Barley M. E. (2004) Geochronology of a Late Archaean flood basalt province in the Pilbara Craton, Australia: constraints on basin evolution, volcanic and sedimentary accumulation, and continental drift rates. *Precambrian Res.* **133**(3–4), 143–173.
- Bolhar R. and Vankranendonk M. (2007) A non-marine depositional setting for the northern Fortescue Group, Pilbara Craton, inferred from trace element geochemistry of stromatolitic carbonates. *Precambrian Res.* **155**(3–4), 229–250.
- Bouton A., Vennin E., Pace A., Bourillot R., Dupraz C., Thomazo C., Brayard A., Désaubliaux G., Visscher P. T. and Lokier S. (2016) External controls on the distribution, fabrics and mineralization of modern microbial mats in a coastal hypersaline lagoon, Cayo Coco (Cuba). *Sedimentology* **63**(4), 972–1016.
- Bouton A., Vennin E., Amiotte-Suchet P., Thomazo C., Sizun J.-P., Virgone A., Gaucher E. C. and Visscher P. T. (2020) Prediction of the calcium carbonate budget in a sedimentary basin: A “source-to-sink” approach applied to Great Salt Lake, Utah, USA. *Basin Res.* **32**(5), 1005–1034.
- Bowlin E. M., Klaus J. S., Foster J. S., Andres M. S., Custals L. and Reid R. P. (2012) Environmental controls on microbial community cycling in modern marine stromatolites. *Sediment. Geol.* **263–264**, 45–55.
- Brantley S. L., Liermann L. and Bullen T. D. (2001) Fractionation of Fe isotopes by soil microbes and organic acids. *Geology* **29**(6), 535.
- Brantley S. L., Liermann L. J., Guynn R. L., Anbar A., Icopini G. A. and Barling J. (2004) Fe isotopic fractionation during mineral dissolution with and without bacteria. *Geochim. Cosmochim. Acta* **68**, 3189–3204.
- Buick R. (1992) The Antiquity of Oxygenic Photosynthesis - Evidence from Stromatolites in Sulfate-Deficient Archean Lakes. *Science* **255**, 74–77.
- Bullen T. D., White A. F., Childs C. W., Vivit D. V. and Schulz M. S. (2001) Demonstration of significant abiotic iron isotope fractionation in nature. *Geology* **29**(8), 699.
- Butler I. B., Archer C., Vance D., Oldroyd A. and Rickard D. (2005) Fe isotope fractionation on FeS formation in ambient aqueous solution. *Earth Planet. Sci. Lett.* **236**, 430–442.
- Canfield D. E., Raiswell R. and Bottrell S. (1992) The Reactivity of Sedimentary Iron Minerals toward Sulfide. *Am. J. Sci.* **292**, 659–683.
- Canfield D. E., Raiswell R., Westrich J. T., Reaves C. M. and Berner R. A. (1986) The Use of Chromium Reduction in the Analysis of Reduced Inorganic Sulfur in Sediments and Shales. *Chem. Geol.* **54**, 149–155.
- Canfield D. E., Stewart F. J., Thamdrup B., De Brabandere L., Dalsgaard T., Delong E. F., Revsbech N. P. and Ulloa O. (2010) A cryptic sulfur cycle in oxygen-minimum-zone waters off the Chilean coast. *Science* **330**(6009), 1375–1378.
- Chapman J. B., Weiss D. J., Shan Y. and Lemburger M. (2009) Iron isotope fractionation during leaching of granite and basalt by hydrochloric and oxalic acids. *Geochim. Cosmochim. Acta* **73**, 1312–1324.
- Choquette P. W. and Pray L. C. (1970) Geologic nomenclature and classification of porosity in sedimentary carbonates. *AAPG Bull.* **54**, 207–250.
- Coffey J. M., Flannery D. T., Walter M. R. and George S. C. (2013) Sedimentology, stratigraphy and geochemistry of a stromatolite biofacies in the 2.72 Ga Tumbiana Formation, Fortescue Group Western Australia. *Precambrian Res.* **236**, 282–296.
- Croal L. R., Johnson C. M., Beard B. L. and Newman D. K. (2004) Iron isotope fractionation by Fe(II)-oxidizing photoautotrophic bacteria. *Geochim. Cosmochim. Acta* **68**, 1227–1242.
- Crosby H. A., Johnson C. M., Roden E. E. and Beard B. L. (2005) Coupled Fe(II)-Fe(III) electron and atom exchange as a mechanism for Fe isotope fractionation during dissimilatory iron oxide reduction. *Environ. Sci. Technol.* **39**(17), 6698–6704.
- Crosby H. A., Roden E. E., Johnson C. M. and Beard B. L. (2007) The mechanisms of iron isotope fractionation produced during dissimilatory Fe(III) reduction by *Shewanella putrefaciens* and *Geobacter sulfurreducens*. *Geobiology* **5**(2), 169–189.
- Crowe S. A., Paris G., Katsev S., Jones C., Kim S.-T., Zerkle A. L., Nomosatryo S., Fowle D. A., Adkins J. F., Sessions A. L., Farquhar J. and Canfield D. E. (2014) Sulfate was a trace constituent of Archean seawater. *Science* **346**(6210), 735–739.
- Czaja A. D., Johnson C. M., Beard B. L., Eigenbrode J. L., Freeman K. H. and Yamaguchi K. E. (2010) Iron and carbon isotope evidence for ecosystem and environmental diversity in the similar to 2.7 to 2.5 Ga Hamersley Province Western Australia. *Earth Planet. Sci. Lett.* **292**, 170–180.

- Dauphas N., John S. G. and Rouxel O. (2017) Iron Isotope Systematics. *Rev. Mineral Geochem.* **82**(1), 415–510.
- Decraene M. N., Marin-Carbonne J., Bouvier A. S., Villeneuve J., Bouden N., Luais B. and Deloule E. (2021) High-spatial-resolution measurements of iron isotopes in pyrites by secondary ion mass spectrometry using the new Hyperion-II radio-frequency plasma source. *Rapid Commun. Mass Spectrom.* **35** e8986.
- Dos Santos Afonso M. and Stumm W. (1992) Reductive dissolution of iron (III)(hydr) oxides by hydrogen sulfide. *Langmuir* **8** (6), 1671–1675.
- Dupraz C., Reid R. P., Braissant O., Decho A. W., Norman R. S. and Visscher P. T. (2009) Processes of carbonate precipitation in modern microbial mats. *Earth Sci. Rev.* **96**, 141–162.
- Eigenbrode J. L. and Freeman K. H. (2006) Late Archean rise of aerobic microbial ecosystems. *Proc. Natl. Acad. Sci. USA* **103** (43), 15759–15764.
- Fike D. A., Bradley A. S. and Rose C. V. (2015) Rethinking the ancient sulfur cycle. *Annu. Rev. Earth Pl. Sc.* **43**, 593–622.
- Flament N., Rey P. F., Coltice N., Dromart G. and Olivier N. (2011) Lower crustal flow kept Archean continental flood basalts at sea level. *Geology* **39**, 1159–1162.
- Flannery D. T., Van Kranendonk M. J., Mazumder R. and Walter M. R. (2014) The ca 2.74 Ga Mopoke Member, Kylene Formation: a marine incursion into the northern Fortescue Group? *Aust. J. Earth Sci.* **61**, 1095–1108.
- Flannery D. T. and Walter M. R. (2012) Archean tufted microbial mats and the Great Oxidation Event: new insights into an ancient problem. *Aust. J. Earth Sci.* **59**(1), 1–11.
- Frierdich A. J., Nebel O., Beard B. L. and Johnson C. M. (2019) Iron isotope exchange and fractionation between hematite (α -Fe₂O₃) and aqueous Fe(II): A combined three-isotope and reversal-approach to equilibrium study. *Geochim. Cosmochim. Acta* **245**, 207–221.
- Guilbaud R., Butler I. B. and Ellam R. M. (2011) Abiotic pyrite formation produces a large Fe isotope fractionation. *Science* **332**(6037), 1548–1551.
- Hansel C. M., Benner S. G., Nico P. and Fendorf S. (2004) Structural constraints of ferric (hydr) oxides on dissimilatory iron reduction and the fate of Fe (II). *Geochim. Cosmochim. Acta* **68**, 3217–3229.
- Haroon M. F., Hu S., Shi Y., Imelfort M., Keller J., Hugenoltz P., Yuan Z. and Tyson G. W. (2013) Anaerobic oxidation of methane coupled to nitrate reduction in a novel archaeal lineage. *Nature* **500**(7464), 567–570.
- Hayes J. (1994) *Global methanotrophy at the Archean-Proterozoic transition*. Columbia University Press, New York, pp. 220–235.
- Heard A. W., Dauphas N., Guilbaud R., Rouxel O. J., Butler I. B., Nie N. X. and Bekker A. (2020) Triple iron isotope constraints on the role of ocean iron sinks in early atmospheric oxygenation. *Science* **370**(6515), 446–449.
- Hinrichs K. U. (2002) Microbial fixation of methane carbon at 2.7 Ga: Was an anaerobic mechanism possible? *Geochem. Geophys. Geosy.* **3**, 1–10.
- Jahnert R. J., Collins L. B. and Ariztegui D. (2013) Controls on microbial activity and tidal flat evolution in Shark Bay, Western Australia. *Sedimentology* **60**(4), 1071–1099.
- Jardine P., McCarthy J. and Weber N. (1989) Mechanisms of dissolved organic carbon adsorption on soil. *Soil Sci. Soc. Am. J.* **53**, 1378–1385.
- Johnson C. M., Roden E. E., Welch S. A. and Beard B. L. (2005) Experimental constraints on Fe isotope fractionation during magnetite and Fe carbonate formation coupled to dissimilatory hydrous ferric oxide reduction. *Geochim. Cosmochim. Acta* **69**, 963–993.
- Johnson C. M., Beard B. L. and Roden E. E. (2008) The iron isotope fingerprints of redox and biogeochemical cycling in the modern and ancient Earth. *Annu. Rev. Earth Pl. Sc.* **36**, 457–493.
- Johnston D. T. (2011) Multiple sulfur isotopes and the evolution of Earth's surface sulfur cycle. *Earth Sci. Rev.* **106**, 161–183.
- Kiczka M., Wiederhold J. G., Frommer J., Kraemer S. M., Bourdon B. and Kretzschmar R. (2010) Iron isotope fractionation during proton- and ligand-promoted dissolution of primary phyllosilicates. *Geochim. Cosmochim. Acta* **74**, 3112–3128.
- Lepot K., Benzerara K., Brown G. E. and Philippot P. (2008) Microbially influenced formation of 2,724-million-year-old stromatolites. *Nat. Geosci.* **1**, 118–121.
- Lepot K., Benzerara K., Rividi N., Cotte M., Brown G. E. and Philippot P. (2009) Organic matter heterogeneities in 2.72 Ga stromatolites: Alteration versus preservation by sulfur incorporation. *Geochim. Cosmochim. Acta* **73**, 6579–6599.
- Lepot K., Williford K. H., Philippot P., Thomazo C., Ushikubo T., Kitajima K., Mostefaoui S. and Valley J. W. (2019) Extreme ¹³C-depletions and organic sulfur content argue for S-fueled anaerobic methane oxidation in 2.72 Ga old stromatolites. *Geochim. Cosmochim. Acta* **244**, 522–547.
- Liu M.-C., McKeegan K. D., Harrison T. M., Jarzebinski G. and Vltava L. (2018) The Hyperion-II radio-frequency oxygen ion source on the UCLA ims1290 ion microprobe: Beam characterization and applications in geochemistry and cosmochemistry. *Int. J. Mass Spectrom.* **424**, 1–9.
- Lyons T. W. and Severmann S. (2006) A critical look at iron paleoredox proxies: New insights from modern euxinic marine basins. *Geochim. Cosmochim. Acta* **70**(23), 5698–5722.
- Mansor M. and Fantle M. S. (2019) A novel framework for interpreting pyrite-based Fe isotope records of the past. *Geochim. Cosmochim. Acta* **253**, 39–62.
- Marin-Carbonne J., Chaussidon M. and Robert F. (2012) Micrometer-scale chemical and isotopic criteria (O and Si) on the origin and history of Precambrian cherts: Implications for paleo-temperature reconstructions. *Geochim. Cosmochim. Acta* **92**, 129–147.
- Marin-Carbonne J., Remusat L., Sforza M. C., Thomazo C., Cartigny P. and Philippot P. (2018) Sulfur isotope's signal of nanopyrates enclosed in 2.7 Ga stromatolitic organic remains reveal microbial sulfate reduction. *Geobiology* **16**(2), 121–138.
- Marin-Carbonne J., Rollion-Bard C., Bekker A., Rouxel O., Agangi A., Cavalazzi B., Wohlgemuth-Ueberwasser C. C., Hofmann A. and McKeegan K. D. (2014) Coupled Fe and S isotope variations in pyrite nodules from Archean shale. *Earth Planet. Sci. Lett.* **392**, 67–79.
- Marin-Carbonne J., Rollion-Bard C. and Luais B. (2011) In-situ measurements of iron isotopes by SIMS: MC-ICP-MS intercalibration and application to a magnetite crystal from the Gunflint chert. *Chem. Geol.* **285**(1–4), 50–61.
- Mata S. A., Harwood C. L., Corsetti F. A., Stork N. J., Eilers K., Berelson W. M. and Spear J. R. (2012) Influence of gas production and filament orientation on stromatolite microfabric. *Palaaios* **27**(4), 206–219.
- McAnena A. (2011) The reactivity and isotopic fractionation of Fe-bearing minerals during sulfidation: an experimental approach. *Newcastle University*.
- Mortimer R. J. G., Galsworthy A. M. J., Bottrell S. H., Wilmot L. E. and Newton R. J. (2011) Experimental evidence for rapid biotic and abiotic reduction of Fe (III) at low temperatures in salt marsh sediments: a possible mechanism for formation of modern sedimentary siderite concretions. *Sedimentology* **58**, 1514–1529.
- Nie N. X., Dauphas N. and Greenwood R. C. (2017) Iron and oxygen isotope fractionation during iron UV photo-oxidation:

- Implications for early Earth and Mars. *Earth Planet. Sci. Lett.* **458**, 179–191.
- Nishizawa M., Yamamoto H., Ueno Y., Tsuruoka S., Shibuya T., Sawaki Y., Yamamoto S., Kon Y., Kitajima K., Komiya T., Maruyama S. and Hirata T. (2010) Grain-scale iron isotopic distribution of pyrite from Precambrian shallow marine carbonate revealed by a femtosecond laser ablation multicollector ICP-MS technique: Possible proxy for the redox state of ancient seawater. *Geochim. Cosmochim. Acta* **74**, 2760–2778.
- Philippot P., Van Kranendonk M., Van Zuilen M., Lepot K., Rividi N., Teitler Y., Thomazo C., Blanc-Valleron M.-M., Rouchy J.-M., Grosch E. and de Wit M. (2009) Early traces of life investigations in drilling Archean hydrothermal and sedimentary rocks of the Pilbara Craton, Western Australia and Barberton Greenstone Belt, South Africa. *Cr. Palevol* **8**(7), 649–663.
- Planavsky N. and Grey K. (2008) Stromatolite branching in the Neoproterozoic of the Centralian Superbasin, Australia: an investigation into sedimentary and microbial control of stromatolite morphology. *Geobiology* **6**, 33–45.
- Polyakov V. B., Clayton R. N., Horita J. and Mineev S. D. (2007) Equilibrium iron isotope fractionation factors of minerals: reevaluation from the data of nuclear inelastic resonant X-ray scattering and Mössbauer spectroscopy. *Geochim. Cosmochim. Acta* **71**(15), 3833–3846.
- Poulton S. W. and Canfield D. E. (2005) Development of a sequential extraction procedure for iron: implications for iron partitioning in continentally derived particulates. *Chem. Geol.* **214**(3–4), 209–221.
- Raiswell R. and Canfield D. E. (1998) Sources of iron for pyrite formation in marine sediments. *Am. J. Sci.* **298**, 219–245.
- Reid R. P., Visscher P. T., Decho A. W., Stolz J. F., Bebout B. M., Dupraz C., Macintyre I. G., Paerl H. W., Pinckney J. L., Prufert-Bebout L., Stepe T. F. and DesMarais D. J. (2000) The role of microbes in accretion, lamination and early lithification of modern marine stromatolites. *Nature* **406** (6799), 989–992.
- Reussel M., Melezhik V. A. and Strauss H. (2012) Sulfur isotopic trends and iron speciation from the c. 2.0 Ga Pilgularji Sedimentary Formation, NW Russia. *Precambrian Res.* **196**, 193–203.
- Rickard D., Mussmann M. and Steadman J. A. (2017) Sedimentary sulfides. *Elements* **13**(2), 117–122.
- Rolison J. M., Stirling C. H., Middag R., Gault-Ringold M., George E. and Rijkenberg M. J. A. (2018) Iron isotope fractionation during pyrite formation in a sulfidic Precambrian ocean analogue. *Earth Planet. Sci. Lett.* **488**, 1–13.
- Sakurai R., Ito M., Ueno Y., Kitajima K. and Maruyama S. (2005) Facies architecture and sequence-stratigraphic features of the Tumbiana Formation in the Pilbara Craton, northwestern Australia: Implications for depositional environments of oxygenic stromatolites during the Late Archean. *Precambrian Res.* **138**(3–4), 255–273.
- Sauvage L., Riquier L., Thomazo C., Baudin F. and Martinez M. (2013) The late Haurerian Faraoni “Oceanic Anoxic Event” at Rio Argos (southern Spain): An assessment on the level of oxygen depletion. *Chem. Geol.* **340**, 77–90.
- Schidlowski M. (1982) Content and isotopic composition of reduced carbon in sediments. *Mineral. Dep. Evol. Bio. Springer*, 103–122.
- Schopf J. W., Kudryavtsev A. B., Czaja A. D. and Tripathi A. B. (2007) Evidence of Archean life: stromatolites and microfossils. *Precambrian Res.* **158**(3–4), 141–155.
- Severmann S., Johnson C. M., Beard B. L., German C. R., Edmonds H. N., Chiba H. and Green D. R. H. (2004) The effect of plume processes on the Fe isotope composition of hydrothermally derived Fe in the deep ocean as inferred from the Rainbow vent site, Mid-Atlantic Ridge, 36 degrees 14' N. *Earth Planet. Sci. Lett.* **225**, 63–76.
- Sforna M. C., Philippot P., Somogyi A., van Zuilen M. A., Medjoubi K., Schoepp-Cothenet B., Nitschke W. and Visscher P. T. (2014) Evidence for arsenic metabolism and cycling by microorganisms 2.7 billion years ago. *Nat. Geosci.* **7**, 811–815.
- Shahar A., Young E. D. and Manning C. E. (2008) Equilibrium high-temperature Fe isotope fractionation between fayalite and magnetite: an experimental calibration. *Earth Planet. Sci. Lett.* **268**, 330–338.
- Sharma M., Polizzotto M. and Anbar A. D. (2001) Iron isotopes in hot springs along the Juan de Fuca Ridge. *Earth Planet. Sci. Lett.* **194**, 39–51.
- Sim M. S., Bosak T. and Ono S. (2011) Large sulfur isotope fractionation does not require disproportionation. *Science* **333** (6038), 74–77.
- Slotznick S. P. and Fischer W. W. (2016) Examining Archean methanotrophy. *Earth Planet. Sci. Lett.* **441**, 52–59.
- Sossi P. A., Foden J. D. and Halverson G. P. (2012) Redox-controlled iron isotope fractionation during magmatic differentiation: an example from the Red Hill intrusion, S Tasmania. *Contribut. Mineral. Petrol.* **164**(5), 757–772.
- Stüeken E. E., Buick R., Anderson R. E., Baross J. A., Planavsky N. J. and Lyons T. W. (2017) Environmental niches and metabolic diversity in Neoproterozoic lakes. *Geobiology* **15**(6), 767–783.
- Stüeken E. E., Buick R., Bekker A., Catling D., Foriel J., Guy B. M., Kah L. C., Machel H. G., Montañez I. P. and Poulton S. W. (2015a) The evolution of the global selenium cycle: Secular trends in Se isotopes and abundances. *Geochim. Cosmochim. Acta* **162**, 109–125.
- Stüeken E. E., Buick R. and Schauer A. J. (2015b) Nitrogen isotope evidence for alkaline lakes on late Archean continents. *Earth Planet. Sci. Lett.* **411**, 1–10.
- Sugisaki R. (1978) Chemical composition of argillaceous sediments on the Pacific margin of southwest Japan.
- Sugitani K., Horiuchi Y., Adachi M. and Sugisaki R. (1996) Anomalously low Al₂O₃/TiO₂ values for Archean cherts from the Pilbara block, western Australia - Possible evidence for extensive chemical weathering on the early earth. *Precambrian Res.* **80**, 49–76.
- Tebbutt G. E., Conley C. D. and Boyd D. W. (1965) Lithogenesis of a distinctive carbonate rock fabric. *Rock. Mount. Geol.* **4**, 1–13.
- Teng F.-Z., Dauphas N., Helz R. T., Gao S. and Huang S. (2011) Diffusion-driven magnesium and iron isotope fractionation in Hawaiian olivine. *Earth Planet. Sci. Lett.* **308**, 317–324.
- Teske A. (2010) Cryptic links in the ocean. *Science* **330**(6009), 1326–1327.
- Thomazo C., Ader M., Farquhar J. and Philippot P. (2007) Multiple Sulfur and Carbon isotopic chemostratigraphy of the 2.73 Ga carbonated Tumbiana formation, new insights for the Fortescue excursion. *Geochim. Cosmochim. Acta* **71**, A1019.
- Thomazo C., Ader M., Farquhar J. and Philippot P. (2009) Methanotrophs regulated atmospheric sulfur isotope anomalies during the Mesoarchean (Tumbiana Formation, Western Australia). *Earth Planet. Sci. Lett.* **279**, 65–75.
- Thomazo C., Oeser M., Strauss H. and Philippot P. (2010) Late Archean oceanic redox fluctuations revealed by iron speciation in the 2.73Ga old Tumbiana Formation. *Geochim. Cosmochim. Acta* **74**, A1042.
- Thomazo C., Ader M. and Philippot P. (2011) Extreme ¹⁵N-enrichments in 2.72-Gyr-old sediments: evidence for a turning point in the nitrogen cycle. *Geobiology* **9**, 107–120.

- Thorne A. and Trendall A. F. (2001) Geology of the Fortescue Group, Pilbara Craton, Western Australia. *Bull. Geol. Surv. West. Aust.* **144**, 1–249.
- Visscher P. T., Reid R. P., Bebout B. M., Hoefl S. E., Macintyre I. G. and Thompson J. A. (1998) Formation of lithified micritic laminae in modern marine stromatolites (Bahamas); the role of sulfur cycling. *Am. Mineral.* **83**(11-12 Part 2), 1482–1493.
- Welch S. A., Beard B. L., Johnson C. M. and Braterman P. S. (2003) Kinetic and equilibrium Fe isotope fractionation between aqueous Fe(II) and Fe(III). *Geochim. Cosmochim. Acta* **67**, 4231–4250.
- White A., Legras M., Smith R. and Nadoll P. (2014) Deformation-driven, regional-scale metasomatism in the Hamersley Basin, Western Australia. *J. Metam. Geol.* **32**, 417–433.
- Whitehouse M. J. and Fedo C. M. (2007) Microscale heterogeneity of Fe isotopes in > 3.71 Ga banded iron formation from the Isua Greenstone Belt Southwest Greenland. *Geology* **35**, 719–722.
- Wiesli R. A., Beard B. L. and Johnson C. M. (2004) Experimental determination of Fe isotope fractionation between aqueous Fe (II), siderite and “green rust” in abiotic systems. *Chem. Geol.* **211**, 343–362.
- Williford K. H., Ushikubo T., Lepot K., Kitajima K., Hallmann C., Spicuzza M. J., Kozdon R., Eigenbrode J. L., Summons R. E. and Valley J. W. (2016) Carbon and sulfur isotopic signatures of ancient life and environment at the microbial scale: Neoproterozoic shales and carbonates. *Geobiology* **14**(2), 105–128.
- Wintsch R. P. and Kvale C. M. (1994) Differential Mobility of Elements in Burial Diagenesis of Siliciclastic Rocks. *J. Sediment. Res. A* **64**, 349–361.
- Yoshiya K., Nishizawa M., Sawaki Y., Ueno Y., Komiyama T., Yamada K., Yoshida N., Hirata T., Wada H. and Maruyama S. (2012) In situ iron isotope analyses of pyrite and organic carbon isotope ratios in the Fortescue Group: Metabolic variations of a Late Archean ecosystem. *Precambrian Res.* **212–213**, 169–193.

Associate editor: Aubrey Zerkle

CHAPTER 6.

MALMANI STROMATOLITES: POST-DEPOSITIONAL HISTORY AND PRESERVATION OF PRIMARY GEOCHEMICAL SIGNATURES

Carbonate platforms are often used to reconstruct the dynamics of ocean chemistry, sea level changes, tectonic and biological activity throughout the Earth history (*Elrick, 1996; Grotzinger and Knoll, 1999; della Porta et al., 2004*). Carbonate platforms are documented since the Mesoarchean, at 2.9 Ga (Red lake; *McIntyre and Fralick, 2017*), but the most commonly studied Archean platform is the Campbellrand-Malmani platform (2.58 to 2.50 Ga, Transvaal Supergroup, South Africa; *Beukes, 1980; Sumner, 1996*). This platform includes a large variety of stromatolites which were deposited shortly before the GOE (*Beukes, 1987; Sumner and Bowring, 1996; Knoll and Beukes, 2009*). Therefore, the 2.58-2.50 Ga stromatolites may give insights on the timing of the major redox transition in Earth history. Indeed, several studies document a production of oxygen related to cyanobacterial photosynthetic activity in the platform (e.g. *Kendall et al., 2010; Czaja et al., 2012*). Consequently, if stromatolites were the site of vigorous oxygen production, these episodes of oxygenation could have influenced the isotope signatures of pyrite. This study aims to investigate the Fe and S isotope signatures of pyrite precipitated under the influence of microbial communities producing oxygen. However, post-depositional processes affected the Campbellrand-Malmani platform, including the large scale dolomitization and metamorphism linked to the emplacement of the 2.06 Ga Bushveld Complex (*Button, 1973; Truswell and Eriksson, 1975; Beukes, 1987; Tyler and Tyler, 1996*). In order to untangle the signal of secondary phases from that of potential preserved primary grains, a petrographic characterization was conducted on samples collected during the fieldwork (September 2019) in the Malmani Subgroup (Transvaal area). Preliminary results of the Fe and S isotope measurements from preserved sedimentary pyrite and late hydrothermal pyrite are also presented here.

1. The Campbellrand-Malmani platform

1.1. Geological context and sections

The stratigraphic studied section is located in the eastern part of the Malmani-Campbellrand platform, located in the Malmani Subgroup (Chuniespoort Group, Transvaal Supergroup, Kaapvaal craton, South Africa; *Eriksson et al., 1993*). The field area is divided in two main outcrops (**Fig. 6.1**) including (1) megadomes (pluri-meter scale) of stromatolites along the R539 roadside (**Fig. 6.1a-c**) and (2) more scattered outcrops in the land above the road (**Fig. 6.1a**), which are made of wavy, domal and concretionary stromatolites, interbedded with laterally discontinuous chert layers (which follow the stratification) and, at the top of the section, climbing ripple beds (**Fig. 6.1d to g**). Because of the highest diversity of the facies, the outcrop (2) was used to describe a 20 m sedimentary section of the Malmani Subgroup (**Fig. 6.1h**). This section is likely part of the 2.55 Ga Upper Monte-Christo Formation (personal communication from W. Altermann), which correlates with the Reivilo and the Lower Nauga Formations in the Griqualand West area and the Prieska area respectively (*Altermann and Nelson, 1998*). The upper Monte Christo Fm deposited in an intertidal to shallow subtidal environment (*Button, 1973*).

1.2. The redox conditions of the Neoproterozoic ocean

Many studies on the Campbellrand-Malmani carbonate platform concentrated on the search of O₂ producing photosynthesis prior to the Great Oxidation Event. Numerous geochemical proxies, including multiple sulfur isotopes, iron speciation and iron isotopes, nitrogen isotopes, molybdenum content and isotope ratios, uranium and rhenium concentrations, evidenced the production of oxygen by photosynthetic organisms in shallow water environments (*Holland et al., 1986; Anbar et al., 2007; Wille et al., 2007; Kamber and Whitehouse, 2007; Godfrey and Falkowski, 2009; Czaja et al., 2012; Fischer et al., 2014; Kurzweil et al., 2016*). However, this oxygen production is portrayed as insufficient to contribute to the global atmospheric oxygenation (*Kendall et al., 2010*).

2. Results

2.1. Petrographic observations

2.1.1. Facies description

Petrographic descriptions are based on macroscopic and microscopic observations of 48 thin sections made from the 44 samples collected on the field (**Fig. 6.1**). Only one thin section

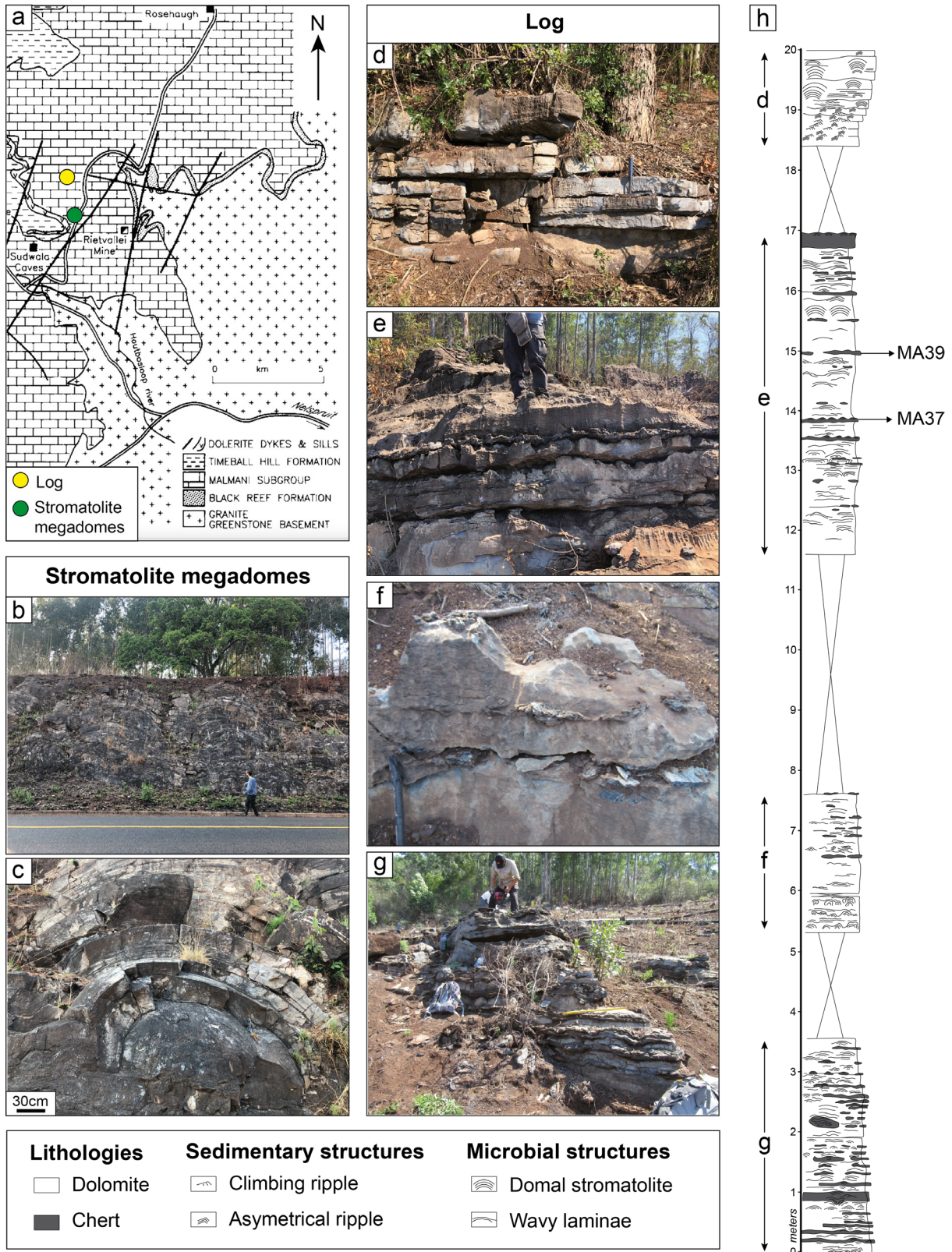


Figure 6. 1: a) Geological map of the studied area with location of the sedimentary section and the outcrop of stromatolite megadomes along the road. Modified from Tyler and Tyler (1996). b) A large-scale view of the outcrop along the road made of large stromatolite megadomes several meters across. c) A close-up of a domal stromatolite. d) to g) Photographs of the different outcrops which composed the log, with rippled-dolomite (non-bioconstructed facies FA1) and stromatolites (bioconstructed facies FA2) at the top and stromatolites with various degrees of silicification throughout the section.

was made in a sample collected from the outcrop of stromatolite megadomes along the road (**Fig. 6.1a-c**) while the other 47 thin sections were made from samples collected in the log (**Fig. 6.1a, d-g**). These observations in reflected and transmitted light microscopy were conducted during the Master projects of Aude Gounelle (*Gounelle, 2021*) and Guillaume Lawnizack (*Lawnizack, 2022*). Two facies associations have been identified, a non-bioconstructed facies (FA1), only observed at the top of the section (**Fig. 6.2a and c**) and a bioconstructed facies (FA2) made of stromatolites (**Fig. 6.2a-b, 6.2d-f**).

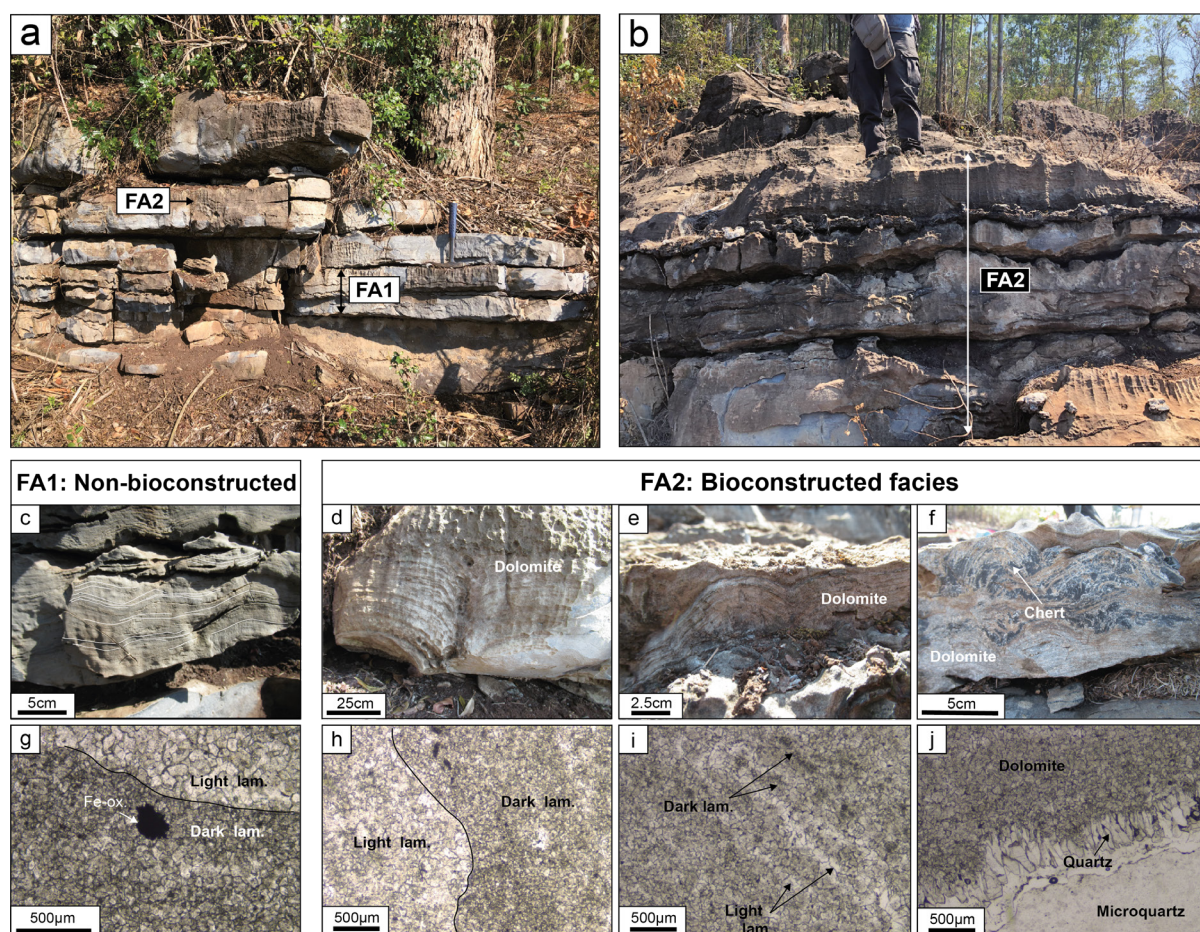


Figure 6. 2: a) Field view of the two facies associations, the non-bioconstructed (ripples) facies FA1 and the bioconstructed (stromatolite) facies FA2, identified at the top of the log. This part of the outcrop displays dolomitization with no signs of silicification. b) Field view of FA2 made of both dolomite and partially silicified stromatolites. c) Climbing ripples forming FA1 and g) microscopic view of FA1, characterized by dark and light laminae. d) Stromatolite at the top of the section (FA2) and h) microscopic view of the laminae constituting FA2. Same for e) and i) in FA2 from a stromatolite interbedded with silicified stromatolites. f) Partially silicified domal stromatolites and j) microscopic view of the dolomite-chert contact.

2.1.1.1. Non-bioconstructed facies (FA1)

Samples belonging to FA1 are dolomitized, categorized as “pure dolomite” hereafter (**Figs. 6.1h and 6.2a**). This facies describes regular laminae forming climbing and asymmetrical ripples. Several occurrences of ripple-laminated ooid grainstones are documented in the Malmani Subgroup, in the Oaktree, Monte Christo and Lyttelton Formations (*Tyler and Tyler, 1996*). Ooid grainstones likely formed the facies FA1 while the intense recrystallization due to dolomitization

erased the morphology of ooids. Microscopic observations revealed dark and light alternations forming ripples (**Fig. 2g**). Dark layers are composed of dolomite (crystal size $\sim 10\text{-}50\ \mu\text{m}$) and carbonaceous material while light layers comprise larger crystals of dolomite of $\sim 10\text{-}90\ \mu\text{m}$ (**Fig. 6.2g**). This facies also preserves carbonaceous ovoid to subangular sedimentary grains, more abundant in the dark layers (**Fig. 6.3a**). Large ($>100\ \mu\text{m}$) euhedral oxides are observed as relics of former pyrite grains (**Fig. 6.2g**). A few disseminated micrometric ($\sim 5\text{-}10\ \mu\text{m}$) pyrite grains preserved from oxidation are also observed.

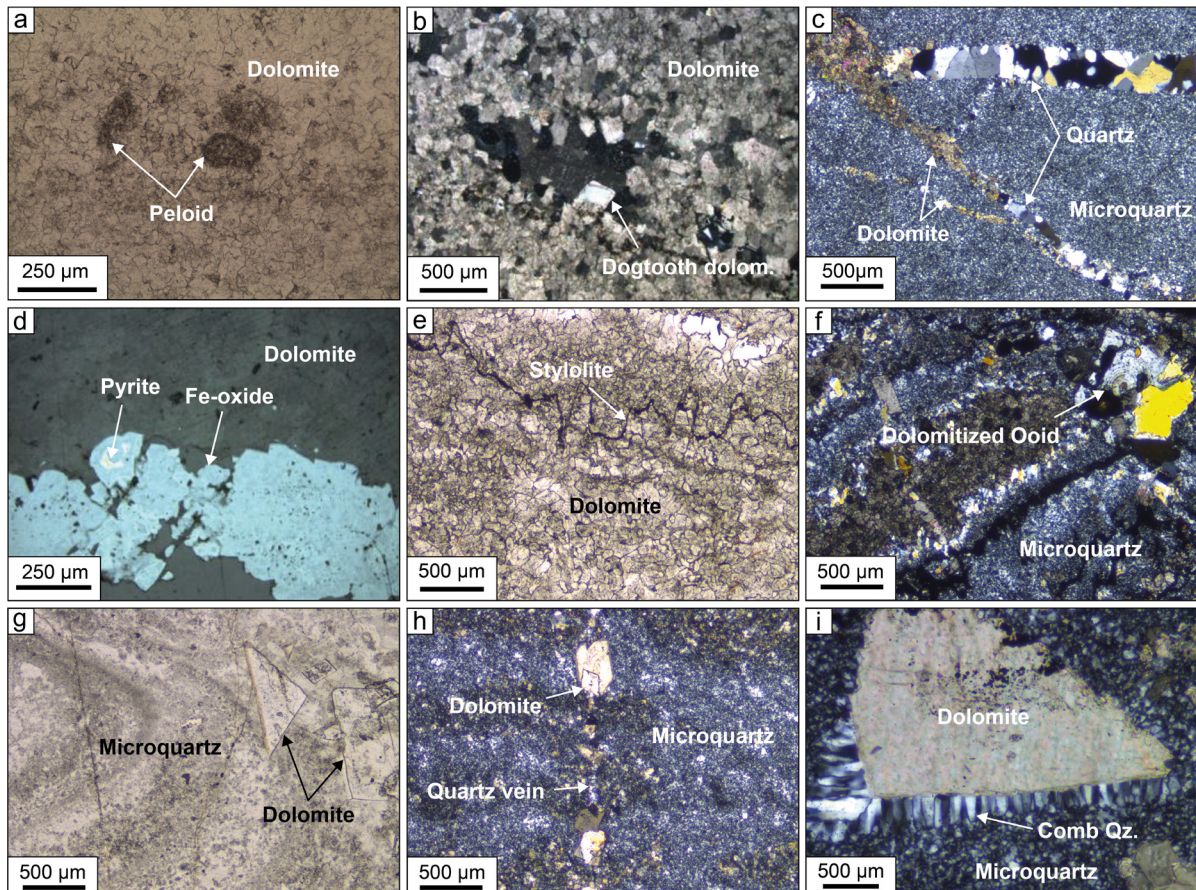


Figure 6.3: Pictures illustrating remarkable (primary and secondary) features observed in samples: a) Peloid in dolomite from FA1; b) Example of a fenestrae with dogtooth crystals of dolomite on the edge; c) Quartz and dolomite veins crosscutting the microquartz in a silicified stromatolite sample; d) Large oxidized pyrite; e) Stylolite in a sample from FA2; f) Preserved dolomitized ooid in a partially silicified stromatolite sample; g) Large dolomite crystal in the microquartz; h) Large crystals of dolomite forming inside a quartz vein; i) Comb quartz between a large dolomite crystal and the microquartz.

2.1.1.2. Bioconstructed facies (FA2)

The bioconstructed facies corresponds to dolomitized stromatolites (**Fig. 6.2d and e**). Several stromatolite morphologies can be observed, including wavy laminae, domes (10-50 cm across), concretionary domes and columns (1-10 cm across). Stromatolite lamination is microscopically identified also as an alternation of dark and light laminae formed by variations of dolomite crystal size and the presence of carbonaceous material (**Fig. 6.2h and i**). Dark laminae are in general thinner than light laminae and contain fenestrae filled with dolomite

or quartz, sometimes bordered by dogtooth dolomite crystals (**Fig. 6.3b**). The lamination can sometimes be disrupted by cross cutting veins filled with dolomite cement (**Fig. 6.3c**). In addition, rounded to angular carbonaceous grains of $\sim 50 \mu\text{m}$ in size can be observed in stromatolite samples from the top of the section similarly to those observed in FA1. These grains are partially dolomitized. Oxides are also abundant and form linear features (**Fig. 6.3d**). Pyrite cores are sometimes preserved in these oxide grains. As in samples from FA1, pyrite is rare and identified disseminated micrometric grains. Stylolites, i.e. planar sutures resulting from intergranular pressure-dissolution, are identified along the lamination (**Fig. 6.3e**).

2.1.2. Episodes of silicification

Dark grey layers of cherts are observed within the section (**Fig. 6.2f and j**). These layers conforming to the stratification but are laterally discontinuous and not observed in the top of the section (therefore only affecting bioconstructed facies FA2; **Fig. 6.1h**). In the field, the discontinuity of cherts results in an abrupt absence of silicification in the dolomite layers, illustrated for example by the half-silicified stromatolite domes. On a micrometer scale, this is expressed by the dolomite cement or dolomitized sedimentary structures (such as fenestrae or ooid; **Fig. 6.3f**) being direct in contact with quartz cement. Several generations of quartz are observed under the microscope. One cement is made of micrometric ($\sim 10 \mu\text{m}$) quartz crystals, referred to microquartz (**Figs. 6.2j and 6.3g**). This microquartz can also include large (hundreds of μm to mm) crystals of dolomite (**Fig. 6.3g**). Another generation of quartz is illustrated by larger crystals (hundreds of μm in size) forming cross-cutting veins (**Fig. 6.3h**). Those veins also exhibit dolomite crystals several mm in length (**Fig. 6.3h**).

2.2. Geochemical analyses

2.2.1. Major and minor elements

The analyses of bulk major and trace elements (**Tables S1 and S2**) performed on 18 samples from FA1 (rippled dolomite) and FA2 (dolomitic stromatolite, silicified stromatolites and partially silicified stromatolite) show low concentrations of detrital elements (**Fig. 6.4a**; sum of $\text{Al}_2\text{O}_3 + \text{Fe}_2\text{O}_3 + \text{MnO} + \text{Na}_2\text{O} + \text{K}_2\text{O} \leq 2 \text{ wt.}\%$). Al_2O_3 and Fe_2O_3 concentrations are respectively less than 0.30 wt.% and 1.21 wt.% (respective detection limits of 0.04 and 0.02 wt.%). MnO content is lower than 0.94 wt.% and positively covaries with the $\text{CaO} + \text{MgO}$ content, showing a substitution of Ca^{2+} or Mg^{2+} by Mn^{2+} in the dolomite atomic structure (**Fig. 6.4b**). TiO_2 and P_2O_5 concentrations are systematically below the detection limit. Those data differ from the major element data published in *Eroglu et al. (2015)*, in which the carbonates of Monte Christo Fm from the western part of the Transvaal area (Malmani Subgroup) have heterogeneous signatures characterized by greater amounts of detrital material and are silicified to various degrees. Pure carbonate samples from FA1 and FA2 are depleted in Sr relative to Ca, which is associated

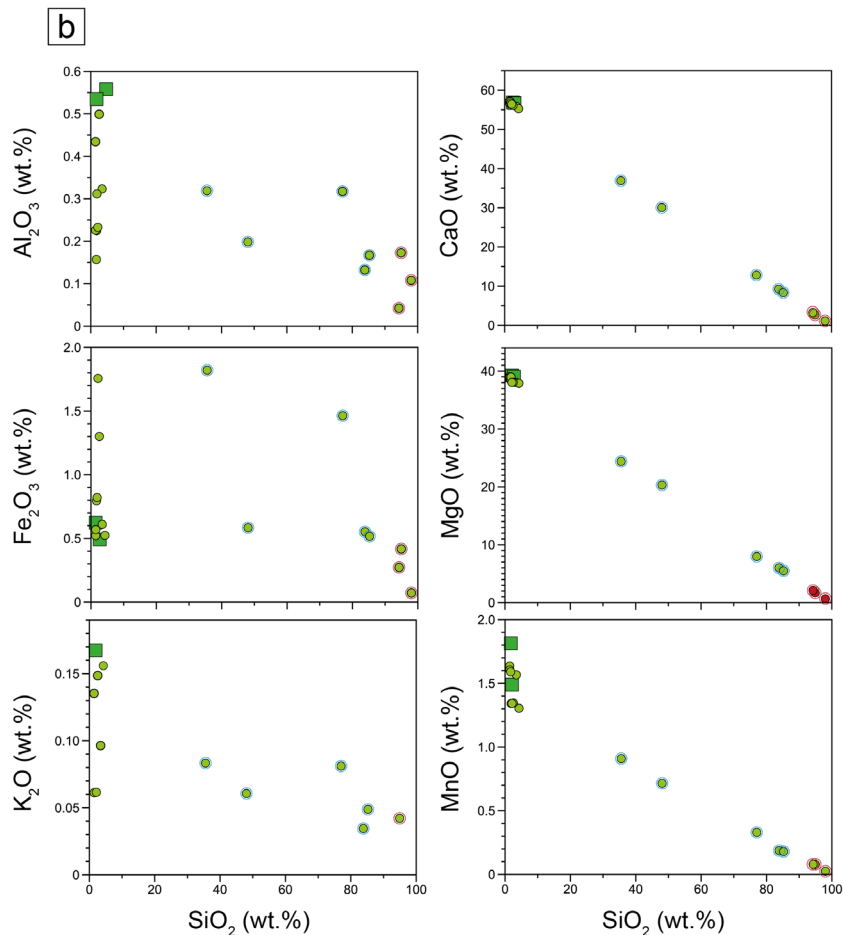
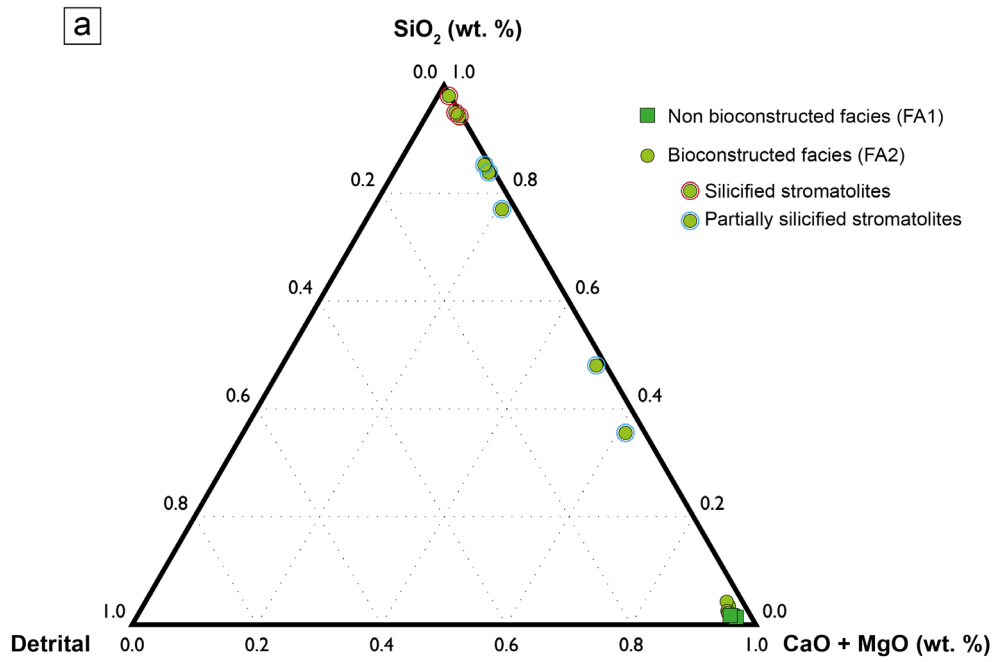


Figure 6. 4: a) Ternary diagram with analyses of stromatolite samples from the studied log (Upper Monte Christo Fm). The detrital fraction is defined as the sum Al₂O₃, Fe₂O₃, MnO, Na₂O and K₂O (in wt.%; TiO₂ and P₂O₅ contents are below the detection limit). b) Harker diagrams with samples from the log, including samples from FA1 (green square) and stromatolite samples from FA2 (green dots) divided into partially silicified stromatolites (green dot with blue line) and fully silicified stromatolites (green dot with red line).

with an enrichment in Mn (**Fig. 6.5a**). This is similar to the carbonate samples of the Malmani Subgroup described by *Eroglu et al. (2017)*. Moreover, the iron content (reported as the ratio Fe/Fe+Mg) is higher in silicified samples than pure dolomite from FA1 and FA2 (**Fig. 6.5b**).

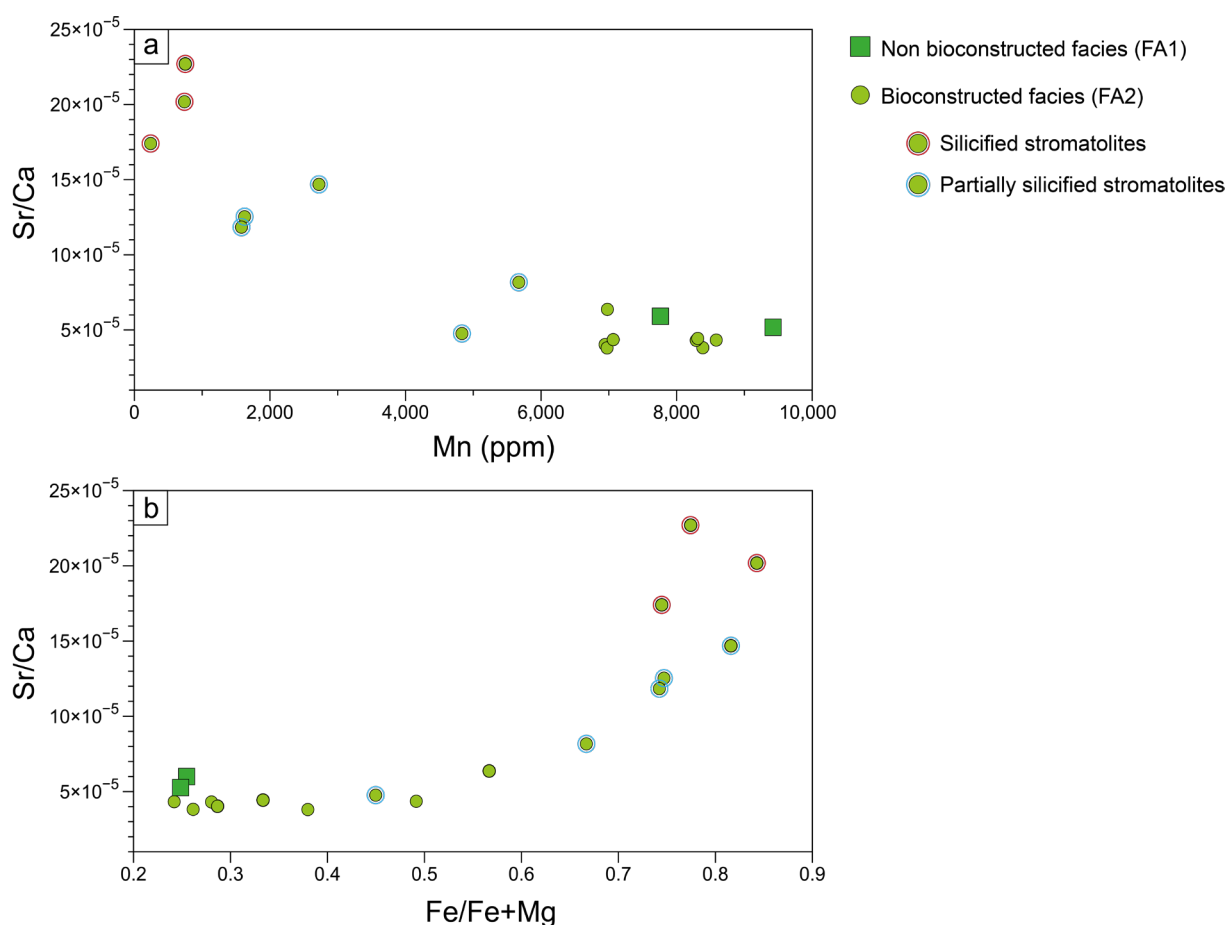


Figure 6.5: Relationship between Sr/Ca ratio and a) the Mn content and b) the ratio Fe/Fe+Mg in samples from the section.

2.2.2. Trace elements plus Rare Earth Element (REE)

The 18 samples selected along the stratigraphic section have been analyzed for their trace element content, including REE concentrations (**Table S3**). Trace element concentrations are low, ranging from 0.01 to 25.91 ppm and can be classified from the most to the least abundant as: Sr > Ba > Cr > Ni > Cu > Zr > V > Rb > W > As > Pb > Co > Ge > Sn > Ga > Y > Th > Sb > Bi > Cs ≥ Nb > Be > Hf = In > U > Ta. Only elements from Sr to As (in the order of abundance) have average concentrations above 1ppm, from 11.92 ppm for Sr to 1.02 ppm for As.

REE concentrations were normalized to post-Archean Australian Shale (PAAS) in order to plot REE+Y distributions (*Taylor and McLennan, 1985*). La, Ce and Eu anomalies are calculated from normalized concentrations and are expressed by the deviation of the shale normalized La/La* ($La/La^* = La_{SN}/(Pr_{SN}^2/Nd_{SN})$), Ce/Ce* ($Ce/Ce^* = Ce_{SN}/(Pr_{SN}^2/Nd_{SN})$) and Eu/Eu* ($Eu/Eu^* = Eu_{SN}/(Sm_{SN}^2/Nd_{SN})$) ratios from 1 (*Lawrence et al., 2006, Tostevin et al., 2016*). Ratios Y/Ho were calculated from absolute concentrations. Samples from FA2 can be categorized as a function

of their REE+Y distributions, which is related to their degree of silicification. REEs are poorly concentrated in chert and rather contained in carbonates.

Two “end-members” REE+Y patterns and two intermediate patterns are identified (**Fig. 6.6**).

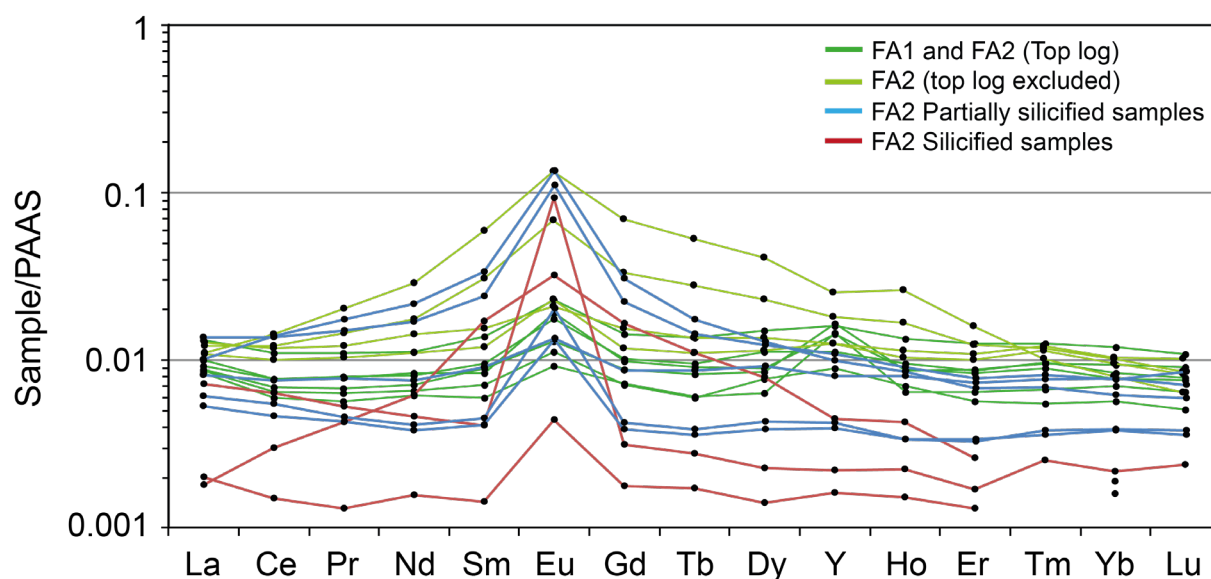


Figure 6. 6: REE+Y spectra normalized to PAAS of samples classified as a function of the lithology and the position in the log. Deep green spectra represent pure dolomite from the top of the section (both FA1 and FA2). Samples from FA2 which are interbedded with silicified samples are in light green. The blue spectra represent partially silicified samples (FA2), and the red spectra refer to silicified samples (FA2). Only the analyses with concentrations above the detection limits are plotted.

The end-member patterns include:

- Samples from FA1 and FA2 at the top of the section (**Fig. 6.1d**) which are characterized by a flat pattern (deep green spectra, **Fig. 6.6**), i.e. without depletion or enrichment of light REEs relative to heavy REEs, a positive La anomaly (average $La/La^* = 1.348$), no Ce anomaly ($Ce/Ce^* = 1.045$), a positive Y anomaly and slightly pronounced Eu anomaly ($Eu/Eu^* = 1.571$). Y/Ho ratios range from 31 to 60, with an average value of 42, the highest through the stratigraphy. Those patterns are comparable with those previously obtained in samples from the Monte Christo Fm (Eroglu *et al.*, 2017).

- Silicified samples from FA2 (**Fig. 6.1e-g**) characterized by lower REE concentrations, slightly enriched light REEs relative to heavy REEs spectra (red spectra, **Fig. 6.6**), a positive La anomaly (average $La/La^* = 1.216$), insignificant positive Ce anomaly (average $Ce/Ce^* = 1.144$) and a well-pronounced positive Eu anomaly (average $Eu/Eu^* = 10.082$), particularly in MA43 sample showing an Eu anomaly of 26.141. The mean Y/Ho is 28, slightly higher than the reference Y/Ho ratio in PAAS (Y/Ho=27).

The intermediate patterns are depicted in:

- Samples from FA2 (interbedded with silicified samples), characterized by regular pattern for light and middle REEs and a depletion of heavy REEs (light green spectra, **Fig. 6.6**), insignificant La and Ce anomalies (averages $\text{La/La}^* = 1.024$ and $\text{Ce/Ce}^* = 1.037$) and less important Eu anomaly (average $\text{Eu/Eu}^* = 1.341$). A slightly higher mean Y/Ho of 29 is measured in those samples.

- Partially silicified samples from FA2, represented by patterns slightly light REEs enriched relative to heavy REEs (blue spectra, **Fig. 6.6**), no La and Ce anomalies (averages $\text{La/La}^* = 1.016$ and $\text{Ce/Ce}^* = 1.000$), a positive Eu anomaly (average $\text{Eu/Eu}^* = 2.840$) and a mean Y/Ho ratio of 31.

2.2.3. Carbonaceous matter

Carbonaceous matter has been either observed in dark laminae of both FA1 and FA2, peloids, in stylolites, included in quartz crystals and in joints between crystals. Raman spectra from a peloid in sample 1.30 (from the sedimentary section) show characteristics of graphitic carbonaceous material. Peak temperature estimations were done following the methodology proposed by *Kouketsu et al. (2014)*. The maximum temperature experienced by the CM was estimated at $395 \pm 30^\circ\text{C}$ (**Fig. 6.7**). This result contrasts with the low-grade metamorphism (greenschist facies) dominant in the platform (*Miyano and Beukes, 1984*) and is rather indicative of the higher grade metamorphism documented in the Bushveld complex area (*Nell, 1985*). However, temperatures compatible with the regional greenschist facies metamorphism ($300\text{--}330^\circ\text{C}$) were documented in carbonate and silicified carbonate samples from the Malmani Subgroup at ~ 80 km south from the Bushveld complex (*Eroglu et al., 2017*). This means that, in the present study, the sedimentary section is located in the most altered part of the platform, and that there is a steep metamorphic gradient within a hundred km around the Bushveld intrusion.

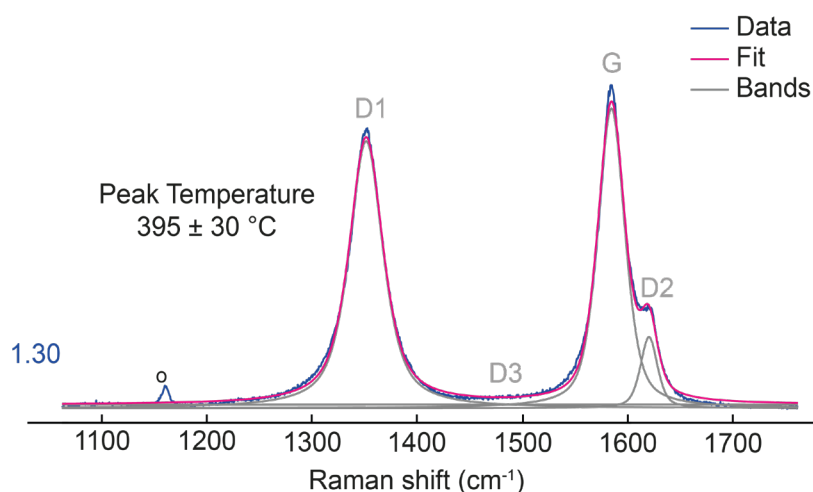


Figure 6. 7: Raman spectra of carbonaceous matter from sample 1.30 (partially silicified stromatolite from the log) fitted to the theoretical G and D-bands. Peak temperature estimation after (*Kouketsu et al., 2014*).

2.2.4. Minor elements in pyrite (EPMA)

The minor and trace element content of pyrite (Co, Ni, As, Au, Pb, Zn and Cu) have been analyzed by EPMA in three silicified stromatolites which were analyzed by SIMS for their S and Fe isotope compositions (**Table S4**). The average concentrations of all trace elements are below 0.1 wt.% and often below the detection limit for Au, Zn and Pb. Co/Ni ratios are widely used to distinguish between the hydrothermal or sedimentary origin of pyrite (*Bajwah et al., 1987; Gregory et al., 2015*). It has been demonstrated that most of pyrite precipitation from hydrothermal fluids has Co:Ni ratios >2 while Co:Ni ratios <2 are indicative for sedimentary pyrite formed in organic-rich environments (*Bajwah et al., 1987*). Here, large euhedral pyrite grains with various degree of oxidation (rims to almost complete oxidation) show Co:Ni ratios from 1.4 to 55.6, with an average value of 23.9 (n=7). In contrast, Co:Ni ratios in micrometric euhedral pyrite grains range between 0.7 to 2, with an average of 1.21 (n=6).

2.2.5. SIMS analyses (Fe and S isotopes)

Iron and sulfur isotope analyses were performed in three silicified stromatolites from FA2 of the Malmani Subgroup (**Fig. 6.8**). Samples MA37 and MA39 are from the sedimentary section and Amal C4 is from the outcrop formed by megadomal stromatolites along the road. Despite the high degree of silicification in those samples, they contain quartz and also dolomite, phyllosilicate minerals ± rutile, pyrite and oxide (**Fig. 6.8**). Samples MA37 and MA39 enclose large euhedral pyrite grains of ~50 to 150 μm affected by various degree of oxidation and always associated with quartz (**Fig. 6.8a-b**). They also include a few micrometric (~15 to 30 μm) disseminated pyrite grains spared from oxidation and spatially associated with dolomite or quartz (**Fig. 6.8c**). Only micrometric pyrite grains of 2 to 35 μm are observed in AmalC4, in spatial association with quartz or dolomite (**Fig. 6.8d**). These pyrite grains are disseminated throughout the sample and are not spatially associated with carbonaceous material. Oxidation rims are not observed in those pyrite grains, but we note the presence of an older generation of sulfide minerals of ~10 μm that are now completely oxidized. Pyrite forms euhedral grains in all studied samples. A total of 32 pyrite Fe isotope analyses were performed in the three samples described above (**Table S5**). Pyrite $\delta^{56}\text{Fe}$ values show a significant variation from -0.87 to +3.85‰ (**Fig. 6.9a**).

In detail, the 12 analyses in sample AmalC4 display $\delta^{56}\text{Fe}$ values between +0.60 and +3.85‰ and the highest average value of +1.71 ± 1.01‰ (1SD). Sample MA37 show the largest isotope range, with $\delta^{56}\text{Fe}$ values varying from -0.87 to +3.53‰ and an average value of +1.31 ± 1.47‰ (1SD, n=14). Finally, $\delta^{56}\text{Fe}$ values in MA39 vary between +0.64 and +1.78‰, with an average of +1.14 ± 0.41‰ (1SD, n=6). Due to repolishing, some of the further S-isotope values were measured from new areas that do not correspond to the areas measured for Fe isotope values. However, the larger grains of pyrites are less susceptible to this consequence of repolishing.

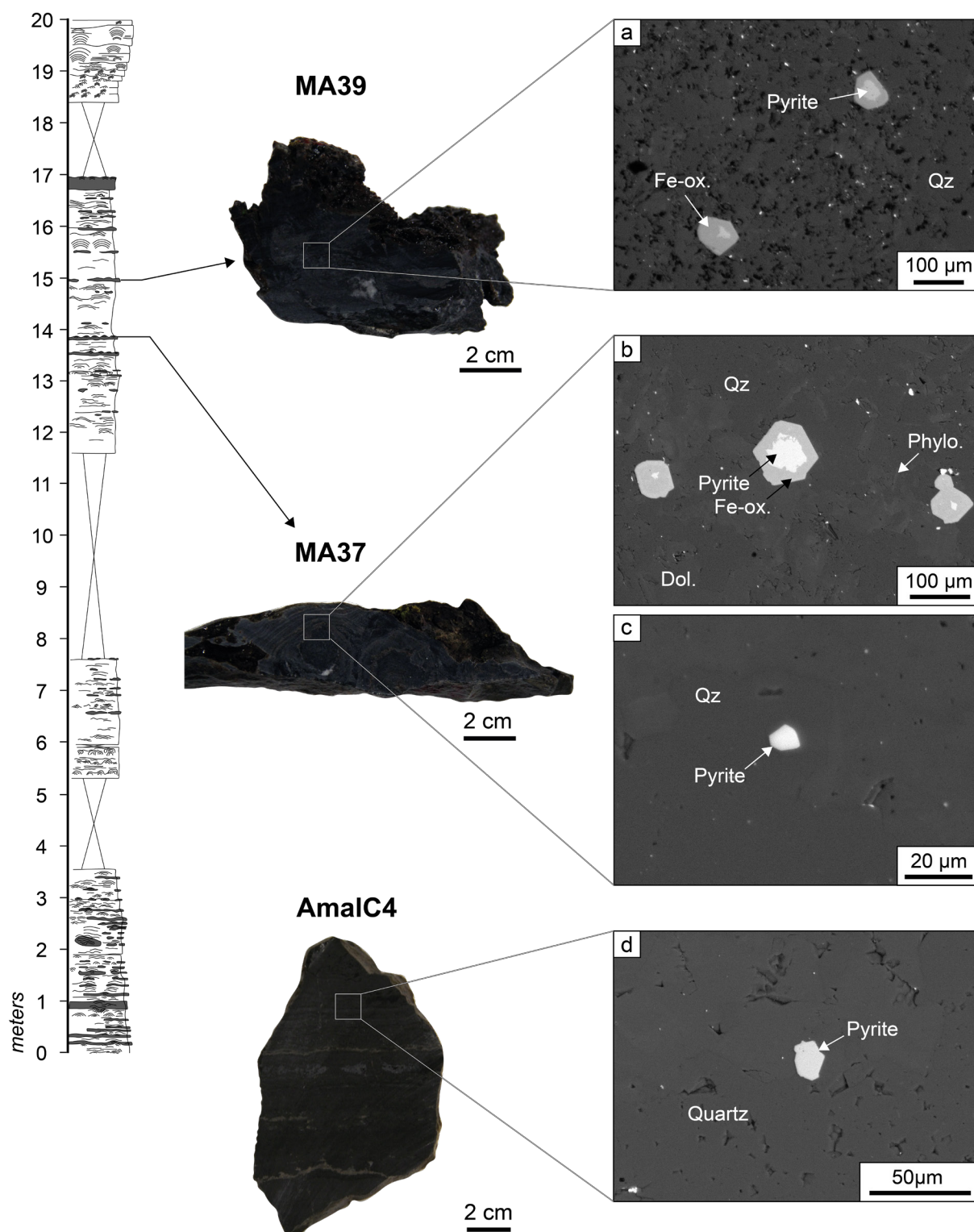


Figure 6. 8: Macroscopic view of samples measured for their pyrite Fe and S isotope compositions by SIMS. The BSE images of pyrite grains in these three samples are shown. a) Partially oxidized euhedral pyrite grains within microquartz in sample MA39 b) Euhedral and aggregated pyrite within microquartz and dolomite in sample MA37. c) Euhedral micrometric pyrite embedded in microquartz in sample MA37. d) Euhedral micrometric pyrite associated with microquartz in sample AmalC4.

For sulfur isotopes, the 42 analyses (**Table S6**) show $\delta^{34}\text{S}$ variation from -24.52 to $+6.43\text{‰}$ and $\Delta^{33}\text{S}$ from $+1.07$ to $+5.63\text{‰}$ (**Fig. 6.9b**). AmalC4 shows the largest isotope range, with $\delta^{34}\text{S}$ values from -24.52 to $+2.57\text{‰}$ and a mean value of $-4.57 \pm 7.11\text{‰}$ (1SD, $n=24$). The $\Delta^{33}\text{S}$ values range between $+1.07$ and $+2.92\text{‰}$, with a mean value of $+1.83\text{‰}$. MA37 shows $\delta^{34}\text{S}$ values from -3.72 to $+6.43\text{‰}$ and an average value of $+1.69 \pm 2.85\text{‰}$ (1SD, $n=11$). This sample shows the heaviest $\Delta^{33}\text{S}$ values, which vary between $+2.64$ and $+5.63\text{‰}$ ($\Delta^{33}\text{S}_{\text{mean}} = +3.11\text{‰}$). The highest $\Delta^{33}\text{S}$ values were measured in MA37, ranging from $+1.55$ to $+2.45\text{‰}$ and an average of $+2.18 \pm 0.30\text{‰}$ (1SD, $n=7$). $\Delta^{33}\text{S}$ values show little variation between $+2.15$ to $+2.36\text{‰}$.

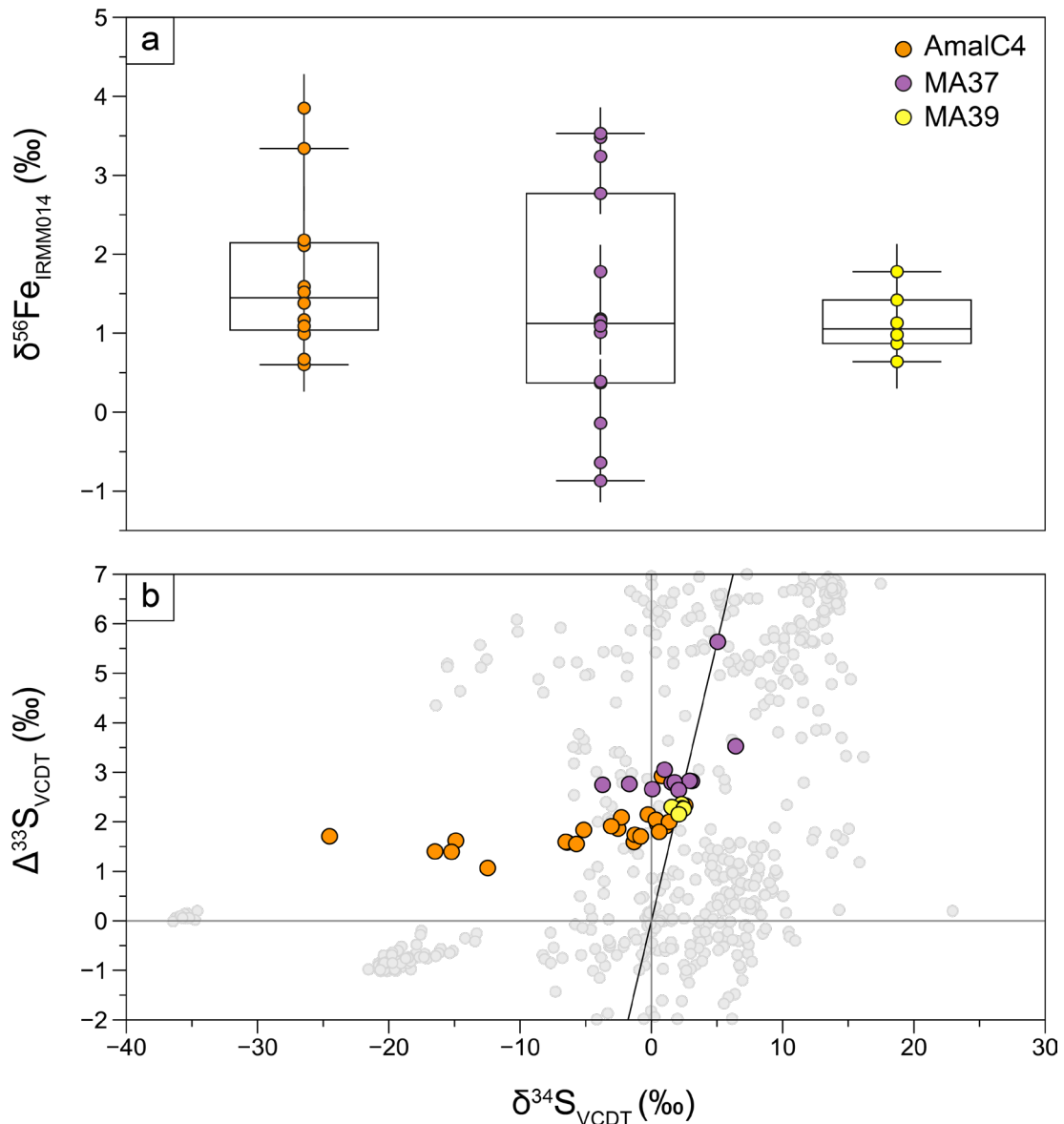


Figure 6.9: a) Fe isotope compositions of pyrite from AmalC4 (orange dots), MA37 (purple dots) and MA39 (yellow dots) reported using outlier box plot representation. Line crossing the box is the median and the edges of the box represent the quartiles (lower line is the 1st quartile $Q1$, i.e. the 25th percentile, and upper line is the 3rd quartile $Q3$, i.e. the 75th percentile). Lower and upper whiskers represent $1.5 \times \text{IQR}$ (interquartile range, i.e. the range between $Q1$ and $Q3$). The minimum and maximum are marked by small lines at the end of whiskers and represent respectively the lowest and highest values of the distribution. b) Multiple sulfur isotopes measured in the same samples that were used for Fe isotope analyses. Grey dots report in situ $\delta^{34}\text{S}$ and $\Delta^{33}\text{S}$ measurements in samples from the Campbellrand-Malmani platform (Farquhar et al., 2013; Fischer et al., 2014; Kamber and Whitehouse, 2007; Ono et al., 2009). $\Delta^{33}\text{S}$ is defined as $\delta^{33}\text{S} - 1000 \times [(1 + \delta^{34}\text{S}/1000)^{33/32} - 1]$.

3. In situ Fe and S isotope signatures previously reported

The Neoproterozoic sulfur cycle has already been investigated through spatially resolved S isotopes analyses along the Campbellrand-Malmani platform. *Farquhar et al. (2013)* documented multiple sulfur isotope variation in pyrite nodules enclosed in carbonates and shales from core GKF01 (Transvaal Supergroup, Griqualand West area). After accounting for alteration, the large $\delta^{34}\text{S}$ isotope range of $\sim 20\%$ evidenced in the nodule was interpreted as a consequence of MSR. From the same drill core, MSR was also identified as an active metabolic pathway in ovoid pyrites grains (negative $\delta^{34}\text{S}$ and $\Delta^{33}\text{S}$ values), while a second pool of atmospheric elemental sulfur was suggested to contribute to the formation of euhedral pyrite grains (positive $\delta^{34}\text{S}$ and $\Delta^{33}\text{S}$ values; *Farquhar et al., 2013*). Mixing of the MSR derived sulfide with the elemental S is also proposed to produce pyrite with negative and variable $\delta^{34}\text{S}$ values and positive $\Delta^{33}\text{S}$ values (Gamoha Formation, Campbellrand Subgroup; *Kamber and Whitehouse, 2007*).

To our knowledge, no study has previously measured the Fe isotope compositions of pyrite in the Malmani-Campbellrand carbonate platform. However, iron cycling in the platform sediments was reconstructed through the Fe isotope bulk rock analyses of carbonates and mudstones (*Czaja et al., 2012; Eroglu et al., 2018*). The iron isotope ratios revealed that the redox Fe cycle was dominated by formation of Fe-oxides related to a significant production of oxygen by oxygenic photosynthesis (*Czaja et al., 2012*). The Fe cycling has been shown to follow a spatial and temporal evolution of the platform architecture, resulting in variations of Fe sources from the steep ramp to rimmed margin. The Fe isotope difference in mudstones from the paleo-shelf (high $\delta^{56}\text{Fe}$ values) and the slope (low $\delta^{56}\text{Fe}$ values) suggests the export of microbially derived Fe according to the Fe shuttle model (*Severmann et al., 2008; Eroglu et al., 2018*).

4. Discussion

4.1. Post depositional history

Samples from the sedimentary section depict a complex post depositional history that can be divided into several episodes, illustrated in **Fig. 6.10**.

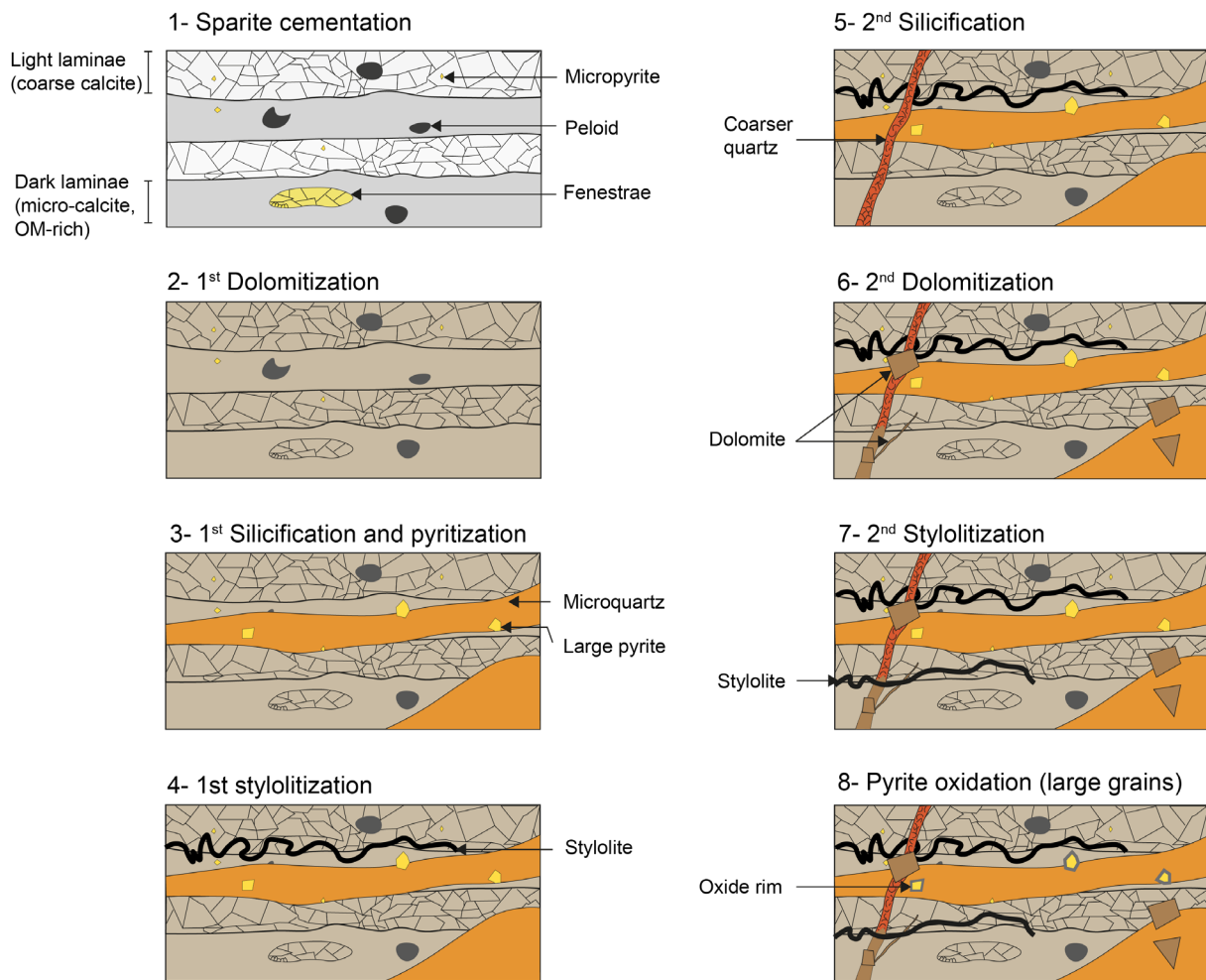


Figure 6. 10: Scheme of the different stages of post-depositional processes experienced by the stromatolite samples of the Malmani Subgroup in the eastern part of the platform. Not to scale, modified from Lawnizack (2022).

They include:

1- Cementation of primary fenestrae filled by sparite (cement of calcite). However, the primary mineralogy (calcite) is not preserved throughout the section.

2- The first stage of dolomitization at expense of primary calcite. This process led to the recrystallization of most of the ooids (lamination removed) in FA1. Only one ooid grain was identified over the 48 thin sections made along the section (Fig. 6.3f). Microscopically, this stage of dolomitization is characterized by a micrometric (10-100 μm) dolomite cement. The size of dolomite crystals varies across the light and dark laminae in samples from FA1 and FA2. This stage of dolomitization is pervasive throughout the Malmani Subgroup (Fig. 6.2), and particularly in the peritidal facies, while some samples of the Campbellrand Subgroup (south part of the platform) still have calcite preserved (Beukes, 1987; Sumner and Grotzinger, 2004; Sumner and Beukes, 2006).

This large scale dolomitization is commonly interpreted as being of the early diagenetic origin (Beukes, 1987; Eriksson and Altermann, 1998). Such scenario would imply circulation of large volume of Mg-rich brines, that were contributed by evaporation in proximal settings

(*Simms, 1984; Machel, 2004*).

3- The first stage of silicification in FA2 (stromatolites) that is typically stratiform but sometimes does not follow the lamination of stromatolites. This silicification is microscopically characterized by a micrometric quartz cement (**Fig. 6.3g**). The silicification of the Malmani Subgroup was previously attributed to the interaction between seawater and acidic meteoric fluids rather than a hydrothermal circulation (*Knauth, 1979; Eroglu et al., 2017*). This hypothesis was further supported by the measurement of high $\delta^{30}\text{Si}$ values which point to quartz precipitation from surface waters (*Eroglu et al., 2015*). However, such a model is not compatible with the observation of silicified layers, which follow the stratification and go through stromatolite lamination. The silicified samples MA12 and MA43 (FA2) show enriched light REEs and a highly pronounced positive Eu anomaly (**Fig. 6.6**). Together with chondritic Y/Ho ratio ~ 27 , these results suggest an increased oceanic input in high temperature hydrothermal fluids (*Michard, 1989; Derry and Jacobsen, 1990; Maier and Barnes, 1998; Bau and Dulski, 1999; Kamber and Webb, 2001*). This Eu anomaly is also observed in partially silicified stromatolites and in non-silicified stromatolites which are interbedded with silicified samples. This means that hydrothermal silica-rich fluids influenced the REE content of stromatolites over an area that is larger than the observed silicification area. From petrographic observations and REE-distributions, a hydrothermal circulation is suggested as the cause of the silicification.

4- The first stage of stylolitization, which affected the dolomite (step 2) and quartz (step 3) cements. Stylolites are only observed in FA2 and represent preferential fluid pathways. These fluid pathways also followed the large oxidized pyrite grains (**Fig. 6.3e**).

5- The second stage of silicification, characterized by 50 to 200 μm -wide veins that crosscut the facies FA2 (silicified and non-silicified, except the top of the log). These veins are filled with quartz.

6- The second stage of dolomitization is represented by formation of dolomite-filled veins (**Fig. 6.3c**). Large (200 μm to 1 mm) dolomite crystal also formed during step (**Fig. 6.3c** and **6.3h**). Multiple dolomite and silica-forming fluid circulation events can be related to magmatic fluid-rock interaction promoted by the Bushveld intrusion. This intrusion is responsible for the ore deposits in the studied area (*Tyler and Tyler, 1996*).

7- These two generations of veins (quartz and dolomite) are crosscut by a second generation of stylolites.

8- Oxidation of large pyrite grains associated with the microquartz (**Figs. 6.3d** and **6.8a-b**). The occurrence of two episodes of dolomitization is further supported by major and trace-

elemental analyses. During secondary alteration, the dissolution of detrital phases can lead to an increase of Mn and Fe content, which can be exchanged with Mg^{2+} , and a decrease of Sr content, which can be exchanged with Ca^{2+} (Banner, 1995). Carbonate samples from FA1 and FA2 show a Sr-depletion and an enrichment of Mn relative to limestone (Fig. 6.5a), which is typical for dolomitization documented in recent sediments (Kretz, 1982; Veizer et al., 1989). Moreover, the positive correlation between Sr/Ca ratio and Fe/Fe+Mg (Fig. 6.5b) suggests that (1) fluids leading to silicification supplied iron in the system and (2) silicified samples retain iron and strontium from leaching.

4.2. Preservation of primary grains and chemical-environmental signals?

Despite the high-grade metamorphism in the Transvaal area, primary structures and grains are still preserved. First, the diversity, in terms of morphology, of stromatolites and the lamination of both stromatolites and ripples have been preserved. Desiccation cracks and one ooid are preserved in samples that even underwent dolomitization. Dogtooth crystals are preserved on the edges of fenestrae and predate the dolomite recrystallization (Flügel, 2004), prior to the entire structure was dolomitized. Abundant carbonaceous rounded to subangular grains are described in both FA1 and FA2. The shape of these grains can be interpreted as detrital in origin and suggests various degrees of transport. Formation of such grains can also be related to the remobilization of laminated carbonaceous mudstones documented in the intertidal to subtidal domains of the platform (Tyler and Tyler, 1996) and can be referred as peloids.

Spectra measured in samples (FA1 and FA2) from the top of the section display different patterns than those in silicified samples. The normalized REE+Y spectra obtained in these dolomite samples from the top of the section (MA1, MA3, MA7 and MA10) exhibit both positive La and Y anomalies and superchondritic Y/Ho ratios up to 60 (Fig. 6.6). Such REE+Y distributions display features characteristic of seawater, including positive La anomaly and high Y/Ho ratios (> 40; Bolhar et al., 2004). However, these measured patterns are less depleted in light REEs compared to seawater. The effect of “flattened” patterns and the correlation between Y/Ho and La anomaly has already been observed in Campbellrand stromatolites samples (Kamber and Webb, 2001) and can be explained by two processes:

- 1- Contamination by clastic material, which tends to flatten the PAAS-normalized REE patterns

- 2- A mixing of seawater with very shallow waters typical of proximal or estuarine settings which preferentially concentrate light REEs (Kamber and Webb, 2001).

However, these two hypotheses are not consistent with petrographic observations and elemental analyses, including the absence of correlation between REEs and elements concentrated in terrigenous phases (e.g. Al, Zr, Th, Ga; Fig. 6.11; Allwood et al., 2010) and the low Al and K content throughout the section, which do not support terrigenous inputs.

Finally, two generations of pyrite have been identified through microscope observations

(Fig. 6.8) and the analyses of minor and trace element concentrations. Only one micrometric “sedimentary” pyrite was measured in sample MA39. The S isotope values in these sedimentary pyrite grains are not distinguishable from those measured in the large and oxidized pyrite grains. The micrometric pyrite grains from sample MA37 display a much larger range of S isotope values than those of large, oxidized grains. Finally, the largest range of $\delta^{34}\text{S}$ values was documented in sample AmalC4 and it was measured in micrometric sedimentary pyrite. Therefore, this large S isotope range may have preserved primary signatures, which are for the moment difficult to interpret as they can be produced by microbial activity or thermochemical sulfate reduction (Kiyosu, 1980; Ono et al., 2009; Watanabe et al., 2009).

Pyrite $\delta^{56}\text{Fe}$ values show large ranges, especially in sample MA37 while samples MA39 and AmalC4 only display positive $\delta^{56}\text{Fe}$ values (Fig. 6.9a). Contrary to the S isotope analyses, the range of $\delta^{56}\text{Fe}$ values in the micrometric pyrite from AmalC4 is similar to the range measured in the oxidized pyrite of MA37 (Fig. 6.9a). The discrepancy between Fe and S isotope compositions in the two pyrite generations can be due to a recrystallization by a S-bearing magmatic fluid which did not contain iron. Therefore, the “hydrothermal” pyrite grains are characterized by a dilution of the S-isotope signal while the Fe isotope signal was not modified.

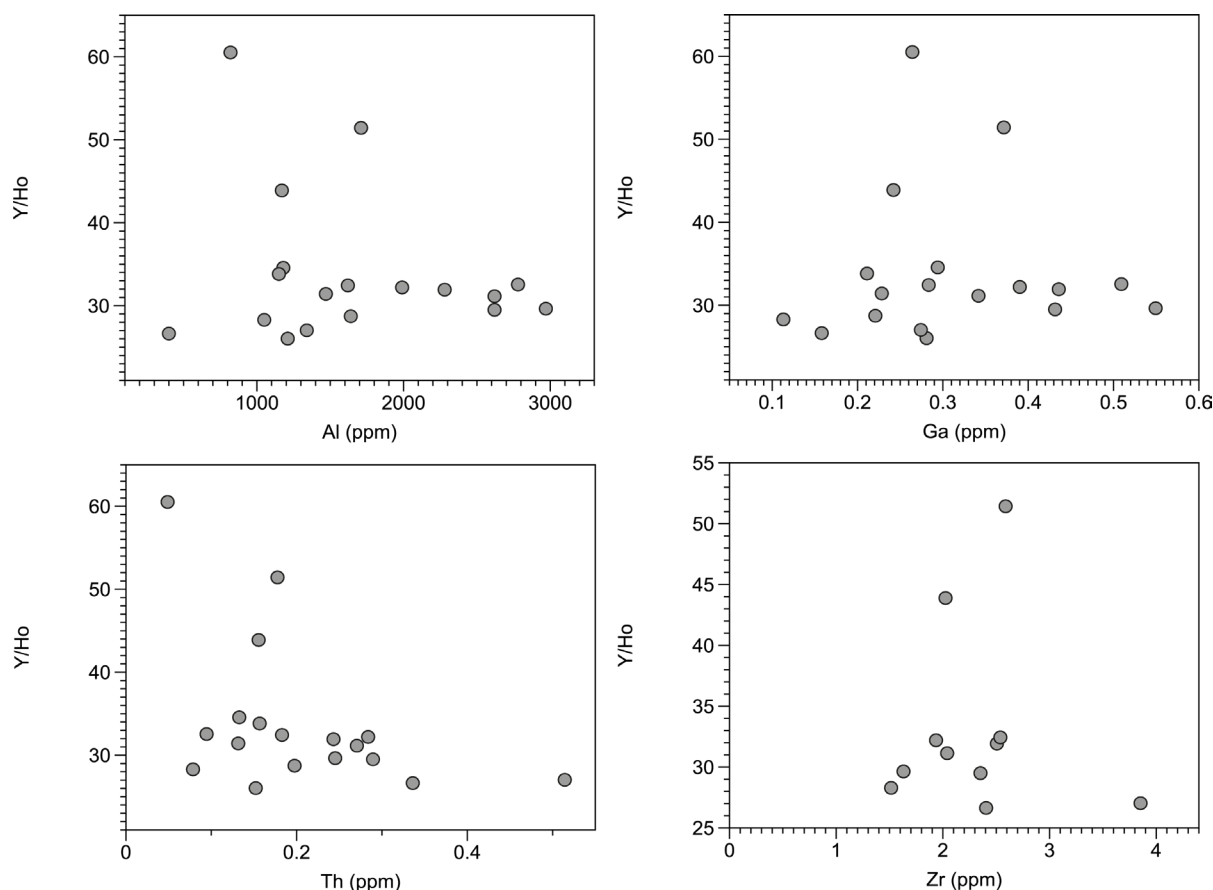


Figure 6.11: Relationship between Y/Ho and element concentrated in terrigenous minerals (Al, Ga, Th and Zr). Detection limits: Y= 0.02 ppm, Ho= 0.001 ppm, Ga= 0.02 ppm, Th=0.015 ppm, Zr= 1.50 ppm

5. Preliminary Conclusions

A complex post-depositional modification of Malmani stromatolites is documented by petrographic observations made in the two facies (FA1 and FA2) of the studied here section. These modifications include several episodes of dolomitization and silicification. However, primary sedimentary grains have been identified as a potential indicator for preservation of primary geochemical proxies. Despite their complete dolomitization, stromatolites and samples with ripple marks from the top of the section retain seawater major- and trace-elemental signatures, while silicified stromatolites or dolomitic stromatolites in the silicification area display REE patterns that were distributed by the hydrothermal circulation.

Pyrite grains were observed in those samples. Two generations of pyrite have been identified, including (1) large (up to 150 μm) euhedral pyrite grains affected by various degrees of oxidation, and (2) micrometric euhedral (10-30 μm) pyrite grains of sedimentary origin. Interestingly, S isotope compositions systematically vary between these two pyrite generations while their $\delta^{56}\text{Fe}$ values are indistinguishable. This suggests that Fe isotope signal was not impacted by post-depositional alteration due to the low Fe content of the late hydrothermal fluids. In order to assess preservation of primary Fe isotopes ratios, pyrite need to be measured in well-preserved stromatolites (courtesy of W. Altermann) from the less altered parts of the platform (see **Chapter 7**, Perspectives). Measurements of preserved samples will provide insights into the robustness of pyrite Fe isotope compositions and their susceptibility to high grade metamorphism and secondary fluid circulation.

6. Literature cited

- Allwood, A.C., Kamber, B.S., Walter, M.R., Burch, I.W., Kanik, I., 2010. Trace elements record depositional history of an Early Archean stromatolitic carbonate platform. *Chemical Geology* 270, 148–163. <https://doi.org/10.1016/j.chemgeo.2009.11.013>
- Altermann, W., Nelson, D.R., 1998. Sedimentation rates, basin analysis and regional correlations of three Neoproterozoic and Palaeoproterozoic sub-basins of the Kaapvaal craton as inferred from precise U–Pb zircon ages from volcanoclastic sediments. *Sedimentary Geology* 120, 225–256. [https://doi.org/10.1016/S0037-0738\(98\)00034-7](https://doi.org/10.1016/S0037-0738(98)00034-7)
- Anbar, A.D., Duan, Y., Lyons, T.W., Arnold, G.L., Kendall, B., Creaser, R.A., Kaufman, A.J., Gordon, G.W., Scott, C., Garvin, J., Buick, R., 2007. A Whiff of Oxygen Before the Great Oxidation Event? *Science* (1979) 317, 1903–1906. <https://doi.org/10.1126/science.1140325>
- Bajwah, Z.U., Seccombe, P.K., Offler, R., 1987. Trace element distribution, Co:Ni ratios and genesis of the big cadia iron-copper deposit, new south wales, australia. *Mineralium Deposita* 22. <https://doi.org/10.1007/BF00204522>
- Banner, Jay.L., 1995. Application of the trace element and isotope geochemistry of strontium to studies of carbonate diagenesis. *Sedimentology* 42, 805–824. <https://doi.org/10.1111/j.1365-3091.1995.tb00410.x>
- Bau, M., Dulski, P., 1999. Comparing yttrium and rare earths in hydrothermal fluids from the Mid-Atlantic Ridge: implications for Y and REE behaviour during near-vent mixing and for the Y/Ho ratio of Proterozoic seawater. *Chemical Geology* 155, 77–90. [https://doi.org/10.1016/S0009-2541\(98\)00142-9](https://doi.org/10.1016/S0009-2541(98)00142-9)
- Beukes, N.J., 1980. Stratigrafie en litofasies van die Campbellrand-subgroep van die Proterofitiese Ghaap-groep, noord-Kaapland. . *South African Journal of Geology* 83, 141–170.
- Beukes, N.J., 1987. Facies relations, depositional environments and diagenesis in a major early proterozoic stromatolitic carbonate platform to basinal sequence, campbellrand subgroup, transvaal supergroup, southern africa, *Sedimentary Geology*.
- Bolhar, R., Kamber, B.S., Moorbath, S., Fedo, C.M., Whitehouse, M.J., 2004. Characterisation of early Archean chemical sediments by trace element signatures. *Earth and Planetary Science Letters* 222, 43–60. <https://doi.org/10.1016/j.epsl.2004.02.016>
- Button, A., 1973. The stratigraphic history of the malmani dolomite in the eastern and north-eastern transvaal.
- Czaja, A.D., Johnson, C.M., Roden, E.E., Beard, B.L., Voegelin, A.R., Nägler, T.F., Beukes, N.J., Wille, M., 2012. Evidence for free oxygen in the Neoproterozoic ocean based on coupled iron–molybdenum isotope fractionation. *Geochimica et Cosmochimica Acta* 86, 118–137. <https://doi.org/10.1016/j.gca.2012.03.007>
- della Porta, G., Kenter, J.A.M., Bahamonde, J.R., 2004. Depositional facies and stratal geometry of an Upper Carboniferous prograding and aggrading high-relief carbonate platform (Cantabrian Mountains, N Spain). *Sedimentology* 51, 267–295. <https://doi.org/10.1046/j.1365-3091.2003.00621.x>
- Derry, L.A., Jacobsen, S.B., 1990. The chemical evolution of Precambrian seawater: Evidence from REEs in banded iron formations. *Geochimica et Cosmochimica Acta* 54, 2965–2977. [https://doi.org/10.1016/0016-7037\(90\)90114-Z](https://doi.org/10.1016/0016-7037(90)90114-Z)
- Ehrick, M., 1996. Sequence stratigraphy and platform evolution of Lower–Middle Devonian carbonates, eastern Great Basin. *Geological Society of America Bulletin* 108, 0392. [https://doi.org/10.1130/0016-7606\(1996\)108<0392:SSAPEO>2.3.CO;2](https://doi.org/10.1130/0016-7606(1996)108<0392:SSAPEO>2.3.CO;2)
- Eriksson, P.G., Altermann, W., 1998. An overview of the geology of the Transvaal Supergroup dolomites (South Africa), Cases and solutions *Environmental Geology*. Springer-Verlag.
- Eriksson, P.G., Schweitzer, J.K., Bosch, P.J.A., Schreiber, U.M., van Deventer, J.L., Hatton, C.J., 1993. The transvaal sequence: an overview. *Journal of African Earth Sciences (and the Middle East)* 16, 25–51. [https://doi.org/10.1016/0899-5362\(93\)90160-R](https://doi.org/10.1016/0899-5362(93)90160-R)
- Eroglu, S., Schoenberg, R., Wille, M., Beukes, N., Taubald, H., 2015. Geochemical stratigraphy, sedimentology, and Mo isotope systematics of the ca. 2.58–2.50 Ga-old Transvaal Supergroup carbonate platform, South Africa. *Precambrian Research* 266, 27–46. <https://doi.org/10.1016/j.precamres.2015.05.007>

org/10.1016/j.precamres.2015.04.014

Eroglu, S., van Zuilen, M.A., Taubald, H., Drost, K., Wille, M., Swanner, E.D., Beukes, N.J., Schoenberg, R., 2017. Depth-dependent $\delta^{13}\text{C}$ trends in platform and slope settings of the Campbellrand-Malmani carbonate platform and possible implications for Early Earth oxygenation. *Precambrian Research* 302, 122–139. <https://doi.org/10.1016/j.precamres.2017.09.018>

Eroglu, S., Schoenberg, R., Pascarelli, S., Beukes, N.J., Kleinhanns, I.C., Swanner, E.D., 2018. Open ocean vs. continentally-derived iron cycles along the neoproterozoic Campbellrand-malmani carbonate platform, South Africa. *American Journal of Science* 318, 367–408. <https://doi.org/10.2475/04.2018.01>

Farquhar, J., Cliff, J., Zerkle, A.L., Kamysny, A., Poulton, S.W., Claire, M., Adams, D., Harms, B., 2013. Pathways for Neoproterozoic pyrite formation constrained by mass-independent sulfur isotopes. *Proceedings of the National Academy of Sciences* 110, 17638–17643. <https://doi.org/10.1073/pnas.1218851110>

Fischer, W.W., Fike, D.A., Johnson, J.E., Raub, T.D., Guan, Y., Kirschvink, J.L., Eiler, J.M., 2014. SQUID-SIMS is a useful approach to uncover primary signals in the Archean sulfur cycle. *Proceedings of the National Academy of Sciences* 111, 5468–5473. <https://doi.org/10.1073/pnas.1322577111>

Flügel, E., 2004. Microfacies Data: Fabrics, in: *Microfacies of Carbonate Rocks*. Springer Berlin Heidelberg, Berlin, Heidelberg, pp. 177–242. https://doi.org/10.1007/978-3-662-08726-8_5

Godfrey, L. v., Falkowski, P.G., 2009. The cycling and redox state of nitrogen in the Archean ocean. *Nature Geoscience* 2, 725–729. <https://doi.org/10.1038/ngeo633>

Gounelle, A., 2021. Caractérisation minéralogique et géochimique des stromatolites de la plateforme de Malmani (Afrique du Sud, 2.5 Ga). Master dissertation, ENS Lyon.

Gregory, D.D., Large, R.R., Halpin, J.A., Baturina, E.L., Lyons, T.W., Wu, S., Danyushevsky, L., Sack, P.J., Chappaz, A., Maslennikov, V. v., Bull, S.W., 2015. Trace Element Content of Sedimentary Pyrite in Black Shales. *Economic Geology* 110, 1389–1410. <https://doi.org/10.2113/econgeo.110.6.1389>

Grotzinger, J.P., Knoll, A.H., 1999. Stromatolites in Precambrian carbonates: Evolutionary Mileposts or Environmental Dipsticks? *Annual Review of Earth and Planetary Sciences* 27, 313–358. <https://doi.org/10.1146/annurev.earth.27.1.313>

Holland, H.D., Lazar, B., McCaffrey, M., 1986. Evolution of the atmosphere and oceans. *Nature* 320, 27–33. <https://doi.org/10.1038/320027a0>

Kamber, B.S., Webb, G.E., 2001. The geochemistry of late Archean microbial carbonate: implications for ocean chemistry and continental erosion history. *Geochimica et Cosmochimica Acta* 65, 2509–2525. [https://doi.org/10.1016/S0016-7037\(01\)00613-5](https://doi.org/10.1016/S0016-7037(01)00613-5)

Kamber, B.S., Whitehouse, M.J., 2007. Micro-scale sulphur isotope evidence for sulphur cycling in the late Archean shallow ocean. *Geobiology* 5, 5–17. <https://doi.org/10.1111/j.1472-4669.2006.00091.x>

Kendall, B., Reinhard, C.T., Lyons, T.W., Kaufman, A.J., Poulton, S.W., Anbar, A.D., 2010. Pervasive oxygenation along late Archean ocean margins. *Nature Geoscience* 3, 647–652. <https://doi.org/10.1038/ngeo942>

Kiyosu, Y., 1980. Chemical reduction and sulfur-isotope effects of sulfate by organic matter under hydrothermal conditions. *Chemical Geology* 30, 47–56. [https://doi.org/10.1016/0009-2541\(80\)90115-1](https://doi.org/10.1016/0009-2541(80)90115-1)

Knauth, L.P., 1979. A model for the origin of chert in limestone. *Geology* 7, 274. [https://doi.org/10.1130/0091-7613\(1979\)7<274:AMFTOO>2.0.CO;2](https://doi.org/10.1130/0091-7613(1979)7<274:AMFTOO>2.0.CO;2)

Knoll, A.H., Beukes, N.J., 2009. Introduction: Initial investigations of a Neoproterozoic shelf margin-basin transition (Transvaal Supergroup, South Africa). *Precambrian Research* 169, 1–14. <https://doi.org/10.1016/j.precamres.2008.10.009>

Kouketsu, Y., Nishiyama, T., Ikeda, T., Enami, M., 2014. Evaluation of residual pressure in an inclusion-host system using negative

frequency shift of quartz Raman spectra. *American Mineralogist* 99, 433–442. <https://doi.org/10.2138/am.2014.4427>

Kretz, R., 1982. A model for the distribution of trace elements between calcite and dolomite. *Geochimica et Cosmochimica Acta* 46, 1979–1981. [https://doi.org/10.1016/0016-7037\(82\)90137-5](https://doi.org/10.1016/0016-7037(82)90137-5)

Kurzweil, F., Wille, M., Gantert, N., Beukes, N.J., Schoenberg, R., 2016. Manganese oxide shuttling in pre-GOE oceans – evidence from molybdenum and iron isotopes. *Earth and Planetary Science Letters* 452, 69–78. <https://doi.org/10.1016/j.epsl.2016.07.013>

Lawnizack, G., 2022. Étude des stromatolithes archéens (Malmani Subgroup, Afrique du Sud, 2,58–2,5 Ga) : caractérisation pétrographique et processus post-dépôt. Master dissertation, Université de Dijon.

Lawrence, M. G., Greig, A., Collerson, K. D., & Kamber, B. S., 2006. Rare earth element and yttrium variability in South East Queensland waterways. *Aquatic Geochemistry*, 12(1), 39–72. <https://doi.org/10.1007/s10498-005-4471-8>

Machel, H.G., 2004. Concepts and models of dolomitization: a critical reappraisal. Geological Society, London, Special Publications 235, 7–63. <https://doi.org/10.1144/GSL.SP.2004.235.01.02>

Maier, W.D., Barnes, S.-J., 1998. Concentrations of rare earth elements in silicate rocks of the Lower, Critical and Main Zones of the Bushveld Complex. *Chemical Geology* 150, 85–103. [https://doi.org/10.1016/S0009-2541\(98\)00054-0](https://doi.org/10.1016/S0009-2541(98)00054-0)

McIntyre, T., Fralick, P., 2017. Sedimentology and geochemistry of the 2930 Ma Red Lake–Wallace Lake carbonate platform, Western Superior Province, Canada. *the Depositional Record* 3, 258–287.

Michard, A., 1989. Rare earth element systematics in hydrothermal fluids. *Geochimica et Cosmochimica Acta* 53, 745–750. [https://doi.org/10.1016/0016-7037\(89\)90017-3](https://doi.org/10.1016/0016-7037(89)90017-3)

Miyano, T., Beukes, N. J., 1984. Phase relations of stilpnomelane, ferri-annite, and riebeckite in very low-grade metamorphosed iron formations. *Transactions of the Geological Society of South Africa* 87, 111–124.

Nell, J., 1985. The Bushveld metamorphic aureole in the Potgietersrus area; evidence for a two-stage metamorphic event. *Economic Geology*, 80(4), 1129–1152. <https://doi.org/10.2113/gsecongeo.80.4.1129>

Ono, S., Kaufman, A.J., Farquhar, J., Sumner, D.Y., Beukes, N.J., 2009. Lithofacies control on multiple-sulfur isotope records and Neoproterozoic sulfur cycles. *Precambrian Research* 169, 58–67. <https://doi.org/10.1016/j.precamres.2008.10.013>

Severmann, S., Lyons, T.W., Anbar, A., McManus, J., Gordon, G., 2008. Modern iron isotope perspective on the benthic iron shuttle and the redox evolution of ancient oceans. *Geology* 36, 487–490. <https://doi.org/10.1130/G24670A.1>

Simms, 1984. Dolomitization by groundwater-flow system in carbonate platforms.

Sumner, D.Y., 1996. Facies, paleogeography, and carbonate precipitation on the Archean (2520 Ma) Campbellrand-Malmani carbonate platform, Transvaal supergroup, South Africa.

Sumner, D.Y., Bowring, S.A., 1996. U-Pb geochronologic constraints on deposition of the Campbellrand Subgroup, Transvaal Supergroup, South Africa. *Precambrian Research* 79, 25–35. [https://doi.org/10.1016/0301-9268\(95\)00086-0](https://doi.org/10.1016/0301-9268(95)00086-0)

Sumner, D.Y., Grotzinger, J.P., 2004. Implications for Neoproterozoic ocean chemistry from primary carbonate mineralogy of the Campbellrand-Malmani Platform, South Africa. *Sedimentology* 51, 1273–1299. <https://doi.org/10.1111/j.1365-3091.2004.00670.x>

Sumner, D.Y., Beukes, N.J., 2006. Sequence Stratigraphic Development of the Neoproterozoic Transvaal carbonate platform, Kaapvaal Craton, South Africa. *South African Journal of Geology* 109, 11–22. <https://doi.org/10.2113/gssajg.109.1-2.11>

Taylor, S. R. and McLennan S. M., 1985. *The Continental Crust: Its Composition and Evolution*. Blackwell, Oxford, 312p

Tostevin, R., Shields, G. A., Tarbuck, G. M., He, T., Clarkson, M. O., & Wood, R. A., 2016. Effective use of cerium anomalies as a redox proxy in carbonate-dominated marine settings. *Chemical Geology*, 438, 146–162. <https://doi.org/10.1016/j.chemgeo.2016.06.027>

Truswell, J.F., Eriksson, K.A., 1975. A palaeoenvironmental interpretation of the Early Proterozoic Malmani dolomite from Zwartkops, South Africa. *Precambrian Research* 2, 277–303. [https://doi.org/10.1016/0301-9268\(75\)90013-3](https://doi.org/10.1016/0301-9268(75)90013-3)

Tyler, R., Tyler, N., 1996. Prerumbrinn Reseurth Stratigraphic and structural controls on gold mineralization in the Pilgrim's Rest goldfield, eastern Transvaal, South Africa, Precambrian Research.

Veizer, J., Hoefs, J., Lowe, D.R., Thurston, P.C., 1989. Geochemistry of Precambrian carbonates: II. Archean greenstone belts and Archean sea water. *Geochimica et Cosmochimica Acta* 53, 859–871. [https://doi.org/10.1016/0016-7037\(89\)90031-8](https://doi.org/10.1016/0016-7037(89)90031-8)

Watanabe, Y., Farquhar, J., Ohmoto, H., 2009. Anomalous Fractionations of Sulfur Isotopes During Thermochemical Sulfate Reduction. *Science* (1979) 324, 370–373. <https://doi.org/10.1126/science.1169289>

Wille, M., Kramers, J.D., Nägler, T.F., Beukes, N.J., Schröder, S., Meisel, Th., Lacassie, J.P., Voegelin, A.R., 2007. Evidence for a gradual rise of oxygen between 2.6 and 2.5Ga from Mo isotopes and Re-PGE signatures in shales. *Geochimica et Cosmochimica Acta* 71, 2417–2435. <https://doi.org/10.1016/j.gca.2007.02.019>

CHAPTER 7.

GENERAL DISCUSSION AND PERSPECTIVES

This chapter outlines the main findings and future perspectives of this thesis work. I studied sedimentary rocks of various ages, some of them from the emblematic Pilbara (Australia) and Kaapvaal (South Africa) Archean cratons, with two initial main goals: (1) determine if Fe isotope signatures are diagnostic for microbial activity, and (2) assess the influence of global oceanic redox changes on Earth. For that, I studied microbial deposits, from periods characterized by contrasting redox conditions. However, because most of my targets have experienced diagenesis and sometimes metamorphism (**Fig. 1**), the first important challenge to overcome was to identify all secondary phases in order to understand the influence of post-depositional processes (**Chapter 7, section 1**). Then, I had to deconvolve the post-depositional history to identify which phases were primary (**Chapter 7, section 2**). The second challenge was to interpret the Fe isotope compositions from these primary pyrite grains (**Chapter 7, section 3**). From this, one main question emerged: does this composition reflect only local environmental processes or is it possible to extract a more global signal from the water column? Two local processes were identified as controlling the pyrite Fe isotope compositions in microbialites: (1) the depositional environment, which is detailed in **section 3.1** and (2) microbial activities, addressed in **section 3.2**. One main result of this thesis is to be cautious when using microbialite pyrite as a proxy for global redox changes (**Chapter 7, section 4**). The final perspective section of this chapter details three possible works I would like to address. They include:

(1) A potential project of analytical development in order to assess the variability of pyrite $<3 \mu\text{m}$ in size.

(2) A project dedicated to the search for a primary signal (biological or not) in Archean sedimentary rocks which record a gradient in their post-depositional history. This work will be conducted on additional samples from the Malmani-Campbellrand platform (collected in the west and east part of the platform).

(3) A possible research question to investigate would aim to determine the influence of methanotrophy on pyrite grain formation and their associated Fe isotope signatures.

1. Importance of post depositional processes

The first important point to discuss is the influence of secondary alteration and metamorphism on the samples I studied, from a petrographic and geochemical point of view. There is a gradient in the magnitude of post-depositional processes between all targets analyzed during this thesis (**Fig. 7.1**). Samples perfectly preserved from secondary processes, experiencing no more than first stages of early diagenesis, are the modern microbialites from the Cayo Coco Lagoon and Atexcac lake (**Chapter 3**). Early Triassic samples (**Chapter 4**) illustrate early diagenetic processes characterized by the precipitation of sparitic (calcite and dolomite) cements filling space between the different sedimentary grains. Early diagenetic processes marked by the presence of sparitic cements are also identified in fenestrae of some stromatolites from the 2.7 Ga Tumbiana Formation (**Chapter 5**). These Tumbiana stromatolites are imprinted by a low-grade metamorphism in the green schist facies (< 300°C). Those samples are affected by post-depositional silicification, illustrated by the presence of microcrystalline quartz cement (*Lepot et al., 2008; Decraene et al., 2021*). This silicification is not well time-constrained but likely occurred early in the post-depositional history of geological formations. Several episodes (at least two identified) of secondary silification were also recorded in Malmani stromatolites (**Chapter 6**). Malmani stromatolites have undergone the highest temperatures recorded in this study, with a temperature of 400 °C at peak metamorphism. Those samples illustrate a complex post-depositional history, with multiple generations of quartz and dolomitic cements. Moreover, the studied Malmani samples have very low concentrations of pyrite and carbonaceous material in contrast to the Tumbiana stromatolite. This can be attributed to secondary leaching, a process which tends to dissolve and/or oxidize primary pyrite grains (*Bierens de Haan, 1991*). Pyrite leaching is further supported in the Malmani samples by the presence of former pyrite grains partially or completely oxidized.

Nonetheless, pyrite is present despite the intensity of post-depositional processes, in varying proportions. I was able to distinguish secondary pyrite formed as a result of late fluid circulation. These latter formed large (thousands of μm) and euhedral pyrite grains, which can be distinguished from sedimentary pyrite through their trace element composition, i.e. Co:Ni ratios. For example, in the Malmani samples, large euhedral pyrite grains (samples MA37 and MA39) revealed high Co:Ni ratios typical of hydrothermal pyrite (*Bajwah et al., 1987*). Moreover, those hydrothermal pyrite grains are associated with narrow ranges of S isotope compositions and $\delta^{34}\text{S}$ values close to 0‰. The preservation of positive S-MIF suggests that late fluid circulation led to the dissolution and recrystallisation of original (sedimentary) pyrite grains (*Ono et al., 2009*).

The effect of late fluid circulation can be also assessed on Fe isotope compositions. Knowing that the $\delta^{56}\text{Fe}$ values of hydrothermal fluids vary from ~ -0.5 to 0‰ (*Dauphas and Rouxel, 2006*) and the equilibrium fractionation factor at 350°C between pyrite and dissolved Fe(II) is +0.99‰ (*Syverson et al., 2013*), the resulting pyrite is characterized by $\delta^{56}\text{Fe}$ values between +0.5 to +1‰. This theoretical range is largely encompassed by Fe isotope ranges ($\delta^{56}\text{Fe}$

from -0.9 to +3.5‰) measured in the hydrothermal pyrite from Malmani samples, meaning that pyrite recrystallization likely occurred with a fluid characterized by a low iron concentration. This suggests that Fe isotope compositions can be resistant to metamorphism, as previously suggested in the literature (Dauphas *et al.*, 2007; Frost *et al.*, 2007; Marin-Carbonne *et al.*, 2020). Although post-depositional processes tend to recrystallize primary mineral phases and homogenize isotope signatures (Large *et al.*, 2009; Marin-Carbonne *et al.*, 2020), it has been demonstrated that some cements, in particular quartz cement formed during early diagenesis, can enhance the preservation of molecular signatures in organic material and pyrite isotope variability (e.g. Wacey *et al.*, 2013; Alleon *et al.*, 2016). Therefore, Fe isotope composition of pyrite can still preserve signatures of primary sedimentary processes, including microbial

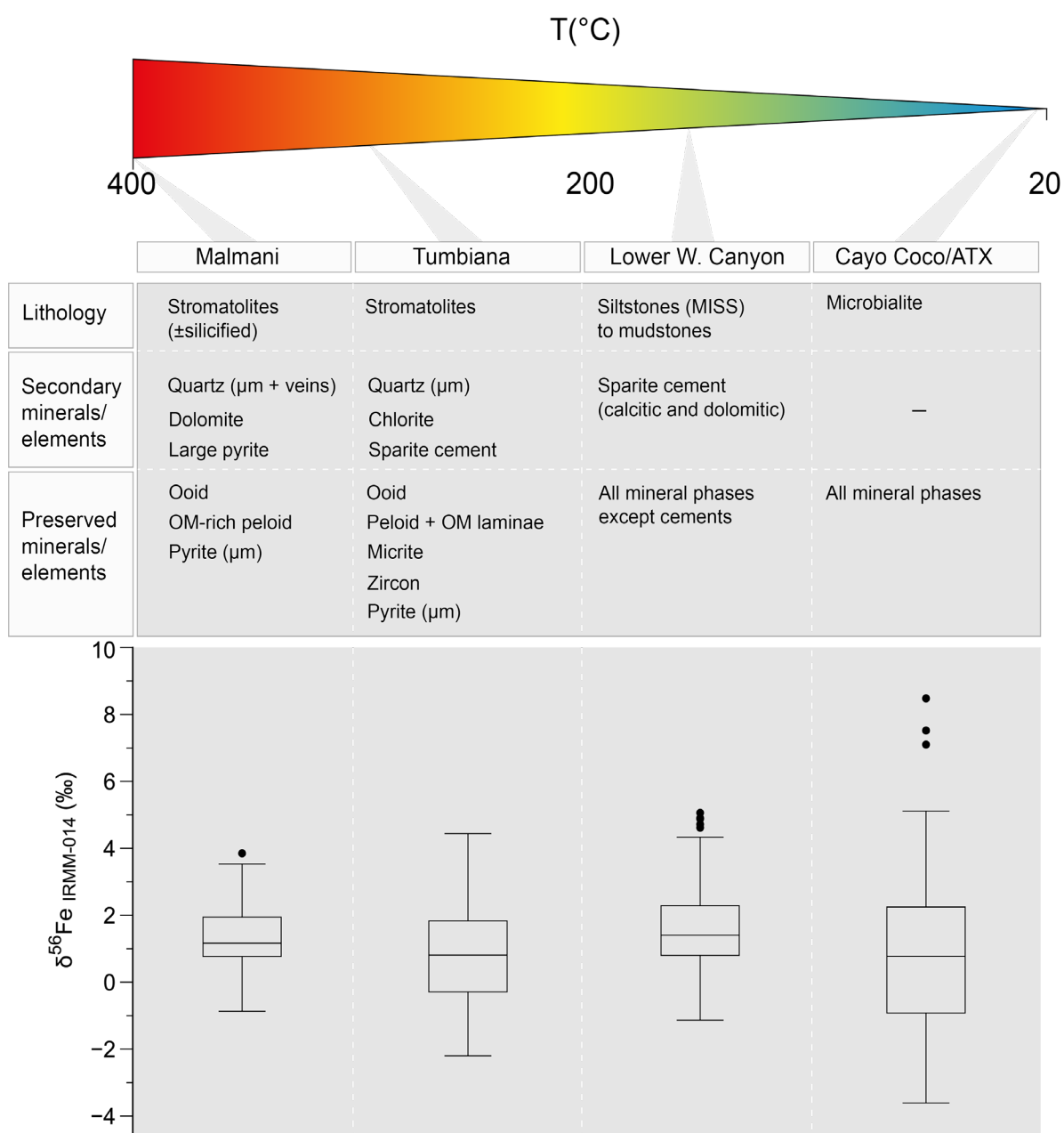


Figure 7. 1: Synthesis of secondary and primary mineral phases observed in all studied samples as a function of the maximum temperature peak they have experience, and comparison of their Fe isotope ranges.

activities (cf. **section 3.2**). A decrease of the extent of Fe isotope range is however noted when the metamorphic grade increases (**Fig. 7.1**). The influence of metamorphism on pyrite Fe and S isotope compositions will be quantitatively assessed through a comparative study between samples from the western and the eastern part of the platform where an increasing metamorphic gradient is documented (cf. **section Perspectives**).

2. Beyond the post-depositional history: identification of primary elements and mineral phases

Over more than 2 Ga of (more or less complicated) post-depositional history, it is quite justified to wonder what has been preserved in all the samples studied. First, it is worth mentioning that the laminated structure of stromatolites is still preserved even at microscopic scale in both Tumbiana and Malmani samples. Modern samples (**Chapter 3**) only show primary (syngenetic to the microbialite formation) phases or grains, including bioclasts, carbonates, kerolite and pyrite. In comparison, early diagenetic samples from the Early Triassic (**Chapter 4**) also preserve primary mineral phases (micrite, phyllosilicates, pyrite of various morphologies, zircons) and grains (including quartz and bioclasts) distributed in a range of facies associations. The identification of primary mineral phases can be more challenging when looking at metamorphic sedimentary rocks. In the Tumbiana stromatolites (maximum peak temperature $\sim 300^{\circ}\text{C}$), chlorite attests the presence of former clays. Micrite is still preserved, as well as a few grains of zircons, peloids and ooids in specific lamina types (cf. **Chapter 5**). Although pyrite of hundreds of μm in size were reported and measured in the Tumbiana stromatolites (*Nishizawa et al., 2010; Yoshiya et al., 2012; Williford et al., 2016*), only one pyrite generation was identified in the different samples measured during this study, all micrometric in size ($<10 \mu\text{m}$) and intimately associated with carbonaceous material (CM; *Thomazo et al., 2009; Marin-Carbonne et al., 2018*). Previous studies identified preserved organic compounds, as well as aragonite crystals associated to CM (*Lepot et al., 2009, 2019*). All of them demonstrate that CM can be a pristine compound. Additionally, CM-associated pyrite may also preserve syndimentary information. The identification of primary phases is more difficult in the Malmani Subgroup compared to the Campbellrand Subgroup samples where fanning aragonite pseudomorphs and ooid grainstones are well preserved (*Sumner, 1996; Sumner and Grotzinger, 2004*). Despite a total dolomitization and partial silicification, Malmani samples still preserved rare ooids and numerous organic-rich peloids that can be interpreted as reworked biofilms (*Lawnizack, 2022*). Moreover, these samples contain micrometric pyrite grains of $\sim 10\text{-}20 \mu\text{m}$ that strongly differ in size and morphology from the hydrothermal pyrite discussed in **section 1**. The trace element analyses of those micrometric pyrite grains revealed Co:Ni below 2, consistent with a sedimentary origin (*Bajwah et al., 1987*). Therefore, these Malmani pyrite grains appear to be good candidates to track a primary geochemical signal, similarly to those identified in the Tumbiana stromatolites. Once the primary phases are identified, particularly pyrite (for the sake of Fe isotopes), it is possible to focus the

analytical work on them and interpret the isotope compositions of these pyrite grains in light of their formation processes within the microbialites.

3. Environmental control on pyrite formation

Spatially resolved analyses of Fe isotopes, sometimes combined with bulk rock or in situ S isotope measurements, revealed that environmental parameter changes control the formation and isotope signatures of pyrite by changing the connectivity between the porewaters and the overlying water column (Thomazo *et al.*, 2019; Pasquier *et al.*, 2021a). Environmental parameters include changes of the eustatic level, sedimentation rate, sediment reworking (bioturbation, waves, storms, fluid escape), and the reactivity of organic matter that modulate microbial reduction rates among others (reviewed in Fike *et al.*, 2015). Here, “environmental” refers to physical, chemical and biological interactions affecting an area (Foucault and Raoult, 1980). This section details two environmental parameters, the depositional environment and microbial activities, controlling pyrite Fe and/or S isotope compositions.

3.1. Influence of depositional settings

At the scale of a carbonate platform, the depositional setting strongly influences the nature of the sediment. The study focusing on the Early Triassic sediments (Lower Weber Canyon, Sonoma Foreland Basin, USA) highlights a clear influence of the sample position along a ramp system on the pyrite Fe isotope compositions (**Chapter 4**). The latter were mostly identified using bulk S isotope compositions (also with Fe isotopes but in a less explicit way). Indeed, the inner ramp S isotope signatures show a negative average value along with much less variable $\delta^{56}\text{Fe}$ values than samples located on the middle and outer ramp settings. Therefore, Fe and S isotope compositions measured in the inner ramp samples (except MISS discussed below) were interpreted as reflecting open sediment conditions, through sediment remobilization, in which porewater iron and sulfate concentrations are buffered by the water column. In contrast, samples from the mid and outer ramp systems show a progressive isotope enrichment in both ^{34}S and ^{56}Fe with a wider Fe isotope range. In these more distal and deeper settings, Fe and S isotope compositions reflect a more ‘closed’ system conditions with respect to Fe-oxides and sulfate, meaning that exchanges with the water column are limited. Therefore, by varying the degree of sediment reworking by tidal current, fair weather or storm waves and/or even bioturbation, it is the environmental conditions that create open or closed system conditions (Aller *et al.*, 2008; Fike *et al.*, 2015).

If sediment reworking has been shown to highly influence the isotope compositions of pyrite (**Chapter 4**; Fike *et al.*, 2015; Thomazo *et al.*, 2019), other environmental parameters do not. For

example, in the Tumbiana stromatolites (**Chapter 5** or *Decraene et al., 2021*), different lamina types were identified and are likely to reflect different environmental conditions, such as variations of terrigenous fluxes that can influence turbidity and mineralization within a biofilm. However, such environmental change does not appear to strongly influence pyrite Fe isotope signals which are comparable between each type of laminae identified in the Tumbiana stromatolite. This can also suggest that variations of turbidity or nutrient input by sediment discharge did not result in drastic microbial community changes, or at least have not disturbed microorganisms involved in pyrite formation (MSR, AOM and DIR; *Thomazo et al., 2009; Marin-Carbonne et al., 2018; Decraene et al., 2021*).

3.2. Influence of microbial activities

This leads us to the final part of this discussion: the influence of microorganisms, gathered in a biofilm, a mat or even in sediments, on the pyrite isotope signals. This section refers more specifically to the influence of sulfate reducers and photosynthetic organisms on pyrite formation and how they influence the Fe isotope compositions of pyrite. While it is demonstrated that MSR controls the sulfur cycle, and thus the formation of pyrites in modern sediments (*Jørgensen and Kasten, 2006*), it is less clear for Archean environments. The activity of various microorganisms has been evidenced, for example, in the 2.7 Ga Tumbiana stromatolites (MSR, AOM coupled to sulfate and Fe-oxide reduction, N fixation; *Hayes, 1994; Hinrichs, 2002; Thomazo et al., 2009, 2011; Marin-Carbonne et al., 2018; Lepot et al., 2019*) or in the 2.5 Ga Malmani stromatolites (e.g. oxygenic photosynthesis, MSR suggested; *Kendall et al., 2010; Farquhar et al., 2013; Fischer et al., 2014*). Based on the Malmani stromatolite results, microbial activity can be supported by the S isotope compositions measured in pyrite from sample AmalC4 (**Chapter 6**), where the wide range of $\delta^{34}\text{S}$ (from -24.52 to +6.43‰) and the positive $\Delta^{33}\text{S}$ can either reflect microbial disproportionation (reduction of elemental sulfur by microorganisms; *Philippot et al., 2007*) or MSR using sulfate with positive $\Delta^{33}\text{S}$ signatures (*Paris et al., 2020*). Nonetheless, even if S isotope measurements were performed on pyrite grains of sedimentary origin, this S isotope range can reflect inorganic sulfate reduction (thermochemical sulfate reduction, TSR) during diagenesis or late fluid circulation (*Kiyosu, 1980; Watanabe et al., 2009*; cf. **section 1**). The origin of S isotope ranges will be investigated in the near future (cf. **section Perspectives**).

In this thesis, I demonstrated that Fe isotope signatures reflect Fe-oxide reduction through the geological record, a result also confirmed by the compilation of in situ $\delta^{56}\text{Fe}$ pyrite during the Archean and Paleoproterozoic (*Dupeyron et al., submitted at EPSL, cf. Appendix 2*). However, the origin of the Fe-oxides reduction can be more or less difficult to identify. For example, the measurement of highly negative $\delta^{56}\text{Fe}$ values ($< 3.5\text{‰}$) allowed to identify DIR as the main driver for complete Fe(III)-oxide reduction in Cayo Coco microbialites (**Chapter 3**). In contrast, Fe-oxide reduction can also occur in several steps including intense redox cycling (multiple steps of partial reduction and oxidation). This intensive redox cycling is suggested to drive the Fe isotope signatures in the Tumbiana stromatolites

(Decraene *et al.*, 2021) and MISS from LWC (Early Triassic samples, **Chapter 4**, Decraene *et al.* submitted at *Palaeogeography, Palaeoclimatology, Palaeoecology*). Fe(III)-oxide reduction can be mediated by H₂S deriving from MSR (evidenced in LWC samples and possibly in Tumbiana samples), DIR (possible but not properly evidenced) and AOM coupled to Fe-oxides (evidenced in Tumbiana but not investigated in LWC). Iron oxidation can be mediated in a biofilm or a mat through the activity of oxygenic and anoxygenic photosynthetic organisms (putative presence of oxygenic photosynthesis in Tumbiana). Such redox cycling can be referred as a cryptic Fe cycle (Teske, 2010; Berg *et al.*, 2016), where the biofilm or mat functions as a closed system dominated by microbial redox reactions leading to an important turnover of Fe species (Hansel *et al.*, 2015; Berg *et al.*, 2019). The regime of Fe-oxide reduction, i.e. complete or partial, is dependent of many parameters. If Fe-oxide reduction is controlled by DIR or MSR, the difference of regime can be due to the reactivity of Fe-oxides, the availability of H₂S or the quantity of organic matter. For example, OM appears to be more abundant in Cayo Coco (>1 wt.%), where Fe isotope compositions point to a complete reduction of Fe-oxides, than in LWC (average TOC ~0.1 wt.%). However, in LWC, pyrite $\delta^{56}\text{Fe}$ values in siltstones (except MISS) are also attributed to a complete reduction of Fe-oxides. This may indicate that (1) Fe-oxide reduction is not only dependent on the quantity of organic matter, and/or (2) the quantity of OM measured in a rock is not necessarily representative of initial conditions (i.e. sediment deposition), as it may have been consumed by microorganisms or secondarily altered. This illustrates the importance of coupling Fe with C (Craddock and Dauphas, 2011) and S (Archer and Vance, 2006) isotope systems to decipher processes leading to pyrite formation.

DIR occurrence in Tumbiana and Lower Weber Canyon?

As mentioned above, the occurrence of DIR is suggested but not properly evidenced. Indeed, the lowest $\delta^{56}\text{Fe}$ value of ~-2‰ measured in both Tumbiana and LWC is not diagnostic for DIR. This can be interpreted as (1) a lack of data, even though DIR was operating or (2) inhibition of microbial Fe reduction by microbial sulfate reduction. Under closed system conditions, the $\delta^{56}\text{Fe}$ - $\delta^{34}\text{S}$ correlation can be the result of coupled DIR and MSR in the sediment porewaters, as previously suggested in the Archean sedimentary record (Archer and Vance, 2006). Although not excluded, the absence of negative values as low as -3‰ do not provide any evidence about the simultaneous occurrence of these two metabolisms. Alternatively, this correlation can reflect the reductive dissolution of Fe(III)-oxides by H₂S. In this case, the reduction of Fe(III)-oxide is fully dependent of the availability of H₂S produced by MSR, i.e. directly link to sulfate reduction rate.

In Malmani stromatolites, the preservation of less extended but still large Fe isotope range and positive mean $\delta^{56}\text{Fe}$ values is fully compatible with a microbially-mediated reduction of Fe-oxide. However, the pristine origin of these signatures should be first assessed by the comparison with pyrite Fe isotope ranges from less altered samples (cf. **section Perspectives**).

4. Closing words: pyrite and global redox changes

The most important point emerging from this thesis is the systematic measurement of very large Fe isotope range in samples from different locations. Such large ranges recognized over geological time clearly indicate that pyrite Fe isotope compositions in microbialites or shallow sediments do not reflect global iron reservoir effects but rather reflect local processes. This suggests that pyrite Fe isotope compositions from various microbialites developed at different geological times and under an evolving oxygenation state is not likely to be a good geochemical proxy for our documentation and understanding of major changes in Earth atmosphere and/or oceanic redox changes. It does not mean that pyrite never records the water column chemistry but rather that local sedimentary parameters (sediment reworking, microbial cycling) acting in shallow environments can dominate pyrite Fe and S isotope compositions. This thesis work demonstrates that, after subtracting the effect of post-depositional processes, it is essential to consider the depositional environment in which the sediments formed (*Fike et al., 2015; Pasquier et al., 2021a*) and the nature of the deposit (i.e. the type of facies).

5. Perspectives

From all the results obtained during my PhD, many ideas for potential future works emerged. Some of them are briefly described earlier in the thesis (**Chapter 3**). Here are the three main perspectives that will be interesting to explore further.

5.1. Development of analytical protocol for nanoscale measurements of Fe isotopes

The analytical protocol for microscale Fe isotope compositions by SIMS developed during this thesis allowed to evidence the largest Fe isotope range in micrometric pyrite. However, such analyses are not trivial. They require a good spotting of pyrite grains before analysis and a lot of patience. Unfortunately, some grains are not thick enough to sustain the primary beam, which is too abrasive ($3\ \mu\text{m}$ depth over a $7'$ analysis). One possibility to overcome this issue is to apply a raster $5 \times 5\ \mu\text{m}$, which will result in a dilution of the primary beam by scanning a $5\ \mu\text{m}^2$ area. This is only possible for pyrite grains included in a matrix devoid of iron. The other possibility is to develop Fe isotope analyses by NanoSIMS. Fe isotope measurements by NanoSIMS are not yet performed because of the difficulty to reach high precision compared to the order of magnitude of Fe isotope fractionations. Such analytical development would bring to light the isotope variability enclosed in pyrite smaller than $3\ \mu\text{m}$ in size, such as the euhedral micropyrrite grains from the modern Cayo Coco microbialite.

5.2. Searching for a primary signal in sedimentary rocks recording a metamorphic gradient

The identification of preserved isotope signatures in pyrite is always challenging in Precambrian sedimentary rocks. This is even more true when these rocks have undergone metamorphic events. At the scale of a carbonate platform that records a gradient of post-depositional processes, it is however possible to target samples affected by various degrees of secondary alteration (e.g. various intensity of silicification). The comparison between well-preserved and altered samples is then useful to (1) assess the effect of temperature on isotope signatures and (2) attempt to extract a primary signal in better preserved samples of the platform. Such comparison will be addressed in a near future by studying samples from the Malmani-Campbellrand carbonate platform which is characterized by an east-west metamorphic gradient (*Button, 1973; Martini, 1976; Clay, 1986*). This carbonate platform developed in several episodes of flooding of the Kaapvaal craton, from a steep margin at the beginning to a rimmed platform with sedimentation rates that have reached 150 m/Ma (*Altermann and Nelson, 1998; Sumner and Beukes, 2006*). Facies variations are documented through the platform, from peritidal stromatolites deposited in the eastern part to basinal shales in the western part (**Fig. 7.2; Beukes, 1987; Knoll and Beukes, 2009**). The preliminary results exposed in **chapter 6** are from the most heated samples ($\sim 400^{\circ}\text{C}$) located in the eastern part of the platform. From these samples, I have evidenced two pyrite generations, one sedimentary and one hydrothermal. While $\delta^{34}\text{S}$ values are highly distinctive, $\delta^{56}\text{Fe}$ values are similar between these two generations. These can be interpreted as late fluid circulation bearing juvenile S isotope compositions, without modifying the Fe isotope signatures. In order to confirm the originality of $\delta^{56}\text{Fe}$ values, new isotope analyses will be conducted in pyrite from stromatolite samples of the west part of the platform which have only experienced low-grade metamorphism in the green-schist facies (i.e. $\sim 300^{\circ}\text{C}$; **Fig. 7.2; Button, 1973**). Measurements of such samples will give insights on the robustness of pyrite Fe and S isotope compositions under variable degree of metamorphism and secondary, early and late, fluid circulation. The interpretation of S isotope compositions can also be facilitated by the acquisition of $\Delta^{36}\text{S}$ signatures to discriminate between microbial versus abiotic (TSR) processes that led to pyrite formation. Moreover, REE spectra obtained in silicified samples from the log suggest a hydrothermal origin of the silicification. This result highly contrasts with a previous study which suggests a sedimentary origin of the microquartz (*Eroglu et al., 2015*). Therefore, the origin of the microquartz cement will be explored through spatially resolved analyses of Si and O isotopes to determine if REE signatures in chert are pristine or if they were reset because of late fluid circulation (*Marin-Carbonne et al., 2012, 2013; Bonnand et al., 2020*).

Samples from the top of the log (**Chapter 6**) have a relatively low concentration of pyrite. However, as those samples retain primary signals in trace elements (i.e. REE+Y spectra), it would be interesting to succeed to analyze their $\delta^{56}\text{Fe}$ range and to compare it with already measured silicified samples (i.e. affected by late diagenesis and/or metamorphism). This approach may

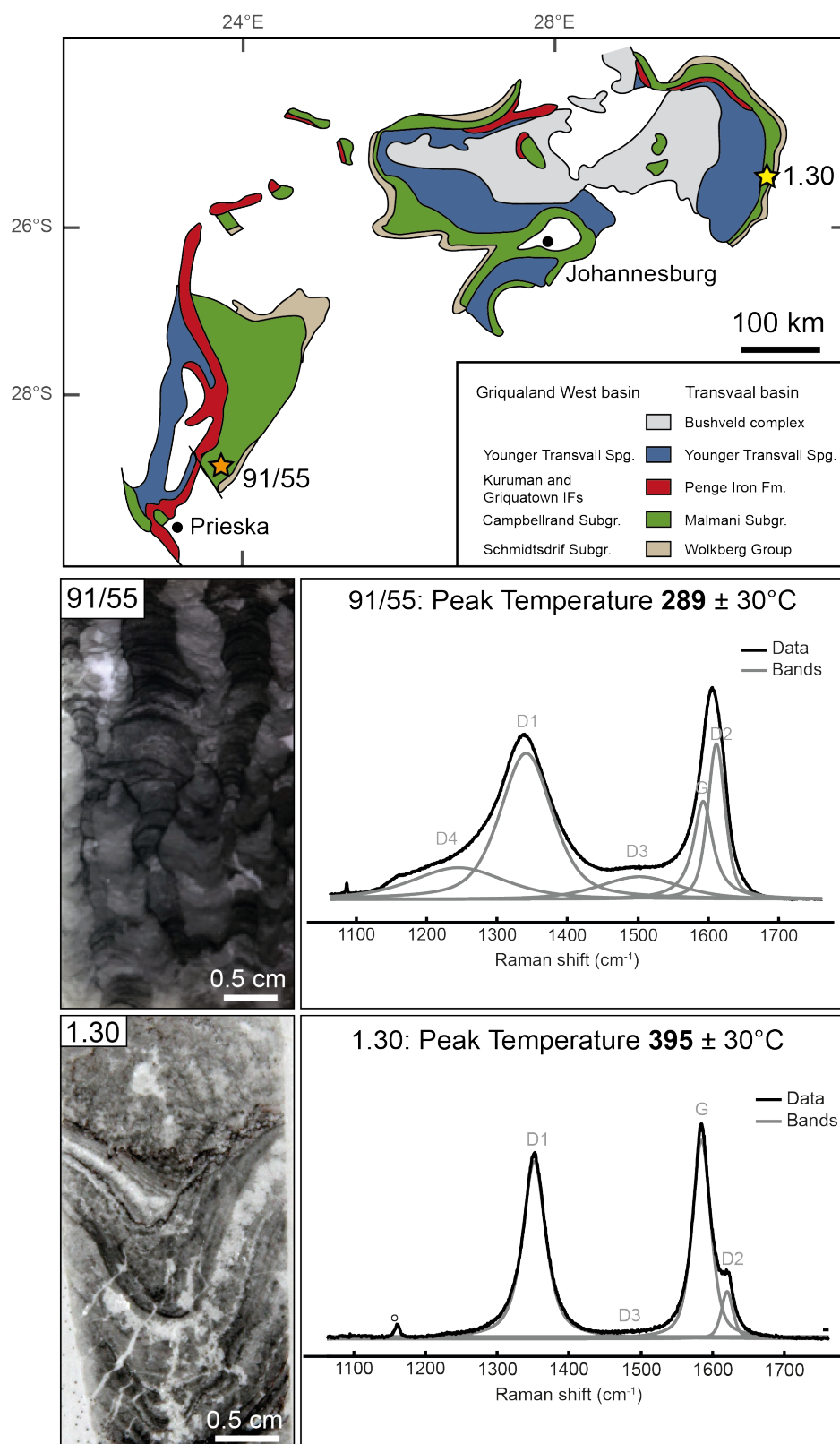


Figure 7. 2: Geological map of the Transvaal sequence (South Africa) with the location of the studied site (yellow star) at the eastern part of the Malmani Subgroup and the site from where the well-preserved stromatolite was sampled (orange star; Griqualand West area; samples provided by W. Altermann; modified after Sumner and Beukes, 2006). Microscopic view of the stromatolite sample 91/55, characterized by dark carbonaceous laminae. The Raman spectra obtained on this carbonaceous material allowed to estimate a maximum peak temperature experienced by the sample of $\sim 290^\circ\text{C}$ (Kouketsu et al., 2014). Comparison with Raman spectra obtained in sample 1.30 (from the log described in Chapter 6), which have experienced a higher peak temperature of $\sim 395^\circ\text{C}$.

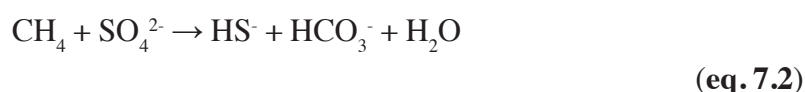
provide insights on the effect of secondary fluid circulation (effect of dolomitization alone and effect of dolomitization and silicification) on pyrite Fe isotope compositions in samples that have experienced the same metamorphic history. The Fe isotope range from the low-grade metamorphic samples (western part of the platform) will be compared to those of the Tumbiana stromatolites, which record a similar metamorphic peak temperature. In addition, samples from the western part of the platform preserved carbonaceous laminae in which pyrite may be abundant. Therefore, the analysis of pyrite associated with CM will be compared to results obtained on pyrite enclosed in OM-rich laminae in the Tumbiana samples.

5.3. Influence of methanotrophy on pyrite formation in modern and ancient sediments

In **chapter 4**, I described a covariation between Fe and S isotope compositions in samples from the mid ramp system. However, samples from the outer ramp setting show a decoupling of those two isotope systems. This has been interpreted as reduction of Fe-oxide located in the upper sediments by a sulfide flux diffusing from deeper zone of the sediment. This raised concerns about the origin, i.e. in terms of microbial activity, of this upward diffusing H₂S flux. In modern sediments, sulfide fluxes are produced by microbes which perform organoclastic sulfate reduction (OSR) and anaerobic methane oxidation coupled to sulfate reduction (AOM-SR). OSR bacteria use sulfate as electron acceptor for its conversion into sulfide and oxidize organic matter (**eq. 7.1**).



Production of sulfide through AOM-SR is based on oxidation of methane (**eq. 7.2**) and is performed by a consortium of methanotrophic archaea and sulfate reducing bacteria (e.g. *Hinrichs et al., 1999; Wegener et al., 2015*).



Methanotrophs can also operate methane oxidation by using Fe(III)-oxide as electron acceptor (AOM-IR). Activities of OSR and AOM function under anoxic conditions in the sediment, although OSR can tolerate suboxic-oxic conditions. They are dependent on sulfate concentration and spatially zoned in sediment with increasing depth. OSR occurs in the shallow sediments where sulfate concentration is high, i.e. where sediment porewaters and water column are well-connected, whereas AOM takes place at lower sulfate concentration at a deeper level in the sediments. In modern sediments, sulfide accumulation resulting from methanotrophy often corresponds to an interval of concurrent decrease of sulfate and increase of methane concentrations named the sulfate-methane transition zone (SMTZ). Recent observations of spatially resolved δ³⁴S values in pyrite show distinct signatures between shallow and deep pyrite in sediments, suggesting pyrite formed through OSR is ³⁴S-depleted compared to pyrite resulting from AOM-

SR (Lin *et al.*, 2017; Pasquier *et al.*, 2021b; Liu *et al.*, 2022). Moreover, a ^{56}Fe -enrichment of $\sim 1\text{‰}$ coupled with an increase of pyritization is reported to illustrate similar processes (Lin *et al.*, 2017).

Although sulfate and methane concentrations are not constrained in **chapter 4**, the reversed trend observed in LWC72 (low $\delta^{56}\text{Fe}_{\text{mean}}$ value and high $\delta^{34}\text{S}_{\text{mean}}$ value) is interpreted as sulfidation of Fe-oxide reservoirs dispersed in the sediments by an upward-diffusing ^{34}S -enriched H_2S . The origin of the H_2S flux could be attributed to activity of AOM-SR organisms deeper in the sediments. Therefore, heavy Fe isotope signatures of sedimentary pyrite might be diagnostic for methanotrophy. Moreover, the activity of methanotrophs has been shown in Archean stromatolites from the Tumbiana Formation (Hayes, 1994; Thomazo *et al.*, 2009) and suggested to have imprinted the Fe isotope signal of pyrite in those stromatolites (e.g. **Chapter 5** or Decraene *et al.*, 2021). Further efforts could be focused on exploring this potential biosignature. These include the systematic measurement of spatially resolved $\delta^{56}\text{Fe}$ and $\delta^{34}\text{S}$ in the same pyrite grains and experimental investigation of Fe and S isotope fractionations during Fe-oxide and sulfate reduction coupled to AOM. Such an approach should couple observations from modern sediments (methanotrophs active in sediments at the sulfate-methane transition zone) and experiments of pyrite precipitation under the influence of methanotrophs performing Fe-oxide reduction. This would allow determination of the Fe isotope fractionation between pyrite and Fe-oxides. The effect of reductive dissolution of Fe-oxides by AOM-derived H_2S would also be important to characterize in controlled experiments.

6. Literature cited

- Alleon, J., Bernard, S., le Guillou, C., Marin-Carbonne, J., Pont, S., Beysac, O., McKeegan, K.D., Robert, F., 2016. Molecular preservation of 1.88 Ga Gunflint organic microfossils as a function of temperature and mineralogy. *Nature Communications* 7, 11977. <https://doi.org/10.1038/ncomms11977>
- Aller, R.C., Blair, N.E., Brunskill, G.J., 2008. Early diagenetic cycling, incineration, and burial of sedimentary organic carbon in the central Gulf of Papua (Papua New Guinea). *Journal of Geophysical Research: Earth Surface* 113. <https://doi.org/10.1029/2006JF000689>
- Altermann, W., Nelson, D.R., 1998. Sedimentation rates, basin analysis and regional correlations of three Neoproterozoic and Palaeoproterozoic sub-basins of the Kaapvaal craton as inferred from precise U–Pb zircon ages from volcanoclastic sediments. *Sedimentary Geology* 120, 225–256. [https://doi.org/10.1016/S0037-0738\(98\)00034-7](https://doi.org/10.1016/S0037-0738(98)00034-7)
- Archer, C., Vance, D., 2006. Coupled Fe and S isotope evidence for Archean microbial Fe(III) and sulfate reduction. *Geology* 34, 153. <https://doi.org/10.1130/G22067.1>
- Bajwah, Z.U., Secombe, P.K., Offler, R., 1987. Trace element distribution, Co:Ni ratios and genesis of the big adia iron-copper deposit, new south wales, australia. *Mineralium Deposita* 22. <https://doi.org/10.1007/BF00204522>
- Berg, J.S., Michellod, D., Pjevac, P., Martinez-Perez, C., Buckner, C.R.T., Hach, P.F., Schubert, C.J., Milucka, J., Kuypers, M.M.M., 2016. Intensive cryptic microbial iron cycling in the low iron water column of the meromictic Lake Cadagno. *Environmental Microbiology* 18, 5288–5302. <https://doi.org/10.1111/1462-2920.13587>
- Berg, J.S., Jézéquel, D., Duverger, A., Lamy, D., Laberty-Robert, C., Miot, J., 2019. Microbial diversity involved in iron and cryptic sulfur cycling in the ferruginous, low-sulfate waters of Lake Pavin. *PLOS ONE* 14, e0212787. <https://doi.org/10.1371/journal.pone.0212787>
- Beukes, N.J., 1987. Facies relations, depositional environments and diagenesis in a major early proterozoic stromatolitic carbonate platform to basinal sequence, campbellrand subgroup, transvaal supergroup, southern africa, *Sedimentary Geology*.
- Bierens de Haan, S., 1991. A review of the rate of pyrite oxidation in aqueous systems at low temperature. *Earth-Science Reviews* 31, 1–10. [https://doi.org/10.1016/0012-8252\(91\)90039-I](https://doi.org/10.1016/0012-8252(91)90039-I)
- Bonnand, P., Lalonde, S.V., Boyet, M., Heubeck, C., Homann, M., Nonnotte, P., Foster, I., Konhauser, K.O., Köhler, I., 2020. Post-depositional REE mobility in a Paleoproterozoic banded iron formation revealed by La-Ce geochronology: A cautionary tale for signals of ancient oxygenation. *Earth and Planetary Science Letters* 547, 116452. <https://doi.org/10.1016/j.epsl.2020.116452>
- Button, A., 1973. The stratigraphic history of the malmani dolomite in the eastern and north-eastern transvaal.
- Clay, A.N., 1986. The stratigraphy of the Malmani Dolomite Subgroup in the Carletonville area, Transvaal: genetic implications for lead-zinc mineralization. *Mineral Deposits of Southern Africa* 853–860.
- Craddock, P.R., Dauphas, N., 2011. Iron and carbon isotope evidence for microbial iron respiration throughout the Archean. *Earth and Planetary Science Letters* 303, 121–132. <https://doi.org/10.1016/j.epsl.2010.12.045>
- Dauphas, N., Rouxel, O., 2006. Mass spectrometry and natural variations of iron isotopes. *Mass Spectrometry Reviews* 25, 515–550. <https://doi.org/10.1002/mas.20078>
- Dauphas, N., Cates, N.L., Mojzsis, S.J., Busigny, V., 2007. Identification of chemical sedimentary protoliths using iron isotopes in the > 3750 Ma Nuvvuagittuq supracrustal belt, Canada. *Earth and Planetary Science Letters* 254, 358–376. <https://doi.org/10.1016/j.epsl.2006.11.042>
- Decraene, M.N., Marin-Carbonne, J., Thomazo, C., Olivier, N., Philippot, P., Strauss, H., Deloule, E., 2021. Intense biogeochemical iron cycling revealed in Neoproterozoic micropyrates from stromatolites. *Geochimica et Cosmochimica Acta* 312, 299–320. <https://doi.org/10.1016/j.gca.2021.07.020>
- Eroglu, S., Schoenberg, R., Wille, M., Beukes, N., Taubald, H., 2015. Geochemical stratigraphy, sedimentology, and Mo isotope

systematics of the ca. 2.58–2.50 Ga-old Transvaal Supergroup carbonate platform, South Africa. *Precambrian Research* 266, 27–46. <https://doi.org/10.1016/j.precamres.2015.04.014>

Farquhar, J., Cliff, J., Zerkle, A.L., Kamyshny, A., Poulton, S.W., Claire, M., Adams, D., Harms, B., 2013. Pathways for Neoproterozoic pyrite formation constrained by mass-independent sulfur isotopes. *Proceedings of the National Academy of Sciences* 110, 17638–17643. <https://doi.org/10.1073/pnas.1218851110>

Fike, D.A., Bradley, A.S., Rose, C. v., 2015. Rethinking the Ancient Sulfur Cycle. *Annual Review of Earth and Planetary Sciences* 43, 593–622. <https://doi.org/10.1146/annurev-earth-060313-054802>

Fischer, W.W., Fike, D.A., Johnson, J.E., Raub, T.D., Guan, Y., Kirschvink, J.L., Eiler, J.M., 2014. SQUID–SIMS is a useful approach to uncover primary signals in the Archean sulfur cycle. *Proceedings of the National Academy of Sciences* 111, 5468–5473. <https://doi.org/10.1073/pnas.1322577111>

Foucault, A., Raoult, J.F., 1980. *Dictionary of geology*. Masson.

Frost, C.D., Blanckenburg, F., Schoenberg, R., Frost, B.R., Swapp, S.M., 2007. Preservation of Fe isotope heterogeneities during diagenesis and metamorphism of banded iron formation. *Contributions to Mineralogy and Petrology* 153, 211–235. <https://doi.org/10.1007/S00410-006-0141-0>

Hansel, C.M., Lentini, C.J., Tang, Y., Johnston, D.T., Wankel, S.D., Jardine, P.M., 2015. Dominance of sulfur-fueled iron oxide reduction in low-sulfate freshwater sediments. *The ISME Journal* 9, 2400–2412. <https://doi.org/10.1038/ismej.2015.50>

Hayes, J.M., 1994. Global methanotrophy at the Archean-Proterozoic transition. *Early Life on Earth* 220–236.

Hinrichs, K.-U., Hayes, J.M., Sylva, S.P., Brewer, P.G., DeLong, E.F., 1999. Methane-consuming archaeobacteria in marine sediments. *Nature* 398, 802–805. <https://doi.org/10.1038/19751>

Hinrichs, K.-U., 2002. Microbial fixation of methane carbon at 2.7 Ga: Was an anaerobic mechanism possible? <https://doi.org/10.1029/2001GC000286>

Jørgensen, B.B., Kasten, S., 2006. Sulfur Cycling and Methane Oxidation, in: *Marine Geochemistry*. Springer-Verlag, Berlin/Heidelberg, pp. 271–309. https://doi.org/10.1007/3-540-32144-6_8

Kendall, B., Reinhard, C.T., Lyons, T.W., Kaufman, A.J., Poulton, S.W., Anbar, A.D., 2010. Pervasive oxygenation along late Archean ocean margins. *Nature Geoscience* 3, 647–652. <https://doi.org/10.1038/ngeo942>

Kiyosu, Y., 1980. Chemical reduction and sulfur-isotope effects of sulfate by organic matter under hydrothermal conditions. *Chemical Geology* 30, 47–56. [https://doi.org/10.1016/0009-2541\(80\)90115-1](https://doi.org/10.1016/0009-2541(80)90115-1)

Knoll, A.H., Beukes, N.J., 2009. Introduction: Initial investigations of a Neoproterozoic shelf margin-basin transition (Transvaal Supergroup, South Africa). *Precambrian Research* 169, 1–14. <https://doi.org/10.1016/j.precamres.2008.10.009>

Large, R.R., Danyushevsky, L., Hollit, C., Maslennikov, V., Meffre, S., Gilbert, S., Bull, S., Scott, R., Emsbo, P., Thomas, H., Singh, B., Foster, J., 2009. Gold and Trace Element Zonation in Pyrite Using a Laser Imaging Technique: Implications for the Timing of Gold in Orogenic and Carlin-Style Sediment-Hosted Deposits. *Economic Geology* 104, 635–668. <https://doi.org/10.2113/gsecongeo.104.5.635>

Lawnizack, G., 2022. Étude des stromatolithes archéens (Malmani Subgroup, Afrique du Sud, 2,58–2,5 Ga) : caractérisation pétrographique et processus post-dépôt. Master dissertation, Université de Dijon.

Lepot, K., Benzerara, K., Brown, G.E., Philippot, P., 2008. Microbially influenced formation of 2,724-million-year-old stromatolites. *Nature Geoscience* 1, 118–121. <https://doi.org/10.1038/ngeo107>

Lepot, K., Benzerara, K., Rividi, N., Cotte, M., Brown, G.E., Philippot, P., 2009. Organic matter heterogeneities in 2.72 Ga stromatolites: Alteration versus preservation by sulfur incorporation. *Geochimica et Cosmochimica Acta* 73, 6579–6599. <https://doi.org/10.1016/j.gca.2009.08.014>

- Lepot, K., Williford, K.H., Philippot, P., Thomazo, C., Ushikubo, T., Kitajima, K., Mostefaoui, S., Valley, J.W., 2019. Extreme ^{13}C -depletions and organic sulfur content argue for S-fueled anaerobic methane oxidation in 2.72 Ga old stromatolites. *Geochimica et Cosmochimica Acta* 244, 522–547. <https://doi.org/10.1016/j.gca.2018.10.014>
- Lin, Z., Sun, X., Lu, Y., Strauss, H., Xu, L., Gong, J., Teichert, B.M.A., Lu, R., Lu, H., Sun, W., Peckmann, J., 2017. The enrichment of heavy iron isotopes in authigenic pyrite as a possible indicator of sulfate-driven anaerobic oxidation of methane: Insights from the South China Sea. *Chemical Geology* 449, 15–29. <https://doi.org/10.1016/j.chemgeo.2016.11.032>
- Liu, J., Pellerin, A., Wang, J., Rickard, D., Antler, G., Zhao, J., Wang, Z., Jørgensen, B.B., Ono, S., 2022. Multiple sulfur isotopes discriminate organoclastic and methane-based sulfate reduction by sub-seafloor pyrite formation. *Geochimica et Cosmochimica Acta* 316, 309–330. <https://doi.org/10.1016/j.gca.2021.09.026>
- Marin-Carbonne, J., Chaussidon, M., Robert, F., 2012. Micrometer-scale chemical and isotope criteria (O and Si) on the origin and history of Precambrian cherts: Implications for paleo-temperature reconstructions. *Geochimica et Cosmochimica Acta* 92, 129–147. <https://doi.org/10.1016/J.GCA.2012.05.040>
- Marin-Carbonne, J., Faure, F., Chaussidon, M., Jacob, D., Robert, F., 2013. A petrographic and isotope criterion of the state of preservation of Precambrian cherts based on the characterization of the quartz veins. *Precambrian Research* 231, 290–300. <https://doi.org/10.1016/J.PRECAMRES.2013.03.019>
- Marin-Carbonne, J., Remusat, L., Sforza, M.C., Thomazo, C., Cartigny, P., Philippot, P., 2018. Sulfur isotope's signal of nanopyrates enclosed in 2.7 Ga stromatolitic organic remains reveal microbial sulfate reduction. *Geobiology* 16, 121–138. <https://doi.org/10.1111/gbi.12275>
- Marin-Carbonne, J., Busigny, V., Miot, J., Rollion-Bard, C., Muller, E., Drabon, N., Jacob, D., Pont, S., Robyr, M., Bontognali, T.R.R., François, C., Reynaud, S., van Zuilen, M., Philippot, P., 2020. In Situ Fe and S isotope analyses in pyrite from the 3.2 Ga Mendon Formation (Barberton Greenstone Belt, South Africa): Evidence for early microbial iron reduction. *Geobiology* 18, 306–325. <https://doi.org/10.1111/gbi.12385>
- Martini, J.E.J., 1976. The fluorite deposits in the Dolomite Series of the Marico District, Transvaal, South Africa. *Economic Geology* 71, 625–635. <https://doi.org/10.2113/gsecongeo.71.3.625>
- Nishizawa, M., Yamamoto, H., Ueno, Y., Tsuruoka, S., Shibuya, T., Sawaki, Y., Yamamoto, S., Kon, Y., Kitajima, K., Komiya, T., Maruyama, S., Hirata, T., 2010. Grain-scale iron isotope distribution of pyrite from Precambrian shallow marine carbonate revealed by a femtosecond laser ablation multicollector ICP-MS technique: Possible proxy for the redox state of ancient seawater. *Geochimica et Cosmochimica Acta* 74, 2760–2778. <https://doi.org/10.1016/j.gca.2010.02.014>
- Ono, S., Kaufman, A.J., Farquhar, J., Sumner, D.Y., Beukes, N.J., 2009. Lithofacies control on multiple-sulfur isotope records and Neoproterozoic sulfur cycles. *Precambrian Research* 169, 58–67. <https://doi.org/10.1016/j.precamres.2008.10.013>
- Paris, G., Fischer, W.W., Johnson, J.E., Webb, S.M., Present, T.M., Sessions, A.L., Adkins, J.F., 2020. Deposition of sulfate aerosols with positive $\Delta^{33}\text{S}$ in the Neoproterozoic. *Geochimica et Cosmochimica Acta* 285, 1–20. <https://doi.org/10.1016/j.gca.2020.06.028>
- Pasquier, V., Bryant, R.N., Fike, D.A., Halevy, I., 2021a. Strong local, not global, controls on marine pyrite sulfur isotopes.
- Pasquier, V., Fike, D.A., Halevy, I., 2021b. Sedimentary pyrite sulfur isotopes track the local dynamics of the Peruvian oxygen minimum zone. *Nature Communications* 12. <https://doi.org/10.1038/s41467-021-24753-x>
- Philippot, P., van Zuilen, M., Lepot, K., Thomazo, C., Farquhar, J., van Kranendonk, M.J., 2007. Early Archaean Microorganisms Preferred Elemental Sulfur, Not Sulfate. *Science* (1979) 317, 1534–1537. <https://doi.org/10.1126/science.1145861>
- Sumner, D.Y., 1996. Facies, paleogeography, and carbonate precipitation on the Archean (2520 Ma) Campbellrand-Malmani carbonate platform, Transvaal supergroup, South Africa.
- Sumner, D.Y., Grotzinger, J.P., 2004. Implications for Neoproterozoic ocean chemistry from primary carbonate mineralogy of the

Campbellrand-Malmani Platform, South Africa. *Sedimentology* 51, 1273–1299. <https://doi.org/10.1111/j.1365-3091.2004.00670.x>

Sumner, D.Y., Beukes, N.J., 2006. Sequence Stratigraphic Development of the Neoproterozoic Transvaal carbonate platform, Kaapvaal Craton, South Africa. *South African Journal of Geology* 109, 11–22. <https://doi.org/10.2113/gssajg.109.1-2.11>

Syverson, D.D., Borrok, D.M., Seyfried, W.E., 2013. Experimental determination of equilibrium Fe isotope fractionation between pyrite and dissolved Fe under hydrothermal conditions. *Geochimica et Cosmochimica Acta* 122, 170–183. <https://doi.org/10.1016/j.gca.2013.08.027>

Teske, A., 2010. Cryptic Links in the Ocean. *Science* (1979) 330, 1326–1327. <https://doi.org/10.1126/science.1198400>

Thomazo, C., Ader, M., Farquhar, J., Philippot, P., 2009. Methanotrophs regulated atmospheric sulfur isotope anomalies during the Mesoproterozoic (Tumbiana Formation, Western Australia). *Earth and Planetary Science Letters* 279, 65–75. <https://doi.org/10.1016/j.epsl.2008.12.036>

Thomazo, C., Ader, M., Philippot, P., 2011. Extreme ^{15}N -enrichments in 2.72-Gyr-old sediments: evidence for a turning point in the nitrogen cycle. *Geobiology* 9, 107–120. <https://doi.org/10.1111/j.1472-4669.2011.00271.x>

Thomazo, C., Brayard, A., Elmeknassi, S., Vennin, E., Olivier, N., Caravaca, G., Escarguel, G., Fara, E., Bylund, K.G., Jenks, J.F., Stephen, D.A., Killingsworth, B., Sansjofre, P., Cartigny, P., 2019. Multiple sulfur isotope signals associated with the late Smithian event and the Smithian/Spathian boundary. *Earth-Science Reviews*. <https://doi.org/10.1016/j.earscirev.2018.06.019>

Wacey, D., McLoughlin, N., Kilburn, M.R., Saunders, M., Cliff, J.B., Kong, C., Barley, M.E., Brasier, M.D., 2013. Nanoscale analysis of pyritized microfossils reveals differential heterotrophic consumption in the ~1.9-Ga Gunflint chert. *Proceedings of the National Academy of Sciences* 110, 8020–8024. <https://doi.org/10.1073/pnas.1221965110>

Watanabe, Y., Farquhar, J., Ohmoto, H., 2009. Anomalous Fractionations of Sulfur Isotopes During Thermochemical Sulfate Reduction. *Science* (1979) 324, 370–373. <https://doi.org/10.1126/science.1169289>

Wegener, G., Krukenberg, V., Riedel, D., Tegetmeyer, H.E., Boetius, A., 2015. Intercellular wiring enables electron transfer between methanotrophic archaea and bacteria. *Nature*. <https://doi.org/10.1038/nature15733>

Williford, K.H., Ushikubo, T., Lepot, K., Kitajima, K., Hallmann, C., Spicuzza, M.J., Kozdon, R., Eigenbrode, J.L., Summons, R.E., Valley, J.W., 2016. Carbon and sulfur isotope signatures of ancient life and environment at the microbial scale: Neoproterozoic shales and carbonates. *Geobiology* 14, 105–128. <https://doi.org/10.1111/gbi.12163>

Yoshiya, K., Nishizawa, M., Sawaki, Y., Ueno, Y., Komiyama, T., Yamada, K., Yoshida, N., Hirata, T., Wada, H., Maruyama, S., 2012. In situ iron isotope analyses of pyrite and organic carbon isotope ratios in the Fortescue Group: Metabolic variations of a Late Archean ecosystem. *Precambrian Research* 212–213, 169–193. <https://doi.org/10.1016/j.precamres.2012.05.003>

APPENDIX 1

DATA TABLES OF THE MALMANI SAMPLES

Appendix. 1. Table S1: Results of major elemental analyses for 18 samples from the Malmani log

Sample #	SiO ₂ (wt. %)	Al ₂ O ₃ (wt. %)	Fe ₂ O ₃ (wt. %)	MnO (wt. %)	MgO (wt. %)	CaO (wt. %)	Na ₂ O (wt. %)	K ₂ O (wt. %)
MA1	0.92	0.12	0.27	0.78	20.30	29.65	0.03	<i>n.a</i>
MA3	0.78	0.28	0.31	0.94	20.11	29.44	0.02	0.09
MA6	0.75	0.23	0.27	0.86	20.49	29.82	<i>n.a</i>	0.07
MA7bas	0.76	0.12	0.30	0.84	20.30	29.89	<i>n.a</i>	0.03
MA10B-1	1.82	0.17	0.32	0.83	20.12	29.60	<i>n.a</i>	0.05
MA10b-2	0.89	0.08	0.42	0.83	20.22	29.83	<i>n.a</i>	<i>n.a</i>
MA12	95.41	0.11	0.07	0.02	0.62	1.09	<i>n.a</i>	<i>n.a</i>
MA13	72.87	0.12	0.48	0.16	5.22	8.04	<i>n.a</i>	0.03
MA15	75.03	0.15	0.46	0.16	4.84	7.36	<i>n.a</i>	0.04
MA18	32.48	0.13	0.40	0.48	13.74	20.32	<i>n.a</i>	0.04
MA23	2.27	0.30	0.28	0.69	20.18	29.43	<i>n.a</i>	0.08
MA24	0.97	0.16	0.43	0.70	20.25	29.49	<i>n.a</i>	<i>n.a</i>
MA28	1.34	0.26	0.68	0.71	19.97	29.46	<i>n.a</i>	0.08
MA30	1.11	0.12	0.91	0.70	19.78	29.34	<i>n.a</i>	0.03
MA32	89.32	0.04	0.26	0.08	2.00	3.06	<i>n.a</i>	<i>n.a</i>
MA35	63.58	0.26	1.21	0.27	6.58	10.59	<i>n.a</i>	0.07
MA37	22.18	0.20	1.14	0.57	15.23	23.04	<i>n.a</i>	0.05
MA43	90.11	0.16	0.40	0.07	1.60	2.53	<i>n.a</i>	0.04

Appendix. 1. Table S2.: Results of trace elemental analyses for 18 samples from the Malmmani log

Sample #	Concentrations (ppm)																											
	As	Ba	Be	Bi	Co	Cr	Cs	Cu	Ga	Ge	Hf	In	Nb	Ni	Pb	Rb	Sb	Sr	Ta	Th	U	V	W	Y	Zr			
MA1	<i>n.a.</i>	7.467	0.053	<i>n.a.</i>	0.423	2.324	0.067	<i>n.a.</i>	0.242	<i>n.a.</i>	0.032	<i>n.a.</i>	0.039	<i>n.a.</i>	0.810	0.835	0.159	0.369	17.526	0.007	0.156	0.056	0.849	<i>n.a.</i>	0.386	2.025		
MA3	1.154	14.290	0.075	0.083	0.570	5.785	0.098	3.575	0.509	<i>n.a.</i>	<i>n.a.</i>	0.030	0.074	2.554	1.140	2.423	0.208	<i>n.a.</i>	15.242	0.012	0.095	0.023	1.802	<i>n.a.</i>	0.436	<i>n.a.</i>		
MA6	0.749	5.941	0.056	0.051	0.268	3.928	0.087	<i>n.a.</i>	0.436	<i>n.a.</i>	0.047	<i>n.a.</i>	0.069	<i>n.a.</i>	0.691	1.930	0.174	0.426	12.908	0.008	0.243	0.019	1.223	<i>n.a.</i>	0.303	2.506		
MA7bas	0.685	<i>n.a.</i>	<i>n.a.</i>	<i>n.a.</i>	0.320	1.993	0.043	2.353	0.294	<i>n.a.</i>	0.031	<i>n.a.</i>	0.035	<i>n.a.</i>	0.746	0.884	0.136	<i>n.a.</i>	11.417	0.005	0.133	0.013	<i>n.a.</i>	<i>n.a.</i>	0.242	<i>n.a.</i>		
MA10B-1	0.550	5.611	<i>n.a.</i>	0.047	0.271	3.316	0.117	<i>n.a.</i>	0.371	<i>n.a.</i>	0.047	<i>n.a.</i>	0.080	<i>n.a.</i>	0.856	1.682	0.273	0.463	12.757	0.011	0.178	0.051	1.058	<i>n.a.</i>	0.447	2.588		
MA10b-2	0.824	<i>n.a.</i>	<i>n.a.</i>	0.052	0.592	1.189	0.033	3.000	0.264	<i>n.a.</i>	<i>n.a.</i>	<i>n.a.</i>	0.026	2.820	1.070	0.586	0.240	<i>n.a.</i>	13.230	0.004	0.049	0.025	<i>n.a.</i>	<i>n.a.</i>	0.393	<i>n.a.</i>		
MA12	<i>n.a.</i>	7.567	<i>n.a.</i>	<i>n.a.</i>	0.350	25.913	0.065	2.825	0.221	0.434	<i>n.a.</i>	<i>n.a.</i>	<i>n.a.</i>	9.757	0.664	0.680	0.088	<i>n.a.</i>	1.903	<i>n.a.</i>	0.198	<i>n.a.</i>	<i>n.a.</i>	<i>n.a.</i>	0.043	<i>n.a.</i>		
MA13	<i>n.a.</i>	5.824	<i>n.a.</i>	<i>n.a.</i>	0.251	7.055	0.069	3.268	0.211	0.390	<i>n.a.</i>	<i>n.a.</i>	0.047	3.238	0.479	0.790	0.166	<i>n.a.</i>	10.079	0.007	0.157	0.021	<i>n.a.</i>	<i>n.a.</i>	0.112	<i>n.a.</i>		
MA15	<i>n.a.</i>	8.879	<i>n.a.</i>	<i>n.a.</i>	1.226	4.412	0.101	<i>n.a.</i>	0.228	0.377	<i>n.a.</i>	<i>n.a.</i>	0.028	3.480	0.805	1.114	0.174	<i>n.a.</i>	8.709	0.004	0.132	0.018	<i>n.a.</i>	<i>n.a.</i>	0.104	<i>n.a.</i>		
MA18	0.506	<i>n.a.</i>	<i>n.a.</i>	<i>n.a.</i>	0.872	5.877	0.096	4.046	0.274	0.177	0.086	<i>n.a.</i>	0.045	3.469	1.239	1.103	0.240	0.357	9.677	0.008	0.514	0.030	<i>n.a.</i>	<i>n.a.</i>	0.214	3.853		
MA23	<i>n.a.</i>	10.076	<i>n.a.</i>	<i>n.a.</i>	0.236	3.725	0.145	<i>n.a.</i>	0.549	<i>n.a.</i>	0.039	<i>n.a.</i>	0.121	<i>n.a.</i>	0.516	2.411	0.159	<i>n.a.</i>	11.853	0.014	0.245	0.061	1.917	<i>n.a.</i>	0.332	1.631		
MA24	<i>n.a.</i>	<i>n.a.</i>	<i>n.a.</i>	<i>n.a.</i>	0.403	1.957	0.086	<i>n.a.</i>	0.283	<i>n.a.</i>	0.044	<i>n.a.</i>	0.060	<i>n.a.</i>	<i>n.a.</i>	0.941	0.151	0.428	11.222	0.009	0.183	0.027	0.900	<i>n.a.</i>	0.331	2.539		
MA28	<i>n.a.</i>	8.892	0.054	<i>n.a.</i>	0.347	3.939	0.060	<i>n.a.</i>	0.432	<i>n.a.</i>	0.062	<i>n.a.</i>	0.158	2.210	<i>n.a.</i>	1.798	0.173	<i>n.a.</i>	12.837	0.019	0.290	0.057	2.203	<i>n.a.</i>	0.484	2.352		
MA30	<i>n.a.</i>	<i>n.a.</i>	<i>n.a.</i>	<i>n.a.</i>	0.405	1.959	0.041	2.978	0.281	<i>n.a.</i>	<i>n.a.</i>	0.035	0.028	<i>n.a.</i>	<i>n.a.</i>	0.723	0.108	<i>n.a.</i>	18.688	0.006	0.152	0.020	<i>n.a.</i>	<i>n.a.</i>	0.669	<i>n.a.</i>		
MA32	<i>n.a.</i>	<i>n.a.</i>	<i>n.a.</i>	<i>n.a.</i>	0.112	4.666	0.032	5.201	0.113	0.783	0.030	<i>n.a.</i>	<i>n.a.</i>	2.073	<i>n.a.</i>	0.254	0.136	0.300	6.947	<i>n.a.</i>	0.079	0.011	<i>n.a.</i>	<i>n.a.</i>	0.119	1.515		
MA35	1.012	17.514	0.050	0.058	1.571	8.760	0.065	<i>n.a.</i>	0.342	0.439	0.054	0.086	0.118	3.985	<i>n.a.</i>	1.693	0.175	<i>n.a.</i>	15.552	0.017	0.271	0.045	<i>n.a.</i>	1.079	0.262	2.040		
MA37	2.761	10.706	0.056	0.211	3.703	4.652	0.063	<i>n.a.</i>	0.390	0.183	0.042	0.054	0.115	2.686	0.452	1.308	0.240	<i>n.a.</i>	18.832	0.014	0.284	0.049	1.632	<i>n.a.</i>	0.287	1.936		
MA43	0.954	16.342	<i>n.a.</i>	0.128	0.680	8.889	0.067	<i>n.a.</i>	0.158	0.503	0.050	0.051	0.025	3.513	<i>n.a.</i>	1.149	0.261	0.374	5.111	<i>n.a.</i>	0.336	0.017	<i>n.a.</i>	<i>n.a.</i>	0.059	2.405		

Appendix. 1. Table S3: REE + Y concentrations in Malammi samples (18 over 43 collected along the log)

Sample #	Facies	REE + Y (ppm)														
		La	Ce	Pr	Nd	Sm	Eu	Gd	Tb	Dy	Y	Ho	Er	Tm	Yb	Lu
MA1	FA1	0.3832	0.6174	0.0705	0.2679	0.0467	0.0210	0.0467	0.0070	0.0396	0.3862	0.0088	0.0242	0.0036	0.0218	0.0033
MA3	FA1	0.5056	0.8834	0.0992	0.3615	0.0779	0.0253	0.0678	0.0106	0.0659	0.4362	0.0134	0.0366	0.0050	0.0336	0.0047
MA6	FA2 (top log)	0.3526	0.6192	0.0712	0.2598	0.0538	0.0195	0.0479	0.0074	0.0492	0.3033	0.0095	0.0250	0.0039	0.0237	0.0034
MA7bas	FA2 (top log)	0.3304	0.5217	0.0570	0.2113	0.0399	0.0123	0.0334	0.0046	0.0341	0.2419	0.0070	0.0164	0.0022	0.0160	0.0022
MA10B-1	FA2 (top log)	0.3335	0.5494	0.0606	0.2279	0.0500	0.0143	0.0417	0.0064	0.0377	0.4474	0.0087	0.0255	0.0038	0.0262	0.0039
MA10b-2	FA2 (top log)	0.3175	0.4783	0.0503	0.1965	0.0333	0.0102	0.0341	0.0047	0.0279	0.3934	0.0065	0.0189	0.0027	0.0196	0.0028
MA12	FA2 silicified	0.0745	0.1177	0.0115	0.0497	0.0079	0.0048	0.0082	0.0013	0.0061	0.0431	0.0015	0.0037	<LD.	0.0044	<LD.
MA13	FA2 partially silicified	0.2282	0.4277	0.0397	0.1295	0.0248	0.0220	0.0194	0.0029	0.0185	0.1116	0.0033	0.0093	0.0015	0.0106	0.0016
MA15	FA2 partially silicified	0.1982	0.3643	0.0373	0.1194	0.0226	0.0143	0.0177	0.0027	0.0166	0.1037	0.0033	0.0096	0.0014	0.0104	0.0015
MA18	FA2 partially silicified	0.3060	0.5896	0.0679	0.2375	0.0496	0.0145	0.0397	0.0065	0.0396	0.2135	0.0079	0.0209	0.0030	0.0214	0.0030
MA23	FA2 non silicified	0.4723	0.9229	0.1069	0.4457	0.0846	0.0225	0.0718	0.0103	0.0584	0.3320	0.0112	0.0308	0.0048	0.0287	0.0043
MA24	FA2 non silicified	0.4073	0.7859	0.0908	0.3460	0.0659	0.0249	0.0543	0.0084	0.0489	0.3309	0.0102	0.0287	0.0045	0.0262	0.0035
MA28	FA2 non silicified	0.4501	0.9534	0.1264	0.5488	0.1702	0.0736	0.1532	0.0212	0.0989	0.4838	0.0164	0.0354	0.0046	0.0279	0.0036
MA30	FA2 non silicified	0.4114	1.1154	0.1775	0.9127	0.3246	0.1435	0.3212	0.0401	0.1765	0.6690	0.0257	0.0455	0.0040	0.0221	0.0027
MA32	FA2 silicified	0.0676	0.2343	0.0377	0.1960	0.0936	0.0351	0.0766	0.0084	0.0341	0.1188	0.0042	0.0075	<LD.	0.0052	<LD.
MA35	FA2 partially silicified	0.3774	1.0973	0.1532	0.6778	0.1841	0.1462	0.1407	0.0132	0.0555	0.2616	0.0084	0.0194	0.0027	0.0169	0.0025
MA37	FA2 partially silicified	0.5085	1.0802	0.1317	0.5308	0.1322	0.1198	0.1031	0.0109	0.0529	0.2866	0.0089	0.0220	0.0032	0.0210	0.0036
MA43	FA2 silicified	0.2716	0.4991	0.0461	0.1462	0.0224	0.1007	0.0145	0.0021	0.0098	0.0586	0.0022	0.0048	0.0010	0.0060	0.0010
PAAS		38	80	8.9	32	5.6	1.1	4.7	0.77	4.4	27	1	2.9	0.4	2.8	0.43

Appendix 1. Table S4: Results of elemental analyses (EPMA) in pyrite grains enclosed in the three Malmani samples analyzed by SIMS

Sample #	Pyrite	Concentrations (wt.%)										Total	Co/Ni		
		S	Co	Ni	Fe	As	Au	Pb	Zn	Cu					
MA37b	Ox. Pyr.	51.67	3.78	0.00	43.18	2.73	0.00	0.00	0.02	0.00	0.00	0.00	0.00	101.38	1.49
MA39	Ox. Pyr.	53.12	0.10	0.07	46.72	0.05	0.00	0.00	0.04	0.00	0.00	0.00	0.00	100.10	12.25
MA39	Ox. Pyr.	53.98	0.30	0.02	46.96	0.21	0.06	0.00	0.00	0.00	0.00	0.00	0.01	101.55	55.63
MA39	Ox. Pyr.	53.58	0.33	0.01	46.89	0.00	0.05	0.00	0.00	0.00	0.00	0.00	0.02	100.88	1.42
MA39	Ox. Pyr.	52.99	0.10	0.07	47.29	0.10	0.04	0.00	0.00	0.00	0.00	0.00	0.06	100.64	22.75
MA37b	Ox. Pyr.	53.24	0.79	0.03	46.58	0.10	0.05	0.00	0.08	0.00	0.00	0.00	0.01	100.87	45.74
MA37b	Ox. Pyr.	53.63	1.72	0.04	45.48	0.00	0.10	0.00	0.02	0.00	0.00	0.00	0.00	100.99	28.19
MA37b	Ox. Pyr.	53.52	1.06	0.04	45.40	0.10	0.00	0.00	0.04	0.00	0.00	0.00	0.00	100.16	
MA37b	μ py.	53.46	0.05	0.04	46.54	0.08	0.03	0.00	0.03	0.00	0.00	0.00	0.07	100.31	1.32
AmalC4	μ py.	53.34	0.05	0.00	45.91	0.00	0.00	0.00	0.00	0.00	0.00	0.00	0.08	99.37	
AmalC4	μ py.	53.05	0.04	0.02	45.99	0.10	0.05	0.16	0.00	0.00	0.00	0.00	0.03	99.44	2.00
AmalC4	μ py.	53.50	0.08	0.11	45.63	0.18	0.09	0.04	0.00	0.00	0.00	0.00	0.02	99.65	0.78
AmalC4	μ py.	53.26	0.06	0.09	46.43	0.11	0.03	0.11	0.00	0.00	0.00	0.00	0.04	100.13	0.73
AmalC4	μ py.	53.37	0.05	0.05	45.91	0.08	0.00	0.01	0.03	0.00	0.00	0.00	0.11	99.60	0.94
AmalC4	μ py.	53.20	0.08	0.05	46.24	0.06	0.08	0.00	0.00	0.00	0.00	0.00	0.00	99.70	1.69
AmalC4	μ py.	53.33	0.07	0.06	46.12	0.04	0.00	0.00	0.07	0.00	0.00	0.00	0.00	99.69	1.11
AmalC4	μ py.	53.39	0.07	0.07	46.61	0.10	0.01	0.00	0.00	0.00	0.00	0.00	0.00	100.26	1.13
AmalC4	μ py.	53.57	0.07	0.00	46.37	0.02	0.00	0.07	0.00	0.00	0.00	0.00	0.00	100.09	

Appendix. 1. Table S5: Pyrite $^{56}\text{Fe}^+$ count rates and Fe isotope compositions obtained for Malmani samples

Analyses #	$^{56}\text{Fe}^+$ intensity (cps)	$\delta^{56}\text{Fe}$ (‰)	2σ
AmalC4a@1	4.13E+07	1.59	0.36
AmalC4a@4	3.94E+07	1.52	0.37
AmalC4a@6	4.21E+07	2.11	0.35
AmalC4a@7	4.33E+07	0.60	0.34
AmalC4a@8	4.34E+07	1.17	0.34
AmalC4a@9	4.22E+07	1.38	0.35
AmalC4a@11	4.22E+07	0.99	0.34
AmalC4a@12	3.44E+07	3.34	0.48
AmalC4a@14	4.26E+07	0.67	0.37
AmalC4a@16	4.39E+07	1.09	0.37
AmalC4a@21	3.79E+07	3.85	0.43
AmalC4a@24	3.75E+07	2.18	0.37
MA37a@1	4.73E+07	0.37	0.27
MA37a@2	4.45E+07	0.39	0.28
MA37a@3	2.19E+07	-0.14	0.32
MA37a@4	3.95E+07	-0.64	0.27
MA37a@5	4.07E+07	-0.87	0.27
MA37a@6	3.29E+07	1.01	0.28
MA37a@8	3.78E+07	1.18	0.27
MA37a@9	4.45E+07	1.16	0.27
MA37a@10	4.33E+07	1.09	0.28
MA37a@12	5.22E+07	2.77	0.26
MA37b@2	3.27E+07	3.48	0.34
MA37b@3	3.13E+07	3.24	0.34
MA37b@4	3.50E+07	1.78	0.34
MA37b@5	3.76E+07	3.53	0.33
MA39@1	3.12E+07	0.87	0.35
MA39@2	3.15E+07	0.98	0.35
MA39@3	3.13E+07	1.42	0.35
MA39@4	3.21E+07	0.64	0.34
MA39@5	3.09E+07	1.13	0.37
MA39@6	2.92E+07	1.78	0.35

Appendix. 1. Table S6: Pyrite ^{32}S count rates and S isotope compositions obtained for Malmani samples

Analysis #	^{32}S - intensity (cps)	$\delta^{34}\text{S}$ (‰)	2σ	$\Delta^{33}\text{S}$	2σ
MA39@01	4.02E+09	2.16	0.09	2.25	0.04
MA39@2	4.59E+09	2.36	0.09	2.31	0.04
MA39@3	4.56E+09	2.30	0.08	2.36	0.04
MA39@4	4.46E+09	2.35	0.08	2.28	0.04
MA39@5	3.72E+09	1.55	0.10	2.30	0.03
MA39@6	4.50E+09	2.45	0.08	2.26	0.04
MA39@7	5.25E+08	2.09	0.09	2.15	0.08
MA37b@01	1.27E+09	3.07	0.11	2.82	0.05
MA37b@2	4.45E+09	2.92	0.08	2.83	0.04
MA37b@3	3.52E+09	1.55	0.10	2.79	0.03
MA37b@4	6.88E+08	0.08	0.13	2.66	0.06
MA37b@5	1.57E+08	-1.68	0.21	2.76	0.17
MA37b@6	9.90E+08	5.05	0.15	5.63	0.04
MA37a@01	3.18E+09	1.78	0.16	2.80	0.00
MA37a@2	3.09E+08	1.01	0.16	3.05	0.05
MA37a@3	6.55E+08	2.08	0.21	2.64	0.01
MA37a@4	9.89E+08	-3.72	0.16	2.75	0.00
MA37a@5	2.10E+09	6.43	0.21	3.53	0.01
AmalC4a@2	7.82E+08	-2.53	0.10	1.86	0.05
AmalC4a@3	4.45E+08	-0.26	0.10	2.15	0.09
AmalC4a@4	2.87E+09	-2.28	0.14	2.09	0.01
AmalC4a@5	1.41E+09	-5.15	0.17	1.84	0.02
AmalC4a@6	5.19E+08	-24.52	0.21	1.71	0.02
AmalC4a@8	1.59E+09	-12.46	0.09	1.07	0.03
AmalC4a@9	7.34E+08	-14.90	0.10	1.62	0.06
AmalC4a@10	5.81E+08	-16.48	0.11	1.40	0.05
AmalC4a@11	2.48E+09	0.80	0.17	2.92	0.04
AmalC4a@12	1.82E+09	2.57	0.18	2.33	0.02
AmalC4b@01	2.42E+09	-6.42	0.14	1.58	0.03
AmalC4b@2	3.23E+08	-3.05	0.14	1.91	0.13
AmalC4b@3	2.65E+09	-1.33	0.13	1.59	0.02
AmalC4b@4	9.68E+08	0.47	0.12	1.95	0.04
AmalC4b@5	3.17E+09	1.10	0.13	1.91	0.03
AmalC4b@6	1.27E+09	-6.52	0.15	1.59	0.03
AmalC4b@7	9.46E+08	-1.26	0.13	1.74	0.04
AmalC4b@8	1.67E+09	0.35	0.18	2.04	0.04
AmalC4b@9	1.97E+09	1.36	0.12	2.00	0.03
AmalC4b@12	1.37E+09	-15.22	0.14	1.39	0.02
AmalC4b@13	2.67E+09	1.90	0.12	2.28	0.03
AmalC4b@14	1.63E+09	-5.71	0.12	1.55	0.03
AmalC4b@15	1.76E+09	0.59	0.20	1.80	0.01
AmalC4b@16	8.04E+08	-0.81	0.28	1.70	0.02

APPENDIX 2

Co-AUTHORED CONTRIBUTION

DUPEYRON ET AL. (SUBMITTED AT *EPSL*)

Highlights

Ferric iron was the dominant source of sedimentary pyrite from Archean to Paleoproterozoic: insights from *in situ* Fe isotope composition

Juliette Dupeyron, Marie-Noëlle Decraene, Johanna Marin-Carbonne, Vincent Busigny

- Compilation of microscale Fe isotope compositions in pyrite from Archean to Paleoproterozoic
- Identification of pyrite formation mechanisms: total and partial Fe (oxy)hydroxide reduction, and kinetic precipitation from dissolved Fe(II)
- Fe (oxy)hydroxide reduction was the dominant pathway of pyrite formation from Archean to Paleoproterozoic

Ferric iron was the dominant source of sedimentary pyrite from Archean to Paleoproterozoic: insights from *in situ* Fe isotope composition

Juliette Dupeyron^{a,b,*}, Marie-Noëlle Decraene^a, Johanna Marin-Carbonne^a,
Vincent Busigny^{b,c}

^a*Institut des Sciences de la Terre, Université de Lausanne, Lausanne, 1015, Switzerland*

^b*Université Paris Cité, Institut de Physique du Globe, CNRS, Paris, F-75005, France*

^c*Institut Universitaire de France, Paris, 75005, France*

Abstract

Iron isotope compositions (expressed as $\delta^{56}\text{Fe}$) in sedimentary pyrite have been widely used as tracers of redox and chemical evolution of the ocean through geological time. Previous studies mostly built on the chemical extraction of sulfides from bulk rock samples, and focused on visible macroscopic pyrites, which may introduce a sampling bias. *In situ* analyses of micropyrrite grains can provide new insights into the processes of pyrite formation and their time evolution. Here, we compile *ca.* 2000 *in situ* iron isotope compositions of Archean to Paleoproterozoic sedimentary pyrite, from previous literature and unpublished data. Contrasting with bulk analyses, micropyrrite displays a large and constant range of $\delta^{56}\text{Fe}$ values, from -4 to +4 ‰, through time. Micropyrrite $\delta^{56}\text{Fe}$ values are not significantly influenced by metamorphic grade. A bimodal distribution of positive *versus* negative $\delta^{56}\text{Fe}$ values can be attributed to two different processes of pyrite forma-

*Corresponding author. *Postal address:* Institut des Sciences de la Terre, Université de Lausanne, 1015, Lausanne, Switzerland. *Email address:* juliette.dupeyron@unil.ch

tion, Fe (oxy)hydroxide sulfidation, *versus* kinetic and possibly microbially mediated pyrite precipitation. These processes are tightly related to rock lithology and thus to sedimentary conditions, and have existed since 3.8 Ga.

Keywords: pyrite, Archean, Fe isotope composition, SIMS

PACS: 0000, 1111

2000 MSC: 0000, 1111

1. Introduction

Iron (Fe) was a dominant chemical element of the early ocean, as illustrated by the deposition of abundant Fe-rich sedimentary rocks such as banded iron formations (BIFs) through the Archean (Klein, 2005; Bekker et al., 2010; Konhauser et al., 2017). Fe played a key role in the development of early life (Lyons et al., 2015), and likely supported microbial activity, in particular anoxygenic photosynthesis and dissimilatory iron reduction (DIR). Some microorganisms can use Fe(II) as an electron donor for anoxygenic photosynthetic carbon fixation, others use Fe(III) as an electron acceptor in anaerobic respiration (Johnson and Beard, 2006). Phylogenetic studies highlight the great degree of conservation of genes responsible for most metabolic reactions involving Fe, suggesting that they evolved close to the root in the tree of life (Lonergan et al., 1996). Moreover, iron metabolic activities can induce Fe isotope fractionation, which can be recorded in Fe mineral phases through the geological record (Johnson et al., 2008). DIR signatures were evidenced in sedimentary sulfides as old as 3.28 Ga (Marin-Carbonne et al., 2020) and more broadly at 2.7 Ga (Archer and Vance, 2006; Craddock and Dauphas, 2011), while fingerprints of anoxygenic photosynthesis have also been reported in the Archean sedimentary record (Czaja et al., 2013; Rego et al., 2021). Significant Fe isotope fractionations occur during oxidation of Fe(II) to Fe(III) (Welch et al., 2003; Balci et al., 2006) and reduction of iron (oxy)hydroxides (Crosby et al., 2005, 2007; Wiederhold et al., 2006; Frierdich et al., 2019). Therefore, Fe isotope composition has been extensively used as a proxy for reconstructing redox and chemical evolution of the ocean (see review in Anbar and Rouxel, 2007; Johnson et al., 2008; Dauphas et al.,

2017).

In a pioneer work, Rouxel et al. (2005) measured bulk Fe isotope composition of pyrite grains in black shales, from late Archean to Paleoproterozoic, and discovered a negative isotope excursion (*i.e.*, enrichment in light Fe isotopes) just before the Great Oxygenation Event (GOE, 2.4 Ga; Bekker et al., 2004). The negative $\delta^{56}\text{Fe}$ values recorded in Neoproterozoic pyrite were interpreted as inherited from extensive seawater Fe(II) oxidation and Fe (oxy)hydroxides precipitation, subsequently reduced to iron sulfides (Rouxel et al., 2005). The evolution to positive $\delta^{56}\text{Fe}$ values during Paleoproterozoic was proposed to reflect the onset of oxidative weathering in the wake of the GOE and increased sulfate delivery to the ocean. Alternatively, the observed negative $\delta^{56}\text{Fe}$ values could reflect the onset of DIR-bacteria, which use ferric iron as an electron acceptor and release light Fe(II) to sediment porewater, from which light pyrite can precipitate (Johnson et al., 2008). Kinetic effects during pyrite precipitation from aqueous FeS precursors could also drive $\delta^{56}\text{Fe}$ variability, with Fe isotope fractionations as low as -3 ‰ produced during abiotic pyrite precipitation (Guilbaud et al., 2011). The expression of kinetic *versus* equilibrium effects during pyrite precipitation is controlled by the Fe/S ratio and the availability of organic material (Mansor and Fantle, 2019). The formation of pyrite follows a complex crystallization pathway with several steps and various soluble and insoluble precursors (Rickard et al., 2017) that can obscure Fe isotope composition record. Recently, Heard and Dauphas (2020) compiled bulk $\delta^{56}\text{Fe}$ values in 3.3 to 1.8 Ga-old pyrite, and highlighted a secular evolution. From Archean through the GOE, $\delta^{56}\text{Fe}$ values are mostly negative and progressively increases, before

reaching positive values after the GOE. This trend, combined with the evolution of iron formation $\delta^{56}\text{Fe}$ and S isotope compositions in sedimentary sulfide from early Archean to late Paleoproterozoic, was proposed to reflect Fe and S availability control over $\delta^{56}\text{Fe}$, and to point to a kinetically driven pyrite precipitation indirectly linked to the redox change of the ocean. Most of these previous studies have focused on millimeter-scale pyrite selected for bulk $\delta^{56}\text{Fe}$ measurement, as large grains are more easily extracted from their matrix. However, this approach may introduce a sampling bias since only large visible pyrite are selected for analysis. Moreover, very few data in pyrite older than 3 Ga are available from bulk measurement, leaving most of the Archean period uncovered. *In situ* analyses of pyrite at the micrometer scale allow to study a larger variability of samples, even in rocks with limited amount of pyrite grains. Microscale $\delta^{56}\text{Fe}$ values previously measured in Precambrian pyrite show a wide range, including positive values throughout the Archean (*e.g.*, Yoshiya et al., 2012; Agangi et al., 2015; Yoshiya et al., 2015b; Marin-Carbonne et al., 2014; Marin-Carbonne et al., 2020), potentially controlled by local environmental variations (*e.g.* Decraene et al., 2021b). *In situ* $\delta^{56}\text{Fe}$ database might bring new perspective on the Fe isotope variations in Archean and Paleoproterozoic pyrite. In the present contribution, we report the first compilation of *in situ* Fe isotope compositions in pyrite, throughout Archean and Paleoproterozoic. Our compilation include data from previous studies (Table S1), as well as additional unpublished data from the Francevillian Group (2.2-2.06 Ga, Gabon), Turee Creek Formation (2.43 Ga, Australia), Tumbiana Formation (2.7 Ga, Australia), Mapepe Formation (3,2 Ga) and Buck Reef Formation (3.4 Ga, South Africa) (see supplementary materials).

From this dataset, we evaluate the effect of metamorphic and lithological variations and revisit the evolution of Fe isotope composition through the Precambrian.

2. Material and Methods

2.1. Data compilation

Both published and previously unpublished *in situ* Fe isotope compositions of iron sulfides from Archean to Proterozoic were compiled (see the supplementary materials). The measurements were performed by secondary ion mass spectrometer (SIMS), or laser ablation multi-collector inductively coupled plasma mass spectrometer (LA-MC-ICP-MS). New data were measured on samples from two IPGP drillcores (TCDP1 and PPDP2), from the BARB3 drillcore (ICDP, 2008) and the Francevillian Group. All samples are described in the supplementary materials. The compilation primarily includes the age, size and morphology of pyrite together with the lithology of the host rock (Table S1). The metamorphic grade and organic matter content were also compiled when available.

2.2. SIMS analyses

Iron isotope compositions were measured with a Cameca ims 1270 ion microprobe at CRPG-CNRS (Nancy, France) for TCDP samples, at UCLA (Los Angeles, USA) for BARB3 samples, and with a Cameca 1280 HR at the SwissSIMS (Lausanne, Switzerland) for the samples from the Francevillian Group, following the procedures described in Marin-Carbonne et al. (2011) and Decraene et al. (2021a). Pyrite grains were sputtered by a $^{16}\text{O}^-$ primary beam of 10 nA intensity focused to a spot of about 10 to 15 μm . $^{54}\text{Fe}^+$ and $^{56}\text{Fe}^+$ were measured in multi-collection mode with two off-axis Faraday cups, with a mass resolving power of $\sim 7,000$. The isobaric interference of ^{54}Cr on ^{54}Fe was monitored at masses 52 and 53, but chromium levels were

negligible in all samples. The internal precision for $\delta^{56}\text{Fe}$ values was typically better than $\pm 0.1 \text{ ‰}$ (2σ), and the external reproducibility based on multiple measurements of our pyrite reference material (Balmat with $\delta^{56}\text{Fe} = -0.399 \text{ ‰}$) was better than $\pm 0.2 \text{ ‰}$ (2σ).

2.3. Statistical analysis

The database presented in this study comprises isotope compositions reported in 12 scientific publications, in addition to our new data (see supplementary material). All data are considered, without being filtered, although the contributions of each publication are unequal among the studies and/or geological formations (from 16 to more than 200 reported $\delta^{56}\text{Fe}$ values). Iron isotope compositions are displayed as distributions, in the form of histogram and often probability density. The former allows to appreciate the amount of data per bin, while the latter is necessary as it reflects both measurement values and errors, which are different for SIMS and LA-MC-ICP-MS. Gaussian function was used for probability density calculation (Equation 1, where μ is the expected value and σ the standard deviation).

$$f(x) = \frac{1}{\sigma\sqrt{2\pi}} e^{-\frac{1}{2}\left(\frac{x-\mu}{\sigma}\right)^2} \quad (1)$$

For histograms and probability density distributions, a small bin size was carefully chosen, so that the distributions do not vary with bin boundaries. However, the small bin size adopted here can induce minor peaks that might not be representative. Histograms and probability density distributions are shown with 0.15 ‰ bin size, in a range from -5.5 to $+5.5 \text{ ‰}$. Finally, the nonparametric Mann Whitney U test was used to evaluate the probability of two independent non-gaussian distributions to be equal.

3. Results

About 2000 Fe isotope compositions of synsedimentary or diagenetic pyrite grains were compiled, with values between -4.87 and +5.04 ‰ (Figure 1, Table 1). This wide range is constant throughout the studied interval (3.8 to 1.8 Ga). The medians show no specific time evolution (Figure 1), strongly contrasting with those compiled for bulk $\delta^{56}\text{Fe}$ values of pyrites (Heard and Dauphas, 2020).

Information on the pyrite grain size was not available in all previous publications. Among the grains for which the size was specified, most of them are millimetric (Figure 2). These large grains have $\delta^{56}\text{Fe}$ values ranging from -4 to +4 ‰, with most values clustering between -2 and +2 ‰. $\delta^{56}\text{Fe}$ values of 0.1 to 1 mm-sized grains range from -3 to +1.5 ‰. Mid-size (50 to 100 μm) grains are mostly positive, with values up to +3 ‰, while small (<50 μm) grains span a $\delta^{56}\text{Fe}$ from -2 to +4 ‰.

Pyrite compiled in the present study experienced various metamorphic grades. The range of $\delta^{56}\text{Fe}$ values in amphibolite facies is slightly narrower compared to prehnite-pumpellyite and greenschist facies, but the corresponding number of data is also lower (316 *vs* > 700; Figure 3).

Fe isotope composition of pyrite depends on host-rock lithology (Figure 4). The distributions observed in stromatolites and cherts are bimodal and similar (Mann Whitney U =102113, p=0.86, two-sided). In contrast, carbonates and BIFs show a monomodal and more restricted range from -3.4 to +0.57 ‰ and from +0.25 to +2.35 ‰ respectively. Interestingly, carbonates display mostly negative values whereas BIFs exclusively contain positive values. It is worth noting that the number of analyses for these lithologies is

the smallest (n=45 for carbonates, and n=90 for BIFs). Detrital sediments show a large multimodal range of distribution from -4.18 to +5.04 ‰.

The $\delta^{56}\text{Fe}$ temporal evolution is represented in Figure 5 for various intervals including Eoarchean (>3.6 Ga), Paleoarchean (3.6-3.2 Ga), Mesoarchean and Neoarchean (3.2-2.8 and 2.8-2.5 Ga). Mesoarchean and Neoarchean intervals were merged because only 11 data were available for Mesoarchean pyrites, at 2.9 Ga. The Paleoproterozoic was subdivided as Siderian and Rhyacian (2.5-2.05 Ga), and Orosirian and Statherian (2.05-1.6 Ga). Data in the Eoarchean and Paleoproterozoic time bins only include 1 or 2 locations, while data in the Paleo-, Meso- and Neoarchean intervals comprise 8 different locations, therefore being statistically more robust. During Eoarchean, a negative and two positive modes are observed, around -1, 0.75 and 1.8 ‰. In the Paleoarchean, negative values are mostly comprised between 0 and -2 ‰, with a mode centered around -1.5 ‰, and one main positive mode is observed at 0.75 ‰. Between Mesoarchean and Neoarchean, the negative mode at -1.5 ‰ is preserved, while the positive one becomes larger, encompassing $\delta^{56}\text{Fe}$ values from 0 to 1 ‰. A 0-centered mode becomes distinct between 2.5 and 2.05 Ga, as the positive and negative modes shift to values of 2.25 and -2.5 ‰, respectively. In the late Paleoproterozoic, the $\delta^{56}\text{Fe}$ range turns into a monomodal distribution, with a main peak around -0.75 ‰. An important observation is that the positive mode is dominant in the $\delta^{56}\text{Fe}$ distributions from Paleoarchean, Mesoarchean, Neoarchean, and the first half of the Paleoproterozoic.

4. Discussion

4.1. Discrepancy between bulk and *in situ* $\delta^{56}\text{Fe}$ evolution

The large and constant range observed for the secular evolution of *in situ* pyrite $\delta^{56}\text{Fe}$ values (Figure 1) is at odds with the shift from negative to positive values visible in the bulk $\delta^{56}\text{Fe}$ compilation from Archean to late Paleoproterozoic (Heard and Dauphas, 2020). For pyrite older than 2.96 Ga, a comparison between bulk and *in situ* $\delta^{56}\text{Fe}$ values is meaningless, due to the difference in number of data (4 *vs* 690). The distinct negative $\delta^{56}\text{Fe}$ excursion between 2.7 and 2.5 Ga determined from bulk analyses has no equivalent in *in situ* data. This discrepancy could arise from a loss of spatial $\delta^{56}\text{Fe}$ heterogeneity when preparing samples for bulk analyses (Yoshiya et al., 2015b). Alternatively, it may reflect a sampling bias. Large pyrite grains are routinely analysed in the case of bulk measurements, as those are easily extracted from their matrix. The compilation presented by Heard and Dauphas (2020) almost exclusively includes millimetre-scale pyrite grains, largely hosted in black shales (see Rouxel et al., 2005; Archer and Vance, 2006; Hofmann et al., 2009; Busigny et al., 2017; Eickmann et al., 2018). In contrast, *in situ* techniques allow the measurement of smaller pyrite grains, at the micrometer-scale, in any type of sedimentary lithology (*e.g.*, Whitehouse and Fedo, 2007; Nishizawa et al., 2010; Yoshiya et al., 2012; Marin-Carbonne et al., 2014; Agangi et al., 2015; Virtasalo et al., 2015; Yoshiya et al., 2015a,b; Galić et al., 2017; Czaja et al., 2018; Marin-Carbonne et al., 2020; Decraene et al., 2021b).

The differences observed in the two compilations can therefore arise from sample bias: pyrite $\delta^{56}\text{Fe}$ could be partially driven by lithology (Figure 4),

and although it is not reflected by the data presented in this study (Figure 2), millimetric and micrometric pyrite grains may not record the same formation processes. These aspects should be further explored in the future, by combining both *in situ* and bulk isotopic analyses on the same rock samples.

4.2. Limited influence of metamorphism on pyrite iron isotope composition

Pyrite samples considered in the present compilation experienced various metamorphic grades, from prehnite-pumpellyite to amphibolite facies conditions. Hence, the effect of post-depositional metamorphism on $\delta^{56}\text{Fe}$ values must be assessed. At high temperature, isotope exchange can proceed and eventually reach equilibrium. This type of exchange homogenizes isotope ratios, leading to narrow Fe isotope distributions (Hyslop et al., 2008). The large $\delta^{56}\text{Fe}$ variability observed in pyrite from all metamorphic grades (Figure 3) indicates that it has not been reset, as also suggested in previous SIMS studies (Whitehouse and Fedo, 2007; Galić et al., 2017; Marin-Carbonne et al., 2020). However, decreasing standard deviation with increasing metamorphic grade may reflect a slight influence of metamorphism. For the amphibolite facies, most data were obtained from a small number of samples from the Isua Greenstone Belt (3.8 Ga, Greenland) and the Talvi-vaara Formation (1.95 Ga, Finland), which may not be widely representative. Interestingly, both modes are present in the $\delta^{56}\text{Fe}$ distribution of pyrite from the Isua Greenstone Belt (Figure 5a, b). This bimodality can hardly be explained by a unique process, such as metamorphism. Therefore, we conclude that primary pyrite $\delta^{56}\text{Fe}$ signatures were likely preserved in Archean and Proterozoic rocks, even in those which experienced amphibolite-facies metamorphism.

4.3. Pyrite records partial iron oxidation

Strictly positive $\delta^{56}\text{Fe}$ values are observed in pyrite from BIFs (Figure 4), most likely reflecting Fe-(oxy)hydroxides reduction in the sediments. In detail, aqueous Fe(II) was first supplied to the ocean by hydrothermal vents with $\delta^{56}\text{Fe}$ of -0.5 to +0.1 ‰ (Rouxel et al., 2005), or by continental weathering (Decraene et al., 2021b). Fe(II) from the deep waters was transferred upwards by upwelling and ocean circulation, where it could be partially oxidized by photo-oxidation, by photosynthetically produced O_2 , and/or by anoxygenic photosynthesis (Dauphas et al., 2004; Bekker et al., 2010; Konhauser et al., 2017). Aqueous Fe(III) readily precipitated as iron (oxy)hydroxide, with an apparent isotope fractionation of +1 to +1.5 ‰ (Bullen et al., 2001; Croal et al., 2004; Nie et al., 2017), producing positive Fe isotope compositions as commonly measured in BIF Fe (oxy)hydroxides (Planavsky et al., 2012; Dauphas et al., 2017). In this context, BIF pyrite grains could form through complete heavy Fe (oxy)hydroxides sulfidation, thus retaining their initial positive isotope composition. Positive $\delta^{56}\text{Fe}$ modes are also present in the distributions of stromatolites and cherts, and we suggest that the corresponding pyrite particles derive from heavy Fe-(oxy)hydroxides. In summary, positive Fe isotope compositions in BIFs, stromatolites and cherts from various geological formations point to partial aqueous Fe(II) oxidation in the Archean oceans, a phenomenon which was often suggested in the literature (*e.g.*, Ostrander et al., 2022). The compilation presented here implies that this mechanism likely existed as early as 3.8 Ga, in good agreement with bulk rock analyses of metamorphic Iron Formations from Greenland (Dauphas et al., 2004; Czaja et al., 2013).

4.4. Pyrite records Fe kinetic abiotic and microbial processes

Iron isotope composition in pyrite from all ages displays a negative $\delta^{56}\text{Fe}$ mode ranging from -2.5 to -1 ‰ (Figure 5). Three main hypotheses could potentially explain such negative $\delta^{56}\text{Fe}$ values in pyrite and are discussed below.

First, Rouxel et al. (2005) proposed that partial oxidation and precipitation of large amounts of seawater Fe(II) as isotopically heavy iron (oxy)hydroxides would leave a pool of light residual dissolved Fe(II) from which pyrite precursors could precipitate. This model implies that pyrite and iron (oxy)hydroxide should record parallel distillation trends from heavy to light isotope compositions (Heard and Dauphas, 2020). As described in subsection 4.3, pyrite with positive $\delta^{56}\text{Fe}$ values probably retains the composition of its iron (oxy)hydroxide precursor. Thus, the shift in opposite directions of the positive and negative $\delta^{56}\text{Fe}$ modes between the 3.2-2.5 and 2.5-2.05 Ga intervals (Figure 5) does not support this formation mechanism. However, data from the latter interval come from only two different locations. Therefore, distillation of the seawater Fe(II) reservoir as a contributor to pyrite formation mechanism cannot completely be ruled out.

Secondly, non-redox kinetic reactions could account for a large part of the negative pyrite Fe isotope compositions (Guilbaud et al., 2011; Heard and Dauphas, 2020). Variable pyrite precipitation rate can induce large isotopic fractionation range (Guilbaud et al., 2011; Mansor and Fantle, 2019). $\delta^{56}\text{Fe}$ values as low as -3 ‰ are obtained when the precipitation rate is faster than the isotope exchange (Mansor and Fantle, 2019). Pyrite precipitation rate depends on Fe/S ratio, whose variation controls the kinetic *vs* equilibrium

extents. In the early Archean ocean, pyrite precipitation was likely slow, due to limited sulfide availability (Mansor and Fantle, 2019). Increased sulfate delivery imparted by the GOE (Lyons et al., 2014) would have increased pyrite precipitation rate and could potentially explain the shift of the negative $\delta^{56}\text{Fe}$ mode to more negative values between 3.2 and 2.05 Ga. However, large variations of S isotope composition were reported in Archean stromatolites, pointing to local enrichments in sulfate (Bontognali et al., 2012; Marin-Carbonne et al., 2018). Following Mansor and Fantle (2019), such conditions should lead to markedly negative pyrite Fe isotope compositions in stromatolites, which are not observed (Figure 4). For other lithologies, like cherts, carbonates and detrital sediments, the sulfate content is poorly constrained (Halevy, 2013). Therefore, a kinetic control cannot be excluded in these environments. Kinetically precipitated pyrites are expected to show a correlation between particle size and Fe isotope composition (Mansor and Fantle, 2019), which is not observed from the present compilation (Figure 2). Similar conclusions were drawn by Decraene et al. (2021b) on micropyrrite from the Tumbiana Formation. Kinetic precipitation should produce a specific isotope profile within a single pyrite grain. Precipitation rate is predicted to slow down as the reaction proceeds (Mansor and Fantle, 2019), thus $\delta^{56}\text{Fe}$ values should gradually increase from light to heavy isotope composition, from inner to outer parts of the pyrite crystal. Such Fe isotope profiles are not observed in pyrite from Mendon black cherts (Marin-Carbonne et al., 2020). We therefore conclude that some of the pyrite grains may be produced by kinetic precipitation, but this process cannot be considered as the sole driver for pyrite formation.

Lastly, isotopically light pyrites could precipitate from partial reduction of iron (oxy)hydroxides, either abiotically or under the influence of DIR bacteria (Crosby et al., 2007; Johnson et al., 2008; Frierdich et al., 2019). Abiotic reduction is associated with isotope fractionation between -2.6 and -3.1 ‰ (Wiederhold et al., 2006; Frierdich et al., 2019), not significantly different from DIR fractionation, -2.9 ‰ (Crosby et al., 2007). Accordingly, iron isotope fractionation alone cannot be used to assess pyrite biogenicity. Stromatolites often contain micropyrrite closely associated with organic matter, likely corresponding to remains of microbial mats (Bontognali et al., 2012; Marin-Carbone et al., 2018; Lepot et al., 2019; Decraene et al., 2021b). In our compilation, stromatolites originating from four different locations display a bimodal $\delta^{56}\text{Fe}$ distributions with a difference of -2.5 ‰ (Figure 4), consistent with DIR microbial activity, of pyrite with positive $\delta^{56}\text{Fe}$ record the composition of primary Fe (oxy)hydroxides. It may also explain the bimodal $\delta^{56}\text{Fe}$ distribution observed in cherts (Figure 4). Specifically, organic carbon-rich cherts show mostly negative $\delta^{56}\text{Fe}$ distributions (Figure 6). Although organic carbon in cherts is rarely measured and these results might therefore not be representative, the latter suggest that organic matter availability controls Fe reduction. Several experimental works showed that organic matter might catalyze Fe(III) reduction and pyrite formation, by providing an active surface for pyrite nucleation and therefore increasing the corresponding reaction rate (Canfield et al., 1998; Rickard et al., 2007; Rickard, 2012; Duverger et al., 2021). Consequently, organic matter availability could drive Fe isotope fractionation during pyrite precipitation. The negative Fe isotope compositions measured in carbonates could also have been produced

by DIR (Figure 4), as previously suggested by Yoshiya et al. (2012) for the Tumbiana Formation.

In summary, the negative $\delta^{56}\text{Fe}$ values cannot be explained by a single process. Partial reduction of Fe (oxy)hydroxides followed by pyrite precipitation, alongside kinetic precipitation from dissolved Fe(II), could both have contributed to pyrite formation during the Archean and Paleoproterozoic.

4.5. Temporal evolution of micropyrrite $\delta^{56}\text{Fe}$ values

The evolution of bulk $\delta^{56}\text{Fe}$ values in sedimentary pyrite through time has been proposed to reflect Fe/S ratio variations in seawater (Guilbaud et al., 2011; Mansor and Fantle, 2019; Heard and Dauphas, 2020). In particular, the shift from negative to positive $\delta^{56}\text{Fe}$ values from Archean to Paleoproterozoic could reflect an increase in sulfate delivery to seawater, imparted by continental oxidative weathering following the GOE (Canfield, 1998; Lyons et al., 2021). Positive correlation between Archean and Paleoproterozoic pyrite $\delta^{56}\text{Fe}$ and S isotope compositions of sulfide led Heard and Dauphas (2020) to suggest a primary control of the Fe/S ratio in the ocean on Fe isotope signatures in pyrite.

Our compilation of *in situ* data shows a different pattern (Figure 1). The quasi-systematic prominence of the positive mode suggests that pyrite was mostly formed via Fe (oxy)hydroxide reduction, starting 3.6 Ga ago. As oxidative weathering after the GOE likely increased the input of Fe (oxy)hydroxide with $\delta^{56}\text{Fe}$ close to 0 ‰, the occurrence of 0 ‰ pyrite grains in stromatolites, cherts or BIFs post-dating the GOE would confirm the proposed pyrite formation mechanism from Fe (oxy)hydroxide quantitative reduction (Section 4.3). However, only few microanalyses were carried out

on such samples (only 18 analyses in 2.32 Ga old stromatolites).

Furthermore, $\delta^{56}\text{Fe}$ values close to 0 ‰ become more significant between 3.2 and 2.05 Ga. These values were measured in pyrite grains hosted in detrital sediments (Figure 4), and they are similar to the crustal average $\delta^{56}\text{Fe}$ value (Beard et al., 2003). Several studies suggest that the lithosphere might have stabilized between 3.2 and 2.5 Ga, leading to the development and thickening of the continental crust (Dhuime et al., 2015; Cawood et al., 2018). This would in turn have led to the onset of continental weathering, that was evidenced in formations as old as 3.2 Ga (Hessler and Lowe, 2006). Delivery of continental Fe(II)-bearing species through rivers before the GOE (Hao et al., 2017) could have supplied the ocean detrital pyrites delivered to the ocean. Pyrite grains from various formations (3.1 to 2.6 Ga) in Zimbabwe and Kaapvaal cratons were described as detrital by Hofmann et al. (2009), based on petrographic evidence, ages greater than the depositional age, and multiple S isotope analyses. They used Fe and S isotope compositions to constrain the pyrite origin, and suggested that $\delta^{56}\text{Fe}$ values clustering around 0 ‰, associated with small variations in $^{34}\text{S}/^{32}\text{S}$ ratios and S mass independent fractionations close to 0 ‰ reflect a crustal origin. Moreover, Agangi et al. (2015) measured Fe isotope compositions in 2.7 Ga pyrite, that they interpreted to be of detrital origin. Inclusion-rich pyrites have a high $\delta^{56}\text{Fe}$ average (2.75 ‰), compared to concentrically laminated pyrites (0.2 ‰). A detrital origin of pyrite cannot be confirmed from the present compilation as only Fe isotope compositions are available and no obvious pyrite shape or size can be used as detrital indicator.

Interpretation of $\delta^{56}\text{Fe}$ distributions in the other time intervals is uncer-

tain and not discussed herein, as the small number of pyrite localities may induce a lack of representativity.

In summary, microscale $\delta^{56}\text{Fe}$ distributions in pyrite point to Fe (oxy)hydroxide precursor as early as 3.6 Ga ago. In addition, an influence of continental weathering might be recorded in Fe isotope signatures from 3.2 Ga. Further investigations of the $\delta^{56}\text{Fe}$ evolution through time would increase the present database and possibly strengthen the tentative conclusions drawn here.

5. Conclusions

In situ Fe isotope compositions in Archean and Paleoproterozoic pyrite show distinct trends from those obtained by conventional bulk measurements of pyrite $\delta^{56}\text{Fe}$ values. The origin of the discrepancy between *in situ* and bulk Fe isotope signatures is not clear, and should be addressed in future works, for instance by coupling *in situ* and bulk techniques on the same samples. The $\delta^{56}\text{Fe}$ distributions in various lithologies point to several pyrite formation mechanisms: total and partial Fe (oxy)hydroxide reduction, that could be abiotic and/or potentially microbially mediated, and kinetic pyrite precipitation from dissolved Fe(II). These mechanisms might have existed since since 3.8 Ga, as suggested by the consistent evolution of the $\delta^{56}\text{Fe}$ distributions throughout early Archean to Paleoproterozoic. The high occurrence of pyrite with positive $\delta^{56}\text{Fe}$ values indicates that Fe(III) reduction was a dominant pyrite formation pathway. Importantly, this study underlines the lack of microanalyses in specific lithologies and time intervals, that hinders robust interpretation of the isotope signature records.

Acknowledgements

We are thankful to Pascal Phillipot, Frantz Ossa Ossa and Axel Hofmann for providing the TCDP, Gabon, and Barberton samples, respectively. V.B. thanks the Institut Universitaire de France for funding (IUF#2017-2021). This research was supported by the European Research Council (ERC) under the European Union's Horizon 2020 research and innovation program (STROMATA, grant agreement 759289). We thank Anne-Sophie Bouvier, Florent Plane and Thomas Bovay for their SIMS expertise. The SwissSIMS is hosted by the Center for Advanced Surface Analyse, CASA, a joint facility between UNIL and EPFL. Virgil Pasquier and Itay Halevy are thanked for fruitful discussions and comments on an earlier version of this manuscript.

References

- Agangi, A., Hofmann, A., Rollion-Bard, C., Marin-Carbonne, J., Cavalazzi, B., Large, R., Meffre, S., 2015. Gold accumulation in the Archaean Witwatersrand Basin, South Africa — Evidence from concentrically laminated pyrite. *Earth-Science Reviews* 140, 27–53. doi:10.1016/j.earscirev.2014.10.009.
- Anbar, A.D., Rouxel, O., 2007. Metal Stable Isotopes in Paleoceanography. *Annual Review of Earth and Planetary Sciences* 35, 717–746. doi:10.1146/annurev.earth.34.031405.125029.
- Archer, C., Vance, D., 2006. Coupled Fe and S isotope evidence for Archean microbial Fe(III) and sulfate reduction. *Geology* 34, 153. doi:10.1130/G22067.1.
- Balci, N., Bullen, T.D., Witte-Lien, K., Shanks, W.C., Motelica, M., Manderack, K.W., 2006. Iron isotope fractionation during microbially stimulated Fe(II) oxidation and Fe(III) precipitation. *Geochimica et Cosmochimica Acta* 70, 622–639. doi:doi:10.1016/j.gca.2005.09.025.
- Bekker, A., Holland, H.D., Wang, P.L., Rumble, D., Stein, H.J., Hannah, J.L., Coetzee, L.L., Beukes, N.J., 2004. Dating the rise of atmospheric oxygen. *Nature* 427, 117–120. doi:10.1038/nature02260.
- Bekker, A., Slack, J.F., Planavsky, N., Kraepel, B., Hofmann, A., Konhauser, K.O., Rouxel, O.J., 2010. Iron Formation: The Sedimentary Product of a Complex Interplay among Mantle, Tectonic, Oceanic, and Biospheric Processes. *Economic Geology* 105, 467–508. doi:10.2113/gsecongeo.105.3.467.

- Bontognali, T.R.R., Sessions, A.L., Allwood, A.C., Fischer, W.W., Grotzinger, J.P., Summons, R.E., Eiler, J.M., 2012. Sulfur isotopes of organic matter preserved in 3.45-billion-year-old stromatolites reveal microbial metabolism. *Proceedings of the National Academy of Sciences* 109, 15146–15151. doi:10.1073/pnas.1207491109.
- Bullen, T.D., White, A.F., Childs, C.W., Vivit, D.V., Schulz, M.S., 2001. Demonstration of significant abiotic iron isotope fractionation in nature. *Geology* 29, 699. doi:10.1130/0091-7613(2001)029;0699:DOSAII;2.0.CO;2.
- Busigny, V., Marin-Carbonne, J., Muller, E., Cartigny, P., Rollion-Bard, C., Assayag, N., Philippot, P., 2017. Iron and sulfur isotope constraints on redox conditions associated with the 3.2 Ga barite deposits of the Mapepe Formation (Barberton Greenstone Belt, South Africa). *Geochimica et Cosmochimica Acta* 210, 247–266. doi:10.1016/j.gca.2017.05.002.
- Canfield, D.E., 1998. A new model for Proterozoic ocean chemistry. *Nature* 396, 450–453. doi:10.1038/24839.
- Canfield, D.E., Thamdrup, B., Fleischer, S., 1998. Isotope fractionation and sulfur metabolism by pure and enrichment cultures of elemental sulfur-disproportionating bacteria. *Limnology and Oceanography* 43, 253–264. doi:10.4319/lo.1998.43.2.0253.
- Craddock, P.R., Dauphas, N., 2011. Iron and carbon isotope evidence for microbial iron respiration throughout the Archean. *Earth and Planetary Science Letters* 303, 121–132. doi:10.1016/j.epsl.2010.12.045.

- Croal, L.R., Johnson, C.M., Beard, B.L., Newman, D.K., 2004. Iron isotope fractionation by Fe(II)-oxidizing photoautotrophic bacteria. *Geochimica et Cosmochimica Acta* 68, 1227–1242. doi:10.1016/j.gca.2003.09.011.
- Crosby, H.A., Johnson, C.M., Roden, E.E., Beard, B.L., 2005. Coupled Fe(II)-Fe(III) Electron and Atom Exchange as a Mechanism for Fe Isotope Fractionation during Dissimilatory Iron Oxide Reduction. *Environmental Science & Technology* 39, 6698–6704. doi:10.1021/es0505346.
- Crosby, H.A., Roden, E.E., Johnson, C.M., Beard, B.L., 2007. The mechanisms of iron isotope fractionation produced during dissimilatory Fe(III) reduction by *Shewanella putrefaciens* and *Geobacter sulfurreducens*. *Geobiology* 5, 169–189. doi:10.1111/j.1472-4669.2007.00103.x.
- Czaja, A.D., Johnson, C.M., Beard, B.L., Roden, E.E., Li, W., Moorbath, S., 2013. Biological Fe oxidation controlled deposition of banded iron formation in the ca. 3770Ma Isua Supracrustal Belt (West Greenland). *Earth and Planetary Science Letters* 363, 192–203. doi:10.1016/j.epsl.2012.12.025.
- Czaja, A.D., Van Kranendonk, M.J., Beard, B.L., Johnson, C.M., 2018. A multistage origin for Neoproterozoic layered hematite-magnetite iron formation from the Weld Range, Yilgarn Craton, Western Australia. *Chemical Geology* 488, 125–137. doi:10.1016/j.chemgeo.2018.04.019.
- Dauphas, N., John, S.G., Rouxel, O., 2017. Iron Isotope Systematics. *Reviews in Mineralogy and Geochemistry* 82, 415–510. doi:10.2138/rmg.2017.82.11.

- Dauphas, N., van Zuilen, M., Wadhwa, M., Davis, A.M., Marty, B., Janney, P.E., 2004. Clues from Fe Isotope Variations on the Origin of Early Archean BIFs from Greenland. *Science* 306, 2077–2080. doi:10.1126/science.1104639.
- Decraene, M.N., Marin-Carbonne, J., Bouvier, A.S., Villeneuve, J., Bouden, N., Luais, B., Deloule, E., 2021a. High-spatial-resolution measurements of iron isotopes in pyrites by secondary ion mass spectrometry using the new Hyperion-II radio-frequency plasma source. *Rapid Communications in Mass Spectrometry* 35, e8986. doi:10.1002/rcm.8986.
- Decraene, M.N., Marin-Carbonne, J., Thomazo, C., Olivier, N., Philippot, P., Strauss, H., Deloule, E., 2021b. Intense biogeochemical iron cycling revealed in Neoproterozoic micropyrrites from stromatolites. *Geochimica et Cosmochimica Acta* 312, 299–320. doi:10.1016/j.gca.2021.07.020.
- Duverger, A., Bernard, S., Viennet, J.C., Miot, J., Busigny, V., 2021. Formation of Pyrite Spherules From Mixtures of Biogenic FeS and Organic Compounds During Experimental Diagenesis. *Geochemistry, Geophysics, Geosystems* 22. doi:10.1029/2021GC010056.
- Eickmann, B., Hofmann, A., Wille, M., Bui, T.H., Wing, B.A., Schoenberg, R., 2018. Isotopic evidence for oxygenated Mesoarchean shallow oceans. *Nature Geoscience* 11, 133–138. doi:10.1038/s41561-017-0036-x.
- Friedrich, A.J., Nebel, O., Beard, B.L., Johnson, C.M., 2019. Iron isotope exchange and fractionation between hematite (α -Fe₂O₃) and aqueous Fe(II): A combined three-isotope and reversal-approach to

- equilibrium study. *Geochimica et Cosmochimica Acta* 245, 207–221. doi:10.1016/j.gca.2018.10.033.
- Galić, A., Mason, P.R., Mogollón, J.M., Wolthers, M., Vroon, P.Z., Whitehouse, M.J., 2017. Pyrite in a sulfate-poor Paleoarchean basin was derived predominantly from elemental sulfur: Evidence from 3.2 Ga sediments in the Barberton Greenstone Belt, Kaapvaal Craton. *Chemical Geology* 449, 135–146. doi:10.1016/j.chemgeo.2016.12.006.
- Guilbaud, R., Butler, I.B., Ellam, R.M., 2011. Abiotic Pyrite Formation Produces a Large Fe Isotope Fractionation. *Science* 332, 1548–1551. doi:10.1126/science.1202924.
- Halevy, I., 2013. Production, preservation, and biological processing of mass-independent sulfur isotope fractionation in the Archean surface environment. *Proceedings of the National Academy of Sciences* 110, 17644–17649. doi:10.1073/pnas.1213148110.
- Heard, A.W., Dauphas, N., 2020. Constraints on the coevolution of oxic and sulfidic ocean iron sinks from Archean–Paleoproterozoic iron isotope records. *Geology* doi:10.1130/G46951.1.
- Hofmann, A., Bekker, A., Rouxel, O., Rumble, D., Master, S., 2009. Multiple sulphur and iron isotope composition of detrital pyrite in Archaean sedimentary rocks: A new tool for provenance analysis. *Earth and Planetary Science Letters* 286, 436–445. doi:10.1016/j.epsl.2009.07.008.
- Hyslop, E.V., Valley, J.W., Johnson, C.M., Beard, B.L., 2008. The effects of metamorphism on O and Fe isotope compositions in the Biwabik Iron For-

- mation, northern Minnesota. *Contributions to Mineralogy and Petrology* 155, 313–328. doi:10.1007/s00410-007-0244-2.
- Johnson, C.M., Beard, B.L., 2006. Fe isotopes: An emerging technique for understanding modern and ancient biogeochemical cycles. *GSA Today* 16, 4. doi:10.1130/GSAT01611A.1.
- Johnson, C.M., Beard, B.L., Roden, E.E., 2008. The Iron Isotope Fingerprints of Redox and Biogeochemical Cycling in Modern and Ancient Earth. *Annual Review of Earth and Planetary Sciences* 36, 457–493. doi:10.1146/annurev.earth.36.031207.124139.
- Klein, C., 2005. Some Precambrian banded iron-formations (BIFs) from around the world: Their age, geologic setting, mineralogy, metamorphism, geochemistry, and origins. *American Mineralogist* 90, 1473–1499. doi:10.2138/am.2005.1871.
- Konhauser, K., Planavsky, N., Hardisty, D., Robbins, L., Warchola, T., Haugegaard, R., Lalonde, S., Partin, C., Oonk, P., Tsikos, H., Lyons, T., Bekker, A., Johnson, C., 2017. Iron formations: A global record of Neoproterozoic to Palaeoproterozoic environmental history. *Earth-Science Reviews* 172, 140–177. doi:10.1016/j.earscirev.2017.06.012.
- Lepot, K., Williford, K.H., Philippot, P., Thomazo, C., Ushikubo, T., Kitajima, K., Mostefaoui, S., Valley, J.W., 2019. Extreme ^{13}C -depletions and organic sulfur content argue for S-fueled anaerobic methane oxidation in 2.72 Ga old stromatolites. *Geochimica et Cosmochimica Acta* 244, 522–547. doi:10.1016/j.gca.2018.10.014.

- Loneragan, D.J., Jenter, H.L., Coates, J.D., Phillips, E.J., Schmidt, T.M., Lovley, D.R., 1996. Phylogenetic analysis of dissimilatory Fe(III)-reducing bacteria. *Journal of Bacteriology* 178, 2402–2408. doi:10.1128/jb.178.8.2402-2408.1996.
- Lyons, T.W., Diamond, C.W., Planavsky, N.J., Reinhard, C.T., Li, C., 2021. Oxygenation, Life, and the Planetary System during Earth's Middle History: An Overview. *Astrobiology* 21, 906–923. doi:10.1089/ast.2020.2418.
- Lyons, T.W., Fike, D.A., Zerkle, A., 2015. Emerging Biogeochemical Views of Earth's Ancient Microbial Worlds. *Elements* 11, 415–421. doi:10.2113/gselements.11.6.415.
- Lyons, T.W., Reinhard, C.T., Planavsky, N.J., 2014. The rise of oxygen in Earth's early ocean and atmosphere. *Nature* 506, 307–315. doi:10.1038/nature13068.
- Mansor, M., Fantle, M.S., 2019. A novel framework for interpreting pyrite-based Fe isotope records of the past. *Geochimica et Cosmochimica Acta* 253, 39–62. doi:10.1016/j.gca.2019.03.017.
- Marin-Carbonne, J., Busigny, V., Miot, J., Rollion-Bard, C., Muller, E., Drabon, N., Jacob, D., Pont, S., Robyr, M., Bontognali, T.R.R., François, C., Reynaud, S., Van Zuilen, M., Philippot, P., 2020. In Situ Fe and S isotope analyses in pyrite from the 3.2 Ga Mendon Formation (Barberton Greenstone Belt, South Africa): Evidence for early microbial iron reduction. *Geobiology* 18, 306–325. doi:10.1111/gbi.12385.

- Marin-Carbonne, J., Remusat, L., Sforza, M.C., Thomazo, C., Cartigny, P., Philippot, P., 2018. Sulfur isotope's signal of nanopyrates enclosed in 2.7 Ga stromatolitic organic remains reveal microbial sulfate reduction. *Geobiology* 16, 121–138. doi:10.1111/gbi.12275.
- Marin-Carbonne, J., Rollion-Bard, C., Bekker, A., Rouxel, O., Agangi, A., Cavalazzi, B., Wohlgemuth-Ueberwasser, C.C., Hofmann, A., McKeegan, K.D., 2014. Coupled Fe and S isotope variations in pyrite nodules from Archean shale. *Earth and Planetary Science Letters* 392, 67–79. doi:10.1016/j.epsl.2014.02.009.
- Marin-Carbonne, J., Rollion-Bard, C., Luais, B., 2011. In-situ measurements of iron isotopes by SIMS: MC-ICP-MS intercalibration and application to a magnetite crystal from the Gunflint chert. *Chemical Geology* 285, 50–61. doi:10.1016/j.chemgeo.2011.02.019.
- Nie, N., Dauphas, N., Greenwood, R.C., 2017. Iron and oxygen isotope fractionation during iron UV photo-oxidation: Implications for early Earth and Mars. *Earth and Planetary Science Letters* 458, 179–191. doi:10.1016/j.epsl.2016.10.035.
- Nishizawa, M., Yamamoto, H., Ueno, Y., Tsuruoka, S., Shibuya, T., Sawaki, Y., Yamamoto, S., Kon, Y., Kitajima, K., Komiya, T., Maruyama, S., Hirata, T., 2010. Grain-scale iron isotopic distribution of pyrite from Precambrian shallow marine carbonate revealed by a femtosecond laser ablation multicollector ICP-MS technique: Possible proxy for the redox state of ancient seawater. *Geochimica et Cosmochimica Acta* 74, 2760–2778. doi:10.1016/j.gca.2010.02.014.

- Ostrander, C.M., Severmann, S., Gordon, G.W., Kendall, B., Lyons, T.W., Zheng, W., Roy, M., Anbar, A.D., 2022. Significance of ^{56}Fe depletions in late-Archean shales and pyrite. *Geochimica et Cosmochimica Acta*, 87–104doi:10.1016/j.gca.2021.10.013.
- Planavsky, N., Rouxel, O.J., Bekker, A., Hofmann, A., Little, C.T., Lyons, T.W., 2012. Iron isotope composition of some Archean and Proterozoic iron formations. *Geochimica et Cosmochimica Acta* 80, 158–169. doi:10.1016/j.gca.2011.12.001.
- Rego, E.S., Busigny, V., Lalonde, S.V., Philippot, P., Bouyon, A., Rossignol, C., Babinski, M., de Cássia Zapparoli, A., 2021. Anoxygenic photosynthesis linked to Neoproterozoic iron formations in Carajás (Brazil). *Geobiology* 19, 326–341. doi:10.1111/gbi.12438.
- Rickard, D., 2012. Sedimentary Pyrite, in: *Developments in Sedimentology*. Elsevier. volume 65, pp. 233–285. doi:10.1016/B978-0-444-52989-3.00006-4.
- Rickard, D., Grimes, S., Butler, I., Oldroyd, A., Davies, K.L., 2007. Botanical constraints on pyrite formation. *Chemical Geology* 236, 228–246. doi:10.1016/j.chemgeo.2006.09.011.
- Rickard, D., Mussmann, M., Steadman, J.A., 2017. Sedimentary Sulfides. *Elements* 13, 117–122. doi:10.2113/gselements.13.2.117.
- Rouxel, O.J., Bekker, A., Edwards, K.J., 2005. Iron Isotope Constraints on the Archean and Paleoproterozoic Ocean Redox State. *Science* 307, 1088–1091. doi:10.1126/science.1105692.

- Virtasalo, J.J., Laitala, J.J., Lahtinen, R., Whitehouse, M.J., 2015. Pyritic event beds and sulfidized Fe (oxyhydr)oxide aggregates in metalliferous black mudstones of the Paleoproterozoic Talvivaara formation, Finland. *Earth and Planetary Science Letters* 432, 449–460. doi:10.1016/j.epsl.2015.09.010.
- Welch, S., Beard, B., Johnson, C., Braterman, P., 2003. Kinetic and equilibrium Fe isotope fractionation between aqueous Fe(II) and Fe(III). *Geochimica et Cosmochimica Acta* 67, 4231–4250. doi:10.1016/S0016-7037(03)00266-7.
- Whitehouse, M.J., Fedo, C.M., 2007. Microscale heterogeneity of Fe isotopes in >3.71 Ga banded iron formation from the Isua Greenstone Belt, southwest Greenland. *Geology* 35, 719. doi:10.1130/G23582A.1.
- Wiederhold, J.G., Kraemer, S.M., Teutsch, N., Borer, P.M., Halliday, A.N., Kretzschmar, R., 2006. Iron Isotope Fractionation during Proton-Promoted, Ligand-Controlled, and Reductive Dissolution of Goethite. *Environmental Science & Technology* 40, 3787–3793. doi:10.1021/es052228y.
- Yoshiya, K., Nishizawa, M., Sawaki, Y., Ueno, Y., Komiya, T., Yamada, K., Yoshida, N., Hirata, T., Wada, H., Maruyama, S., 2012. In situ iron isotope analyses of pyrite and organic carbon isotope ratios in the Fortescue Group: Metabolic variations of a Late Archean ecosystem. *Precambrian Research* 212–213, 169–193. doi:10.1016/j.precamres.2012.05.003.
- Yoshiya, K., Sawaki, Y., Hirata, T., Maruyama, S., Komiya, T., 2015a. In situ iron isotope analysis of pyrites in ~ 3.7 Ga sedimentary protoliths from

the Isua supracrustal belt, southern West Greenland. *Chemical Geology* 401, 126–139. doi:10.1016/j.chemgeo.2015.02.022.

Yoshiya, K., Sawaki, Y., Shibuya, T., Yamamoto, S., Komiya, T., Hirata, T., Maruyama, S., 2015b. In situ iron isotope analyses of pyrites from 3.5 to 3.2 Ga sedimentary rocks of the Barberton Greenstone Belt, Kaapvaal Craton. *Chemical Geology* 403, 58–73. doi:10.1016/j.chemgeo.2015.03.007.

Time interval (Ga)	Locations	Number of analyses	References		
3.8 - 3.6	Isua Greenstone Belt	178	Yoshiya et al. (2015a)		
			Whitehouse and Fedo (2007)		
3.6 - 3.2	Hooggenoeg complex	37	Yoshiya et al. (2015b)		
	Noisy complex	94	Marin-Carbonne et al. (2020)		
	Kromberg complex	23	Galić et al. (2017)		
	Buck Reef	145	Unpublished data		
	Mendon Formation	227	Marin-Carbonne et al. (2014)		
	Mapepe Formation	156	Czaja et al. (2018)		
	Fig Tree	5	Agangi et al. (2015)		
	Moodies	33	Yoshiya et al. (2012)		
3.2 - 2.5	Nsuze group	11	Nishizawa et al. (2010)		
			Unpublished data		
				Bubi Greenstone Belt	35
				Wilgie Mia Formation	13
				Ventersdorp Contact Reef	121
				Tumbiana formation	430
				Maddina formation	19
				Jerrinah Formation	35
2.5 - 2.05	Turee Creek Formation	181	Nishizawa et al. (2010)		
			Unpublished data		
				Francevillian Formation	101
2.05 - 1.8	Talvivaara Formation	138	Virtasalo et al. (2015)		

Table 1: List of geological locations from which pyrite grains were sampled, the corresponding number of analyses, and references in which the data were published, per time interval used in Figure 5. References are given by time interval.

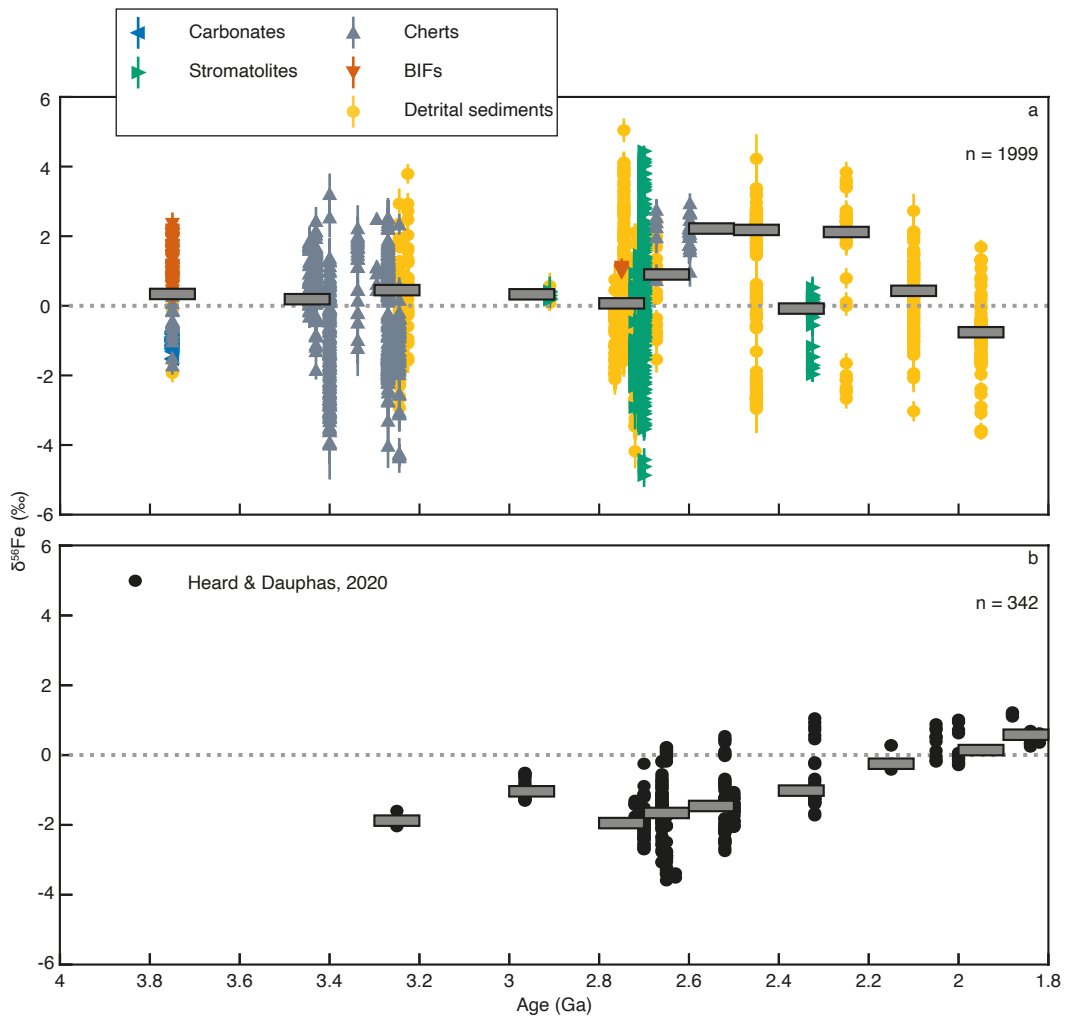


Figure 1: Archean and Paleoproterozoic sedimentary $\delta^{56}\text{Fe}$ records. (a) $\delta^{56}\text{Fe}$ compilation of this study, classified by lithology. The $\delta^{56}\text{Fe}$ were measured by *in situ* analytical methods. (b) Adapted from Heard and Dauphas (2020). The $\delta^{56}\text{Fe}$ values were acquired by bulk conventional techniques. The number of analyses (n) is reported for each study. Medians are plotted as time-bins of 100 Ma.

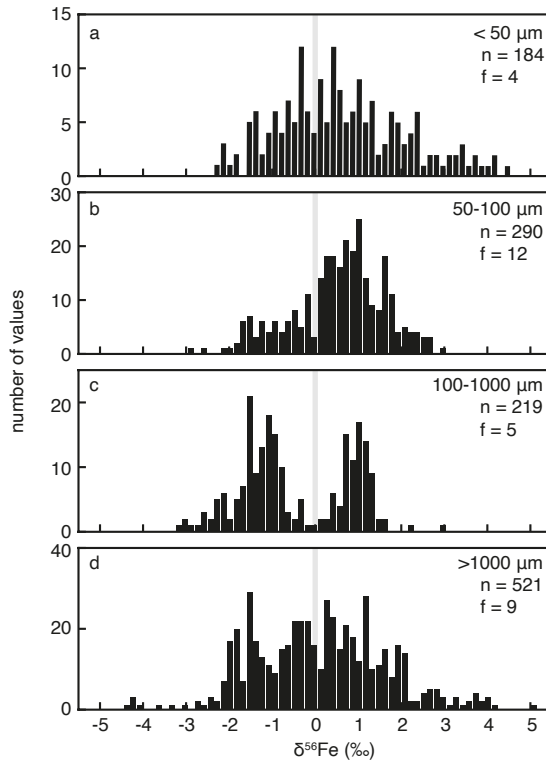


Figure 2: Pyrite $\delta^{56}\text{Fe}$ distributions as a function of pyrite grain size. Four groups are differentiated: (a) grains with size $<50 \mu\text{m}$, (b) grains with size comprised between 50 and $100 \mu\text{m}$, (c) grains with size of a few hundreds of microns, and (d) millimetric grains. Information on pyrite grain size was not systematically available in previous publications. Further detail on grains with size comprised between 100 and $1000 \mu\text{m}$ was not always available. The numbers of values (n) and geological formations (f) are indicated for each histogram. The vertical grey bar represents a $\delta^{56}\text{Fe}$ value of 0 ‰ and is drawn to facilitate comparison between plots.

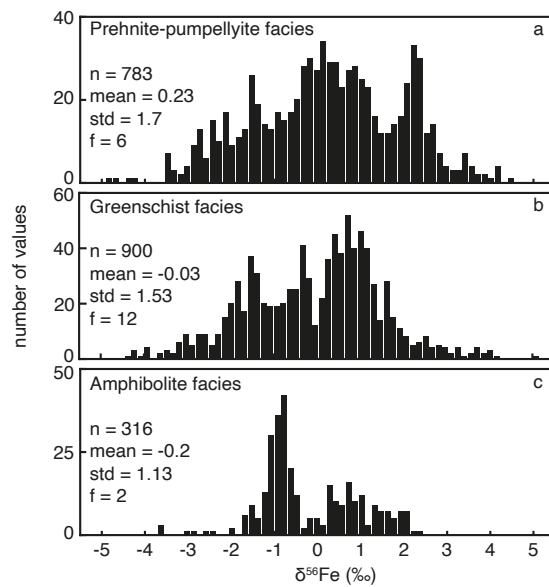


Figure 3: Pyrite $\delta^{56}\text{Fe}$ as a function of metamorphic grade. The number of values (n), mean value, standard deviation (std) and the number of geological formations (f) from which pyrite originates are indicated for each histogram.

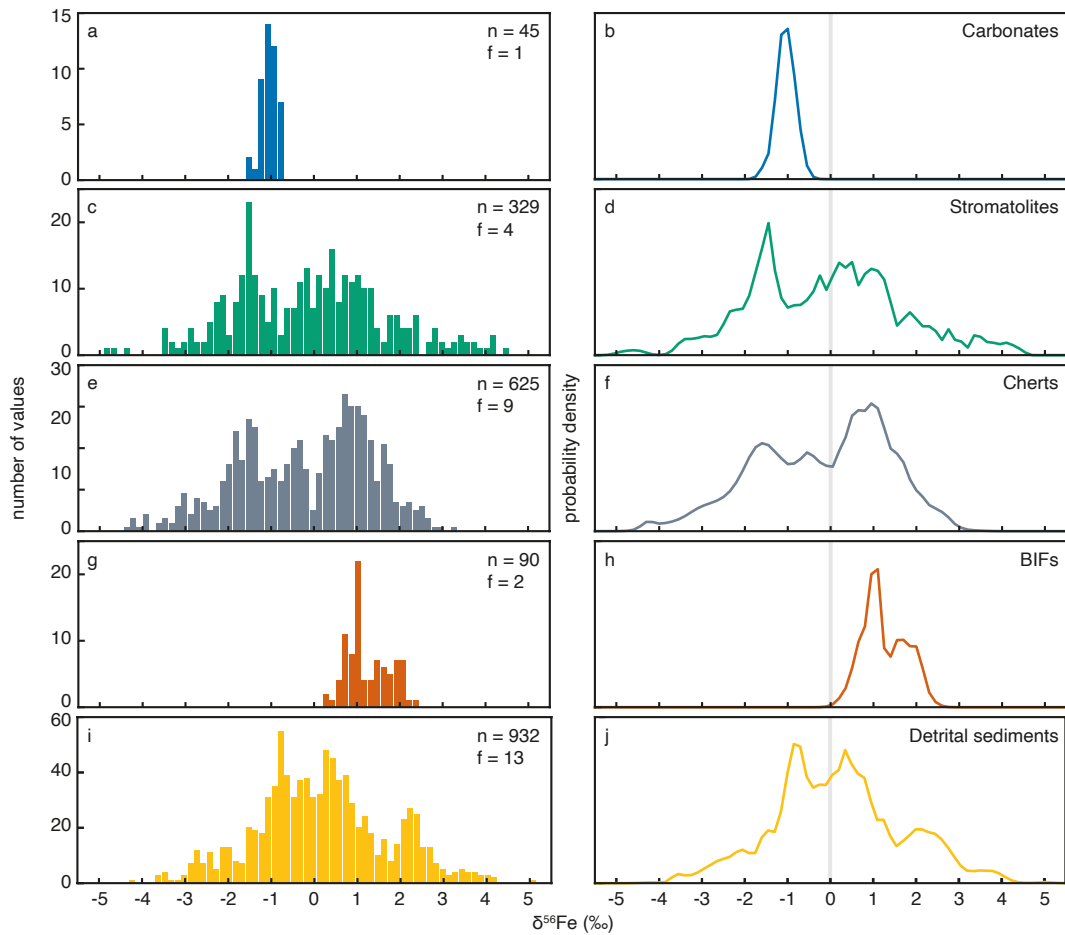


Figure 4: Pyrite $\delta^{56}\text{Fe}$ distributions in carbonates (a, b) stromatolites (c, d), cherts (e, f), BIFs (g, h), and detrital sediments (i, j). The distributions are shown as histograms (a, c, e, g, i) and the corresponding probability density plots (b, d, f, h, j). The numbers of values (n) and geological formations (f) from which pyrite originates are indicated on the histograms. The vertical grey bar on the right panels represents a $\delta^{56}\text{Fe}$ value of 0 ‰ and is drawn to facilitate comparison between plots.

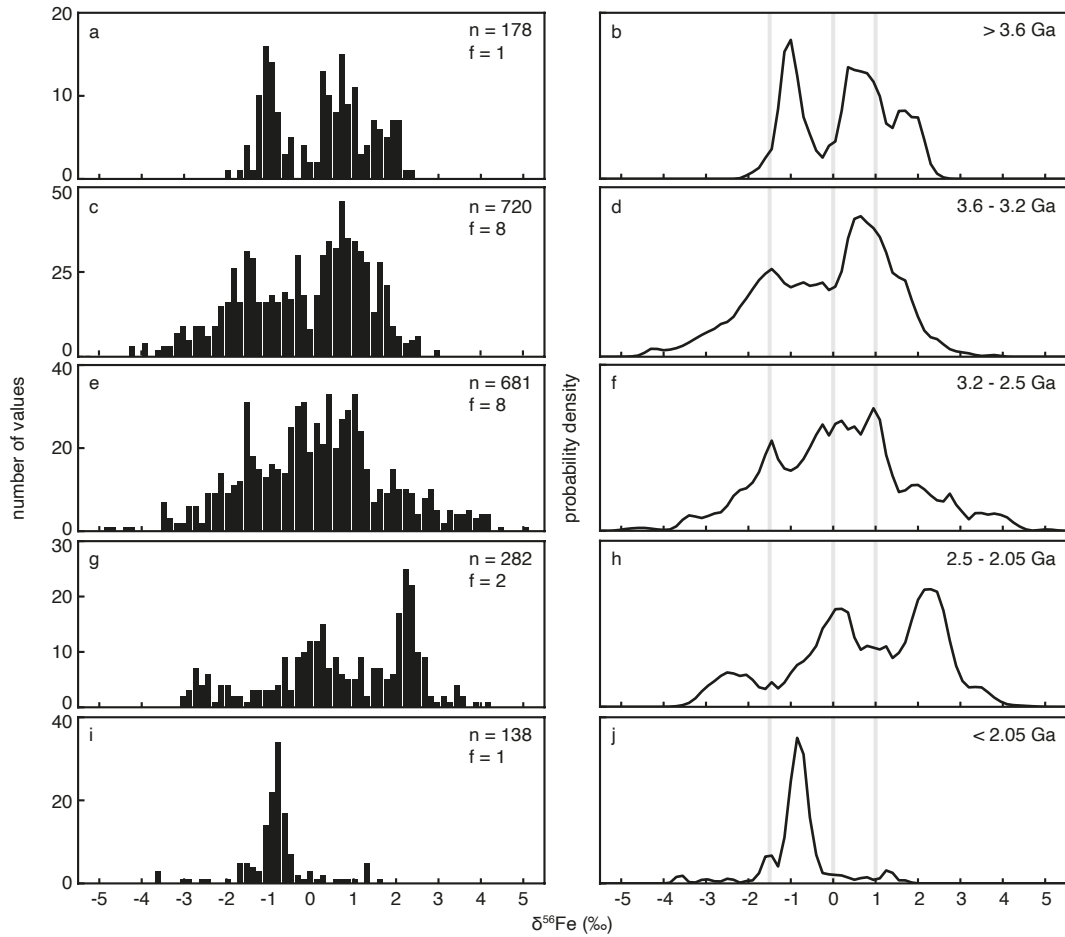


Figure 5: Evolution of pyrite $\delta^{56}\text{Fe}$ distribution over time, shown as histograms (a, c, e, g, i) and the corresponding probability density plots (b, d, f, h, j). The numbers of values (n) and geological formations (f) from which pyrite originates are reported on the histograms. The Eoarchean and late Paleoproterozoic $\delta^{56}\text{Fe}$ distributions (a, b, and i, j) are not discussed, as they each represent only one location, Isua Greenstone Belt and Talvivaara Formation, that are both highly metamorphosed. The three vertical grey bars on the right panels represent $\delta^{56}\text{Fe}$ values of -1.5, 0 and +1 ‰, and are drawn to facilitate comparison between plots.

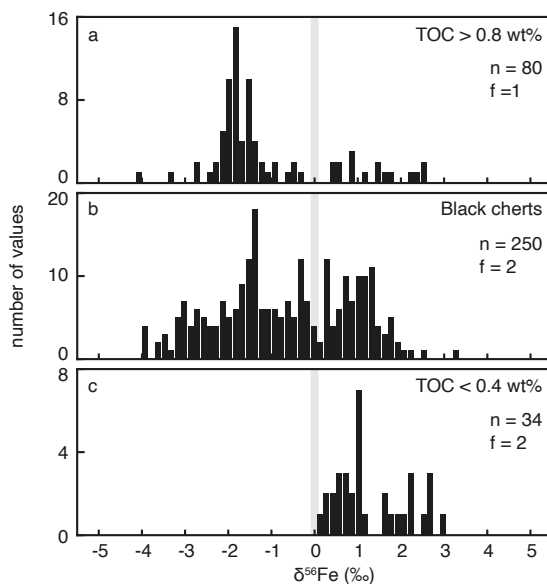


Figure 6: Pyrite $\delta^{56}\text{Fe}$ distributions in cherts with variable total organic carbon (TOC) content. Experimental works suggested that organic matter could catalyze pyrite formation by providing active surfaces for pyrite nucleation (Rickard et al., 2007; Rickard, 2012; Duverger et al., 2021). The upper plot (a) comprises pyrite $\delta^{56}\text{Fe}$ values from cherts containing 0.82 to 1.51 wt% organic carbon. The middle plot (b) includes $\delta^{56}\text{Fe}$ values measured in black cherts for which no specific information about the organic carbon content was given. We suggest that they can reasonably be considered as organic matter-rich host rocks. In the lower plot (c), $\delta^{56}\text{Fe}$ values were measured in pyrites associated with cherts presenting TOC values from less than 0.05 to 0.38 wt%. The numbers of values (n) and geological formations (f) from which pyrite originates are indicated. Pyrite particles in organic matter-poor and organic matter-rich (TOC > 0.8 wt%) cherts have one location in common (Mendon Formation). The three other locations are distinct. The grey bar represents a $\delta^{56}\text{Fe}$ value of 0 ‰ and is drawn to facilitate comparison between plots.

